

Research
Engineering
Structures
Materials

P-ISSN: 2148-9807 E-ISSN: 2149-4088

www.jresm.org

Volume
9

Issue
3

September
2023

The International Journal of **Research on Engineering Structures and Materials (RESM)** is a peer-reviewed open access journal (p-ISSN: 2148-9807; o-ISSN: 2149-4088) published by MIM Research Group. It is published in February, June, September, and December.

The main objective of RESM is to provide an International academic platform for researchers to share scientific results related to all aspects of mechanical, civil, and material engineering areas.

RESM aims the publication of original research articles, reviews, short communications technical reports, and letters to the editor on the latest developments in the related fields.

All expenditures for the publication of the manuscripts are most kindly reimbursed by *MIM Research Group*. Thus, authors do not need to pay for publishing their studies in the journal.

The scope of the journal covers (but not limited to) behavior of structures, machines and mechanical systems, vibration, impact loadings and structural dynamics, mechanics of materials (elasticity, plasticity, fracture mechanics), material science (structure and properties of concrete, metals, ceramics, composites, plastics, wood, etc.), nano-materials performances of new and existing buildings and other structural systems, design of buildings and other structural systems, seismic behavior of buildings and other structural systems, repair and strengthening of structural systems, case studies and failure of structural systems, safety and reliability in structural and material engineering, use of new and innovative materials and techniques in energy systems and mechanical aspects of biological systems (biomechanics and biomimetics).

The topics covered in JRESM include:

- Structural Engineering
- Mechanical Engineering
- Material Engineering
- Earthquake Engineering
- Nano-technology
- Energy Systems (Focus on Renewable)
- Biomechanics and Biomimetics
- Environment (Material and Engineering System Related Issues)
- Computer Engineering and Data Science (Material and Engineering System-Related Issues)

Abstracting and Indexing

Please visit <http://www.jresm.org> for more information.

Graphics and Design

Yunus Demirtaş

ydemirtas@jresm.net



**RESEARCH on
ENGINEERING STRUCTURES &
MATERIALS**

RESEARCH on ENGINEERING STRUCTURES & MATERIALS

Editorial Board

Editor in Chief		
Hayri Baytan Özmen	Usak University	Turkey
Editor		
Canan Kandilli	Usak University	Turkey
Editor		
Antonio F. Miguel	University of Evora	Portugal
Editor		
Michele Barbato	University of California Davis	USA
Editor		
Alp Karakoç	Aalto University	Finland
Editor		
Faris Tarlochan	Qatar University	Qatar
Editor		
Mehmet Palancı	Arel University	Turkey
Editor		
Francesco D'Annibale	University of L'Aquila	Italy
Editor		
Tadesse G. Wakjia	University of British Columbia	Canada
Editor		
Samson Olalekan Odeyemi	Kwara State University Malete	Canada
Editor		
Saifulnizan Jamian	Universiti Tun Hussein Onn Malaysia	Malaysia
Editor		
Chitaranjan Pany	Vikram Sarabhai Space Centre	India
Editor		
Daniel Cruze	Hindustan Institute of Technology and Science	India
Editor		
Badrinarayan Rath	Wollega University	Ethiopia

Editorial Office

Publishing Assistant

Yunus Demirtaş	Eskişehir Technical University	Turkey
Yusuf Öztürk	MIM Resarch Group	Turkey

Language Editors

Gaye Kuru	Usak University	Turkey
Mete Çal	Niğde Ömer Halisdemir University	Turkey

Editorial Board Members

Farid Abed-Meraim	Arts et Metiers ParisTech	France
P. Anbazhagan	Indian Institute of Science	India
Raffaele Barretta	University of Naples Federico II	Italy
R.S. Beniwal	Council of Scientific and Industrial Research	India
Antonio Caggiano	University of Buenos Aires	Argentina
Noel Challamel	University of South Brittany	France
Abdulkadir Çevik	Gaziantep University	Turkey
J. Paulo Davim	University of Aveiro	Portugal
Hom Nath Dhakal	University of Portsmouth	UK
Ali Faghidian	Islamic Azad University	Iran
S. Amir M. Ghannadpour	Shahid Beheshti University	Iran
Ali Goodarzi	Harvard University	USA
Jian Jiang	National Institute of Standards and Technology	USA
Ramazan Karakuzu	Dokuz Eylül University	Turkey
Arkadiusz Kwiecien	Cracow University of Technology	Poland
Stefano Lenci	Universita Politecnica delle Marche	Italy
Silva Lozančić	University of Osijek	Croatia
Fabio Mazza	University of Calabria	Italia
Yuan Meini	North University of China	China
Stergios A. Mitoulis	University of Surrey	UK
Vinayagam Mohanavel	Anna University	India
Ehsan Noroozinejad Farsangi	Kerman Graduate University of Technology	Iran
Alaa M. Rashad	Shaqra University	Saudi Arabia
Mohammad Mehdi Rashidi	University of Tongji	China
Pier Paolo Rossi	University of Catania	Italy
Neritan Shkodrani	Polythecnic University of Tirana	Albania
Y.B. Yang	National Taiwan University	Taiwan

Advisory Board

Name and Surname	Affiliation	Country
Waleed A Abbas	University of Technology	Iraq
Muna Khethier Abbass	University of Technology-Iraq	Iraq
Abdul Razak Abdul Karim	University Malaysia Sarawak	Malaysia
Yunika Kirana Abdul Khalik	UNIMAS	India
Mohammad Abdul Mannan	University Malaysia Sarawa	Malaysia
Ahmed Abdullahi	Higher Colleges of Technology	Dubai
Mehmet Ada	Usak University	Turkey
Mohammad Afrazi	Tarbiat Modares University	Iran
B. Akbari	University of Tehran	Iran
Mustafa Akpolat	Munzur University	Turkey
Ali Özhan Akyüz	Burdur Mehmet Akif Ersoy University	Turkey
Waleed Khalid Al- azzawi	Al-Farahidi University	Iraq
Tawalo Ali	Università degli di Napoli Federico II	Italy
Thaer Alrudaini	University of Basrah	Iraq
Raheem Al-Sabur	University of Basrah	Iraq
Denis Anders	Cologne University of Applied Sciences	Germany
Gabriel Arce	Louisiana State University	USA
Nur Farhayu Ariffin	University Malaysia Pahang	Malaysia
E. Arunraj	Karunya Institute of Technology and Sciences	India
Hidayati Asrah	University Malaysia Sabah	Malaysia
Siva Avudaiappan	University of Santiago	Chile
Samuel Awe	Automotive Components Floby AB	Sweden
Chioma Awodiji	University Of Port-Harcourt	Nigeria
Kemal Aydın	Gümüşhane University	Turkey
Ameer Baiee	University of Babylon	Iraq
Carlos Eduardo Tino Balestra	Western Paraná State University	Brazil

Mohammad Saleh Baradaran	Islamic Azad University of Mashhad	Iran
Peyman Beiranvand	Razi University	Iran
Hadj Bekki	University Ibn Khaldoun of Tiaret	Algeria
Abdelhalim Bensaada	University of Yahia Fares of Medea	Algeria
Mohammed Bentahar	Tahar Moulay University of Saida	Algeria
H. Alperen Bulut	Erzincan University	Turkey
Esitake Cebolina		Iraq
Halit Cetiner	Isparta University	Turkey
Kamel Chaoui	Badji Mokhtar University	Algeria
Venkatesh Chava	CVR College of Engineering	India
Maheswaran Chellapandian	Mepco Schlenk Engineering College	India
Xinrong Chengil	Tongji University	China
Sonali Sri Durga Chereddy	CVR College of Engineering	India
Anna Chiaradonna	DICEAA, University of L'Aquila	Italy
Ajay Chourasia	Central Building Research Institute	India
Daniel Cruze	Mohamed Sathak A J College of Engineering	India
Zhaoyan Cui	Nanjing Forestry University	China
Ashish Kumar Dash	Indian Institute of Technology	Indian
Cengiz Grkem Dengiz	Ondokuz Mayıs University	Turkey
Arindam Dey	Indian Institute of Technology Guwahati	India
Marwan Effendy	Universitas Muhammadiyah Surakarta	Indonesia
Ashraf El-Shamy	National Research Centre	Egypt
Ali Ercetin	Bandırma Onyedi Eylül University	Turkey
Kemal Ermis	Sakarya University of Applied Science	Turkey
Uchechi Eziefula	University of Agriculture and Environmental Sciences, Umuagwo	Nigeria
Mingjing Fang	Wuhan University of Technology	China
Christopher Fapohunda	Federal University Oye-Ekiti	Nigeria
Abdelkader Fidjah	University of Djelfa	Algeria
Saeid Foughi	Konya Technical University	Turkey

Sharanabasava V. Ganachari	KLE Technological University	India
Zhong Ge	Yunnan University	China
Gökhan Gece	Bursa Teknik University	Turkey
Mahesh Gopal	College of Engineering and Technology	Ethiopia
Chandrasekhar G L Gotur	Atria Institute of Technology	India
Mert Göksüzöğlü	SAMPA	Turkey
Layachi Guelmine	B.B.A University	Algeria
Kadir Günaydın	GE Aviation, Marmara Technology Center	Turkey
Endalkachew Mosisa Gutema	College of Engg and Tech	Ethiopia
Ahmet Güral	Gazi University	Turkey
Hussein Hamada	University Malaysia Pahang	Malaysia
Taihao Han	Missouri University of Science and Technology	USA
Md. Zia Ul Haq	Panjab University	India
Md. Naimul Haque	East West University	India
Noor Sheena Herayani Harith	University Malaysia Sabah	Malaysia
Shrikant Harle	Ram Meghe College of Engineering and Management	India
Catur Harsito	Universitas Sebelas Maret	Indonesia
Muttaqin Hasan	Syiah Kuala University	Indonesia
Maboud Hekmatifar	Islamic Azad University	Iran
Mohammad Heydari Vini	Islamic Azad University	Iran
Qing Hong	Midwestern University	USA
Oleksii Hrechanyi	Zaporizhzhia National University	Ukraine
Md. Saiful Islam	University Putra Malaysia	Malaysia
Mehmet Zerrakki Işık	Batman University	Turkey
Ghassan Subhi Jameel	University of Anbar	Iraq
Saifulnizan Jamian	University Tun Hussein Onn Malaysia	Malaysia
Girish M. Joshi	VIT University	India
Bhuria Jyothi		Nepal

Arunkumar K		India
Hossein Kabir	University of Illinois	USA
Pulitha Kavutri		Sri Lanka
Mehmet Kaya	Bozok University	Turkey
Emre Kemer	Usak University	Turkey
Pallavi Pradeep	Rungta College of Engineering and	
Khobragade	Technology	India
Cemal Kochan	Dokuz Eylul University	Turkey
Ali Koçak	Yıldız Technical University	Turkey
Nitin Kumar	University of California Davis	USA
A. Suresh Kumar	Kalasalingham Academy of Research and	
	Education	India
Sanjeev Kumar	Sanjeev Agrawal Global Educational	
	University	India
Josephine Chang Hui		
Lai	University Malaysia Sarawak	Malaysia
Ravichandran M	K. Ramakrishnan College of Engineering	India
Uma Mageshwari		India
Lomesh Mahajan	Dr. Babasaheb Ambedkar Technological	
	University	India
Natt Makul	Phranakhon Rajabhat University	Thailand
Anirban Mandal	National Institute of Technology	India
Tahara Ramadan Md		
Kassim	International Islamic University Malaysia	Malaysia
Priyansha Mehra	Manipal University	India
Adamah Messan	Laboratoire Eco Matériaux de Construction	
	(LEMC)	France
Suruchi Mishra		Malaysia
Khairul Anwar		
Mohamad Said	UNIMAS	Malaysia
Fadzli Mohamed Nazri	University Sains Malaysia	Malaysia
Mohsin Talib		
Mohammed	Kufa University	Iran
Noor Azline Mohd		
Nasir	University Putra Malaysia	Malaysia

Mohd Syahrul Hisyam	University Teknologi MARA (UiTM)	Malaysia
Mohd Sani	Cawangan Pahang	
Mahmoud Mokhtar	Housing & Building National Research Center	Egypt
Alaa M. Morsy	Arab Academy for Science	Egypt
Rini Mulyani	Senior Lecturer at University Bung Hatta, Padang, Indonesia	Indonesia
Yasmin Murad	University of Jordan Amman	Jordan
Nahida Nazim Musayeva	Azerbaijan National Academy of Sciences	Azerbaijan
Arslan Mushtaq	NUST Institute of Civil Engineering	Pakistan
Maheswaran Muthiah	Kalasalngam Academy of Research and Education	India
Madeva Nagaral	Aircraft Research and Design Centre, Hindustan Aeronautics Limited	India
Salem Nawel	University of Gabes	Tunisia
Amarachi Nkwoada	Federal University of Technology Owerri	Nigeria
Mehrab Nodehi	University of California	USA
Samson Olalekan Odeyemi	Kwara State University	Nigeria
Hayri B. Ozmen	Usak University	Turkey
İbrahim Öz	Ahi Evran University	Turkey
Gurusamy P	Chennai Institute of Technology	India
Partheeban	Chennai Institute of Technology	India
Pachaivannan		
Chitaranjan Pany	Vikram Sarabhi Space Center	India
Rajesh Kumar Paswan	National Institute of Technology Jamshedpur	India
Vikas Patel	National Council for Cement and Building Materials	India
Hiteshkumar Patil	Dr. Babasaheb Ambedkar Technological University	India
Zühtü Onur Pehlivanlı	Kırıkkale University	Turkey
Amin Moslemi Petrudi	Tehran University	Iran
Hemadri Prasad Raju	Sree Vidyanikethan Engineering College	India

Kalappa Prashantha	Adichunchanagiri University	India
Harris Priya	Kurukshetra University	India
Kavendra Pulkit		India
Helogi Putin		India
Ajibola Ibrahim Quadri	Federal University of Technology	Nigeria
Md. Mijanur Rahman	Military Institute of Science and Technology	Bangladesh
Azida Rashidi	UNIMAS	Malaysia
Badrinarayan Rath	Wollega University	Ethiopia
T.V. Reshma		India
Pier Paolo Rossi	University of Catania	Italy
Md Jalal Uddin Rumi	Military Institute of Science and Technology	Bangladesh
Abbasali Sadeghi	Islamic Azad University	Iran
Mohammed A. Sakr	Tanta University	Egypt
M.Helen Santhi	Vellore Institute of Technology	India
Tamer Saraçyakupoğlu	Istanbul Gelişim University	Turkey
Divya Sharma	NITTTR Chandigarh	India
Fatheali Shilar	Jain College of Engineering Belgaum	India
Lenganji Simwanda	Stellenbosch University	South Africa
Brijesh Singh	National Council for Cement and Building Materials	India
Navdeep Singh	Dr B R Ambedkar National Inst. of Tech.	India
Rami Sldozian	University of Technology	Iraq
M. Somasundaram	PSG College of Technology	India
Rajkumar Srinivasan	SRM TRP Engineering College Irungalur	India
Rianti Dewi Sulamet- Ariobimo	Universitas Trisakti	Indonesia
Marthin Dody Josias Sumajouw	Sam Ratulangi University	Indonesia
Gülsah Susurluk	Beykent University	Turkey
Jumrik Taipodia	NIT Arunachal Pradesh	India
Ayktut Tamer	Imperial College London	England
Chan Sin Tan	University Malaysia Perlis	Malaysia
Hamide Tekeli	Süleyman Demirel University	Turkey

Delsye Ching Lee Teo	Melbourne Polytechnic	Australia
Mehmet Topuz	Van Yüzüncü Yıl University	Turkey
Tuan Norhayati Tuan Chik	University Tun Hussein Onn	Malaysia
Hasan Ulus	Selcuk University	Turkey
Dilay Uncu	Celal Bayar University	Turkey
Prem Kumar V	VIT Chennai	India
Harinadh	Sri Venkateswara College of Engineering and Technology	India
Vemanaboina		
Tadesse Gameda Wakjira	University of British Columbia	Canada
Gustavo Bosel Wally	Federal University of Rio Grande do Sul	Brazil
Narong Wichapa	Kalasin University	Thailand
I Wiryadi	Mahasaraswati Denpasar University	Indonesia
Omid Aminoroayai Yamani	K. N. Toosi University of Technology	Iran
Guney Guven Yapici	Ozyegin University	Turkey
Salih Hakan Yetgin	Kütahya Dumlupınar University	Turkey
Sevim Yolcular Karaoğlu	Ege University	Turkey
Ana Sakura Zainal Abidin	UNIMAS	Malaysia

In This Issue

Research Article

675 **Turgay Coşkun, Erdal Çetkin**

Vascularized mini cooling channels to achieve temperature uniformity: Battery thermal management and electronic cooling

Research Article

687 **Naga Sudha Rani Behara, Putti Srinivasa Rao**

Vibration energy harvesting using telescopic suspension system for conventional two-wheeler and EV

Research Article

709 **Mohamed Kafeel Delvi, K Mohamed Kaleemulla**

Tensile and compressive mechanical properties of ZA27/ molybdenum disulfide, metal matrix composite

Research Article

719 **Ayşe Pınar Tüzüm Demir**

Kinetic evaluation of the stabilization efficiency of the phosphite and urea derivative based stabilizers against epoxy based stabilizers on the thermal degradation of plasticized poly (vinyl chloride)

Research Article

743 **Elaf Khalid Dahamm, Sheelan Mahmoud Hama, Ibrahim A. AL-Jumaily**

Effect of nano-sized clay and waste glass powder on rheological and hardened properties of self-compacting concrete

Technical Note

763 **Pallavi Pradeep Khobragade, Ajay Vikram Ahirwar**

Seasonal variation in aerosol optical depth and study of PM2.5-AOD empirical relationship in Raipur, Chhattisgarh, India

Review Article

775 **Uzoma S. Nwigwe, Chukwuka I. Nwoye**

Green corrosion inhibitors for steel and other metals in basic media: A mini-review

Research Article

791 **Didem Kale, Nazmiye Yoldaş, M. Özgür Seydibeyoğlu**

The effect of mechanical surface roughness for polyvinyl chloride (PVC) and aluminum joining

Research Article

- 805 **Md Jalal Uddin Rumi, Muhammad Muzibur Rahman**
Prediction and optimization of heat treatment effects on hardness and electrical conductivity of aluminum composite reinforced with nano alumina based on response surface methodology

Research Article

- 827 **T V Vineeth Kumar, N Shanmugapriya, Arun S, Madeva NagaraI**
Influence of MWCNTS on mechanical and in vitro biocompatibility properties of PMMA bone cement for orthopedic application

Research Article

- 843 **Naveen Arasu A, Natarajan Muthusamy, Balasundaram Natarajan, Parthasaarathi R**
Optimization of high performance concrete composites by using nano materials

Research Article

- 861 **Dwi Nurtanto, Mochammad Roziqin, Krisnamurti, Wiwik Yunarni Widiarti, Roy Firmawan**
Integral waterproofing concrete mechanical properties with the addition of fly ash

Technical Note

- 875 **Andi Yusra, Hesti Meliana, Lissa Opirina, Andrisman Satria**
Investigation of normal concrete properties with the addition of micro reinforcement

Research Article

- 885 **Santosh V Janamatti, Veerabhadrapa Algur, Madeva NagaraI, V Auradi**
Mechanical behavior and fractography analysis of Zn-Sn alloy matrix composites reinforced with nano B4C particles

Research Article

- 901 **Jahanvi Suthar, Sharadkumar Purohit**
Seismic behaviour of re-entrant dominant RC frame buildings

Research Article

- 921 **Rizwanullah, H.K. Sharma**
Prediction of performance of UHPFRC flexural member under blast loading

Research Article

- 947 **Philip Jun Celerinos, Patrick Miguel Dedel, Nesty Vince Fernandez, Kathleen Ira Muñoz, Fatima Alaiizza Suelan**
An assessment of rebound hammer test in estimating the concrete compressive strength in seawater

Research Article

969 **Noor Azim Mohd. Radzi, Muhaimim Kamal, Shareen Azuha, Nur Izzatie Aqilah Mansor, Roszilah Hamide**

Nonlinear coupled thermal-structural analysis of precast concrete beam-to-column connections at high temperatures

Review Article

989 **Vishal Kumar Mourya, Gaurav Pandey, Dharendra Patel, Rajesh Kumar**

Approaches considering non-linearity in soil-foundation-interaction: A State-of-the-Art Review

Research Article

1015 **Nehal Mahadevbhai Desai, Sandip Vasanwala**

Sensitivity indices of RC beams considering construction sequence analysis for RC high-rise building

Research Article

1039 **Monali Kirange, Lomesh Mahajan**

Predicting strength of concrete by ensemble technique

Research Article

1061 **CH Ajay, K Durga Rani**

Evaluation of cement-treated ferrochrome slag and quarry dust composites for base and sub-base layers of flexible pavement

Research Article

1081 **Lalit Pawar, Keshav K. Sangle, Yuvaraj L. Bhirud**

Experimental investigation along with 3-D Finite Element Analysis to determine the stress bearing ability of concrete containing waste plastic aggregates

Free access to tables of content, abstracts and full text of papers for web visitors.

Copyright © 2023

Research on Engineering Structures & Materials

MIM Research Group Publications

P-ISSN: 2148-9807

E-ISSN: 2149-4088

<http://www.jresm.org>



ABSTRACTING / INDEXING

The international journal of Research on Engineering Structures and Materials (RESM) is currently Abstracted/Indexed by Asos Indeks, CiteFactor, Cosmos, CrossRef, Directory of Research Journal Indexing, Engineering Journals (ProQuest), EZB Electronic Journal Library, Global Impact Factor, Google Scholar, International Institute of Organized Research (I2OR), International Scientific Indexing (ISI), Materials Science & Engineering Database (ProQuest), Open Academic Journals Index, Publication Forum, Research BibleScientific Indexing Service, Root Indexing, Scopus, Ulakbim TR Index (Tubitak), Universal Impact Factor and under evaluation by many other respected indexes.

Check web site for current indexing info, www.jresm.org

Scopus®





Research Article

Vascularized mini cooling channels to achieve temperature uniformity: Battery thermal management and electronic cooling

Turgay Coşkun^b, Erdal Çetkin^{*a}

Department of Mechanical Engineering, Izmir Institute of Technology, Izmir, Turkey

Article Info

Article history:

Received 21 Nov 2022
Revised 02 Mar 2023
Accepted 03 Apr 2023

Keywords:

*Silicon Heater;
Battery Cell Mimicking
Structures;
Thermal Management;
Cooling System*

Abstract

Here we propose to use of distinct vascularized plates to be used in the applications of battery thermal management and electronic cooling. The temperatures of battery cells increase during charge and discharge; and elevated temperature values in them accelerated degradation and even may trigger battery fire because of the thermal runaway. Therefore, thermal management system is a necessity for battery packs to increase the battery performance and diminish the risk factors in the electric vehicles. Generally, high amount of heat is released in the high capacity (>15 Ah) cells in short time interval under fast charge/discharge conditions; thus, thermal management of the battery system can be achieved with liquid cooling in that situation. A silicon heater system which represents the thermal behavior of a battery cell is manufactured based on the literature and it is used in experiments. Such a method has not proposed up to now in the literature, so the study may be creating a new experimental procedure for future studies without the risk of battery fire/degradation to uncover even extreme conditions experimentally. Electronic cooling is also in prime importance due to enhanced computing requirement of current systems, and vascularized plates can solve the hot spot problems occurring with decreased energy consumption. According to the results, the cooling capacity of the vascularized plates are calculated as 20W, and a battery cell can be kept within its optimal operating temperature range when the heat loads up to 30W. Also, the temperature uniformity along the surface of mimic of the battery is satisfied by vascularized plates.

© 2023 MIM Research Group. All rights reserved.

1. Introduction

Recent developments in rechargeable batteries and limited energy sources of the world increase the interest of researchers on the electric vehicle industry. Vehicles are responsible for 50% of the final oil consumption in the world [1] and seen as one of the main sources of air pollution. These are key factors in the progression of electric vehicle industry. Developing electric vehicle industry bring out new issues for researchers, i.e. safety problems and performance decrements in battery cells due to overheating. Battery cell is one of the main and the most vital component in the electric vehicle. The capacity and performance of the electric vehicle mostly depend on the battery system, and it is responsible for the most of safety problems in the electric vehicle [2-4]. There are various types of battery cells and lithium-ion is one of the most commonly used types in electric vehicles. It is most popular because of high specific energy density and high specific power than others [2].

A lithium-ion battery cell consists of a negative current collector, a negative electrode, a separator, a positive electrode and a positive current collector, respectively [5, 6]. Battery cell is the basic component of the electric vehicle. A battery unit consists of many battery

*Corresponding author: erdalchetkin@iyte.edu.tr

^a orcid.org/0000-0003-3686-0208; ^b orcid.org/0000-0002-1921-3896

DOI: <http://dx.doi.org/10.17515/resm2022.585ma1121>

Res. Eng. Struct. Mat. Vol. 9 Iss. 3 (2023) 675-685

cells. A battery module is created by connecting many battery units in serial or parallel form and a battery pack is formed by connecting many battery modules [7]. The number of battery units in a battery pack is defined with respect to the desired voltage and capacity. The heat is generated in battery cell during charging, discharging and in operation. Therefore, the temperature of the battery cell increases. The increment in the temperature effects the capacity, performance and lifetime of the battery cell [8]. There is not uniform heat generation along the battery surface, and it is dense near the tabs. In the design of the cooling system for a battery pack, eliminating safety issues due to high temperature values (i.e. thermal runaway) and distributing heat uniformly along the battery surface and between the batteries in a battery module should be the priority. Vascularized cooling channels can be used in the cooling of the battery cells. They are commonly used in the cooling of deterministic and random heat loads [9]. Vascularized cooling channels are known for their high thermal performance and low energy consumption [10-12].

Here, a cooling system is developed for a silicon heater system which mimics the characteristics of a lithium-ion battery cell (pouch shape). A schematic view of the pouch cell is shown in Figure 1. The battery cell separated into two sections: active area and tabs. A silicon heater which is sandwiched between the steel plates was used during the experiments instead of a real battery cell. Yamada et al. [13] was used electric heater instead of real battery in the experiments. However, they were not considered the non-homogenous temperature distribution along the battery surface and heat generation rate change with charge/discharge capacity. The silicon heater reflects the thermal behavior of the battery cell and various heating loads are supplied to it in order to represent heat generation rate of a real battery under various charge/discharge rates. Using mimics of battery cells in the experimental studies eliminate some challenges associated with real battery like short-circuit, explosion, capacity fade and etc. Moreover, designed cooling system can be tested under extreme heating loads via silicon heater and will be used for electronic cooling.

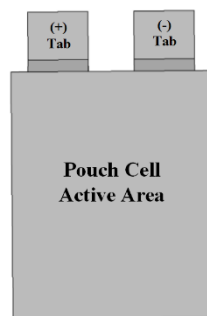


Fig. 1 A schematic of a lithium-ion pouch cell

2. Battery Thermal Properties

In the study, a silicon heater is used instead of real battery cell in the experiment. Therefore, the heat generation profile and thermal behavior of the battery cell need to be deeply understood to establish mimic the battery cell accurately.

2.1. Heat Generation in Battery Cells

The heat generation rate of the battery cell needs to be defined before introducing a cooling system for an electric vehicle. There are two main sources of generation in a battery cell. First one is the entropic heat, occurs due to the entropy change. The second one is the ohmic heat and it occurs because of the current transfer between the internal resistances

[7]. The basic equation used in the calculation of heat generation rate in a battery cell is shown in Equation 1 [14, 15].

$$q = q_{irr} + q_{rev} = I(E_{oc} - V) - \left[IT \frac{dE_{oc}}{dT} \right] \quad (1)$$

In Equation 1, q is heat generation rate, I is current ($I > 0$ for discharge and $I < 0$ for charge), E_{oc} is equivalent potential (open circuit voltage), V is cell voltage, T is cell temperature and $\frac{dE_{oc}}{dT}$ is the temperature coefficient. The first term in the Equation 1, $I(E_{oc} - V)$, ohmic heat generation (also called as Joule heat or irreversible heat), the second term, $-\left[IT \frac{dE_{oc}}{dT} \right]$, represents the entropic heat (reversible heat) which is created by electrochemical reactions.

Heat generation at the tabs should be added to the Equation 1 to calculate total heat generation rate. The heat generation at the connection points is studied in the study of Yi et al. [16] and represented by Equation 2:

$$q_{tab} = (r + r_c)i^2 \quad (2)$$

In Equation 2, i , r and r_c represent current density, internal resistance and contact resistance, respectively.

To sum up, the heat generation in the battery cell is shown in Equation 3 [17];

$$q_{sum} = q_{irr} + q_{rev} + q_{tab} \quad (3)$$

The total heat generation in a battery cell can be calculated by using the Equations (1), (2), (3), but, some terms in the equations are time dependent, like $\frac{dE_{oc}}{dT}$, so the change of these term with respect to time should be taken from experimental studies. So, if a study will be conducted without using a real battery, time dependent parameters should be defined by checking the results of experimental studies from literature or calculated using a software including battery module.

2.2. Parameters Effecting Heat Generation Rate in Battery Cells

Heat generation rate in a battery cell changes with respect to battery type, capacity, charge-discharge duration and ambient temperature. In addition, chemical reactions occurring inside of the battery cell also change the heat generation rate of a battery cell. The heat generation rate in a battery cell increases with enhancement in battery capacity [18]. Arora and Kapoor [18] compared heat generation rate of three different capacity cells and they figure out that heat generation rate is directly proportional to the battery capacity.

The duration of charge/discharge is symbolized by C . The charging/discharging of battery cell is completed in one hour at 1C rate. In a similar manner, $C/2$ and $2C$ means that charging/discharging will be completed in 2 hours and a half hour, respectively. So, charge/discharge duration is inversely related to C rate and high amount of heat releases in a short time interval at high C rates. In addition, heat generation rate in a battery cell increases logarithmically with increasing C rate [19-21].

In the study of Xie et al. [22], the heat generation rate during charging and discharging process is compared. The results of the study show that the more heat is released during discharging process when compared to charging process. The studies in the literature support the situation [17].

Ambient temperature is another parameter that has a significant effect on the heat generation rate. The effect of ambient temperature on the heat generation rate can be

explained by the change of battery internal resistances. The internal resistance of the battery is high at low temperature values. The heat generation rate is known to increase with decreasing electrical conductance at low temperature values. According to studies, the heat generation rate is inversely proportional to the ambient temperature [19, 21, 23]

The heat generation at the connections points (tabs) should be take into consideration in the calculation of total heat generation rate. The heat generation in the connection points can be observed at module and pack level in the battery systems. In the study of Keyser et al. [24], it is indicated that a cell is generated more heat when it is in a battery module rather than just a single cell. The heat generation difference between the cell in a battery module and a single cell can be reached 30% with respect to the current rate. This situation provides evidence as to how total heat generation rate is change in module or pack level.

2.3. Temperature Distribution on the Battery Surface

The temperature distribution on the battery surfaces is studied detailly in the literature. The heat generation rate is denser near the tabs; therefore, the highest temperature values observed near the tabs. There are two main reasons for that situation. First one is the ionic distribution between positive and negative tabs. In the study of Li et al. [25], the effect of ionic distribution on the heat generation rate investigated numerically. Their results yield that heat generation increase with increasing ionic distribution. Second parameter is that heat generation at the tabs and it is explained in the heat generation part.

2.4. Battery Thermal Management

The capacity and performance of the battery cell are changing with changing operating temperatures. There is an optimum working temperature for batteries, and it is changed with respect to battery type. Generally, lithium-ion battery cells operate best at 25-40 °C [26, 27]. The performance of the battery cell gets worse because of decrease in ion transfer at low temperatures (<15 °C). At high temperature values (>35 °C), the chemical reactions occur very fast, and it causes a decrease in the lifetime of the battery cell [28]. In addition to the operating temperatures, temperature difference along the battery surface and between the battery cells in a battery module also affect the battery performance and it causes safety problems for the electric vehicles. The temperature difference along the battery surface and between the battery cells should be kept lower than 5 °C. Because thermal runaway occurs in battery pack at high temperature values accompanying the higher temperature differences and may result in fire of the electric vehicle.

A thermal management system which satisfies the battery requirements in terms of heat generation and capacity values should be developed. In the literature, it is stated that air cooling is effective when the heat generation rate per cell is lower than 10W [29]. Therefore, liquid cooling can be sufficient in the thermal management of a high-capacity battery cell operating at high C rate.

3. Experimental Procedure

A silicon heater system is used instead of real battery in the experiments. So, a silicon heater is manufactured. It is aimed to reflect battery heat generation rates and temperature distribution via the silicon heater system. So, the temperature distribution on the surface on the silicon heater is defined by benefiting from literature studies such as Wu et. al. [30], Murashko et al. [31], and Zhu et al. [32]. According to these studies, the heat generation is dense near the tabs, and it becomes less dense far away from the tabs. So, a silicon heater yielding non-homogeneous temperature distribution along the surface is manufactured. The silicon heater is sandwiched between the metal plates to have same thermal conductivity in thickness direction as it in real battery and a mimic of battery cell is created. A liquid cooling system is designed to cool the mimic of a battery cell. HEXs

having different cooling channel orientations (parallel and hybrid) are used in the cooling system. The experimental setup is shown in Figure 2. Metal plates have the thermal conductivity of 15 W/mK, which is very close to thermal conductivity of battery cell in axial directions (Figure 3). The experimental setup mainly consists of a silicon heater, a power supply, mini heat exchangers, a water bath and a data logger. There is a contact surface between the HEX and silicon heater to allow heat transfer. The remaining surfaces are insulated. The coolant liquid is supplied at the desired temperature by a water bath. The flow rate of the coolant is aligned firstly by a needle valve and then measured via a flowmeter. The temperature of the coolant liquid at the inlet and outlet of the HEX is measured via thermocouples. Also, the temperature of silicon heater is measured by thermocouples which are positioned on the surface of the silicon heater system. All the measured data are recorded via data logger.

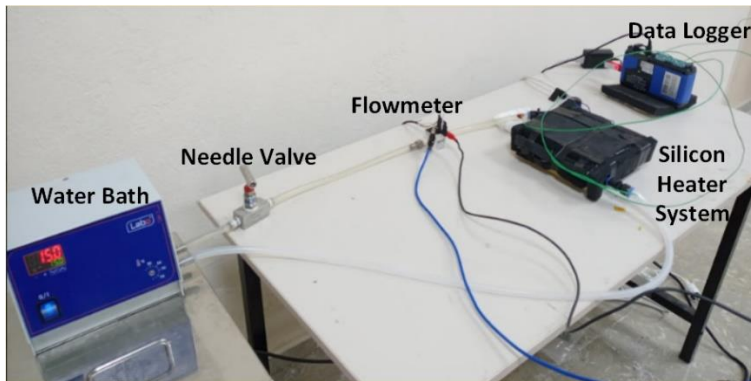


Fig. 2 Experimental setup with its components



Fig. 3 20V Silicon heater and a mimic of battery cell

4. Results and Discussion

The silicon heater system under various heating load is cooled by using different HEXs. Silicon heater voltage is 20V and maximum power extends up to 50W. The temperature and flow rate of the coolant liquid are 15 °C and 0.0218 kg/s, respectively. The power of the silicon heater is adjusted to 8W, 17W, 30W and 48W by changing the current value on the power supply. In a real battery case, heat generation rate varies under distinct C rates. In the silicon heater, heat generation in a real battery under various C rate is reflected by supplying various heating load to silicon heater. In the study, two HEXs having different heat transfer channel orientations are used: parallel and hybrid. The details of HEXs is given in Figure 4 and Table 1 [28].

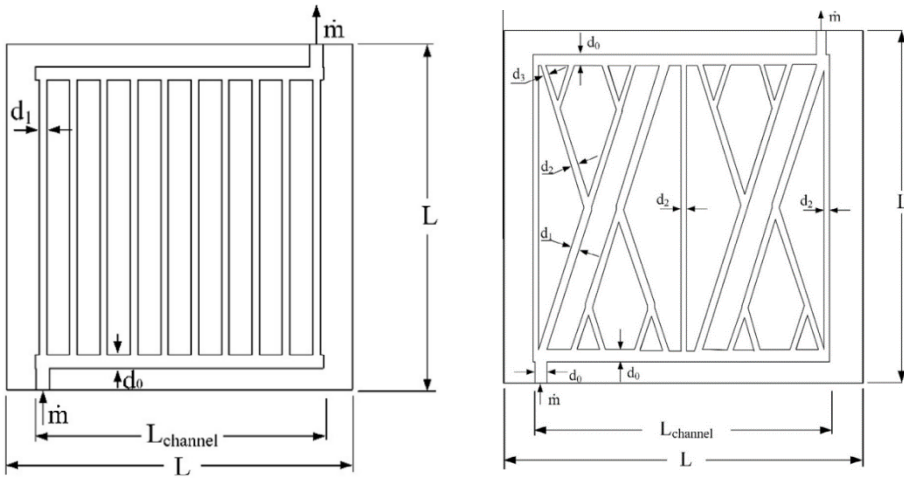


Fig. 4 Parallel and Hybrid HEXs [9]

Table 1. Dimensions of the heat exchangers [9]

#	d_0 (m)	d_1 (m)	d_2 (m)	d_3 (m)	L (m)	$L_{channel}$ (m)
Parallel Design	0.004	0.003	-	-	0.17	0.15
Hybrid Design	0.004	0.003	0.0025	0.002	0.17	0.15

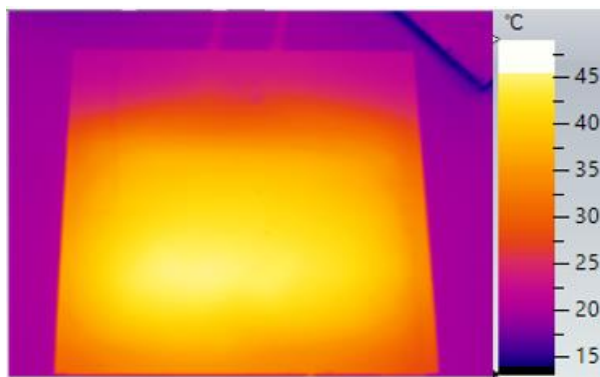


Fig. 5 Thermal image of the silicon heater surface under 30W heating load

Infrared thermal imaging of the silicon heater, when the heating load is 30W, is shown in Figure 5. According to the Figure 5, the temperature distribution is not uniform throughout the surface of the silicon heater as it in real battery case.

The silicon heater is cooled by parallel HEX and the change of temperature with respect to various heating load is shown in Figure 6. According to the Figure 6, the temperature of the silicon heater exceeds critical values when the heating load is 30W. Furthermore, the temperature of the silicon heater is kept between the operating limits when the cooling load is 17W and coolant temperature is 15°C.

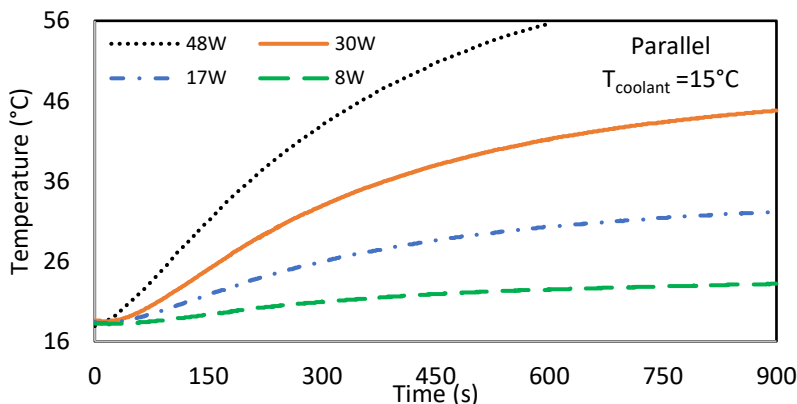


Fig. 6 The change of temperature on the surface of the silicon heater system under various heating loads (Coolant liquid: 15 °C)

The effect of cooling system on the maximum temperature values under 30W heating load when the ambient temperature is 30°C, is shown in Figure 7. The maximum temperature value reaches up to 45°C in 7.5 min when there is natural convection. In the liquid cooling, the temperature of the silicon heater reaches up to 45°C in 15 minutes when the coolant temperature is 15°C. The coolant temperature is decreased from 15°C to 10°C to keep system temperature below the critical values. According to the Figure 7, the maximum temperature values is kept below 45°C at the end of 15 minutes when the coolant temperature decreased from 15°C to 10°C.

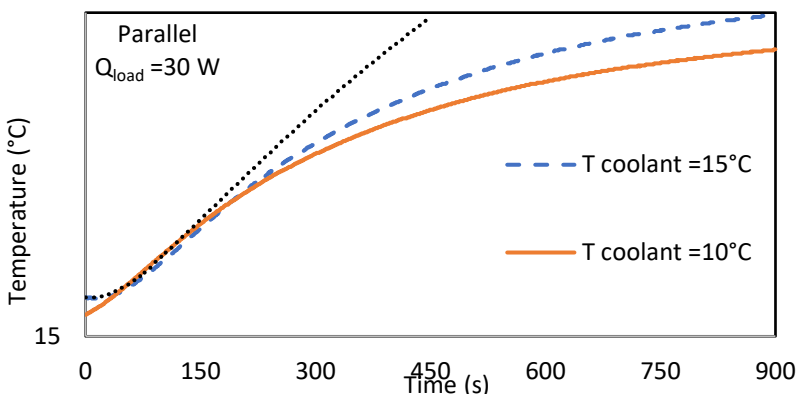


Fig. 7 The change of temperature on the surface of the silicon heater system with respect to type cooling mode and coolant temperatures (Heating load: 30 W)

In the second part of the experiment, different kinds of HEXs (parallel and hybrid) are used under various heating loads. In the following experiments, the coolant liquid temperature is fixed at 20°C. Three thermocouples are located on the surface of the silicon heater to measure temperature change during the experiments. The temperature of the silicon heater keeps below critical values for heating loads 8 W and 17 W when compared to 30W heating load, according to Figure 8 (a), (b), (c). The cooling system does not satisfy the requirements of the battery system at 30W heating load. The lowest temperature values are observed at point 3 which is very close to connection point. In addition, the temperature differences between the measurement points are lower than the 5°C.

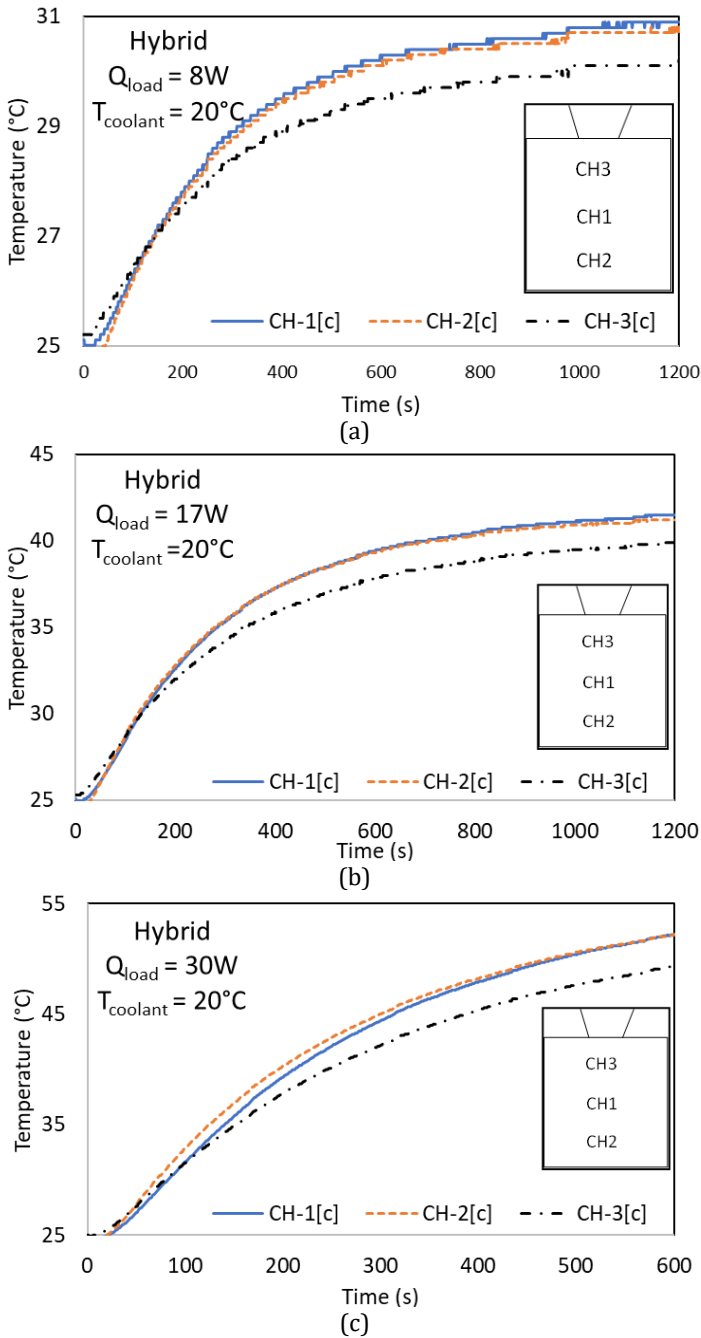


Fig. 8 The change of temperature on the surface of the silicon heater system for various heating loads: (a) 8 W, (b) 17 W and (c) 30 W

The silicon heater system cooled by parallel design HEX when the heating load is 30 W (Figure 9). Parallel design gives similar results with the hybrid design. The temperature homogeneity is satisfied by two types of HEXs ($\Delta T < 5^{\circ}C$).

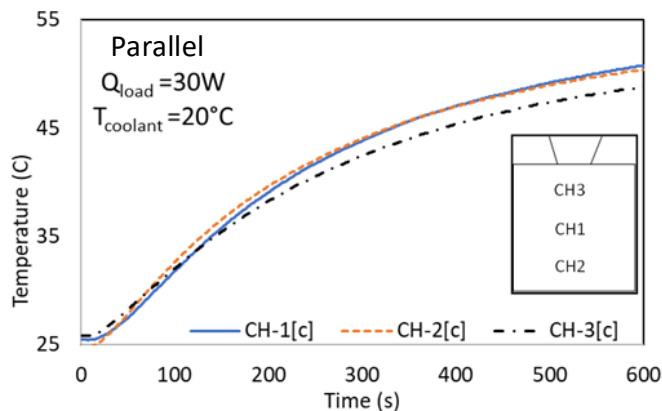


Fig. 9 The change of temperature on the surface of the silicon heater system for 30 W heating load in parallel design HEX

5. Conclusions

The heat generation in a battery cell is changed by many parameters such as type, capacity, charge/discharge duration and ambient temperature. The performance of the electric vehicle is highly affected by operating temperatures. So, the temperature in the battery pack should be controlled in order to improve performance and eliminate safety issues. In that study, a silicon heater system which represents the thermal behavior of a battery cell is developed to design a cooling system for a battery cell. The various heating loads (8W, 17W, 30W, 48W) are applied to the silicon heater and the cooling capacity of the vascularized cooling channels are determined. Parallel and hybrid shape cooling channels (categorized with respect to cooling channel orientations) are used in the experiments. According to the results, the temperature of the silicon heater is kept within operating limits ($< 40^{\circ}\text{C}$) when the heating loads are 8W and 17W. The temperature homogeneity on the surface of silicon heater is satisfied by the cooling channels while the cooling requirements is not satisfied when the heating load is 30W. However, the temperature of the silicon heater is kept within the operating limits (under 30W heating load) at low ambient temperature (18°C) when the coolant liquid is 10°C . The study is an only a proximity for the cooling system of a battery cell because thermal behavior of a real battery cell under various working circumstances cannot be reflected by silicon heater system exactly. Some of the examples are chemical reactions occurring in a battery cell and the change of heat distribution on the surface of the battery cell by time. These situations are not estimated by silicon heater system. However, this method is a good approximation to design cooling system for batteries.

Acknowledgement

The authors acknowledge that this study is supported by Izmir Institute of Technology, Scientific Research committee.

References

- [1] IEA, 2021, Retrieved from: <https://www.iea.org/reports/key-world-energy-statistics-2021/final-consumption>.
- [2] Bandhauer TM, Garimella S, Fuller TF. A Critical Review of Thermal Issues in Lithium-Ion Batteries. *Journal of the Electrochemical Society*, 2011; 158: R1 - R25. <https://doi.org/10.1149/1.3515880>

- [3] Safari M, Delacourt C. Mathematical modeling of lithium iron phosphate electrode: galvanostatic charge/discharge and path dependence. Journal of the Electrochemical Society, 2011; 158: A63 - A73. <https://doi.org/10.1149/1.3515902>
- [4] Horie H, Abe T, Kinoshita T, Shimoida Y. A Study on an Advanced Lithium-ion Battery System for EVs. The World Electric Vehicle Journal, 2008; 2: 25 - 31. <https://doi.org/10.3390/wevj2020113>
- [5] Hosseinzadeh E, Marco J, Jennings P. Electrochemical-Thermal Modelling and Optimisation of Lithium-Ion Battery Design Parameters Using Analysis of Variance. Energies, 2017; 10: 1278(1-22). <https://doi.org/10.3390/en10091278>
- [6] Smith K, Wang CY. Power and thermal characterization of a lithium-ion battery pack for hybrid-electric vehicles. Journal of Power Sources, 2006; 160: 662 - 673. <https://doi.org/10.1016/j.jpowsour.2006.01.038>
- [7] Karimi G, Li X. Thermal management of lithium-ion batteries for electric vehicles. International Journal of Energy Res., 2013; 37: 13 - 24. <https://doi.org/10.1002/er.1956>
- [8] Mastali M, Foreman E, Modjtahedi A, Samadani E, Amirfazli A, Farhad S, Fraser RA, Fowler M. Electrochemical-thermal modeling and experimental validation of commercial graphite/LiFePO₄ pouch lithium-ion batteries. International Journal of Thermal Sciences, 2018; 129: 218 - 230. <https://doi.org/10.1016/j.ijthermalsci.2018.03.004>
- [9] Yenigün O, Cetkin E. Experimental and numerical investigation of constructal vascular channels for self-cooling: Parallel channels, tree-shaped and hybrid designs. International Journal of Heat and Mass Transfer, 2016; 103: 1155 - 1165. <https://doi.org/10.1016/j.ijheatmasstransfer.2016.08.074>
- [10] Mosa M, Labat M, Lorente S. Constructal design of flow channels for radiant cooling panels, International Journal of Thermal Sciences, 2019; 145: 106052(1 - 14). <https://doi.org/10.1016/j.ijthermalsci.2019.106052>
- [11] Mosa M, Labat M, Lorente S. Role of flow architectures on the design of radiant cooling panels, a constructal approach, Applied Thermal Engineering, 2019; 150: 1345-1352. <https://doi.org/10.1016/j.applthermaleng.2018.12.107>
- [12] Sahin G, Cetkin E. Enhanced temperature uniformity with minimized pressure drops in electric vehicle battery packs at elevated C-rates. Heat Transfer, 2022; 51: 7540-7561. <https://doi.org/10.1002/htj.22654>
- [13] Yamada T, Koshiyama T, Yoshikawa M, Yamada T, Ono N. Analysis of a lithium-ion battery cooling system for electric vehicles using a phase-change material and heat pipes, Journal of Thermal Science and Technology, 2017; 12: 17-00104. <https://doi.org/10.1299/jtst.2017jtst0011>
- [14] Bernardi D, Pawlikowski E, Newman J. A general energy balance for battery systems, Journal of the Electrochemical Society, 1984; 132: 5 - 12. <https://doi.org/10.1149/1.2113792>
- [15] Chen Y, Evans JW. Thermal analysis of lithium polymer electrolyte batteries by a two-dimensional model-thermal behaviour and design optimization. Electrochimica Acta, 1994; 39: 517 - 526. [https://doi.org/10.1016/0013-4686\(94\)80095-2](https://doi.org/10.1016/0013-4686(94)80095-2)
- [16] Yi J, Kim US, Shin CB, Han T, Park S. Three-Dimensional Thermal Modeling of a Lithium-Ion Battery Considering the Combined Effects of the Electrical and Thermal Contact Resistances between Current Collecting Tab and Lead Wire. Journal of the Electrochemical Society, 2013; 160: A437 - A443. <https://doi.org/10.1149/2.039303jes>
- [17] Xiao M, Choe SY. Theoretical and experimental analysis of heat generations of a pouch type LiMn₂O₄/carbon high power Li-polymer battery. Journal of Power Sources, 2013; 241: 46 - 55. <https://doi.org/10.1016/j.jpowsour.2013.04.062>

- [18] Arora S, Kapoor A. Experimental Study of Heat Generation Rate during Discharge of LiFePO₄ Pouch Cells of Different Nominal Capacities and Thickness. *Batteries*, 2019; 5: 1 - 22. <https://doi.org/10.3390/batteries5040070>
- [19] Lin C, Xu S, Liu J. Measurement of heat generation in a 40 Ah LiFePO₄ prismatic battery using accelerating rate calorimetry. *International Journal of Hydrogen Energy*, 2018; 43: 8375 - 8384. <https://doi.org/10.1016/j.ijhydene.2018.03.057>
- [20] Bazinski SJ, Wang X. Predicting heat generation in a lithium-ion pouch cell through thermography and the lumped capacitance model. *Journal of Power Sources*, 2016; 305: 97 - 105. <https://doi.org/10.1016/j.jpowsour.2015.11.083>
- [21] Chen K, Unsworth G, Li X. Measurements of heat generation in prismatic Li-ion batteries. *Journal of Power Sources*, 2014; 261: 28 - 37. <https://doi.org/10.1016/j.jpowsour.2014.03.037>
- [22] Xie Y, Shi S, Tang J, Wu H, Yu J. Experimental and analytical study on heat generation characteristics of a lithium-ion power battery. *International Journal of Heat and Mass Transfer*, 2018; 122: 884 - 894. <https://doi.org/10.1016/j.ijheatmasstransfer.2018.02.038>
- [23] Arora S, Shen W, Kapoor A. Neural network based computational model for estimation of heat generation in LiFePO₄ pouch cells of different nominal capacities. *Computers and Chemical Engineering*, 2017; 101: 81 - 94. <https://doi.org/10.1016/j.compchemeng.2017.02.044>
- [24] Keyser M, Pesaran A, Li Q, and et al. Enabling fast charging - Battery thermal considerations, *Journal Power Sources*, 2017; 367: 228 - 236. <https://doi.org/10.1016/j.jpowsour.2017.07.00>
- [25] Li Y, Qi F, Guo H, Guo Z, Li M, Wu W. Characteristic investigation of an electrochemical-thermal coupled model for a LiFePO₄/Graphene hybrid cathode lithium-ion battery, *Case Studies in Thermal Engineering*, 2019; 13: 100387(1-11). <https://doi.org/10.1016/j.csite.2018.100387>
- [26] Pesaran AA. Battery thermal models for hybrid vehicle simulations. *Journal of Power Sources*, 2002; 110: 377 - 382. [https://doi.org/10.1016/S0378-7753\(02\)00200-8](https://doi.org/10.1016/S0378-7753(02)00200-8)
- [27] Yeow K, Teng H, Thelliez M, Tan E. Thermal Analysis of a Li-ion Battery System with Indirect Liquid Cooling Using Finite Element Analysis Approach. *SAE International Journal Alt. Power*, 2012; 1: 65 - 78. <https://doi.org/10.4271/2012-01-0331>
- [28] Xu J, Lan C, Qiao Y, Ma Y. Prevent thermal runaway of lithium-ion batteries with minichannels cooling. *Applied Thermal Engineering*, 2017; 110: 883 - 890. <https://doi.org/10.1016/j.applthermaleng.2016.08.151>
- [29] Teng H, Yeow K. Design of Direct and Indirect Liquid Cooling Systems for High Capacity, High-Power Lithium-Ion Battery Packs. *SAE International Journal of Alternative Powertrains*, 2012; 1: 525 - 536. <https://doi.org/10.4271/2012-01-2017>
- [30] Wu B, Li Z, Zhang J. Thermal Design for the Pouch-Type Large-Format Lithium Ion Batteries, I. Thermo-Electrical Modeling and Origins of Temperature Non-Uniformity. *Journal of The Electrochemical Society*, 2015; 162: A181 - A191. <https://doi.org/10.1149/2.0831501jes>
- [31] Murashko K, Pyrhönen J, Laurila L. Three-Dimensional Thermal Model of a Lithium Ion Battery for Hybrid Mobile Working Machines: Determination of the Model Parameters in a Pouch Cell. *IEEE Transactions on Energy Conversion*, 2013; 28: 335 - 343. <https://doi.org/10.1109/TEC.2013.2255291>
- [32] Zhu J, Sun Z, Wie X, Dai H, Song L. Preliminary Study of a Distributed Thermal Model for a LFP Battery in COMSOL Inc. Multiphysics (MP) Software. *Vehicle Power and Propulsion Conference (VPPC)*, Beijing, China, 1-5, 2013. <https://doi.org/10.1109/VPPC.2013.6671700>

Blank Page



Research Article

Vibration energy harvesting using telescopic suspension system for conventional two-wheeler and EV

Naga Sudha Rani Behara^{*a}, Putti Srinivasa Rao^b

Department of Mechanical Engineering, Andhra University College of Engineering(A), Visakhapatnam 530003, Andhra Pradesh, India

Article Info

Abstract

Article history:

Received 12 Dec 2022

Accepted 27 Feb 2023

Keywords:

*Mechanical Vibrations;
Electric Vehicles;
Energy harvesting;
telescopic Suspension system;
Air pollutants;
Electronic devices*

Energy harvesting (EH), a fairly recent technological advancement, is the technique of capturing and converting environmental energy sources—such as load, mechanical vibrations, temperature changes, light energy, wind energy, and so on—into extremely small amounts of power within a specified voltage range. When there is no accessibility to conventional power sources, energy harvesting is employed to power electronic devices. In addition to reducing vibration brought on by road imperfections, an energy-harvesting telescopic shock absorber can collect energy that would otherwise be wasted in suspension vibration. It can act as an energy generator as well as a controlled damper. In order to increase the effectiveness of energy harvesting, this research indicates analyzing and testing a telescopic shock absorber structure that has the benefit of lowering spring vibrations and resisting unneeded spring motion. Focusing on energy harvesting and vibration analysis in shock absorbers is the main objective of this effort. The first telescopic suspension system, which consists of a spring, rack, and pinion, was created using Solid works 20 and then every portion was examined using Ansys Workbench. The spring, rack, and pinion were then practically constructed on a two-wheel bike using a rack and pinion mechanism that was created using 3D printing technology, and testing was then done to determine how much energy was harvested in terms of voltage in relation to the distance (in kilometers) travelled for different loading conditions observed how the voltage can be harvested for conventional two-wheeler and Electric Vehicle. Throughout the observation we found that the vibration harvesting in Electric bike is low compared to Conventional bike. Finally, the unwanted vibrations were harvested and boost up, stored in 5V, 12 V rechargeable dead battery which is used to recharge the mobile phone and low power electric devices.

© 2023 MIM Research Group. All rights reserved.

1. Introduction

Automobiles have long been utilized as a form of transportation around the world, but their usage of exhaust gas and gasoline has resulted in environmental problems. Automobile technologies for environmentally friendly cars, such as electric and hybrid cars that use electric energy to alleviate this environmental problem, are actively being developed. Fuel economy improvements are always a focus. Energy lost by shock absorbers is a significant source of power recovery since only 10–16 % of energy production is required to actively propel cars and trucks through road friction with air drag [1]. Recent research [2] show that vehicle suspension significantly affects fuel efficiency. Regenerative shock absorbers were already developed for more than 20 years to make up for the kinetic energy lost by conventional oil shock absorbers. The two groups of regenerative vehicle shock absorbers, the subject of several investigations, can be split into two categories. The power from the relative linear movement of magnetic with coils is produced by the first, which is founded on a novel linear generating architecture. The

^{*}Corresponding author: nsrani@mail.com

^a orcid.org/0000-0002-1234-9053; ^b orcid.org/0000-0003-1379-4906

DOI: <http://dx.doi.org/10.17515/resm2022.589me1212>

Res. Eng. Struct. Mat. Vol. 9 Iss. 3 (2023) 687-707

second type uses rotational permanent magnetic DC or AC converters to transform linear suspension vibration into oscillatory spinning in contrast to linear regenerative shock absorbers. Examples of mechanical mechanisms include the hydraulic transmission, ball screw, with rack and pinion.

Up-and-down suspension vibrations are transformed into bi-directional electricity generating vibrations by the rotating energy recovery absorber, which then generate power. Due to the availability of low-cost, off-the-shelf rotary rotors, they seem to be more affordable but also small. However, the unequal oscillation of the motion machinery leads to a number of problems, such as inadequate mechanical durability with subpar vibration effectiveness. For instance, even with active control at high frequency above 7–10 Hz [7,8], the ball screw mechanics investigated in [3-6] have outstanding power density, however the absorbers are too rigid to regulate at high frequency because to significant motion inertia. As a result, ride comfort is reduced. To power automobile electronics or recharge battery, the voltage should be commutated through an electrical rectifier, as the forward voltage of the diodes has a permanent impact on the circuit's effectiveness. Minimizing vehicle energy losses is necessary for increasing fuel efficiency, reducing pollutants, and fulfilling the power requirements of other systems [9–11]. In addition to improving engine and powertrain efficiency, we may recover energy lost in automobiles by recovering wasted heat energy [12–14], regenerative braking energy [15–17], including vibrational energy on shock absorbers [18, 19].

Although contemporary regenerative shock absorbers may recover a significant proportion of vibration energy, there are several downsides to replacing conventional shock absorbers entirely. Various elements in regenerative shock absorbers continue to pose problems for researchers. Regenerative shock absorbers can be improved by focusing on the two major issues listed below. For starters, regenerative shock absorbers are often inefficient and perform poorly in comparison to traditional shock absorbers. Second, the uses of recovered energy must be thoroughly investigated. Previous research proposed a regenerative shock absorber using a pair of gear rack structures to achieve high efficiency and apply to range-extended EVs [20]. Thus, we are using a different material for increasing the efficiency of energy harvesting and shock absorbers. Our proposed approach therefore achieves greater energy harvesting with vibration analysis with shock absorbers. The paper's primary contribution is:

- The first telescopic suspension system, which comprises of a spring, rack, and pinion, was created in Solid Works 20. This was followed by an investigation of several shock absorber materials in Ansys Workbench.
- A rack and pinion system that was modelled using 3D printing technology was used to test the telescopic shock absorber on a two-wheeler and make a comparison.
- Meshing was done in Hyper Mesh software tool for the shock absorbers.

Finally, our proposed solution outperforms all previous strategies. The research article is also included in the next section. Part 2 of the current model survey goes deep. Part 3 contains information about the proposed structure. Part 4 looks at the experimental setting for the proposed approach. Part 5 goes over the design and analysis sections in depth. Results and discussion is presented in part 6, Part 7 shows the comparative analysis and Part 8 the paper closes.

2. Literature Survey

A passive or semi-active electromechanical damper based on the linear electric motor using permanent magnets (PMs) whose electric terminals are shunted by a resistance was proposed by Karnopp [21]. According to the mechanics of the automobile, the shunt

resistance may be used to modify the damping coefficient. To achieve good vibration suppression performance with little energy consumption, Suda et al. [22] built an active suspension with an energy conversion system as well as a linear DC generator based on linear electrodynamic motors.

Goldner et al [23] just completed a proof-of-concept study to investigate the possibility of using an optimised regenerative magnetic shock absorber to produce significant energy savings in automobiles. Aside from other potential applications, using such shock absorbers could improve energy efficiency in electric vehicles by turning normally parasitic mechanical power losses into stored electrical energy, allowing for longer battery recharge times.

The feasibility study of an electromagnetic damper for use as a sensor and actuator in automotive suspension applications was finished by Ebrahimi et al [24]. This electromagnetic damper is founded on the tubular, linear, brushless DC motor principle that operates in three modes: passive, semi-active, and active. The proposed damper, being a self-powered active shock absorber, has the capability of acting as both a sensor and an actuator at the same time. Even in the absence of external power, the calculated damping force appears reasonable for car suspension applications.

Zuo et al. [25] constructed and prototyped a linear electromagnetic frequencies harvester capable of producing more than 16-64 watts of electricity from all four shock absorbers with 0.2-0.5 m/s RMS suspension velocity. These versions can be used as actuators for active or semi-active control, but they are mostly used for energy harvesting. Martins et al. [26] shown the practicality of electromagnetic active suspensions by pioneering some breakthroughs in power devices, permanent magnetic compounds, and microelectronic devices.

Chen and Liao [27], as well as Sapinski [28], designed linear electromagnetic energy harvesters to power MR dampers in order to provide active/semi-active control. In order to supply energy, the second type of linear regenerative shock absorbers employs rotating permanent magnetic DC or AC converters to convert linear suspension vibrations into oscillatory spinning. Hydraulic transmission, rack and pinion, and ball screw are examples of mechanical systems. A comparison among a linear as well as a rotary shock absorber was done by Gupta et al [29]. The energy lost in shock absorbers can be recovered using regenerative electromagnetic shock absorbers, it was discovered that the rotary shock absorber may possess a higher energy density.

An energy-regenerative electrical suspension was created by Zhang et al. [30] which uses a permanent-magnet direct-current motor, a ball screw, as well as a nut as the motor actuator. The ability of the suspension to regenerate and convert vibration energy from road excitement into electric energy while keeping outstanding suspension effectiveness is its most noticeable characteristic. The performance of the DC motor is evaluated. The regeneration and vibration control features are validated through full-vehicle testing on the IST Road Lab four post rig. The results of tests conducted with an electrical device that acts as a passive suspension mechanism show the practicality of vibration energy regeneration.

Avadhany et al [31] patented that the straight movement of the piston can be turned into rotational motion using reasonable pressure driven gear, which drives the rotating engine of the generator. The vehicle's shock is lessened by the engine's electromotive power using hydraulic transmission.

Additionally, Choi et al. [32] provide vibration control of an automobile suspension system without the use of exterior power sources by using an electrorheological (ER) shock absorber that is adjustable as well as activated by an energy generator. The linear motion

of the piston is changed into a spinning movement via the rack and pinion operation of the ER shock absorber. The rotational motion is accelerated by gears, which subsequently turns on a generator to produce electricity. Experiments have demonstrated a significant reduction in suspension vibration when the ER shock absorber is activated using the suggested regenerative energy method.

A unique regenerative shock absorber architecture put forth by Zhang and Zuo [33,34] has the benefit of significantly increasing energy harvesting effectiveness while reducing oscillation-induced impact forces. The model is capable of concurrently analyzing mechanical and electrical elements. The MMR shock absorber, which generates more than 15 Watts of power while travelling at 15 mph on a smooth, paved road using a rack and pinion system, is also put through road tests to show its viability.

The adoption of piezoelectric as well as electromagnetic techniques was suggested by Howells CA and Ju S, Ji C-H [35,36] for the conversion of mechanical to electrical energy. The piezoelectric design is typically utilized for small-scale vibration harvesting, including in milliwatt & microwatt harvesters like those that generate power from the motion of human bodies.

Dr. Seema Tiwari et.al [37] Some operation wastes a lot of fuel energy, which can be recovered by using a regenerative suspension system. A regenerative suspension framework can successfully retain these vibrations while reducing the amount of energy lost to the surrounding. This study examines the most recent studies on regenerative shock absorbers. It first investigates the dispersal of energy from cars and then the feasibility of recouping this scattered energy using a regenerative shock absorber. It also analyses the many unique work done on the regenerative shock absorber.

Zhanwen Wang et.al [38] proposed a high-efficiency regenerative shock absorber based on a pair of ball screws is proposed in this research for range-extended EVs. The vibration energy is captured and transformed into electricity, which is then dissipated as heat in the suspension system. The suspension vibration input module, transmission mechanism module, generator module, and power storage module comprise the regenerative shock absorber. The simulation section depicts the force-displacement loop at various amplitudes and frequencies, the angular velocity of the generator shaft at sinusoidal inputs, and the damping coefficients at various external resistances.

Cyriacus Okpalike and colleagues [39] proposed to explore the effects of building rehabilitation on ventilation and energy savings in Achara layout, Enugu City, Nigeria, a qualitative research approach was used. Using a judgmental sampling technique, the sample size was determined to be four blocks of flat residential buildings. To collect empirical data relating the window system, physical measurements, an observation schedule, and oral interviews with site employees focused on window size, area, property, and fenestration type were used. The results show a very significant difference in all analyzed variables between the as-built and modified window design systems. Its finding was based on the fact that a restored structure does not promote adequate natural ventilation, requiring more energy for cooling and lighting.

F. E. Tahiri et. Al [40] This research provides optimal control strategies for a standalone Hybrid Power System (HPS) in order to provide sustainable and optimal energy to an isolated site while improving electrical energy quality. In addition, a unique control approach for maximizing PVS power has been developed in this work. This suggested technique, which is based on the combination of the Perturb and Observe (P&O) algorithm and the Fuzzy PI Controller (FPIC), outperforms the traditional algorithm P&O, especially in the dynamic state. A supervisory control algorithm has been developed to manage the energy flows between the hybrid system's devices in order to determine the ideal

operating mode in order to provide a continuous supply of the load with minimal battery usage.

A. Laabid et al [41] The purpose of this article is to examine, evaluate, and develop options for integrating hybrid energy sources (Solar Photovoltaic PV/Batteries/Diesel Generator (DG)) in mobile service units (MSU) meant to serve rural communities. The initial goal is to assess the functioning of two previously deployed solar systems installed on truck roofs, with respective outputs of 2.12 and 3.54 kWp. We created a model of the energy conversion chain and simulated its behaviour throughout the year. The simulated findings are then compared to the measurements taken on-site. Several association possibilities are then investigated in order to propose the best combination, taking into account the surface available for PV module installation (truck roof), weight, and battery longevity.

According to the preceding study of shock absorbers on mechanical vibrations, there are many constraints for generating high energy harvest. This method offered a strategy that is explained in detail in the next section.

3. Principle and Methodologies of Proposed Technique

Motorcycles are the main application for a telescopic suspension built of steel and aluminium alloy, and because of its weight and shock-absorbing capacity, it is very effective. A rack and pinion modelled using 3D printing technology, a shock absorber made of spring stainless steel, as well as a dynamo that converts mechanical displacement into voltage stored in a rechargeable battery have all been created and attached to both ends of the rear wheel of a motorcycle with a gasoline engine. The circuit also includes a pump up device but a diode to boost the voltage of the energy that has been captured so that it can be used to power portable devices and signal lights. Results from a comparison of boost up voltage are recorded on several roadways, accounting for different loading scenarios such as kilometers.

An experimental procedure using piezoelectric material was also utilized to capture vibrations, however it failed due to strong vibrations. Numerous researchers have incorporated energy harvesting absorbers to decrease fuel usage, improve ride comfort, and improve road handling using techniques like adjustable damping and variable inverter [42–44].

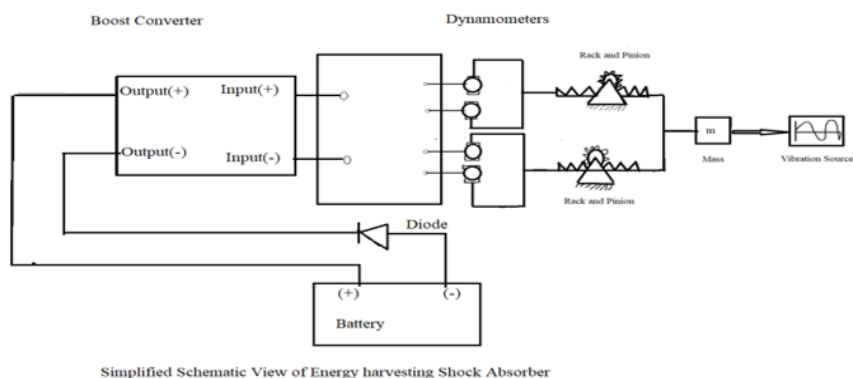


Fig. 1 Circuit diagram

The circuit diagram for the proposed approach is shown in Figure 1. In the illustration, the boost converter has two inputs and two outputs. Two outputs are linked to the battery, one of which incorporates a diode. Two inputs are transmitted to a medium to create

dynamometers. The Solid works 20 version and ANSYS Workbench software were used to analyse a 3D model of a telescopic suspension system. Stress analysis has been carried out under different load conditions, while material properties of helical compression springs for various materials, such as Spring Steel telescopic shock absorbers, have been explored. We concluded by employing these materials that we monitor and harvest the voltage in rechargeable batteries, and the boost converter is used to raise the voltage, which may be used to power low electrical devices. Our ASTM A313 shock absorber material is the optimum material for bikes to load one or more people and performs well.

4. Experimental Setup

Figure 2 depicts the proposed method's experimental setup with conventional two-wheeler and electric vehicle. A diode, dynamometer, battery, and multimeter are set up with the rack and pinion in order to calculate the kilometers and load that shock absorbers support. Our method's shock absorber is made of a spring-like steel substance that retains its elasticity while having exceptional tensile qualities. This compression load shock absorber has a 250kg loading capability. We employed this kind of shock absorbers to lessen vibration and shock on machinery. The tyres are always in contact with the road due to these shock absorbers. As a result, our research shows that mechanical vibrations, such as shock absorbers, can be used to harvest energy.



Fig. 2 Experimental setup conventional Two wheeler (Passion Pro) and Electric Vehicle (Hero NYXe5)



Fig. 3 Circuit connected for EV

4.1. Components and Its Uses

The components employed in our experiment are briefly described in this section. Diode (4007), rack and pinion, dynamometers, battery, boost converter, multimeter, and other components are used in our method. Let's take a quick look at these elements.

4.1.1. Diode 4007

Our proposed process uses a diode 4007. The 1N4007 diode is a traditional recovery rectifier with a plastic casing. In our proposed solution, this diode is coupled with a rack and pinion to handle greater current capacities. Figure4 presents the diode (4007).



Fig. 4 Diode (4007)

4.1.2. Rack and Pinion

A longitudinal controller with a rack and pinion consists of a pinion (circular gear) that engages a rack (linear gear) to transformation of rotational motion into constant speed. In a rack and pinion drive, both linear and spiral gears can be employed. The rack and pinion is shown in Figure 5.



Fig, 5 Rack and pinion

4.1.3. Dynamometers

A dynamometer, often known as a "dyno," is a machine that simultaneously monitors the torque and speed of rotation (RPM) of an engine, motor, or other rotating prime mover to determine its instantaneous power, which is commonly shown as kW or bhp by the dynamometer. This dynamometer is used by our method to measure mechanical

vibrations and to absorb power. The dynamometers utilized in our method are shown in Figure 6.

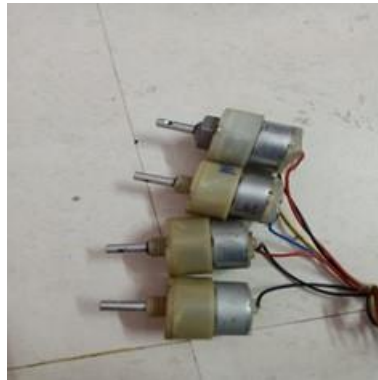


Fig. 6 Dynamometers

4.1.4. Battery

In our proposed method we are using 12V (1.3AH) battery. In order to store energy and provide a steady supply of voltage, we linked this battery to the diode and dynamometers in our experimental setup. The 12V battery for our proposed solution is depicted in Figure 7.



Fig. 7 12V Battery

4.1.5. Boost Converter

Our proposed method consumes LM6009 Boost Converter shown in figure8. A boost converter (sometimes called a step-up manipulator) is a DC-to-DC power manipulator that increases voltages while depressing power from its source to destination.

4.1.6. Multimeter

A multimeter is an instrument for measuring a broad variety of electric characteristics. A multimeter that can calculate voltage, resistance, and current is known as a volt-ohm-milliammeter because it contains voltmeter, ammeter, and ohmmeter operations. Figure 9 shows our proposed model multimeter.

We designed our innovative energy harvesting shock absorbers employing mechanical vibrations based on all of the above materials. With SOLIDWORKS 20 and ANSYS model

methodologies, our method harvests an amount of energy and outperforms all existing methods.



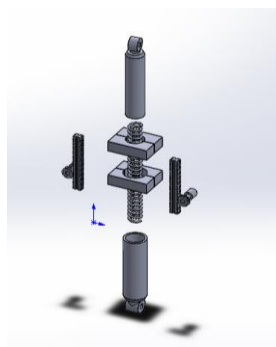
Fig. 8 Boost Converter



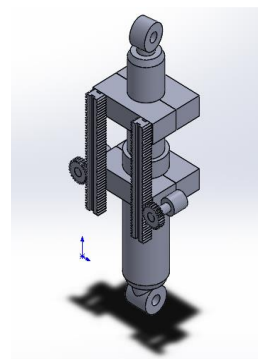
Fig. 9 Multimeter

5. Design and Analyzing

SolidWorks 20 is a top end, parametric, feature-based, solidwork software that was used to develop this study. It gives mechanic designers a method for automating mechanical design that is founded on built-in intelligence and removes the element of guesswork from 3D design.



Exploded view



Isometric view

Fig. 10 Exploded and Isometric views

Figure 10 shows the exploded and isometric views of our proposed method designed using Solid works 20. The rack and pinion, spring steel, top mount, and bottom mount components of the proposed approach make up our technique.

5.1. Design Parameters of Telescopic Suspension System

5.1.1. Design Specifications of a Shock Absorber

Our proposed approach includes a telescopic suspension system in which a Spring Body Shock Absorber is an integral part along with rack & Pinions with adjustable loading capacity is considered. The bike used in our method is Hero Passion Pro Bike 110CC and the weight of the bike is 117 kg. The following Table 1 shows the Loading descriptions of the weight for our proposed method.

Table 1. Loading descriptions

Loading Description	Considering load in kg	In N
Weight of 1 person + weight of bike	187 kg	1834.47 N
Weight of bike + two persons	257 kg	2521.17
Assuming 60% of overall vehicle weight =154.2kg=1512.7N		

Steel and Aluminum Alloy is the Telescopic Suspension Material used in this method. Spring material used is Stainless 17-7 ASTM A313 and the type is Helical Closed and Ground Type Spring. The proposed parameters and dimensions are displayed in Table 2. Also our proposed modelled is designed using these factors.

Table 2. Proposed parameters and dimensions

Parameter	Dimension
Weight of one spring	0.3849 kg
Wire diameter	5mm
Outer diameter	35mm
Inner diameter	25mm
Free length	285mm
Mean diameter	30mm
Number of active turns	24
Total coils	26
Spring Index	6
Pitch coil	11.458 mm
Rise angle of Coils	6.93 Degrees
Modulus of Rigidity G	75.68 GPa
Maximum Shear stress	725.8 MPa
Wahl Correction Factor W	1.253
Spring Rate K	9.124 N/mm
Maximum load carrying Capacity	948.278 N

5.1.2. Design Parameters of Rack and Pinion

The rack and pinion materials used in this process are Polyacetal and MC Nylon. The length of rack is 14cm and the diameter of pinion is 3cm. Teeth on the Rack and pinion is 30 and

25 respectively. Linear circle is 3cm with module 1 and pitch circle is 3.5 cm. 154.2 kg is the mass to be moved with speed 11.11m/s. Acceleration time t is 5.55 sec and the acceleration due to gravity g : 9.81m/sec². Proposed Variables are shown in Table 3. Our technique is modelled using the Poisson's ratio, the load factor, and the lifetime factor of the rack and pinion.

Table 3. Proposed Variables

Properties	Dimensions
Poisson's Ratio μ	0.4
Load factor KA	1.5
Life time Factor F_n	1.05
Safety Coefficient SB	1.4
Linear Load Distribution Factor $LKH\beta$	1.3

Maximum Permissible Feed Force $F_u = (m.g. \mu + m. a)/1000 = 2.3\text{KN}$ and Permissible Feed Force $F_{U.tab}$ is 9 KN (For Rack & Pinion of module:1 & of Polymer Type) from Atlanta Rack & Pinion Drive Calculation Table. Permissible Feed Force is F_u . Per: $F_u \text{ tab} / (KA.F_n.SB.LKH\beta) = 3.13\text{KN}$. $F_u \text{ Per} > F_{U}$ (Condition is fulfilled) for our proposed method.

5.2. Analyzing Properties

When loads are applied to a body, the structure deforms as well as the weights' effects are dispersed throughout the body. The body enters a condition of equilibrium as a result of the internal forces and reactions caused by the external stresses. Meshing is done in our method using ANSYS work.

5.2.1. Meshing

Figure 11 shows that the Shock Absorber Assembly has been fully mesh. One of the most crucial elements in running a precise simulation is meshing. A mesh is composed of elements that have nodes in them that represent the geometry's shape. Meshing is done in Hyper Mesh. Hyper Mesh is a pre-processing software where you divide the model into no. Of elements and nodes for a solver to apply the mathematical functions on it.

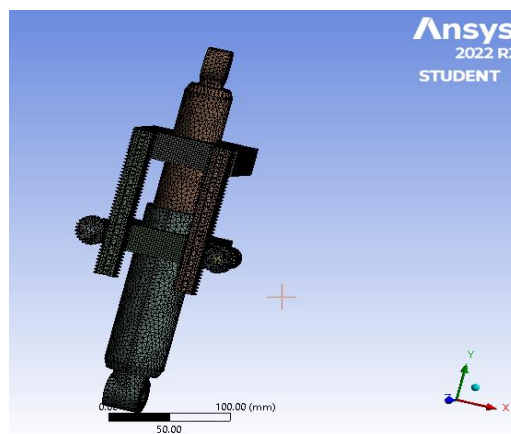


Fig. 11 Mesh model for shock absorber

5.2.2. Applying Material Properties

Material properties employed in our technique are shown in table 4 in accordance with how it is proposed to conduct the analysis for materials.

Table 4. Material Properties

Material	Density Kg/m-3	Poisson 's ratio	Young's Modulus MPa	Tensile strength MPa	Yield Strength MPa
ASTM A313	7800	0.25	2.04 E + 05	1170	965
Steel & Aluminum Alloy	5260	0.33	1.3 E + 05	2.43 E + 08	2.43 E + 08

The bottom eye is a fixed contact, while the top eye is attached to the axle of the back wheel, in which the force is applied, in the actual installation of the shock absorber to a two-wheeler. The struts rod is in sliding motion with the upper mounting, as well as the spring is constrained within the top and bottom mounts. Our model for a shock absorber is proposed using these materials and the attribute values. The next section shows the results and discussion of our proposed method.

6. Results and Discussion

Results from a comparison of boost up voltage are recorded on various roadways, taking into account different loading scenarios such kilometers. The datasets for bike load, voltage, and distance travelled are determined by the instances below.

Conventional Bike (Passion Pro 110 CC)

Case: 1

Table 5. Bike Load (117 Kg) + one Person (70 Kg) (Driver)

S.NO	Condition(distance travelled by bike)	Initial Voltage (Volts)	Boost up Voltage (Volts)
1	Rest Condition	0	0
2	10Km	0.35 - 0.5 V	0
3	50km	2 - 2.5 V	0
4	100 km	4 - 5 V	0 - 10 V
5	150 Km	6 - 7 V	15 - 20 V
6	200 km	8.5 - 9 V	25 - 30V

Table 5 shows the weight of the bike in kilograms, the initial and boost up voltage in volts, and the distance travelled in kilometers. The bike load is 117kg and the loaded one person (driver) weight is 70kg.

Figure 12 depicts a line graph based on the Bike Load and a single person. The bike weighs 117 kilograms, while the (driver) person weighs 70 kilograms. The kms travelled in harvested voltage are 5 and the volt is 1.5V. However, we travelled 26 kilometers with a load and increased the voltage by 12V in boost up voltage. X-axis depicts the distance travelled and Y-axis depicts the voltage.

Table 6 illustrates the bike load and the measurements of two people. The bike weight is 117 kg, with one person weighing 70 kg and the driver weighing 70 kg. The distance travelled is in kilometers, while the voltages are in volts.

Figure 13 depicts a line graph created using the Bike Load and two people. The bike load is 117kg, the passenger weight is 70kg, and the driver is 70kg. The combined weight of two people is 140kg. We boost up energy by 37.5 kms with 16V and energy harvesting is done. X-axis depicts the distance travelled and Y-axis depicts the voltage.

Note: Minimum voltage to boost up is to be 5V.

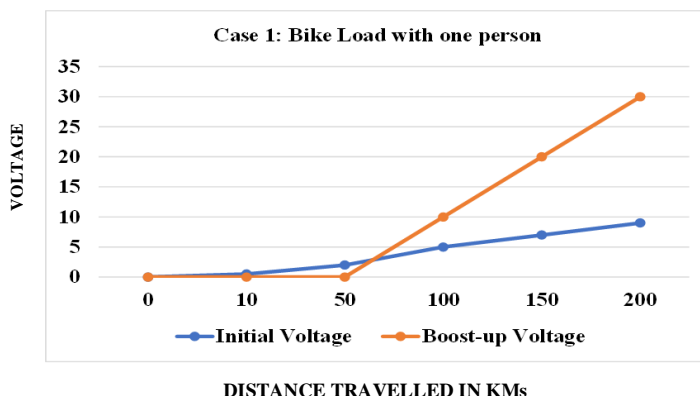


Fig. 12 A plotted line graph

Case: 2

Table 6. Bike Load (117 Kg) + one Person (70Kg) + Driver (two persons 140kg)

S.NO	Condition (distance travelled by bike)	Initial Voltage (Volts)	Boost up Voltage (Volts)
1	Rest Condition	0	0
2	10Km	1.2 - 1.5 V	0
3	50km	3.5 - 4 V	0
4	100 km	6.5- 7V	0 - 15 V
5	150 Km	9 - 10 V	20 -30 V
6	200 km	10 - 12 V	35 - 40 V

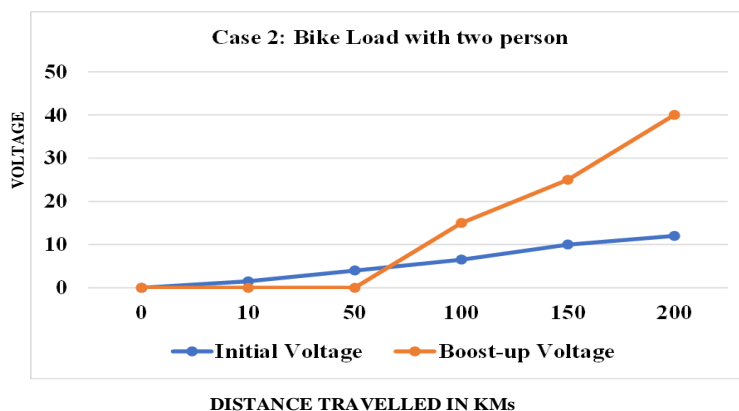


Fig. 13 A line graph

Electric bike (Hero NYXe5)

Specifications: Lithium ion 51.2 V,30AH battery

Case: 1

Table 7. Bike Load (77 Kg) + one Person (70 Kg) (Driver)

S.NO	Condition (distance travelled by bike)	Initial Voltage (Volts)	Boost up Voltage (Volts)
1	Rest Condition	0	0
2	10Km	0	0
3	50km	1-2.5 V	0
4	100 km	3-4.5 V	0 – 8 V
5	150 Km	5-7V	10-15 V
6	200 km	8.5 – 9 V	18-20V

Figure 14 depicts a line graph created using the Bike Load with one people on Electric vehicle. The bike load is 77kg, and the driver weight is 70kg. X-axis depicts the distance travelled and Y-axis depicts the voltage.

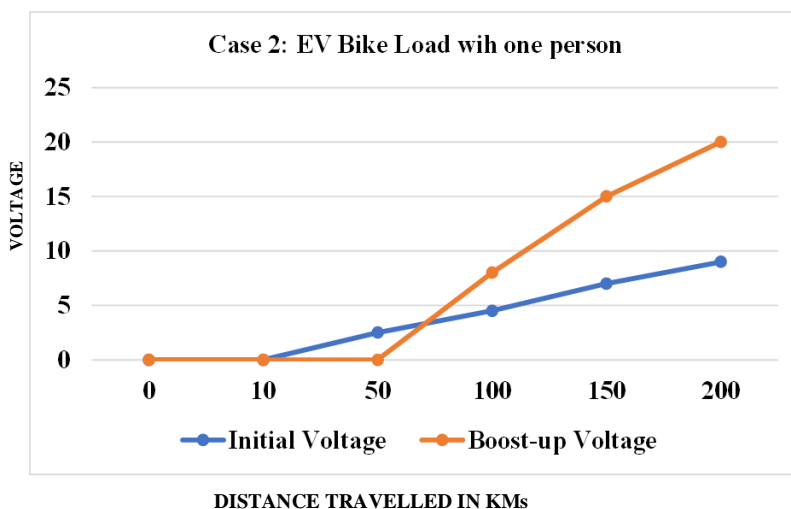


Fig. 14 A line graph

Case: 2

Figure 15 depicts a line graph created using the Bike Load with two people on Electric vehicle. The bike load is 77kg, the person weight is 70kg and the driver weight is 70kg. X-axis depicts the distance travelled and Y-axis depicts the voltage.

Figure 16 depicts mobile charging with a harvested stored rechargeable battery. The energy captured by the shock absorbers is connected to the cell phone for charging. As a result, we can store energy in a rechargeable battery and gain energy to recharge mobile phones, outperforming all other methods.

Table 8. Bike Load (77 Kg) + one Person (70Kg) + Driver (two persons 140kg)

S.NO	Condition (distance travelled by bike)	Initial Voltage (Volts)	Boost up Voltage (Volts)
1	Rest Condition	0	0
2	10Km	0	0
3	50km	0-1V	0
4	100 km	2-3 V	0 - 5V
5	150 Km	3-5V	5-10V
6	200 km	5-7V	10-15V

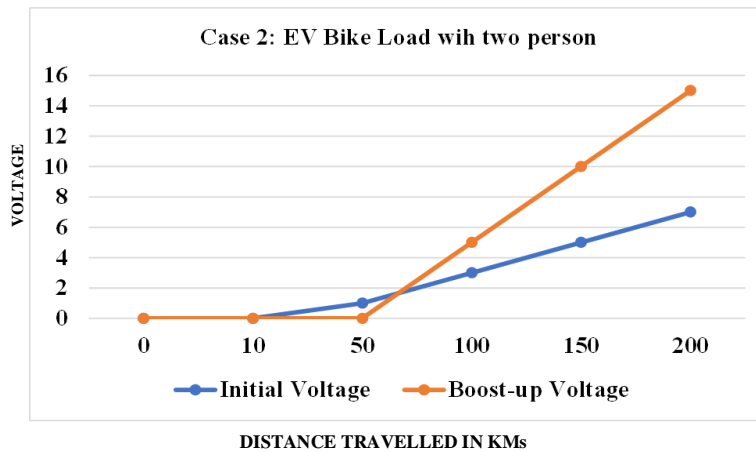


Fig. 15 A line graph



Fig. 16 Mobile charging using stored harvested rechargeable battery

6.1. Modal Analysis

An elastic structure will oscillate around its equilibrium position if a force is applied to initially displace it from its stationary state, and then the force is removed. Free vibration is the name given to this sort of oscillation caused merely by the initial disturbance. Natural frequencies are frequencies that naturally exist, but their typical values exhibit

specific deformation patterns known as mode shapes. The analysis of such free vibrations is crucial for determining the system's dynamic response. All materials are tested for their first six modal frequencies:

Table 7. Results of Modal Analysis (Freq-Hz)

Mode	Frequency
Mode 1	247.34 Hz
Mode 2	253.32 Hz
Mode 3	315.66 Hz
Mode 4	345.28 Hz
Mode 5	561.6 Hz
Mode 6	566.1 Hz

Table 7 shows the results of modal analysis for our proposed method. At mode 1 our material attains 247.34 minimum frequency and at mode 6 we gain maximum of 566.11 frequency for our material ASTM A313.

7. Comparative Analysis

This part compares all the materials used in this method to design the Spring Steel Shock Absorber for energy harvesting. We used Spring steel and its dimensions are given in the table1. In this method, we used a Von mises stress analysis for analyzing load material.

Table 8. Loading condition for shock absorber analysis

S.no	Loading Description	Considering dynamic load in double	In N
1	Bike load + 1 person	187 Kg	1834.47N
2	Bike load + 2 person	257Kg	2521.17N

Assuming 60% of overall vehicle weight =154.2kg=1512.7N. Table 8 shows the loading condition for shock absorber analysis. In this table, the load is mentioned in kilograms and numbers are mentioned in natural numbers.

7.1. Von mises Stress Analysis

Figure 17 shows Von mises stress analysis 3D modeling in Ansys for loading one person (1373.4N). A statistic that determines if a substance may give or fracture is the Von Mises stress. It is typically frequently applied to ductility, such as metals. A material will yield, according to the von Mises yield criterion, if its von Mises strain during load is equal to or higher than that of the yield point of the identical substance under simple tension. Our method employs 6.952 max tensile strength for our shock absorbers.

Figure 18 illustrates the Von Mises stress analysis for loading two persons (2521.17N) using the proposed approach. Our proposed solution employs a rack and pinion with a maximum yield of 12.762 in the shock absorber.

7.2. Deformation

We develop a method termed deformation after comparing loading people in the proposed materials. Deformation refers to the change in shape. When enough force is exerted to a metal or other structural material, the substance will change shape. Deformation of the materials is given as follows.

Figure 19 depicts the deformation when one person is loaded (1373.4N). We can get a maximum of 0.0061586 by loading one person in the shock absorbers.

Figure 20 shows the deformation of loading two persons in the shock absorber (2521.17N). For loading two people in the shock absorber we achieve maximum values of 0.011305 and minimum values tends to 0.

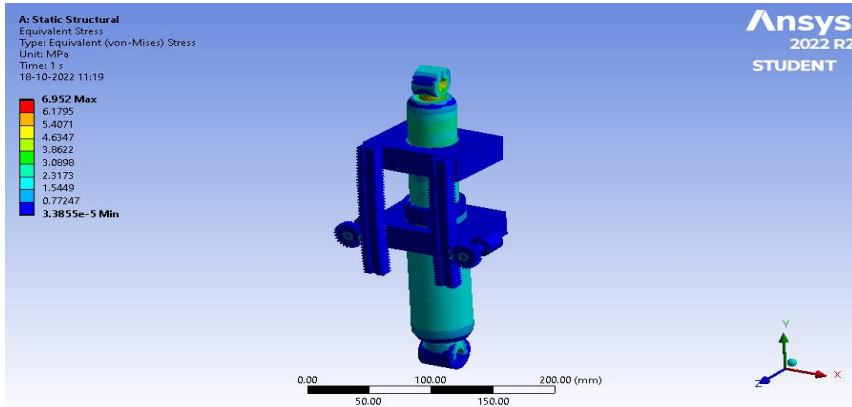


Fig. 17 Von mises stress analysis for loading one person

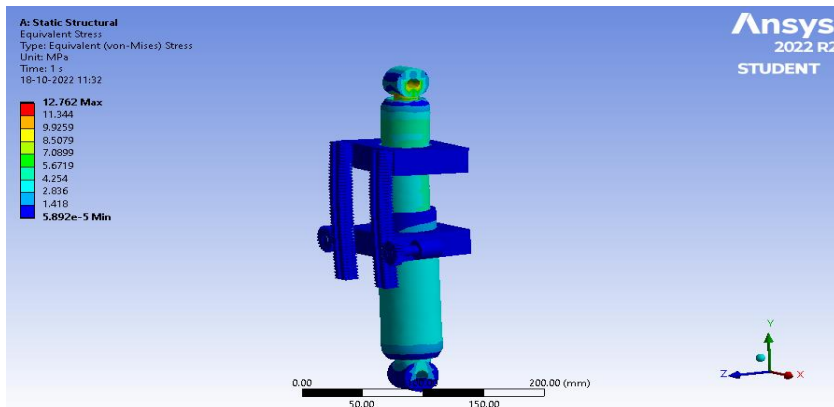


Fig. 18 Von mises stress analysis for loading two persons

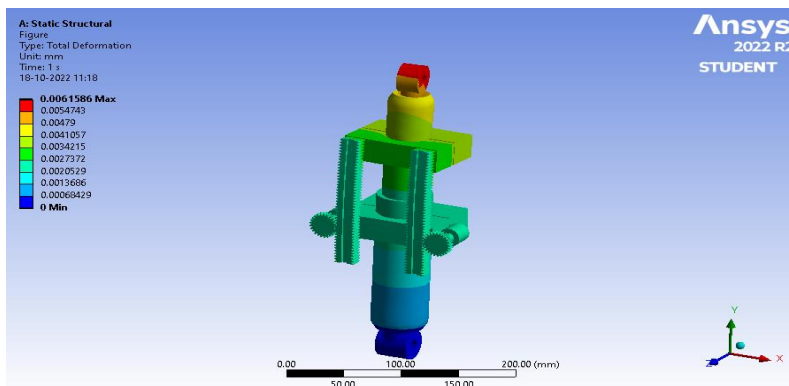


Fig. 19 Deformation for loading one person

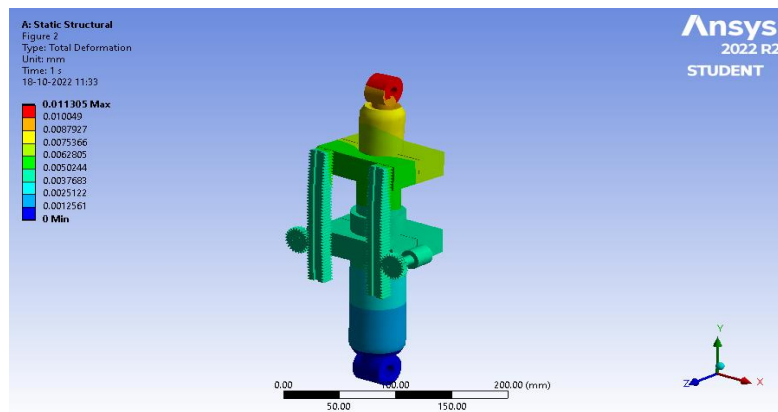


Fig. 20 Deformation for loading two persons

8. Conclusion and Future Work

In this study, we developed a brand-new energy collecting technique depends on shock absorbers' mechanical vibrations. This technique demonstrates the detailed difference between loading one or more persons in a shock absorber using a displayed line graph. In the existing paper, only the harvested power vs load is analyzed, however in our work, we monitor and harvest the voltage in rechargeable batteries, and the boost converter is utilized to raise the voltage, which may be used to power low electrical devices. Then, to compare the Spring steel, we used Solid works 20, 3D printing and ANSYS technology. Our study area's major purpose is to concentrate on energy harvesting and vibration analysis in shock absorbers. After modelling the shock absorber with Solid works 20, ANSYS Workbench was used to analyze the shock absorber for Conventional bike and Electric Vehicle for different load conditions over the distanced travelled in Kilometers. Later, the shock absorber was tested on a two-wheeler bike using a rack and pinion mechanism. Compared to Conventional the vibrations in Electric bike were low so the that energy harvesting takes over the long distance. Mesh is performed using ANSYS technology for shock-absorber and is also shown in the paper. The modal analysis for our material ASTM A313 is also performed from mode 1 to mode 6, and the maximum and minimum modes are calculated. Von Mises stress analysis for loading one and two persons and also maximum tensile strength is also calculated by using ANSYS method. Deformation is also done for loading one and two persons is also calculated in this method. Finally, the Vibrations were harvested, boosted up voltage stored in dead rechargeable battery can be used to recharge the mobile. The future scope of the work is to use the piezo electric material for vibration energy to the suspension system in convention and EV two wheelers, Four wheelers.

References

- [1] Kobayashi S, Plotkin S, & Ribeiro SK. Energy efficiency technologies for road vehicles. *Energy Efficiency*, 2009; 2: 125-137. <https://doi.org/10.1007/s12053-008-9037-3>
- [2] Efatpenah K, Beno JH, & Nichols SP. Energy requirements of a passive and an electromechanical active suspension system. *Vehicle System Dynamics*, 2000; 34(6): 437-458. <https://doi.org/10.1076/vesd.34.6.437.2050>
- [3] Song X, & Li Z. U.S. Patent No. 6,920,951. Washington, DC: U.S. Patent and Trademark Office, 2005.

- [4] Song X, Li Z, Edmondson JR. inventors; Visteon Global Technologies Inc, assignee. Regenerative passive and semi-active suspension. United States patent US 7,087,342, 200.
- [5] Amati N, Canova A, Cavalli F, Carabelli S, Festini A, Tonoli A, & Caviasso G. Electromagnetic shock absorbers for automotive suspensions: electromechanical design. In *Engineering Systems Design and Analysis 2006*; 42495: 131-140. <https://doi.org/10.1115/ESDA2006-95339>
- [6] Cassidy IL, Scruggs JT, & Behrens S. Design of electromagnetic energy harvesters for large-scale structural vibration applications. In *Active and Passive Smart Structures and Integrated Systems 2011*; 7977: 253-263. <https://doi.org/10.1117/12.880639>
- [7] Goldner RB, Zerigian P, & Hull JR. A preliminary study of energy recovery in vehicles by using regenerative magnetic shock absorbers. *SAE transactions* 2001: 53-59. <https://doi.org/10.4271/2001-01-2071>
- [8] Zhang Y, Huang K, Yu F, Gu Y, & Li D. Experimental verification of energy-regenerative feasibility for an automotive electrical suspension system. In *2007 IEEE international conference on vehicular electronics and safety 2007*: 1-5.
- [9] Ali MKA, Xianjun H, Abdelkareem MA, Gulzar M, & Elsheikh AH. Novel approach of the graphene nanolubricant for energy saving via anti-friction/wear in automobile engines. *Tribology International* 2018; 124: 209-229. <https://doi.org/10.1016/j.triboint.2018.04.004>
- [10] Wang H, Jasim A, & Chen X. Energy harvesting technologies in roadway and bridge for different applications-A comprehensive review. *Applied energy* 2018; 212: 1083-1094. <https://doi.org/10.1016/j.apenergy.2017.12.125>
- [11] Ali MKA, Fuming P, Younus HA, Abdelkareem MA, Essa FA, Elagouz A, & Xianjun H. Fuel economy in gasoline engines using Al₂O₃/TiO₂ nanomaterials as nanolubricant additives. *Applied energy* 2018; 211: 461-478. <https://doi.org/10.1016/j.apenergy.2017.11.013>
- [12] Zhang Y, Guo K, Wang D, Chen C, & Li X. Energy conversion mechanism and regenerative potential of vehicle suspensions. *Energy* 2017; 119: 961-970. <https://doi.org/10.1016/j.energy.2016.11.045>
- [13] Pancharoen K, Zhu D, & Beeby SP. Temperature dependence of a magnetically levitated electromagnetic vibration energy harvester. *Sensors and Actuators A: Physical* 2017; 256: 1-11. <https://doi.org/10.1016/j.sna.2017.01.011>
- [14] Zhao D. Waste thermal energy harvesting from a convection-driven Rijke-Zhao thermo-acoustic-piezo system. *Energy conversion and management* 2013; 66: 87-97. <https://doi.org/10.1016/j.enconman.2012.09.025>
- [15] Pugi L, Pagliai M, Nocentini A, Lutzemberger G, & Pretto A. Design of a hydraulic servo-actuation fed by a regenerative braking system. *Applied Energy* 2017; 187: 96-115. <https://doi.org/10.1016/j.apenergy.2016.11.047>
- [16] Itani K, De Bernardinis A, Khatir Z, & Jammal A. Comparative analysis of two hybrid energy storage systems used in a two front wheel driven electric vehicle during extreme start-up and regenerative braking operations. *Energy Conversion and Management* 2017; 144: 69-87. <https://doi.org/10.1016/j.enconman.2017.04.036>
- [17] Li L, Zhang Y, Yang C, Yan B, & Martinez CM. Model predictive control-based efficient energy recovery control strategy for regenerative braking system of hybrid electric bus. *Energy conversion and management* 2016; 111: 299-314. <https://doi.org/10.1016/j.enconman.2015.12.077>
- [18] Wei C, & Jing X. A comprehensive review on vibration energy harvesting: Modelling and realization. *Renewable and Sustainable Energy Reviews* 2017; 74: 1-18. <https://doi.org/10.1016/j.rser.2017.01.073>
- [19] Zuo L, & Tang X. Large-scale vibration energy harvesting. *Journal of intelligent material systems and structures* 2013; 24(11): 1405-1430. <https://doi.org/10.1177/1045389X13486707>

- [20] Zhang Z, Zhang X, Chen W, Rasim Y, Salman W, Pan H, & Wang C. A high-efficiency energy regenerative shock absorber using supercapacitors for renewable energy applications in range extended electric vehicle. *Applied Energy* 2016; 178: 177-188. <https://doi.org/10.1016/j.apenergy.2016.06.054>
- [21] Karnopp D. Permanent magnet linear motors used as variable mechanical dampers for vehicle suspensions. *Vehicle System Dynamics* 1989; 18(4): 187-200. <https://doi.org/10.1080/00423118908968918>
- [22] Suda Y, Nakadai S, & Nakano K. Hybrid suspension system with skyhook control and energy regeneration (development of self-powered active suspension). *Vehicle system dynamics* 1998; 29(S1): 619-634. <https://doi.org/10.1080/00423119808969590>
- [23] Goldner RB, Zerigian P, & Hull JR. A preliminary study of energy recovery in vehicles by using regenerative magnetic shock absorbers. *SAE transactions* 2001: 53-59. <https://doi.org/10.4271/2001-01-2071>
- [24] Ebrahimi B, Khamesee MB, & Golnaraghi MF. Feasibility study of an electromagnetic shock absorber with position sensing capability. In 2008 34th Annual Conference of IEEE Industrial Electronics 2008: 2988-2991. <https://doi.org/10.1109/IECON.2008.4758436>
- [25] Zuo L, Scully B, Shestani J, & Zhou Y. Design and characterization of an electromagnetic energy harvester for vehicle suspensions. *Smart Materials and Structures* 2010; 19(4): 045003. <https://doi.org/10.1088/0964-1726/19/4/045003>
- [26] Martins I, Esteves J, Marques GD, & Da Silva FP. Permanent-magnets linear actuators applicability in automobile active suspensions. *IEEE Transactions on vehicular technology* 2006; 55(1): 86-94. <https://doi.org/10.1109/TVT.2005.861167>
- [27] Chen C, & Liao WH. A self-sensing magnetorheological damper with power generation. *Smart Materials and Structures* 2012; 21(2): 025014. <https://doi.org/10.1088/0964-1726/21/2/025014>
- [28] Sapiński B. Vibration power generator for a linear MR damper. *Smart Materials and Structures* 2010; 19(10): 105012. <https://doi.org/10.1088/0964-1726/19/10/105012>
- [29] Gupta A, Jendrzeczyk JA, Mulcahy TM, & Hull JR. Design of electromagnetic shock absorbers. *International Journal of Mechanics and Materials in Design* 2006; 3: 285-291. <https://doi.org/10.1007/s10999-007-9031-5>
- [30] Huang K, Zhang Y, & Yu F. Predictive controller design for electromagnetic suspension based on mixed logical dynamical model. *Journal of Vibration and Control* 2012; 18(8): 1165-1176. <https://doi.org/10.1177/1077546311409609>
- [31] Avadhany S, Abel P, Tarasov V, & Anderson Z. U.S. Patent No. 8,376,100. Washington, DC: U.S. Patent and Trademark Office 2013.
- [32] Choi SB, Seong MS, & Kim KS. Vibration control of an electrorheological fluid-based suspension system with an energy regenerative mechanism. *Proceedings of the Institution of Mechanical Engineers, Part D: Journal of Automobile Engineering* 2009; 223(4): 459-469. <https://doi.org/10.1243/09544070JAUTO968>
- [33] Zhang PS. Design of electromagnetic shock absorbers for energy harvesting for energy harvesting from vehicle suspensions (Doctoral dissertation, The Graduate School, Stony Brook University: Stony Brook, NY.) 2010.
- [34] Li Z, Zuo L, Kuang J, & Luhrs G. Mechanical motion rectifier based energy-harvesting shock absorber. In *International Design Engineering Technical Conferences and Computers and Information in Engineering Conference* 2012; 45059: 595-604. <https://doi.org/10.1115/DETC2012-71386>
- [35] Howells CA. Piezoelectric energy harvesting. *Energy Conversion and Management* 2009; 50(7): 1847-1850. <https://doi.org/10.1016/j.enconman.2009.02.020>
- [36] Ju S, & Ji CH. Impact-based piezoelectric vibration energy harvester. *Applied Energy* 2018; 214: 139-151. <https://doi.org/10.1016/j.apenergy.2018.01.076>
- [37] Tiwari S, Singh MK, & Kumar A. Regenerative Shock Absorber: Research Review.

- [38] Wang Z, Zhang T, Zhang Z, Yuan Y, & Liu Y. A high-efficiency regenerative shock absorber considering twin ball screws transmissions for application in range-extended electric vehicles. *Energy and Built Environment* 2020; 1(1): 36-49. <https://doi.org/10.1016/j.enbenv.2019.09.004>
- [39] Okpalike C, Okeke FO, Ezema EC, Oforji PI, & Igwe AE. Effects of renovation on ventilation and energy saving in residential building. *Civil engineering journal* 2022; 7: 124-134. <https://doi.org/10.28991/CEJ-SP2021-07-09>
- [40] Tahiri FE, Chikh K, & Khafallah M. Optimal management energy system and control strategies for isolated hybrid solar-wind-battery-diesel power system. *Emerging Science Journal* 2021; 5(2): 111-124. <https://doi.org/10.28991/esj-2021-01262>
- [41] Laabid A, Saad A, & Mazouz M. Integration of Renewable Energies in Mobile Employment Promotion Units for Rural Populations. *Civil Engineering Journal* 2022; 8(7): 1406-1434. <https://doi.org/10.28991/CEJ-2022-08-07-07>
- [42] Li P, & Zuo L. Influences of the electromagnetic regenerative dampers on the vehicle suspension performance. *Proceedings of the Institution of Mechanical Engineers, Part D: Journal of Automobile Engineering* 2017; 231(3): 383-394. <https://doi.org/10.1177/0954407016639503>
- [43] Zhang H, Guo X, Xu L, Hu S, & Fang Z. Parameters analysis of hydraulic-electrical energy regenerative absorber on suspension performance. *Advances in Mechanical Engineering* 2014; 6: 836502. <https://doi.org/10.1155/2014/836502>
- [44] Yu L, Huo S, Xuan W, & Zuo L. Assessment of ride comfort and braking performance using energy-harvesting shock absorber. *SAE International Journal of Passenger Cars-Mechanical Systems* 2015; 8(2015-01-0649): 482-491. <https://doi.org/10.4271/2015-01-0649>

Blank Page



Research Article

Tensile and compressive mechanical properties of ZA27/ molybdenum disulfide, metal matrix composite

Mohamed Kafeel Delvi ^{*1,a}, K Mohamed Kaleemulla ^{2b}

¹Mechanical Eng. Dept., Bearys Inst.of Technology (Affiliated to VTU Belgavi) Mangalore, Karnataka, India

²Mechanical Eng. Dept., University B.D.T. College of Eng. (Constituent College of VTU Belgavi) Davangere, Karnataka, India.

Article Info

Abstract

Article history:

Received 12 Nov 2022

Accepted 24 Mar 2023

Keywords:

ZA 27 alloy;

Molybdenum disulfide

(MoS₂);

SEM;

The present investigation aims to study the mechanical properties of ZA-27 alloy/ Molybdenum disulfide composites containing Molybdenum disulfide (MoS₂) particles of size 40 μm. 1% and 2% of molybdenum disulfide are reinforced with ZA 27 alloy (which mainly consists of Aluminium 27%, Copper 0.5%, Tin 1-2% balance is Zinc) through the stir casting method. In this method, MoS₂ particles are poured into the molten ZA 27 alloy, for the uniform distribution of the particle stirrer used. The results of the present investigation showed that as MoS₂ composition increased, there were significant monotonic increases in the elastic load strength, plastic load strength, ultimate tensile strength (UTS) and compressive strength of MoS₂-reinforced ZA27 alloy as compared to unreinforced ZA 27 alloy. The present work gives explanations for these obtained results with the help of Scanning Electron Microscope (SEM) images.

© 2023 MIM Research Group. All rights reserved.

1. Introduction

Among zinc-based cast alloys, the ZA family has enjoyed great popularity in recent years. Compared to aluminium-based alloys, The increased strength and lower casting temperature of ZA alloys are significant advantages [1,2,3]. It has been proposed that adding silicon carbide reinforcement to zinc alloys will increase the alloys' strength-to-weight ratio and dimensional stability while taking advantage of their low processing temperatures and low cost [4]. Similar to graphite, Alumina, and silicon carbide, MoS₂ is a reinforcing material and can likely be used to strengthen zinc-based matrixes [5]. In recent years, remarkable work has happened on MoS₂ as reinforced material in the metal matrix composite. Molybdenum-reinforced material exhibits good anti-sizing characteristics, low friction and less wear [6,7,8]. The MoS₂ projected out from the specimen during pin-on-disc wear testing, from the tribo layer which prevents wear loss of the specimen, as result composite presumably imparts enhanced tribological properties, in other words, it acts as a solid lubricant. MoS₂ particles of sizes ranging from 1 μm to 100 μm are generally used for dry lubricating purposes. It is also used in an automotive engine, coating rifle barrels to easily pass bullets, etc. The presence of MoS₂ in the matrix increases the spreadability of the oil on the contact surface, thereby reducing the tendency to score or scratch or seize as result it is also used as a solid lubricant [9]. The zinc-aluminium alloy ZA-27 with the chemical composition mentioned in the abstract was used as the matrix material in this study. Among the various ZA alloy series, ZA 27 alloy has the highest ductility and strength, excellent wear properties, and good machineability and bearing properties. ZA 27 alloy is used for medium load, low speed and moderate temperature applications such as bearings and gears. The stir casting method is used in this work, in which MoS₂ particles with sizes

*Corresponding author: rulerkafeel@yahoo.co.in

^a orcid.org/0000-0002-0349-3926; ^b orcid.org/0000-0002-7450-7782

DOI: <http://dx.doi.org/10.17515/resm2022.583me1112>

Res. Eng. Struct. Mat. Vol. 9 Iss. 3 (2023) 709-718

ranging from 40 μm to 50 μm are preheated and added to molten ZA 27 alloy that has been heated above its melting temperature. The mechanical stirrer is used for the proper mixing of matrix and reinforcement material. The elastic strength, Plastic strength, ultimate tensile strength (UTS) and ultimate compressive strength of the composite material and unreinforced ZA 27 alloy are studied. The present investigation aims to study these properties in the ZA 27 alloy/MoS₂ particle composites.

2. Experimental Procedure

2.1. Preparation of Composite

To prepare tensile and compressive specimens, the stir casting method has been adopted [10]. The measured quantity of ZA 27 alloy was placed in the furnace's crucible. The crucible is heated at a constant temperature of 600°C until the solid ZA27 changes to a liquid phase. The molten matrix is brought to a temperature of 485-490°C at which the calculated amount of (1% weight of taken ZA 27) preheated MoS₂ is poured. At this temperature, the mixing of both molten matrix and MoS₂ is carried out at the speed of 320-340 rpm with the help of a mechanical stirrer for 5 minutes. The molten composite is poured into a circular preheated mould of cast iron. The molten metal matrix composite inside the mould allowed it to solidify at room temperature. A casted circular specimen was taken out from the mould. The same procedure was repeated to prepare ZA 27 alloy reinforced with 2% Molybdenum disulfide, but instead of 1% weight of ZA 27 alloy, 2% weight of ZA 27 alloy, MoS₂ is used. The Same procedure repeats to prepare base ZA 27 alloy.

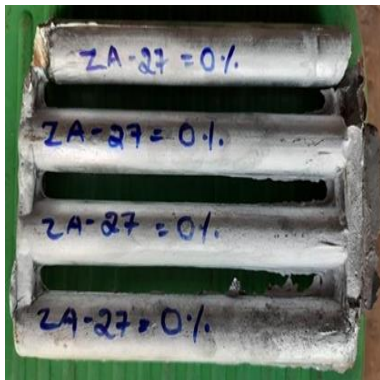


Fig. 1 ZA27 without MoS₂ moulded specimen

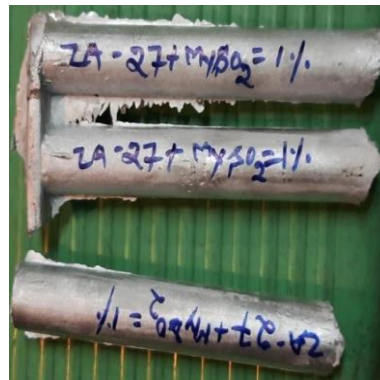


Fig. 2 ZA 27 with 1% MoS₂ moulded specimen

2.2. Preparation of Tensile and Compressive Specimens

Specimens obtained after removal from the mould are shown in Fig. 1 and Fig. 2 From these figures, it has been observed that moulded specimens are irregular in shape, and are surrounded by an oxide scale. The size of the specimen in terms of length and diameter is greater than the required dimension. All moulded specimens are machined and turned as per the requirement of ASTM (American Society for testing material) Standards. For the tensile test, specimens are prepared as per ASTM E 8 standard [11], the specification of the tensile specimen as per ASTM E8 is given in Table 1. schematic representation of the tensile specimen is given in Fig. 3 Similarly, for the compressive test, moulded specimens are machined as per the ASTM standard E 9 which is the ASTM standard for compressive test [12,13]. The compressive specimen should be a 1.5 to 2 length-to-diameter ratio as per

ASTM standard E9 A schematic representation of the compressive specimen is given in Fig. 5 and the prepared compressive specimen as per ASTM standard E9 is shown in Fig. 6.

Table 1. Specification of tensile specimen as ASTM standard E8

Specification	Dimension(mm)
G—Gauge length	62.5 + 0.1
D—Diameter	12.5 + 0.2
R—Radius of fillet	10
A—Length of reduced section	75



Fig. 4 Prepared tensile specimen as per ASTM standard E8

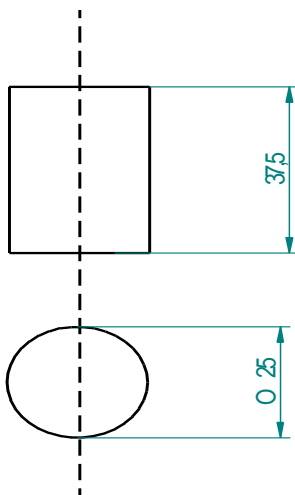


Fig. 5 Schematic representation of compressive specimen as per ASTM standard E 9



Fig. 6 Prepared compressive specimen asper ASTM standard E 9

2.3. Procedure to Perform the Tensile and Compressive Test

At room temperature, both tensile and compressive tests are conducted using the universal testing machine. The standard procedure was followed to conduct both tensile and compressive tests.

- The tensile specimen is held between the jaws of the UTM machine in such a way that the test specimen is held by both jaws perfectly

- The extensometer is fixed within the gauge length marked on the specimen dial of the extensometer is adjusted and the dial of the machine scale is set to zero and further load indicator also is set to zero.
- A suitable increment of load selected is applied so that corresponding elongation is measured in the case of a tensile specimen and reduction is measured in the case of the compressive specimen from dial gauge by keeping the speed of the machine uniform to record all displacement points for applied load till break or failure of specimen takes place.
- From each composition, 3 tensile specimens are tested, and from the average values of ultimate tensile strength, young's modulus and plasticity are represented in form of a graph. Similarly, from each composition, three compressive specimens are tested for compressive strength and the average values of the ultimate compressive specimen is calculated.
- A gradual load in KN is applied in UTM for both tensile and compressive and the corresponding displacement in mm is recorded. Based on the results obtained load v/s displacement graph was plotted to analyze the mechanical properties of the specimen both for tension and compression [13,14].

3. Result and Discussion

Young's modulus in terms of elastic load, ductility (in terms of plastic load) or plastic load ultimate tensile strength (UTS) in terms of breaking load and ultimate compressive strength in terms of breaking load are determined for the ZA 27 alloy and ZA 27 alloy reinforced with 1% and 2% MoS₂ with help of a universal testing machine. For each composition, three tensile and compressive specimens are tested to find out the tensile and compressive strength of the specimen respectively. The average value of three tests is taken for each composition. The repeatable results are obtained. The individual results do not deviate more than 5% from their mean value. All mentioned parameter results are represented graphically from Fig. 7 to Fig. 10

3.1 Elastic Behavior

Average three values of elastic loads are plotted for both ZA 27 base alloy and 1%, as well as 2% MoS₂, reinforced ZA27 alloy as shown in Fig. 7. Generally, young's modulus is defined, as stress is proportional to strain within the elastic limit. the specimen comes to its original position after the removal applied load, that load is called elastic load. In the current study, for the applied load, if zero deflection is shown on the extensometer, that load is referred to as elastic load. From the plotted graph shown in Fig. 7, it can be seen that the elastic load range increases for an increase in the quantity of MoS₂ in ZA 27 base alloy. It can be observed from Fig. 7, ZA 27 reinforced with 1% of MoS₂ has 3 times elastic strength compared to the base ZA 27 alloy. Similarly, ZA 27 reinforced with 2% of MoS₂ showed four times the elastic load applied as compared to unreinforced ZA 27 alloy.

3.2. Plastic Behavior

Average three values of plastic loads are plotted for both ZA 27 base alloy and 1%, as well as 2% of MoS₂, reinforced ZA27 alloy as shown in Fig 8. load at which specimen does not return to its original size after removal applied load, such load is called plastic load. plastic load of ZA 27 base alloy and ZA 27 reinforced with 1% and 2% of MoS₂ are given in Fig. 8. In the present research work, the load at which the specimen starts to elongate which can be indicated through deflection in the extensometer which is fixed to the tensile specimen during tensile testing. Such load is referred to as plastic load. It can be seen from Fig. 8, ZA 27 alloy has experienced a plastic load of around 4000N, ZA 27 alloy reinforced with 1% of MoS₂ has experienced a plastic load of around 7900N which is twice that of the base ZA 27 alloy. ZA 27 alloys reinforced with 2% MoS₂ have experienced a plastic load of around

9800N, which is around 3 times greater than ZA 27 base alloy. This substantial increase in ductility is probably because zinc, with its compact hexagonal crystalline structure, is a relatively brittle material in the solid state, while added MoS₂, as an effective solid lubricant, facilitates the movement of grains, along with the slide planes, a similar observation made while graphite is added instead of MoS₂[15].

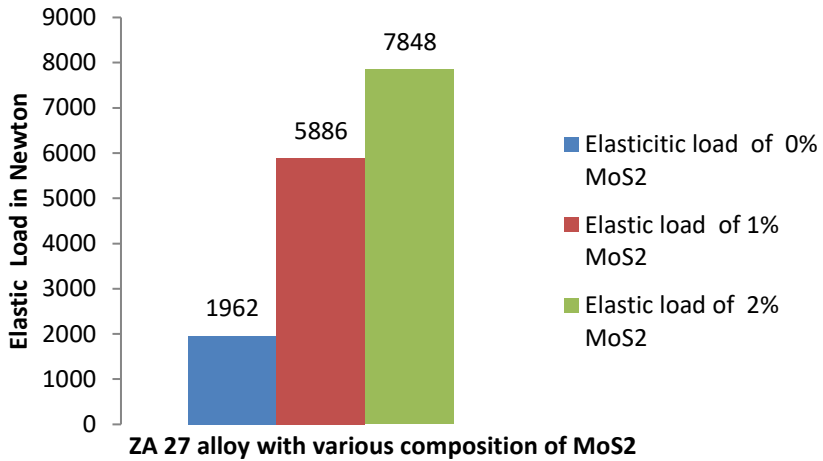


Fig. 7 Change of elastic behaviour of ZA 27 alloy with the addition of MoS₂ particle

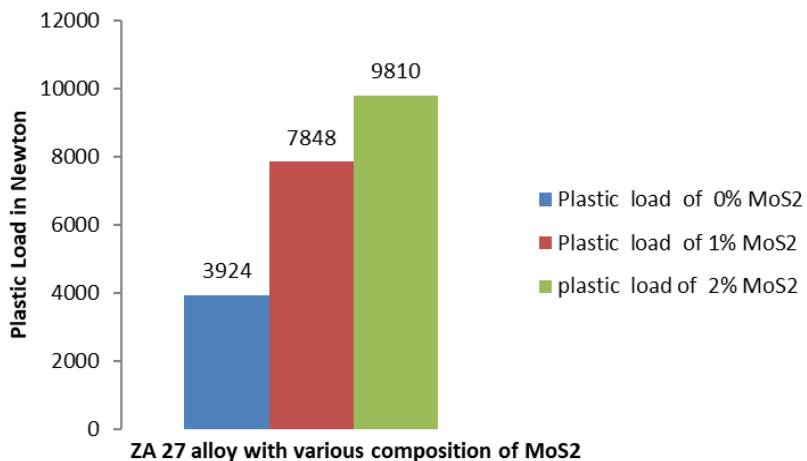


Fig. 8 Change of plastic behaviour of ZA 27 alloy with the addition of MoS₂ particle

3.3. Ultimate Tensile Strength

Average three values of ultimate tensile loads are plotted for both ZA 27 base alloy and 1%, as well as 2% of MoS₂, reinforced ZA27 alloy as shown in Fig. 9. Ultimate tensile load is the maximum load applied to a specimen during tensile testing, at which the testing specimen will break. The ultimate tensile load of ZA 27 base alloy and ZA 27 reinforced with 1% and 2% of MoS₂ are given in Fig. 9. In the present work, the load at which the specimen breaks, that load is referred as the ultimate tensile load. It can be observed from Fig. 9, ZA 27 alloy

is broken at a load of around 22500N, ZA 27 reinforced with 1% MoS₂ is broken at a load of around 25500, and ZA 27 alloy reinforced with 2% MoS₂ is broken around 28400N. It is observed from Fig. 9 that the Ultimate tensile strength of ZA 27 alloy increased with an increase in the composition of MoS₂. This increase in tensile strength may be due to the MoS₂ particles acting as barriers to dislocations in the microstructure as a similar observation made by other researchers. [16,17,18]

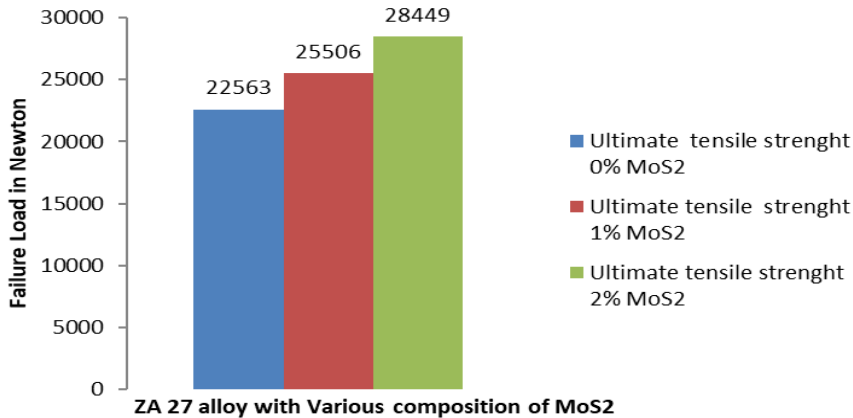


Fig. 9 Ultimate tensile strength of ZA 27 alloy with addition of MoS₂ particle

3.4 Ultimate Compressive Strength

Fig. 10 is a graph showing the effect of MoS₂ content on the compressive strength of cast ZA-27 base alloy. Effects of elasticity, plasticity and ultimate tensile strength of ZA 27 alloy and ZA 27 reinforced with 1% and 2% of MoS₂ are discussed in the previous section. It can be seen from Fig. 10 that as the MoS₂ content increases, the compressive strength of the composite material increases significantly. As the MoS₂ content is increased from 0% to 2%, the compressive strength increases by about 45%. As in the case of UTS described above, this increase in compressive strength may be due to the MoS₂ particles acting as barriers to dislocations in the microstructure as the same thing was observed by the other researcher for graphite reinforcement, the same explanation can be given as explained for ultimate tensile strength [16,17,18].

3.5 SEM Analyses

The SEM images of the middle portion of a tested surface of ZA 27 alloy, ZA 27 alloy reinforced with 1% MoS₂ and ZA 27 reinforced with 2% MoS₂ are shown in Fig. 11(a, b, c). All SEM images are taken at the magnification of 200X. It can be seen in Fig. 11(a), a relatively large void is formed on the surface of the tensile tested specimen for the base ZA27 alloy. A weak spot within the specimen will create a small internal void when a tensile load is applied. As the load rises, this void will progressively get bigger. The material cross-section area cannot withstand high loads when the internal resistance of the specimen exceeds the applied load and the specimen ultimately fails by ductile fracture as a result of significant plastic deformation and the formation of a micro void. After reinforcement of 1% MoS₂ in ZA 27 alloy, there is a change in the size of the void can be seen in Fig. 11(b). It showed that due to the addition of MoS₂ particle, the size of the void decreased between ZA 27 particles, and the more refined structure of ZA 27 alloy can be seen from the same Fig. 11(b), further increase in the percentage of MoS₂ to 2% further reduction in size and depth of void of ZA 27 alloy can be seen in Fig. 11 (c). So, SEM images give more support to

the interpretation given for all tensile results. To check the presence and distribution of MoS₂ inside the ZA 27 alloy EDX analysis is carried out which is shown in Fig. 12.

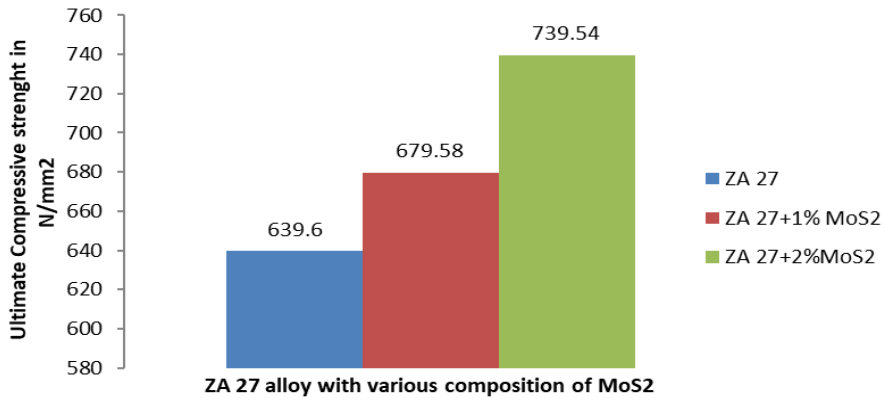
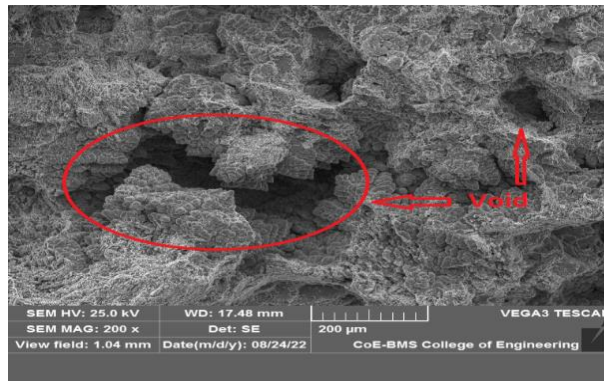
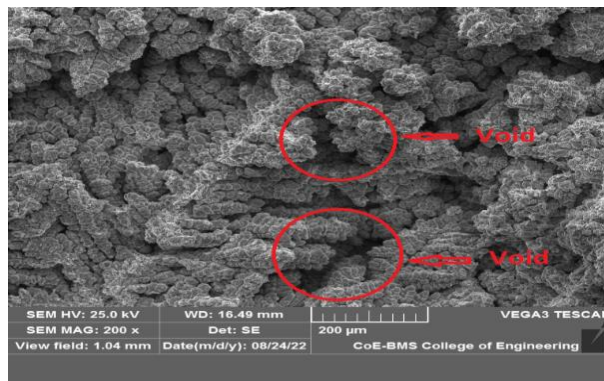


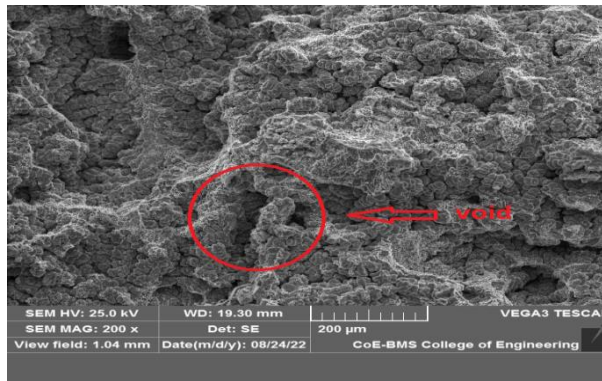
Fig. 10 Ultimate compressive strength of ZA 27 alloy and its MoS₂ reinforcement



(a) SEM image of ZA 27 alloy without reinforcement



(b) SEM image of ZA 27 alloy with 1% of MoS₂



(c) SEM image of ZA 27 alloy with 2% of MoS₂

Fig. 11 SEM images

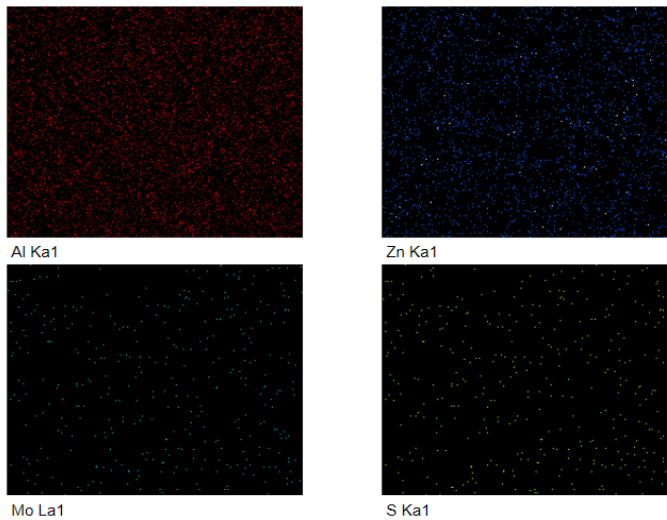


Fig. 12 EDX image of the distribution of MoS₂ in ZA 27 base alloy

4. Conclusions

The ZA 27 alloy possesses excellent physical, mechanical and tribological properties such as low weight, high strength, excellent foundry castability fluidity, good machining properties, low initial cost, and environmentally- friendly as compared to plastics, cast iron, or even steels when being applied under conditions of high mechanical loads and moderate sliding speeds under moderate operation temperatures. Many researchers tried to improve its mechanical, tribological and other physical properties through reinforcing it with various reinforced materials such as silicon carbide, graphite, zircon, Manganese, Magnesium, Aluminium oxide, short glass fibre, Titanium and titanium diboride etc. Some Researchers tested the same ZA 27 alloy by subjecting it to various heat treatment processes to check the change in its mechanical properties. In the present investigation, important mechanical properties such as tensile strength and compressive strength of ZA 27 alloy and ZA 27 alloy reinforced with one percentage (1%) and two per cent (2%) of MoS₂ were investigated. To get repeatability, each composition is tested three (3) times.

The comparative studies were carried out with unreinforced ZA 27 base alloy with ZA 27 alloy reinforced with 1% and 2% MoS₂ particles. Mechanical analyses or tensile and compressive analyses indicated that the presence of the MoS₂ particles in the Zinc aluminium alloy remarkably changed through reinforcing 1% and 2% amounts of MoS₂. It was found that increasing the MoS₂ content within the ZA-27 matrix results in significant increases in the elasticity or elastic strength, plasticity or plastic strength, ultimate tensile strength and ultimate compressive strength. This change in the result is completely attributed to the presence of MoS₂ inside the ZA 27 alloy. Scanning Electron Microscopic images showed the changes in surface structure and decrease in the size of voids due to the addition of MoS₂ particles and the Energy Dispersive X-ray (EDX) image showed the distribution of reinforced particles inside the ZA 27 alloy. Both SEM and EDX images also support the explanation of the positive effect of MoS₂ particles in the Mechanical properties of ZA 27 alloy. Compressive strength is increased as a result of MoS₂ particles acting as barriers to dislocations occurring due to the application of compressive load. So, it can be concluded that MoS₂ particles positively influence the tensile and compressive properties of ZA 27 alloy. The good mechanical characteristics of MoS₂ and their adequate facial interaction with the matrix surface can be used to explain this behaviour.

References

- [1] Babic M, Slobodan M, Džunic D, Jeremic B, Ilija B. Tribological Behavior of Composites Based on ZA-27 Alloy Reinforced with Graphite Particles. Tribol. Lett. 2010, 37 (2), 401-410. <https://doi.org/10.1007/s11249-009-9535-2>
- [2] Mitrović S, Babić M, Bobić I. ZA- 27 Alloy Composites Reinforced with Al₂O₃ Particles. Tribol. Ind. 2007, 29 (3-4), 35-41.
- [3] Babić M, Mitrović S, Ninković R. Tribological Potencial of Zinc- Aluminium Alloys Improvement. Tribol. Ind. 2009, 31 (1-2), 15-28.
- [4] Auras R, Schvezov C. Wear Behavior , Microstructure , and Dimensional Stability of As-Cast Zinc-Aluminum / SiC (Metal Matrix Composites) Alloys. 2004, 35 (May),1579-1590. <https://doi.org/10.1007/s11661-004-0264-8>
- [5] Daniel AA, Murugesan S, Sukkasamy S, Coimbatore C. Dry Sliding Wear Behaviour of Aluminium 5059 / SiC / MoS₂ Hybrid Metal Matrix Composites 2 . Experimental Work. 2017, 20 (6), 1697-1706. <https://doi.org/10.1590/1980-5373-mr-2017-0009>
- [6] Delvi MK, Kaleemulla KM. Dry Sliding Wear Behaviour of ZA27/MoS₂ Metal Matrix Composite. Adv. Sci. Technol. Eng. Syst. J. 2021, 6 (3), 263-270. <https://doi.org/10.25046/aj060329>
- [7] Delvi MK, Kaleemulla KM. Sliding Wear Behaviour of Al 7039 / MoS₂ Metal Matrix Composite. Int. J. Sci. Technol. Eng. Manag. VTU Publ. 2021, 5844 (1), 8.
- [8] Senthil Kumar P, Manisekar K, Subramanian E, Narayanasamy R. Dry Sliding Friction and Wear Characteristics of Cu-Sn Alloy Containing Molybdenum Disulfide. Tribol. Trans. 2013, 56 (5), 857-866. <https://doi.org/10.1080/10402004.2013.806685>
- [9] Farr JPG. MoS₂in Lubrication. a Review. wear 1975, 35, 1-22. [https://doi.org/10.1016/0043-1648\(75\)90137-4](https://doi.org/10.1016/0043-1648(75)90137-4)
- [10] Amirkhanlou S, Niroumand B. Synthesis and Characterization of 356-SiC p Composites by Stir Casting and Compocasting Methods. Trans. Nonferrous Met. Soc. China 2010, 20,788-793.
- [11] E8M ASTM. Standard Test Methods for Tension Testing of Metallic Materials [Metric]. ASTM Stand. 1989, 02, 1-11.
- [12] ASTM E 9. Standard Test Methods of Compression Testing of Metallic Materials at Room Temperature. Annu. B. ASTM Stand. 2000, 03.01(Reapproved), 9.
- [13] Suryanarayana AVK. Testing of Metallic Materials, 2nd edition.; B S publication: Hyderabad, India, 2013.

- [14] Sajaniemi V, Karakoç A, Paltakari J. Mechanical and thermal behaviour of natural fiber polymer composites without compatibilizers. *Res. Eng. Struct. Mater.*, 2020; 6(1): 63-73. <https://doi.org/10.17515/resm2019.124ma0308>
- [15] Rohatgi PK, Ray S, Liu Y. Tribological Properties of Metal Matrix-Graphite Particle Composites. *Int. Mater. Rev.* 1992, 37 (1), 129- 152. <https://doi.org/10.1179/imr.1992.37.1.129>
- [16] Ramesh A, Prakash JN, Gowda ASSS, Appaiah S. Comparison of the Mechanical Properties of AL6061/Albite and AL6061/Graphite Metal Matrix Composites. *J. Miner. Mater. Charact. Eng.* 2009, 08 (02), 93-106. <https://doi.org/10.4236/jmmce.2009.82009>
- [17] Seah KHW. Mechanical Particulate Properties Composites of Cast ZA = 27 / Graphite. 1995, 16 (5), 1-5. [https://doi.org/10.1016/0261-3069\(96\)00001-5](https://doi.org/10.1016/0261-3069(96)00001-5)
- [18] Demircan O, Ansaroudi NR, Uzunoglu FB. Tensile and flexural properties of MWCNT-COOH and hBN integrated polyamide 66/short glass fiber composites. *Res. Eng. Struct. Mater.*, 2022; 8(1): 1-18. <https://doi.org/10.17515/resm2021.334me0822>



Research Article

Kinetic evaluation of the stabilization efficiency of the phosphite and urea derivative based stabilizers against epoxy based stabilizers on the thermal degradation of plasticized poly (vinyl chloride)

Ayşe Pınar Tüzüm Demir

Usak University, Faculty of Engineering, Chemical Engineering Department, Usak, TR64200, Turkey

Article Info

Article history:

Received 24 Apr 2023

Accepted 14 Aug 2023

Keywords:

Poly (vinyl chloride) (PVC);

Epoxy stabilizers;

Phenyl stabilizers;

Plasticizer migration;

Thermal stability;

Element Method

Abstract

Poly(vinyl chloride) (PVC) is difficult to process because of its low thermal stability. Therefore, stabilizers are used. Epoxidized vegetable oils are environmentally friendly stabilizers, but they degrade at high temperatures, causing the polymer to become brittle and discolored. Also, unreacted double bonds in it can reduce the compatibility between plasticizer and PVC, causing greater migration of plasticizer from PVC. This study focuses on the evaluation of the effect of phosphite and urea derivative stabilizers against epoxy stabilizers on the thermal degradation of PVC and plasticizer diffusion from PVC. Plastisols were prepared by mixing plasticizers (di-octyl terephthalate and di-2-ethyl-hexyl phthalate), primary, and secondary stabilizers (epoxidized soybean oil (EPSO), epoxidized linseed oil (ELO), tri-phenyl phosphite (TPP) and diphenyl urea (DPU)) into PVC. Plastigels were cured and thermally aged. Thermal degradation in terms of color changes, oxidation index, and polyene concentration was investigated by using colorimetry, Fourier Transform Infrared Spectroscopy (FTIR) and Ultraviolet (UV)-visible spectroscopy, respectively. As a result, phosphite and urea derivative stabilizers provided better long-term stability than the EPSO. However, EPSO was more affected by the plasticizer migration than the others. An effort has been made in this study to shed light on the improvement of the thermal stability of PVC by means of non-toxic secondary stabilizers.

© 2023 MIM Research Group. All rights reserved.

1. Introduction

Poly(vinyl chloride) (PVC) is amongst the most widely used polymers worldwide since it is unique properties and low cost [1, 2]. However, PVC is difficult to process due to the high melt viscosity and rigid chain structure caused by polar chlorine atoms. As a result, the processing temperature increases and its thermal stability decreases [3-5]. Before its processing temperature reached, it will release hydrogen chloride (HCl) gas resulting in a performance decline [6]. The decomposition product, HCl, accelerates the degradation and plays a role in the autocatalytic process [7]. Degraded PVC is characterized by intense discoloration caused by the formation of conjugated double bonds (polyenes). When PVC has 4, 6, 8, and 11 polyenes in its chain, its color appears light yellow, yellow, orange, and red, respectively [8-10]. This problem can be solved by the use of plasticizers and thermal stabilizers [5, 11]. Stabilizers provide thermal stability by the absorption and neutralization of HCl gas, and thus prevents or delays the degradation process [7]. Conventional primary stabilizers such as calcium/zinc (Ca/Zn) stabilizers are widely used for thermal stabilization. However, it causes some problems in the long-term stability of PVC due to zinc chloride ($ZnCl_2$) formed during the process and can catalyze the

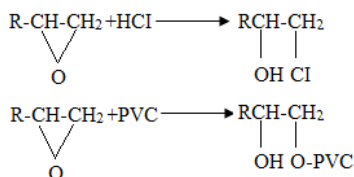
*Corresponding author: pinar.demir@usak.edu.tr

orcid.org/0000-0002-0822-5728

DOI: <http://dx.doi.org/10.17515/resm2023.749ma0424>

Res. Eng. Struct. Mat. Vol. 9 Iss. 3 (2023) 719-742

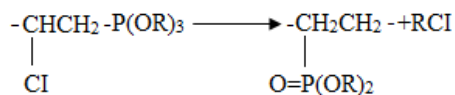
degradation of PVC. This causes a sudden zipper dehydrochlorination [6, 12]. When primary stabilizers and secondary stabilizers are used together, their stabilizing effects increase [6]. Ca/Zn stabilizers are supported by epoxidized vegetable oils as secondary stabilizers or by co-stabilizers because of their non-toxic structures [11, 13, 14]. Epoxidized vegetable oil based from renewable bio-resources, which are epoxidized triglyceride oils from rubber seed oil, sunflower oil, soybean oil, linseed oil, epoxidized cardanol, epoxidized triglyceride oils and oleic acid polyester with their low toxicity, they attract attention as PVC stabilizers or plasticizers [4, 5, 15]. The researches on epoxidized vegetable oils and their synergism with metal carboxylates for stabilization have been reported [3-5, 11, 16-19]. Ferrer et al. al., (2010) showed that PVC-based formulations containing different amounts of EPSO improved compatibility and thermal stability. They stated that the thermal stability of materials depends on the plasticizer concentration [11]. Karmalm et al., (2009) tested the effectiveness of EPSO as the primary plasticizer for PVC. They compared the stabilization of materials with different conventional stabilizers. They reported that the addition of traditional stabilizers for instance Ca/Zn-stearate, reduced the stability of PVC-EPSO [17]. Benaniba et al., (2003), studied PVC stabilization of epoxidized sunflower oil (ESO) with Ca/Zn stearate. They calculated the induction and dehydrochloride initial rates of dehydrochlorination before depletion of the stabilizers. The addition of this stabilizers increased the induction time and decreased the dehydrochlorination rate. The effectiveness of ESO found to depend on the amount of epoxy groups in the molecule and the high epoxy groups increased efficiency [18]. Scheme 1 represented the reaction with PVC in the presence of metal salts of epoxy thermal stabilizers [20]. Epoxy groups act as HCl scavengers and getting excellent thermal stability to PVC [5]. EPSO stabilization involves a reaction between the epoxide ring of EPSO and HCl. Then labile chlorine atoms return into the polymer chains. This reaction prevents further dehydrochlorination at high temperatures [17].



Scheme 1. Schematic representation of the reaction between epoxy thermal stabilizer with PVC in the presence of metal salts

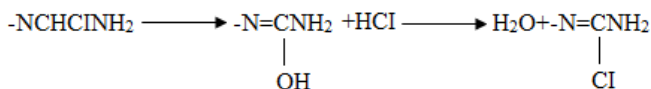
Such functional copolymers provide a strong auxiliary effect to the Ca/Zn-stabilizer system on the stabilization of PVC. This effect increasing with increasing hydroxy or epoxy group content. [13] but also problematic due to the tendency to degrade, causing the polymer to become brittle and discolored during heat aging. Also, many of vegetable oils are include of oleic, linoleic and linolenic acids containing conjugated double bonds. These oils are triglyceride mixtures formed by different unsaturated fatty acids [21]. The benefit of phosphite stabilizers is to prevent the chemical compounds resulting from chlorine disintegration, from causing color distortion and turbidity in the polymer. However, when organic phosphites used alone, they can cause metal chloride formation. Therefore, they used with metal heat stabilizers to prevent this. The most known organic phosphites are; triphenylphosphite and tris (nonylphenyl) phosphate [22]. Organic phosphites, reacts with hydroperoxides generated from the thermooxidative degradation of the polymer. The phosphite stabilizers can also act as metal-complexing agents. Therefore, phosphites classify as secondary antioxidants in these applications [23]. The effect of thermal stability

of organic phosphites showed in Scheme 2 [24]. Some phosphites increase the efficiency of other thermal stabilizers with anti-rust effect.



Scheme 2. Schematic representation of the thermal stability of organic phosphites

Urea derivatives have proven to be effective stabilizers for PVC when used with primary thermal stabilizers for PVC stabilization [25]. Phenyl urea and phenyl urea derivatives have a variety of functional groups that can interact with the evolved HCl gas released from degraded PVC. Due to their ability to form stable complexes with various metal ions, they react with metal chloride by-products formed during the thermal degradation of PVC stabilized with metallic stabilizers [19]. Urea derivatives act according to the mechanism in Scheme 3.



Scheme 3. Schematic representation of the thermal stability of α -phenylindole and urea derivatives

The presence of chlorine in PVC resin increases the interchain attraction that makes PVC rigid and stiff [26]. Plasticizers are added to resin to lowering glass transition temperature (T_g) and break up chain-chain interactions, leading to flexibility [4, 5, 26-28]. Low molecular weight monomeric plasticizers derived from phthalic acids are the most widely used plasticizers [26, 28]. Because of the high migration to contact media, some plasticizers, in particular phthalates, especially diethylhexyl phthalate (DEHP), (dioctyl phthalate, DOP), which are commonly used in PVC formulations has been questioned due to their potential toxicity risk to human health and the environment, food contaminations as well as deformation of material due to losing its flexibility [3, 4, 11, 14, 27, 28]. Therefore, many of the phthalate esters were restricted in the world are listed in the Substances of Very High Concern (SVCH) by European Chemicals Agency (ECHA). Therefore, there is a need for greener and safer alternatives [4, 5, 26, 29] or plasticizer migration must be controlled [28]. However, their plasticisation performance are similar, dioctyl terephthalate (DOTP) is less volatile than DEHP [5, 29]. DOTP are used for main fields of applications as coatings, floorings, electric connectors etc. As far as currently known, DOTP has no carcinogenic, or developmental effects [29]. As a result, PVC, is difficult to process, due to its low thermal stability. This problem is solved the use of stabilizers. Epoxidized vegetable oils are environmentally friendly but, it is problematic as it degrades at high temperatures, causing the polymer to become brittle and discolored upon thermal aging. Also, unreacted double bonds in it can reduce the compatibility between PVC and plasticizer, causing greater migration of the plasticizer from the PVC matrix to the environment. This study focuses on the evaluation of the effects of the phosphite and urea derivative stabilizers against epoxy stabilizers on the thermal degradation of plasticized-PVC (p-PVC) films and plasticizer diffusion from films. EPSO, ELSO, TPP and DPU were used as secondary stabilizers for p-PVC formulations and their thermal stabilization behaviour were investigated. The p-PVC films were prepared with DOTP and DEHP as plasticizers and their plasticizer diffusion efficiencies were investigated also. EPSO and DEHP were used for comparison at the same conditions in the

study. Thermal aging studies were carried out in an oven at 100 and 150°C up to 420 minute. This study focused on the decomposition of the films and plasticizer migration out of the films into air. Oxidation index were determined by FTIR spectroscopy. Stabilization behaviour as color changes and dehydrochlorination were investigated by colorimetry, and, UV-visible spectroscopy respectively. Diffusion coefficients of plasticizers were calculated from mass loss of the films. Conjugated double bonds (CDB) were determined by UV spectroscopy and degradation kinetics of the films were evaluated. The novelty of this study is the comparison study of the effect of phosphite and urea derivative stabilizers against epoxy stabilizers on the thermal degradation of PVC and their effect of migration of plasticizers to air from plasticized PVC composite films for use in flexible PVC cable sheath applications.

2. Materials and Methods

2.1. Materials

Emulsion-type PVC was purchased from Petkim Co., Aliğa, Izmir, Turkey. Dioctyl terephthalate (DOTP), dioctyl phthalate (DOP) ((di-2-ethyl hexyl phthalate (DEHP)), CaSt₂, ZnSt₂, epoxidized soy bean oil (EPSO), epoxidized linseed oil (ELSO), tri phenyl phosphite (TPP), diphenyl urea (DPU) were supplied by Sigma Aldrich, Germany. The additives and their molecular formulas are given in Table 1.

2.2. Methods

The experimental method mainly involves the preparation of p-PVC films by gelation of prepared plastisols, their thermal degradation under controlled conditions and the assessment of degradation and degradation kinetics by means of instrumental methods as well as the plasticizers migration and diffusion kinetics through mass loss measurements.

2.2.1 Plastisol Preparation

Plastisols were produced by mixing 60 parts of plasticizer (DOTP and DEHP), 5 parts of secondary thermal stabilizers (EPSO, ELSO, TPP and DPU), and 3 parts of Ca-Zn St₂ mixture as primary stabilizers with 100 parts of PVC, on the mass basis. Formulations of the films and their codes are given in Table 2. Samples containing EPSO and DEHP (EP-DE) were used for comparison.

2.2.2 Plastigel Preparation

P-PVC films which have 150µm thickness were drawn from plastisol and cured under the same conditions, as in our previous study [29].

2.2.3 Thermal Degradation Studies

P-PVC films were cut into about 4x4cm² pieces and were heat treated at 100 and 150°C in an oven up to 420 minutes.

2.3. Analysis Methods

2.3.1 Spectroscopic Analysis

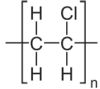
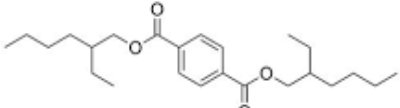
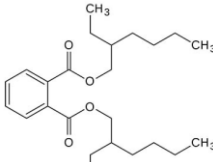
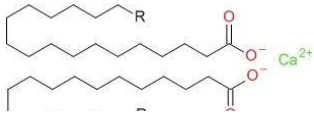
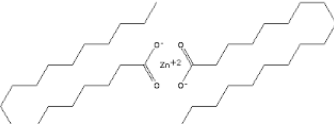
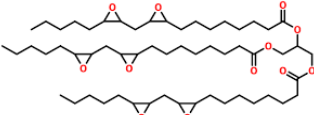
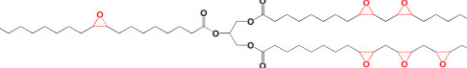
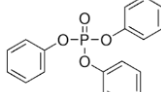
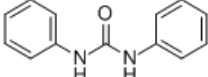
Oxidation index values were analyzed using Perkin Elmer (Spectra 100) FTIR spectrometer.

Light absorbances of the films were determined by using a Perkin Elmer (Spectra 100) UV spectrophotometer.

Raman spectra of thermally degraded p-PVC films were recorded using a WITech alpha 300R Raman Microspectrometer. Diffraction grating was used in conjunction with air-

cooled DPSS laser source excitation up to 100mW at 532nm. The Raman spectra were acquired from 500 cm⁻¹ to 3500 cm⁻¹. Raman analyzes were made by Atatürk University East Anatolia High Technology Application and Research Center, DAYTAM, Erzurum, Turkey. It has OECD ILU (GLP) conformity certificate.

Table 1. Additives used in the study

Material	Chemical Formula	Molecular Weight, g/mol	Molecular Formula
Polivinyll chloride, PVC, PETKIM Emulsion type	$-(C_2H_3Cl)_n-$	97300-110643	
Diocetyl terephthalate, DOTP	$C_{24}H_{38}O_4$	391	
Diethylhexyl phthalate, DEHP	$C_{24}H_{38}O_4$	390	
Calcium stearate, CaSt ₂	$C_{36}H_{70}O_4Ca$	607	
Zinc stearate, ZnSt ₂	$C_{36}H_{70}O_4Zn$	632.3	
Epoxidized soybean oil, EPSO (Epoxy value % 6.8-7.1)	$C_{57}H_{98}O_{12}$	975.5	
Epoxidized linseed oil, ELSO			
Triphenyl phosphite, TPP	$C_{18}H_{15}O_3P$	310.3	
Diphenyl ürea, DPU	$C_{13}H_{12}N_2O$	212.3	

2.3.2 Colorimetric Analysis

Yellowness index of the films were measured by placing the tip of the measuring head of B&W Tek Glacier X Model Color Spectrophotometer.

Table 2. Sample codes with respect to the variables as secondary thermal stabilizers and plasticisers in formulations of p-PVC plastisols

Secondary thermal stabilizer	Plasticizer/ Film codes	
	DOTP	DEHP
Epoxidized soybean oil, EPSO	EP -DO	EP-DE
Epoxidized linseed oil, ELSO	EL -DO	EL-DE
Triphenyl phosphite, TPP	TP-DO	TP-DE
Diphenyl urea, DPU	DP-DO	DP-DE

3. Theoretical

3.1. Determination of Oxidation

The oxygen diffused into the polymer during decomposition reacts with the free radicals inside, causing further oxidation. As a result, the oxidized surface layer becomes thicker. This thickening is also assessed via the oxidation index (OI), which is determined using infrared spectroscopy.

OI values were calculated by using Eq (1) considering the absorbance of carbonyl band ($C=O$) around 1720 cm^{-1} and the absorbance of a reference group of $-CH_2-$ at 1363 cm^{-1} , 1420 cm^{-1} or 2920 cm^{-1} band [9].

$$OI = \frac{A_{C=O}}{A_{ref}} = \frac{A_{[1722\text{ cm}^{-1}]}}{A_{[2920\text{ cm}^{-1}]}} \times 100 \quad (1)$$

3.2. Following of Polyene Formation by Spectroscopic Method

Thermal stabilization behaviour in terms of concentration of polyenes formed due to the released HCl during thermal treatment were determined by spectroscopic technique. Concentration of polyenes were calculated using light absorbance by UV-visible spectroscopy [30]. There is a wide absorption peak at 200-350 nm for PVC in the UV spectrum. Dehydrochlorination rate can be determine using molar absorption coefficients from the concentration of conjugated dienes in the range of 268–447 nm in the UV spectrum [9]. Polyenes absorb light of a certain wavelength (λ) with a certain molar absorption coefficient (ξ_λ).

The number of double bonds of the different lengths of polyenes were given in literature [31]. The concentrations of polyene sequences, C_n (mol/L), calculated by using Eq (2).

$$C_n = A / (\xi_\lambda \times b) \quad (2)$$

Where; A is the absorbance, b (cm) is the thickness of the films, ξ_λ (L/mol cm) is the molar absorption coefficient.

3.3. Kinetic Evaluation of the Dehydrochlorination

The distribution values of n number of polyene sequences after dehydrochlorination is determined from its absorption spectra. The mol fraction of polyene sequences containing n conjugated double bonds are determined as Eq (3);

$$N_n = \frac{C_n}{C} \quad (3)$$

Where C is the concentration of vinyl chloride repeat units in films. N_{ps} is the mol fractions of polyene sequences and N_{db} (ND) is the mol fractions of the polyenes, are given by Eq (4) and Eq (5), respectively;

$$N_{ps} = \sum N_n \quad (4)$$

$$N_{db} = \sum n N_n \quad (5)$$

This is a first order reaction [32], Eq (6) was obtained;

$$-\ln(1 - N_{db}) = k_1 \times t \quad (6)$$

Where k_1 is the reaction rate constant, t is time, and N_{db} is the mol fraction of polyenes. Plotting $-\ln(1 - N_{db})$ versus time lines the rate constants can be determine [9].

3.4. Determination of Polyene Number Using Raman Spectroscopy

For excitation wavelengths from 425 nm to 625 nm to estimate the excitation wavelength for which the optimum resonance effect occurs derived an equation Eq (7) [33] as below.

$$\lambda = 700 - 537.7 \times \exp(-0.0768 \times n) \quad (7)$$

where, λ is excitation wavelength (nm) and n is the number of conjugated double bonds.

The other equation is related the wavenumber (cm^{-1}) of the C=C stretching vibration between n (Eq (8)) [34].

$$\nu_{1521} = 1461 + 151.2 \times \exp(-0.07808 \times n) \quad (8)$$

3.5. Determination of Yellowness Index by Colorimetric Method

Color changes observed according to the numbers of polyenes formed from polymer degradation were determined by using tristimulus values of color. When PVC degrades as a result of thermal treatment, yellowing occurs. The coloration caused by the formation of polyenes is determined by the spectroscopy technique. The yellowness index (YI) is a measure of color change compared to a white standard. PVC color is calculated with $L^*a^*b^*$ color coordinates (tristimulus values) (Eq (9)) [35].

$$YI = (0.72a + 1.79b) \times [100/L] \quad (9)$$

3.6. Determination of the Plasticizer Migration

Aging of p-PVC involves dehydrochlorination, oxidation and loss of plasticizers by migration processes. When analyzing the migration of the plasticizer, it is necessary to analyze the diffusion through the polymer matrix to the surface of the material and the transporting from the surface to the surrounding environment [29]. For analyzing the rate of migration, diffusion coefficient would be desirable by Fick's law. Diffusion coefficient of the plasticizers calculates from the corresponding mass loss data when the other evaporating or decomposing components are negligible [29]. Eq (10) is able to explain the migration of plasticizer from p-PVC films [36].

$$\frac{M_t}{M_\infty} = (4/l) \times (D t/\pi)^{0.5} \quad (10)$$

Where M_t and M_∞ are the measured mass of plasticizer diffused at time t and after time infinite, respectively, D is the diffusivity and l is the film thickness.

4. Results

The stabilizing efficiency of secondary stabilizers, the formation of polyene sequences, the yellowness index, and structural changes were evaluated. The degradation kinetics of the films were evaluated.

4.1. Evaluation of the Structural Changes and Oxidation

During the decomposition, oxygen diffuses into the polymer, and the polymer is oxidized by the formation of free radicals. The oxidation is observed through the increase in OI values by the FTIR spectroscopy technique. Fig. 1 depicts the FT-IR spectrum of the films during heat treatment at 150°C for 420 minutes between 1800-1400 cm^{-1} wave numbers. The intensity of the 1570 and 1530 cm^{-1} bands belonging to the thermal stabilizers generally decreased after heat treatment due to their consumption. The bands at around 1720 cm^{-1} belong to the carbonyl C=O vibrations of an ester plasticizer [29], and the decreasing peak height suggests the migration of the plasticizer by heat treatment in all films. However, in the films containing epoxy soybean oil (EP-DO and EP-DE) the peak height was reduced less than in the other films. When the effect of different thermal stabilizers on the migration of plasticizers is examined for DOTP and DEHP-containing films, the order of decrement of the ester peak during heat treatment is as follows: DP-DO = EL-DO = TP-DO > EP-DO and DP-DE = TP-DE = EL-DE > EP-DE, respectively. The oxidation index (OI) values given in Table 3 were calculated from the ratio of absorbance values of the 1720 cm^{-1} carbonyl peak to the absorbance values of the reference group at 2920 cm^{-1} using Eq (1).

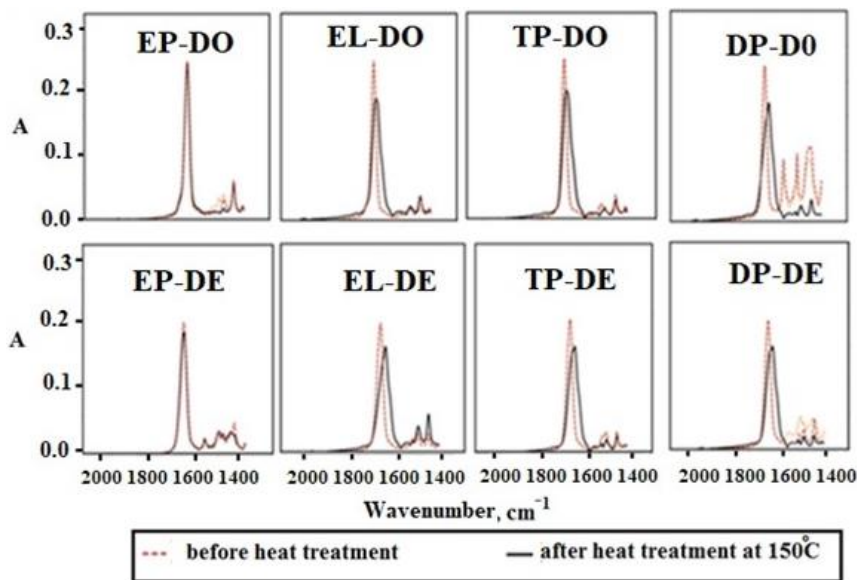


Fig. 1 Change of 1720 cm^{-1} peaks of p- PVC films with temperature for 420 minutes

Table 3. OI values of the films during heat treatment

Time. min.	0	120	240	360	420	120	240	360	420
Films	OI (at 100°C)					OI (at 150°C)			
EP-DO	173.7	174.3	158.2	186.2	152.8	189.5	140.3	146.4	176.0
EL-DO	207.9	216.5	211.5	212.6	213.4	216.5	156.0	44.7	46.3
TP-DO	217.8	224.9	190.8	234.8	228.5	263.9	154.7	47.3	47.5
DP-DO	193.2	254.6	230.8	226.4	224.2	256.8	149.3	34.6	41.5
EP-DE	176.7	205.1	203.4	186.8	184.9	205.0	203.4	186.8	184.9
EL-DE	185.3	189.0	188.5	203.7	184.0	174.8	142.6	41.5	37.7
TP-DE	200.9	229.0	186.1	233.9	233.5	234.7	66.1	42.8	48.7
DP-DE	192.9	175.2	172.8	177.5	167.6	151.9	33.4	39.1	51.2

Change in OI values during the heat treatment process belongs to the plasticizer migration and degradation. Diffusion and carbonyl formation are two competing processes; while plasticizer diffusion results in decrementing carbonyl, its formation results in the increment of the same peak. This can be explained by the loss of ester resulting from plasticizer migration and the carbonyl formed as a result of decomposition on the same peak. Therefore, the observation of ester loss and carbonyl formation on the same peak made it difficult to explain the change in OI with heat treatment.

4.2. Evaluation of Polyene Formation by UV-Visible Spectroscopy

Polyolefins are permeable in the UV zone. They give absorbance in the UV region depending on the color change after degradation. HCl is released by the dehydrochlorination of PVC during the heat treatment. Conjugated double bonds formed after degradation give maximum absorbance in the UV spectrum in the wavelength range of 268-447 nm. Between these wavelengths, namely at (268, 304, 334, 364, 390, 410, 428, and 447 nm), 3-10 conjugated polyenes are formed. The ratio of absorbance (A) values to 1100 nm reference absorbance (A_{1100}) values normalized the change in film thicknesses by heat treatment. A_{λ}/A_{1100} and polyene number during heat treatment at 100 and 150°C are depicted in Fig. 2 and 3, respectively. The number of polyenes increased with heat treatment. Three conjugated polyenes were observed at 268 nm wavelength even at 100°C and 3-10 double bonds were observed at 150°C. Although there are no major differences as compared to the one with DEHP, the film with DOTP formed a somewhat higher amount of shortest polyenes upon heat treatment. Diphenyl urea having a film had divergence from the others with lower absorbance, that is, a lower amount of conjugated double bonds. It was observed that the samples with the highest triple conjugated bond at 268 nm at 100°C are EL-DE and TP-DE, and at 150°C it is EP-DE. For the strongest heat treatment (at 150°C, 420 min), the lowest absorbance having sample was the one containing DP-DE, while the highest total absorbance having sample was the one containing EP-DO. While the order of the UV absorbance at 268-447 nm wavelength of the plasticizers DOTP>DEHP and of the secondary heat stabilizers is EPSO> ELSO> TPP> DPU, respectively. Fig. 4 shows the UV-vis relative total absorbances of the samples.

An increase in the slope of the relative UV absorbance curves of the films is due to the formation of polyene by heat treatment. The number of polyenes increases with heat treatment. Although total absorbance values increased in all films with heat treatment, the least change was observed in the film containing EL-DE, and the highest change was observed in the film containing EP-DO. The order of the UV total absorbance at the 268-447 nm wavelength of the plasticizers is as DOTP> DEHP. For the high heat treatment (at 150°C, 420 min), the lowest total absorbance value was observed in the sample containing DP-DE, while the highest was observed in the sample containing EP-DO. The order of the

total absorbance values for secondary heat stabilizers is $ELSO > TPP > EPSO > DPU$ and $EPSO > ELSO \approx TPP > DPU$ at 100 and 150°C, respectively. Diphenyl urea having film had divergence from the others with lower absorbance, that is, lower conjugated double bond amount. The stability of phenyl urea derivatives is high due to their chemical structure, which includes two amide linkages, two aromatic rings, a phthalimide moiety, and various substituent groups known to be thermally highly stable [37].

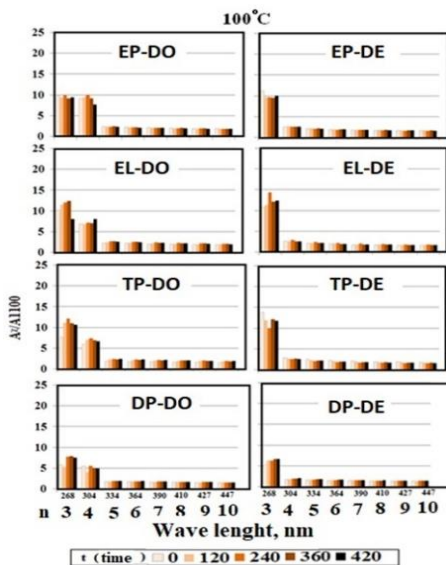


Fig. 2 A_{λ}/A_{1100} values of the films at 100°C (n; number of conjugated polyene at specified wave length [31] (for 120, 240, 360, and 420 minutes)

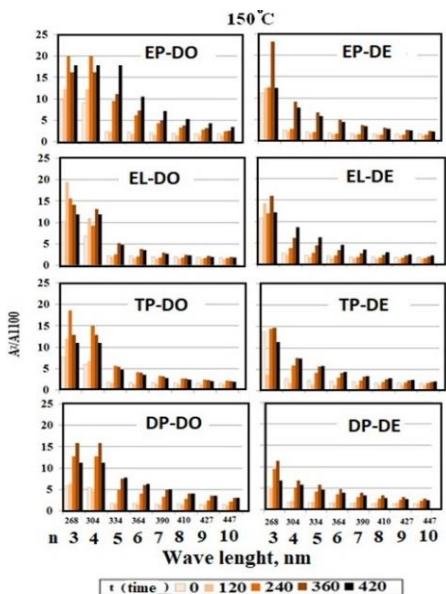


Fig. 3 A_{λ}/A_{1100} values of the films at 150°C (n; number of conjugated polyene at specified wave length)

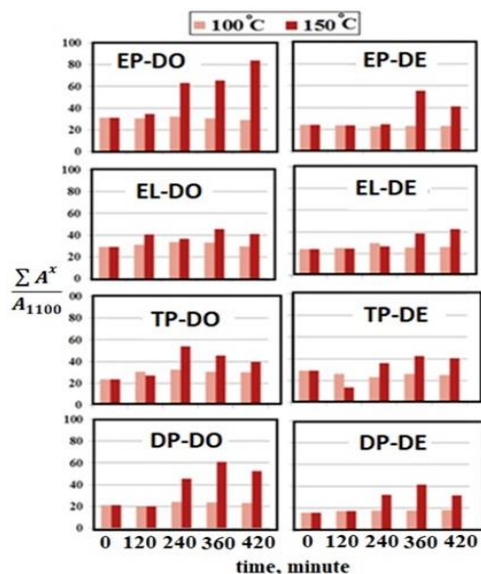


Fig. 4 Total relative absorbance values of P-PVC films

4.3. Evaluation of the Polyene Concentrations of Degraded p-PVC Films by UV/Visible Spectrum

Polyene concentrations, C_n (mol/L), were calculated by using Eq (2). In Table 4, the polyene concentrations of the films were given. The mol fraction of polyenes at each n value and the mol fractions of conjugated double bond (x_{cdlb}) were given in our previous study [9]. The concentration of the polyenes formed after degradation in films increased with temperature. The concentration of polyenes formed in heat-treated films up to 420 minutes at 150°C at 268 nm wavelength (the number of conjugated dienes formed at this wavelength is three) in the UV spectrum was mostly observed in films containing EP-DE. Whereas it was observed that they were the lowest in EL-DO-containing films. However, the highest increase in triple conjugated double bond concentrations compared to the initial values was observed in EP-DO film, while the least increase was observed in DP-DE film. The order of the increment of the concentration at 268 nm wavelength for the films is as follows: EP-DO > TP-DO > EL-DO > EL-DE > EP-DE > DP-DO > TP-DE > DP-DE. The order of the increment of the concentration at 268 nm wavelength for the films in terms of plasticizers is DOTP > DEHP. Fig. 5 shows the total concentration of the polyenes. With the increase in heat treatment time and temperature, the total concentrations of polyenes observed in the wavelength range of 268-447 nm in all films increased. The total concentration of polyenes formed in the films at 150°C for 420 minute remained in the range of 14-22 10^{-3} mol/L. In general, the total concentration of polyenes formed as a result of degradation was higher in films containing DOTP than in films containing DEHP plasticizers. The order of the total polyene concentration of the films is as follows: EP-DO > TP-DO > EP-DE > TP-DE > DP-DO > EL-DE > EL-DO > DP-DE. Mohamed et al. (2014) suggested that the stabilizing effect of various maleimido phenyl urea stabilizers is due to a radical mechanism that blocks the single electron sites formed in PVC chains [38].

4.4. Degradation Kinetics for Dehydrochlorination Reaction of PVC

The mol fractions of polyene sequences formed after degradation were determined from their UV spectra. These values for each films containing n polyene (N_n) were determined

by using Eq (3). Mol fractions of polyene sequences and double bonds (N_{ps} and N_{db}) were calculated by using Eq (4) and Eq (5). These values were given in Table 5. Then, the degradation rate constants for each film were calculated at 15 (°C up to 420 minutes by using Eq (6). Thermal dehydrochlorination is a first order reaction [9]. Therefore Eq (6) was used for the reaction rate constant calculation. The polyene formation rate constants for each film were determined by plotting $-\ln(1-N_{db})$ versus time lines. The dehydrochlorination rate constants (Table 6) were calculated using the slope of these curves (Fig. 6). Polyene formation rate constants calculated from the slopes of the lines in Fig. 6. These are between $1.68 \cdot 10^{-4}$ - $2.34 \cdot 10^{-4} \text{ min}^{-1}$ at 150°C (as given in Table 6). The degradation rate constant of the film containing EPSO is higher than that of the other stabilizers.

Table 4. Concentration of polyenes, $C_n \cdot 10^3, \text{ mol/L}$

N, number of polyene raysı		Polyene concentration, $C_n \cdot 10^3, \text{ mol/L}$								$\sum C_n \times 10^3, \text{ mol/L}$
		3	4	5	6	7	8	9	10	
T, °C	A Film	A_{268}	A_{304}	A_{334}	A_{364}	A_{390}	A_{410}	A_{428}	A_{447}	
25	EP-DO	5.93	2.65	0.41	0.34	0.25	0.24	0.17	0.15	10.14
100		9.40	3.66	0.65	0.53	0.40	0.38	0.28	0.24	15.54
150		10.05	4.83	2.87	1.48	0.80	0.59	0.36	0.26	21.24
25	EL-DO	5.99	1.92	0.39	0.32	0.24	0.23	0.17	0.14	9.4
100		8.03	3.86	0.73	0.61	0.45	0.43	0.31	0.26	14.68
150		9.25	4.44	1.08	0.69	0.42	0.35	0.23	0.18	16.64
25	TP-DO	6.68	2.50	0.47	0.39	0.30	0.29	0.21	0.18	11.02
100		9.55	2.88	0.62	0.51	0.38	0.37	0.27	0.23	14.81
150		11.12	5.34	1.37	0.90	0.57	0.48	0.32	0.25	20.35
25	DP-DO	7.92	3.54	0.70	0.59	0.45	0.43	0.32	0.27	14.22
100		9.18	2.87	0.70	0.58	0.44	0.42	0.31	0.26	14.76
150		9.71	4.67	1.91	1.37	0.86	0.70	0.46	0.36	20.04
25	EP-DE	9.63	1.04	0.51	0.41	0.30	0.29	0.21	0.18	12.57
100		10.61	1.31	0.64	0.51	0.38	0.36	0.26	0.23	14.3
150		12.04	3.67	1.63	1.08	0.67	0.55	0.36	0.28	20.28
25	EL-DE	8.38	0.97	0.48	0.38	0.28	0.27	0.19	0.16	11.11
100		11.01	1.10	0.56	0.44	0.33	0.31	0.23	0.19	14.17
150		11.01	3.80	1.63	1.05	0.63	0.50	0.32	0.25	19.19
25	TP-DE	9.88	1.00	0.51	0.40	0.30	0.28	0.20	0.17	12.74
100		11.22	1.15	0.58	0.46	0.34	0.33	0.24	0.21	14.53
150		11.68	3.70	1.70	1.13	0.70	0.59	0.39	0.30	20.19
25	DP-DE	9.18	1.51	0.82	0.67	0.51	0.49	0.36	0.31	13.85
100		9.63	1.42	0.76	0.61	0.46	0.44	0.32	0.28	13.92
150		9.92	2.84	1.36	1.02	0.67	0.56	0.38	0.30	17.05

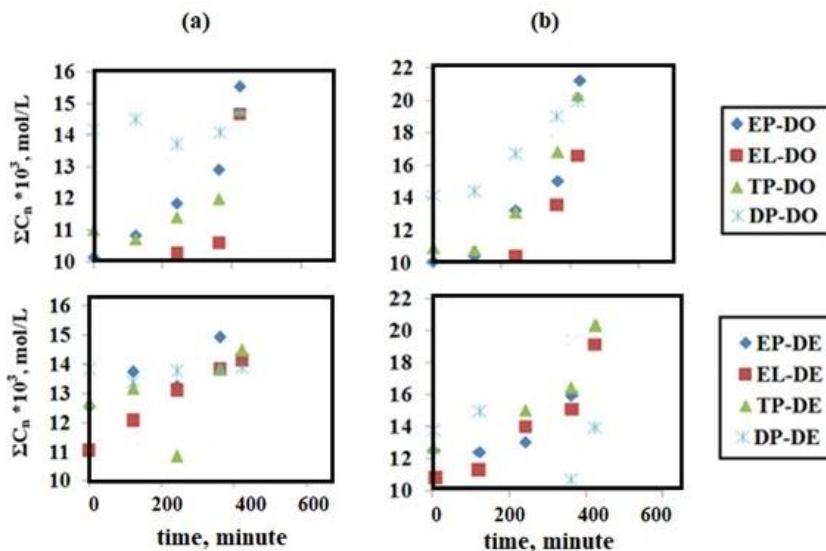


Fig. 5 Total concentration of polyenes at (a) 100°C and (b) 150°C for 420 minute

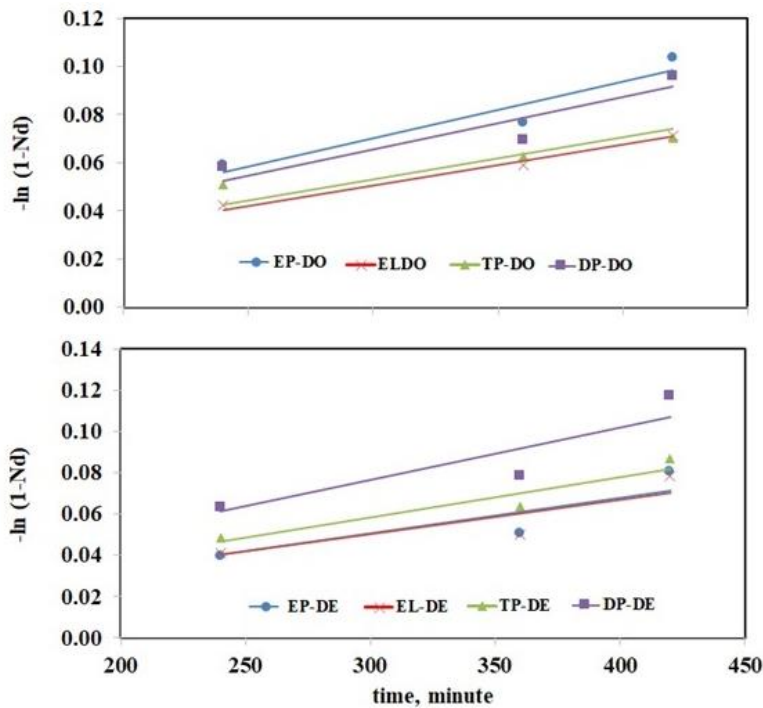


Fig. 6 Time dependence of the mole fraction of polyenes

Table 5. Mol fraction of the polyene sequences for each films at 150°C

Film code	time .min	$N_3 \cdot 10^4$	$N_4 \cdot 10^4$	$N_5 \cdot 10^4$	$N_6 \cdot 10^4$	$N_7 \cdot 10^4$	$N_8 \cdot 10^4$	$N_9 \cdot 10^4$	$N_{10} \cdot 10^4$	$N_{ps} \cdot 10^4$	$N_{db} \cdot 10^4$
EP -DO	0	7.34	3.28	0.51	0.42	0.31	0.30	0.22	0.184735	12.56	48.57
	120	7.54	3.62	0.40	0.28	0.19	0.18	0.13	0.112418	12.47	45.94
	240	8.22	3.95	1.12	0.63	0.35	0.27	0.17	0.131063	14.85	57.36
	360	9.41	4.52	1.85	1.05	0.58	0.44	0.27	0.200257	18.32	73.86
	420	11.12	5.34	3.18	1.64	0.88	0.65	0.40	0.287200	23.50	98.28
EL -DO	0	7.34	2.36	0.48	0.40	0.30	0.28	0.20	0.173983	11.53	44.12
	120	7.59	2.06	0.23	0.17	0.13	0.12	0.09	0.076427	10.46	36.58
	240	7.98	2.27	0.37	0.27	0.19	0.18	0.13	0.110738	11.50	41.55
	360	8.60	3.84	0.90	0.57	0.35	0.29	0.20	0.155737	14.91	57.21
	420	9.83	4.72	1.15	0.73	0.44	0.37	0.25	0.195383	17.69	68.77
TP-DO	0	7.34	2.75	0.52	0.43	0.33	0.31	0.23	0.196947	12.11	47.05
	120	7.54	2.04	0.30	0.23	0.18	0.17	0.13	0.108669	10.69	38.49
	240	8.10	3.15	0.72	0.46	0.28	0.24	0.16	0.123662	13.22	49.76
	360	8.54	4.10	1.02	0.67	0.42	0.35	0.23	0.178177	15.49	60.61
	420	9.41	4.52	1.16	0.77	0.48	0.40	0.27	0.212139	17.23	67.86
DP-DO	0	7.34	3.28	0.65	0.55	0.42	0.40	0.29	0.251949	13.18	52.98
	120	7.65	2.70	0.58	0.47	0.35	0.34	0.25	0.215568	12.56	49.05
	240	7.92	3.81	0.88	0.64	0.40	0.34	0.23	0.182921	14.40	56.68
	360	8.88	4.27	1.21	0.85	0.54	0.45	0.29	0.224912	16.71	67.10
	420	10.49	5.04	2.06	1.48	0.93	0.75	0.50	0.383177	21.62	91.57
EP-DE	0	7.34	0.79	0.39	0.31	0.23	0.22	0.16	0.137323	9.58	35.19
	120	7.75	0.66	0.30	0.24	0.18	0.18	0.13	0.110908	9.55	33.77
	240	8.54	0.92	0.40	0.29	0.21	0.20	0.15	0.127120	10.84	38.75
	360	9.49	1.80	0.79	0.51	0.30	0.25	0.16	0.122712	13.42	49.42
	420	11.59	3.54	1.57	1.04	0.64	0.52	0.34	0.265530	19.52	77.46
EL-DE	0	7.34	0.85	0.42	0.33	0.24	0.23	0.17	0.144207	9.73	36.03
	120	7.86	0.57	0.26	0.21	0.15	0.15	0.11	0.095499	9.41	32.62
	240	8.16	1.25	0.53	0.35	0.24	0.22	0.15	0.130552	11.02	40.30
	360	9.33	1.75	0.75	0.48	0.30	0.26	0.18	0.143454	13.19	48.85
	420	10.90	3.76	1.62	1.03	0.62	0.49	0.32	0.246071	18.99	75.63
TP-DE	0	7.34	0.75	0.38	0.30	0.22	0.20	0.15	0.125160	9.46	34.44
	120	8.04	0.51	0.25	0.20	0.15	0.15	0.11	0.097244	9.50	32.81
	240	8.88	1.75	0.74	0.47	0.30	0.26	0.18	0.144458	12.72	47.37
	360	10.29	2.57	1.13	0.73	0.45	0.38	0.25	0.195817	16.00	61.60
	420	11.97	3.79	1.74	1.16	0.72	0.60	0.40	0.307941	20.68	83.21
DP-DE	0	7.34	1.21	0.65	0.54	0.41	0.39	0.29	0.251487	11.09	44.50
	120	8.60	1.75	0.92	0.75	0.56	0.54	0.39	0.342034	13.86	57.13
	240	9.10	2.37	1.15	0.86	0.56	0.48	0.33	0.265470	15.13	61.14
	360	10.69	3.02	1.53	1.12	0.72	0.61	0.41	0.321782	18.42	75.35
	420	12.66	5.19	2.48	1.86	1.22	1.02	0.69	0.554517	25.67	110.75

Table 6. Polyene formation rate constants

p-PVC films	$k_1 \cdot 10^4, \text{min}^{-1}$	R^2
EP-DO	2.34	0.91
EL-DO	1.69	0.98
TP-DO	1.77	0.52
DP-DO	2.18	0.82
EP-DE	1.69	0.78
EL-DE	1.68	0.77
TP-DE	1.95	0.90
DP-DE	2.25	0.82

4.5. Degradation of PVC Using Raman Spectroscopy

Raman spectroscopy is a very useful technique for detecting polyenes in PVC. Degraded PVC contains polyene sequences of various lengths, which chain lengths of 10–30 exhibit various absorption bands in the spectrum [34]. Typically, the wavenumbers of the C-C and C=C stretching vibrations are denoted as 1122 and 1500 cm^{-1} , respectively [33, 34]. These correspond to polyene sequences in the Raman spectrum of p-PVC films shown in Fig. 7. Therefore these peaks reflect PVC degradation. Measurements were obtained by dividing the absorbance peak at 1122 cm^{-1} by the peak at 2911 cm^{-1} , which is unaffected by degradation due to C-H to eliminate effects of film thickness and instrument variation on this peak value [33]. An increase in the peak intensities of C-C and C=C was observed with heat treatment. However, due to strong Raman scattering due to darkening of the color of the samples at high heat treatment time, the spectrum was as in Fig. 7 (c). Using Eq (7), it is found that polyene sequence lengths for excitation wavelengths from 425 to 625 nm correspond to 9 to 26 [33]. In this work, for the laser light wavelength of 532 nm, polyene lengths were 15. Calculations were made for this polyene length. When 1122 cm^{-1} peak (C-C) was divided by 2911 cm^{-1} reference peak (C-H), 92.5 % increase in peak intensity was observed as a result of heat treatment at 150°C for 240 minutes. When 1500 cm^{-1} peak (C=C) was divided by 2911 cm^{-1} reference peak (C-H), 79.3 % increase in peak intensity was observed as a result of heat treatment at 150°C for 240 minutes.

4.6. Evaluation of Discoloration of the Films

The colors of the films were evaluated by the yellowness index (YI) measurements (Eq (9)) calculated using Tristimulus (L.a.b) values. Fig. 8 shows the YI values of the films at 100 and 150°C. The yellowing of the films indicates that dehydrochlorination has taken place with the formation of polyenes. Color changes were observed in all films as a result of decomposition due to the increase in heat treatment time and temperature. This can be seen from the increase in the YI values. The YI values of all films increased with heat treatment. In general the YI values and YI increments of films containing DOTP as a plasticizer were higher than those containing DEHP. The order of the YI values at 150°C for 420 minutes was determined to be DP-DO > DP-DE > TP-DO > TP-DE > EP-DO > EL-DO > EL-DE > EP-DE. The order of the YI increment at 150°C for 420 minute is as follows: EP-DO > EP-DE > EL-DE > TP-DO > DP-DO > TP-DE > DP-DE. EPSO including films that consisted of the highest number of polyenes, had YI values were also high. However, the film including diphenyl urea consisted of the lowest number of polyenes. According to the initial values, the highest increment in yellowness index values during the long heat treatment process was observed in the film including EPSO. The lowest increment in yellowness index values during the long heat treatment process was observed in films including DPU (Fig. 9). The photographs of films given in Fig. 10 showed the discoloration on the films, which were plasticized with two different plasticizers and contained four different secondary

stabilizers during heat treatment. No significant change in the color of the films was observed at low temperatures, while no darkening was observed at 150°C. The films began to turn yellow and brown during heat treatment. The types of stabilizers have shown a difference. After 150°C 240 minutes, yellowing was observed on the films due to heat treatment. During the 150°C 240-minute heat treatment, the maximum yellowing was observed in films containing EPSO, while the least yellowing was observed in ELSO, including films. The film containing ELSO did not show early color change compared to other films. The yellowing of the films proves that dehydrochlorination occurs via polyene formation. In many applications, in addition to thermal stability, stability against discoloration caused by the action of light is desirable. Butler et al. (1968) have found that monophenyl urea and diphenyl urea have a good light stabilising effect [39].

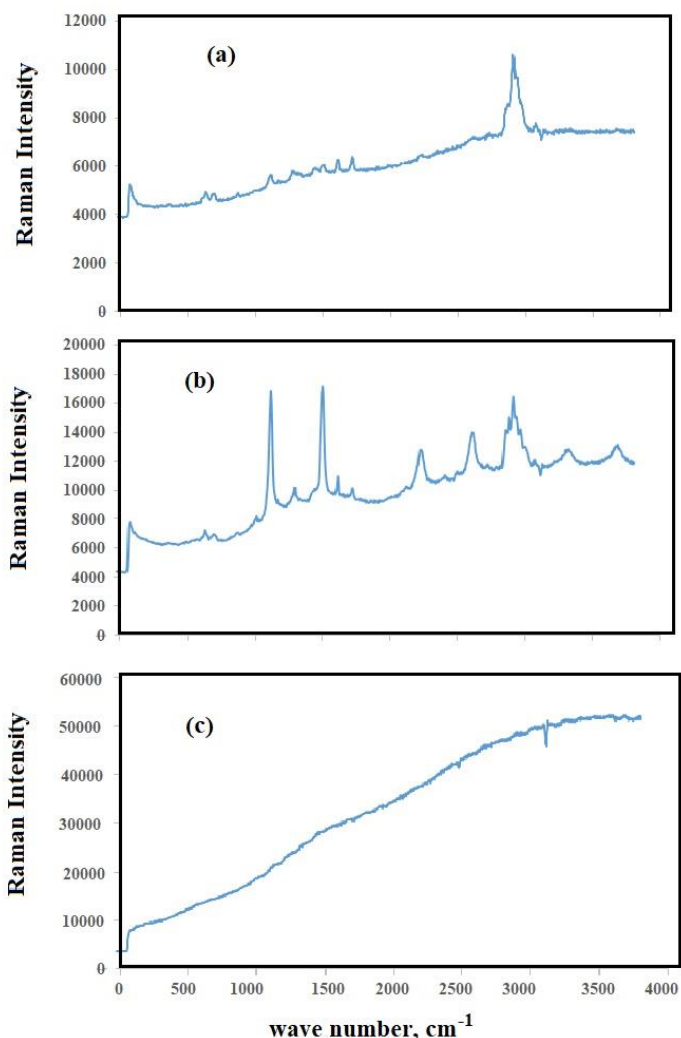


Fig. 7 Resonance Raman spectrum of thermally degraded p-PVC film (DP-DO) a) before heat treatment b, and c) after heat treatment at 150°C for 240, and 420 minute, respectively (using 532 nm laser).

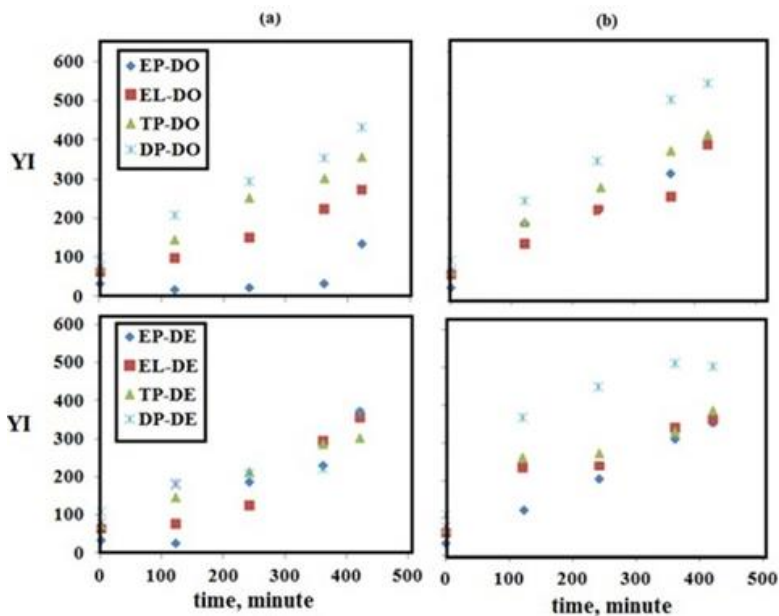


Fig. 8 YI values of the films (a) at 100°C and (b) at 150°C

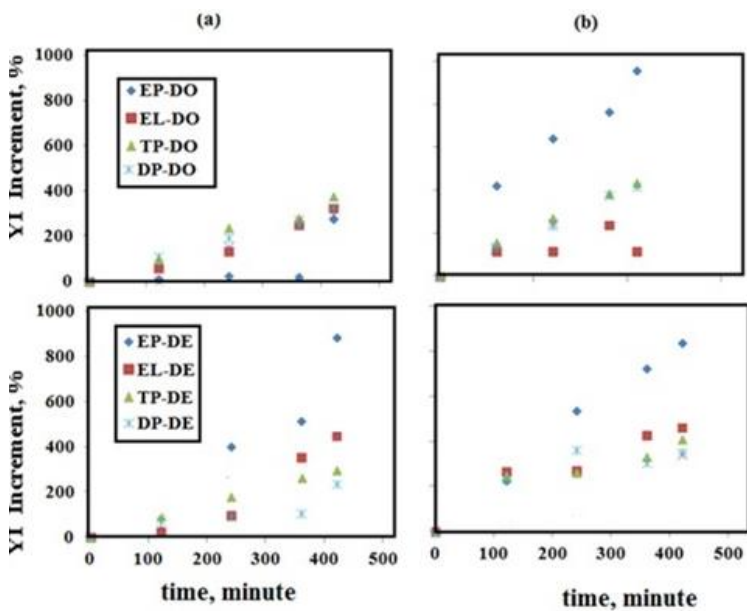


Fig. 9 YI increment (%) values of the films during thermal treatment (a) at 100°C and (b) at 150°C

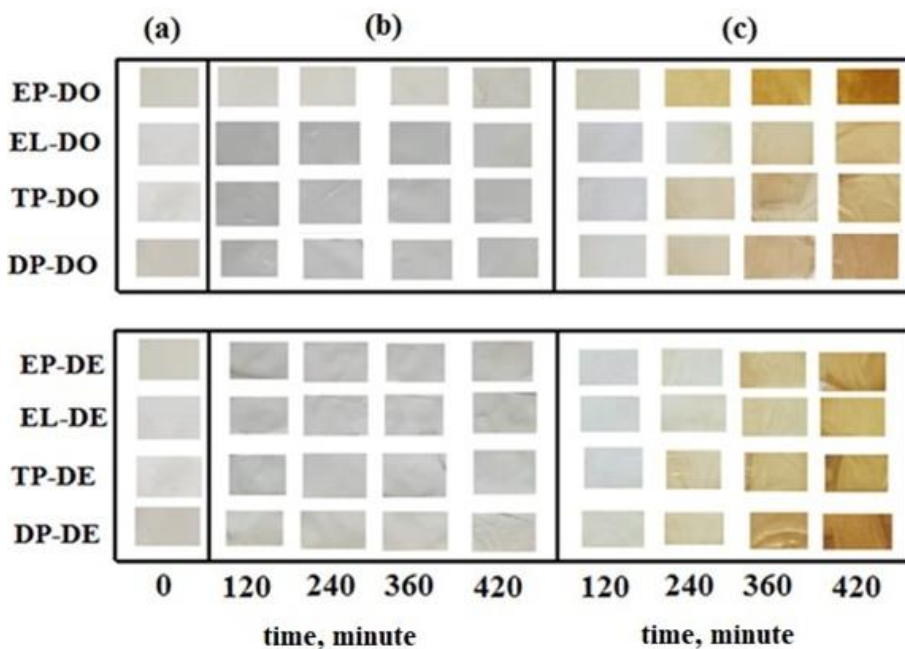


Fig. 10 The photographs of the films during heat treatment

4.7. Determination of Mass Loss and Diffusion Coefficient

When the plasticized PVC films are exposed to air, mass loss occurs by evaporating the plasticizer from the surface. The mass loss of the films having DOTP and DEHP during the heat treatment at 100 and 150°C are given in Fig. 11 (a) and (b), respectively. Since the amount of the initial primary and secondary stabilizers are very low, 5% and 8.3% of the plasticizer mass, respectively, in the formulation used herein, and they have very high molar masses, their contribution to mass loss due to the consumption of heat stabilizers is negligible [40]. However, long heat treatments at high temperatures cause decomposition, most likely due to the consumption of heat stabilizers. Therefore, it is suggested that the mass loss of the films during short to medium heat treatment periods depends mainly on the evaporation of plasticizers [29]. The mass loss of the films increased with heat treatment. While the mass loss for EP-DO, EL-DO, TP-DO, DP-DO having films for 420 minutes at 100°C are 0.8, 0.5, 0.9, and 1.0 %, those at 150°C 11.7, 8.4, 12.9, and 12.0 %, respectively. While the mass losses for EP-DE, EL-DE, TP-DE, and DP-DE having films for 420 minutes at 100°C are 1.0, 0.9, 1.6, and 0.8 %, those at 150°C 20.2, 18.3, 23.2, and 23.5 %, respectively. The mass loss of the films containing DEHP was higher compared to the DOTP-containing films. Considering the effect of secondary thermal stabilizers on the mass loss of the films, it was observed that films containing tri phenyl phosphite (TP) were higher at high temperature than others, whereas the films having epoxidized linseed oil (EL) were lower. The order of the mass loss was determined as TP-DO > DP-DO > EP-DO > EL-DO at 150°C for DOTP-containing films. Similarly, the order of the mass loss is TP-DE > DP-DE > EP-DE > EL-DE for DEHP-containing films at 150°C. For examining the migration behavior of plasticizers from p-PVC films into air, diffusion coefficients were calculated by plotting against Mt/M_∞ versus $t^{0.5}$ at 100°C and 150°C, as given in Fig. 12 (a) and (b), respectively. From the slope of the linear part of this graph, the diffusivity of the molecules diffused from the polymeric membrane is also calculated. Diffusion coefficients calculated from Eq (8) are given in Table 7. The effective diffusivity of plasticizer increased with heat

treatment. The migration of plasticizers from films containing DEHP was higher than that of DOTP- containing films. Parameters such as molar mass, polarity of molecules, nature and amount of plasticizer, contact medium, and temperature affect plasticizer migration [29, 41]. Table 1 shows the molecular structure of plasticizers. DOTP is an aromatic terephthalate plasticizer, while DEHP is an aromatic ortho phthalate. Although DOTP and DEHP have the same molar mass, the planar spatial arrangement of DOTP likely makes it more compatible with PVC polymer chains. Therefore, the mass loss of DOTP film is thought to be less than that of DEHP [29]. Considering the effect of secondary thermal stabilizers on the effective diffusion of plasticizers from p-PVC films, it was observed that diffusion coefficients of the films having triphenyl phosphite (TP) were higher than the others at high temperatures. Whereas the films having epoxidized linseed oil (EL) were the lowest. Due to the linear structure of ELSO, it is thought to result in lower plasticizer diffusion. Plasticizer migration from the films having DEHP was higher than that from the films having DOTP. For example, while the effective diffusion coefficient of the p-PVC films at 150°C is $1.4 \times 10^{-14} \text{ m}^2/\text{sec}$ for EP-DO, and $4.0 \times 10^{-14} \text{ m}^2/\text{sec}$ for EP-DE. The order of the diffusion coefficients was determined as TP-DO > DP-DO > EP-DO > EL-DO at 150°C for DOTP containing films as plasticizers. Similarly, the order of the diffusion coefficients was determined as the TP-DE > DP-DE > EP-DE > EL-DE at 150°C for DEHP- containing films as plasticizer. The diffusivity values belonging to the films subjected to 100°C thermal treatments also have the same order. Although they have a similar chemical formula, the use of DOTP as a plasticizer instead of DEHP due to its linear structure would be advantageous in terms of plasticizer migration in PVC. Because the films are identical, the diffusivity results are in line with the mass loss, except for differences arising from the type of plasticizer and secondary heat stabilizer.

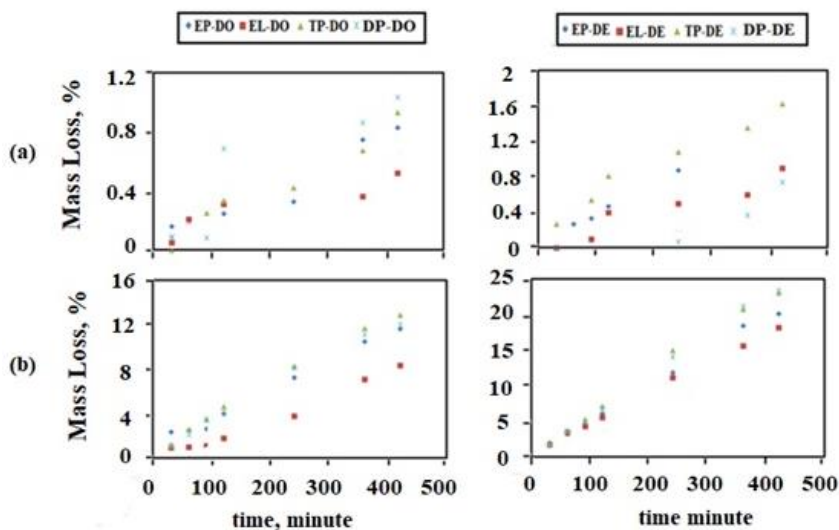


Fig. 11 The mass loss of the films

Ekelund et al. (2008) reported that the diffusion of plasticizer from PVC films to air was controlled by diffusion, where the evaporation rate was independent of plasticizer amount at low temperatures [42]. When examined in terms of thermal stability, DPU and TPP showed higher stability than EPSO and ELSO due to the phenyl rings in their chemical structures, while the linear structures of EPSO and ELSO ensured less plasticizer migration from PVC when examined in terms of the effects of thermal stabilizers on plasticizer

migration. However, the phenyl groups in the structures of DPU and TPP opened the interchain spaces, causing more plasticizer migration.

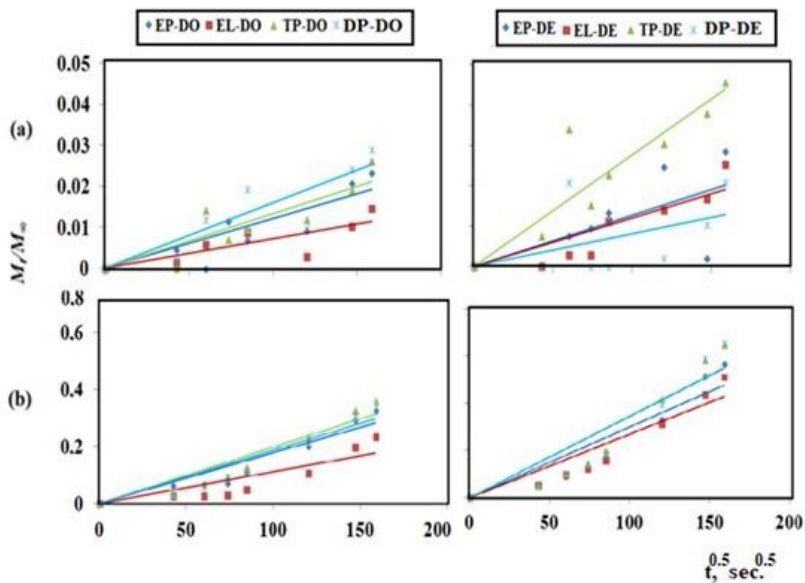


Fig. 12 Fractional loss of the films at (a) 100°C (b)150°C

Table 7. Diffusion coefficients of P-PVC films

T, °C	100		150	
Film Codes	De*10 ¹⁶ , m ² /s	R ²	De*10 ¹⁶ , m ² /s	R ²
EP-DO	0.7	0.8	141.1	0.9
EL-DO	0.2	0.7	55.1	0.8
TP-DO	0.8	0.8	174.3	0.9
DP-DO	1.1	0.8	154.5	0.9
EP-DE	1.3	0.9	399.7	0.9
EL-DE	0.6	0.8	322.1	0.9
TP-DE	3.4	0.8	535.0	0.9
DP-DE	0.3	0.6	525.2	0.9

4. Conclusion

PVC is difficult to process due to its relatively high processing conditions and low thermal stability. The use of plasticizers and thermal stabilizers solves this problem. Epoxidized vegetable oils are known to be co-stabilizers for PVC resins, environmentally friendly, and good nominees for PVC secondary stabilizers. However, they are problematic and tend to deteriorate as they cause the polymer to become brittle and discolored at high temperatures. Also, unreacted double bonds in epoxidized vegetable oils reduce compatibility between PVC and plasticizer. This may cause more plasticizer to migrate from the PVC matrix to the surrounding environment. This study focuses on the thermal stabilization efficiency of phosphite and urea derivative-based stabilizers that are non-

toxic against epoxy-based stabilizers on the thermal degradation of p-PVC films. As a result, phosphite and urea derivative-based stabilizers generally provided better long term thermal stability than epoxidized vegetable oils stabilizers. Diphenyl urea, relative to all other thermal stabilizers, showed higher long-term stability than the other stabilizers in terms of the number of polyenes, concentration of polyenes, and yellowness index. Diphenyl urea has a variety of functional groups that can interact with the evolved HCl gas obtained from degraded PVC. It is recommended to use e-PVC in 0.3-0.5 part [25]. In this study, diphenyl urea was used in 3 parts for 100 parts of e-PVC. It performed better than other stabilizers, even 10 times over the specified amount. Therefore, it will be economically beneficial if it is used in lower amounts. In addition, it is also advantageous that it represents a class of compounds with a wide variety of biological properties, such as bactericidal, fungicidal and anticancer activities. However, epoxidized vegetable oil stabilizers generally more affected by the prevention of plasticizer migration than phosphite and urea derivative-based stabilizers.

The findings of this study and the publication of these results will contribute to studies on improving the thermal stability of PVC with different stabilizers, solving the structural degradation problem of PVC, PVC stabilization and plasticizer diffusion.

Acknowledgement

The financial support of Usak University Research Fund (Project No: 2016/MF002) is gratefully acknowledged as well. The present study partially based on the presented at the International Congress on Chemistry and Materials Science organized by Ankara University, Ankara, Turkey. 5-7 October 2017.

References

- [1] Taghizadeh MT, Nalbandi N, Bahadori A. Stabilizing effect of epoxidized sunflower oil as a secondary stabilizer for Ca/Hg stabilized PVC. *Express Polymer Letters*. 2008;2(1):65-76. <https://doi.org/10.3144/expresspolymlett.2008.9>
- [2] Boughattas I, Ferry M, Dauvois V, Lamouroux C, Dannoux-Papin A, Leoni E, Balanzat E, Esnouf S. Thermal degradation of γ -irradiated PVC: I-dynamical experiments. *Polym Degrad Stab*. 2016;126: 219-226. <https://doi.org/10.1016/j.polymdegradstab.2015.03.014>
- [3] Jia P, Zhang M, Liu C, Hu L, Feng G, Bo C, Zhou Y. Effect of chlorinated phosphate ester based on castor oil on thermal degradation of poly(vinyl chloride) blends and its flame retardant mechanism as secondary plasticizer. *Rsc Advances*. 2015;51. <https://doi.org/10.1039/C5RA05784A>
- [4] Liu T, Jiang P, Liu H, Li M, Dong Y, Wang R, Wang Y. Performance testing of a green plasticizer based on lactic acid for PVC. *Polymer Testing*. 2017;61:205-213. <https://doi.org/10.1016/j.polymertesting.2017.05.012>
- [5] Li M, Li S, Xia J, Ding C, Wang M, Xu L, Yang X, Huang K. Tung oil based plasticizer and auxiliary stabilizer for poly(vinyl chloride). *Materials & Design*. 2017;122:366-375. <https://doi.org/10.1016/j.matdes.2017.03.025>
- [6] Wu B, Wang Y, Chen S, Wang M, Ma M, Shi Y, Wang X. Stability, mechanism and unique "zinc burning" inhibition synergistic effect of zinc dehydroacetate as thermal stabilizer for poly(vinyl chloride). *Polym Degrad Stab*. 2018;152:228-234. <https://doi.org/10.1016/j.polymdegradstab.2018.04.025>
- [7] Liu J, Chen G, Yang J. Preparation and characterization of poly(vinyl chloride)/layered double hydroxide nanocomposites with enhanced thermal stability. *Polym*. 2008;49(18):3923-3927. <https://doi.org/10.1016/j.polymer.2008.07.014>
- [8] Mohammed FS, Conley M, Rumble AC, Saunders SR, Switzer J, Urena-Benavides E, Jha R, Cogen JM, Chaudhary BI, Pollet P, Eckert CA, Liotta CL. Enhanced thermal

- stabilization and reduced color formation of plasticized poly(vinyl chloride) using zinc and calcium salts of 11-maleimideundecanoic acid. *Polym Degrad Stab.* 2015;111:64-70. <https://doi.org/10.1016/j.polymdegradstab.2014.10.021>
- [9] Tüzüm-Demir AP, Ulutan S. Assessment Of Degradation Of Plasticized Poly(Vinyl Chloride) Films Through Polyene Formation Under Isothermal Conditions. *J Appl Polym Sci.* 2018;135:46092. <https://doi.org/10.1002/app.46092>
- [10] Ureta E, Cantú ME. Zinc maleate and zinc anthranilate as thermal stabilizers for PVC. *J Appl Polym Sci.* 2000;2603-2605. [https://doi.org/10.1002/1097-4628\(20000919\)77:12<2603::AID-APP70>3.0.CO;2-2](https://doi.org/10.1002/1097-4628(20000919)77:12<2603::AID-APP70>3.0.CO;2-2)
- [11] Bueno-Ferrer C, Garrigós MC, Jiménez A. Characterization and thermal stability of poly(vinyl chloride) plasticized with epoxidized soybean oil for food packaging. *Polym Degrad Stab.* 2010;95(11):2207-2212. <https://doi.org/10.1016/j.polymdegradstab.2010.01.027>
- [12] Xu X, Chen S, Tang W, Qu Y, Wang X. Investigation of basic zinc cyanurate as a novel thermal stabilizer for poly(vinyl chloride) and its synergistic effect with calcium stearate. *Polym Degrad Stab.* 2014;99:211-218. <https://doi.org/10.1016/j.polymdegradstab.2013.11.003>
- [13] Braun D. Poly(vinyl chloride) on the Way from the 19th Century to the 21st Century. *Journal of Polymer Science: Part A: Polymer Chemistry.* 2004;42:78-586. <https://doi.org/10.1002/pola.10906>
- [14] Gupta S, Agarwal DD, Banerjee S. Synthesis and characterization of hydrotalcites: Potential thermal stabilizers for PVC. *Indian Journal of Chemistry.* 2008;47A:1004-1008.
- [15] Suzuki AH, Botelho BG, Oliveira LS, Franca AS. Sustainable synthesis of epoxidized waste cooking oil and its application as a plasticizer for polyvinyl chloride films. *European Polymer Journal.* 2018;99:142-149. <https://doi.org/10.1016/j.eurpolymj.2017.12.014>
- [16] Gobin M, Loulergue P, Audic JL, Lemiègre L. Synthesis and characterisation of bio-based polyester materials from vegetable oil and short to long chain dicarboxylic acids. *Industrial Crops and Products.* 2015;70:213-220. <https://doi.org/10.1016/j.indcrop.2015.03.041>
- [17] Karmalm P, Hjertberg T, Jansson A, Dahl R. Thermal stability of poly(vinyl chloride) with epoxidised soybean oil as primary plasticizer. *Polym Degrad Stab.* 2009;94:2275-2281. <https://doi.org/10.1016/j.polymdegradstab.2009.07.019>
- [18] Benaniba MT, Belhaneche-Bensemra N, Gelbard G. Stabilization of PVC by epoxidized sunflower oil in the presence of zinc and calcium stearates. *Polym Degrad Stab.* 2003;82:245-249. [https://doi.org/10.1016/S0141-3910\(03\)00178-2](https://doi.org/10.1016/S0141-3910(03)00178-2)
- [19] Sabaa MW, Mohamed RR, Yassin AA. Organic thermal stabilizers for rigid poly(vinyl chloride) VIII. Phenylurea and phenylthiourea derivatives. *Polym Degrad Stab.* 2003;81(1):37-45. [https://doi.org/10.1016/S0141-3910\(03\)00060-0](https://doi.org/10.1016/S0141-3910(03)00060-0)
- [20] Haryono A, Triwulandari E, Jiang P. Interaction between vegetable oil based plasticizer molecules and polyvinyl chloride, and their plasticization effect. *AIP Conference Proceedings.* 2017;1803(1). <https://doi.org/10.1063/1.4973172>
- [21] Gamage PK, Farid AS, Karunnanayake L. Kinetics of degradation of PVC containing novel neem oil as stabilizer. *J Appl Polym Sci.* 2009;112:2151-2165. <https://doi.org/10.1002/app.29686>
- [22] Craver C, Carraher C. *Applied Polymer Science: 21st Century First Edition* Elsevier Applied Science Publishers, Oxford. 2000;231-257. <https://doi.org/10.1016/B978-008043417-9/50004-0>
- [23] Howe SR, Surana P, Jakupca MR, Borodinsky L. Potential dietary exposure to p-nonylphenol from foodcontact use of tris(nonylphenyl)phosphite (TNPP). *Food Additives and Contaminants.* 2001;18(11)1021-1039. <https://doi.org/10.1080/02652030110050320>

- [24] Folarin OM, Sadiku ER. Thermal stabilizers for poly(vinyl chloride): A review. *Int J Phys Sci.* 2011;6(18):4323-4330.
- [25] Mohamed NA, Abd El-Ghany NA. Evaluation of the stability of rigid poly(vinyl chloride)/biologically active phthalimido phenyl urea composites using thermogravimetric analysis. *Polym Degrad Stab.* 2017;140:95-103. <https://doi.org/10.1016/j.polymdegradstab.2017.04.019>
- [26] Altindag IA, Akdogan Y. Spectrophotometric characterization of plasticizer migration in poly(vinyl chloride)-based artificial leather. *Materials Chemistry and Physics.* 2021;258: 123954. <https://doi.org/10.1016/j.matchemphys.2020.123954>
- [27] Pyeon HB Park JE, Suh DH. Non-phthalate plasticizer from camphor for flexible PVC with a wide range of available temperature. *Polymer Testing.* 2017;63:375-381. <https://doi.org/10.1016/j.polymertesting.2017.08.029>
- [28] Ambrogi V, Brostow W, Carfagna C, Pannico M, Persic P. Plasticizer migration from cross-linked flexible PVC: Effects on tribology and hardness. *Polymer Engineering and Science.* 2012;52(1): 211-217. <https://doi.org/10.1002/pen.22070>
- [29] Tüzüm-Demir AP, Ulutan S. Migration of phthalate and non-phthalate plasticizers out of plasticized PVC films into air. *J Appl Polym Sci.* 2013;128:1948-1961. <https://doi.org/10.1002/app.38291>
- [30] Manzoor W, Yousaf SM, Ahmad Z. Degradation of PVC: Effect of zinc chloride on the concentration of polyenes. *Polym Degrad Stab.* 1996;51:295-299. [https://doi.org/10.1016/0141-3910\(95\)00186-7](https://doi.org/10.1016/0141-3910(95)00186-7)
- [31] Baltacıoğlu H, Balköse D. Effect of zinc stearate and/or epoxidized soybean oil on gelation and thermal stability of PVC-DOP plastigels. *J Appl Polym Sci.* 1999;74:2488-2498. [https://doi.org/10.1002/\(SICI\)1097-4628\(19991205\)74:10<2488::AID-APP18>3.0.CO;2-B](https://doi.org/10.1002/(SICI)1097-4628(19991205)74:10<2488::AID-APP18>3.0.CO;2-B)
- [32] Castañeda-Facio A, Benavides R, Martínez-Pardo ME. Thermal stability of PVC formulations gamma irradiated at different dose rates. *Radiat. Phys. Chem.* 2014;97:75-80. <https://doi.org/10.1016/j.radphyschem.2013.11.004>
- [33] Gilbert M, Ho KC, Hitt DJ, Vrsaljko D. Assessment of PVC stabilisation using hydrotalcites -Raman spectroscopy and other techniques. *Polymer Degradation and Stability.* 2013;98:1537-1547. <https://doi.org/10.1016/j.polymdegradstab.2013.04.005>
- [34] Kuznetsov SM, Sagitova EA, Prokhorov KA, Nikolaeva GY, Mendeleev DI, Donack P, Materny A. Raman spectroscopic detection of polyene-length distribution for high-sensitivity monitoring of photo- and thermal degradation of polyvinylchloride. *Spectrochimica Acta Part A: Molecular and Biomolecular Spectroscopy.* 2021; 252:119494. <https://doi.org/10.1016/j.saa.2021.119494>
- [35] Awad WH, Beyer G, Benderly D, Ijdo WL, Songtipya P, del Mar Jimenez-Gasco M, Manias E, Wilkie CA. Material properties of nanoclay PVC composites. *Polymer.* 2009;50 (8): 1857-1867. <https://doi.org/10.1016/j.polymer.2009.02.007>
- [36] Kim JH, Kim SH, Lee CH, Nah JW, Hahn A. DEHP Migration Behavior from Excessively Plasticized PVC Sheets. *Bull. Korean Chem. Soc.* 2003;24:3:345. <https://doi.org/10.5012/bkcs.2003.24.3.345>
- [37] Mohamed NA, Abd El-Ghany NA. Evaluation of the stability of rigid poly(vinyl chloride)/biologically active phthalimido phenyl urea composites using thermogravimetric analysis. *Polym Degrad Stab.* 2017;140:95-103. <https://doi.org/10.1016/j.polymdegradstab.2017.04.019>
- [38] Mohamed NA, Abd El-Ghany NA, Fahmy MM, Ahmed MH. Thermally stable antimicrobial PVC/maleimido phenyl urea composites. *Polym. Bull.* 2014;71:2833-2849. <https://doi.org/10.1007/s00289-014-1225-z>
- [39] Butler MR, Llewellyn LI. Chlorine-containing resins stabilized with mixtures comprising a phenyl urea and a phosphite, and optionally a magnesium compound US Patent 3,396,131, 1968.

- [40] Kovacic, T, Mrklic Z. The kinetic parameters for the evaporation of plasticizers from plasticized poly(vinyl chloride). *Thermodyn. Acta.* 2002;381, 49. [https://doi.org/10.1016/S0040-6031\(01\)00643-8](https://doi.org/10.1016/S0040-6031(01)00643-8)
- [41] Zoller A, Marcilla A. Soft PVC foams: Study of the gelation, fusion, and foaming processes. I. Phthalate ester plasticizers. *J. Appl. Polym. Sci.* 2011;121:1495. <https://doi.org/10.1002/app.33671>
- [42] Ekelund M, Azhdar B, Hedenqvist MS, Gedde U W. Long-term performance of poly(vinyl chloride) cables, Part 2: Migration of plasticizer. *Polym. Degrad. Stab.* 2008;93:1704. <https://doi.org/10.1016/j.polymdegradstab.2008.05.030>



Research Article

Effect of nano-sized clay and waste glass powder on rheological and hardened properties of self-compacting concrete

Elaf Khalid Dahamm^a, Sheelan Mahmoud Hama^{*b}, Ibrahim A. AL-Jumaily^c

Department of Civil Engineering, University Of Anbar, Ramadi, Iraq

Article Info

Abstract

Article history:

Received 26 Oct 2022

Accepted 13 Mar 2023

Keywords:

Mechanical properties;

Nano-clay;

Rheological properties;

Self-compacting

concrete;

Waste glass powder

Two types of pozzolanic materials nano-clay (NC) and waste glass powder (WGP) have been utilized in this work, which has been carried out in three stages. The first stage is to partially replace the cement with nano-clay (2.5, 5, 7.5, and 10%). The second stage is replacing cement with 15% of the waste glass powder, and the third and final stage is partially replacing the waste glass powder partially with nano-clay (2.5%NC+12.5%WGP, 5%NC+10%WGP, 7.5%NC+7.5%WGP, and 10%NC+2.5%WGP). The results were evaluated by studying the rheological and mechanical properties of self-compacting concrete (SCC) for each stage to find out the best replacement ratio for the best properties. The results of the tests on the fresh concrete showed that the nano-clay reduces the fluidity and flowability of the mixtures, while the addition of glass has almost no effect. While the addition of glass and NC leads to an additional decrease in the flowability of the mixture. From the results of mechanical properties, it was found that the mix with 2.5% NC and 12.5% WGP gave the highest strength.

© 2023 MIM Research Group. All rights reserved.

1. Introduction

In 1988 in Japan the Self-compacting concrete (SCC) was first been applied by Okamura to avoid the problems related to the concrete structures' durability caused by the lack of skilled builders to provide sufficient compaction [1]. This concrete can be considered the most sustainable type of concrete for complex shapes and elements and use under difficult conditions [2]. SCC can spread and fill all corners and all parts into complex forms of formwork under its weight and can be fully compacted without external vibration even with congested steel reinforcement. SCC is known as an innovative production of flowing concrete due to its excellent properties which provide many benefits. Concrete can be classified as SCC when the desired features of rheological behavior are achieved as stipulated in EFNARC Guidelines [3]. In addition, SCC provides significant benefits in improved construction productivity, reduced placing cost, good surface finish, short mandatory casting time, reduced labor cost as well as no noise pollution, excellent build quality, and ease of casting even with reinforced steel's encapsulation areas, which are allowing more of options in the design of building systems [4, 5].

The total annual output of domestic and industrial waste is increasing more and more due to the increase in population and development in the industrial sector. This waste represents a significant pollution source that requires increased attention to find efficient ways to get rid of it [6]. Sustainable building means creating and managing an integrated system for the environment and health as a result of efficient resource management and environmental protection [7].

Nowadays, the environmental trend aims to exploit waste as a total or partial substitute for raw materials in the construction industry. This provides many advantages in

*Corresponding author: drsheelan@uoanbar.edu.iq

^a orcid.org/0009-0005-8922-5306; ^b orcid.org/0000-0001-7265-583X; ^c orcid.org/0000-0001-9354-4864

DOI: <http://dx.doi.org/10.17515/resm2022.563ma1026>

Res. Eng. Struct. Mat. Vol. 9 Iss. 3 (2023) 743-761

developing sustainable systems and not only ensures waste consumption but also provides a cleaner and greener environment at an economical cost [8, 9]. One of the main problems facing the production of SCC is the high production cost because of the need for a high cement content and chemical additives and the environmental problems caused by significant emissions, especially carbon dioxide (CO₂) resulting from cement manufacturing [10].

This issue can be solved by partially replacing cement with alternative materials such as waste glass powder, and thus it is possible to reduce the use of cement and at the same time reduce waste glass and achieve double environmental benefits. Recently there have been some investigations on the use of ground glass powder in the construction industry as a partial substitute for cement [6]. To some extent, recent work has indicated that discarded glass when grounded into small-size particles ($\leq 75 \mu\text{m}$) had a high response to pozzolanic activity and provided a higher level of hydration products and a more uniform distribution [7]. When the calcium hydroxide Ca(OH)₂ from cement hydration combines chemically with the pozzolanic materials that have a large amount of SiO₂ like waste glass powder, cementitious compounds known as C-S-H (calcium-silicate-hydrate) gel are formed, which can enhance the strength of concrete [8]. According to a different experiment, the ultimate load of beams with 10% and 15% waste glass powder increased by +4 to 39% in situations where reinforcement beams were present. This led to more brittle behavior because WGP concrete had a higher compressive strength [9]. Researchers found that at age of 28 days after water curing, the compressive strength of specimens with 10%, 15%, and 20% of WGP increased by 27.62%, 41.46%, and 20.18%. While, these specimens showed an increase of 22.11%, 41.75%, and 21.36% at 56 days, and 27.05%, 30.81%, and 17.2% at 90 days. But the 25% of WGP reduced compressive strength by 14.34%, 20.5%, and 19.41% at 28, 56, and 90 days, respectively, compared with referenced mixes [10,11]. In another research, the pozzolanic behavior of glass powder was investigated at concentrations of 0, 5, 10, 15, 20, and 25% by cement weight. The results showed an average of 16% increase in compressive strength [12]. Vanjare and Mature [13] produced an SCC by incorporating ground glass powder, to encourage its application in on-site construction. They pointed out that replacing cement with glass powder contributed to reducing raw materials in the SCC and creating a healthy green environment. Rahman et al. [14] studied the combined effect of using two types of industrial wastes in concrete which include glass powder and granular steel slag also as substitute materials for cement and fine aggregate on the fresh and hardened characteristics of SCC. The cement has been replaced partially with glass powder by 20%, 30%, and 40% of the weight of cement. Fine aggregate substitutes for fine slag aggregate were 40%, 60%, and 80%. The results indicated that the workability of the mixtures improved with the presence of glass powder, while the increased amount of steel slag led to a decrease in their workability. The results also showed that compressive strength, modulus of elasticity, and flexural strength were increased with a 20% cement replacement with glass powder. However, there is a downward trend in these properties with increasing glass powder ratio at a constant ratio of steel slag. Liu [15] utilized two types of ground glass of different colors were used: white glass and green glass. The cement replacement rates were 5%, 10%, 5%, and 10% while the sand replacement rates were 5%, 10%, 4%, and 9%. Liu concluded that an SCC with new desirable properties could be produced by incorporating approximately 104 kg/m³ of glass waste, replacing 10% of the cement and sand.

An important part of the widespread acceptance of nanotechnology provides improved system reliability, extends functionality beyond traditional applications, and reduces cost, size, and energy consumption.

The incorporation of nanotechnology into the field of materials facilitates an increase in the durability of materials and provides materials with superior performance. It also

allows for more efficient use of natural resources and achieving the properties of the necessary materials with minimal effort [16]. Pozzolanic materials such as nano-silica, nano-alumina, and nano-clay (NC) are characterized by Pozzolanic reacting with CaOH producing additional C-S-H gel that increases the strength of the mortar or concrete. [17, 18]. Niewiadomski et al. studied the effect of nanoparticles with different amounts of SiO₂, TiO₂, and Al₂O₃ nanoparticles on the microstructure of SCC. They found an improvement in the microstructure, toughness properties, and a higher density microstructure [15]. Al-Ani [19] utilized nano-clay (NC) from the local Iraqi natural kaolin clay in SCC production. The study was conducted using three different proportions of NC as a partial cement substitution (2%, 4%, 6%) with the use of quicklime powder (QLP) with (50, 75, and 100) kg. The results showed that the addition of NC alone has a greater effect on SCC samples than reference SCC without any addition of NC and QLP. The best value was obtained for SCC with 6% NC. The addition of NC and QLP has a noticeable effect on strength and durability properties. It found that using 4% NC with 100 kg QLP could improve the workability, strength, and durability of SCC. Hosseini et al. [20] showed through their experimental work that the addition of NC up to 1% resulted in a decrease in the flow diameter spread in the slump test. Also, an increase in flow time (for the V-funnel flow and slump flow tests) was noticed indicating an increase in the viscosity of the fresh SCC. According to test results, 0.5% NC gave the highest strength at both 7 and 28 days of water-curing treatment. But 0.25% of NC content gave the highest compressive strength at 56 days of water-curing treatment. By adding 0.25, 0.50, 0.75, and 1.00% NC to the reference SCC mixture, the water penetration depth was decreased by 17, 27, 39, and 43%, respectively. This means improving the durability of SCC mixtures and acting as dense barriers against the penetration of chemical solutions. Researches show a scientific debate about the global warming phenomenon. One of the main reasons for this phenomenon is carbon dioxide emissions.

As mentioned earlier, the cement industry accounts for about 5-8 of the total global CO₂ value. One of the main disadvantages of SCC is the need for a large amount of cement according to EFNORAC, the recommended amount is 400-600 kg/m³ to achieve the required rheological properties, which in turn increases the risks of environmental pollution because of increases the amount of carbon dioxide emitted [21]. It has been found that incorporating alternative materials into concrete is a successful way to reduce cement and thus reduce carbon dioxide emissions. In this current work, the focus was on three-point:

- Using nano-clay as a partial replacement for cement
- The use of 15% waste glass powder as a partial substitute for cement in concrete mixtures.
- Used a combination of waste glass powder and nano-clay by replacing 15% glass powder partially with nano-clay.

2. Materials and Methods

2.1. Materials

Ordinary Portland cement (OPC) with fineness and specific gravity of 325 m²/kg and 3.15 respectively, was utilized for casting all the concrete mixtures. The chemical properties from the XRF test for cement are illustrated in Table 1, which satisfied the Iraqi specification No.5/1984 [22].

The raw material for Iraqi natural kaolin clay is abundantly available in the quarries of Wadi Houran in the western desert of Anbar Governorate. When this clay is been burned at 700 ° C for two hours, it turns into metakaolin. Its effectiveness can be increased by the ground of the metakaolin to particle size up to the nanoscale and obtained nano-clay (NC). Al-Ani [19] showed in her study the possibility of producing NC from Iraqi metakaolin and

using it effectively in SCC. The NC used in this work was verified by a particle size distributions test (PSD) and scanning electron microscopy (SEM) test, as shown in Figures 1 and 2, respectively. one can see that the particle size of NC is not homogeneous as illustrated by the PSD test results and a wide range of shapes from irregular, spherical particles and agglomerates to rounded nanoparticles were noticed as illustrated in the SEM test result. The XRF test results to illustrate the chemical composition of NC is listed in Table 1. The pozzolanic activity of NC was found to be 106.46 at 28 days. So, NC used in this work meets the ASTM C618-12 [23] requirements for pozzolanic materials.

Table 1. The main chemical composed from XRF test results for cement, NC, and WGP

Oxide composition	Cement	Nano-clay powder	Waste glass powder
CaO	65.26	< 15	1.460
SiO ₂	20.11	50	79.400
Al ₂ O ₃	6.42	42	0.822
Fe ₂ O ₃	3.37	<0.5	0.204

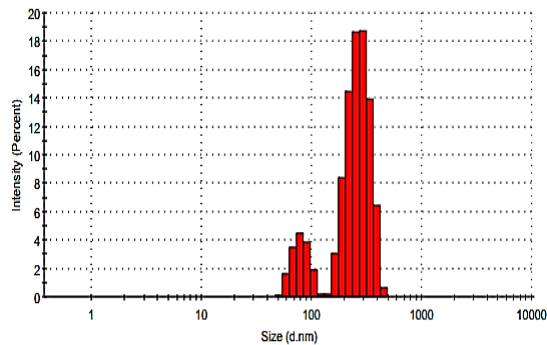


Fig. 1 Particle size distribution for NC

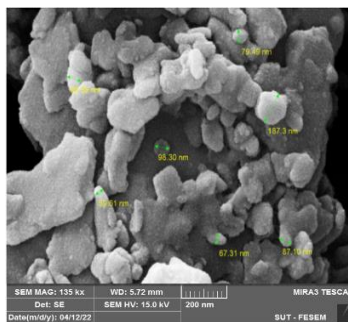


Fig. 2 SEM test for NC

To prepare glass powder, the waste of broken window glass was collected from glass sell shops, and after the collection was completed, the steps for preparing glass powder began as follows: First, wash the collected glass to clean it from dust or any other substance, and then crush it into fine aggregate. Finally, it was ground into a fine powder and passed through the No. 200 sieve, as illustrated in Figure 3. The waste glass powder (WGP) was verified by XRF (see Table 1), PSD, and SEM tests, as shown in Figures 4 and 5, respectively. The pozzolanic activity of WGP was found to be 92.07 at 28 days. So, WGP used in this work meets the ASTM C1240-05 [24] requirements for pozzolanic materials.

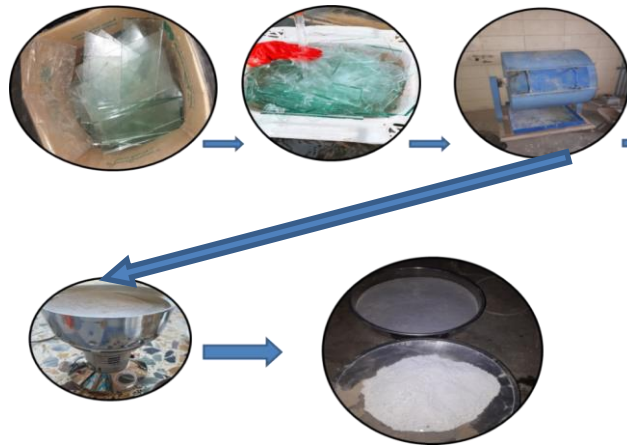


Fig. 3 Glass powder preparation stages

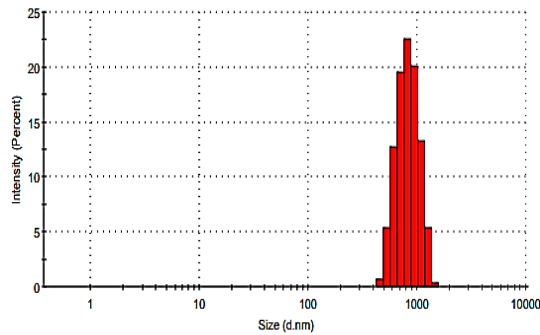


Fig. 4 Particle size distribution for WGP

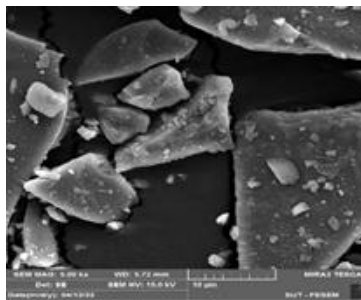


Fig. 5 SEM test for WGP

An aqueous solution of polycarboxylic (sika discrete – 5930) type F was used as a superplasticizer, which meets the ASTM C 494 limitation [25]. Tap water was used for the mixing and curing process.

Natural local sand of 2.5 fineness was used as a fine aggregate. The specific gravity of used sand was 2.62, while percentage of sulfur trioxide (SO_3 %), and the absorption ratio were, 0.1%, and 0.13%, respectively, and these properties were all within the limits of Iraqi Standard No. 45/1984 [26].

Crushed gravel was used in this work with a maximum size of 10 mm as coarse aggregate and has a specific gravity of 2.67. while SO₃%, and the absorption ratio for used coarse aggregate were 0.05%, and 0.3%, respectively, and these values were all within the limits of the Iraqi specification No. 45/1984 [26]. The sieve analysis of fine and coarse aggregates is listed in Table 3.

Table 3. Sieve Analysis of All Used Aggregate

Sieve size (mm)	Cumulative passing %	
	Coarse aggregate	Fine aggregate
12.5	100	100
10	86.76	100
4.75	14.12	95.3
2.36	0.6	85.9
1.18	-	77.3
0.6	-	62.4
0.3	-	16.8
0.15	-	2.0
0.075	-	0.005

2.2. Mix Proportion, Procedure and Tests

The EFNARC Guidelines [3] were utilized as a reference for designing the reference mixture (without NC or WGP). Experimental mixes were made in the laboratory to design the reference mix, which was achieved by trial-and-error method to obtain the best concrete mix design and the best rheological properties of SCC without separating and bleeding, the quantity of mixes constituted are listed in Table 4.

Ten mixes with the same water/binder ratio of 0.365 and a superplasticizer dose of 0.86% by weight of the binder were prepared for the current investigation. The mixes included one reference mix, four sets were completed by partially substituting the cement with various amounts of NC ranging from (2.5 to 10 percent) by weight, one mix with 15% waste glass powder, and four sets were completed by partially substituting the cement with various amounts of NC and waste glass powder, as shown in Table 4. Cement is added to the mixer after the coarse and fine aggregates have been combined for 30 seconds. How to include nanoparticles into concrete mixtures without affecting their original composition and physical qualities is one of the most essential aspects to take into account. In this work, a wet mixing approach was used, in which NC was gradually added to the concrete mixture after being completely mixed for two minutes with some mixing water. The remaining water was used to dissolve the superplasticizer. After the superplasticizer was gradually added, the mixture was mixed for an additional three minutes to achieve complete dissolution, Figure 6 illustrated the mixing process.

The flow capacity of the SCC was evaluated by measuring slump flow diameter (mm), T500 (the time at flow diameter be 500 mm) (sec), V-funnel (sec), and L-box test. For evaluating the ability to pass with the appropriate viscosity that is needed for the fresh mix to remain homogeneous in its composition, a segregation test was adopted, see Figure 7. The results of fresh tests were compared with the limitations of EFNARC standards [3].

For each mix, three 100×100×100 mm cubes for compressive strength based on BS EN 12,390–3 [30], three prisms of 100×100×500 mm sizes for the modulus of rupture test based on ASTM C78-15a [31], three cylinders of diameter 100 mm and height 200 mm for

splitting strength based on, ASTM C496-C [32], and three cylinders of diameter 150 mm and height 300 mm for modulus of elasticity ASTM C469-14 [33], were made. The mechanical properties tests are illustrated in Figure 8.

Table 4. Mixes proportions for one cubic meter

Mixes	Cement kg	Nano- clay kg	Waste glass powder kg	FA kg	CA kg	Water kg	Sp kg
0NC0WGP	465	0	0	870	800	175	4
2.5NC0WGP	453.375	11.62 5	0	870	800	175	4
5NC0WGP	441.75	23.5	0	870	800	175	4
7.5NC0WGP	430.125	34.87 5	0	870	800	175	4
10NC0WGP	418.5	46.5	0	870	800	175	4
0NC15WGP	395.25	0	69.75	870	800	175	4
2.5NC12.5WGP	395.25	11.62 5	58.125	870	800	175	4
5NC10WGP	395.25	23.5	46.5	870	800	175	4
7.5NC7.5WGP	395.25	34.87 5	34.875	870	800	175	4
10NC5WGP	395.25	46.5	23.5	870	800	175	4

NC: Nano-Clay, WGP: Waste Glass Powder, 0NC0WGP: refer to 0% NC and 0% WGP
 SP: Superplasticizer, FA: Fine Aggregate, CA: Coarse Aggregate

All specimens were cast for each mix and poured into moulds without using any vibration. Before this, all casting moulds are cleaned, and the internal surfaces are lubricated with a suitable liquid. All specimens were prepared at the laboratory conditions with a temperature of $20 \pm 2^\circ\text{C}$ and a relative humidity of $60 \pm 5\%$. After casting, the concrete samples were covered with nylon plates in the laboratory for 24 hours before being demoulded and transferred to a water-curing tank for 28 days. All specimens are tested after 28 days of curing.



Fig. 6 Mixing processes



Fig. 7 Fresh Properties' Tests

3. Results and Discussion

3.1. Rheological tests results

3.1.1. Flow diameter, T500, and V-funnel fresh tests

Figure 9 shows the slump flow diameters (SFDs) for each SCC mix. According to EFNARC guidelines [3], the SFD results for all SCC mixes were divided into the SF2 and SF3 groups. Additionally, the SFDs results showed that the reference mix (0NC0WGP), 2.5NC0WGP, 0NC15WGP, and 2.5NC12.5WGP belonged to the SF3 classification and the highest recorded value was 780 mm for 0NC0WGP.

In SCC mixes with NC alone, the SFD values decrease from 780 mm for 0NC0WGP to 708 mm for the 10NC0WGP mix. Figure 10 shows the recorded time required to reach a flow diameter of 500 mm i.e. T500 in a second. The higher recorded value was 3.45 sec. for the 10NC5WGP mix and the lower value was 1.95 for 0NC0WGP. According to these results, all mixes lie in VS2 classification except the 0NC0WGP mix, which lies in VS2 classification. Where the VS1 and VS2 presented viscosity classes expressed by T500.

Figure 11 shows the recorded time required to pass through V shape funnel in a second. The higher recorded value was 23.6 sec. for 10NC5WGP mix and the lower value was 8 sec. for 0NC0WGP. According to these results, all mixes lie in the VF2 classification. The reason why the SFDs for NC mixes are smaller than the SFD for the control mix while T500 is higher compared to the control mix is primarily due to the high surface area of nanoparticles that led to an increase in the surface area of cementitious paste. In addition, the finer nanoparticles are causing an increase in water demand and absorbing more water, leaving less free water and contributing to the flow ability. Also, the stiffening influence of NC, which likewise decreased the SFDs is another factor [34, 35].

While the increase in V-funnel time can be attributed to the flocculation mechanism, which results in a thickened fresh mix because NC particles increase the flocculation ability of fresh concrete mixture. In reality, flocculation draws particles into the water, increasing the volume of solids and stiffening the fresh mixture as a result [36, 37]. and similar results were found by Al-Ani [19].

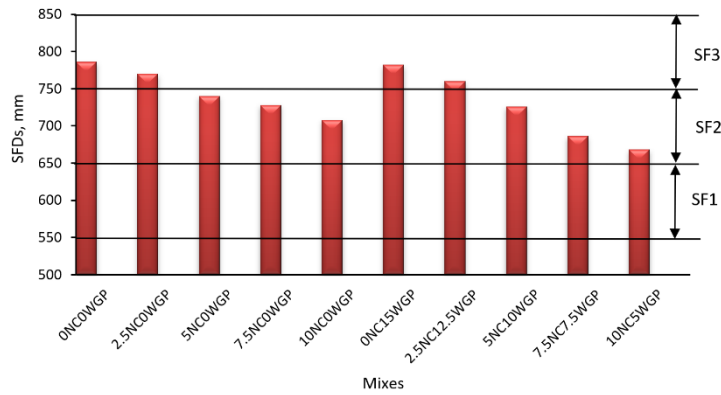


Fig. 9 SFDs for all SCC mixes

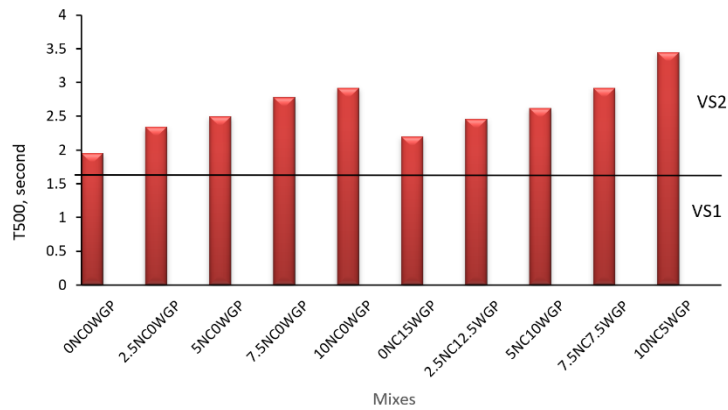


Fig. 10 T500 for all SCC mixes

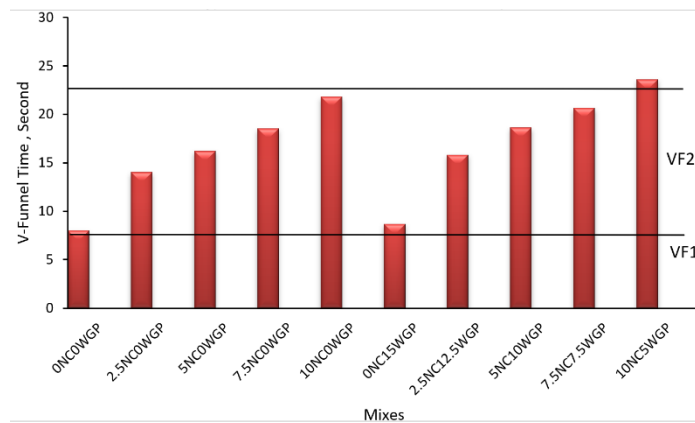


Fig. 11 V-funnel time for all SCC mixes

The SCC mixes with 15% WGP alone and has an SFD of 782 mm. This means that adding waste glass powder did not affect the flow diameter of the mixture. The recorded T500 value was 2.2 sec. for the 0NC15WGP mix vs. 1.95 sec. for 0NC0WGP. While the recorded V-funnel time value was 8.86 sec. for 0NC15WGP mix vs. 8 sec. for 0NC0WGP. This outcome

may be attributable to the fact that the particle size distribution of cement and WGP is somewhat close [38]. Similar results were found by Khudair et al. [38]. By using recycled glass powder as a partial cement replacement, they looked at the characteristics of self-compacting concrete both while it was fresh and when it had hardened. Five mixtures were prepared for their study, each with a different percentage of ground glass powder used as a cement replacement: 0%, 10%, 20%, 30%, and 40% by weight. The rheological characteristics of the produced self-compacting concrete were examined using the following metrics: slump flow diameter, the time required to reach a flow diameter of 500 mm, sieve segregation resistance, and L-box height ratio. The test findings show that increasing the partial substitution of cement with glass powder resulted in a minor reduction in T500 mm time and maintenance of flow ability. The SCC mixes with the combination of WGP and NC show a decrease in SFDs and an increase in flow time. This may be due to the combined effect of these two pozzolanic materials that led to an increase in the volume of solids and stiffening of the fresh mixture as a result [11], [20].

Figure 12 illustrates the relationship between V-funnel flow and T500 flow time and these results are within the EFNARC 2005-recommended viscosity scale. A linear relation was found between Tv-funnel and T500 with R2 equal to 0.8909 as follows:

$$T_{v-funnel} = 11.526(T_{500}) - 13.546 \tag{1}$$

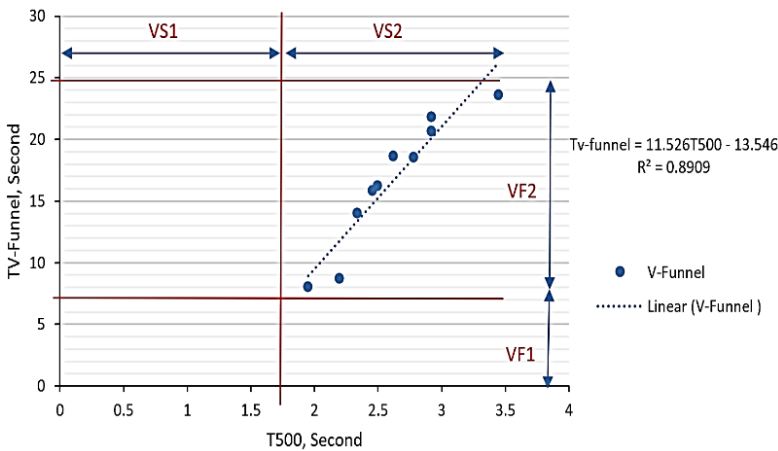


Fig. 12 V-funnel time vs. T500 for all SCC mixes

3.1.2 L-box and Sieve Segregation tests

The blocking ratio can be defined as the ratio between the concrete height at the end of the horizontal section (H2) of the L-box, and the height of the remaining concrete in the vertical section (H1) of the L-box.

The highest blocking ratio from L-Box's test was obtained for the ONC0WGP mix (0.94) and ONC15WGP (0.93) and the lowest ratio was obtained for the 10NC5WGP mix (0.82), as shown in Figure 13. Replacing cement with NC or NC with WGP gradually reduced the L-box ratio results, whereas WGP did not affect the L-box ratio results of the SCC mix. The same behavior was noticed in the segregation test, the segregation ratio was decreased with replacing cement with NC and WGP, as shown in Figure 14. The reason for this is that NC has a large specific surface area, it easy to form a flocculent network microstructure, and can absorb more free water during hydration [39] and along with the fact that both NC

and WGP have active pozzolanic reactions, which raise the need for water demand and decrease workability.

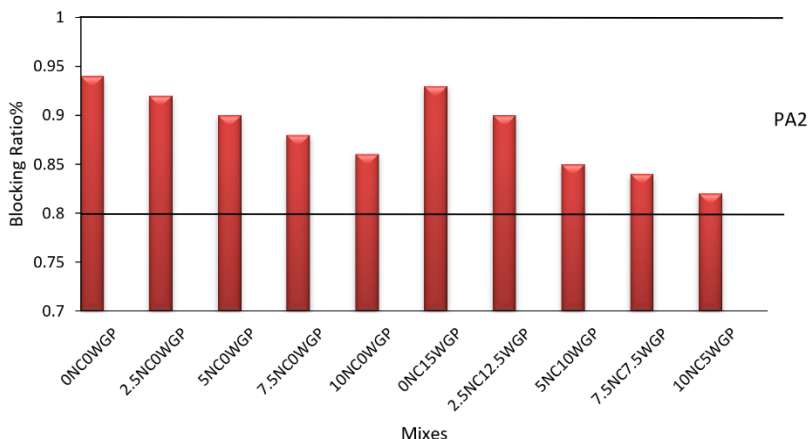


Fig. 13 Blocking ratio for all SCC mixes

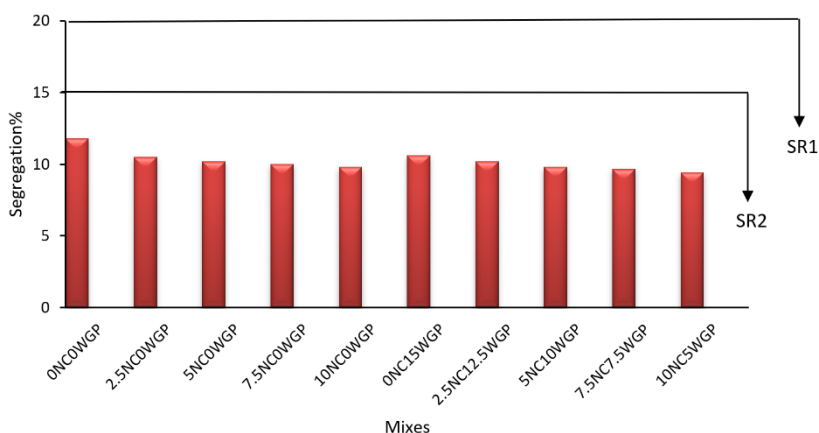


Fig. 14 Segregation ratio for all SCC mixes

3.2. Mechanical Properties

3.2.1. Compressive strength and modulus of elasticity

Figure 15 shows the compressive strength of reference and SCC mixes incorporating various weight percentages of NC and WGP. The highest compressive strength was found for 2.5NC12.5WGP (80.6 MPa). for all mixes, the compressive strength was higher than the one for the reference mix (62 MPa) except for the 10NC0WGP mix (58.8 MPa), which has the lowest compressive strength and 10NC5WGP (60.28).

The modulus of elasticity of concrete is mostly correlated with compressive strength [40]. The modulus of elasticity is calculated through the compression test of the cylinder, where the resulting stress and strain are recorded so that the modulus of elasticity is calculated from the following equation:

$$E_c = \frac{S_2 - S_1}{\epsilon_2 - 0.00005} \tag{2}$$

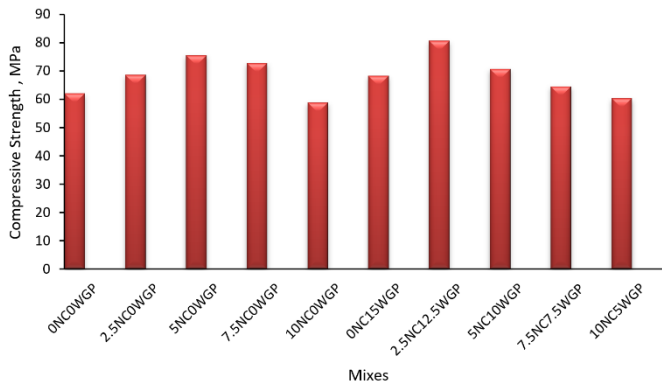


Fig. 15 Compressive strength for all SCC mixes

Where E_c is the static modulus of elasticity (MPa), S_2 is stress corresponding to (40%) of ultimate strength (MPa), S_1 is stress corresponding to a longitudinal strain ($\epsilon_1=0.00005$) (Mpa), and ϵ_2 is Longitudinal strain formed by stress S_2 . The results of the modulus of elasticity are illustrated in Figure 16. The highest modulus of elasticity was found for 2.5NC12.5WGP and the lowest modulus of elasticity was for 10NC0WGP.

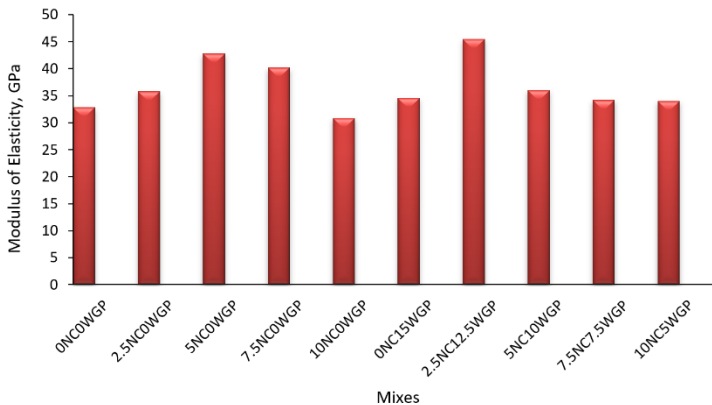


Fig. 16 Modulus of elasticity for all SCC mixes

As a result of NC and WGP particles' pozzolanic behavior in the cementitious matrix and their reaction with $Ca(OH)_2$, which results from cement hydration, form a dense Calcium Silicate-Hydrate (C-S-H) gel, so the compressive strength of SCC mixed with NC has increased. Additionally, NC particles can fill the micropores and strongly bond with the bulk volume of the matrix to create a more compact and integrated microstructure [41].

But increased NC content of more than 7.5% led to a decrease in compressive strength. This is because of a weakening of the interfacial transition areas in the mortar or concrete matrix [42] The scattering defect results in fewer matrix contact points and has a negative influence on bonding with cement particles [43, 44]. According to experimental results, a

linear relationship between compressive strength and modulus of elasticity is suggested as shown in Figure 17 and illustrated in the following equation:

$$E_c = E_c = 0.6341f_c - 6.5585 \tag{3}$$

Where: E_c = is static modulus of elasticity (GPa) and f_c = compressive strength (MPa)

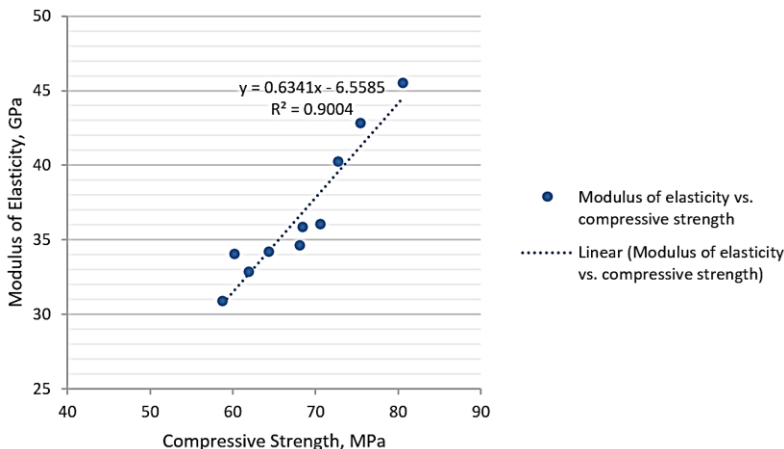


Fig. 17 Modulus of elasticity vs. compressive strength for all SCC mixes

3.2.2. Flexural and splitting strengths

Figure 18 and Figure 19 show the flexural and splitting strengths, respectively of reference and SCC mixes incorporating various weight percentages of NC and WGP. The highest flexural tensile strength was found for 2.5NC12.5WGP (5.84 MPa) and 5NC0WGP (5.5 MPa). While the lowest flexural tensile strength was for 10NC0WGP (3.88 Mpa). The highest splitting tensile strength was found for 5NC0WGP (4.64 MPa) and it was closed for 2.5NC12.5WGP (4.6 MPa). While the lowest splitting tensile strength was also for 10NC0WGP (2.8 Mpa), as shown in Figure 19. This is because the specimens' bonding and hydration were enhanced by the finer size and specific gravity of NC and the pozzolanic nature of both NC and WGP [8, 45, 46]. According to experimental results, a linear relationship between compressive strength and indirect tensile strengths are suggested as shown in Figure 20 and 21 and illustrated in the following equations:

$$f_t = 0.6341f_c - 6.5585 \tag{4}$$

$$f_{st} = 0.6341f_c - 6.5585 \tag{5}$$

Where: f_t = is flexural tensile strength (MPa) and f_{st} = splitting tensile strength (MPa).

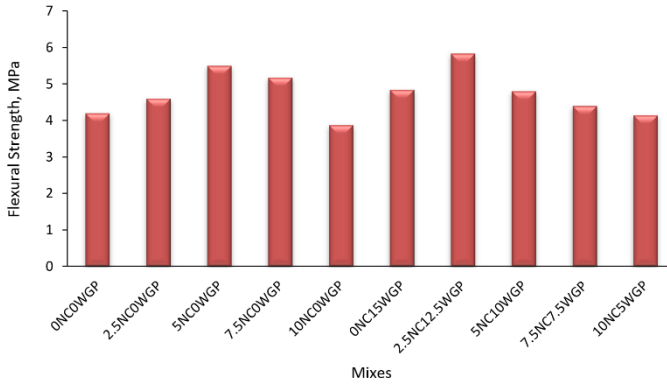


Fig. 18 Flexural strength for all SCC mixes

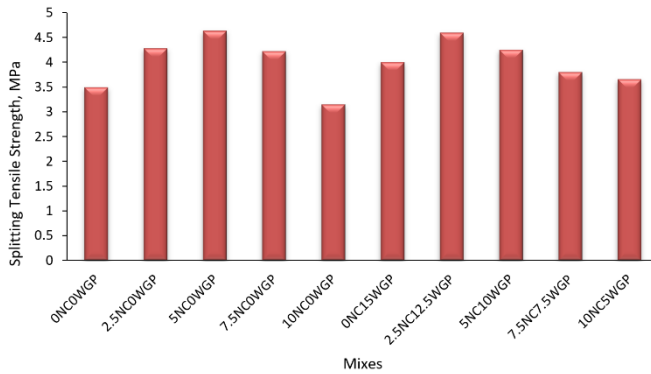


Fig. 19 Splitting strength for all SCC mixes

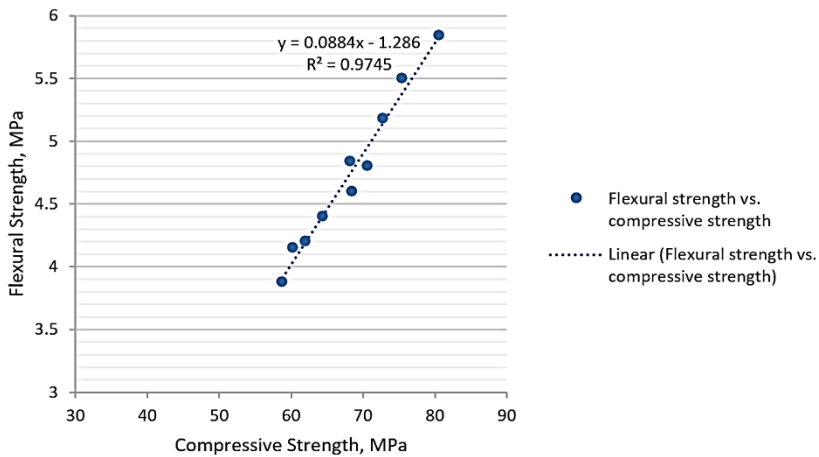


Fig. 20 Flexural strength vs. compressive strength for all SCC mixes

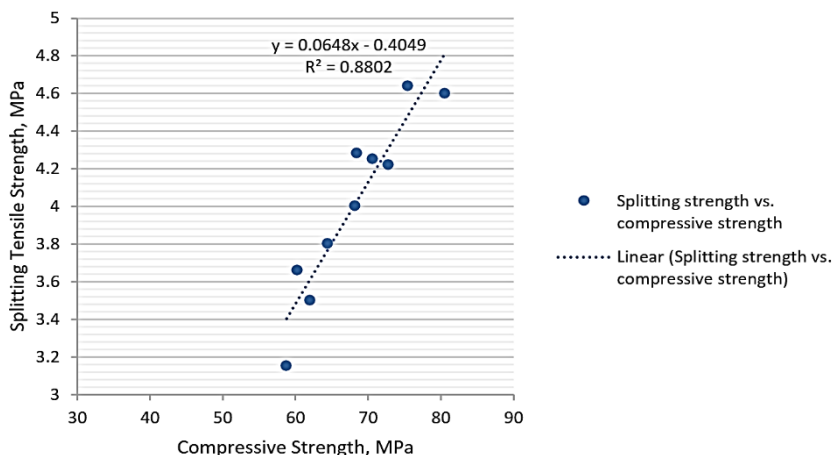


Fig. 21 Splitting strength vs. compressive strength for all SCC mixes

3.3. Permeation's Properties

The results of the experiments on absorption and permeable void ratios are shown in Figure 22 and 23, respectively. The findings showed that the SCC mixes' water absorption was reduced by the addition of NC and WGP. Additionally, compared to the reference SCC, the water absorption values for NC and WGP were lower. Additionally, the higher weight percentages of NC (> 7.5%), in contrast to all other contents of NC alone or with WGP in SCC, resulted in higher water absorption than the reference mix.

The amount of free water that can be kept in a mixture depends on the surface area of the solid particles and their fineness. Additionally, free water is not disturbed when there is no compacting procedure. As a result, the ITZ has fewer pores since there is less of a tendency for water to flow into and concentrate around aggregates [47, 48]. Lower water absorption is shown when more fillers or pozzolanic materials, such as NC and WGP, are added to the SCC mixture [47]. This effect may be attributed to improved particle distribution, less inter-particle friction, and increased packing density. A Higher NC replacement value (10%), however, may result in higher water absorption. Therefore, using NC and WGP to replace the cement has a favorable effect on SCC.

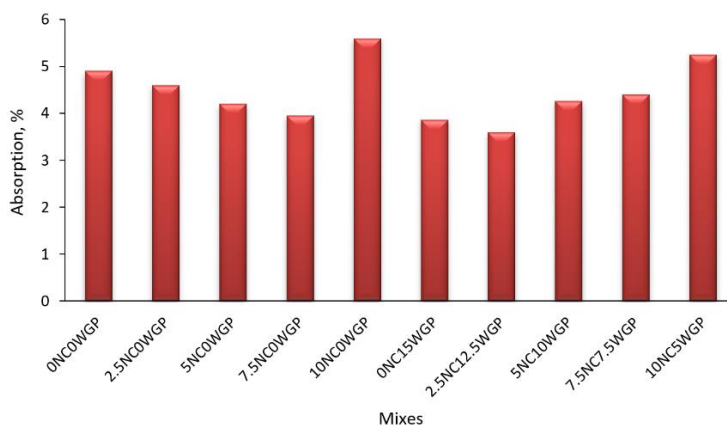


Fig. 22 Water absorption% of all mixes

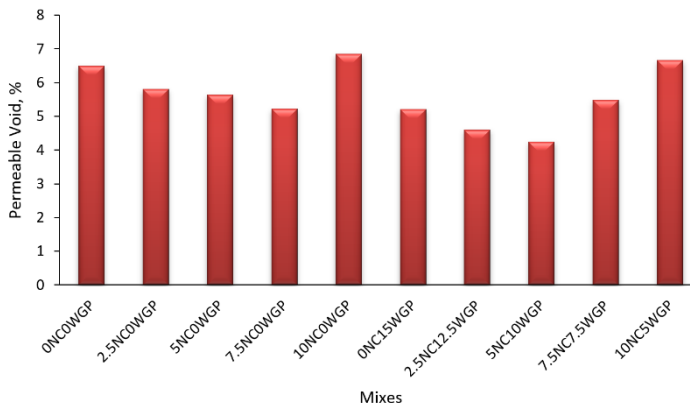


Fig. 23 Permeable voids % of all mixes

4. Conclusions

Based on experimental work the following conclusions are drawn:

- For all SCC mixes contain NC, the SFD values decrease from 780 mm for 0NC0WGP to 708 mm for the 10NC0WGP mix.
- The SCC mix with 15% WGP has an SFD of 782 mm. This means that adding waste glass powder did not affect the flow diameter of the mixture. The recorded T500 value was 2.2 sec. for the 0NC15WGP mix vs. 1.95 sec. for 0NC0WGP. While the recorded V-funnel time value was 8.86 sec. for 0NC15WGP mix vs. 8 sec. for 0NC0WGP.
- The higher recorded T500 value was 3.45 sec. for the 10NC5WGP mix and the lower value was 1.95 for 0NC0WGP. According to these results, all mixes lie in the VS2 classification except the 0NC0WGP mix, which lies in the VS2 classification.
- The results of the tests on the fresh concrete showed that the NC reduces the fluidity and flowability of the mixtures, while the addition of glass has almost no effect. While the addition of WGP with NC led to an additional decrease in the flowability of the mixture.
- The highest compressive strength was found for 2.5NC12.5WGP and 5NC0WGP. For all mixes, the compressive strength was higher than the one for the reference mix (62 MPa) except 10NC0WGP and 10NC5WGP.
- The highest modulus of elasticity of SCC is found at 45.5 GPa for 2.5NC12.5WGP, while the lowest value was found for 10NC0WGP.
- The highest flexural tensile strength was found for 2.5NC12.5WGP and 5NC0WGP. While the lowest flexural tensile strength was for 10NC0WGP.
- The highest splitting tensile strength was found for 5NC0WGP and it was closed for 2.5NC12.5WGP. While the lowest splitting tensile strength was also for 10NC0WGP
- The results showed that the SCC mixes' water absorption was reduced by the addition of NC and WGP. Additionally, compared to the reference SCC, the water absorption values for NC and WGP were lower. Additionally, the higher weight percentages of NC (> 7.5%) water absorption than the reference mix.
- Finally, it can be concluded that the replacing cement with 2.5%NC and 12.5%WGP gave the best fresh and hardened properties for SCC mix.

References

- [1] Malherbe JS. (2015). Self-compacting concrete versus normal compacting concrete: a techno-economic analysis. MSc. Thesis, Stellenbosch: Stellenbosch University.
- [2] Mastali M, Dalvand A, Sattarifard A. The impact resistance and mechanical properties of the reinforced self-compacting concrete incorporating recycled CFRP fiber with different lengths and dosages. *Composites Part B: Engineering*, 2017; 112: 74-92. <https://doi.org/10.1016/j.compositesb.2016.12.029>
- [3] EFNARC (2005). Specification and guidelines for self-compacting concrete. European Federation for Specifications Construction Chemical & Concrete System. <http://www.efnarc.org>.
- [4] Ahmad S, Umar A. Fibre-reinforced Self-Compacting Concrete: A Review. IOP Conference Series: Materials Science and Engineering, 2018. <https://doi.org/10.1088/1757-899X/377/1/012117>
- [5] Memon NA, Memon MA, Lakho NA, Memon FA, Keerio MA, Memon AN. A review on self-compacting concrete with cementitious materials and fibers. *Engineering, Technology & Applied Science Research*, 2018; 8: 2969-2974. <https://doi.org/10.48084/etasr.2006>
- [6] Keryou AB, Ibrahim GJ. Effect of using windows waste glass as coarse aggregate on some properties of concrete. *Engineering and technology journal*, 2014; 32: 1519-1529.
- [7] Islam GS, Rahman M, Kazi N. Waste glass powder as partial replacement of cement for sustainable concrete practice. *International Journal of Sustainable Built Environment*, 2017; 6: 37-44, 2017. <https://doi.org/10.1016/j.ijbsbe.2016.10.005>
- [8] Mohammed TK, Hama SM. Mechanical properties, impact resistance and bond strength of green concrete incorporating waste glass powder and waste fine plastic aggregate. *Innov. Infrastruct. Solut.*, 2022; 7, 49. <https://doi.org/10.1007/s41062-021-00652-4>
- [9] Hama SM, Ali ZM, Zayan HS, and Mahmoud AS. Structural behavior of reinforced concrete incorporating glass waste as coarse aggregate. *Journal of Structural Integrity and Maintenance*, 2023; 8(1): 59-66. <https://doi.org/10.1080/24705314.2023.2165470>
- [10] Yassen MM, Hama SM, Mahmoud AS (2018) Reusing of Glass Wastes as Powder as Partial of Cement in Production of Concrete. 2018 11th International Conference on Developments in eSystems Engineering (DeSE) 2018.00065. <https://doi.org/10.1109/DeSE.2018.00065>
- [11] Mahmoud AS, Yassen MM, Hama SM (2019). Effect of Glass Powder as Partial Replacement of Cement on Concrete Strength and Stress-Strain Relationship. 12th International Conference on Developments in eSystems Engineering (DeSE), 2019. <https://doi.org/10.1109/DeSE.2019.00030>
- [12] Aliabdo AA, Abd Elmoaty M, Aboshama AY. Utilization of waste glass powder in the production of cement and concrete. *Construction and Building Materials*, 2016; 124:866-877 8. <https://doi.org/10.1016/j.conbuildmat.2016.08.016>
- [13] Vanjare MB, Mahure SH. Experimental investigation on self compacting concrete using glass powder. *International Journal of Engineering Research and Applications (IJERA)*, 2012;2:488-149.
- [14] Rehman S, Iqbal S, Ali A. Combined influence of glass powder and granular steel slag on fresh and mechanical properties of self-compacting concrete. *Construction and Building Materials*, 2018;178: 153-160. <https://doi.org/10.1016/j.conbuildmat.2018.05.148>
- [15] Liu M. Incorporating ground glass in self-compacting concrete," *Construction and Building Materials*, 2011;25: 919-925. <https://doi.org/10.1016/j.conbuildmat.2010.06.092>

- [16] Hunashyal A, Banapurmath N, Jain A, Quadri S, Shettar A. Experimental investigation on the effect of multiwalled carbon nanotubes and nano-SiO₂ addition on mechanical properties of hardened cement paste," *Adv. Mater.*, 2014; 3(5):45-51. <https://doi.org/10.11648/j.am.20140305.13>
- [17] Said AM, Zeidan MS, Bassuoni MT, Tian Y. Properties of concrete incorporating nano-silica. *Construction and Building Materials*, 2012;36: 838-844. <https://doi.org/10.1016/j.conbuildmat.2012.06.044>
- [18] Niewiadomski P, Stefaniuk D, Hoła J. Microstructural Analysis of Self-compacting Concrete Modified with the Addition of Nanoparticles. *Procedia Eng.*, 2017;172: 776-783. <https://doi.org/10.1016/j.proeng.2017.02.122>
- [19] Al-Ani NYR. (2021). Effect of Nano-clay on Flexural behavior and some Hardened properties of lightweight self-compacting concrete. MSc. thesis University of Anbar, Iraq.
- [20] Hosseini P, Afshar A, Vafaei B, Booshehrian A, MolaeiRaisi E, Esraflia A. Effects of nano-clay particles on the short-term properties of self-compacting concrete. *Eur J Environ CivEng*, 2017; 21(2):127- 147. <https://doi.org/10.1080/19648189.2015.1096308>
- [21] WJ. Long, Y. Gu, J. Liao, and F. Xing, "Sustainable design and ecological evaluation of low binder self-compacting concrete," *Journal of Cleaner Production*, vol. 167, pp. 317-325, 2017. <https://doi.org/10.1016/j.jclepro.2017.08.192>
- [22] Iraqi Specification No.5. Portland Cement. The cement Agency for Standardization and Quality Control, Baghdad,1984.
- [23] ASTM C618-12a. Standard Specification for Coal Fly Ash and Raw or Calcined Natural Pozzolan for Use in Concrete. ASTM Int. West Conshohocken, PA, 2012.
- [24] ASTM C1240-05. Standard Specification for Silica Fume Used in Cementitious Mixtures. *Annu B ASTM Stand.* 2005;1-7.
- [25] ASTM C494/C494M-13. Standard Specification for Chemical Admixtures for Concrete. *Annu B ASTM Stand.* 2013.
- [26] Iraqi Specification No. 45, 1984. Aggregate from natural sources for concrete and construction. Baghdad, Iraq. 1984.
- [27] B. S. EN (2002) 12390-3, Testing hardened concrete-Part 3: Compressive strength of test specimens. *Br. Stand. Inst.* 39.
- [28] ASTM C496/C496M-17 (2017) Standard Test Method for Splitting Tensile Strength of Cylindrical Concrete Specimens. ASTM International, West Conshohocken, PA
- [29] ASTM C78/C78M-15a (2015) Standard Test Method for Flexural Strength of Concrete. ASTM International, West Conshohocken, PA 40.
- [30] BS 12390-3. Testing Hardened Concrete: Compressive Strength of Test Specimens. British Standard Institution, London. 2009.
- [31] ASTM C78-15. Standard test method for flexural strength of concrete (using a simple beam with third-point loading). American Society for Testing and Material, 2015.
- [32] ASTM C496-05. Splitting tensile Strength of Cylindrical Concrete Specimens. American Society of Testing and Material International, 2005.
- [33] ASTM C469, "Standard test method for static modulus of elasticity and Poisson's ratio of concrete in compression." American Society for Testing and Material, 2014.
- [34] Kwalramani MA, Syed ZI. Application of nanomaterials to enhance microstructure and mechanical properties of concrete. *Int. J. Integr. Eng.*, 2018;10(2). <https://doi.org/10.30880/ijie.2018.10.02.019>
- [35] Kawashima S, Kim JH, Corr DJ, Shah SP. Study of the mechanisms underlying the fresh-state response of cementitious materials modified with nanoclays. *Construction and Building Materials*, 2012;36: 749-757. <https://doi.org/10.1016/j.conbuildmat.2012.06.057>
- [36] Newman J, Choo BS. *Advanced concrete technology 2: concrete properties.* Elsevier, 2003.

- [37] Tregger NA, Pakula ME, Shah SP. Influence of clays on the rheology of cement pastes. *Cem. Concr. Res.*, 2010;40(3):384-391. <https://doi.org/10.1016/j.cemconres.2009.11.001>
- [38] Khudair AY, Mohammed MK, and Hama SM. Optimization of glass powder content in self-compacting concrete as partial replacement of cement. 2nd International Scientific Conference of Al-Ayen University (ISCAU-2020). IOP Conf. Series: Materials Science and Engineering 928 (2020) 022140. <https://doi.org/10.1088/1757-899X/928/2/022140>
- [39] Amin M, Abu el-Hassan K. Effect of using different types of nano materials on mechanical properties of high strength concrete. *Construction and Building Materials*, 2015;80: 116-124. <https://doi.org/10.1016/j.conbuildmat.2014.12.075>
- [40] Dinakar P, Reddy MK, Sharma M. Behaviour of self compacting concrete using Portland pozzolana cement with different levels of fly ash. *Mater. Des.*, 2013;46: 609-616. <https://doi.org/10.1016/j.matdes.2012.11.015>
- [41] Hosseini P, Hosseinpourpia R, Pajum A, Khodavirdi MM, Izadi H, Vaezi A. Effect of nano-particles and aminosilane interaction on the performances of cement-based composites: An experimental study. *Construction and Building Materials*, 2014; 66:113-124. <https://doi.org/10.1016/j.conbuildmat.2014.05.047>
- [42] Liao KY, Chang PK, Peng YN, Yang CC. A study on characteristics of interfacial transition zone in concrete," *Cem. Concr. Res.*, 2004; 34(6):977-989. <https://doi.org/10.1016/j.cemconres.2003.11.019>
- [43] Abdel Gawwad HA, Abd El-Aleem S, Faried AS. Influence of nanosilica and-metakaolin on the hydration characteristics and microstructure of air cooled slag-blended cement mortar. *Geosystem Eng.*, 2017; 20(5):276- 285. <https://doi.org/10.1080/12269328.2017.1323678>
- [44] Nadeem A, Memon SA, Lo TY. The performance of fly ash and metakaolin concrete at elevated temperatures. *Construction and Building Materials*, 2014; 62: 67-76. <https://doi.org/10.1016/j.conbuildmat.2014.02.073>
- [45] Ibrahim AM. The effect of nano metakaolin material on some properties of concrete. *Diyala J. Eng. Sci.*, 2013;6(1):50-61. <https://doi.org/10.24237/djes.2013.06105>
- [46] Alrashedi B, Hassan M. Effects of nano and micro size of clay particles on the compressive and tensile strength properties of self-consolidating concrete. *MATEC Web Conf.*, 2018;162:1-5. <https://doi.org/10.1051/mateconf/201816202030>
- [47] Kristiawan SA, Murti GY. Porosity of Self-Compacting Concrete (SCC) incorporating high volume fly ash. *IOP Conference Series: Materials Science and Engineering*, 2017; 176(1):12043. <https://doi.org/10.1088/1757-899X/176/1/012043>
- [48] Valcuende M, Parra C, Marco E, Garrido A, Martínez E, Cánoves J. Influence of limestone filler and viscosity-modifying admixture on the porous structure of self-compacting concrete. *Construction and Building Materials*, 2012; 28(1):122-128, 2012. <https://doi.org/10.1016/j.conbuildmat.2011.07.029>

Blank Page



Technical Note

Seasonal variation in aerosol optical depth and study of PM_{2.5}-AOD empirical relationship in Raipur, Chhattisgarh, India

Pallavi Pradeep Khobragade^{*1,a}, Ajay Vikram Ahirwar^{2,b}

¹Department of Civil Engineering, Rungta College of Engineering and Technology, Raipur, India

²Department of Civil Engineering, National Institute of Technology, Raipur, India

Article Info

Article history:

Received 08 Oct 2022

Accepted 12 Apr 2023

Keywords:

PM_{2.5};
Aerosol Optical Depth;
Aerosol Optical
Thickness;
Back-trajectory
analysis;
Ozone Monitoring
Instrument;
Modern-Era
Retrospective Analysis
for Research and
Application

Abstract

Owing to urbanization and industrialization, PM_{2.5} (particulate matter with a diameter of less than 2.5 m) pollution has developed into a severe environmental issue. The limited geographical precision and inadequate coverage of PM_{2.5} measurement stations hinders research into the sources of contamination and the associated health hazards. The complex link between PM_{2.5} and aerosol optical depth (AOD), which is again confounded by meteorological conditions, makes retrieving PM_{2.5} from space difficult. AOD dataset was obtained from multiple satellite data retrieval tools including MERRA and OMI for the year 2020. Assessment of annual, seasonal and monthly AOD variation was carried out. The average aerosol optical depth obtained from OMI and MERRA is 1.60 ± 0.56 and 1.33 ± 0.12 respectively. Maximum AOD value was recorded in the summer, while the lowest value was recorded in the winter. Both the OMI and the MERRA AOD monthly change trends were similar, according to the comparative data. The months with the highest AOD values were July and October, and the months with the lowest AOD values were April and November. In the region, aerosol optical thickness (AOT) shows a significant seasonal change. Back-trajectory analysis indicated the contribution from local as well as distant sources. A significant association between PM_{2.5}-AOD was found with R -square = 0.71 with validated model showing good model performance and can be used for predicting future ground-based PM_{2.5} concentrations in the region. Substantial site-specific AOD-PM_{2.5} associations enable OMI AOD to be used to monitor pollution levels.

© 2023 MIM Research Group. All rights reserved.

1. Introduction

Pollution caused by PM_{2.5} aerosols (particulate matter with a diameter less than 2.5 m) has long been a concern for the environment and for people's health [1,2]. The optical and microphysical properties of aerosols continue to be one of the largest sources of uncertainty when assessing the climatic forcing attributable to particles [2]. Aerosols can have significant impacts on the climate on local to global dimensions, but the magnitude and relevance of these effects are largely unknown [3]. Aerosols impact on the radiative equilibrium by scattering and absorbing radiation through solar energy [4]. Indirect effects on climate due to aerosols include aerosol-cloud interactions [5]. Aerosols' role in the atmosphere is determined by their physical, chemical, and optical properties, as well as complicated aerosol interactions changing greatly in both space and time [6]. Significant parameters controlling the radiative impacts include aerosol optical depth (AOD) or aerosol optical thickness (AOT), single scattering albedo (SSA) and Angstrom exponent (AE) [7]. The most important factors for determining the AOD are aerosol bulk load and aerosol extinction efficiency [8].

*Corresponding author: khobragadepallavi19@gmail.com

^a orcid.org/0000-0002-0861-1709; ^b orcid.org/0009-0003-0035-2030

DOI: <http://dx.doi.org/10.17515/resm2023.548ma1008tn>

Res. Eng. Struct. Mat. Vol. 9 Iss. 3 (2023) 763-773

The most important methods used and customized to study aerosol optical characteristics and the radiative impact that aerosols have on climatic conditions are satellite and ground-based multispectral data. Ground-based devices are the easiest to calibrate and, as a result, the least precise, and hence serve as the foundation for satellite algorithm calibration [9]. In China, the Pearson correlation coefficient of surface $PM_{2.5}$ and AOD indicates large inter-annual changes (27%) but no statistically significant trends. However, their application is limited to the area in which they operate [10]. Increasing AOD product geographic coverage is critical for mapping $PM_{2.5}$ variance, particularly in metropolitan regions [11]. Remote sensing technology, on either side, has become progressively popular in the recent decade for quantifying aerosols around the world [12]. Because of its fundamental virtue of giving full and comprehensive mapping of huge areas in single snap-shots, it is a new but strong technique for examining aerosol spatial distribution and attributes. Satellite data give global views of the Earth and enable for the retrieval of the spatiotemporal aerosol dispersion, which is caused by spatial heterogeneities and brief aerosol lifetimes [13]. As a result, aerosol spatial data from long-term operating satellites offers a once-in-a-lifetime opportunity to examine aerosol load and attributes globally and seasonally [14].

A range of satellite sensors (MERRA, OMI, MODIS) and methodologies have been applied for aerosol estimation and pollution load from local to global scales at varying spatial resolutions. The limited temporal resolution, the impacts of surface albedo, and the inclusion of clouds are all downsides of using satellite sensor systems. The aerosol mass concentration, mass extinction efficiency, hygroscopic growth factor, and effective scale height all play a role in the AOD- $PM_{2.5}$ association [15]. The vertical distribution of aerosols is a significant element in the AOD- $PM_{2.5}$ relationship [16]. Previous research indicated good correlation between AOD- $PM_{2.5}$ which will help to predict air quality through satellite data [17]. The relationship between AOD and $PM_{2.5}$ can be used for air quality monitoring, model verification, and data assimilation. The vertical distribution of aerosols is a significant element in the AOD- $PM_{2.5}$ relationship [16].

There are two types of methodologies for estimating near-surface $PM_{2.5}$ using space-borne AOD: observation-based and simulation-based methods [18]. Observation-based approaches rely heavily on statistical correlations among AOD and $PM_{2.5}$ measurements at the surface level [19]. $PM_{2.5}$ and AOD correlation is influenced by regional heterogeneity. Meteorological characteristics such as cloud cover, wind speed, boundary layer, and humidity were used to construct more advanced algorithms for estimating $PM_{2.5}$ from space improving correlation between $PM_{2.5}$ and AOD. If the association among AOD and PM concentration is proven (including $PM_{2.5}$ and PM_{10}), the satellite output can be used to determine the concentration of particulate matter (PM, including $PM_{2.5}$ and PM_{10}) over a vast area [20]. Recent investigations have been conducted across the globe, primarily over the Indo Gangetic Plains (IGP) [5, 21]. As far as we are aware, there are no specific investigations on the aerosol optical characteristics over the central research region. AOD and $PM_{2.5}$ frequently exhibit high connections when particles are in the boundary layer (since they are well mixed). Future research should focus on examining the AOD-PM connection with regard to the types of land uses, the sources of air pollution, and aerosol characterisation [22]. The nature and sources of aerosols and air pollution, as well as the intensity of the correlation between AOD and PM, vary widely, therefore the observed association between AOD and PM in one region cannot be extrapolated to other regions [22]. The present study investigates on annual, seasonal and monthly AOD variations and comparison between data retrieved through satellite sensors during 2020. A model was developed to identify the relationship between $PM_{2.5}$ and AOD with the inclusion of relative humidity in the study area using linear regression analysis approach.

2. Methodology

2.1. Study Area

Raipur, capital of state is a study area of about 1,760,411 people geographically located at the Chhattisgarh state of India Extends from latitude $21^{\circ} 23''$ to longitude $81^{\circ} 65''$. It is a developing city with an area of 226 square kilometers. The maximum temperature in Raipur district is 44.3° C, while the lowest temperature is 12.5° C. The district's total average rainfall is 1370 mm. The city has moderate temperature throughout the year. The area has experienced rapid industrial development and has emerged as a key industrial center in the state. Although the iron and steel industries help the city thrive economically, the city's industrial and vehicular activity lead to urbanization.

2.2. Data Collection

The set of data used in this research consists of one year of observations made during 2020. The data was collected from January 2020 to December 2020 derived from Ozone monitoring instrument (OMI) and Modern-Era Retrospective analysis for Research and Applications (MERRA) satellite data. OMI is a mission to the Earth Observing System (EOS) Aura project from the Netherlands Agency for Aerospace Programs (NIVR) in partnership with the Finnish Meteorological Institute (FMI). The OMI gadget delivers daily global coverage over a 2600-kilometer swath. The AOD data used here was generated using the UV method (OMAERUV) [16, 23, 24]. MERRA was based on a 2008-frozen version of the GEOS-5 atmospheric data assimilation system. MERRA data was created on a $0.5^{\circ} 0.66^{\circ}$ grid with 72 layers [25]. $PM_{2.5}$ data was obtained through online data collection from air quality index data [26].

3. Results and Discussions

3.1. Annual, Seasonal and Monthly AOD Variations

Based on the seasonal changes identified from OMI and MERRA data, the highest AOD value occurred in summer and lowest value occurred in winter. Figure 1. shows the comparison of seasonal AOD variation during Jan 2020 to Dec 2020 from OMI and MERRA satellite data. Table 1 and 2 shows the descriptive statistics of AOD obtained from OMI and MERRA respectively. The comparison results show that both the OMI and MERRA AOD monthly change trends were similar and were compatible with $PM_{2.5}$ seasonal trends. OMI and MERRA show that during summer the concentrations values were maximum which remains constant during spring when observed from MERRA results. The mean AOD values were less during spring as observed through OMI data. The intricacy of the Earth's surface and atmosphere makes it difficult to retrieve AOD from satellites, and it also leads to inconsistencies between the various sensors that are employed [27, 28]. The trend change was similar during autumn and winter using both OMI and MERRA satellite retrieval. In terms of maximum aerosol optical depth, OMI and MERRA reanalysis produce quite similar results. High AOD occurred in summer and is often associated with dusty weather conditions occurring in this season. Low AOD values in winter is attributed to reduced winter wind and dust activity. The downward trend increases from summer to winter during 2020 and is reflected from the perspective that atmospheric conditions would have been more severe in summer than in autumn and winter and the air quality is relatively poor. Typically, places with high $PM_{2.5}$ concentrations also have elevated AOD loads in China and the presence of dust storms results in high PM_{10} and AOD concentrations indicating comparable variation [19].

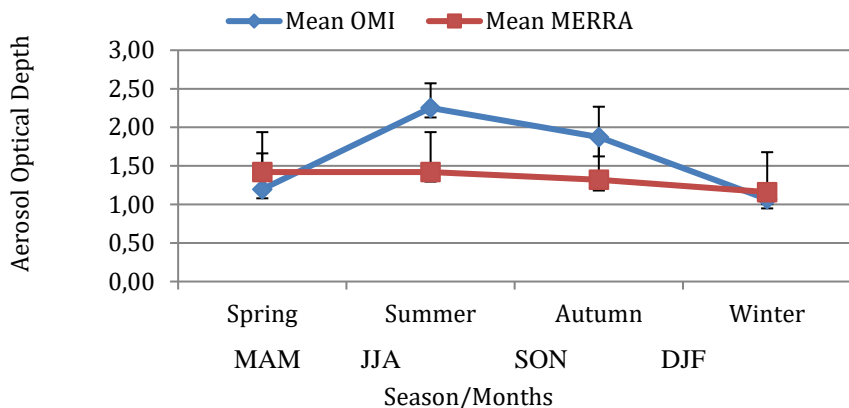


Fig. 1 Seasonal AOD variation during 2020 retrieved from OMI and Merra satellite data

Table 1. Seasonal AOD concentrations during 2020 retrieved from OMI

Season	Mean	Min	Max	Std dev	Std error
Spring	1.20	0.60	1.91	0.47	0.12
Summer	2.25	1.86	2.72	0.32	0.12
Autumn	1.87	1.24	2.32	0.39	0.25
Winter	1.07	0.80	1.38	0.19	0.06

Table 2. Seasonal AOD concentrations during 2020 retrieved from MERRA

Season	Mean	Min	Max	Std dev	Std error
Spring	1.42	0.43	1.84	0.67	0.11
Summer	1.42	0.64	1.92	0.45	0.14
Autumn	1.32	0.61	2.01	0.51	0.21
Winter	1.16	0.50	1.38	0.30	0.01

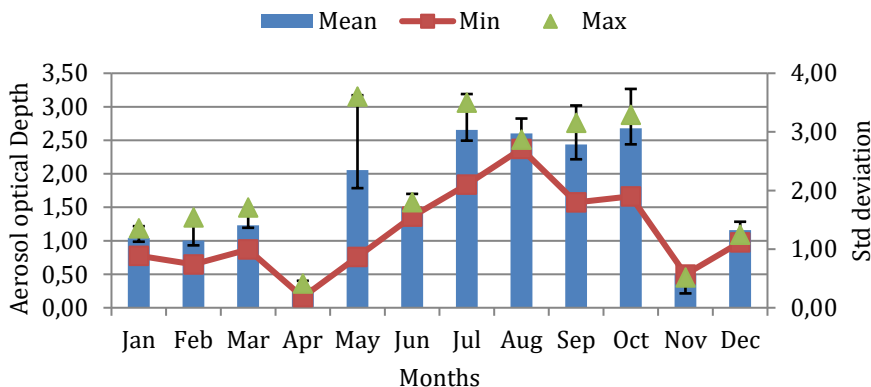


Fig. 2 Monthly AOD variation during 2020 retrieved from OMI satellite data

Figure 2. shows the AOD Data from OMI (-Aura_L2-OMAERUV_2020m0501t0758-o84012_v003-2020m0503t164542.SUB.he5). As monsoon approaches after June, peak values of AOD can be seen arising due to higher wind speeds which may be due to advection of dust particles and increase in columnar water vapour. The high AOD values were observed mainly during July & October and low AOD values during April & November. Excluding the monsoon months, from June to September, October month observed highest OMI mean value over the region which may be attributed from regional crop residue and biomass burning activities. During May, Jun and July transported dust might be the significant contributors to high AODs.

3.2 Seasonal Classification of Aerosols

Figure 3. shows the seasonal AOD variation during summer, monsoon and winter. AOT shows a distinct seasonal variation in the region. The averages of AOT were higher in summer (1.58) than in winter (1.38) and found minimum in monsoon (1.14) season during 2019 to 2020. This indicates that precipitation levels and humidity accumulate the particles and settle them down minimizing their concentration in the air. AOT mainly comprises of fine particles. This signifies that even during summer, the concentration of fine particulates in the region is higher from a stable source. Also, dust aerosol concentrations rise during summer as compared to winter season. Similar seasonal trends are observed in Raipur city with minimum AOD values in winter (0.44 ± 0.15) and maximum values during spring and summer (0.98 ± 0.21) from 2019 to 2021 showing the presence of scattering aerosols in summer and absorbing aerosols in winter season [29]. By utilizing a sunphotometer and the AERONET network, seasonal and yearly fluctuations in the optical characteristics of aerosols in Kanpur, Karachi, and Ahemdabad were tracked [30]. When compared to other sites, the AOD and angstrom exponent were found to be greater in Kanpur. AOD was investigated in Bhubaneswar utilizing satellite and ground-based assessment methods [31]. They discovered that AOD ranged from 0.39 to 0.96, with the highest concentration in February and the lowest in July. In 2013 and 2014, the optical characteristics of Lumbini, Nepal, a UNESCO World Heritage Site were measured [32]. They discovered an average AOD (0.64) with a greater AOD (0.72) post-monsoon. The pre-monsoon month's high AOD suggest that natural desert dust aerosols with a preference for coarse mode particulate have been loaded into the atmosphere in Jodhpur [33].

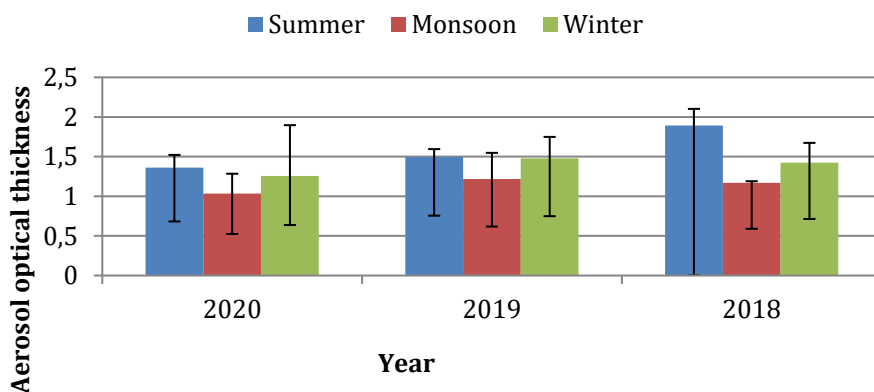


Fig. 3 Monthly mean of aerosol optical thickness at 550 nm during 2018-2020 retrieved from GIOVANNI

3.3 Back Trajectory Analysis

Back trajectory analysis was performed to find the significance of local sources contributing to high aerosol concentrations using Hybrid Single Particle Lagrangian Integrated Trajectory (HYSPPLIT) model developed by National Oceanic and Atmospheric Administration. The trajectories were calculated at 500 m, 1000 m and 2000 m above ground level at latitude 21.25 N and longitude 81.62 E during periods of higher concentrations (GDAS 1 degree, global, 2006-present). Maximum concentrations were observed on 14th May 2020 and 15th May 2020. Local air masses inside the boundary layer enhanced by anthropogenic aerosols are related with the UI type, resulting in high AOD550 and FM values (0.54 and 0.98, respectively) [14]. Figure 4 shows the back trajectories during periods of maximum concentrations. Contribution from local along with distant sources is observed during the period indicating that aerosol in the region is contributed from both natural i.e., windblown mineral dust as well as anthropogenic sources like industrial emissions, vehicular pollution and anthropogenic activities at urban areas.

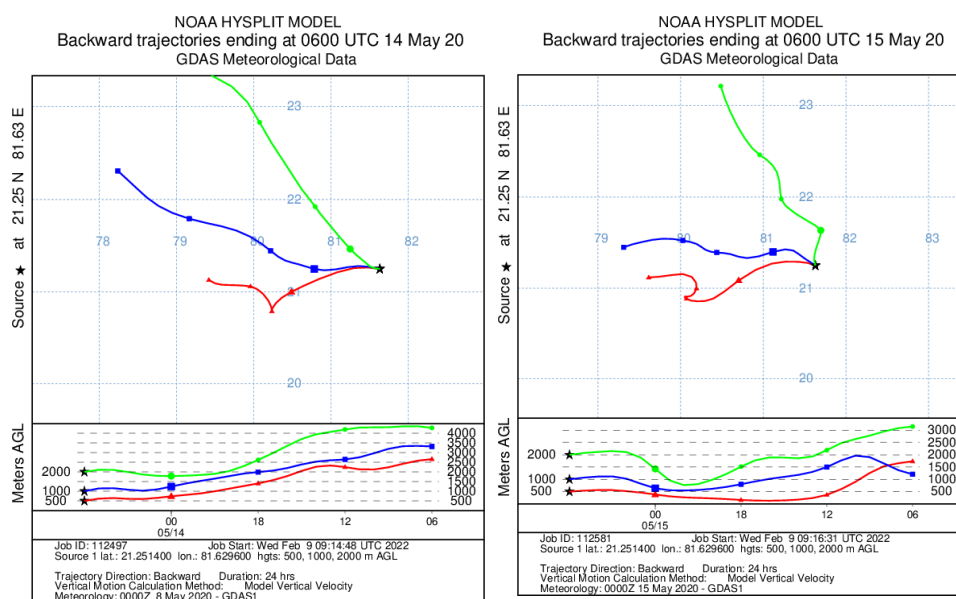


Fig. 4 Back trajectories during periods of maximum concentrations using HYSPLIT model

3.4 Particulate Matter and AOD Correlation

Aerosol particles with a large aerodynamic diameter are responsible for the region's high AOD. Globally, MODIS AOD has a geographic pattern analogous to that of PM_{2.5}. This suggests that areas with high AOD are also likely to have elevated PM_{2.5} levels [19]. Also, aerosol particle hygroscopic expansion was discovered to be widespread, which necessarily results in uncertainty of variable degrees when obtaining AOD from satellite data [34]. Hence, regression analysis was conducted to find out the relation between PM_{2.5}, AOD and RH. Statistical analysis was performed between the parameters to check the significance of the parameters on the PM_{2.5} values. The p-value was found to be significant for AOD (<0.05), however it is observed to be insignificant for RH. Correlation analysis was conducted and correlation co-efficient between AOD and PM_{2.5} was observed to be 0.83 making it significant parameter, whereas for RH it is -0.03 considering the parameter as insignificant. Through statistical analysis, F-value was found to be greater than F-critical

indicating the R^2 value is significant and t-test was performed and observed that t-critical is less than t-value, hence the R^2 value was significant. The R^2 value between $PM_{2.5}$ and AOD was observed as 0.70 ($p < 0.05$). Figure shows the relation between predicted and observed $PM_{2.5}$ values with $R^2 = 0.71$ ($p < 0.05$). Sensitivity analysis was conducted and AOD was observed as an influencing parameter with $R^2 = 0.81$ ($p < 0.05$). Equation 1 represents the developed model. Satellite AOD was utilized in order to obtain $PM_{2.5}$ data from a total of 15 sites in India [35]. They came to the conclusion that the co-efficient was 77%, and the diurnal scale co-efficient ranged from 0.45 to 0.75. AOD- $PM_{2.5}$ correlation studies have yielded conflicting results depending on the study area's size, geographic location, and spatial resolution [21]. On days where there is no discernible relationship between AOD and $PM_{2.5}$, this variability is likely due to a number of different causes. Numerous factors, such as local aerosol origins and weather patterns, greatly affect $PM_{2.5}$ levels. $PM_{2.5}$ fluctuation can be caused by a variety of reasons. Few factors influencing urban PM concentrations include local origins of primary PM, topographic boundaries between locations, intermittent generation episodes, meteorological processes, changes in the behaviour of semi volatile constituents, and measurement imprecision [36]. A strong linear association (coefficient = 0.96) between the daily mean satellite AOD and ground-based $PM_{2.5}$ measurements for a total of 26 cities around the world has been observed [37]. In Finland, correlation values involving AOD and $PM_{2.5}$ were ranged from 0.57 to 0.91 [38]. The paucity of a substantial AOD- $PM_{2.5}$ association during certain days in the region could be attributed to the fact that AOD is a marker of light attenuation by particles in a vertical column, whereas terrestrial $PM_{2.5}$ is a marker of aerosol content (less than 2.5 m) on the surface. AOD is susceptible to the vertical atmospheric pattern, which is primarily determined by the structure of the aerosol cover and the elevation of the layer's higher or lower boundary [39]. In the research area, however, a region-specific steady and persistent seasonal AOD- $PM_{2.5}$ association is observed.

$$PM_{2.5} = 91.32 + 52.85 * AOD \tag{1}$$

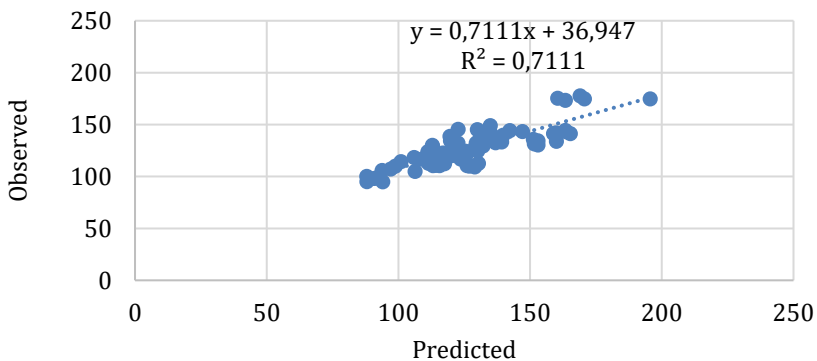


Fig. 5 Scatterplots and relationship between observed and predicted $PM_{2.5}$ values

3.5 Model Validation

The 25% dataset was used for model validation with R^2 value as 0.81. Statistical testing was conducted to check the statistical acceptance of the data and it was found that the model is statistically acceptable. Also, error analysis was carried out and mean absolute percentage error was found as 0.07 which is acceptable. Hence the developed model was statistically significant. Figure 6. shows the association between actual and predicted $PM_{2.5}$ values estimated using the developed model.

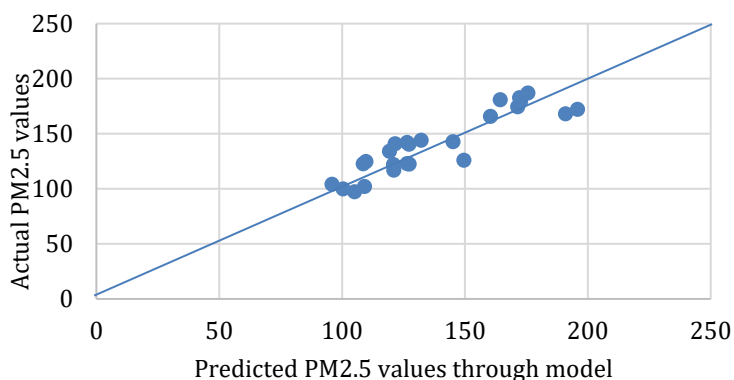


Fig. 6 PM_{2.5}-AOD model validation

4. Conclusion

This study highlights the importance of monitoring aerosol concentrations in regions with high anthropogenic activities, to mitigate their negative impact on human health and the environment. The findings provide valuable insights into the temporal and spatial variability of aerosols and their impact on the Earth's radiation balance. It is worth noting that aerosol concentrations are not only affected by natural sources but also by anthropogenic activities. The average AOD concentrations obtained from OMI and MERRA is 1.60 ± 0.56 and 1.33 ± 0.12 respectively over 2020 indicating variability in aerosols in the region. AOD levels were high over the summer, which is generally associated with dusty weather conditions. Winter wind and dust activities are reduced, resulting in lower AOD readings. AOT averages were greater in the summer (1.58) than in the winter (1.38) and were lowest during the monsoon (1.14) season from 2019 to 2020 indicating high amounts of precipitation and humidity collecting the particles and settling them down, reducing their concentration in the air. The results obtained through back-trajectory analysis indicate that both wind-blown mineral dust and anthropogenic activities are significant contributors to aerosol concentrations in the study region. High correlations were observed between annual PM_{2.5} and AOD concentrations during the study period. AOD is found as an influencing parameter to PM_{2.5} with $R^2 = 0.71$ ($p < 0.05$). The mean absolute percentage error is less than 10% indicating good prediction accuracy. The validated model demonstrated good prediction accuracy and is suitable for making accurate projections about possible potential ground-based PM_{2.5} concentrations in the region. Therefore, it can assist policymakers and environmentalists in making informed decisions about air quality management and the development of effective mitigation measures. OMI AOD can be used to assess possible levels of pollution as there are substantial site-specific connections between AOD and PM_{2.5}. Further research is needed to improve our understanding of the sources and transport of aerosols to develop more effective mitigation measures.

References

- [1] Song Z, Chen B, Zhang P, Guan X, Wang X, Ge J, Hu X, Zhang X, Wang Y. High temporal and spatial resolution PM_{2.5} dataset acquisition and pollution assessment based on FY-4A TOAR data and deep forest model in China. *Atmospheric Research*. 2022 Aug 15;274:106199. <https://doi.org/10.1016/j.atmosres.2022.106199>

- [2] Gui K, Che H, Li L, Zheng Y, Zhang L, Zhao H, Zhong J, Yao W, Liang Y, Wang Y, Zhang X. The significant contribution of small-sized and spherical aerosol particles to the decreasing trend in total aerosol optical depth over land from 2003 to 2018. *Engineering*. 2022 Sep 1;16:82-92. <https://doi.org/10.1016/j.eng.2021.05.017>
- [3] Dunstone NJ, Smith DM, Booth BB, Hermanson L, Eade R. Anthropogenic aerosol forcing of Atlantic tropical storms. *Nature Geoscience*. 2013 Jul;6(7):534-9. <https://doi.org/10.1038/ngeo1854>
- [4] Saidou Chaibou AA, Ma X, Sha T. Dust radiative forcing and its impact on surface energy budget over West Africa. *Scientific reports*. 2020 Jul 22;10(1):12236. <https://doi.org/10.1038/s41598-020-69223-4>
- [5] Che H, Qi B, Zhao H, Xia X, Eck TF, Goloub P, Dubovik O, Estelles V, Cuevas-Agulló E, Blarel L, Wu Y. Aerosol optical properties and direct radiative forcing based on measurements from the China Aerosol Remote Sensing Network (CARSNET) in eastern China. *Atmospheric Chemistry and Physics*. 2018 Jan 15;18(1):405-25. <https://doi.org/10.5194/acp-18-405-2018>
- [6] Jacobson MZ. Strong radiative heating due to the mixing state of black carbon in atmospheric aerosols. *Nature*. 2001 Feb 8;409(6821):695-7. <https://doi.org/10.1038/35055518>
- [7] Kang N, Kumar KR, Yu X, Yin Y. Column-integrated aerosol optical properties and direct radiative forcing over the urban-industrial megacity Nanjing in the Yangtze River Delta, China. *Environmental Science and Pollution Research*. 2016 Sep;23:17532-52. <https://doi.org/10.1007/s11356-016-6953-1>
- [8] Kaskaoutis DG, Badarinath KV, Kumar Kharol S, Rani Sharma A, Kambezidis HD. Variations in the aerosol optical properties and types over the tropical urban site of Hyderabad, India. *Journal of Geophysical Research: Atmospheres*. 2009 Nov 27;114(D22). <https://doi.org/10.1029/2009JD012423>
- [9] Feenstra B, Papapostolou V, Hasheminassab S, Zhang H, Der Boghossian B, Cocker D, Polidori A. Performance evaluation of twelve low-cost PM_{2.5} sensors at an ambient air monitoring site. *Atmospheric Environment*. 2019 Nov 1;216:116946. <https://doi.org/10.1016/j.atmosenv.2019.116946>
- [10] Qi L, Zheng H, Ding D, Wang S. Effects of Anthropogenic Emission Control and Meteorology Changes on the Inter-Annual Variations of PM_{2.5}-AOD Relationship in China. *Remote Sensing*. 2022 Sep 19;14(18):4683. <https://doi.org/10.3390/rs14184683>
- [11] Mirzaei A, Bagheri H, Sattari M. Data level and decision level fusion of satellite multi-sensor AOD retrievals for improving PM_{2.5} estimations, a study on Tehran. *Earth Science Informatics*. 2023 Jan 7:1-9. <https://doi.org/10.1007/s12145-022-00912-6>
- [12] Xu Q, Chen X, Rupakheti D, Dong J, Tang L, Kang S. Evaluation and Comparison of Spatio-Temporal Relationship between Multiple Satellite Aerosol Optical Depth (AOD) and Near-Surface PM_{2.5} Concentration over China. *Remote Sensing*. 2022 Nov 18;14(22):5841. <https://doi.org/10.3390/rs14225841>
- [13] Santese M, Perrone MR, Zakey AS, De Tomasi F, Giorgi F. Modeling of Saharan dust outbreaks over the Mediterranean by RegCM3: case studies. *Atmospheric Chemistry and Physics*. 2010 Jan 11;10(1):133-56. <https://doi.org/10.5194/acp-10-133-2010>
- [14] Kosmopoulos, P.G., Kaskaoutis, D.G., Nastos, P.T. and Kambezidis, H.D., 2008. Seasonal variation of columnar aerosol optical properties over Athens, Greece, based on MODIS data. *Remote Sensing of Environment*, 112(5), pp.2354-2366. <https://doi.org/10.1016/j.rse.2007.11.006>
- [15] Zhang T, He W, Zheng H, Cui Y, Song H, Fu S. Satellite-based ground PM_{2.5} estimation using a gradient boosting decision tree. *Chemosphere*. 2021 Apr 1;268:128801. <https://doi.org/10.1016/j.chemosphere.2020.128801>
- [16] Li J, Carlson BE, Laci AA. How well do satellite AOD observations represent the spatial and temporal variability of PM_{2.5} concentration for the United States?. *Atmospheric*

- Environment. 2015 Feb 1;102:260-73. <https://doi.org/10.1016/j.atmosenv.2014.12.010>
- [17] Zhang H, Hoff RM, Engel-Cox JA. The relation between Moderate Resolution Imaging Spectroradiometer (MODIS) aerosol optical depth and PM_{2.5} over the United States: a geographical comparison by US Environmental Protection Agency regions. Journal of the Air & Waste Management Association. 2009 Nov 1;59(11):1358-69. <https://doi.org/10.3155/1047-3289.59.11.1358>
- [18] Lin C, Li Y, Yuan Z, Lau AK, Li C, Fung JC. Using satellite remote sensing data to estimate the high-resolution distribution of ground-level PM_{2.5}. Remote Sensing of Environment. 2015 Jan 1;156:117-28. <https://doi.org/10.1016/j.rse.2014.09.015>
- [19] Guo J, Xia F, Zhang Y, Liu H, Li J, Lou M, He J, Yan Y, Wang F, Min M, Zhai P. Impact of diurnal variability and meteorological factors on the PM_{2.5}-AOD relationship: Implications for PM_{2.5} remote sensing. Environmental Pollution. 2017 Feb 1;221:94-104. <https://doi.org/10.1016/j.envpol.2016.11.043>
- [20] Kong L, Xin J, Zhang W, Wang Y. The empirical correlations between PM_{2.5}, PM₁₀ and AOD in the Beijing metropolitan region and the PM_{2.5}, PM₁₀ distributions retrieved by MODIS. Environmental pollution. 2016 Sep 1;216:350-60. <https://doi.org/10.1016/j.envpol.2016.05.085>
- [21] Yang Z, Zdanski C, Farkas D, Bang J, Williams H. Evaluation of Aerosol Optical Depth (AOD) and PM_{2.5} associations for air quality assessment. Remote Sensing Applications: Society and Environment. 2020 Nov 1;20:100396. <https://doi.org/10.1016/j.rsase.2020.100396>
- [22] Kumar N, Chu A, Foster A. An empirical relationship between PM_{2.5} and aerosol optical depth in Delhi Metropolitan. Atmospheric Environment. 2007 Jul 1;41(21):4492-503. <https://doi.org/10.1016/j.atmosenv.2007.01.046>
- [23] Torres O, Tanskanen A, Veihelmann B, Ahn C, Braak R, Bhartia PK, Veeffkind P, Levelt P. Aerosols and surface UV products from Ozone Monitoring Instrument observations: An overview. Journal of Geophysical Research: Atmospheres. 2007 Dec 27;112(D24). <https://doi.org/10.1029/2007JD008809>
- [24] Fasnacht Z, Vasilkov A, Haffner D, Qin W, Joiner J, Krotkov N, Sayer AM, Spurr R. A geometry-dependent surface Lambertian-equivalent reflectivity product for UV-Vis retrievals-Part 2: Evaluation over open ocean. Atmospheric Measurement Techniques. 2019 Dec 19;12(12):6749-69. <https://doi.org/10.5194/amt-12-6749-2019>
- [25] Smith N, Barnet CD. CLIMCAPS observing capability for temperature, moisture, and trace gases from AIRS/AMSU and CrIS/ATMS. Atmospheric Measurement Techniques. 2020 Aug 17;13(8):4437-59. <https://doi.org/10.5194/amt-13-4437-2020>
- [26] Stein AF, Draxler RR, Rolph GD, Stunder BJ, Cohen MD, Ngan F. NOAA's HYSPLIT atmospheric transport and dispersion modeling system. Bulletin of the American Meteorological Society. 2015 Dec 1;96(12):2059-77. <https://doi.org/10.1175/BAMS-D-14-00110.1>
- [27] Aldabash M, Bektas Balcik F, Glantz P. Validation of MODIS C6.1 and MERRA-2 AOD using AERONET observations: A comparative study over Turkey. Atmosphere. 2020 Aug 26;11(9):905. <https://doi.org/10.3390/atmos1109090>
- [28] Fan X, Xia X, Chen H. Intercomparison of multiple satellite aerosol products against AERONET over the north China Plain. Atmosphere. 2019 Aug 21;10(9):480. <https://doi.org/10.3390/atmos10090480>
- [29] Ahirwar AV, Khobragade PP. Aerosol optical properties over an urban industrial area, Raipur, Chhattisgarh, India. Spatial Information Research. 2022 Nov 17:1-0. <https://doi.org/10.1007/s41324-022-00496-9>
- [30] Ramachandran S, Kedia S. Aerosol optical properties over South Asia from ground-based observations and remote sensing: a review. Climate. 2013 Oct 21;1(3):84-119. <https://doi.org/10.3390/cli1030084>

- [31] Mukherjee T, Vinoj V. Atmospheric aerosol optical depth and its variability over an urban location in Eastern India. *Natural Hazards*. 2020 Jun;102(2):591-605. <https://doi.org/10.1007/s11069-019-03636-x>
- [32] Rupakheti D, Kang S, Rupakheti M, Cong Z, Tripathee L, Panday AK, Holben BN. Observation of optical properties and sources of aerosols at Buddha's birthplace, Lumbini, Nepal: environmental implications. *Environmental Science and Pollution Research*. 2018 May;25:14868-81. <https://doi.org/10.1007/s11356-018-1713-z>
- [33] Bhaskar VV, Safai PD, Raju MP. Long term characterization of aerosol optical properties: Implications for radiative forcing over the desert region of Jodhpur, India. *Atmospheric Environment*. 2015 Aug 1;114:66-74. <https://doi.org/10.1016/j.atmosenv.2015.05.043>
- [34] Remer LA, Kaufman YJ, Tanré D, Mattoo S, Chu DA, Martins JV, Li RR, Ichoku C, Levy RC, Kleidman RG, Eck TF. The MODIS aerosol algorithm, products, and validation. *Journal of the atmospheric sciences*. 2005 Apr 1;62(4):947-73. <https://doi.org/10.1175/JAS3385.1>
- [35] Krishna RK, Ghude SD, Kumar R, Beig G, Kulkarni R, Nivdange S, Chate D. Surface PM_{2.5} estimate using satellite-derived aerosol optical depth over India. *Aerosol and Air Quality Research*. 2019;19(1):25-37. <https://doi.org/10.4209/aaqr.2017.12.0568>
- [36] Pinto JP, Lefohn AS, Shadwick DS. Spatial variability of PM_{2.5} in urban areas in the United States. *Journal of the Air & Waste Management Association*. 2004 Apr 1;54(4):440-9. <https://doi.org/10.1080/10473289.2004.10470919>
- [37] Gupta P, Christopher SA, Wang J, Gehrig R, Lee YC, Kumar N. Satellite remote sensing of particulate matter and air quality assessment over global cities. *Atmospheric Environment*. 2006 Sep 1;40(30):5880-92. <https://doi.org/10.1016/j.atmosenv.2006.03.016>
- [38] Natunen A, Arola A, Mielonen T, Huttunen J, Komppula M, Lehtinen KE. A multi-year comparison of PM_{2.5} and AOD for the Helsinki region. 2010 Dec 30; 15: 544-552
- [39] Wu Y, De Graaf M, Menenti M. The sensitivity of AOD retrieval to aerosol type and vertical distribution over land with MODIS data. *Remote Sensing*. 2016 Sep 17;8(9):765. <https://doi.org/10.3390/rs8090765>

Blank Page



Green corrosion inhibitors for steel and other metals in basic media: A mini-review

Uzoma S. Nwigwe ^{1,a,*}, Chukwuka I. Nwoye ^{2,b}

¹Department of Mechanical Engineering, Alex Ekwueme Federal University, Ebonyi State, Nigeria

²Department of Metallurgical and Materials Engineering, Nnamdi Azikiwe University, Awambra State, Nigeria

Article Info

Article history:

Received 16 Jan 2023

Accepted 11 Apr 2023

Keywords:

Corrosion inhibitors;
Surface engineering;
Metallic materials;
Alkaline plant extracts

Abstract

This work aims to investigate briefly, the effectiveness of plant extracts so far used for steel and other metals as inhibitors in combating the metallic corrosion in basic media. Corrosion inhibitors have been recommended by various researchers as one of the ways to slow down the rate of corrosion and to reduce the financial losses associated with it. Corrosion inhibitors can be organic or inorganic in nature. But due to their eco-friendly and regenerative nature, green corrosion inhibitors of natural origin are the preferred candidates as against synthetic inhibitors. Majority of corrosion studies today are focused on the application of plant extracts for corrosion protection in acidic media, whereas alkaline media has been used only in few studies, and yet with little or no recent work. Even the result of this review shows that plant-based inhibitors have been used mostly on steel products, aluminum products, and copper in that descending order for minimizing corrosion in alkaline media, while it has been rarely used on metals such as tin, iron, and zinc in the same alkaline media. As a result, it is beneficial to encourage more review and research on the use of plant extracts as corrosion inhibitors in basic media for steel and other metals. And the novelty of this review is based on this concept. Hence, this study is very vital for key players/readers in this field to improve their awareness regarding on how to design extract of plants origin according to their suitability and reproducibility for corrosion protection of metallic structures.

© 2023 MIM Research Group. All rights reserved.

1. Introduction

Metallic materials are critical to the advancement of technology and economy development of any nation. Numerous improvements in design development have been made possible as a result of material innovations, such as high-speed airplanes, bridges, contemporary dwellings, electronics, automobiles, and so on. Due to their exceptional qualities, metallic materials might be considered the most essential engineering materials [1], [2]. In spite of all, metals are still known to be the least corrosion resistant of all the engineering materials. This is because, while ceramics are an important class of material with desirable properties such as corrosion resistance, they are more difficult to design with than metals because they lack some vital properties which limits their uses when put side by side with metals [3]. Corrosion of metals can be thought of as extractive metallurgy in reversed manner as illustrated in Fig. 1, while extractive metallurgy itself is largely concerned with the extracting of metal from the ore and refining or alloying it for a better application. Verse majority of iron ores holds within them oxides of iron, and rusting of steel by water and oxygen results in a hydrated iron oxide. Therefore, rusting is a term designated for steel and iron corrosion, despite the fact that many other metals form their oxides when corrosion attack happens [4].

*Corresponding author: nwigweuzoma@gmail.com

^a<http://orcid.org/0000-0002-5712-9812>; ^b<https://orcid.org/0000-0003-3131-3432>

DOI: <http://dx.doi.org/10.17515/resm2023.643ma0116>

Res. Eng. Struct. Mat. Vol.9 Iss. 3 (2023) 775-789

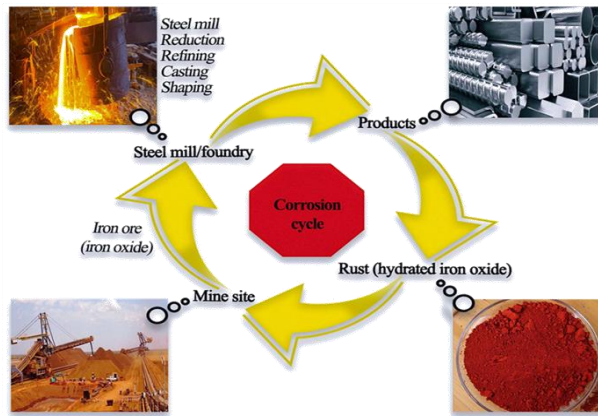


Fig. 1 Metallurgy in the reverse nature

Metallic corrosion has an impact on a variety of domains, including bridges, railways, buildings, industries, traffic lights, and household device [5]. According to a recent study [6] conducted by NACE, the economic impact of corrosion is estimated to be around 2.5 trillion dollars (USA). The financial costs of corrosion are depicted in detail in Fig. 2. However, if corrosion protection techniques are used, this loss can be minimized by up to 15–35 percent [6].

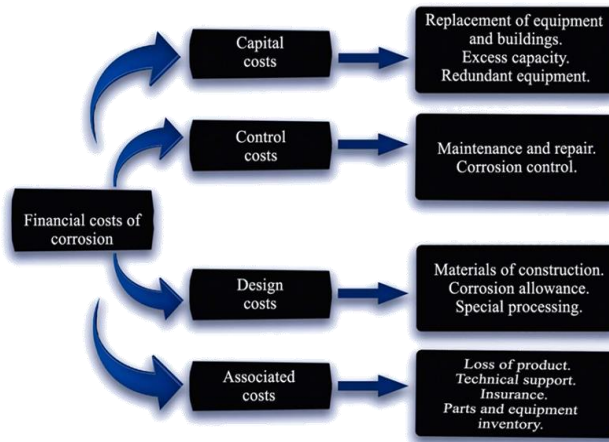


Fig. 2 The financial costs associated with corrosion

Thanks to the use of corrosion inhibitors, which have been recommended by various researchers as a way to slow down the rate of corrosion and so reduce the financial losses suffered by all major users of metallic materials. Corrosion inhibitors are organic or inorganic chemical substances that act as cathodic, anodic or mixed inhibitors by adsorbing on a corroding metal surface when added to a corrosive media, hence suppressing to a great extent the metal's corrosion rate [7], [8]. The presence of organic substances comprising O, S, and N atoms in their compounds with numerous bonds through which they can adsorb on the metal surface makes most inorganic inhibitors harmful to the environment. This has fueled the search for green corrosion inhibitors that are biodegradable, eco-friendly, low-cost, incredibly easy to find, and regenerative, and yet having no heavy metals [9] – [12].

Most corrosion studies today are concentrated on the use plant inhibitors for corrosion protection in strong acidic media like sulfuric acid, hydrochloric acid and other weak acidic media like H_3PO_4 , CH_3COOH , and $HCOOH$, etc. While only little investigations were done using alkaline media. Therefore, it has become imperative to encourage a review on the use of plant extracts on steel and other metals as corrosion inhibitor in basic media. Under this premise lies the novelty of this review, hence, been unique, it is believed that it will contribute immensely to knowledge and learning in the area of corrosion of metals, and on how to create plant extracts in accordance with their suitability and reproducibility for protecting metallic structures from corrosion.

2. Corrosion Inhibitors and Their Functions

Corrosion inhibitor might function in two different ways. Firstly, through contact with the corrosive species, the added inhibitors can sometimes transform the corrosive medium into a noncorrosive or less corrosive medium. In other circumstances, the corrosion inhibitor can react only with the metal surface, and through which, prevents the metal from corroding. As a result, there are two broad types of inhibitors based on how they interact [5]:

- Environment modifiers.
- Adsorption.

The action and method of inhibition in the case of environment modifiers is just by a simple interaction with the aggressive species in the environment, which leads to reduction in the aggressive species' attack on the metal. Oxygen scavengers like Na_2SO_3 or N_2H_4 , as well as cobaltous nitrate and biocides used to prevent microbiological corrosion, are examples of this. The cathodic reaction in corrosion in neutral and alkaline environments involves oxygen reduction, which can be resisted by oxygen scavengers and so impede corrosion [5].

There are two processes in the case of inhibitors that adsorb on metal surfaces and control corrosion: (a) transport of the inhibitor to the metal surface; and (b) metal – inhibitor reactions. The procedure is similar to drug molecule transport in the human's body to the needed location and its engagement with the location to provide relief from the symptoms. The interaction of the metal surface with the inhibitor molecule is perhaps the most crucial step. But however, depending on whether the added inhibitor decreases the cathodic or anodic interaction, inhibitors could be further categorized as follows [5];

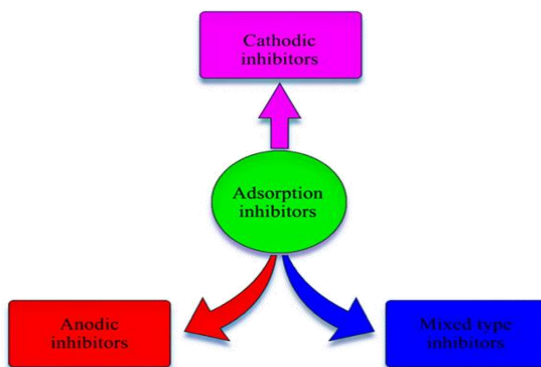


Fig. 3 Different types of adsorption inhibitors

2.1 Cathodic Inhibitors

Cathodic inhibitors inhibit hydrogen from forming in acidic media and/or reduce oxygen formation in neutral or alkaline media. Cathodic inhibitors are substances that have a high hydrogen overpotential in acidic solutions and those that produce insoluble compounds in alkaline solutions. Inorganic phosphates, silicates, and borates in alkaline solutions are examples of inhibitors that prevent oxygen reduction at the cathodic sites. Cathodic sites are blocked by substances like calcium and magnesium carbonates, which have a low solubility [5], [13].

2.2 Anodic Inhibitors

In the pH range of 6.5–10.5 (which is near neutral to basic), anodic inhibitors are often effective. Oxyanions such as molybdates, chromates, sodium nitrite and tungstates, among others, are particularly potent anodic inhibitors. These oxyanions are believed to have a role in mending deficiencies in the iron surface's passive iron oxide layer. The concentration of the inhibitor applied in the case of chromate or dichromate is crucial. When a significant amount of inhibitor is employed, corrosion is slowed, but when the inhibitor is insufficient, corrosion is increased. As an inhibitor, dichromate exhibits this common behavior [13].

2.3 Mixed Type Inhibitors (both Cathodic and Anodic)

Organic substances are commonly used to represent mixed type inhibitors. Regardless of the type of inhibitor, the inhibition process entails transporting the inhibitor to the metal location, and through the subsequent interaction of the inhibitor with the metal's surface, corrosion protection will result. Organic inhibitors when deposited on the metal surface act as a barrier to anode dissolution and cathodic oxygen reduction. The organic mixed-type inhibitors' protective functional groups can be carboxyl, amino, or phosphonate [5], [13].

3. Use of Plant Extracts as Corrosion Inhibitors

Plant extracts are versatile and cost-effective group of corrosion inhibitors. The application of plant extracts as a corrosion inhibitor is done in accordance with green chemistry principles, making the procedure more environmentally benign [14]. Plants produce phytochemicals as a result of their primary or secondary fermentation. Phytochemicals are divided into two classes based on their role in plant metabolism: primary and secondary metabolites. Carbohydrates, proteins, amino acids, and chlorophylls are examples of primary metabolites, while saponins, alkaloids, steroids, tannins, flavonoids, and other secondary metabolites are examples of secondary metabolites [15] - [16]. The phytochemical ingredients in plant extracts have the capacity to inhibit steel and other metals from corroding. These chemicals establish a protective coating on the metal surface by adsorbing to it. The plant population is extremely diverse, containing a vast spectrum of phytochemicals with different redox potential. If we understand the mechanism of action of phytochemicals, we can take advantage of their varied properties to harness them on a commercial scale for corrosion inhibition of metals, since phytochemicals offer a cost-effective, environmentally acceptable, non-toxic, and non-hazardous alternative to conventional corrosion inhibitors [14].

The type of metal, the test medium, the chemical structure of the inhibitor, the kind of substituents present in the inhibitor, the presence of additives, the solution temperature, and the solution concentration all influence the adsorption of green corrosion inhibitors on metal surfaces [17]. Table 1 below shows some latest studies by host of numerous researchers where plant extracts have been employed successfully as excellent steel and other metals corrosion inhibitors in various alkaline media.

Table 1. List of plant extracts evaluated as green corrosion inhibitors in various alkaline media for steel and other metals.

S. no.	Inhibitor	Electrolyte/metal	Method	Nature of adsorption/isotherm	Max. IE (%)	Ref.
1	Moringa Oleifera, Psidium Quajava	NaOH/mild steel	WL	-	> 80	[18]
2	Jatropha curcas, Hibiscus Sabdariffa calyx	NaCl/mild steel	3D SI, ATR, FTIR, LC-MS, EIS, WL, PDP, EDS, SEM	Formation of inhibitor film on mild steel surface	90.26	[19]
3	Hibiscus sabdariffa	NaOH/aluminum	HE, WL, PDP, EIS	Physical adsorption, Langmuir, Dubinin- Radushkevich	84.68	[20]
4	Gum arabic	NaOH/aluminium	HE, TM	Chemical adsorption, Langmuir, Freundlich	> 75	[21]
5	Vigna unguiculata	NaOH/aluminium	WL	Chemical adsorption, Freunlich, Temkin	79.63	[22]
6	Ipomoea involcrata	NaOH/aluminium	HE	Physical adsorption, Langmuir	60	[23]
7	Gossipium hirsutum	NaOH/aluminium	WL	Adsorption of the phytochemicals in the plant	97	[24]
8	Phyllanthus amarus	NaOH/aluminium	WL	Langmuir	76	[25]
9	Gongronem a latifolium	KOH/aluminium	HE	Physically adsorbed	97.54	[26]
10	Garlic	Rain water/aluminium	WL, FTIR	Protective film formed	98	[27]
11	Lupine, Fenugreek, Pomegrana e, Doum, Mango, Aloe eru, Opuntia, Orange	NaOH/aluminium	WL		84,80, 85, 56, 65, 54, 85, 64	[28]
12	Peony	NaCl/carbon steel	WL, FTIR, EIS, GIXD, FESEM, XPS, LC- MS, PDP, XRD, SEM	Frumkin	65.8	[29]
13	Kudingcha	NaCl/steel	FTIR, EIS, SEM,PDP	Langmuir	96.53	[30]
14	Tomato pomace	NaCl/mild steel	SEM, PDP, GC-MS, AFM	Protective layer formed on the metal surface	93.01	[31]

15	Myrmecodia pendans	NaCl/carbon steel	PDP, EIS, FTIR	Langmuir	91.41	[32]
16	Rosmarinus officinalis	NaCl/Al-Mg alloy	PDP, EIS	Freundlich	-	[33]
17	Equisetum arvense	Seawater/copper	PDP, EIS, LPR, SEM, FTIR, GC-MS	Mixed-type inhibitor adsorbed onto the metal surface	87.5	[34]
18	Ziziphus lotus	Natural seawater/copper	WL, SEM, PDP, FTIR	Formation of chemisorbed films	93	[35]
19	Olive	NaCl/copper	WL, PDP, EIS	Cathodic-type corrosion inhibitor	90	[36]
20	Saffron	Seawater/copper	WL, PDP	Cathodic-type inhibitor	84	[37]
21	Beta vulgaris	Well water/mild steel	WL, PDP, FTIR, SEM, ACI, AFM	Mixed-type inhibitor	94	[38]
22	Cleome droserifolia	NaOH/aluminium	WL, SEM	Temkin	78.6	[39]
23	Psidium guajava	NaOH/mild steel	WL, PDP, SEM, FTIR	Langmuir	89.0	[40]
24	Pterocarpus	Na ₂ CO ₃ /mild steel	WL, HE	Langmuir	64.29	[41]
25	Amaranthus cordatus	NaCl/mild steel	WL	Physical adsorption	99.51	[42]
26	Allium sativum	NaCl/mild steel	FTIR, XRD, SEM, PDP, EIS	Mixed-type inhibitor	95	[43]
27	Ricinus communis	NaCl/steel	EIS, PDP, AFM	Temkin	87	[44]
28	Thyme	NaCl/mild steel	WL, PDP	Temkin	80.49	[45]
29	Neem	Ca(OH) ₂ /mild steel	WL, PDP	Chemisorption	86	[46]
30	Morinda lucida	NaCl/steel	WL, CST	Optimal corrosion inhibition	95.64	[47]
31	Rice straw	NaCl/steel	WL, EDX, XRD, FTIR, PDP, SEM	Interphase inhibition	92	[48]
32	Rhizophora mangle	NaCl/steel	AAS, FTIR	-	-	[49]
33	Arecanut husk	NaOH/copper, mild steel	WL, PDP, SEM, ATR-FTIR, XRD	Langmuir	94.34, 93.75	[50]
34	Origanum majorana	NaCl/mild steel	PDP	Physical adsorption	90	[51]
35	Euphorbia hirta, Dialium guineense	NaOH/aluminium	WL	Langmuir, Temkin	87.5, 87.5	[52]
36	Henna	NaOH/tin	WL, FTIR	Physical adsorption	95.45	[53]

37	Water hyacinth	NaOH/iron, aluminium	WL, OM, PDP	Adsorption of the phytochemical constituents of the extract on the surface of the metals	98.93	[54]
38	Citrullus colocynthis	NaCl, NaOH/copper	WL, PDP	Langmuir	77.08, 84.61	[55]
39	Gnetum africana	NH ₄ OH/copper	WL, PDP	Langmuir	87.83	[56]
40	Piper longum	NaOH/aluminium	PDP, EIS, WL	Mixed-type character	89	[57]
41	Mansoa alliacea	NaCl/zinc	PDP, EIS, FTIR, HPLC	Mixed-type inhibitor	92	[58]
42	Cascabela thevetia	NaCl/carbon steel	WL, PDP, EIS, AFM, EFM	Freundlich	95	[59]
43	Bitter leaf	NaOH/Al-Si alloy	WL	Physical adsorption	91	[60]
44	Calotropis	NaOH/mild steel	WL, SEM	Formation of layer on the mild steel	80.89	[61]
45	Robinia pseudoacacia	NaCl/copper	PDP, WL, SEM, EDX	Mixed inhibitory effect	93.5	[62]
46	Gelatin	NaOH/Al-Si alloy	PDP, EIS, CV	Freundlich	65.71	[63]
47	Garcinia indica	NaOH/aluminium	PDP, WL	Chemisorption	70.25	[64]
48	Derris Indica	NaOH/aluminium	WL, PDP, EIS, OP	Langmuir	60.2	[65]
49	Skytanthus acutus meyen	NaCl/carbon steel	WL, EIS, LC-MS	Formation of protective film	90	[66]
50	Litchi chinensis	NaCl/aluminium	PDP, EIS, FTIR, SEM	Langmuir	90	[67]
51	Cardamom, Nutmeg	Sea water/mild steel	WL, PDP, EIS, SEM, FTIR	Protective coating formed	99	[68]
52	Cymbopogon citratus	Seawater/mild steel	UV-Vis, FTIR, WL, EIS, SEM	Formation of a protective film due to the adsorption of inhibitor on the mild steel	34	[69]
53	Vicia faba peel	Marine water/mild steel	GC-MS, PDP, EIS, SEM	Langmuir	97.84	[70]

3.1 Inhibitors are Used in Four Types of Environments

1. Supply waters, natural waters, industrial cooling waters in the 5–9 pH range.
2. Liquid acid media utilized in pickling of metallic materials, and post-service cleaning of metal surfaces.

3. In primary and secondary oil production and refining.
4. Environments of many other types, [13].

3.2 pH Impact on Inhibitor Performance

When choosing a corrosion inhibitor with high inhibition and cost effectiveness, the electrolyte solution's pH is crucial. It is frequently important to evaluate the pH value to guarantee the constant inhibitory performance of the inhibitor during treatment. All inhibitors have a pH range in which they are most efficient. The formation of stable surface layers needs a certain minimum pH. Temperature, chemical species, and flow rate are only a few of the additional factors that affect this minimum pH value. Several inhibitors lose their effectiveness at pH levels that are either too low or too high. Inhibitors of polyphosphates, for instance, must be utilized between pH 6.5 and 7.5. Nitrites are ineffective at pH levels below 5.5-6. Despite the fact that chromates are less prone to pH changes, it is typically used at pH 8.5. Because no insoluble protective iron benzoate film can form at lower pH values, sodium benzoate is ineffective in electrolytes with pH less than 5.5 [71-74].

3.3 Inhibitors and Some Influencing Factors

The performance of inhibitors depends on various factors. The Figure 4 below provides the discussion concerning them [75-76].

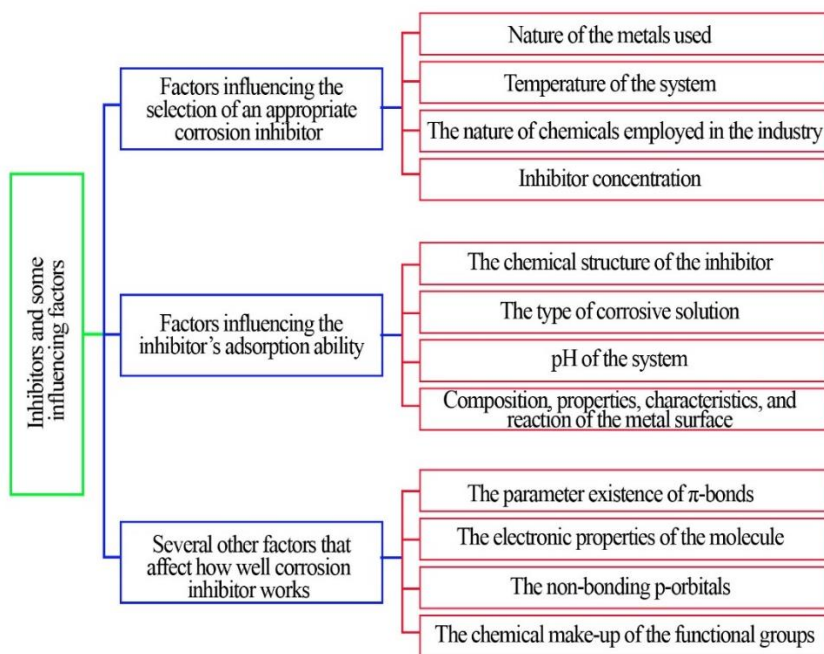


Fig. 4 Inhibitors and some influencing factors

4. Conclusion and Future Outlook

This paper has successfully examined the most recent developments in corrosion protection of metallic materials by different plant extracts in alkaline environments. From the literatures looked into, it can be summarized that,

- Plant extracts are excellent candidates to be harnessed on a commercial quantity as better replacement to inorganic corrosion inhibitors against metal corrosion, which are both costly and very harmful to the environment.
- Researchers suggested using corrosion inhibitors of plant origin as a strategy to slow down corrosion in metallic materials.
- The pH of the system has a significant impact on the corrosion inhibition process and must be considered when selecting the appropriate corrosion inhibitor.
- The phytochemical ingredients in plant extracts are said to have the capacity to inhibit steel and other metals from corroding by adsorbing to it.
- This study has also identified and briefly reviewed the wide varieties of corrosion inhibitors and their functions, plant extracts, and corrosion characterization methods employed by different researchers in their search of ideal inhibitors of natural origin for corrosion protection of metallic materials.
- This work is highly important for key participants and readers in this field to increase their understanding of how to create plant extracts based on their appropriateness and reproducibility for protecting metallic structures from corrosion.
- It has also looked into the economic costs of corrosion as it impacts the economy of a nation, the use of steel and other metals in alkaline environments.
- Majority of the existing studies concentrated more on alkaline media like NaCl and NaOH, while there were less researches on alkaline media like Na₂CO₃, NH₄OH, and Ca(OH)₂.
- According to the findings of this review, plant-based inhibitors have been employed most notably in steel products, followed by aluminum products, and copper, in that order. But only one piece of literature supports the use of plant extracts in alkaline medium for other metals like tin, iron, and zinc.

Therefore, it is advantageous to promote/recommend more reviews and studies on the application of plant extracts as corrosion inhibitors in basic media for steel and other metals in the near future using other basic media like Mg(OH)₂, NaHCO₃ and / or KOH.

Acknowledgement(s)

For their encouragement and assistance, the authors of this research study are grateful to their colleagues in the department of Materials and Metallurgical Engineering at Nnamdi Azikiwe University in Awka, Anambra State, Nigeria.

Conflicts of Interest

The authors of this research work have no conflicts of interest to disclose.

Abbreviations

OM:	Optical Microscope
EFM:	Electrochemical frequency modulation
WL:	Weight loss
AFM:	Atomic force microscope
GIXD:	Grazing incidence X-ray diffraction
FTIR:	Fourier transform infrared spectroscopy
DFT:	Density functional theory
HE:	Hydrogen evolution
N ₂ H ₄ :	Hydrazine
MDS:	Molecular dynamics simulation

ATR:	Attenuated total reflection spectroscopy
XRD:	X-ray diffraction
KOH:	Potassium hydroxide
NaCl:	Sodium chloride
Mg(OH) ₂ :	Magnesium hydroxide
Na ₂ SO ₄ :	Sodium sulfate
3D SI:	3D Surface inspection
LPR:	linear polarization resistance
EDS:	Energy-dispersive X-ray spectroscopy
Na ₂ SO ₃ :	Sodium sulfite
FESEM:	Field emission scanning microscopy
CV:	Cyclic voltammetry
HPLC:	High-performance liquid chromatography
EIS:	Electrochemical impedance spectroscopy
PDP:	Potentiodynamic polarization
Ca(OH) ₂ :	Calcium hydroxide
OPM:	Optical microscope
Max. IE (%):	Maximum inhibition efficiency
ACI:	AC impedance
LC-MS:	Liquid chromatography-mass spectrometry
XPS:	X-ray photoelectron spectroscopy
NaOH:	Sodium hydroxide
NH ₄ OH:	Ammonium hydroxide
GC-MS:	Gas chromatography-mass spectrometry
NaHCO ₃ :	Sodium bicarbonate
CST:	Compressive-strength testing
ATR-FTIR:	Attenuated total reflection-Fourier transform infrared
AAS:	Atomic absorption spectroscopy
TM:	Thermometric method
UV-Vis:	Ultraviolet-visible spectroscopy

References

- [1] Jimoh SO, Abhulimen UI, Kubeyinje LI. Importance of engineering materials in the mandate of iron and steel industry. *Int. J. Sci. Technol. Res.* 2013;2(12):1-10.
- [2] Alves G. The importance of metallic materials as biomaterials. *Adv. Tissue Eng. Regen. Med.* 2017;3(1):300-302. <https://doi/10.15406/atroa.2017.03.00054>
- [3] Ashby MF. *Materials selection in mechanical design*, second edition, Butterworth-Heinemann Publishing Ltd, Oxford, 1999, England.
- [4] M. G. Fontana, *Corrosion engineering* third edition, McGraw-Hill Book Company, 1987, Singapore.
- [5] Sastri VS, Ghali E, Elboujdaini M. *Corrosion prevention and protection: Practical solutions*. John Wiley & Sons Ltd., 2007, England.
- [6] Guo H, Dong Y, Bastidas-Arteaga E, Gu XL. Probabilistic failure analysis, performance assessment, and sensitivity analysis of corroded reinforced concrete structures. *Eng. Fail. Anal.* 2021;124:1-46. <https://doi.org/10.1016/j.engfailanal.2021.105328>
- [7] Chen L, Lu D, Zhang Y. Organic Compounds as Corrosion Inhibitors for Carbon Steel in HCl Solution: A Comprehensive Review, *Materials*. 2023;15(6):1-59. <https://doi.org/10.3390/ma15062023>
- [8] Gadaw HS, Fakeeh M. Green inhibitor of carbon steel corrosion in 1 M hydrochloric acid: *Eruca sativa* seed extract (experimental and theoretical studies). *RSC Adv.* 2022;12(5):8953-8986. <https://doi.org/10.1039/d2ra01296k>

- [9] Farhadian A, Kashani A, Rahimi S, Oguzie E, Javidparvar A. Modified hydroxyethyl cellulose as a highly efficient eco-friendly inhibitor for suppression of mild steel corrosion in a 15% HCl solution at elevated temperatures. *J. Mol. Liq.* 2021;338:1-16. <https://doi.org/10.1016/j.molliq.2021.116607>
- [10] Yang HM. Role of organic and eco-friendly inhibitors on the corrosion mitigation of steel in acidic environments—a state-of-art review. *Molecules.* 2021;26(11):1-20. <https://doi.org/10.3390/molecules26113473>.
- [11] Siti H, Sunarya Y, Anwar B, Priatna E, Risa H, Koyande A. Protoporphyrin Extracted from Biomass Waste as Sustainable Corrosion Inhibitors of T22 Carbon Steel in Acidic Environments. *Sustainability.* 2022;14(3622)1-14, <https://doi.org/10.3390/su14063622>
- [12] Ahmed RK, Zhang S. Atriplex leucoclada extract: A promising eco-friendly anticorrosive agent for copper in aqueous media. *J. Ind. Eng. Chem.* 2021;99:334-343. <https://doi.org/10.1016/j.jiec.2021.04.042>
- [13] Sastri VS. Green corrosion inhibitors, John Wiley & Sons, Inc., New Jersey, USA, 2011.
- [14] Bhardwaj N, Sharma P, Kumar V. Phytochemicals as steel corrosion inhibitor: An insight into mechanism. *Corros Rev.* 2021;39(1):27-41, <https://doi.org/10.1515/corrrev-2020-0046>
- [15] Mohan M, Krishna MP. Identification of Phytochemical Constituents of Michelia nilagirica Leaves Phytochemistry & Biochemistry. *J Phytochem. Biochem.* 2019;3(1):1-5.
- [16] A. Kumar, Ilavarasan R, Jayachandran T, Decaraman M, Aravindhnan P. Phytochemicals Investigation on a Tropical Plant, Syzygium cumini from Kattuppalayam, Erode District, Tamil Nadu, South India. *Pakistan J. Nutr.* 2009;8(1):83-85.
- [17] Chigondo M, Chigondo F. Recent Natural Corrosion Inhibitors for Mild Steel: An Overview. *J. Chem.* 2016;1-7. <https://doi.org/10.1155/2016/6208937>
- [18] Idu HK, Nwofe PA, Idenyi NE. Investigations on the Inhibitive Properties of Moringa Oleifera and Psidium Quajava Leaves Extract on the Corrosion Susceptibility of Mild Steel. *Am. J. Sci. Res.* 2016;11(2):119-124. <https://doi.org/10.5829/idosi.aejsr.2016.11.2.22748>
- [19] Afandi MA, Saud SN, Hamzah E. Green-based corrosion protection for mild steel in 3.5% NaCl and distilled water medias: Jatropha curcas and Roselle extracts. *J. Met. Mater. Miner.* 2020;30(2):91-104. <https://doi.org/10.14456/jmmm.2020.25>
- [20] Noor EA. Potential of aqueous extract of Hibiscus sabdariffa leaves for inhibiting the corrosion of aluminum in alkaline solutions Potential of aqueous extract of Hibiscus sabdariffa leaves for inhibiting the corrosion of aluminum in alkaline solutions, *J Appl Electrochem*, 2009;39:1-12. <https://doi.org/10.1007/s10800-009-9826-1>
- [21] Umoren SA, Obot IB, Ebenso EE, Okafor PC. Gum arabic as a potential corrosion inhibitor for aluminium in alkaline medium and its adsorption characteristics. *Anti-Corrosion Methods Mater.* 2004;53(5):227-282. <https://doi.org/10.1108/00035590610692554>
- [22] Umoren SA, Obot IB, Akpabio LE, Etuk SE. Adsorption and corrosive inhibitive properties of Vigna unguiculata in alkaline and acidic media. *Pigment Resin Technol.* 2008;37(2):98-105. <https://doi.org/10.1108/03699420810860455>
- [23] Obot IB, Obi-Egbedi NO. Ipomoea Involcrata as an Ecofriendly Inhibitor for Aluminium in Alkaline Medium. *Port. Electrochim. Acta.* 2009;27(4):517-524. <https://doi.org/10.4152/pea.200904517>
- [24] Olusegun KA, Otaigbe JO, Kio JO. Gossipium hirsutum L. extracts as green corrosion inhibitor for aluminum in NaOH solution. *Corros. Sci.* 2009;52:1879-1881. <https://doi.org/10.1016/j.corsci.2009.04.016>
- [25] Olusegun KA, Otaigbe JO. The effects of Phyllanthus amarus extract on corrosion and kinetics of corrosion process of aluminum in alkaline solution. *Corros. Sci.* 2009;51(11):2790-2793. <https://doi.org/10.1016/j.corsci.2009.07.006>

- [26] Oguzie EE, Onuoha GN, Ejike EN. Effect of Gongronema latifolium extract on aluminium corrosion in acidic and alkaline media. *Pigment Resin Technol.* 2007;36(1):44–49. <https://doi/10.1108/03699420710718751>
- [27] Priya SL, Chitra A, Rajendran S, Anuradha K. Corrosion behaviour of aluminium in rain water containing garlic extract. *Surf. Eng.* 2005;21(3):229–231, <https://doi/10.1179/174329405X50073>
- [28] Saleh RM, Ismail AA, EL Hosary AA. The effect of the aqueous extracts of some seeds, leaves, fruits and fruit-peels on the corrosion of Al in NaOH, *Corros. Sci.* 1983;23(1):1239–1241.
- [29] Mehdi H, Mehdi S, Eden A, Xianming S. A peony-leaves-derived liquid corrosion inhibitor: protecting carbon steel from NaCl. *Green Chem. Lett. Rev.* 2017;10(4):1–22. <https://doi.org/10.1080/17518253.2017.1388446>
- [30] Chen S, Singh A, Wang Y, Liu W, Deng K, Lin Y. Inhibition effect of Ilex kudingcha C. J. Tseng (Kudingcha) extract on J55 Steel in 3. 5wt % NaCl Solution Saturated with CO₂. *Int. J. Electrochem. Sci.* 2017;12:782–796. <https://doi/10.20964/2017.01.21>
- [31] Vorobyova V. Potential of Tomato Pomace Extract as a Multifunction Inhibitor Corrosion of Mild Steel. *Res. Sq.* 2022:1–43. <https://doi.org/10.21203/rs.3.rs-539323/v1>
- [32] Pradityana A, Shahab A, Noerochim L, Susanti D. Inhibition of Corrosion of Carbon Steel in 3. 5 % NaCl Solution by Myrmecodia Pendans Extract. *Int. J. Corros.* 2016:1-7. <https://doi.org/10.1155/2016/6058286>
- [33] Gudic S, Katalinic V. Aqueous extract of Rosmarinus officinalis L. as inhibitor of Al-Mg alloy corrosion in chloride solution. *J. Appl. Electrochem.* 2000;30:823–830. <https://doi.org/10.1023/A:1004041530105>
- [34] Esquivel-Rojas A, Cuevas-Arteaga C, Valladares-Cisneros MG. Study of corrosion inhibition of copper in synthetic seawater by Equisetum arvense as green corrosion inhibitor. *Rev. Mex. Ing. Química.* 2020;8(3):603–616. <https://doi.org/10.24275/rmiq/Mat629>
- [35] Oukhrib R, Issami E, El Ibrahim B, El Mouaden K. Ziziphus lotus as Green Inhibitor of Copper Corrosion in Natural Sea Water. *Port. Electrochim. Acta.* 2017;35(4):187–200. <https://doi/10.4152/pea.201704187>
- [36] Rahal C, et al. Olive leaf extract as natural corrosion inhibitor for pure copper in 0.5 M NaCl solution: A study by voltammetry around OCP. *J. Electroanal. Chem.* 2016:1–43. <https://doi.org/10.1016/j.jelechem.2016.03.010>
- [37] Oukhrib R, El Issammi S, Chaouay A, El Mouaden K, Jmiai A. The inhibitory effect of Saffron extract (*Crocus sativus*, L) on copper corrosion in seawater. *Chem. Sci. Rev. Lett.* 2016;4(13):241–251.
- [38] Joyce SC, Raja AS, Amalraj AS, Rajendran S. Corrosion mitigation by an eco-friendly inhibitor: Beta vulgaris (beetroot) extract on mild steel in simulated oil well water medium. *Int. J. Corros. Scale Inhib.* 2022;11(1):82–101. <https://doi/10.17675/2305-6894-2022-11-1-4>
- [39] Qudah M. Inhibition of Aluminum in NaOH Solution using Cleome droserifolia Leaves Extract. *Res. Rev. J. Chem.* 2015;4(4): 40–45.
- [40] Amoo KS, Jatau JS, Abdulwahab M. Corrosion Inhibitive Effect of Psidium Guajava Leaves on Mild Steel in an Induced Alkaline Solution. *J. Sci. Eng. Res.* 2019;6(6):116–127.
- [41] Onukwube D, Awomukwu A, Brown N. Inhibition of Corrosion of Mild Steel in Alkaline Medium by Ethanol Extract of Pterocarpus Soyauxii Taub. *Ewemen J. Anal. Environ. Chem.* 2016;2(1):38–44.
- [42] Nwankwo M, Offor P, Neife S, Oshionwu L, Idenyi N. Amaranthus cordatus as a Green Corrosion Inhibitor for Mild Steel in H₂SO₄ and NaCl. *J. Miner. Mater. Charact. Eng.* 2014;2:194–199. <https://doi/10.4236/jmmce.2014.23024>

- [43] Devikala S, Kamaraj P, Arthanareeswari M, Patel M. Green corrosion inhibition of mild steel by aqueous *Allium sativum* extract in 3.5 % NaCl. *Materials Today: Proceedings*. 2019;14:580–589. <https://doi/10.1016/j.matpr.2019.04.182>
- [44] Palanisamy S, Maheswaran G, Selvarani A, Kamal C, Venkatesh G. *Ricinus communis* – A green extract for the improvement of anti-corrosion and mechanical properties of reinforcing steel in concrete in chloride media. *J. Build. Eng.* 2018:1–31. <https://doi/10.1016/j.jobe.2018.05.020>
- [45] Premkumar P, Kannan K, Natesan M. Thyme extract of *Thymus Vulgar L.* as volatile corrosion inhibitor for mild steel in NaCl environment. *Asian J. Chem.* 2008;20(1):445–451. http://krc.cecni.res.in/ro_2008/006-2008.pdf
- [46] Baitule J, Manivannan R. Corrosion inhibitory effect of neem leaf extract on mild steel in alkaline solution containing chloride ions. *J. Indian Chem. Soc.* 2020;97: 1061–1065.
- [47] Olusegun J, Akintoye C, Idowu A. *Morinda lucida* effects on steel-reinforced concrete in 3.5 % NaCl: Implications for corrosion-protection of wind-energy structures in saline / marine environments. *Energy Procedia*, 2014;50:421–428. <https://doi/10.1016/j.egypro.2014.06.051>
- [48] Othman N, Yahya S, Ismail M. Corrosion inhibition of steel in 3.5% NaCl by rice straw extract. *J. Ind. Eng. Chem.* 2018: 1-40. <https://doi/10.1016/j.jiec.2018.10.030>
- [49] Joshua M, Olusegun O, Akinlabi E, Ikotun J, Akinlabi S, Okeniyi E. *Rhizophora mangle* L. Leaf biochemical characterization: natural-green total- corrosion inhibition prospect on concrete steel-reinforcement in 3.5% NaCl. *J. Teknol.* 2019:11–21. <http://hdl.handle.net/10210/290662>
- [50] Raghavendra N, Bhat J. Chemical Components of Mature Arecanut Husk Extract as Potential Corrosion Inhibitor for Mild Steel and Copper in Both Acid and Alkali Media. *Chem. Eng. Commun.* 2017;6445:1-48. <https://doi.org/10.1080/00986445.2017.1370709>
- [51] Challouf H, Souissi N, Messaouda M, Abidi R, Madani A. *Origanum majorana* Extracts as Mild Steel Corrosion Green Inhibitors in Aqueous Chloride Medium. *J. Environ. Prot.* 2016;7:532–544. <https://doi.org/10.4236/jep.2016.74048>
- [52] Nnanna L, Anozie I, Akoma C, Mejeha I, Okeoma K, Meje K. Corrosion Control of Aluminium Alloy in Alkaline Solution Using Some Leave Extracts. *Am. J. Mater. Sci.* 2011;1(2):76–80. <https://doi.org/10.5923/j.materials.20110102.12>
- [53] Ibrahim M, Sulaiman Z, Usman B, Ibrahim A. Effect of Henna Leaves on the Corrosion Inhibition of Tin in Acidic and Alkaline Media. *World J. Appl. Chem.* 2019;4(4): 45–51. <https://doi.org/10.11648/j.wjac.20190404.11>
- [54] Oloruntoba D, Adesina O, Abraham O, Akinluwade K. Corrosion Mitigation of Gray Cast Iron and Aluminum in NaOH Using Water Hyacinth (*Eichhornia crassipes*) Plant Extract. *Chem. Sci. Int. J.* 2019;27(4):1–15. <https://doi.org/10.9734/CSJI/2019/v27i430120>
- [55] Mohsin H, Al-Dokheily E, Rasha N. Inhibition of Copper Corrosion in H₂SO₄, NaCl and NaOH Solutions by *Citrullus colocynthis* Fruits Extract. *J. Nat. Sci. Res.* 2014;4(17):60–74.
- [56] Aliyu A, Onyedikachi E. Corrosion Inhibition Effect of Phenolic Extract of *Gnetum africana* on Copper in 1.0 mol / dm³ Ammonium Hydroxide. *Am. Chem. Sci. J.* 2014;4(6): 952-962.
- [57] Singh A, Ahamad I, Quraishi M. Piper longum extract as green corrosion inhibitor for aluminium in NaOH solution. *Arab. J. Chem.* 2012:1–6. <https://doi.org/10.1016/j.arabjc.2012.04.029>
- [58] Suedile F, Robert F, Roos C, Lebrini M. Corrosion inhibition of zinc by *Mansoa alliacea* plant extract in sodium chloride media: Extraction, Characterization and Electrochemical Studies. *Electrochim. Acta* 2013:1–27. <https://doi.org/10.1016/j.electacta.2013.12.070>

- [59] Fouda A, Emam A, Refat R, Nageeb M. Cascabela thevetia plant extract as corrosion inhibitor for carbon steel in polluted sodium chloride solution. *J. Anal. Pharm. Res. Res.* 2017;6(1):1–8. <https://doi.org/10.15406/japlr.2017.06.00168>
- [60] Ayeni F, Madugu A, Sukop P, Ihom A, Okara R. Effect of Aqueous Extracts of Bitter Leaf Powder on the Corrosion Inhibition of Al-Si Alloy in 0.5 M Caustic Soda Solution. *J. Miner. Mater. Charact. Eng.* 2012;11:667–670.
- [61] Kumar S, Surendra A, Manish S, Paresh A, Suraj PM. Synergistic effect of calotropis plant in controlling corrosion of mild steel in basic solution. *J. Chil. Chem. Soc.* 2009;1:83–88. <http://dx.doi.org/10.4067/S0717-97072009000100020>
- [62] Pourzarghan V, Nasab BF. The use of Robinia pseudoacacia L fruit extract as a green corrosion inhibitor in the protection of copper - based objects. *Herit. Sci.* 2021;9(75):1–14. <https://doi.org/10.1186/s40494-021-00545-w>
- [63] Abdallah M, Kamar EM, El Etre AY, Eid S. Gelatin as Corrosion Inhibitor for Aluminum and Aluminum Silicon Alloys in Sodium Hydroxide Solutions. *Prot. Met. Phys. Chem. Surfaces.* 2016;52(1):140–148. <https://doi.org/10.1134/S2070205116010020>
- [64] Deepa P, Padmalatha J. Corrosion Inhibition of 6063 Aluminum Alloy in 0.5 M Sodium Hydroxide Medium by Aqueous Extract of Seeds of Garcinia indica. *Mater. Sci. Forum.* 2017;880:119–123. <https://doi.org/10.4028/www.scientific.net/MSF.880.119>
- [65] Nambiar NK, Brindha D, Punniyakotti P, Venkatraman BR, Angaiah S. Derris Indica Leaves Extract as a Green Inhibitor for the Corrosion of Aluminium in Alkaline Medium. *Eng. Sci.* 2022;17:167–175. <https://doi.org/10.30919/es8d540>
- [66] Cáceres L, Frez Y, Galleguillos F, Soliz A, Gómez-silva B, Borquez J. Aqueous dried extract of L. Aqueous dried extract of skytanthus acutus meyen as corrosion inhibitor of carbon steel in neutral chloride solutions. *Metals.* 2021;11(12):1–23. <https://doi.org/10.3390/met11121992>
- [67] Pliego-Arreaga R, Regalado C, Amaro-Reyes A, García-Almendárez BE. Corrosion inhibition of aluminum 2024-T3 in 3.5% NaCl by using litchi chinensis extract. *Uso del extracto de litchi chinensis como inhibidor de la corrosión del aluminio 2024-T3 en 3.5% NaCl.* *Rev. Mex. Ing. Química.* 2022;12(3):505–511.
- [68] Dorothy R, Sasilatha T, Rajendran S. Corrosion resistance of mild steel (Hull plate) in sea water in the presence of a coating of an oil extract of plant materials. *Int. J. Corros. Scale Inhib.* 2021;10(2):676–699. <https://doi.org/10.17675/2305-6894-2021-10-2-13>
- [69] Ismail N, Ghazali MS, Fakhratul M, Zulkifli R, Umoren SA, Kamal C, Haque J, Nik MW. Employing Cymbopogon citratus (Lemongrass) as Eco-friendly Corrosion Inhibitor for Mild Steel in Seawater. *J. Sustain. Sci. Manag.* 2021;16(3):71–82. <https://doi.org/http://doi.org/10.46754/jssm.2021.04.006>
- [70] Abdelshafeek, KA, Abdallah WE, Elsayed WM, Eladawy HA, El-Shamy AM. Vicia faba peel extracts bearing fatty acids moieties as a cost-effective and green corrosion inhibitor for mild steel in marine water: computational and electrochemical studies. *Scientific Reports.* 2022;12(1):1–26. <https://doi.org/10.1038/s41598-022-24793-3>
- [71] Legrand L, Abdelmoula M, Géhin A, et al. Electrochemical formation of a new Fe (II) Fe (III) hydroxy-carbonate green rust: characterisation and morphology. *Electrochim. Acta.* 2001;46:1815–1822.
- [72] Migahed MA. Environmental factors affecting corrosion inhibition in oil and gas industry, first edition., Wiley-VCH Verlag GmbH & Co. KGaA, 2020. <https://doi.org/10.1002/9783527822140.ch3>
- [73] Simpson LJ, Melendres CA. Surface-enhanced Raman spectroelectrochemical studies of corrosion films on implant Co-Cr-Mo alloy in biosimulating solutions. *J. Electrochem. Soc.* 1996;143(7):2146–2152. [https://doi.org/10.1002/\(SICI\)1097-4555\(199902\)30:2<97::AID-JRS352>3.0.CO;2-X](https://doi.org/10.1002/(SICI)1097-4555(199902)30:2<97::AID-JRS352>3.0.CO;2-X)

- [74] Wang W, Robert D, Zhou A, Li C. Factors Affecting Corrosion of Buried Cast Iron Pipes. *J. Mater. Civ. Eng.* 2018;30(11):1–12. [https://doi.org/10.1061/\(ASCE\)MT.1943-5533.0002461](https://doi.org/10.1061/(ASCE)MT.1943-5533.0002461)
- [75] Ahmed J, Ganesh G. A Comprehensive Overview on Corrosion in RCC and Its Prevention Using Various Green Corrosion Inhibitors. *Buildings.* 2022;12:2–48.
- [76] Montemor MF. Fostering green inhibitors for corrosion prevention, *Active Protective Coatings*, Springer Series in Materials Science, 2016:107–137. https://doi.org/10.1007/978-94-017-7540-3_6

Blank Page



Research Article

The effect of mechanical surface roughness for polyvinyl chloride (PVC) and aluminum joining

Didem Kale^{1,a}, Nazmiye Yoldaş^{1,b}, M. Özgür Seydibeyoğlu^{*2,3,4,c}

¹Ege Profil, MPIO SB Atatürk Plastik O.S.B Mah. 5. Cad. No:4 Menemen, İzmir, Turkey

²Department İzmir Katip Çelebi University, Department of Materials Science and Engineering, 35620, Çiğli, İzmir, Turkey

³Advanced Structures and Composites Center, University of Maine, Orono, Maine, 04473, USA

⁴Thermoplastic Composites Application Center (TPAC), Saxion University, Netherlands

Article Info

Abstract

Article history:

Received 14 Dec 2022

Accepted 05 Mar 2023

Keywords:

Polyvinyl Chloride(PVC);
Aluminum; Bonding;
Surface Roughness;
Deflection;; Joined

In this study, the joining technique of two different materials such as polyvinyl chloride (PVC) and aluminum that can replace steel insertion in the PVC profile industry was investigated. The aim was to improve the interface structure for joining PVC and aluminum with different geometries on the aluminum surface. The effects of mechanical surface roughness were studied for the joining performance. Aluminum samples with mechanically deformed surfaces were prepared and joined with PVC strips. Lap-shear, interlaminar shear strength (ILSS), 3-Point (3P) bending, and coefficient of linear thermal expansion (CTE) tests were performed. Microstructural investigations were conducted with an optical microscope and scanning electron microscope. According to the results obtained, mechanical surface roughness on the aluminum improved the joining interface between PVC and aluminum. The side-punched and perforated samples achieved the best results in terms of geometrical variations on the aluminum surface. Improvement in surface roughness resulted in a 2-fold increase in lap-shear shear strength and 45% reduction in 3-point bending test results. Optical microscopy was performed on the interface layer, the cavity structures were examined. In the samples with good adhesion results, it was observed that the desired locking mechanism was formed in joined structures as a result of the abrasion on the metal surface and the filling of holes with PVC.

© 2023 MIM Research Group. All rights reserved.

1. Introduction

The construction industry plays an important role in the development of human history. Building materials can be divided into structural materials, decorative materials, and special materials. [1].

Aluminum and its alloys have many outstanding attributes that lead to a wide range of applications, including good corrosion and oxidation resistance, high electrical and thermal conductivities, low density, high reflectivity, high ductility and reasonably high strength, and relatively low cost [2]. Extruded aluminum profiles are used to make ladders, doors, windows, showers, and scaffolding, among other industrial applications. Roofs, facades, panels, components, awnings, cladding gutters & downpipes, ceilings, and many more structures in the building and construction business use our coated and uncoated building goods [3].

*Corresponding author: seydibey@gmail.com

^a orcid.org/000-0003-1096-6733; ^b orcid.org/0000-0001-8162-1092; ^c orcid.org/0000-0002-2584-7043;

DOI: <http://dx.doi.org/10.17515/resm2022.604ma1214>

Res. Eng. Struct. Mat. Vol. 9 Iss. 3 (2023) 791-804

PVC is one of the most widely used plastic compounds in the world, with a wide range of applications. UPVC has piqued the construction industry's attention as low-maintenance material [4].

PVC is widely employed in the construction sector for a variety of purposes, including pipelines, windows, flooring, roofing, and lighter constructions. The building industry consumes 67% of global PVC production [5]. Windows are available in a variety of frame materials in the construction industry, including aluminum, PVC, timber, and aluminum cover of PVC on timber, joined, composite, and fiberglass. Some observations concerning these building materials are relevant to an understanding of the PVC requirements [6].

The idea of having joined materials of PVC and aluminum is a solid product within an improved joining structure that can replace steel sheets. The current PVC window fabrication process includes additional labor costs for steel insertion and screwing. However, the modulus of elasticity of steel is approximately 3 times higher than aluminum, there is a positive reduction in deflection values in the moment of inertia for joined materials when used in multiple structures. For this reason, it was necessary to initiate a study with enhanced bonding properties at the PVC and aluminum interface.

Joining structure between interface layers can be improved with surface roughness, adhesive bonding, and plasma applications. Surface roughness is one of the important factors which influence the mechanical properties of the joints. Having surface roughness on aluminum material can be preferable in joining [7]. The importance of the surface and its favorable impact on bond strength was noted by the majority of the studies [8].

In this study, we used aluminum and PVC to create a new joined profile that overcomes the barriers for steel reinforcement in conventional PVC profiles. During the project evaluation phase, shear stress (lap-shear test) for adhesion strength, interlaminar shear stress for bending, and 3-point bending tests were performed. In addition, linear thermal expansion tests were performed on the samples prepared at different temperature ranges determined under laboratory conditions. With the use of an optical microscope, the interface layer and surface morphology between aluminum - PVC were investigated. After the results were minimized, the surface topography of the test sample showing the best adhesion was examined by Scanning Electron Microscope (SEM) analysis.

The experiment design was made in DOE using full factorial design techniques. DOE was created to deal with complex problems where more than one variable may influence response and two or more factors may interact [9]. DOE which is the dependent variables (responses) consist of the test results as lap-shear, 3-point bending, ILSS, and CTE performed as a result of the study. The independent variables (factor) were determined as aluminum surface roughness and process types. There are 6 levels for aluminum surface roughness and they are described as S1 to S6.

2. Material and Methods

2.1. Materials

2.1.1 PVC

PVC strips have been obtained from suspension u-PVC from Petkim S65. It has some properties which are 67 ± 2 K-value, 0.55 ± 005 g/cm³ bulk density, and $0.250 \mu\text{m}$ (Max 8%) and $0.063 \mu\text{m}$ (Min 90%) particle size. These materials were prepared from extruded u-PVC window profiles.

2.1.2 Aluminum

The alloy of 5052H18 which is the strongest temper produced through the action of only strain hardening decided to use for the preparation of aluminum strips in the study. It

has some properties which are 2.7 g/cm³ density, 70 GPa Young Modulus, and 178 MPa Yield Strength.

Samples are prepared in the required dimensions from aluminum rolls.

2.2. Experimental Methods

2.2.1 Design of Experiments (DOE)

To analyze the effect of the design of the experimental parameters, the aluminum surface roughness and the process types were used for the improvement of two material joining. MINITAB 19 software Design of Experiment Full Factorial method was used to examine the main effect and interaction plots.

2.2.2 Preparation of PVC Samples

PVC profiles that are the origin of the samples were produced in the extrusion process. As the third step, the strips were prepared from extruded PVC profiles. The thickness of PVC samples was preferred as 3.2 mm.

2.2.3 Preparation of Aluminum Samples

To obtain the patterns on the aluminum surface, the modeling of different patterns was studied. During this study, the resistance to applied forces (such as lap-shear, 3P bending, ILSS, and linear thermal expansion) on the interface layer has been considered. Surfaced deformed, planned to apply on the aluminum surface, have been designed on CAD software. 3D modeling of patterns was created on a jig to have this effect on the aluminum surface. Having a patterned surface on an aluminum surface is included in the pressing process (Figure 1).

After the pressing process, surfaces of aluminum are prepared according to the pattern on these jigs. Six different types of roughness were applied to the aluminum surface. These are Flat, Perforated, Side Punched, Surface Deformed, Side Punched+Surface Deformed, and Side Punched+Perforated surfaces which are abbreviated as S1 to S6 (Table 1).

The thickness of the aluminum samples was 0.8 mm.

In the study, the aluminum surface type definitions will be expressed with the abbreviations explained in Table 1.

2.2.4 Preparation of Joined Samples as PVC Aluminum







The joined samples were prepared using a hot-pressing process is shown in Figure 1. In this method firstly, PVC and aluminum samples were preheated and joined in a hot press machine to obtain joined samples.

Hot-press equipment which provides 6 bar compression pressure is shown in Figure 2 includes two metal plates as horizontally on top and bottom with heating resistance.

180 °C, 190 °C, and 200 °C temperatures have been studied for preheating rigid PVC samples to optimize the properties. The temperature (180 °C, 190 °C, 200 °C), pressure (6 bar), preheating time (10,15,20 minutes), and compression time (3, 4, 5 min) were varied to find the optimum joining properties.

The compression pressing conditions were optimized to 190 °C, 10 minutes for preheating, and 3 minutes for compression time. PVC and aluminum samples were placed on a customized tool and started tests as shown in Figure 3.

Table 1. Abbreviations of Aluminum Surface Types

#	Aluminum Surface Types	Sample Pictures	Codification
1	Flat		S1
2	Side Punched		S2
3	Perforated		S3
4	Perforated + Side Punched		S4
5	Surface Deformed		S5
6	Surface Deformed + Side Punched		S6

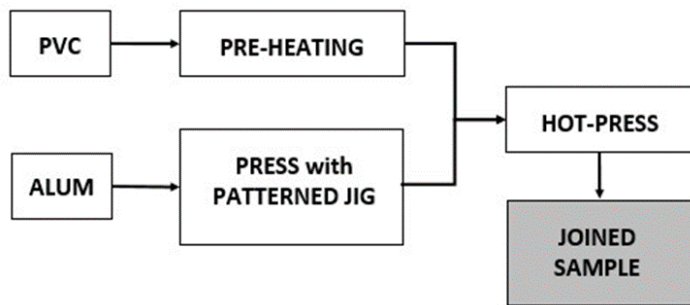


Fig. 1 A schematic picture of the sample preparation process

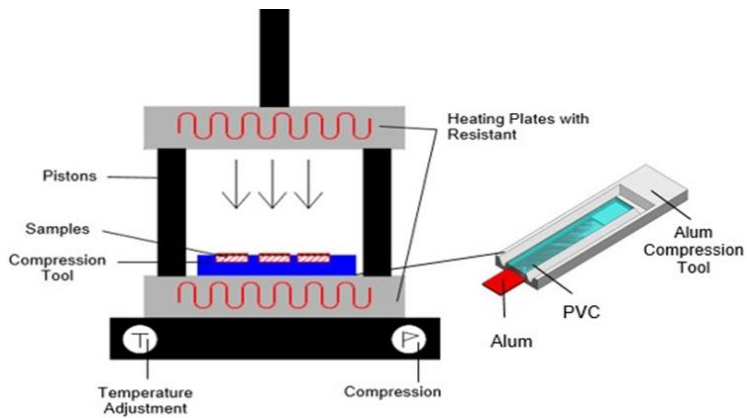


Fig. 2 Schematic representative of hot press equipment

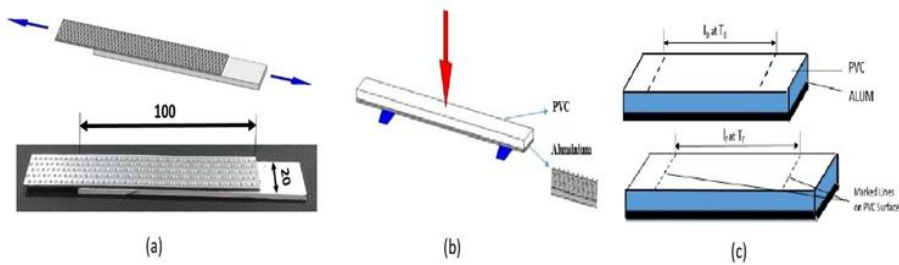


Fig. 3 Sample preparation and tests (a) Lap-Shear, (b) 3P Bending, (c) CTE

2.3. Characterization

2.3.1 Mechanical Testing

2.3.1.1 Lap-Shear Test

The lap-shear tests were conducted on a Zwick mechanical tensile testing equipment with a load cell of 20 kN. During the tensile/shear testing, the displacement control mode with a rate of 1 mm/min was utilized. After the peak loads were recorded, the experiments were terminated.

The test specimen in the lap-shear arrangement is formed by two rectangular pieces with an overlapping area large enough to cause failure. The subsequent tensile testing determines the lap-shear strength, which is given by:

$$\sigma = \frac{P}{b \cdot L} \quad (1)$$

where,

P - Maximum load (N),

b- Joint width (mm),

L- Joint length (mm),

σ - Stress (N/mm²)

Lap-shear properties of composite materials were measured with Zwick Roell 20 kN. Samples dimensions were 20x100 mm. The measurements were done at 23 ± 2 °C and relative humidity %45 ± 10.

2.3.2 3-Point Bending

A flexural strength test imposes tensile stress in the convex side of the specimen and compressive stress in the concave side. Test has been performed with 30 kN.

2.3.3 Inter Laminar Shear Strength (ILSS)

The short beam strength test of high modulus reinforced composite materials is determined in ASTM D 2344. The samples have dimensions of 4x24x8 mm. The ILSS values were evaluated from the short beam shear test according to the following relation:

$$ILSS = 0.75 \times Pb / (b \times d) \quad (2)$$

Where P_b = breaking load (N), b = width (mm) and d = thickness (mm) of the specimen.

2.3.4 Thermal Tests

2.3.4.1 Coefficient of Linear Thermal Expansion (CTE)

Different substances expand by different amounts. Over small temperature ranges, the linear thermal expansion of uniform objects is proportional to temperature change.

The test specimens were marked as l_0 at T_0 , after the test, l_f has been recorded at temperature T_f . By measuring the length at room temperature, the expansion, and the temperature difference, the α value can be calculated as the formulation given below.

$$(l_f - l_0) / l_0 = \alpha_1 \times (T_f - T_0) \quad (3)$$

$$\Delta l / l_0 = \alpha_1 \times \Delta T \Rightarrow \alpha_1 = 1 / l (dl/dT) \quad (4)$$

where l_0 and l_f represent, respectively, where l_0 and l_f represent, respectively, the original and final lengths with the temperature change from T_0 to T_f . The parameter α_1 has units of reciprocal temperature (K^{-1}) such as $\mu m/mK$ or $10^{-6}/K$.

The length of the marked sample is measured at room temperature, and again when it has been heated up. The test has been performed in a Nuve heating oven at 20 °C (T_0) to 70 °C with 10 °C increasing temperature intervals.

2.3.5 Microscopic Analysis

2.3.5.1 Optical Microscope

The interface layer of sections of joined samples were analyzed in the Optical Microscope of Eclipse LV100ND model in Nikon. The section of joined samples were prepared to have 100X magnifications.

According to tests explained in this study, overview of test performed samples as shown in Figure 4.



Fig. 4 Overview of test samples

3. Results and Discussion

3.1. Design of Experiment (DOE)

MINITAB software was used to examine the main effect and interaction plots.

Main effect plots provide information about which is the most influencing factor and the classic relationship between availability, performance, and quality rate [10].

DOE which is shown in Figure 5; the dependent variables (responses) consist of the test results as lap-shear, 3-point bending, ILSS, and CTE performed as a result of the study. The independent variables (factors) were determined as aluminum surface roughness and process types. The determined independent variables are classified as levels and described in Minitab software. There are 6 levels for aluminum surface roughness and they are described as S1 to S6.

In the study of Rafidah et al. (2014) on “Comparison Design of Experiment (DOE): Taguchi Method and Full Factorial Design in Surface Roughness”, they compared the effectiveness of Taguchi and full factorial design methods on surface roughness using both Taguchi and full factorial design techniques [11]. According to the obtained results in their paper, the full factorial design looks better DOE technique than the Taguchi method, since the mean square error is lower, the parameter design of the full factorial design provides a simple, systematic, and efficient methodology for optimizing process parameters. When the available techniques in DOE analysis were evaluated, full factorial design has been decided to use in the current study.

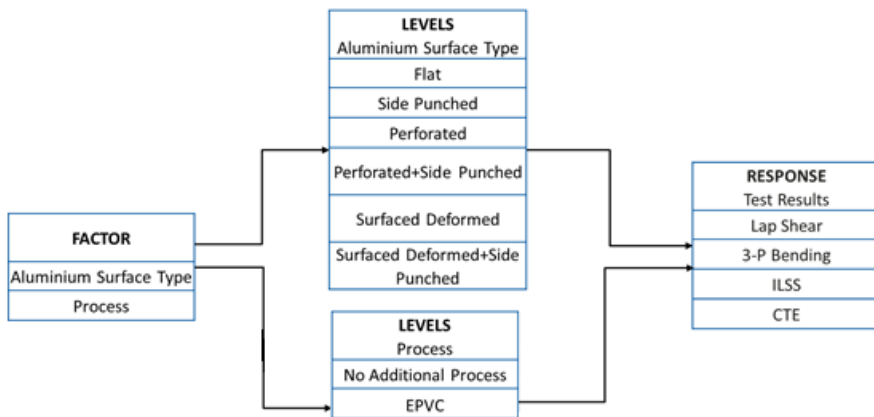


Fig. 5 DOE analysis in the study (factors, levels and responses)

The brief contents of the results from the DOE results are as follows:

The lap-shear tests were performed on the modified samples which have the effect of surface roughness and adhesions. The results show that increasing sanding time as higher surface roughness, was improving mechanical locking. But, after having maximum shear strength, the surface roughness degraded the bond strength of the adhesive which means reducing in shear strength at higher roughness. The results of the lap-shear relationship between the different samples were explained in the first main effect plot. These plots show the mean value of that parameter based on different roughness and process types.

The other purpose was to describe how different surface roughness classes affected flexural performance. In the current study, the flexural strength of the surface roughness has increased. The 3-point bending test results showed that the fracture surfaces in the

samples with surface roughness were filled with plastic material, enhancing the interface and contributing to the study's findings of a decrease in deflection. The detected deflection on test samples is explained by a 3P bending main effect plot.

ILSS was measured as a function of surface roughness. Roughness and surface energy variations effectively improve laminate bonding strength. In our study, the measured ILSS results were higher for the specimens which having pretreated processes on surfaces. Roughness has improved the results identically for the samples S4, S5, and S6 (perforated, punched, and deformed surfaces).

The measured results for CTE show that the roughness on the aluminum surface affects expansion property. The lowest values in the S range, which are identical to the joined structure were obtained in S2, S4, and S5 samples.

According to the plots of the main effect in DOE studies, the surface roughness examined on the aluminum surface contributes positively to the joining interface. Additional processes also resulted positively when they are compared to the untreated process. DOE study results show that S2, S4, and S5 specimens achieved better results among all samples.

3.1.1 Main Effect Plots

Main effect plots provide information about which is the most influencing factor and the classic relationship between availability, performance, and quality rate [10].

In this study, main effect plots describe the relations of levels between aluminum surface roughness and process types. The mean values of test results were shown on main effect plots. Therefore, these plots provide a good overview of the data.

Lap-shear, ILSS, and 3P bending tests were examined to focus on mechanical properties deviation. CTE test was set to see how enhancing the joining affects the thermal expansion behavior.

3.1.1.1 Main Effect Plot of Lap-shear

Kwon et. al researched "Comparison of interfacial adhesion of joined materials of aluminum/ carbon fiber reinforced epoxy composites with different surface roughness" in 2019. They have modified the surface of aluminum using some sanding processes. The lap-shear tests were performed on the modified samples which have the effect of surface roughness and adhesions. The results show that increasing sanding time as higher surface roughness, was improving mechanical locking. In other words, the increased energy of the surface results in improved mechanical adhesion with higher lap-shear values [12].

Similar to these results, the different roughness types have improved the results positively in our study. Because of the locking mechanism, PVC material filled the deformations on the aluminum surface, the results were obtained identically higher than the S1-flat surface.

Hamdi et. al (1995) studied "Improving the adhesion strength of polymers: effect of surface treatments" on PVC, ABS, and EPDM materials. According to their outputs on graphs for lap-shear tests, PU application on PVC surface has a lower effect than other adhesives selected as silicone and modified silane. On the other hand, the samples which were treated had better results [13]. Pretreatment had also a similar influence on the outcomes of the present study specimens. The samples which were premiered as a pre-treatment on the aluminum surface have higher values on lap-shear tests.

The surface treatment of effect on aluminum was studied by Boutar et.al (2016) for automotive applications. They determined the effect of surface roughness and wettability on the strength of single lap joints on three abraded surfaces. The results indicate that

shear strength appears to increase from not abraded to a polishes surface with abrasive paper that provides 0.6 μm surface roughness. But, after having maximum shear strength, the surface roughness degraded the bond strength of the adhesive which means reducing in shear strength at higher roughness. They have summarized that joint durability cannot be provided by higher surface roughness, it also depends on the characterization of the interphase and its formation mechanism [14].

In the present study, the customized tool has been designed to deform and increase the surface area like roughness. While the values were expected to go up, the results were worse than expected, because of air in the gap remained closed, it had a negative impact on the outcomes. Equivalent to their study, the depth of roughness must be optimized. Otherwise, the roughness can have a negative effect on the results.

The results of the lap-shear relationship between the different samples were explained in the first main effect plot. These plots show the mean value of that parameter based on different roughness and process types. According to the given results, the addition of roughness and process types have positive effects on the results. While S1 (untreated flat surfaces) have the lowest value, the additional processes and mechanical operations on the surface have an impact on the values as variations. The main effect plots for lap-shear test results were summarized that S2, S3 and S4 samples in surface types have resulted as higher than 2 MPa which was 1.08 MPa without any roughness.

3.1.1.2 Main Effect Plot of 3P Bending

Lee et al. (2016) studied carbon fiber-reinforced plastic/Al5052 joined samples. When the flexural stress of the composite was measured about the surface roughness, it was found that if the specimen surface was treated with sandblasting, the flexural stress remained relatively constant regardless of the surface roughness; nevertheless, it was lower when the specimen surface was not treated. This shows that surface treatment improved the flexural strength of the material. The specimen had a flexural stress of 480–500 MPa after sandblasting, whereas it was only 220 MPa in the absence of surface treatment [15].

In the present study, the roughness on the surface has increased in flexural strength. The 3-point bending test results showed that in the samples with surface roughness, the fracture surfaces were filled with plastic material, thus improving the interface, which also led to a positive decrease in the deflection results in this study.

Zal et al. (2016) studied the effect of the surface roughness of aluminum on fiber metal laminates (FML) which include fiberglass, PVC film (0.2 mm), and aluminum. Four different surface treatments (pickled with HCl, cold rolled, holes, grinding, and mechanically roughened) were applied on three-point bending samples to measure flexural strength. The least flexural strength has been measured in the etched aluminum layered sample, because of pickling removed contaminant substances from the aluminum surface and tend to form a chemical bond. In this case, PVC polymer tolerates delaminating shear stress which also provides an improvement in flexural strength. The overview of the results showed that mechanical treatment and roughening of the aluminum surface was found to be a good treatment method to obtain a high-strength PVC matrix/aluminum layer interface bonding in the produced FMLs [16] some processes as surface treatment and having some holes similar to S2 and S3 specimens look close to principally. The created holes improved the interlock mechanism in both studies were resulted in higher values. Piercing on aluminum allowed the PVC filling which is similar to S2-side punched and S3-perforated specimens, resulting in better outcomes.

The “Effects of surface roughness and bond enhancing techniques on flexural performance of CFRP/concrete composites” subject has been studied by Ariyachandra et al (2017). The surface preparation and bonding alternative techniques on joined performance were

performed with the three-point bending test method. The purpose was to define the effects of dissimilar surface roughness classes on flexural performance. Polymer anchorages' effect for delaying the end debonding was studied. The surface roughness of concrete substrates has significant effects on the bond strength of CFRP-concrete composites. Samples with shorter leg – anchorages results were not big improvements, which means longer leg-anchorage geometry provided better outputs in three-point bending results [17].

Interface assessment has been studied by Karakaya (2020) They have investigated an alternative joining method on the over-molding of thermoplastics on thermoset composites. The peel ply treated over-molding on the surface indicates better adhesion performance. The tests reveal that the peel-ply application increases the roughness by providing a good effect on flexural strength and modulus. This effect was more evident in the sample which was prepared with 80 oC temperature mold [18].

In that study higher temperatures provided the softening phase for polymers to improve the joining. Similarly to that, the temperature in the hot press was 190 °C in the current study, which allowed the softened PVC higher than the Vicat temperature. The roughness on the aluminum surface was filled with a soft polymer that enabled good adhesion. 3P bending main effect plot explains the measured deflection on test samples. The highest deflection value was measured in S1, which decreased roughly from 2.5 mm to lower than 1.0 mm with surface roughness and adding extra treatments. The results indicated that the pretreatment on the aluminum surface with primer provided a lower displacement. The main effect plots for 3P bending indicated that decrease in the deflection after surface modifications and treatments. S4, S5, and S6 in surface types have lower deflection with the result of good joining properties.

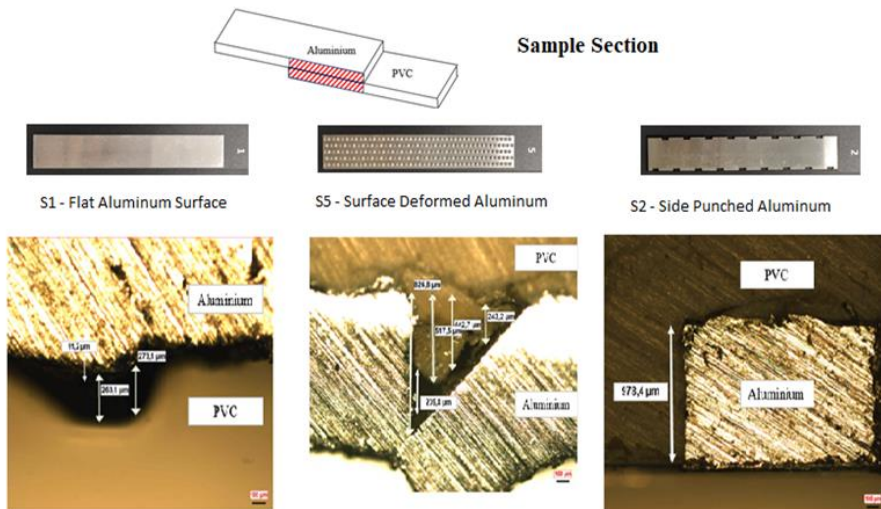


Fig. 6 Optical microscope result of interface on S1, S5 and S2

3.1.1.3 Main Effect Plot of ILSS

Choi et al (2010), investigated the interface of a metal sheet–prepreg. The studies were carried out on aluminum sheets with different roughness levels of surface textures (sanding and nylon-pad abrasion) and chemical etches systematically changing the surface

morphology. ILSS was measured as a function of surface roughness. Roughness and surface energy variations effectively improve laminate bonding strength [19].

In our study, similar to their outputs, the measured ILSS results were higher for the specimens which having pretreated processes on surfaces. Roughness has improved the results identically for the samples S4, S5, and S6 (perforated, punched, and deformed surfaces).

Wu et al.2014, studied the impacts of various surface treatments on fiber metal laminate ILSS. For the surface treatment of aluminum, they utilized solvent degreasing, mechanical abrasion, alkaline cleaning, and plasma treatment. Sandpaper and alkaline cleaning with NaOH had the greatest ILSS among the various surface treatments. The reason for the greater ILSS value is that when metal is abraded with a lower-grit sandpaper, it achieves a higher roughness than when metal is abraded with a higher-grit sandpaper. With alkaline washing, an interface layer was created, causing a bridging effect between aluminum and composite, resulting in greater adhesion. As the concentration of NaOH rises, the thickness of this interface layer increases [20].

As lower grit sandpaper provided higher roughness in their study, ILSS measurements of S5 surface deformed samples have resulted more than others, which is identical to outcomes of higher roughness. The results of the ILSS test indicated that the surface roughness on the Aluminum surface has an effect in a positive direction on the values. From aluminum surface types, S4 and S5 have higher values in their range. Small sizes of ILSS specimen needs to prepare the sampling more sensitively. It is the one reason for these deviations in the results. If the location of the roughness was not centered correctly on the specimen, it creates some deviations in unexpected direction.

3.1.1.4 Main Effect Plot of CTE

The main effect plot for CTE results has been indicated. The measured results for CTE show that the roughness on the aluminum surface affects expansion property. The lowest values in the S range, which are identical to the joined structure were obtained in S2, S4, and S5 samples. The main effect plot was created for CTE which is critical for the products that need to be exposed to outside weathering conditions. Therefore, the thermal expansion of each material for the joined structure must be examined if the value is a limitation at certain temperature differences. The results revealed that S2, S4, and S5 have lower coefficients than other types.

According to the plots of the main effect in DOE studies, the surface roughness examined on the aluminum surface contributes positively to the joining interface. Additional processes also resulted positively when they are compared to the untreated process. DOE study results show that S2, S4, and S5 specimens achieved better results among all samples. Main Effect plots for Lap Shear, Deflection, Short Beam Strength, and CTE results were given in Figure 7.

3.2. Microscopic Analysis

3.2.1 Optical Microscope

S1- Flat Aluminum surface;

On flat samples, Figure 6 illustrates the gaps between the PVC and aluminum interface regions. In some local areas of the interface, there is a gap of nearly 263 μm , which has a significant impact on the result of the sample, which has no surface roughness.

S5 - Surface deformed Aluminum;

In Figure 6, the optical microscope result of the S5 joined sample is shown. OM picture indicates that PVC material penetrated through the cavity on the aluminum surface. The dimension of PVC penetration was measured as 517.5 μm which provides an advantage as interlocking on test results. But, there is still a void (239.8 μm) on this joining structure that PVC can't fill since it is a closed gap with air. Air in these gaps could not be replaced with PVC.

S2 - Side punched Aluminum surface;

The optical microscope output for side-punched aluminum samples is shown in Figure 6. OM result presents on the cross section that removed part of aluminum were filled by PVC material. The depth of penetrated PVC was measured to be 978.4 μm , which is the best interlocking mechanism among the other surface roughness.

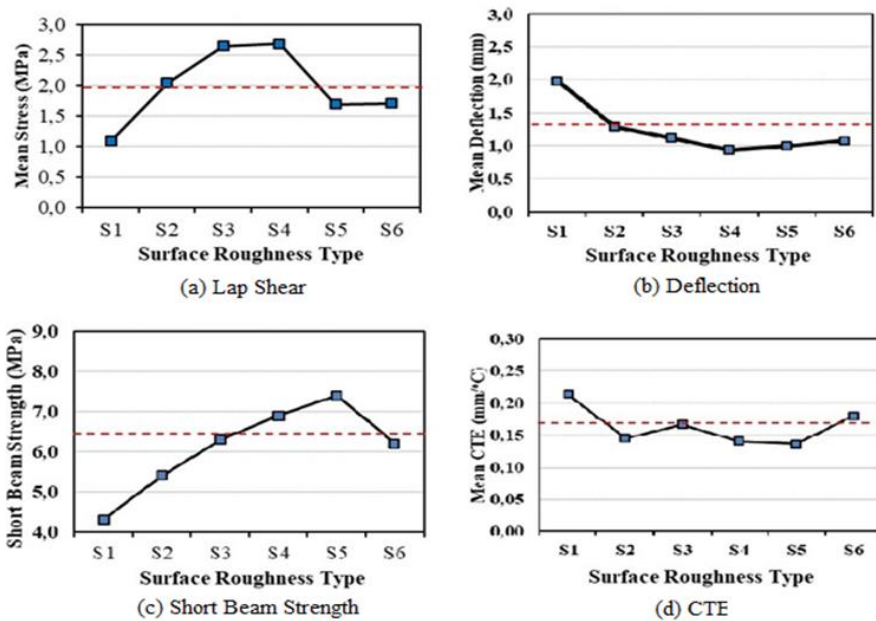


Fig. 7 Main Effect plots (a) Lap Shear (b) Deflection (c) Short Beam Strength (d) CTE- Based on Roughness

4. Conclusion

In this study, the idea of having joined PVC and aluminum a solid product within an improved joining structure that can replace the steel sheet. However, the modulus of elasticity of steel is approximately 3 times higher than aluminum. It has a positive reduction in the deflection values in the moment of inertia for joined materials when using aluminum in multiple structures. For this reason, it was necessary to initiate a study with enhanced bonding properties at the PVC and aluminum interface.

Before any experimental study, the design of the experiment methodology was exploited for all the parametric studies. In the study, which aims to strengthen the joining between PVC and aluminum, good results were obtained from the samples of the metal surface, with side punched and perforated aluminum surfaces with a positive increase of around 40%.

The specimens with side cuts and perforated holes with interlock mechanisms resulted in the expected direction, where shear forces appear to be difficult due to the plastic raw

material filling the emptied space. This view was also supported by cross-sectional images taken with an optical microscope. In the side punched samples, it was observed that PVC and aluminum formed an interlocked structure which provides an advantage on joined structure. Contrary to expectations, in the surface deformed samples, the PVC material could not fill the deformed area on the surface, since the air is trapped inside.

Considering all of the parameters and findings of this study, it has been determined that surface roughness has a critical effect on joining structure and that mechanical and thermal results can be improved by adding additional processes to the specified surface.

When the findings of these studies are analyzed, new coupling techniques or parameter adjustments are still in discussion, and the potential implications of new applications on the results will be investigated further in the study's subsequent steps.

In further steps of this study, it is thought that the interface formation on the process-based parameters on aluminum surfaces has a positive effect on the bonding. For this reason, several processes such as emulsion PVC, adhesives, and plasma will be evaluated in further studies. This is an area where we scratched the surface and there are many studies to conduct in this area, we are also working on the adhesive type for the joining that has the optimized roughness.

References

- [1] Shen J, Liang J, Lin X, et al. Recent Progress in Polymer-Based Building Materials. *International Journal of Polymer Science*. 2020;58(23):1-15
<https://doi.org/10.1155/2020/8838160>
- [2] Campbell FC. *Aluminum. Elements of Metallurgy and Engineering Alloys*, 1st edition, ASM International USA, 2008:487-506, ISBN 0-87170-867-1
- [3] Hulamin Think Future Think Aluminum. *Integrated Report 2016*. [Internet] 2020; Available from: https://www.hulamin.com/iar2016/Business_products_applications_aluminium.html
- [4] Eskandari N, Motahari S, Atoufi Z, et al. Thermal, mechanical, and acoustic properties of silica-aerogel/UPVC composites. *Journal of Applied Polymer Science*. 2017;134(14)
<https://doi.org/10.1002/app.44685>
- [5] *PVC Stabilizers Market - Growth, Trends, COVID-19 Impact, and Forecasts (2021 - 2026)*. Mordor Intelligence Pvt Ltd. 2021
- [6] Asif M. Sustainability analysis of window frames. *Building Services Engineering Research and Technology*. 2005;26(1):71-87
<https://doi.org/10.1191/0143624405bt118tn>
- [7] Harris AF. The effects of grit blasting on surface properties for adhesion. *International Journal of Adhesion and Adhesives*. 1999;19(1):445-452
[https://doi.org/10.1016/S0143-7496\(98\)00061-X](https://doi.org/10.1016/S0143-7496(98)00061-X)
- [8] Plasma Treat. *Atmospheric plasma solutions: High-efficiency plasma cleaning, activation and nanocoating of surfaces*. [Internet]. Available from: <https://www.plasmatreat.com/plasma-technology/openair-atmospheric-plasma-technique.html>
- [9] Petrie EM. *Adhesive. Handbook of Adhesives and Sealants*, 2nd edition, McGraw-Hill Companies New York, 2007:451-479, ISBN: 978-0-07-170981-1
- [10] Mathews PG. *DOE Language and Concepts. Design of Experiments with MINITAB*. 1st edition, American Society for Quality USA, 2004: 93-95, ISBN 0-87389-637-8
- [11] Rafidah A, Nurulhuda A, Azrina A, et al. Comparison Design of Experiment (DOE): Taguchi Method and Full Factorial Design in Surface Roughness. *Applied Mechanics and Materials*. 2014;660:275-279
<https://doi.org/10.4028/www.scientific.net/AMM.660.275>

- [12] Kwon D, Kim J, Kim Y, et al. Comparison of interfacial adhesion of hybrid materials of aluminum/carbon fiber reinforced epoxy composites with different surface roughness. *Composites Part B: Engineering*. 2019;170:11-18 <https://doi.org/10.1016/j.compositesb.2019.04.022>
- [13] Hamdi M, Saleh M, Poulis J.A. Improving the adhesion strength of polymers effect of surface treatments. *Journal of Adhesion Science and Technology*. 2020;34(17): 1853-1870 <https://doi.org/10.1080/01694243.2020.1732750>
- [14] Boutar Y, Naïmi S, Mezlini S, et al. Effect of surface treatment on the shear strength of aluminium adhesive single-lap joints for automotive applications. *International Journal of Adhesion&Adhesives*. 2016;67:38-43 <https://doi.org/10.1016/j.ijadhadh.2015.12.023>
- [15] Lee MS, Kim SJ, Lim OD, et al. A study on mechanical properties of Al5052/CFRP/Al5052 composite through three-point bending tests and shear lap tests according to surface roughness. *Journal of Composite Materials*. 2016;54(12):1549-1559 <https://doi.org/10.1177/00219983166636458>
- [16] Zal V, Naeini HM, Bahramian AR. Evaluation of the effect of aluminum surface treatment on mechanical and dynamic properties of PVC/aluminum/fiber glass fiber metal laminates. *Journal of Process Mechanical Engineering*. 2016;231(6):1-9 <https://doi.org/10.1177/0954408916657371>
- [17] Ariyachandra MREF, Gamage JCPH, Al-Mahaidi R, et al. Effects of Surface Roughness and Bond Enhancing Techniques on Flexural Performance Of Cfrp/Concrete Composites. *Composite Structures*. 2017;178:476-482 <https://doi.org/10.1016/j.compstruct.2017.07.028>
- [18] Karakaya N, Papila M, Özkoç G. Overmolded hybrid composites of polyamide-6 on continuous carbon and glass fiber/epoxy composites: 'An assessment of the interface'. *Composites Part A*, 2020;131:105771 <https://doi.org/10.1016/j.compositesa.2020.105771>
- [19] Choi WJ, Choi HS, Parka SY, et al. Effects of surface pre-treatment and void content on GLARE laminate process characteristics. *Journal of Materials Processing Technology*. 2010;210(8):1008-1016 <https://doi.org/10.1016/j.jmatprotec.2010.01.017>
- [20] Wu W, Abliz D, Jiang B, et al. A novel process for cost effective manufacturing of fiber metal laminate with textile reinforced pCBT composites and aluminum alloy. *Composite Structures*. 2014;108(1):172-180 <https://doi.org/10.1016/j.compstruct.2013.09.016>



Prediction and optimization of heat treatment effects on hardness and electrical conductivity of aluminum composite reinforced with nano alumina based on response surface methodology

Md Jalal Uddin Rumi^{*1, a}, Muhammad Muzibur Rahman^{2, b}

¹Dept. of Aeronautical Eng. Military Inst. of Science and Tech., Mirpur Cantonment, Dhaka-1216, Bangladesh

²Dept. of Naval Architecture and Offshore Eng., Bangabandhu Sheikh Mujibur Rahman Maritime University, Dhaka-1216, Bangladesh

Article Info

Abstract

Article history:

Received 27 Jan 2023

Accepted 02 May 2023

Keywords:

Aluminum Composite;
Heat Treatment;
Mechanical and
Electrical Behavior;
Response Surface
Methodology;
Microstructure

In this study, three non-linear mathematical models were developed using a central composite design for the prediction of heat treatment effects on Vickers micro hardness (HV), Rockwell hardness (RHN), and electrical conductivity (%IACS) of nano Al₂O₃ reinforced Al composite fabricated by a two-step stir casting method. As per the investigation, both process variables of heat treatments such as solution temperature and aging temperature considerably influence the changes in hardness and electrical conductivity of Al composite. For the two-way interaction analysis of variance test, the R² values for HV, RHN, and %IACS were 89.29%, 96.23%, and 91.50%, respectively, with a 95% confidence level and 5% significance level. As per the regression equation, the optimized process variables of heat treatment such as solution temperature and aging temperatures are 531.428°C and 180°C which can provide an improvement of 23.15%, 33.57%, and 9.57% respectively for HV, RHN, and %IACS in contrast to their as-cast conditions. Here, the maximum error (%) measured between experimental and prediction are respectively 3.52%, 6.09%, and 2.69%. The microstructure reveals an almost uniform distribution of nano Al₂O₃ in Al composite with fewer agglomeration. The formation of intermetallic compounds at different heat treatment processes identified in SEM impacted the changes in the electro-mechanical properties of fabricated Al composite.

© 2023 MIM Research Group. All rights reserved.

1. Introduction

Aluminum composites (Al composites) are a type of materials that hold great potential for use in the automotive and aerospace sectors. This is because they possess characteristics such as low weight, high specific strength, and effective resistance to wear and corrosion [1, 2]. Researchers all over the world are constantly studying how to enhance the electro-mechanical characteristics of aluminum composites. They do this by using various manufacturing methods, adjusting process parameters, and applying heat treatment techniques. A variety of fabrication techniques are available to create Al composites, including stir casting, ultrasonic assisted casting, composite casting, powder metallurgy process, etc. [3]. When making Al composites, the stir casting method is preferred to its counterparts since it is more widely applicable [4]. The stir casting technique's benefits stem from its ease of use, adaptability, and suitability for large-scale production [5]. Al composites with reinforcement volume fractions up to 30% can be developed using this fabrication method [6]. The main drawback of this fabrication technique is that the distribution of the reinforcing particles in the matrix might not be entirely uniform [7]

*Corresponding author: jalal.rumi@ae.mist.ac.bd

^aorcid.org/0000-0002-6404-4438; ^borcid.org/0000-0002-7444-9009

DOI: <http://dx.doi.org/10.17515/resm2023.672ma0127>

Res. Eng. Struct. Mat. Vol. 9 Iss. 3 (2023) 805-825

because of density variations and the development of porosity, which reduces the material properties of the composite. Two-step stir casting [8-10] is one of many methods available to mitigate the said issue.

The fabrication process, the types, and sizes of reinforcement particles, the interaction between reinforcement and matrix, the morphology, and the volume fraction reinforcement all have a significant impact on the properties of an Aluminum Metal Matrix Composite (Al MMC) [11]. Numerous researchers from all over the world are constantly investigating whether it is possible to create straightforward, affordable, and effective processing conditions for the production of MMCs [12-13]. According to number of research papers and textbooks, the characteristics of developed Al MMCs are largely dependent on the various stir casting processes and parameters including speed of stirring [14], duration of stirring [15], casting temperature [16], squeeze pressure [17-18], reinforcement size [19], and preheating temperature [20-22]. Constant attempts are also being made to enhance the electro-mechanical properties of Al MMC by including different reinforcing particles such as Al_2O_3 , SiC, Gr, B4C, and TiC [23-28]. Due to its greater interfacial affinity and resistance to chemical deterioration by molten aluminum alloys, Al_2O_3 is the most often used reinforcing material among them [29-30]. When the heat treatment technology is used in a different way, the characteristics of the Al composites are considerably altered. Aluminum Associations have standardized a number of heat treatment procedures, including T4, T5, T6, T8, etc. [31]. The effect of heat treatment on the electro-mechanical properties of aluminum composites can vary depending on the type of heat treatment, the temperature, and the cooling rate. Therefore, it is important to carefully select the heat treatment process and parameters to achieve the desired mechanical properties for the specific application. Chandra et al. (32) fabricated MoS_2 -reinforced AA6061 by a stir casting technique and carried out heat treatment at a solutionized temperature of 540°C for 1 hour. On completion of solution treatment, test specimens were quenched immediately in water and then thermally aged at 180°C . They observed improvement in hardness, and flexure strength compared with as-cast composites. Tiwari et al. (33) investigated the influence of heat treatment on the mechanical properties of aluminum alloy-fly ash composites, where the solution temperature was maintained at 490°C followed by thermal aging at various temperatures of 130°C , 150°C , 170°C , 200°C , and 240°C , respectively, and observed a gradual improvement in the mechanical properties.

Response surface methodology (RSM) is utilized for creating, enhancing, and optimizing the process variables of different heat treatment processes [34]. Orthogonal array designs employed in trials are scarce and might not be able to evaluate all interactions between the process variables being studied [35]. A two-level factorial design has been employed in numerous experimental studies to investigate how heat treatment affects electro-mechanical properties. However, for analyzing the nonlinearity of output characteristics, this method allows for the creation of linear input-output interactions, and each factor must have at least three levels [36]. As the number of parameters and their levels rises, so does the number of experiments.

It may be mentioned that RSM is a type of regression analysis that examines the connections between a number of explanatory factors and one or more response variables. It relies on findings estimated at various places in the design space to create an approximation mathematical model in place of a complex one [37].

In a study, Vickers micro hardness, Rockwell hardness, and Electrical conductivity of 2.5 wt. % of Al_2O_3 reinforced Al composite were obtained respectively as 35.72 HV, 24.33 RHN, and 45.15 %IACS as a casted condition [38], which can be improved further by various heat treatment processes. However, a single heat treatment process is insufficient to achieve

the desired characteristics as per the requirement of the automotive and aerospace industry. For the fabricated Al composite to work at its best, a combination of natural and artificial heat treatment processes can be taken into account to observe the changes in the electro-mechanical properties of fabricated Al composites. Reviewing the effects of different solution and thermal aging temperatures on electro-mechanical properties of fabricated Al composites carried out by different researchers, two factors, i.e., factor 1 and factor 2 have been set as a solution treatment temperature and thermal aging temperature respectively. The purpose of the present study was to identify the most accurate correlation between solution temperature and thermal aging for the highest improvement of Vickers micro hardness (HV), Rockwell hardness (RHN), and Electrical Conductivity (%IACS) of fabricated Al composite under different heat treatment processes in comparison. Another objective of the study was to predict the Hardness and Electrical conductivity of Al composite and optimization of the Heat treatment process based on the Response Surface Methodology.

2. Material under Study

The base metal used for the casting of composites is aluminum ingots collected from RUSAL of Russia. Olympus Vanta C Series XRF Analyzer was used to analyze the chemical composition of the aluminum, and the results are shown in Table 1. The reinforcement particle used for the fabrication of Al composite is Alumina (Al_2O_3) in grain size of 20 nm provided by Hebei Suoyi New Material Technology Co. Ltd. in China. Its physical properties are shown in Table 2 and its microstructure is presented in Fig.1. In this current study, an Al composite was fabricated having 97.5 wt. % of Al along with 2.5 wt. % of Alumina.

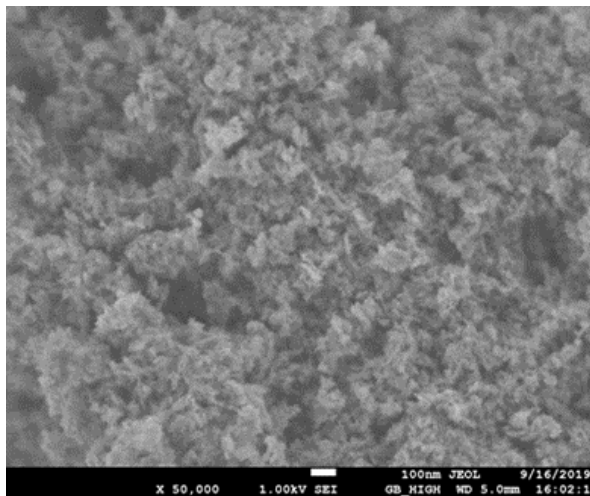


Fig. 1 SEM of Reinforcement particles Al_2O_3 with grain size of (05-20) nm

Table 1. Composition of Aluminum

Element	Al	Si	Fe	Cu	Zn	Zr	Pb
Percentage (%)	99.052	0.614	0.323	0.002	0.008	0.0007	0.0009

Table 2. Physical Properties of Alumina (Al_2O_3)

Melting point (°C)	Boiling point(°C)	Limit of application (°C)	Bulk Density (g/cm ³)	Hardness (Moh's Scale)	Molecular weight (g/mol)	Fracture toughness (MPa-m ^{1/2})
2072	2977	1175	.1-.3	7.5	101.96	3.5

3. Experimental Details

3.1 Selection of Two-Step Stir Casting Technique

In order to optimize the dispersion of reinforcing particles in aluminum composites, the two-step stir-casting method modifies the traditional stir-casting process. The procedure entails two stirring stages with a little break in between, and it can produce a more uniform distribution of the reinforcing particles. The molten aluminum is swirled in the initial step of the process to better moisten the reinforcing particles. This ensures that the particles are spread evenly throughout the molten metal and lessens the agglomeration of the particles. Agglomerates of the reinforcement particles are dispersed during the first step of stirring, resulting in a more even distribution of the particles. In order to further homogenize the composite mixture, the molten aluminum is churned once more during the second step of the process. This guarantees that the reinforcement particles are dispersed uniformly throughout the matrix and that any leftover agglomerates are broken up. The deposition of the reinforcing particles during casting can also be decreased by using the two-step stir casting technique. This is due to the fact that while the first round of stirring serves to suspend the particles in the molten aluminum, the second round of stirring makes sure they stay suspended. Overall, the two-step stir casting technique can aid in enhancing the dispersion of reinforcing particles in aluminum composites, producing composites with more consistent mechanical properties.

3.2 Selection of Process and Parameters

The characteristics of developed Al composites are largely dependent on the various stir-casting processes and parameters, including speed of stirring, duration of stirring, casting temperature, squeeze pressure, reinforcement size, preheating temperature, etc. which are discussed here. In the case of low stirrer rpm, there is no room for the reinforcement particles (dispersed phase) to scatter evenly throughout the matrix due to the low stirrer rpm's reduced shearing force on the matrix metal. Moreover, the scattered phase has the propensity to cluster and agglomerate in lower rpm as it occurs because there isn't enough force to overcome it. In the case of higher stirrer rpm, the dispersed phase can flow inside through the vortex that is formed by stirring because there is more shearing force being applied to the matrix metal. The energy generated by the stirrer's high-speed spinning is sufficient to disperse the dispersed phase's particles, resulting in the dispersed phase's uniform distribution throughout the matrix. With faster stirrers, there is a potential that the matrix's porosity will increase as the gas particles move around inside it. Therefore, an optimum stirring speed of 400 rpm has been selected.

The duration of stirring is crucial in ensuring that dispersed phases are distributed evenly throughout the matrix. The clustering of the reinforcement particles results from less stirring time. Moreover, it can be noticed that some of the matrix lacked inclusions of the reinforcing particles. Increased porosity and oxidation development are two potential drawbacks of longer stirring times, which can also serve to improve the homogeneity and distribution of the reinforcing particles. The mechanical properties of the composite may be significantly impacted by increasing porosity brought on by air entrainment as a result of prolonged stirring durations. Moreover, a prolonged stirring of the molten metal can

promote greater oxide development, which can impact the composite's mechanical properties. In summary, whereas extended stirring durations can increase the homogeneity and distribution of the reinforcing particles, they can also have a negative impact on the composite's cost and attributes. The ideal stirring period will vary depending on the particular materials and manufacturing conditions. Based on the literature review, the time duration of stirring has been selected as 5 minutes in a two-step.

Preheating the mold and reinforcing material is essential to reducing porosity. The entrapped gases from the metal and reinforcement particles are released through preheating. Reviewing recent works from different researchers, preheating of base metal Al selected at a temperature of 500°C for 60 minutes and reinforcement particle Al₂O₃ at a temperature of 300°C for 120 minutes. One of the most important factors that influence the stir-casting process is casting temperature. Due to an increased chemical reaction between the reinforcement particles and the metal matrix, the viscosity reduces as the casting temperature rises, and the distribution of the particles is impacted. The reinforcing particles in the casting temperatures of 750°C and 800°C were discovered to be uniformly dispersed based on the microstructure analysis of several study articles. Due to variations in the viscosity of the liquid Al matrix, particle agglomerations were observed at processing temperatures of 700°C, 850°C, and 900°C. Therefore, casting temperature was set at 800°C.

3.3 Fabrication Procedure of Al Composite

The Al metal was placed in the crucible and heated in the furnace without activating the blower, which generated around 300°C heat. After 15 minutes, the electric blower was activated, and the base metal was preheated at 500°C for 60 minutes. At the same time, the reinforcement particles were preheated in the oven at 300°C for 120 minutes. It took approximately 60 minutes to fully melt the metal. Then, the stirring machine was used for 5 minutes with an rpm of 400 in two steps to ensure proper mixing of the molten metal with Al₂O₃. Once ready, the metal was poured into a sand mold. The mixing rate of Al₂O₃ in the crucible was maintained at 20 gm/minute. Fig.2 depicts the layout of the fabrication procedure.

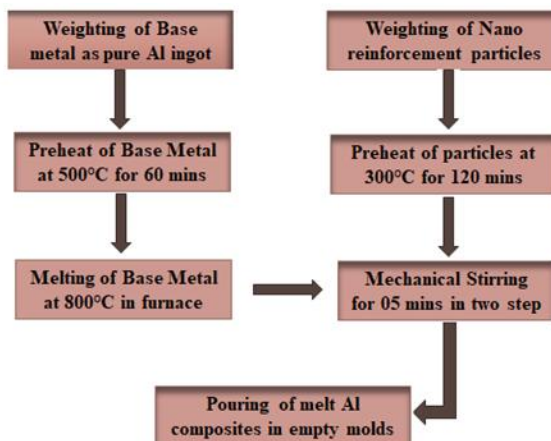


Fig. 2 Fabrication step of Al Composite

3.4 Test Sample Preparation

The Al composite developed had a rough surface and contained few air bubbles, which made it unsuitable for testing electro-mechanical properties directly. In order to improve the surface quality, a Model VF-2 type CNC machine was used for surfacing, as illustrated

in Fig. 3(a). A tungsten carbide end mill with a diameter of 12 mm was employed as the cutting tool for the surfacing process, as shown in Fig. 3(b). The casted sheet had an initial thickness of 30 mm, but after surfacing, the thickness was reduced to 26 mm, and the metal surface on both sides were smoothed out, as depicted in Fig. 3(b). The test specimens were prepared for hardness (Rockwell and Vickers micro) and electrical conductivity as per ASTM standards E18-20, E92-17, and E1004-17 with the same dimensions of 20 mm×20 mm×08 mm, as shown in Fig. 3(c).

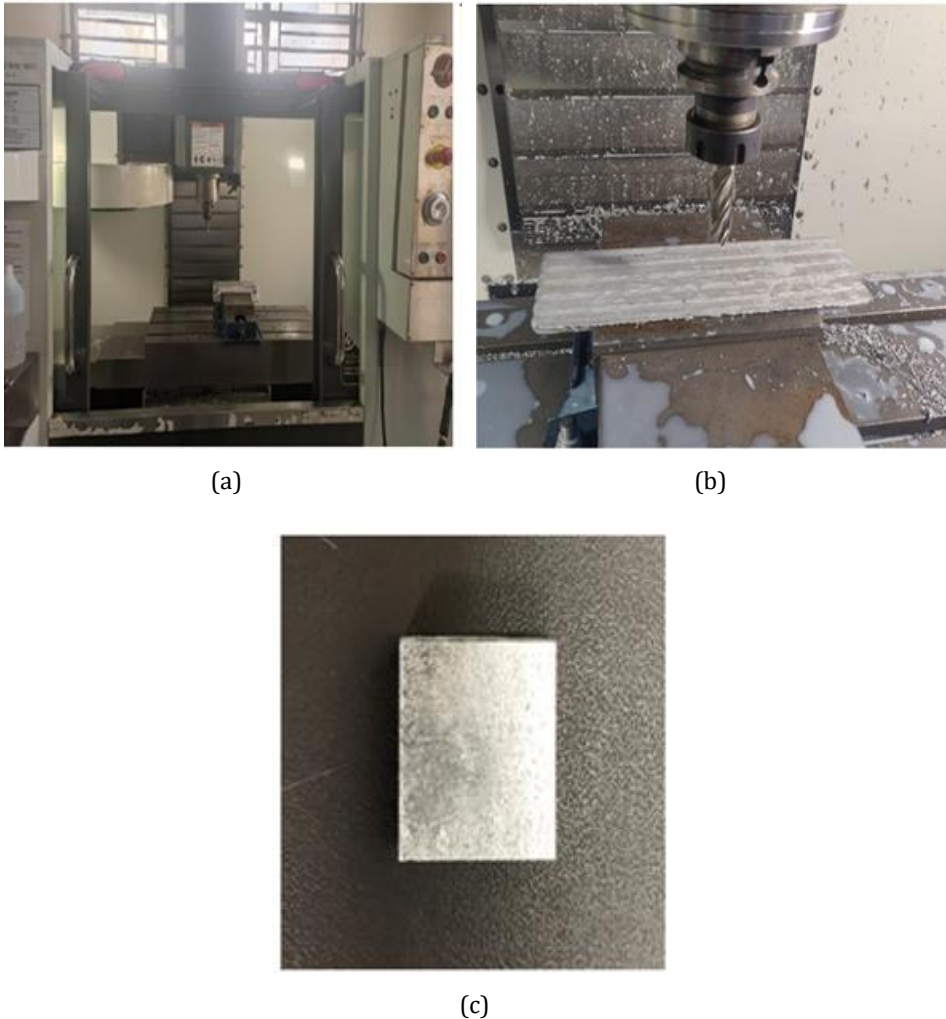


Fig. 3 (a) CNC machining set up; (b) End mill tool with smooth surface; (c) Test specimen

3.5 Process of Heat Treatment

A Carbolite laboratory chamber furnace, model CWF 13/13 from the United Kingdom, with a maximum operating temperature range of 1300°C, was used to perform the heat treatment. During the heat treatment process, the chamber furnace's reported heating rate was 16.66°C per minute. Heat treatment involves solution treatment of test specimens at different temperatures from 501°C to 550°C and thermal aging at different temperatures

from 123°C to 236°C as per the design matrix from RSM. All heat treatment procedures took place for 60 minutes, were followed by water quenching, and were then allowed to naturally age for 72 hours at room temperature in both solution treatment and thermal aging. After the aforementioned heat treatment steps were finished, tests on Vickers micro hardness, Rockwell hardness, and electrical conductivity were done. The step-by-step procedure of heat treatment are shown in Fig.4.

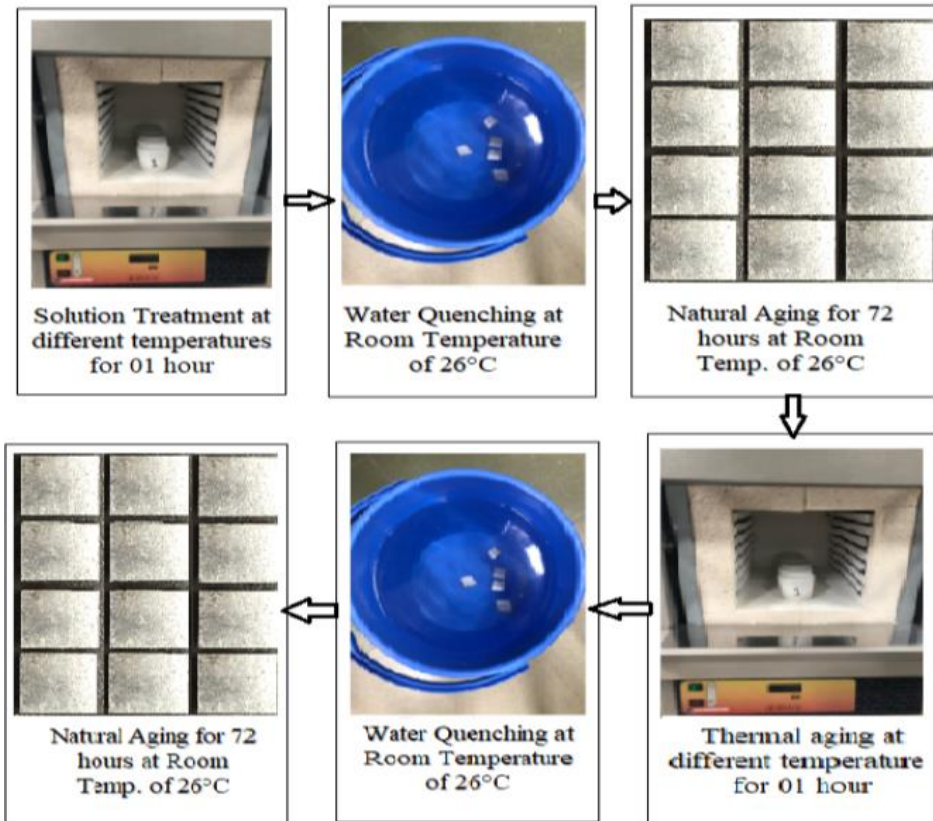


Fig. 4 Heat treatment process of Al composite

3.6 Response Surface Methodology

The goal of the current study was to use Response Surface Design, based on Central Composite design, to simulate and optimize the various heat treatment processes of manufactured Al composite. Below is presented the equation for the second-order polynomial response surface methodology.

$$y = \beta_0 + \sum_{k_j=1} \beta_j X_i + \sum_{k_j=1} \beta_{jj} X_2^j + \sum \sum_{k_i < j=2} \beta_{ij} X_i X_j \quad (1)$$

The relationship between the answer and a number of independent variables is mathematically modeled. The coefficients of mathematical modeling based on the response surface regression form were determined using the MINITAB program version 18. As indicated in Table 3, Central Composite design of RSM, DOE ran a total of 14 experiment runs using the optimized model of heat treatment for Al MMC. According to the best results obtained from DOE, a confirmation experiment was carried out. Table 3 displays the experimental findings for the specified matrix for Vickers microhardness

(HV), Rockwell hardness (RHN), and electrical conductivity (%IACS). The non-linear mathematical model based on CC has been developed for the response of HV, RHN and %IACS having continuous factor of Solution temperature (lower level: 510°C and higher level: 550°C) and Thermal aging (lower level: 140°C and higher level: 220°C). Significance and ANOVA tests have been carried out to check the statistical adequacy of the models.

Table 3. Design matrix and experimental results

Run Order	Pt Type	Blocks	Solution Temperature(°C)	Thermal Aging Temperature(°C)	HV	RHN	%IACS
1	0	2	530.00	180.00	43.99	32.50	49.47
2	-1	2	501.72	180.00	42.08	30.04	48.53
3	-1	2	530.00	123.43	42.15	26.90	48.33
4	-1	2	530.00	236.57	43.83	27.25	45.70
5	-1	2	558.28	180.00	43.42	30.15	47.93
6	0	2	530.00	180.00	43.99	32.50	49.47
7	0	2	530.00	180.00	43.99	32.50	49.47
8	0	1	530.00	180.00	43.99	32.50	49.47
9	1	1	510.00	140.00	40.61	26.25	46.16
10	1	1	550.00	220.00	41.95	27.25	45.99
11	1	1	550.00	140.00	41.33	26.75	48.12
12	1	1	510.00	220.00	43.39	26.00	45.41
13	0	1	530.00	180.00	43.99	32.50	49.47
14	0	1	530.00	180.00	43.99	32.50	49.47

4. Statistical Analysis

4.1 Analysis of Electro-mechanical properties

According to the established model, 89.29% and 80.12%, respectively, are the derived values of R^2 and adj R^2 for Vickers micro hardness. R^2 and adj R^2 for Rockwell hardness were calculated to be 96.23% and 92.99%, respectively. Additionally, for electrical conductivity, R^2 and adj R^2 values were determined to be 91.5% and 84.22%, respectively. The polynomial performs better at characterizing the system's behavior when the R^2 values are higher. This set of parameters is the only set where the model is valid (solution temperature and thermal aging temperature). The model shown in the Eq (1) is created using the regression coefficients.

4.2 Study of Variance

A 95% confidence level and a 5% significance level were used in the regression analysis for Vickers micro hardness (HV), Rockwell hardness (RHN), and electrical conductivity (%IACS). The relevance of numerous aspects, including the regression model, linear terms, 2-way interaction terms, and lack of fit, was determined by analysis. To determine whether or whether the results are statistically significant, one uses the P-value. Regression equations (2) through (4) were determined based on the analysis, and they are as follows for Vickers microhardness, Rockwell hardness, and electrical conductivity:

Regression Equation of;

$$HV = -663 + 2.467ST + 0.547TA - 0.002206ST*ST - 0.000477 TA*TA - 0.000675 ST*TA \quad (2)$$

Regression Equation of;

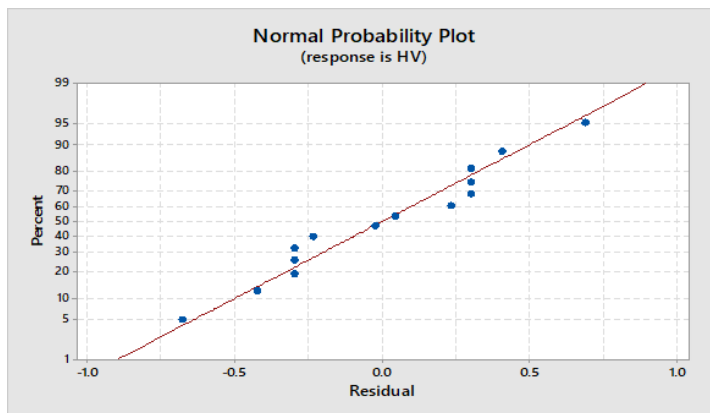
$$RHN = -1217 + 4.496 ST + 0.602 TA - 0.004270 ST*ST - 0.002011 TA*TA + 0.000234 ST*TA \quad (3)$$

Regression Equation of;

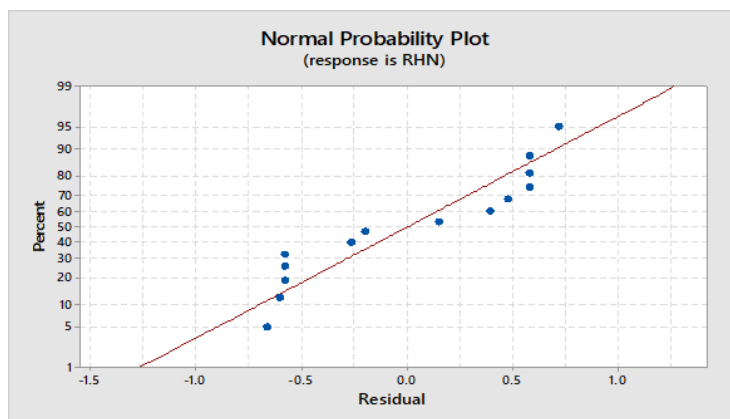
$$\%IACS = -670 + 2.524 ST + 0.550 TA - 0.002298 ST*ST - 0.000954 TA*TA - 0.000429 ST*TA \quad (4)$$

Where ST is Solution temperature at °C and TA is Thermal Aging at °C.

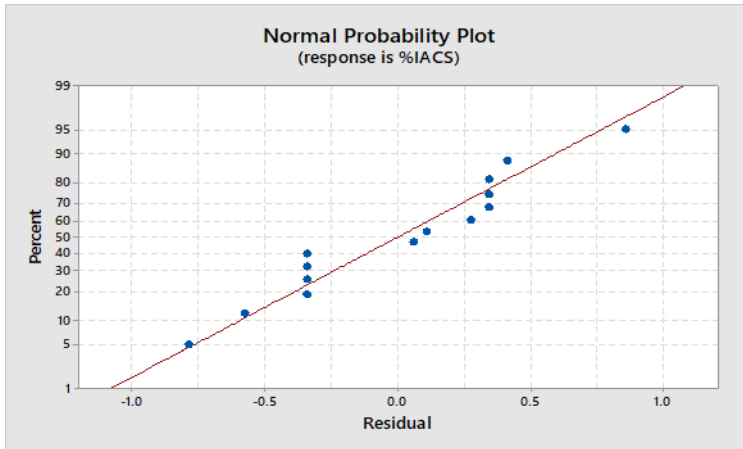
Vickers micro hardness, Rockwell hardness, and electrical conductivity of the manufactured Al MMC are all impacted by linear and two-way interactions. Eqs (2)–(4) shows that the HV, RHN, and %IACS are affected by positive sign parameters for increasing and negative sign parameters for decreasing, respectively. The normal probability plots for Vickers micro hardness, Rockwell hardness, and electrical conductivity are shown in Fig. 5 (a) through (c) respectively.



(a)



(b)



(c)

Fig. 5. Normal probability plot for (a) Vickers micro hardness; (b) Rockwell hardness; (c) Electrical Conductivity

4.3. Comparison between Experimental and Predicted Results

Mathematical modeling provided Equation (2)-(4) for predication of Vickers micro hardness (HV), Rockwell hardness number (RHN) and Electrical conductivity (%IACS) respectively for fabricated Al MMC. For each solution temperature (ST) and aging temperature (AT), Eqs (2)-(4) provides a predicated value of HV, RHN and %IACS respectively as shown in Table 4. We also calculated the Error percentage (%) of predicated HV, RHN and % IACS with respect to the experimental results as below. The negative (-) sign in Error % Calculation means that predicated results are found higher in some cases than the experimental results.

Table 4. Analysis of Experimental and Predicated Results with % of Error

Factor 1	Factor 2	Experimental Results			Predicted Results			Error (%) Calculation		
		HV	RHN	%IACS	HV	RHN	%IACS	HV	RHN	%IACS
ST (°C)	AT (°C)									
530.00	180.00	43.99	32.50	49.47	43.45	31.96	49.38	1.22%	1.65%	0.18%
501.72	180.00	42.08	30.04	48.53	41.49	28.21	47.23	1.41%	6.09%	2.69%
530.00	123.43	42.15	26.90	48.33	40.94	25.41	47.50	2.88%	5.53%	1.72%
530.00	236.57	43.83	27.25	45.70	42.92	25.65	45.15	2.08%	5.89%	1.21%
558.28	180.00	43.42	30.15	47.93	41.89	28.89	47.85	3.52%	4.19%	0.17%
530.00	180.00	43.99	32.50	49.47	43.45	31.96	49.38	1.22%	1.65%	0.18%
530.00	180.00	43.99	32.50	49.47	43.45	31.96	49.38	1.22%	1.65%	0.18%
530.00	180.00	43.99	32.50	49.47	43.45	31.96	49.38	1.22%	1.65%	0.18%
510.00	140.00	40.61	26.25	46.16	40.43	26.90	47.20	0.46%	-2.50%	-2.26%
550.00	220.00	41.95	27.25	45.99	42.11	27.55	45.97	-0.39%	-1.09%	0.05%
550.00	140.00	41.33	26.75	48.12	41.79	27.01	48.32	-1.11%	-0.96%	-0.43%
510.00	220.00	43.39	26.00	45.41	42.91	26.70	46.22	1.11%	-2.67%	-1.79%
530.00	180.00	43.99	32.50	49.47	43.45	31.96	49.38	1.22%	1.65%	0.18%
530.00	180.00	43.99	32.50	49.47	43.45	31.96	49.38	1.22%	1.65%	0.18%

5. Analysis of Response Optimization

It is possible to derive the Vickers micro hardness (HV), electrical conductivity (%IACS), Rockwell hardness (RHN), and optimality searches based on the proposed second-order response surface equations, i.e., Eqs (2)–(4). This is done in order to figure out the best electro-mechanical parameter combination and how it will affect the required response criterion [39]. Response surface methodology is the foundation of the optimality search model for the various process variable positions for optimizing the %ICAS, RHN, and HV values.

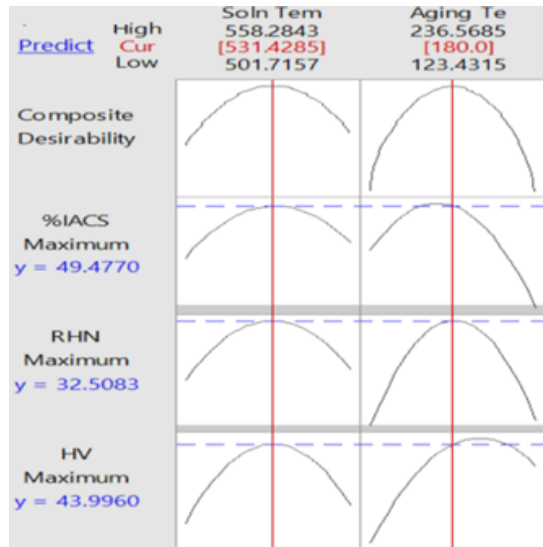


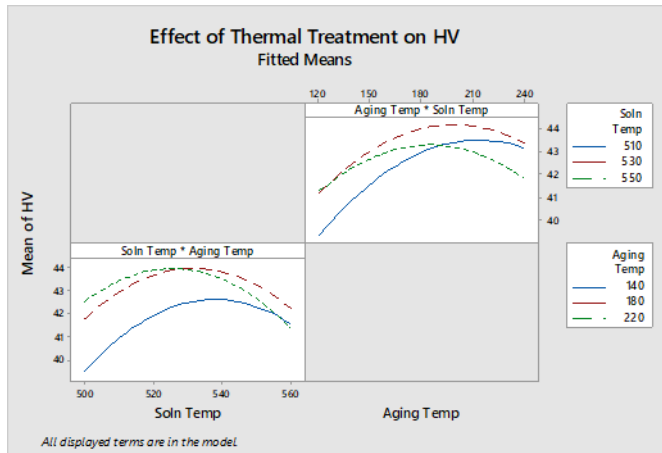
Fig. 6 Optimum Response results for maximum %IACS, RHN and HV

Fig. 6 shows that Solution Temperature of 531.428°C and Aging Temperature of 180°C as the most favorable values of Electrical Conductivity (%IACS), Rockwell hardness (RHN) and Vickers micro hardness (HV) which are 49.4770 % IACS, 32.5083 RHN and 43.9960 HV, respectively, through the optimized parametric combination.

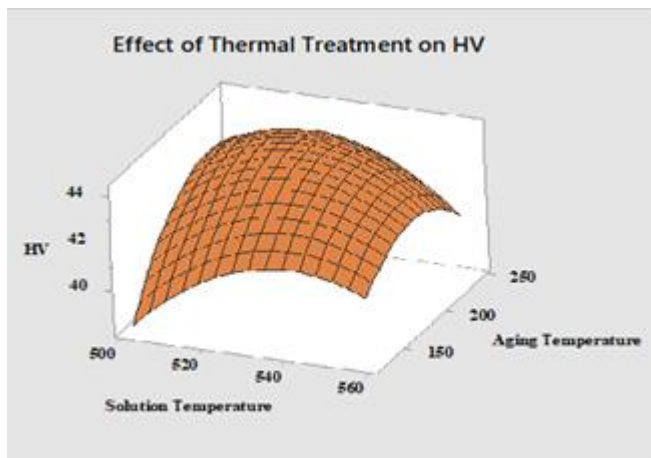
6. Results and Discussion

6.1 Effect of Heat Treatment on Vickers Micro hardness

As per the central composite (CC) design of RSM, a total 14 sets of heat treatments were carried out with different solution temperatures from 500°C to 560°C and aging temperatures from 120°C to 240°C for 1 hour for investigation of Vickers micro hardness. As per Fig. 7 (a) and Fig. 7 (b), the highest Vickers micro hardness of 43.99 HV was obtained for the solution temperature of 530°C and thermal aging at 180°C which is an improvement of 23.15% of HV in comparison to as-casted condition. Rajasekaran et al. (40) investigated T4 and T6 heat treatment effects on Al-15 Vol. % SiCP composite. As per their observation, the hardness profile of aging showed a sharp increase in hardness after the solution heat treatment at 558°C for 1 hour. In our current investigation, we also observed heat treatment at a solution temperature of 530°C and thermal aging at 180°C. We also observed that aging at higher temperatures, especially after 200°C led to softening of the alloy and the ductility also decreased. As a result, hardness also decreased with an increase in aging temperature which goes in line with the observation of Mahadevan et al. [41].



(a)

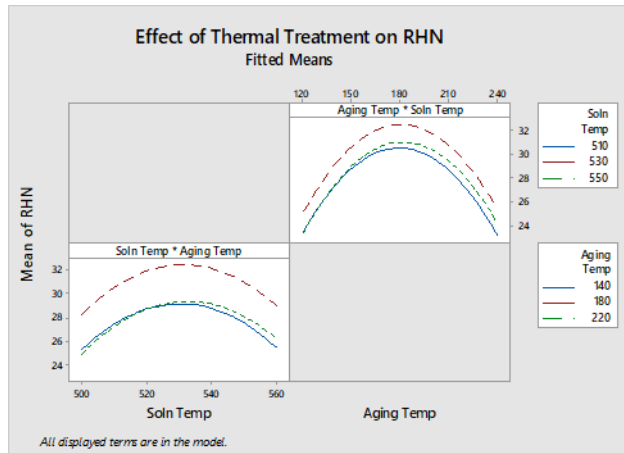


(b)

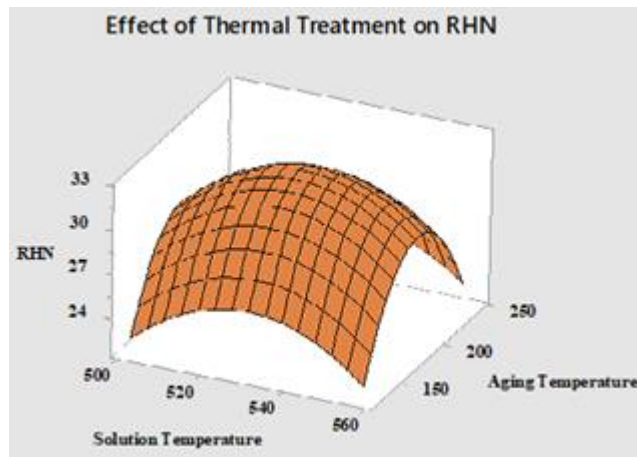
Fig.7 (a) Fitted means and (b) Surface plot for Vickers micro hardness of Al Composite

6.2 Effect of Heat Treatment on Rockwell hardness

As per the central composite (CC) design of RSM, a total of 14 set heat treatments were carried out with different solution temperatures from 500°C to 560°C and aging temperatures from 120°C to 240°C for 1 hour for investigation of Rockwell hardness. As per Fig. 8(a) and Fig. 8(b), the highest Rockwell hardness of 32.5 RHN was obtained for the solution temperature of 530°C and thermal aging at 180°C which is an improvement of 33.57% of RHN in comparison to the as-casted condition. Salleh et al. (42) studied the optimization of T6 heat treatment for aluminum alloy where they investigated the hardness values for different solution temperatures such as 510°C, 520°C, and 530°C and thermal aging temperatures such as 160°C, 170°C, and 180°C. As per their investigation, the highest hardness value was obtained for the solution temperature of 530°C and thermal aging temperature of 180°C. Therefore, our finding goes in line with the findings from Salleh et al. (42).



(a)



(b)

Fig.8 (a) Fitted means; (b) Surface plot for Rockwell hardness of Al Composite.

The results of this study indicate that heat treatment has a significant effect on the hardness of the aluminum composite. The hardness of the composite increases with an increase in the aging temperature, up to a certain point, and then decreases with a further increase in the aging temperature. This behavior can be explained by the precipitation of hardening phases during the aging process, which increases the strength and hardness of the composite up to a certain point. Beyond this point, over-aging can lead to the coarsening of these phases, which can decrease the hardness and strength of the composite. The results also show that the composite exhibits higher hardness values when subjected to a combination of solution treatment and aging compared to just aging. This can be attributed to the fact that the solution treatment allows for a more uniform distribution of the hardening phases, leading to an overall increase in the hardness of the composite. Farokhpour et al. (43) investigated the heat treatment effect of aluminum alloy at an aging temperature from 180°C to 230°C and observed the hardness and microstructure. As per their investigation, they observed the highest hardness values of an

aluminum alloy at an aging temperature of 180°C. Our findings and microstructure observation goes in line with Farokhpour et al. (43).

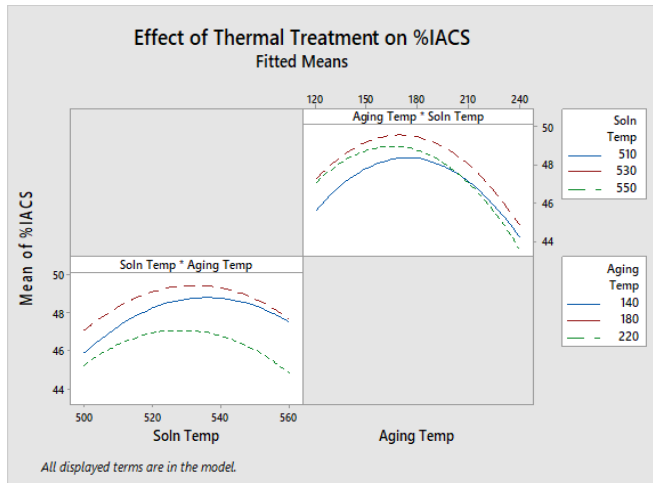
6.3 Effect of Heat Treatment on Electrical Conductivity

Heat treatment of aluminum composites affected the electrical conductivity due to changes in their microstructure. During the heat treatment process, the alloying elements in the Al composite form precipitate, which enhanced or hindered the flow of electrical current through the material as the temperature changed.

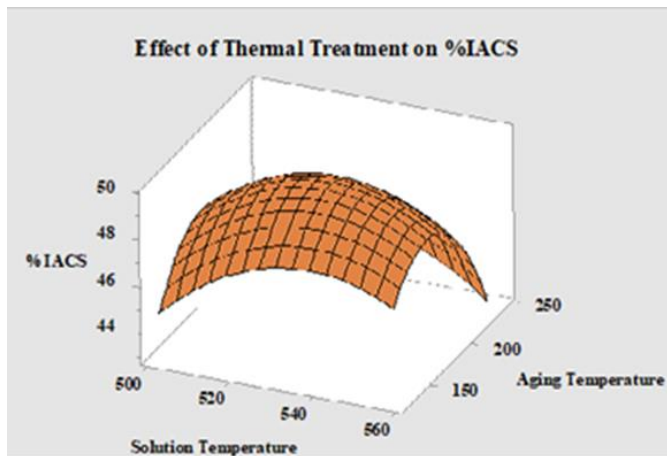
In particular, the formation of intermetallic compounds during heat treatment can negatively impact the electrical conductivity of the composite by hindering the movement of electrons. These compounds can act as barriers to the flow of current, reducing the number of conductive pathways in the material. Additionally, the coarsening of the precipitates during over-aging further decreases the electrical conductivity of the composite. This is because coarser precipitates can lead to a reduction in the number of conductive pathways, as the particles are further apart, and the composite becomes less conductive. On the other hand, heat treatment can also improve the electrical conductivity of aluminum composites by reducing the number of intermetallic compounds and increasing the number of conductive pathways through the material. This can be achieved by controlling the heat treatment process to ensure that the precipitates are uniformly distributed throughout the composite, leading to a more homogeneous microstructure and enhanced conductivity. By carefully selecting the heat treatment parameters, it is possible to optimize the electrical conductivity of aluminum composites for specific applications.

As per the central composite (CC) design of RSM, a total of 14 set heat treatments were carried out with different solution temperatures from 500°C to 560°C and aging temperatures from 120°C to 240°C for 1 hour for investigation of electrical conductivity. As per Fig.9(a) and Fig.9(b), the highest electrical conductivity of 49.47 %IACS was obtained for the solution temperature of 530°C and thermal aging at 180°C which is an improvement of 9.57% of electrical conductivity in comparison to the as-casted condition.

Diehl et al. (44) investigated that electrical conductivity increases significantly at various temperatures and constant times. They observed the removal of foreign atoms from the lattice of the parent alloy during precipitation hardening eliminates much distortion of electron disturbance in the lattice. Hence, these actions favor the movement of electrons through the metal and therefore result in higher conductivity. Pankade et al. (45) also investigated the influence of heat treatments on the electrical conductivity of AA 7075-T6 aluminum alloy where duplex aging at 163°C. The study reveals that duplex aging at 163°C shows better results for electrical conductivity. Debih et al. (46) investigated the influence of heat treatment on mechanical properties and electrical conductivity of AA6101 Aluminum alloy. In their experiment, they performed heat treatment of Al alloy in three categories namely natural aging, artificial aging and combination of natural aging. As per their investigation, they observed highest improvement of micro hardness (HV) and electrical conductivity (%IACS) at combination of natural aging at 20°C for 72 hours and artificial aging at 180°C for 6 hours. In our present research work, we performed combination of natural aging of 72 hours and artificial aging of a constant time of 1hr at different temperatures from 120°C to 240°C as per CC of RSM. Here we observed the progressive improvement of electrical conductivity up to an aging temperature of 180°C. Therefore, our current findings go in line with the results outcome of Diehl et al. (44), Pankade et al. (45) and Debih et al. (46).



(a)



(b)

Fig. 9 (a) Fitted means; (b) Surface plot for electrical conductivity of Al composite

7. Microstructure

Two test samples of Al composite with dimensions of 05mm x 05mm x 05mm were prepared for microstructure observation using a scanning electron microscope (SEM), model TESCAN VEGA 4. As we noticed improvements in the electromechanical properties of our Al composite at various solution temperatures, the microstructure of the first sample was observed respectively at a solution temperature of 510°C, and the second sample was observed at a solution temperature of 550°C. In order to better understand how different heat treatment settings affected the distribution of reinforcement particles in Al composite, which helped to increase electromechanical parameters including hardness and electrical conductivity, SEM microstructure observation was used. The heat treatment at solution temperatures from 501°C to 550°C for 01 hour resulted in a breakdown of the course of Al dendrites and Al₂O₃ particles.

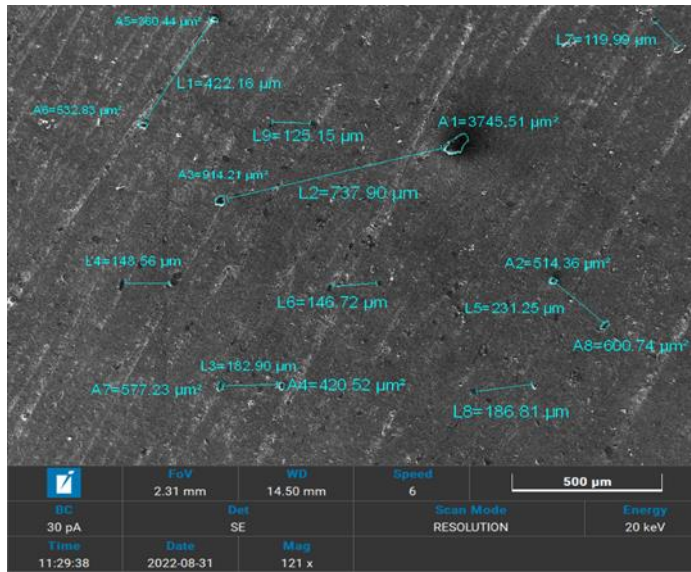


Fig.10 Microstructure observation of Al composite at solution temperature of 510°C.

As seen in Fig. 10, microstructure observation of an Al composite was done at a solution temperature of 510°C, with a FoV of 2.32 mm, WD of 14.5 mm, speed of 6 mm, 20 keV energy, 121 x magnification, and 500 μm. The shape of Al_2O_3 particles, as depicted in Fig. 10, is primarily amorphous or almost elliptical. The metal matrix contains Al_2O_3 particles that are evenly dispersed at a solution temperature of 510°C. SEM measurements are depicted in Fig.10 for the elliptical area submerged by some of the reinforcements (Al_2O_3) in the Al composite, labeled as A1 to A8. At a solution temperature of 510°C, the distances between some of the reinforcement particles in the metal matrix were also measured and designated as L1 to L9, as shown in Fig. 10.

As seen in Fig. 11, image processing is used to determine the distance and area that the reinforcement particles Al_2O_3 are submerged in the matrix after undergoing a 550°C solution treatment, respectively. Al_2O_3 reinforcement particles spread out in the matrix as a result of the heat treatment. We found that the measured distance between reinforcement Al_2O_3 particles in thermally treated conditions is greater than in cast conditions by comparing the microstructure images of the two situations. The electro-mechanical characteristics, such as hardness and electrical conductivity, displayed better conditions than when the reinforcement Al_2O_3 particles were cast, as a result of the solution and aging temperature effects on the matrix.

The use of proper process parameters during stir casting has helped in achieving the uniform distribution of reinforcement Al_2O_3 at base Aluminum with minor clustering. The fabrication of Al composites reinforced with SiC particles by a stir casting method, which was a low-cost way of MMC production, was carried out by Singla et al. (9) using a two-step mixing/stirring methodology. Their approach and testing with various SiC weight percentages on the assumption that all other factors would remain constant produced positive results for uniform matrix reinforcement dispersion, which effectively improved the strength and hardness of made-to-order Al composites. While we used a two-step stirring procedure to create our Al composite, we also see a similar uniform distribution of reinforcement particles in both Figs. 10 and 11. This discovery is consistent with Singla et al (9).

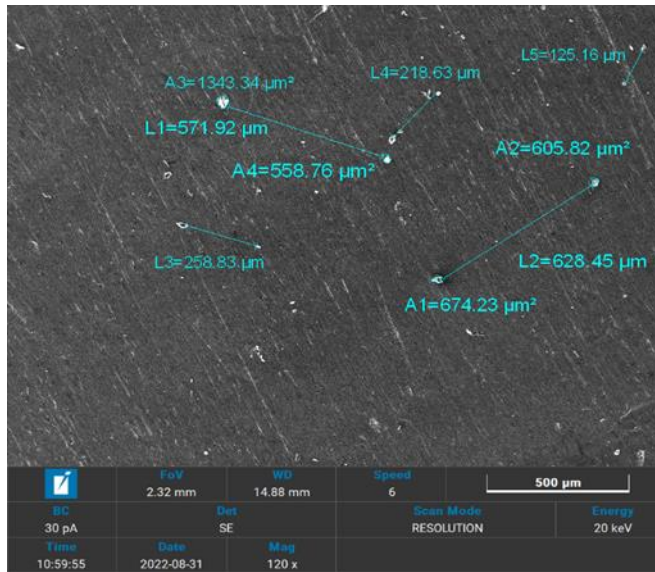


Fig.11 Microstructure observation of Al composite at solution temperature of 550°C.

It is also seen that higher solution temperatures create a uniform distribution of Al_2O_3 particles and dispersion of agglomeration in the Al matrix. Also, higher temperatures followed by rapid cooling (quenching) cause Al_2O_3 to diffuse more homogeneously across the interface. As per the analysis of microstructure, we can verify the changes in readings/test results through Hardness (Vickers and Micro & Rockwell) and Eddy Current Electrical Conductivity. The changes in electro-mechanical properties such as hardness and electrical conductivity have been revealed by microstructure with a clear distribution of reinforcement particles Al_2O_3 in Al composite for different heat treatment processes. The impact of heat treatment on the microstructure characteristics of Al 6063 alloy was examined by Azeez et al. (47). Taking into account the size and dimensions of the sample specimen, they used a heat treatment furnace to execute heat treatment at 450°C and soaked it for an hour. They then quickly quenched the water. Their composites' morphology showed that the Al 6063 alloy used for heat treatment had reinforcing particles distributed evenly and uniformly throughout. In this investigation, we also used SEM to observe the microstructure under the following conditions: (a) at a solution temperature of 510°C, and (b) at a solution temperature of 550°C. Moreover, we saw a reasonably homogeneous distribution of reinforcement particles in both the heat-treated and as-cast conditions, which is consistent with Azeez et al. (47).

8. Conclusion

In the current study, an Al MMC has been developed using a two-step stir casting method, and its properties were investigated in a series of experiments as well as predicted using customized models. The following is the summary of the current work:

- Three non-linear mathematical models have been developed through Central Composite design based on response surface methodology (RSM) for prediction of Hardness such as Vickers micro & Rockwell hardness and Electrical conductivity of manufactured Al MMC where R^2 obtained for HV, RHN and % IACS are respectively 89.29%, 96.23% and 91.50%.
- The most favorable values of HV, RHN, and %IACS achieved respectively as 43.99 HV, 32.5 RHN, and 49.47% IACS through the optimized parametric combination

of solution temperature of 531.428°C and aging temperature of 180°C. The optimized parameters of heat treatments contributed to the improvement of 23.15%, 33.57% and 9.57% respectively for Vickers micro, Rockwell hardness, and Electrical conductivity in comparison to as casted condition.

- As per the regression equation, the lowest and highest error (%) calculated between the experimental and prediction of HV are respectively 0.39% and 3.52%. For Rockwell hardness, the lowest and highest error (%) calculated between the experimental and prediction of RHN are respectively 0.96% and 6.09%. For Electrical conductivity, the lowest and highest error (%) calculated between the experimental and prediction of %IACS are respectively 0.05% and 2.69%.
- The microstructure reveals an almost uniform distribution of nano Al₂O₃ in Al composite with fewer agglomeration. The use of proper process parameters during stir casting has helped in achieving the uniform distribution of reinforcement Al₂O₃ at base Aluminum with minor clustering. It also revealed the formation of intermetallic compounds at different heat treatment processes which impacted the changes in the electro-mechanical properties of fabricated Al composite.
- As a whole the developed mathematical models can be considered useful for predicting purposes of thermal treatment effects of Al MMCs.

Acknowledgments

The authors are grateful to BITAC, BUET and MIST for utilizing their laboratory/test facilities. This research work was supported by a Research grant from the Military Institute of Science and Technology (MIST).

References

- [1] Swamy PK, Mylraiah S, Gowdru Chandrashekarappa MP, Lakshmikanthan A, Pimenov DY, Giasin K, Krishna M. Corrosion Behaviour of High-Strength Al 7005 Alloy and Its Composites Reinforced with Industrial Waste-Based Fly Ash and Glass Fibre: Comparison of Stir Cast and Extrusion Conditions. *Materials*. 2021;14(14):3929. <https://doi.org/10.3390/ma14143929>
- [2] Naik MH, Manjunath L, Koti V, Lakshmikanthan A, Koppad PG, Kumaran SP. Al/Graphene/CNT hybrid composites: Hardness and sliding wear studies. *FME Trans*. 2021;49:414-421. <https://doi.org/10.5937/fme2102414N>
- [3] Gebre Fenta Aynalem. Processing Methods and Mechanical Properties of Aluminum Matrix Composites. *Advances in Materials Science and Engineering*. 2020;2020:3765791. <https://doi.org/10.1155/2020/3765791>
- [4] Kumar KV, Jayahari L. Study of mechanical properties and wear behaviour of aluminum 6063 matrix composites reinforced with steel machining chips. *Materials Today: Proceedings*. 2018;5(9):20285-20291. <https://doi.org/10.1016/j.matpr.2018.06.400>
- [5] Singh J, Jawalkar CS, Belokar RM. Analysis of mechanical properties of AMC fabricated by vacuum stir casting process. *Silicon*. 2020;12(10):1-7. <https://doi.org/10.1007/s12633-019-0078-3>
- [6] Sable AD, Deshmukh SD. Preparation of MMCs By Stir Casting Method. *International Journal of Mechanical Engineering and Technology*. 2012;3(3):299-305.
- [7] Reddy BR, Srinivas C. Fabrication and characterization of silicon carbide and fly ash reinforced aluminum-metal matrix hybrid composites. *Materials Today: Proceedings*. 2018;5(2):8374-8381. <https://doi.org/10.1016/j.matpr.2017.11.531>
- [8] Gopalakrishnan S, Murugan N. Production and wear characterisation of AA 6061 matrix titanium carbide particulate reinforced composite by enhanced stir casting method.

- Composites Part B: Engineering. 2012;43(2):302-308. <https://doi.org/10.1016/j.compositesb.2011.08.049>
- [9] Singla M, Dwivedi DD, Singh L, Chawla V. Development of aluminum based silicon carbide particulate metal matrix composite. Journal of Minerals and Materials Characterization and Engineering. 2009;8(6):455-467. <https://doi.org/10.4236/jmmce.2009.86040>
- [10] Dehghan Hamedan A, Shahmiri M. Production of A356-1wt% SiC nanocomposite by the modified stir casting method. Materials Science and Engineering A. 2012;556:921-926. <https://doi.org/10.1016/j.msea.2012.07.093>
- [11] Hassen SB, Aponbide O, Aigbodion VS. Precipitation hardening characteristics of Al-Si-Fe/SiC particulate composites. Journal of Alloy Compounds. 2008;466:268-272. <https://doi.org/10.1016/j.jallcom.2007.11.023>
- [12] Soboyejo W. Mechanical Properties of Engineered Materials. New York: Marcel Dekker, Inc.; 2003. <https://doi.org/10.1201/9780203910399>
- [13] Miracle DB. Metal Matrix Composites: From Science to Technological Significance. Composites Science and Technology. 2005;65(15):256-262. <https://doi.org/10.1016/j.compscitech.2005.05.027>
- [14] Aqida SN, Ghazali MI, Hashim J. The effects of stirring speed and reinforcement particles on porosity formation in cast MMC. Jurnal Mekanikal. 2003;(16):22-30. ISSN 0127-3396.
- [15] Mathur S, Barnawal A. Effect of Process Parameter of Stir Casting on Metal Matrix Composites. International Journal of Science and Research (IJSR). 2013;2(12):1-6. ISSN 2319-7064.
- [16] Kumar R, Parshuram M. Preparation of Aluminum Matrix Composite by Using Stir Casting Method. IJEAT. 2013;3:570-575.
- [17] Sozhamannan GG, Prabu SB, Venkatagalapathy VSK. Effect of Processing Parameters on Metal Matrix Composites: Stir Casting Process. Journal of Surface Engineered Materials and Advanced Technology. 2012;2:11-15. <https://doi.org/10.4236/jseamat.2012.21002>
- [18] Seo YH, Kang CG. The effect of applied pressure on particle-dispersion characteristics and mechanical properties in melt-stirring squeeze-cast SiCp/ Al composites. J Mater Process Technol. 1995;55:370-379. [https://doi.org/10.1016/0924-0136\(95\)02033-0](https://doi.org/10.1016/0924-0136(95)02033-0)
- [19] Kumar A, Singh RC, Chaudhary R. Recent progress in production of metal matrix composites by stir casting process: An overview. Materials Today: Proceedings. 2019;16:2441-2450.
- [20] Dao V, Zhao S, Lin W, Zhang C. Effect of process parameters on microstructure and mechanical properties in AlSi9Mg connecting-rod fabricated by semi-solid squeeze casting. Mater Sci Eng A. 2012;558:95-102. <https://doi.org/10.1016/j.msea.2012.07.084>
- [21] Saravanakumar P, Soundararajan R, Deepavasanth PS, Parthasarathi N. A review on effect of reinforcement and squeeze casting process parameters on mechanical properties of aluminium matrix composites. Int J Innov Res Sci Eng Technol. 2016;5:58-63.
- [22] Das DK, Mishra PC, Singh S, Pattanaik S. Fabrication and heat treatment of ceramic-reinforced aluminium matrix composites - a review. Int J Mech Mater Eng. 2014;9(6):1-14. <https://doi.org/10.1186/s40712-014-0006-7>
- [23] Sakthivelu S, Sethusundaram PP, Meignanamoorthy M, Ravichandran M. Synthesis of metal matrix composites through stir casting process-a review. Mechanics and Mechanical Engineering. 2018;22(1):351-363. <https://doi.org/10.2478/mme-2018-0029>
- [24] Surappa MK. Aluminium matrix composites: Challenges and opportunities. Sadhana. 2003;28(1-2):319-334. <https://doi.org/10.1007/BF02717141>

- [25] Bhoi NK, Singh H, Pratap S. Developments in the aluminum metal matrix composites reinforced by micro/nano particles - A review. *Journal of Composite Materials*. 2020;54(6-7):857-878. <https://doi.org/10.1177/0021998319865307>
- [26] Saravanan C, Subramanian K, Ananda Krishnan V, Sankara Narayanan R. Effect of particulate reinforced aluminium metal matrix composite -A review. *Mechanics and Mechanical Engineering*. 2015;19(1):23-30.
- [27] Yuan Z, Li F, Zhang P, Chen B, Xue F. Mechanical properties study of particles reinforced aluminum matrix composites by micro-indentation experiments. *Chinese Journal of Aeronautics*. 2014;27(2):397-406. <https://doi.org/10.1016/j.cja.2014.02.010>
- [28] [Kok M. Production and mechanical properties of Al₂O₃ particle-reinforced 2024 aluminium alloy composites. *J. Mater. Process. Technol.* 2005;161:381-387. <https://doi.org/10.1016/j.jmatprotec.2004.07.068>
- [29] Pilania G, Thijsse BJ, Hoagland RG, Laziä I, Valone SM, Liu XY. Revisiting the Al/Al₂O₃ interface: coherent interfaces and misfit accommodation. *Sci. Rep.* 2014;4:1-9. <https://doi.org/10.1038/srep04485>
- [30] 30Aybarç U, Ertugrul O, Seydibeyoğlu M. Effect of Al₂O₃ Particle Size on Mechanical Properties of Ultrasonic-Assisted Stir-Casted Al A356 Matrix Composites. *International Journal of Metal casting*. 2020;14:609-619. <https://doi.org/10.1007/s40962-020-00490-7>
- [31] ASM Handbook. Aluminum and Aluminum Alloy Specialty Handbook. ASM International: Materials Park, OH, USA, 2002.
- [32] Manda CS, Surendra Babu B, Ramaniah N. Effect of Heat Treatment on Mechanical properties of Aluminium metal matrix composite (AA6061/MoS₂). *Advances in Materials and Processing Technologies*. 2022;8(sup1):205-222. <https://doi.org/10.1080/2374068X.2020.1860593>
- [33] Tiwari SK, Soni S, Rana RS, Singh A. Effect of Heat Treatment on Mechanical Properties of Aluminium alloy-Fly ash Metal Matrix Composite. *Materials Today: Proceedings*. 2017;4(2):3458-3465. <https://doi.org/10.1016/j.matpr.2017.02.235>
- [34] Myers RH, Montgomery DC, Anderson-Cook CM. *Response Surface Methodology*. 3rd ed. Hoboken, NJ: Wiley; 2009.
- [35] Mukherjee I, Ray PK. A review of optimization techniques in metal cutting processes. *Comput Ind Eng*. 2006;50(1-2):15-34. <https://doi.org/10.1016/j.cie.2005.10.001>
- [36] Patel MGC, Krishna P, Parappagoudar MB. Modelling of squeeze casting process using design of experiments and response surface methodology. *Int J Cast Met Res*. 2015;28(3):167-180. <https://doi.org/10.1179/1743133614Y.0000000144>
- [37] Wang H, Li GY. Optimization of draw bead design in sheet metal forming based on intelligent sampling by using response surface methodology. *J Mater Process Technol*. 2008;206(1-3):45-55. <https://doi.org/10.1016/j.jmatprotec.2007.12.002>
- [38] Md Jalal Uddin Rumi, Muhammad Muzibur Rahman, Effect of Heat Treatment on Hardness and Electrical Conductivity of nano Al₂O₃ reinforced Al MMC, *Metal Science and Heat Treatment*, Springer 2023 (in Press).
- [39] Llorca J. Fatigue of particle and whisker reinforced metal matrix composites. *Programme Material Science*. 2002;47:283-353. [https://doi.org/10.1016/S0079-6425\(00\)00006-2](https://doi.org/10.1016/S0079-6425(00)00006-2)
- [40] Rajasekaran S, Udayashankar NK, Nayak J. T4 and T6 Treatment of 6061 Al-15 Vol.%SiCP Composite. *ISRN Mater Sci*. 2012;2012:374719. doi:10.5402/2012/374719 <https://doi.org/10.5402/2012/374719>
- [41] Mahadevan K, Raghukandan K, Pai BC, Pillai UTS. Influence of precipitation hardening parameters on the fatigue strength of AA 6061-SiCp composites. *J Mater Process Technol*. 2008;198:277-281. <https://doi.org/10.1016/j.jmatprotec.2007.06.075>

- [42] Salleh MS, Hashim H, Omar MZ, Sulong AB, Rahman SA, Yahaya SH, Rashid MWA, Zubaidi SA. T6 Heat Treatment Optimization of Thixoformed LM4 Aluminium Alloy using Response Surface Methodology. *Malays J Compos Sci Manuf.* 2020;3(1):1-13. <https://doi.org/10.37934/mjcs.3.1.113>
- [43] Farokhpour M, Aghareb Parast MS, Azadi M. Evaluation of Hardness and Microstructural Features in the Piston Aluminum-Silicon Alloys after Different Heat Treatments. *SSRN Electronic Journal.* 2022;10.2139/ssrn.4112917. <https://doi.org/10.2139/ssrn.4112917>
- [44] Diehl D, Köhler C, Schneider EL, Gabriel T, Clarke R. Eddy Current at High Temperatures for In-Situ Control of Heat Treatment Precipitation in Hardening Aluminum Alloys. *IEEE Sens J.* 2020;20(17):9699-9705. <https://doi.org/10.1109/JSEN.2020.3008629>
- [45] Pankade SB, Khedekar DS, Gogte CL. The Influence of Heat Treatments on Electrical Conductivity and Corrosion Performance of AA 7075-T6 Aluminium Alloy. *Procedia Manuf.* 2018;20:53-58. <https://doi.org/10.1016/j.promfg.2018.02.007>
- [46] Debih A. Influence of heat treatment on mechanical properties and electrical conductivity of AA6101 Aluminum alloy. 2023.
- [47] Azeez TM, Lateef M, Adeleke A, Ikubanni P, Olayinka A, Adesina OS. Effect of Heat Treatment on Micro Hardness and Microstructural Properties of Al 6063 Alloy Reinforced with Silver Nanoparticles (AgNps). *IOP Conf Ser Mater Sci Eng.* 2021;1107(1):012013. <https://doi.org/10.1088/1757-899X/1107/1/012013>



Research Article

Influence of MWCNTs on mechanical and in vitro biocompatibility properties of PMMA bone cement for orthopedic application

T V Vineeth Kumar^{1,a}, N Shanmugapriya^{2,b}, Arun S^{3,c}, Madeva Nagaral^{4,d}

^{1,2}Department of Mechanical Engineering, Siddaganga Institute of Technology (Autonomous Institution Affiliated to Visvesvaraya Technological University, Belagavi), Tumakuru 572 103, Karnataka, India

³Advanced Composites Division, CSIR - National Aerospace Laboratories, Bengaluru 560 017, Karnataka, India

⁴Aircraft Research and Design Centre, Hindustan Aeronautics Limited, Bengaluru 56003, Karnataka, India

Article Info

Abstract

Article history:

Received 14 Jan 2023

Accepted 02 May 2023

Keywords:

Bone Cement;

Carbon Nanotubes;

Compressive Strength;

Hardness;

Orthopedics;

Biocompatibility

Polymethyl methacrylate (PMMA) serves as sealing material in securing the implant and distributing the load between the implant and bone. Fast polymerization and speedy patient recovery after surgery are the main benefits of using PMMA bone cement. Considering PMMA for orthopedic applications, the mechanical properties and biocompatibility studies are important. In this study, Simplex P bone cement is reinforced with carboxyl functionalized multiwall carbon nanotubes (MWCNTs-COOH) to evaluate compressive strength, Shore D hardness, and in vitro biocompatibility properties. MWCNTs are added to the PMMA powder in different amounts using a geometric dilution technique. The PMMA/MWCNT nanocomposite is prepared with MWCNTs varying from 0.1 wt. % to 0.7 wt. %. The compressive strength and Shore D hardness values increased to a maximum of 69.21% and 4.84%, respectively for 0.3 wt. % loading. The in vitro cytotoxicity studies on MG-63 cells show a percentage cell viability of 81.37 % for 0.3 wt. % and 83.25 % for 0.7 wt. % MWCNTs loading. Hemolysis studies on human B+ve blood exhibited a low hemolytic potential of 15.12% for 0.3 wt. % and 16.38% for 0.7 wt. % MWCNTs loading on human RBCs. It is concluded that the prepared PMMA/MWCNT nanocomposites are found to have enhanced mechanical properties compared to Simplex P bone cement.

© 2023 MIM Research Group. All rights reserved.

1. Introduction

Bone cement, also known as polymethyl methacrylate, is a widely used biomaterial in orthopedic surgeries [1]. It is a thermosetting material that is used to fix artificial joint implants to the bone, as well as to fill voids or defects in bones caused by fractures or disease. The bone cement is injected into the bone in a viscous state, and then hardens and sets within a few minutes, creating a stable and durable bond between the implant and the bone. PMMA bone cement is often used in joint replacement surgery, where the cement mantle acts as an interface in transferring loads between the implant and bone [2]. PMMA bone cement offers several advantages in the preparation of the cement mantle and its application. One of the main advantages is its ability to provide immediate fixation and stability to the implant or bone [3]. This allows for early weight-bearing and faster rehabilitation for the patient. However, there are a few disadvantages, such as impaired mechanical properties due to pore entrapment, and monomers that can cause toxicity or adverse effects. The poor abrasion resistance can make bone cement susceptible to wear and lose its original shape or surface finish, leading to implant loosening and failure [4].

*Corresponding author: madeva.nagaral@gmail.com

^a orcid.org/0000-0002-0814-8531; ^b orcid.org/0000-0002-4028-3813; ^c orcid.org/0000-0001-5266-7542;

^d orcid.org/0000-0002-8248-7603

DOI: <http://dx.doi.org/10.17515/resm2023.639me0114>

Res. Eng. Struct. Mat. Vol. 9 Iss. 3 (2023) 827-842

The development of novel bone cement has undergone significant improvements over the years in terms of its composition and properties. The researchers have added different fillers like graphene, hydroxyapatite, glass-ceramic, silver nanoparticles and chitosan to augment the mechanical properties and biocompatibility of PMMA bone cement [5][6][7][8][9]. Nanomaterials have gained special importance and extensively investigated as fillers due to their unique properties [10]. Nanoparticles are typically less than 1000 nm in size and have a high reactivity and substantial surface area-to-mass ratio, distinguishing themselves from bulk materials of the same composition [11]. Among the nanomaterials, carbon nanotubes possess superior mechanical and thermal properties [12]. Carbon nanotubes are cylindrical structures formed by folding single or several sheets of graphene and are characterized by a zigzag, chiral, or armchair configurations based on the direction of hexagons [13]. Multi-walled carbon nanotubes (MWCNTs) were incorporated into PMMA bone cement at a low weight percentage and resulted in notable improvements in the mechanical properties as well as cytotoxicity [14][15]. The MWCNT's performance mainly depends on the homogeneous dispersion in the matrix material. The MWCNTs dispersion within the bone cement microstructure was mainly decided by the method used to integrate into the bone cement [16]. Three different methods have primarily been described for the preparation of composite bone cement. In the first, an ultrasonic disintegrator was used to incorporate MWCNTs into liquid monomers by dispersion. In the second method, high-temperature mechanical shear mixing or Rheomix was used to blend MWCNTs with commercial bone cement powder. In the third method, MWCNTs were incorporated into the methylmethacrylate (MMA) component using a magnetic stirrer. Ormsby et al. (2010) [17] evaluated the mechanical properties of 0.1 wt. % loaded both functionalized and unfunctionalized MWCNTs. The compressive strength of PMMA bone cement was reduced by 13% when 0.1 wt. % functionally loaded MWCNTs were added using the magnetic-stirring method. However, the same was increased by 4% and 13% in the dry blending and sonication synthesis process, respectively.

The literature review indicates that MWCNTs were used to enhance the properties of bone cement. However, the incorporation of MWCNTs into PMMA bone cement may present some challenges, including:

- Dispersion - Achieving a uniform and stable dispersion of MWCNTs in PMMA bone cement is challenging due to the tendency of MWCNTs to agglomerate. Poor dispersion can lead to heterogeneous mechanical properties and may negatively affect the overall performance of the cement.
- Cytotoxicity - The use of MWCNTs in biomedical applications raises concerns about their potential cytotoxicity. While some studies have shown that MWCNTs can induce cell death and inflammation, others have suggested that MWCNTs may not be toxic at low concentrations. Further research is needed to fully understand the toxicity of MWCNTs in PMMA bone cement.

Mechanical properties - The addition of MWCNTs to PMMA bone cement can alter its mechanical properties, such as strength and stiffness. Achieving the desired balance between the mechanical properties of the cement and the MWCNT content can be challenging.

In this study, the geometric dilution method was used to distribute MWCNTs in the powder medium. The geometric dilution method is expected to achieve uniform distribution of MWCNTs into MMA powder without causing any damage to the walls of nanotubes. However, the lower weight percentage of MWCNTs was selected to minimize the possibility of agglomeration [18]. The mechanical properties and in vitro biocompatibility of the nanocomposite bone cement were evaluated and compared with the commercial Simplex P bone cement. X-ray diffraction analysis (XRD), Scanning electron microscopy (SEM), and Differential scanning calorimetry (DSC) are used for material characterization.

2. Materials and Methods

The two-part acrylic-based Surgical Simplex® P radiopaque bone cement consisting of liquid and powder components is purchased from Stryker Howmedica Osteonics in the Republic of Ireland. The monomer used in this solution is methyl methacrylate, and N, N-Dimethyl-p-Toluidine is employed as an activator, while a small amount of hydroquinone is included in the solution to prevent polymerization during storage. The powder component of the solution contains polymethyl methacrylate polymer units, benzoyl peroxide - polymerization initiator, and either barium sulfate or zirconium dioxide, which are radiopaque substances that facilitate X-ray imaging. In the composite composition, carboxyl functionalized MWCNTs of 10-15 nm outer diameter and 2-10 µm length are used as nanofillers, which are purchased from Platonic Nanotech Pvt. Ltd. in Kachwa Chowk, Mahagama, Jharkhand.

The weight proportions of the composite bone cement are shown in Table 1. The powder and liquid medium are mixed in a 2:1 proportion according to the manufacturer's guidelines. A geometrical dilution method with the measured size is employed by combining fine powders of an equal proportion of MWCNTs with MMA powder. This MMA/MWCNTs powder is then added to N, N-Dimethyl-p-Toluidine (liquid monomer solution) to initiate self-polymerization. The sticky, working, and hardening phases are involved in the mixing of the powder and liquid components. The resulting dough stage mixture is then transferred into polypropylene molds of diameter 6 mm and height 12 mm to form cylindrical specimens. After 24 hours of curing at room temperature, the cylindrical specimens are sectioned and polished using SiC paper with grits ranging from 220-2400.

Table 1. Composite identification and composition

Sl. No.	Sample identification	Material composition	MMA g	Liquid mL	MWCNT wt. %
1	C	PMMA (control)	10	5	-
2	C1	PMMA+0.1% MWCNT	9.99	5	0.1
3	C2	PMMA+0.3% MWCNT	9.97	5	0.3
4	C3	PMMA+0.5% MWCNT	9.95	5	0.5
5	C4	PMMA+0.7% MWCNT	9.93	5	0.7

2.1. Mechanical Tests

The hardness of the composites is measured using a Yuzuki Shore D Durometer with a 5% tolerance (ASTM D2240-05). The samples are loaded against an indenter with a diameter of 1.15 to 1.40 mm and a height of 6.5 mm. Measurements are taken at room temperature using five samples of each composition, with dimensions of 10x40x3 mm.

Cylindrical nanocomposite samples of 6x12 mm are prepared and allowed to harden in PBS at pH 7.4. After drying for 24 hours, the samples are tested for compressive strength using the Tinius Olsen Universal Testing Machine (Model 50ST) at a crosshead speed of 5 mm/min following ASTM F-451-08 standard. The compressive strength is estimated using Equation 1.

$$\text{Compressive strength} = \frac{4F}{\pi d^2} \quad (1)$$

where, 'F' is the fracture load in Newton, and 'd' is the cylindrical specimen diameter in mm.

2.2. Characterization Techniques

The phase and crystalline nature of the nanocomposite samples are investigated using X-ray diffraction (XRD). Nanocomposite bone cement samples of 8x2 mm are prepared as described previously and hardened in PBS at pH 7.4. After 24 hours, the samples are subjected to XRD testing using an X-ray diffractometer (PAN Analytical). The measurements are taken at room temperature using Cu-K α source radiation with 1.541 Å^o wavelengths, 40 kV voltage, and 30 mA current. The XRD data are acquired at a scanning frequency of 0.50 min⁻¹ with a step size of 0.001^o over a Bragg angle range of 10-80^o.

The morphology of the specimens of composite bone cement reinforced with MWCNTs is examined by SEM (JEOL 6500, JSM, Japan) at working voltages of 5.0 kV and 4 Torr vacuum pressure. Energy dispersive spectroscopy is obtained to investigate the elemental composition of the composite bone cement. Samples of size 8x5 mm are prepared as previously noted and allowed to harden in PBS with a pH of 7.4. The samples are then dried for 24 hours, polished using SiC paper (220-2400 grits), sputter coated and analyzed.

The thermal endurance and glass transition temperature (T_g) of the bone cement are studied using DSC in a nitrogen gas atmosphere, with a heating rate of 100°C/minute from room temperature up to 700°C. The samples are allowed to harden in a pH 7.4 PBS solution and air-dried for 24 hours, then crushed and analyzed.

2.3. In Vitro Biocompatibility Tests

2.3.1 Cytotoxicity Evaluation

Cytotoxicity is the degree to which a substance can cause damage to a cell. In this work, cell growth and cytotoxicity are measured using a colorimetric test. The samples are tested for cytotoxicity on mitochondrial lactate dehydrogenase produced by MG-63-Human Osteosarcoma cell lines (NCCS, Pune). It turns MTT into insoluble formazan crystals that, when dissolved in the right solvent, show a purple color, the intensity of which is related to the number of live cells and is measured spectrophotometrically at 570 nm. Since the composite bone cement is meant to encourage osteointegration, MG-63 cells are chosen as a model of osteoblast cells. This cell line is frequently used to conduct preliminary in vitro research on the cytocompatibility of biomaterials for bone substitutes.

Maintenance of cell lines: The MG-63 cell line is purchased from NCCS, Pune, India. The cells are kept in Dulbecco's modified eagle medium, a high glucose medium supplemented with 10% fetal bovine serum and the 1% antibiotic-antimitotic solution at 37°C in a CO₂ incubator. The cells are subcultured every two days.

Cell viability: The MG-63 cell suspension (1000 µl) is seeded in a twelve well-plate at a density of 50,000 cells per well and allowed to grow for about 24 hours. The composite bone cement samples are sterilized beneath UV light for 30 min and washed with PBS for 2 mins to ensure sterility. After sterilization, the samples are carefully kept in each well of twelve well plates. Cells without any sample are considered untreated and cells treated with doxorubicin at 1 µM/ml concentration are considered positive controls for the study. The plates are kept in an environment of 5% CO₂ and incubated for 24 hours at 37°C. After incubation, the plates and used medium are removed. Finally, MTT reagent is added, and plates are incubated for 3 hours. Upon removing MTT, 100 µl of solubilization medium is added. The absorbance is read on a spectrophotometer at 570 nm wavelength. The % cell viability is calculated from Equation 2,

$$\% \text{ cell viability} = \left(\frac{\text{Mean abs of treated cells}}{\text{Mean abs of untreated cells}} \right) \times 100 \quad (2)$$

2.3.2 Hemolysis

A hemolysis assay is performed as per ASTM F756 to check whether the composite bone cement contains compounds that can induce the lysis of red blood cells (RBCs). To assess the lysis of hemoglobin spectrophotometrically, RBCs are separated from the blood sample and treated with the test chemicals. A positive control is one in which the detergent lyses the cells, whereas a negative control shows completely undamaged cells. A healthy individual donated about 5 mL of blood, which is then centrifuged at 1000 rpm for 10 minutes at 4°C to separate the RBCs from the new blood and keep the blood healthy (B+ve). After removing the supernatant (plasma), 1 ml of PBS is used to wash the collected erythrocytes. Diluted RBCs (500µL) are added to each well of 12 well-plate and sterilized bone cement samples are placed. The untreated, standard control of 1% sodium dodecyl sulfate (SDS) and blank controls are used for comparison. The RBCs are incubated for 24 hours at 37°C, and the reaction is centrifuged for 5 minutes at 300 rpm. Each reaction's supernatant is put on a 96-well ELISA plate, and the absorbance is checked at 590 nm. The proportion of hemolysis is calculated using Equation 3.

$$\text{Haemolysis} = \left(\text{Mean abs} \frac{\text{Sample}}{\text{Positive Control}} \right) \times 100 \tag{3}$$

2.3.3 Statistical analysis

Two sample t-test statistical analysis is used to determine whether the results for compressive strength and hardness tests. The mean standard deviation is used to represent the findings. The level of statistical significance is set at p<0.05.

3. Results and Discussion

3.1. Mechanical Tests

The Shore D hardness of the composite bone cement is depicted in Table 2. It is observed that the addition of MWCNTs enhanced the composites' Shore D hardness. The reason is that MWCNTs-COOH reinforcement helps in better interaction with the PMMA matrix and acts as a barrier for crack propagation [19]. Although MWCNTs increase the hardness of the PMMA, the trend is not proportional to the MWCNTs added. Hardness increased significantly (p=0.023) by 4.84% for 0.3 wt. % loading, but the increase is marginal for 0.5 and 0.7 wt. % of MWCNT concentrations. Greater hardness is seen in C2 samples of which had fewer voids and a more evenly dispersed matrix. The undissolved beads spotted in SEM images (Figure 7) may have caused the creation of voids and poor adherence of the MWCNTs to the PMMA in samples C3 and C4. Therefore, there is no substantial increase in the C3 and C4 sample's hardness.

Table 2. Percentage variation in Shore D hardness

Bone cement samples	Shore D hardness %↑
C1	3.03↑
C2	4.84↑
C3	3.63↑
C4	2.42↑

The compressive strength of the bone cement samples is depicted in Figure 1, it can be observed that with increasing MWCNTs up to 0.3 wt. % ($p=0.03$), compressive strength rose significantly. This is attributed to the nanotubes' high density of interfaces, and a tendency to resist crack propagation. The homogeneous distribution of MWCNTs in the PMMA matrix also helped in effective load transmission between the PMMA and MWCNT [20]. However, with a further increase of MWCNTs in C3 and C4 samples (0.5 and 0.7 wt %), due to the existence of undissolved PMMA beads and voids inside the PMMA matrix, the compressive strength reduced[21][22].

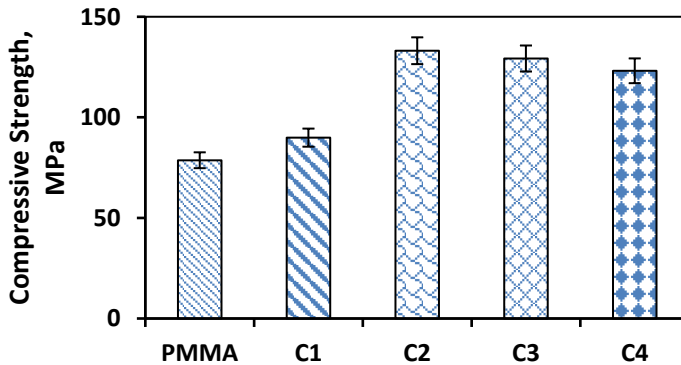


Fig. 1 Compressive strength of composite bone cement composition

The compressive strength of the C1, C2, C3, and C4 samples increased by 14.28%, 69.21%, 64.29%, and 56.27%, respectively, compared to PMMA bone cement. These findings are consistent with previous studies by Mu et al. (2018) [23] and Nien et al. (2010) [24], which also reported increased compressive strength due to the addition of MWCNTs.

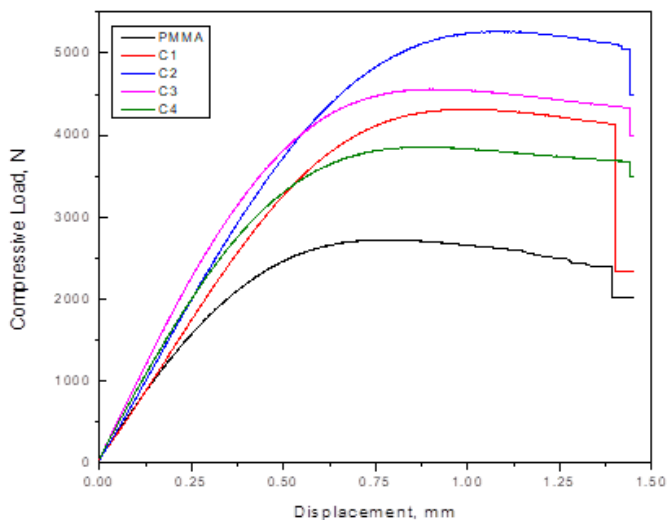


Fig. 2 Behavior of composite bone cement under compressive loading

The load versus compression plots obtained for test samples are shown in Figure 2. All the samples exhibited similar loading trends for a compressive load up to 25kN and are found to be elastic below 20kN. The resistance to the applied load is notably high up to 0.3 wt. % and beyond which it decreased gradually.

Figure 3 displays the compressive modulus of the bone cement composites. The highest modulus of elasticity, reaching 3854 MPa, is achieved at 0.3 wt.% MWCNT loading. The optimal value at 0.3 wt.% is attributed to the efficient stress transfer between the MWCNTs and PMMA, facilitated by a strong interfacial bonding [25]. However, the modulus decreases beyond this point, which is mainly attributed to agglomerations of MWCNTs.

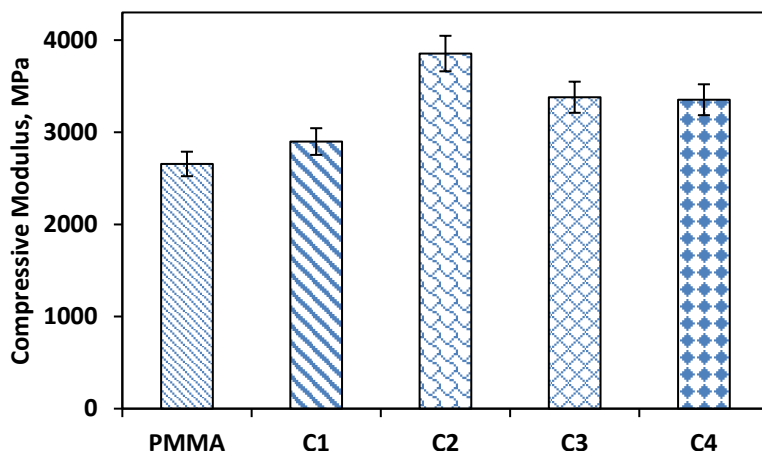


Fig. 3 Influence of MWCNTs on the compressive modulus of composite bone cement

3.2. Reasons for the Enhanced Mechanical Property

The plausible justifications for the increase in mechanical properties of composite bone cement up to 0.3 wt. % MWCNTs loadings are discussed in this section. The mechanical properties of PMMA/MWCNTs composites are improved due to MWCNT's intrinsic features. The modulus of elasticity of an individual CNT was reported to be up to 1TPa [26]. In this study, the modulus of elasticity and compressive strength of PMMA is experimentally determined as 2.66 GPa and 78.67 MPa, respectively. Hence, it is evident that the modulus of elasticity and strength of nanotubes is superior compared with PMMA bone cement. So, the addition of MWCNTs to PMMA is expected to improve the mechanical properties. The improvement in compressive strength for lower loadings of MWCNTs is due to MWCNTs' proclivity to withstand compression load and high-density interfaces (bonding between matrix and MWCNTs) of nanomaterial [27].

The effect of MWCNTs on the degradation temperature of PMMA is shown in Figure 4. The weight loss pattern is observed to be identical for the synthesized samples. However, the degradation temperature of PMMA is increased with the MWCNTs reinforcement, which acts as an impediment to PMMA degradation. The rise in degradation temperature observed from the derivative of the thermogravimetric curve (DTG) confirms the interfacial bonding of PMMA with MWCNTs [28].

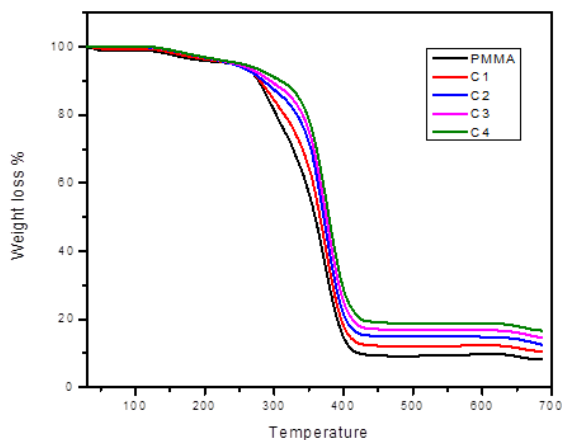


Fig. 4 TGA curves of PMMA/MWCNT composites

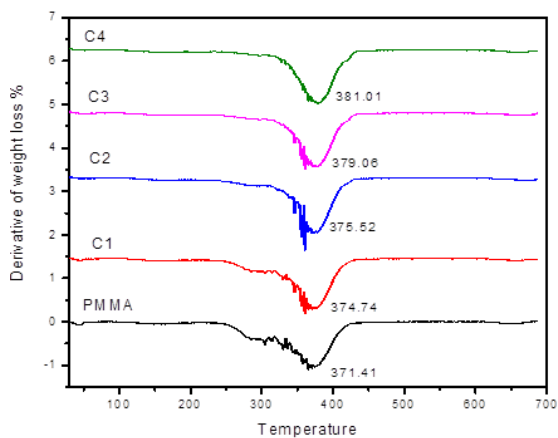


Fig. 5 Derivative of TGA curves of composite bone cement

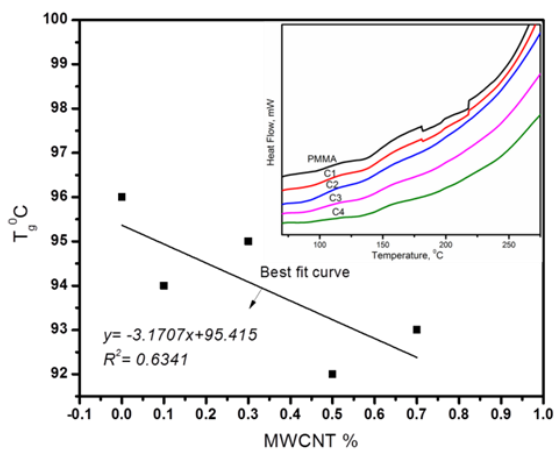


Fig. 6 Glass transition temperatures of composite bone cement

The DTG of PMMA/MWCNTs composites are illustrated in Figure 5. The DTG plot revealed that the addition of MWCNTs delayed the thermal degradation of PMMA and increased its thermal stability. The degradation temperature of PMMA is obtained as 371.41°C, which is increased by 0.89%, 1.1%, 2.1%, and 2.58% for C1, C2, C3, and C4 samples, respectively.

The behavior of T_g of PMMA/MWCNT composites with varying MWCNT concentrations is represented in Figure 6. The variations in T_g are observed to decrease prominently compared to PMMA with the increase in MWCNT concentration. However, among the PMMA/MWCNT composites, both increasing and decreasing trends are observed, which was also reported by Tomova et. al (2017) [29]. The T_g value is found to be maximum for PMMA and among the composites, it is maximum for 0.3 wt. % and minimum for 0.5 wt. % MWCNTs loading. The linear fitting of T_g revealed a high slope, indicating the considerable effect of MWCNTs on T_g due to the strong interfacial bonding among PMMA and MWCNTs [23]. The correlation between PMMA and MWCNTs is demonstrated by the elevated thermal stability and T_g of the composite, resulting in improved compressive strength and hardness. However, the decrease in T_g may be attributed to the plasticizing effect of MWCNTs on PMMA [24].

3.3. Reasons for Diminution of Mechanical Properties

This section outlines the most likely reasons for the reduction in mechanical properties of composite bone cement upon the addition of more than 0.3% MWCNTs, as evidenced by SEM images. The SEM images (300 nm scale) of PMMA/MWCNT composites are depicted in Figure 7.

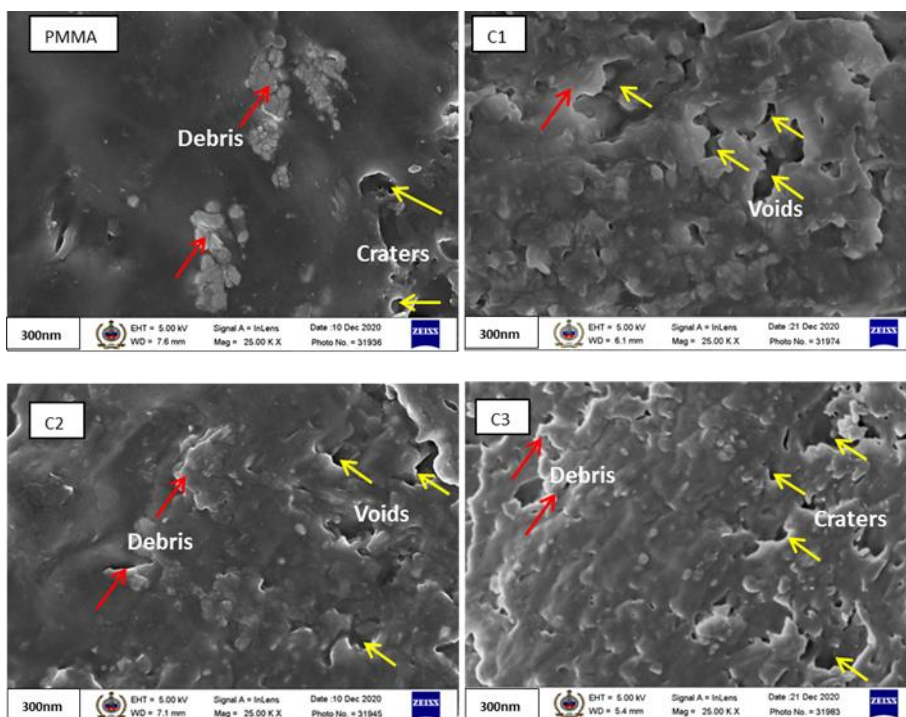


Fig. 7 SEM images of composite bone cement

The nodular-like particles and voids are observed on C1 and C2 samples. The nodular-like particles present in the images are likely to be Benzoyl peroxide and Zirconium dioxide,

which serve as initiator and radio-opacifier, respectively, in the MMA powder. When the MWCNTs loading exceeds 0.3 wt. %, there is an increase in voids, craters, and agglomerations observed in the SEM images (Figure 7-C3). Muthu et al. (2018) [30] attributed the agglomerations to the inherent van-der Waals forces among the individual Nanotubes. Incorporating more wt. % of MWCNTs into the PMMA matrix increased the composite's density, resulting in a higher viscosity. However, due to the higher viscosity of the PMMA matrix, it was unable to wet the surface area of the MWCNTs completely during composite preparation by hand mixing. Thus, the micro-voids and agglomeration of MWCNTs in the cement matrix are responsible for the drop in compressive strength beyond 0.3 wt. % loading [31][18].

The XRD pattern of PMMA/MWCNTs composites with 2θ ranges of $10\text{--}80^\circ$ is depicted in Figure 8. PMMA is an amorphous polymer with two large peaks found at 2θ values of 30.67° and 31.96° . The strong peak around 42° and the next prominent peaks around 30° and 26° are observed in all prepared samples. The presence of sharp and narrow peaks implies that the nanotubes served as nucleating agents, initiating the formation of new crystallites [32].

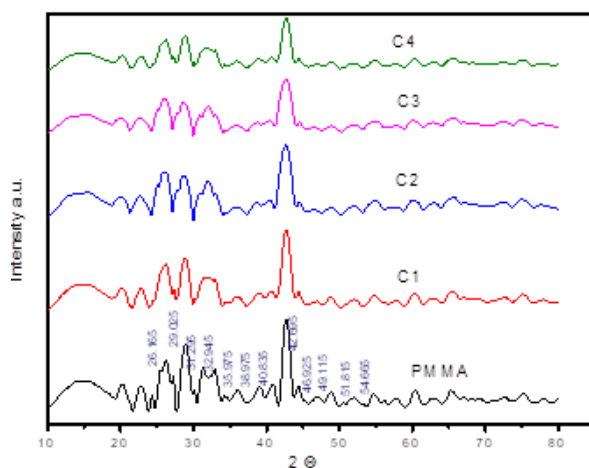


Fig. 8 XRD of PMMA composite bone cement

The composite's crystallinity is a factor that influences the mechanical properties of polymer composites. The presence of strong Bragg peaks in the XRD pattern is a direct indication of material's crystallinity. The area of crystalline peaks divided by the total area of all peaks yields the percentage crystallinity. The crystallinity measurement by XRD is due to the total coherent scattering as a constant independent of the arrangement of the atoms in the sample [33]. This study found that the crystallinity of PMMA is 46.83%. However, the crystallinity of composite bone cement reinforced with 0.1, 0.3, 0.5, and 0.7 wt. % MWCNTs is calculated to be 49.52%, 53.87%, 52.25%, and 50.50%, respectively. The interfacial bonding between MWCNTs and PMMA has resulted in maximum crystallinity of 52.25% at 0.3 wt. % loading.

3.3. In Vitro Biocompatibility Tests

3.3.1 Cytotoxicity Evaluation

The composite bone cement samples, C2 and C4 are subjected to cytotoxicity effect on MG-63 cells. Figure 9 illustrates the results of the cytotoxicity study, which is conducted using the MTT assay. The study found that the test samples are non-cytotoxic on MG-63 cells,

with a percentage cell viability of 81.37% and 83.25% after a treatment period of 72 hours. Doxorubicin is used as a standard control for the study, which showed effective cytotoxicity on MG-63 cells with 11.32% cell viability.

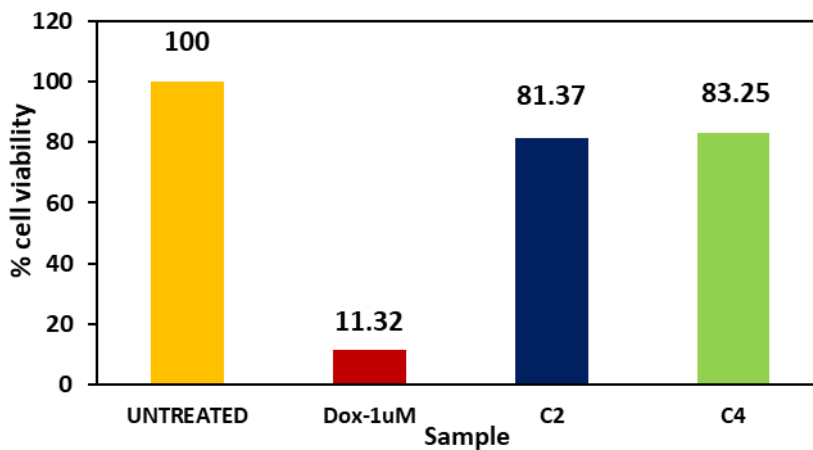


Fig. 9 Percentage of cell viability against MG-63 cells

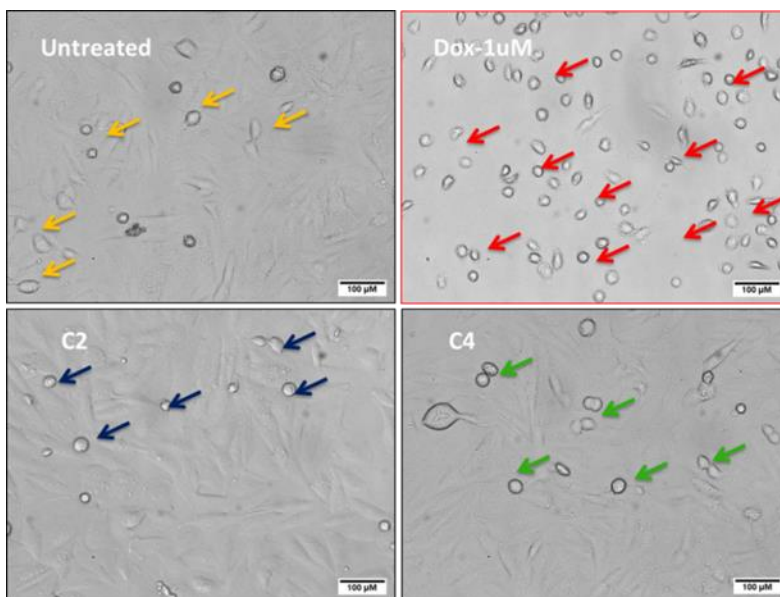


Fig. 10 Optical images of samples after cytotoxicity evaluation

The microscopic observations of cell-treated images of test samples after 72 hours of incubation are shown in Figure 10. The MTT assay results showed that the samples are non-cytotoxic on human bone cancer cells and further studies could be carried out to control the molecular mechanism.

3.3.2 Hemolysis

The composite bone cement samples, C2 and C4 are subjected to hemolysis test on a healthy human blood (B+ve). After a treatment period of 24 hours, the samples did not demonstrate significant hemolytic potential on human RBCs in comparison to 1% SDS, which exhibited effective hemolysis on human RBCs. Figure 11 displays the comparative percentage hemolysis potency of the samples C2 (15.12 %) and C4 (16.38%), along with the control, after an incubation period of 24 hours. The results indicate that the samples, C2 and C4, are non-toxic and safe for human health, without any adverse effects on normal human health.

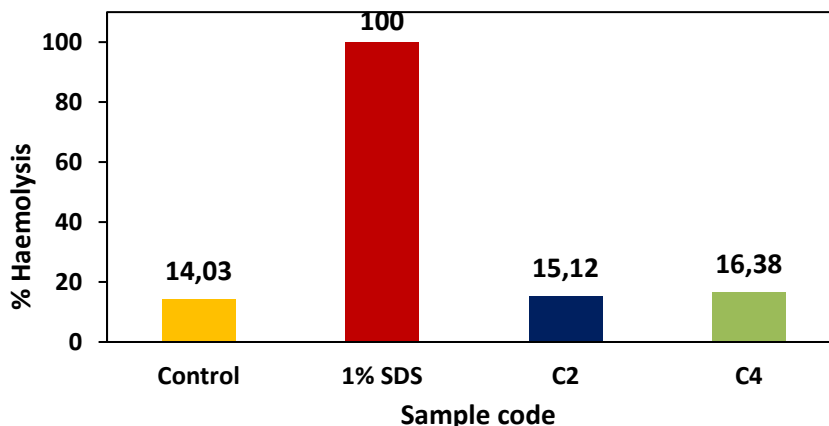


Fig. 11 Percentage Haemolysis of composite bone cement samples

3.4 Discussion

The two major purposes of bone cement are to quickly secure implants after surgery and to distribute implant stresses to the surrounding bone bed. When incorporating fillers to meet bone cement specifications, it is crucial to ensure that the fundamental properties of the cement are not significantly altered. In this work, the post-fabrication drying time of 24 ± 2 hours is followed for testing the static mechanical properties. It's interesting to note that, compared to commercial Simplex P cement, the compressive strength and Shore D hardness of the cement improved with the inclusion of MWCNTs.

The mechanical properties of bone cement play a critical role in serving as a linkage between the prosthesis and bone, as it is responsible for transmitting the load to the surrounding bone tissue. Compressive strength and hardness tests have revealed that this characteristic holds for all composite cement that is loaded with multi-walled carbon nanotubes (MWCNTs). The present study demonstrates a notable 69.21% increase in compressive strength upon the addition of 0.3 wt. % MWCNTs-COOH to the bone cement. In comparison, earlier research by Nien (2011) [18] observed a 23% increase in compressive strength for MWCNT-modified bone cement, while Ormsby et al. (2014) [34] reported a mere 2% increase in compressive strength for PMMA/MWCNT bone cement. Xu et al. (2013) [35] dispersed MWCNTs using ultrasonic disintegration and observed a 24.5% increase in compressive strength. Therefore, the increase in compressive strength exhibited by the composite bone cement developed in this study is significantly superior to the previous findings [18] [34] [35]. The incorporation of 0.3 wt. % MWCNTs-COOH into the bone cement results in a modulus of elasticity of 3.85 GPa. In contrast, cancellous bone has Young's modulus of 0.33 GPa, while metals commonly utilized for implants possess

Young's modulus values ranging from 110 GPa to 230 GPa [36]. Notably, the composite bone cement developed in this study exhibits a 44.7% increase in modulus of elasticity compared to conventional bone cement. This enhanced stiffness characteristic may aid in reducing the stress shielding effect (due to difference in stiffness) at the interface between the cement and bone [37]. The addition of 0.3 wt. % MWCNTs-COOH, the Shore D hardness of the bone cement increased by 4.84%. This improved hardness can enhance the wear resistance of the cement and enable the cement mantle to regain its original shape and surface finish without failure and causing implant loosening.

In this study, the MWCNTs are integrated into the bone cement matrix using a geometric dilution technique, which resulted in a relatively well-dispersed cement mixture at 0.3 wt. % optimum loading. However, there are certain acknowledged limitations in the present study. Firstly, only one type of cement (Simplex P) is employed, and the results may vary depending on the chemical composition and viscosity of other types of cement. Simplex P is chosen as it is one of the most commonly used bone cement formulations for total hip and knee replacements [38]. Secondly, although fatigue is a crucial factor in *in vivo* cement failure, the fatigue parameters of the MWCNT-loaded cement are not evaluated [39]. This is because testing for fatigue is beyond the scope of the current project. Lastly, the biocompatibility assessment only measured cell viability, while other relevant markers such as cell proliferation and lactate dehydrogenase are not examined. Future studies should explore dynamic mechanical properties and biocompatibility in greater detail.

4. Conclusions

This study builds upon previous research to enhance the mechanical properties and biocompatibility of Simplex P bone cement. Specifically, the geometric dilution method is utilized to incorporate MWCNT-COOH into the cement, avoiding the possible agglomerations without damaging MWCNTs. The influence of 0.1, 0.3, 0.5, and 0.7 wt. % MWCNTs on the MMA powder of Simplex P bone cement on mechanical properties and *in vitro* biocompatibility of the cured cement are examined. The results of this study indicate that the C2 samples exhibited the highest increase in compressive strength (69.21%) and compressive modulus (44.75%). The observed positive interaction between PMMA and MWCNTs at a concentration of 0.3 wt.% is likely due to the uniform distribution of MWCNTs in the PMMA matrix, which is also supported by the increased thermal stability of the resulting bone cement. The results of cytotoxicity (82.31% average cell viability) and hemolysis (15.75% average) tests confirm that the composite bone cement formulations prepared in this study are non-toxic and safe for use in therapeutic applications related to human bone treatment. The overall findings of this research propose that it is difficult to predict the performance of synthesized bone cement by *in vitro* characterization only. It is worthwhile to conduct *in vivo* biocompatibility studies of PMMA loaded with -COOH functionalized MWCNTs to assess the viability and potential clinical usage impairments.

Funding

This work is supported by the Vision Group on Science and Technology, Department of Electronics, Information Technology, Biotechnology and Science & Technology, Government of Karnataka [GRD NO 605, 2016-17].

Acknowledgment

Authors are thankful to Siddaganga Institute of Technology, Tumakuru for providing a research facility, Visvesvaraya Technological University, Belagavi, Karnataka, India for supporting this research work, and Biotechnology Department, Siddaganga Institute of Technology, Tumakuru, BioEdge Solutions, Peenya, Bengaluru 560058, for supporting in

conducting Biocompatibility studies. Department of Applied Sciences (Nanotechnology), Visvesvaraya Technological University, Center for Post Graduate Studies, Bengaluru Region, Muddenahalli, Chikkballapura 562101, Karnataka, India for supporting in characterization. Advanced Composites Division, CSIR - National Aerospace Laboratories, Bengaluru 560017, Karnataka, India and Center of Applied Research and Nanotechnology, Siddaganga Institute of Technology, Tumakuru for carryout this research work.

References

- [1] Hasandoost L. The role of poly (methyl methacrylate) in management of bone loss and infection in revision total knee arthroplasty: a review. *Journal of Functional Biomaterials*, 2020;11 (2):25. <https://doi.org/10.3390/jfb11020025>
- [2] Ko DO, S. Lee S, Kim KT, Lee J, Kim JW, Yi SM. Cement mantle thickness at the bone cement interface in total knee arthroplasty: comparison of PS150 RP and LPS-Flex Knee Implants. *Knee Surgery and Related Research*, 2017;29 (2):115-121. <https://doi.org/10.5792/ksrr.16.013>
- [3] Zapata MEV, Tovar CDG, Hernandez JHM. The role of chitosan and graphene oxide in bioactive and antibacterial properties of acrylic bone cements. *Biomolecules*, 2020;10 (12): 1616. <https://doi.org/10.3390/biom10121616>
- [4] Dunne N, Clements J, Wang JS. Acrylic cements for bone fixation in joint replacement. *Joint Replacement Technology*, 2014; 212-256. <https://doi.org/10.1533/9780857098474.2.212>
- [5] Hamizah AS, Mariatti M, Othman R, Kawashita M, Noor Hayati AR. Mechanical and thermal properties of polymethylmethacrylate bone cement composites incorporated with hydroxyapatite and glass-ceramic fillers. *Journal of Applied Polymer Science*, 2012; 125 (S1) <https://doi.org/10.1002/app.35295>
- [6] Hernández ML, Alonso LM, Pradas MM, Lozano OEL, Bello DG. Composites of poly (methyl methacrylate) with hybrid fillers (micro/nanohydroxyapatite): Mechanical, setting properties, bioactivity and cytotoxicity in vitro. *Polymer Composites*, 2013; 34 (11):1927-1937. <https://doi.org/10.1002/pc.22600>
- [7] Kang IG, Park CI, Lee H, Kim HE, Lee SM. Hydroxyapatite Microspheres as an Additive to Enhance Radiopacity, Biocompatibility, and Osteoconductivity of Poly(methyl methacrylate) Bone Cement. *Materials*, 2018; 11 (2): 258 <https://doi.org/10.3390/ma11020258>
- [8] Slane J, Vivanco J, Rose W, Ploeg HL, Squire M. Mechanical, material, and antimicrobial properties of acrylic bone cement impregnated with silver nanoparticles. *Materials Science and Engineering C*, 2015; 48: 188-196. <https://doi.org/10.1016/j.msec.2014.11.068>
- [9] Tham DQ. PMMA bone cements modified with silane-treated and pmma-grafted hydroxyapatite nanocrystals: preparation and characterization. *Polymers (Basel)*, 2021;13 (22):3860. <https://doi.org/10.3390/polym13223860>
- [10] Mahmood T, Ullah A, Ali R. Improved nanocomposite materials and their applications. *Nanocomposite Materials*, Intech Open, 2022; <https://doi.org/10.5772/intechopen.102538>
- [11] Ikram M. Carbon Nanotubes. In *21st Century Advanced Carbon Materials for Engineering Applications - A Comprehensive Handbook*, IntechOpen, 2021; <https://doi.org/10.5772/intechopen.92494>
- [12] Patel KD, Singh RK, Kim HW. Carbon-based nanomaterials as an emerging platform for theranostics. *Materials Horizons*, 2019; 6 (3):434-469. <https://doi.org/10.1039/C8MH00966j>
- [13] Wang RM, Zheng SR, Zheng YP. Introduction to polymer matrix composites. *Polymer Matrix Composites and Technology*, 2011 <https://doi.org/10.1533/9780857092229.1>

- [14] Ormsby R, McNally T, Mitchell C, Dunne N. Influence of multiwall carbon nanotube functionality and loading on mechanical properties of PMMA/MWCNT bone cements. *Journal of Materials Science: Materials in Medicine*, 2010;21 (8):2287-2292. <https://doi.org/10.1007/s10856-009-3960-5>
- [15] Ormsby R, McNally T, Hare PO, Burke G, Mitchell C, Dunne N. Fatigue and biocompatibility properties of a poly(methyl methacrylate) bone cement with multi-walled carbon nanotubes. *Acta Biomaterials*, 2012; 8 (3):1201-1212. <https://doi.org/10.1016/j.actbio.2011.10.010>
- [16] Soleymani SEB. Polymethyl Methacrylate-Based Bone Cements Containing Carbon Nanotubes and Graphene Oxide: An Overview of Physical, Mechanical, and Biological Properties. *Polymers (Basel)*, 2020;12 (7):1469. <https://doi.org/10.3390/polym12071469>
- [17] Ormsby R, McNally T, Mitchell C, Dunne N. Incorporation of multiwalled carbon nanotubes to acrylic based bone cements: Effects on mechanical and thermal properties. *Journal of Mechanical Behavior of Biomedical Materials*, 2010;3(2) <https://doi.org/10.1016/j.jmbbm.2009.10.002>
- [18] Dunne N. MWCNT Used in Orthopedic Bone Cements. *Carbon Nanotubes - Growth and Applications*, Carbon Nanotubes. Open Intech, 2011. <https://doi.org/10.5772/20317>
- [19] Brković DV. Structural properties of the multiwall carbon nanotubes/poly(methyl methacrylate) nanocomposites: Effect of the multiwall carbon nanotubes covalent functionalization. *Polymer Composites*, 2017;38: 472-489. <https://doi.org/10.1002/pc.23996>
- [20] Arun S, Rama Sreekanth PS, Kanagaraj S. Mechanical characterisation of PMMA/SWNTs bone cement using nanoindenter. *Materials Tehnology*, 2014; 29 (S1):B4-B9. <https://doi.org/10.1179/1753555713Y.0000000111>
- [21] Shen SC, Letchmanan K, Chow PS, Tan RBH. Antibiotic elution and mechanical property of TiO₂ nanotubes functionalized PMMA-based bone cements. *Journal of Mechanical Behavior of Biomedical Materials*, 2019; 91:91-98. <https://doi.org/10.1016/j.jmbbm.2018.11.020>
- [22] Valencia Zapata ME, Mina Hernandez JH, Grande Tovar CD. Acrylic Bone Cement Incorporated with Low Chitosan Loadings. *Polymers (Basel)*, 2020; 12 (7):1617. <https://doi.org/10.3390/polym12071617>
- [23] Mu M, Teblum E, Figiel L, Nessim GD, McNally T. Correlation between MWCNT aspect ratio and the mechanical properties of composites of PMMA and MWCNTs. *Materials Research Express*, 2018; 5 (4): 045305. <https://doi.org/10.1088/2053-1591/aab82d>
- [24] Nien YH, Huang C. The mechanical study of acrylic bone cement reinforced with carbon nanotube. *Materials Science and Engineering B*, 2010;169 (1-3):134-137. <https://doi.org/10.1016/j.mseb.2009.10.017>
- [25] Chen J, Yan L, Song W, Xu D. Interfacial characteristics of carbon nanotube-polymer composites: A review. *Composites Part A: Applied Science and Manufacturing*, 2018; 114:149-169. <https://doi.org/10.1016/j.compositesa.2018.08.021>
- [26] Kim H. Tensile properties of millimeter-long multi-walled carbon nanotubes. *Science Reports*, 2017; 7(1):9512. <https://doi.org/10.1038/s41598-017-10279-0>
- [27] Nurazzi NM. Mechanical Performance and Applications of CNTs Reinforced Polymer Composites-A Review. *Nanomaterials*, 2021;11 (9): 2186. <https://doi.org/10.3390/nano11092186>
- [28] Arun S, Kanagaraj S. Performance enhancement of epoxy based sandwich composites using multiwalled carbon nanotubes for the application of sockets in trans-femoral amputees. *Journal of Mechanical Behavior of Biomedical Materials*, 2016;59: 1-10. <https://doi.org/10.1016/j.jmbbm.2015.12.013>
- [29] Tomova A. Multinanosensors Based on MWCNTs and Biopolymer Matrix - Production and Characterization. *Acta Physica Polonica A*, 2017;132 (4):1251-1255. <https://doi.org/10.12693/APhysPolA.132.1251>

- [30] Arif M, Muthu J. Characterization of CNT properties using space-frame structure. *Journal of Mechanics of Materials and Structures*, 2018; 13(4):443-461. <https://doi.org/10.2140/jomms.2018.13.443>
- [31] Shubha A, Manohara SR, Siddlingeshwar B, Daima HK, Singh M, Revaprasadu N. Ternary poly(2-ethyl-2-oxazoline)-polyvinylpyrrolidone-graphene nanocomposites: Thermal, electrical, dielectric, mechanical, and antibacterial profiling. *Diamond and Related Materials*, 2022; 125: 109001. <https://doi.org/10.1016/j.diamond.2022.109001>
- [32] Arun S, Kanagaraj S. Mechanical characterization and validation of poly (methyl methacrylate)/multi walled carbon nanotube composite for the polycentric knee joint. *Journal of Mechanical Behavior of Biomedical Materials*, 2015; 50: 33-42. <https://doi.org/10.1016/j.jmbbm.2015.06.002>
- [34] Ormsby RW, Modreanu M, Mitchell CA, Dunne NJ. Carboxyl functionalized MWCNT/polymethyl methacrylate bone cement for orthopedic applications. *Journal of Biomaterials Applications*, 2014;29(2) <https://doi.org/10.1177/0885328214521252>
- [35] Xu Y, Wang Y, Cui L. An efficient functionalization method for the multiwalled carbon nanotubes and their applications in PMMA bone cement. *Sensors & Transducers*, 2013;21(5):36.
- [36] Fouad H. In vitro evaluation of stiffness graded artificial hip joint femur head in terms of joint stresses distributions and dimensions: finite element study. *Journal of Materials Science: Materials in Medicine*, 2011;22 (6):1589-1598, <https://doi.org/10.1007/s10856-011-4319-2>
- [37] Sumner DR. Long-term implant fixation and stress-shielding in total hip replacement. *Journal of Biomechanics*, 2015; 48 (5):797-800, <https://doi.org/10.1016/j.jbiomech.2014.12.021>
- [38] Kim S, Bishop AR, Squire MW, Rose WE, Ploeg HL. Mechanical, elution, and antibacterial properties of simplex bone cement loaded with vancomycin. *Journal of Mechanical Behavior of Biomedical Materials*, 2020;103:103588, <https://doi.org/10.1016/j.jmbbm.2019.103588>
- [39] Lewis G. Injectable bone cements for use in vertebroplasty and kyphoplasty: State-of-the-art review. *Journal of Biomedical Materials Research - Part B Applied Biomaterials*, 2006 <https://doi.org/10.1002/jbm.b.30398>



Research Article

Optimization of high performance concrete composites by using nano materials

Naveen Arasu A^{*1,a}, Natarajan Muthusamy^{1,b}, Balasundaram Natarajan^{1,c}, Parthasaarathi R^{2,d}

¹ Dept. of Civil Eng., Karpagam Acedamy of Higher Education, Coimbatore, Tamilnadu, India

² Dept. of Civil Eng., Hindusthan College of Engineering and Technology, Coimbatore, Tamilnadu, India.

Article Info

Abstract

Article history:

Received 13 Dec 2022

Accepted 13 Mar 2023

Keywords:

Silica fume;

Fly ash;

Graphene oxide (GO)

Investigating the mechanical properties of high-performance concrete (HPC) employing mineral admixtures including fly ash, silica fume, and graphene oxide was the primary goal of this investigation. The HPC utilised in this study was created using regular OPC fine and coarse aggregate, portable water, and mineral and chemical admixtures such as fly ash, silica fume, and graphene oxide at varied replacement levels, in addition to super plasticizer. In compliance with IS 10262:2019, which calls for the use of HPC mix grade M60 with a w/c ratio of 0.33, super plasticizer was added to the concrete to increase its workability. In order to evaluate different mixtures, cube and cylinder beam specimens with extra mechanical and durability features were all cast. Partial cement replacements of 0%, 5%, 10%, and 15% composed of fly ash and silica fume, graphite oxide with a concentration of 0.04 % were used in the casting of M1 through M4, respectively. The concrete's mechanical behaviour, which was measured in terms of compressive strength, was then put to the test seven, fourteen, and 28 days after it was cast. The results of the tests demonstrate that including mineral admixtures usually improves the combinations' mechanical and durability attributes.

© 2023 MIM Research Group. All rights reserved.

1. Introduction

Due to its excellent workability, high density, high elastic modulus, and high dimensional stability with strong abrasion and impact resistance, high soundness, and cavitation resistance, High Performance Concrete (HPC) is currently utilized extensively across the world. As a result of its toughness and protection from salt probing, HPC is sometimes referred to as "durable" concrete since it outlives conventional concrete by a significant margin. The standard components of water, Portland cement, fine and coarse aggregates, and admixtures are included in this designed concrete, which also contains the classic ingredients. ACI's definition of high-performance concrete states that it "meets unusual combinations of performance and uniformity requirements that cannot always be routinely attained with conventional components and standard mixing, placing, and curing techniques."

HPC is incredibly well-known for achieving financial benefits through environmentally friendly construction methods. There is only one option to lessen the impact of an external chemical assault on concrete, and that is to decrease the concrete's porosity and permeability in order to lessen or at least moderately slow down the penetration of the aggressive chemicals. When typical concrete is subjected to compressive stresses, failure might take place either inside the hydrated cement paste itself or along the interface

*Corresponding author: naveenanbu07@gmail.com

^a orcid.org/0000-0002-5708-0086; ^b orcid.org/0000-0001-8226-8307; ^c orcid.org/0000-0002-4831-1209;

^d orcid.org/0000-0001-9614-0769

DOI: <http://dx.doi.org/10.17515/resm2022.602ma1213>

Res. Eng. Struct. Mat. Vol. 9 Iss. 3 (2023) 843-859

between the cement paste and aggregate particles. Normal concrete has a weak spot at this interface, which is referred to as the transition zone.

A change in the microstructure of the concrete composite, namely a reduction in the thickness, related voids, and micro cracks, as well as a more uniform distribution of the particles in the transition zone, is what accounts for the improved attributes of high-performance concrete. Utilizing both chemical and mineral admixtures, such changes in microstructure are accomplished. In order to make HPC, a significant decrease in the amount of mixing water is required. Concrete that has a lower w/c ratio will be more durable. In order to obtain the high levels of reactivity, silica fume, an additive made from a low-calcium aluminium silicate mineral, has its particle size distribution carefully managed. The ultrafine particles' fineness and strong reactivity contribute to a more effective hydration process. Silica fume addition enhances the particle packing of paste ingredients, which is correlated in concrete with increased strength and life span of concrete. To create more cementitious components and hence boost long-term strength, fly ash grain reacts with free lime in the cementitious components.

Fly ash will diminish the amount of water entering into the concrete by diminishing the w/c ratio and, consequently, the quantity of capillary pores in the mass. As a result, less water is required. The high specific area, however, increases the requirement for water. The combined effect of these two results in a net increase in water consumption when compared to standard-strength concrete for a given degree of workability.

Water usage is decreased by using a super plasticizer. By deflocculating the cement lump, producing cement water mixes, as well as dispersion systems, water lowering admixtures, and super plasticizers, provide the optimal conditions for full hydration of cement. The likelihood of anhydrous cement grains being present in the concrete structure is decreased, and the pore structure is enhanced by bringing almost all cement particles into complete contact with water during the hydration process. Superplasticizers may be able to cut back on water consumption by about 30%.

2. Literature Review

By incorporating nano particles into cementitious composites, fibres have been shown to regulate nano and microscale fractures in the early stages, improving the quality of cement-based composites. (12). Consider graphene oxide nano alumina carbon nano tubes as an example of a reinforced material in cementitious composite structures. (4)

The impact of GO on enriching the cementitious materials' microstructure had a favourable effect on speeding up the hydration process. (7). The mechanical strength, thus, saw a substantial improvement. By adding GO, the moisture transport in the cementitious matrix was successfully constrained. GO successfully prevented the intrusion of chlorides into the cementitious matrix as a result. (1,15)

Among the brodie's approach, the staudenmaier method and the hummer and offeman method, the hummer and offeman method is the most commonly utilised in the production of graphene oxide. The pros and cons of the three ways the brodie's synthesis process was explored, and it was discovered that the brodie's approach produces the cleanest and most stable graphene oxide samples. (2)

The workability of new concrete is the most important factor in influencing its uniform mixing, ease of transport, placement and compaction. The addition of extra components to concrete causes it to lose its workability. Worse, adding nanoparticles to the cementitious matrix alters the rheological properties of cement pastes, making cement mortar and concrete mixes considerably more difficult to work with. (8). This might be due to a decrease in free water, which is needed for lubrication at a certain water-to-cement ratio

w/c to moisten the nanomaterial's increased surface area. (6). Superplasticizers were provided to the fresh mix in order to keep it flowing. Superplasticizers based on polycarboxylate ethers have been discovered to be an efficient additive for sustaining cementitious matrix workability. (3)

In a minor slump test, the slump diameter was decreased by 41.7 percent when compared to the reference sample at a GO dose of 0.05 percent, and there was a 34.6 percent drop in slump. A 0.2 percent polycarboxylate superplasticizer added to the cementitious matrix increased flow by 34%, indicating that it is an important additive for preserving the workability of new mixes by reducing water consumption.(9)

The researchers studied the influence of graphene oxide nanosheets on compressive tensile and flexural strength tests using dosages of 0.01 percent, 0.02 percent, 0.03 percent, and 0.05 percent by weight of cement. In a cement composite made up of 165 g of water, 450 g of cement, 1350 g of normal sand, and a trace of graphene oxide, 0.9 g of polycarboxylate superplasticizer was utilised. The graphene oxide nanosheets are 8 nm thick and range in size from 80 to 260 nm. They are 8 nm thick and contain 29.75 percent oxygen. (11)

For 28, 56, and 90 days of cure, the initial surface absorption and sorptivity tend to decline as GO content rises. The non-destructive method's (UPV) findings demonstrated that the homogeneity of the GO reinforced concrete composite remained unaltered as GO concentration increased, and that the mix made with 0.08% had the highest average velocity across all curing ages when compared to the control mix and the other mixes. (10,16)

It's possible that the improved performance of GO cement-based composites is due to GO dispersion in the cementitious matrix. Thus, the process for efficient GO mixing is critical in increasing the performance of cementitious composites, and further research is needed in this area in concrete since excessive GO sheet dosage has a negative impact on performance. (13, 14). Many studies on the microstructure of GO cementitious composites found a significant improvement in the pore structure reduction in porosity and filler effect of GO in cement pastes and cement mortars, but more research is needed before GO can be widely used in concrete. (5) Previous studies on the durability of GO-incorporated cementitious composites found that they were resistant to the freeze-thaw phenomenon, indicating that more study into the durability qualities of cement-based materials is needed.

Slump values decrease almost linearly with increase in silica fume content. The increase in replacement level of cement with silica fume there is an increase in compressive strength up to 20% when compared with conventional concrete. [17] By the usage of silica fume and fly ash in concrete will reduce the land pollution and helps in recycling of waste materials [18].

Particularly in the mixtures having high foam content, silica fume introduction resulted in superior compressive strength values and greater compressive strength/thermal conductivity ratios than fly ash introduction. [19] Based on the analysis of the results of microstructural tests and the evaluation of the propagation of macroscopic cracks, it was established that along with the substitution of the cement binder with the combination of mineral additives, the composition of the cement matrix in these composites changes, which implies a different, i.e., quasi-plastic, behavior in the process of damage and destruction of the material. [20]

The effect of F/S ratio depended strongly on the curing condition. Under ambient curing, the optimum F/S ratio of 90/10 was observed. For accelerated curing, the addition of silica fume provided negative effect on the mechanical properties. The optimum F/S ratio was

observed in mix without silica fume.[21] The best compressive strength was attained by the mix containing 80% FCA and 20% GGBFS, and hence could be implemented for normal construction works [22]

3. Material Properties

3.1. Cement

All of the specimens were cast using Portland pozzolana cement 53 grade conformities to IS 12269-1987 and with a relative density of 3.15. Cement has been tested for fineness using a sieve analysis with a 90-micron sieve, specific gravity with le-chatliers equipment, and ultimate setting time using a vicat device. The ultra-modern OPC 53 grade cement that was used was procured from Ariyalur. Table 1 shows the properties of cement.

Table 1. Properties of cement

Tests on cement	Results
Specific gravity test	3.15
Fineness test (m ² /Kg)	274
Consistency test (%)	25.0
Initial setting time (min)	135
Final setting time (min)	290
Strength test (N/mm ²)	38.26
	48.30
	61.80
Soundness test (mm)	1.2

3.2. Fine Aggregate

Fine aggregate was taken from Karanempettai and confirmed to be M-sand according to IS 383-1970. Its sp. gr. is 2.860. Tests on fine aggregate include grading and sp. gr. using a pycnometer to measure fineness ratio. Table 2 shows the properties of fine aggregate.

3.3. Course Aggregate

Crushed angular granite stone confirming to a size of 12.5mm and 20mm confirming to table 7 of IS 383: 1970 was used, having a sp. gr for 12.5 mm is 2.87 and for 20mm is 2.82. Coarse aggregate was obtained from Karanempettai. Table 3 shows the properties of course aggregate.

3.4. Silica Fume

Having a low calcium aluminium silicate grading reactivity, silica fume is a mineral-based additive. The hydration process is brought on by the enhanced reactivity and grading of SF. When SF is used to increase the particle packing of paste components, the resulting concrete is stronger and also possesses a longer life span.

The manufacturer of silica fume is called Silica fume & Admixtures Pvt. Ltd., and is located in Nagpur, Maharashtra. 2.71 is the specific gravity. Table 4 shows the properties of silica fume.

3.5. Fly Ash

Fly ash is a thin grey powder that is a byproduct of combustion power plants and is mostly made up of spherical glassy particles. When pulverised coal is burned, a finely divided residue called fly ash is produced, which is used in combustion power plants.

In Metturs (MTPP), collected fly ash has a specific gravity of 2.13. Table 5 shows the properties of fly ash.

Table 2. Properties of fine aggregate

Tests on fine aggregate	Results
Sieve analysis (Fineness modulus) (m ² /Kg)	2.85
Density	
Loose (Kg/m ³)	1683.00
Rodded (Kg/m ³)	1780.00
Specific gravity	2.860
Water absorption (%)	1.06

Table 3. Properties of course aggregate

Tests on Coarse Aggregate	Results (12.5mm)	Results (20mm)
Density		
Loose (Kg/m ³)	1736	1680
Rodded (Kg/m ³)	1786	1777
Specific gravity	2.82	2.87
Water absorption (%)	0.23	0.24
Flakiness index (%)	10.6	7.2
Elongation index (%)	11.20	13.6

Table 4. Properties of silica fume

Tests on Silica Fume	Results
Fineness (m ² /Kg)	2730
Particle size range	
D ₅₀ (µm)	3.85
(b) D ₉₅ (µm)	8.79
Slag Activity Index	
7 days	87.20%
28 days	110%

Table 5. properties of fly ash

Test on Fly ash	Results
Bulk density (gm/cc)	0.9-1.3
Specific gravity	1.6-2.6
Plasticity	Lower or non-plastic
Shrinkage limit (vol stability)	Higher
Free swell index	Very low
Porosity (per cent)	30-65
Surface area (m ² /kg)	500-5000
Lime reactivity (MPa)	1-8

3.6. Graphene Oxide

Chemical admixtures like graphene oxide are used to improve the durability and strength of concrete.

The Karnataka-based Ad-nano technologies company produces grapheme oxide. Table 6 shows the properties of graphene oxide. Figure 1 (a & b), 2 and 3 shows the GO FE SEM images and GO FTIR image shows the variations of wane number and transmittance.

Table 6. Properties of GO

GO	Value
Elastic modulus	23.42
Elongation at break	0.6%
Electrical conductivity	Non conductive
Dispensability in water	Highly dispersible

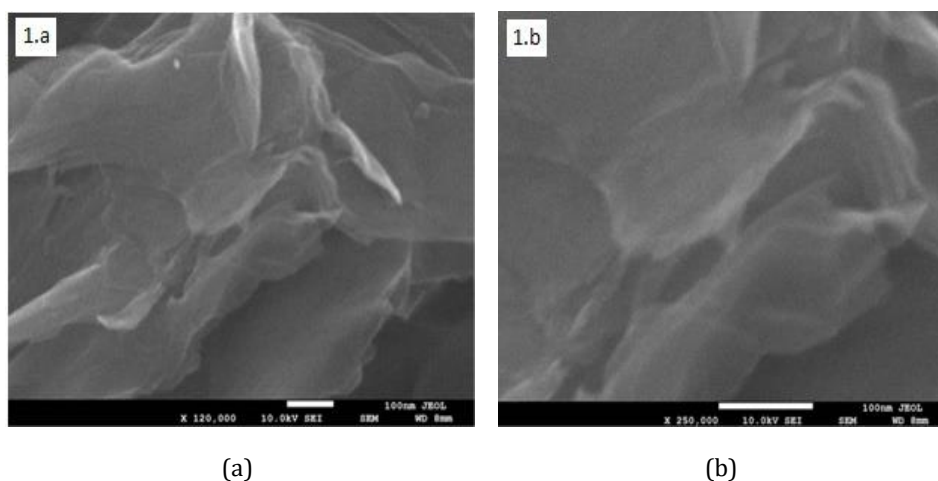


Fig. 1 (a) and (b) GO FE SEM

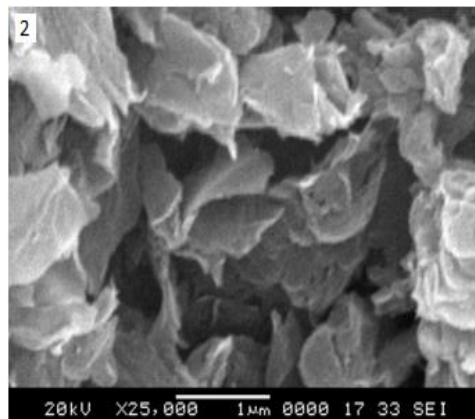


Fig. 2 GO SEM

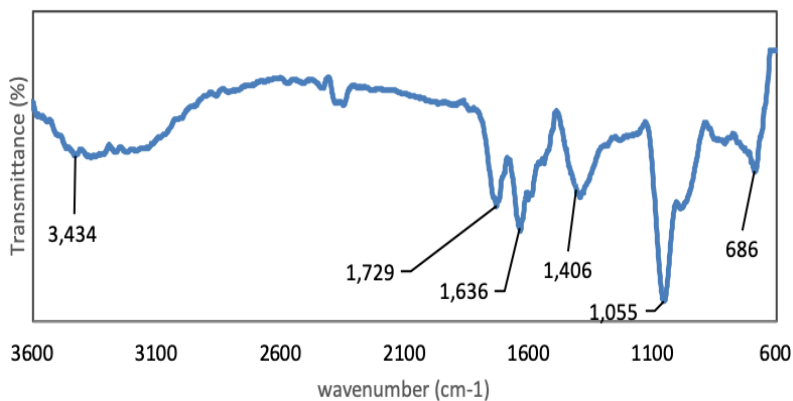


Fig. 3 GO FTIR

3.7. Super Plasticizer

In order to improve the flow ability of concrete, a chemical additive called CAC Hyperfluid plus (H5), which is readily accessible, was utilized.

A concrete super plasticizer called CAC-HYPERFLUID PLUS (H5), which is based on polycarboxylic ether, is used to decrease the amount of water in admixed concrete as well as to make it easier to work with. In order to provide substantial water reductions of up to 40% without sacrificing flow ability or to manufacture high-quality concrete with decreased permeability, CAC-HYPERFLUID PLUS (H5) has been particularly designed. Table 7 shows the properties of superplasticizer.

Hydrostatic pressure from one side to a concrete specimen with known dimensions that is inside a specially designated cell, and measuring the amount of water that percolates through the specimen in a certain amount of time through the other end of the specimen. The permeability is inversely correlated with the amount of water collected. For a full day, the test pressure was maintained. This shows the lowering concrete's water permeability, improving the material's resilience.

4. Mix Proportions and Casting

The mix proportioning for a concrete of M60 grade concrete using Fly ash, Silica Fume and Graphene oxide is given below in the table 8 various mix.

Table 7. Properties of super plasticizer

Property	Result
Appearance	Brown free flowing liquid
Base material	Modified poly-carboxylic ether
Specific gravity at 25o C	1.080+/- 0.020
Chloride content	Maximum 0.2%
pH	Minimum 6

Table 8. Quantity of materials used in kg/m³

Mix	Description	Cement (Kgs.)	GO (Gms)	Fly ash (Kgs.)	SF (Kgs.)	Water (Kgs.)	FA (Kgs.)	CA (Kgs.)	SP (Lits)
M1	Conventional % GO +	470	0.00	0	0	141	659	1324	4.70
M2	5% Fly ash + 5 % Silica Fume % GO +	422.81	0.19	23.5	23.5	141	659	1324	4.70
M3	10 % Fly ash + 10 % Silica Fume 0.04 % GO +	375.81	0.19	47.0	47.0	141	659	1324	4.70
M4	15% Fly ash + 15 % Silica Fume	328.81	0.19	70.5	70.5	141	659	1324	4.70

5. Test Method

5.1. Fluidity Test

Slump cone tests and compaction factor tests are conducted to determine the fluidity of fresh concrete. The test results are given below in table 9. Figure 4 (a, b, c & d) shows slump test. Figure 5 and 6 shows how slump value and compaction factor decrease with increase in fly ash, silica fume and graphene oxide with various mix.

Table 9. Slump value and compaction factor

Mix	Description	Slump Value (mm)	Compaction Factor
M1	Conventional	110	0.904
M2	0.04% GO + 5% Fly ash + 5 % Silica Fume	105	0.900
M3	0.04% GO + 10 % Fly ash + 10% Silica Fume	99	0.895
M4	0.04 % GO + 15% Fly ash + 15% Silica Fume	93	0.890

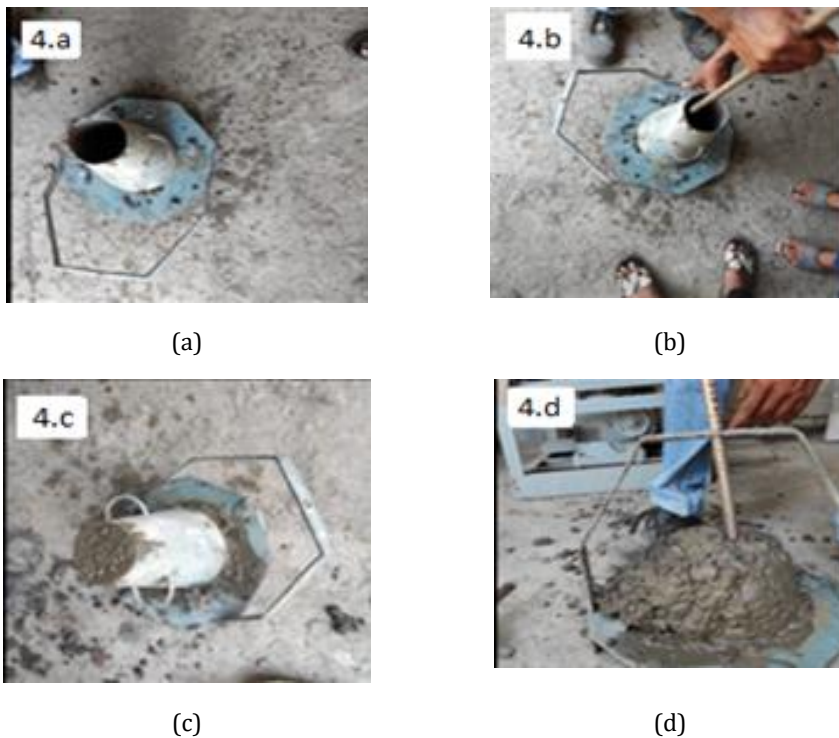


Fig. 4 Slump test

5.2. Strength Test

Compressive, Split tensile, and flexural tests were conducted to find the physical properties of concrete and the results are given below in tables 10, 11, and 12. Figure 7 (a, b, c & d), 9 (a & b) and 11 shows the image of compression test on cube of various mixes, the compressive strength increases in mix M1, M2 and M3 and reduces in M4 mix for cylinder and beam. Figure 8, 10 and 12 shows the variation of compressive and split tensile strength increase with addition in percentage of fly ash, silica fume and graphene oxide for various mix.

The compressive strength of the hardened concrete cubes of size 150mm x 150mm x 150mm was found using the compression testing machine of capacity 200kN. The tests

were carried out at a uniform rate of $14\text{N}/\text{mm}^2/\text{min}$ after the specimen had been centered in the testing machine.

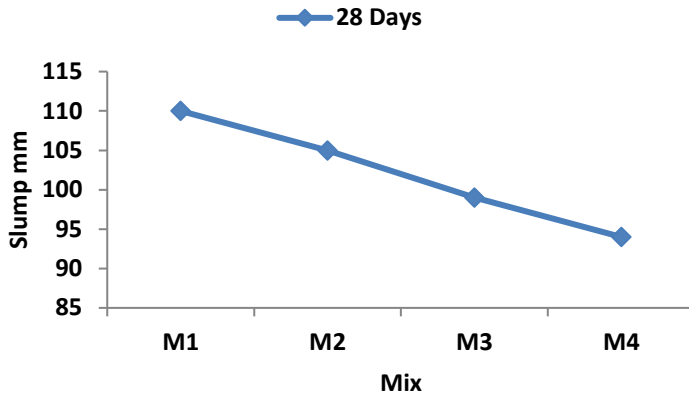


Fig. 5 Slump value

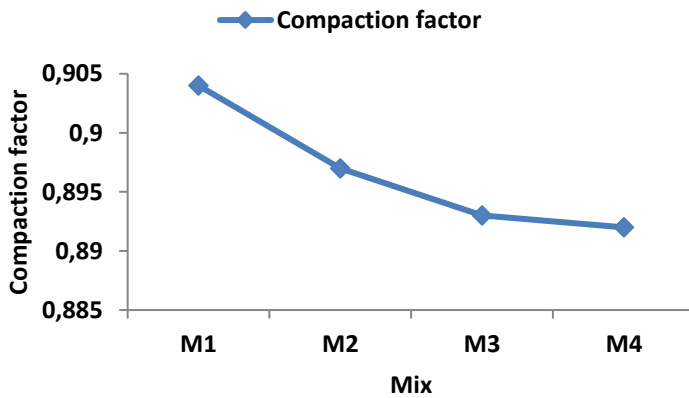


Fig. 6 Compaction factor



(a)



(b)

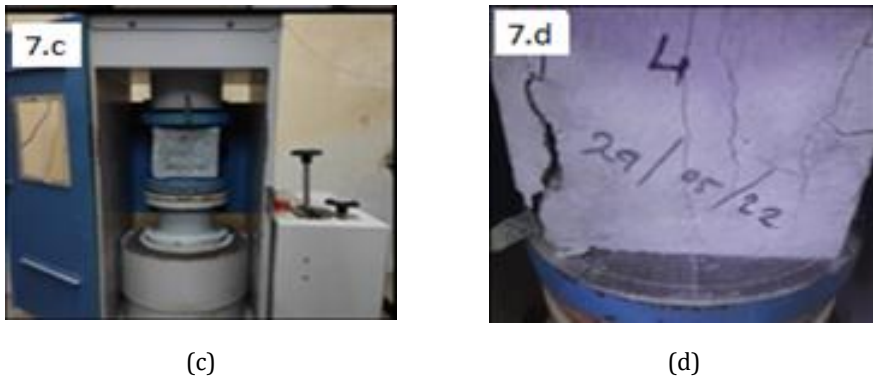


Fig. 7 Compression test

Table 10. Compressive Strength

Mix Proportion	7 Days N/mm ²	14 Days N/mm ²	28 Days N/mm ²
M1	40.02	47.82	66.31
M2	57.04	61.83	74.88
M3	62.68	67.44	82.15
M4	38	49.68	76.33

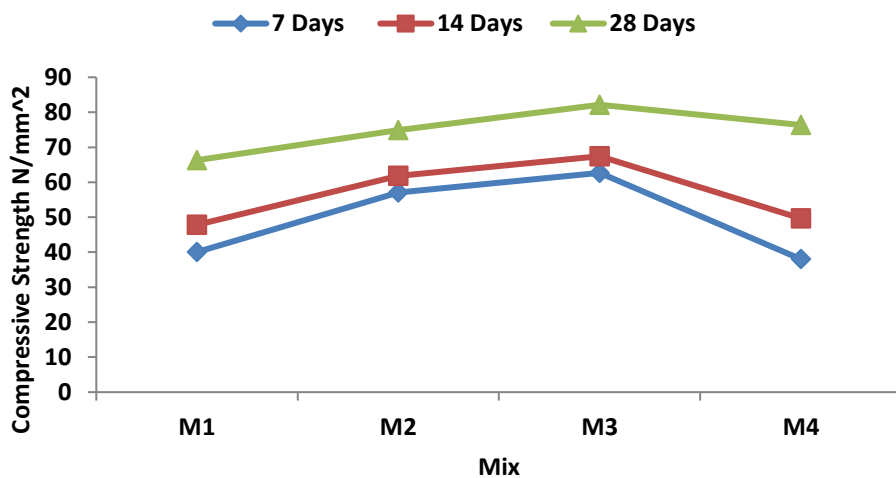


Fig 8. Compressive strength

Table 11. Split tensile strength

Mix Proportion	7 Days N/mm ²	14 Days N/mm ²	28 Days N/mm ²
M1	4.60	4.96	5.04
M2	4.68	5.13	5.32
M3	5.08	5.41	5.83
M4	5.02	5.33	5.67

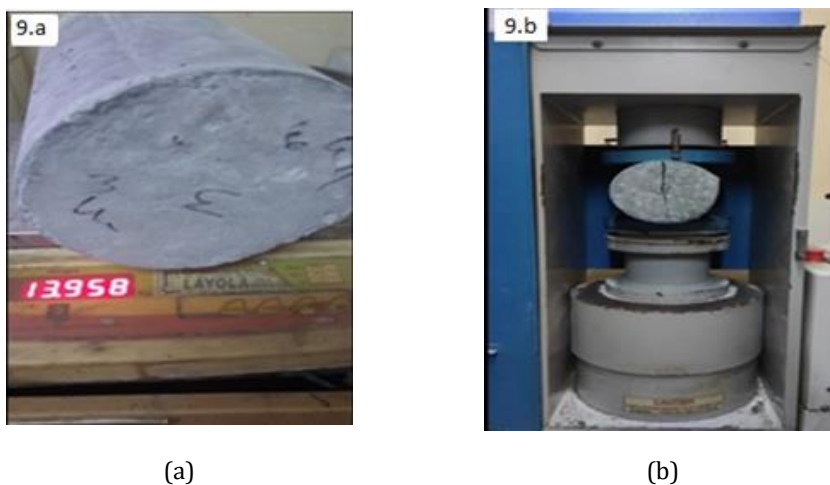


Fig. 9 Split tensile test

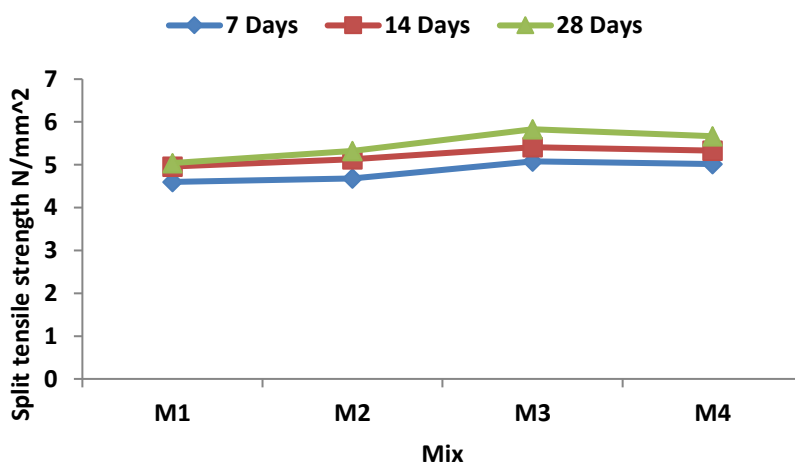


Fig 10. Split tensile strength

Table 12. Flexural test

Mix Proportion	28 Days N/mm ²
M1	6.79
M2	7.32
M3	7.81
M4	7.63



Fig. 11 Flexural test on beam

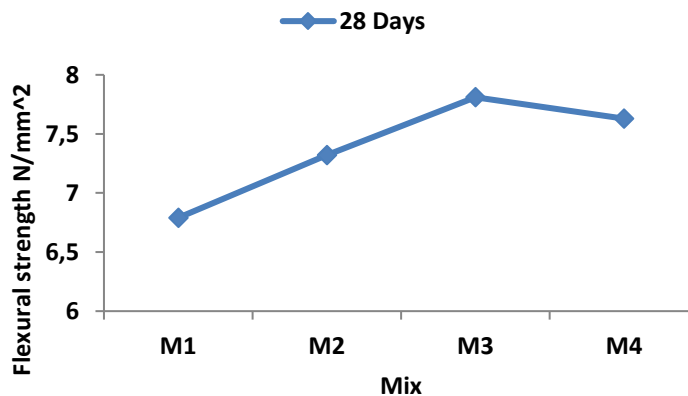


Fig. 12 Flexural strength

5.3. Test for Permeability

The equation, which is provided in the code, was used to compute the coefficient of permeability during permeability tests that were carried out in accordance with IS 3085-1965.

The device comprises a reservoir that is connected to the cell via a metal pipe that is 500 millimetres long and 50 to 100 millimetres in diameter. The permeability cell measures

115 mm in height and 115 mm in diameter. A scale has been installed in the reservoir. The permeability cell is equipped with the necessary valves for admitting water, compressed air, and water drainage. The permeability cell assembly is coupled to a 5 hp air compressor to maintain a pressure between 5 and 15 kg/cm². To remove all laitance, the specimen was extensively cleaned with a hard wire brush. Water that was clean and in sufficient supply was made available for the permeability test. This investigation has been conducted at a pressure of 5 kg/cm². The test involves applying a known hydrostatic pressure from one side to a concrete specimen with known dimensions that is inside a specially designated cell, and measuring the amount of water that percolates through the specimen in a certain amount of time through the other end of the specimen. The permeability is inversely correlated with the amount of water collected. For a full day, the test pressure was maintained.

Table 13. Permeability test

Mix Proportion	Permeability 10 ⁻⁹ cm/sec
M1	0.48
M2	0.46
M3	0.43
M4	0.38

5.4 Microstructural Observation

To compare the structural cytology of the fly ash, silica fume and GO concrete composites and conventional mix, scanning electron microscopy was used. In mixes made with fly ash, silica fume and GO, huge hydrated crystals, calcium silicate hydrates (C-S-H), were seen in contrast to the presence of ettringites, pointed crystals, and holes in the control mix as seen on the SEM micrograph. The hydrated crystals in Fig. 13 prevented pore capillaries from forming, making the concrete less porous and increasing its strength and endurance. Fig. 14. Represents the SEM pictures of 0.04% GO and 10% silica fume and 10% fly ash with 90 day old concrete.

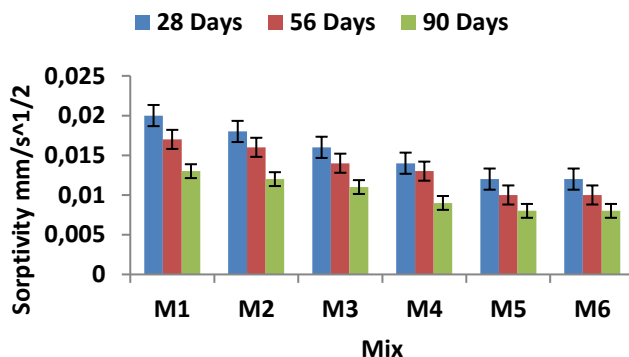


Fig. 13 Sorptivity of all the mixes at 28, 56 and 90 days curing age

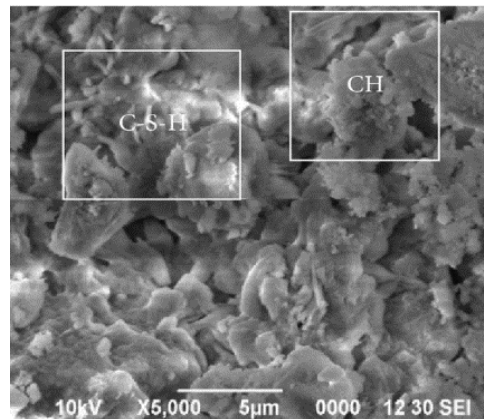


Fig. 14 SEM of mix GO 0.04%

6. Conclusion

In the previous study they have optimized only the graphene oxide. The present study concluded that how fly ash, silica fume, and graphene oxide can be made possible and how they performed when used in place of certain cements to create high-performance concrete. For a water-binder ratio of 0.30, silica fume is place of cement in the following percentages: 0%, 5%, 10%, and 15% for fly ash is place of cement in the following percentages: 0%, 5%, 10%, and 15% and for graphene oxide dispersion is added to cement by 0.04% percentage.

The workability of the fresh concrete reduces the by adding silica fume, fly ash and graphene oxide to counteract the reduction of workability super plasticizer is added. The super plasticizer called CAC-HYPERFLUID PLUS (H5), which is based on polycarboxylic ether, is used to enrich the flow ability property of concrete.

- The findings of this research show that optimization for the M60 grade of concrete by replacing 10% of silica fume, 10% of fly ash, and 0.04% of graphene oxide for cement in concrete shows better results when compared to all the mix including the conventional concrete.
- Due to increase in fly ash and silica fume in concrete it reduces the workability of fresh concrete due to that after M3 mix the strength also reduces.
- There is an appreciable increase in compressive strength of about 24 percentage, split tensile strength of about 16 percentage, and flexural strength of about 15 percentage while maintaining other mix design parameters at their original levels.
- Due to improved permeability of concrete for about 26 percentage, the durability of concrete also increases. And with increasing curing age the value decreases drastically indicating the improvement of porosity at the micro-level of the concrete.
- The size of the hydrated crystals grows as the proportion of GO content does, showing that GO nano materials are filling the pores. The hydrated crystals prevents the pore capillaries from forming, making the concrete less porous and increasing its strength and endurance.
- Fly ash, silica fume, and GO were incorporated into the concrete to reinforce it and improve its mechanical and durability properties. These might be the best option among the various nanomaterials in the near future for building stronger, better robust, and longer-lasting concrete.

References

- [1] Mohammed A, Al-Saadi NTK, Sanjayan J. Inclusion of graphene oxide in cementitious composites: state-of-the-art review. Australian Journal of Civil Engineering. 2018; 1-15. <https://doi.org/10.1080/14488353.2018.1450699>
- [2] Gong K, Pan Z, Korayem AH, Qiu L, Li D, Collins FG, Wang CM, Duan W. Reinforcing effects of graphene oxide on Portland cement paste. Journal of Materials in Civil Engineering. 2015; 27: 1-6. [https://doi.org/10.1061/\(ASCE\)MT.1943-5533.0001125](https://doi.org/10.1061/(ASCE)MT.1943-5533.0001125)
- [3] Wille K, Loh KJ. Nanoengineering ultra-high-performance concrete with multiwalled carbon nanotubes. Transportation Research Record. 2010; 2142: 1; 119-126. <https://doi.org/10.3141/2142-18>
- [4] Sanchez F, Sobolev K. Nanotechnology in concrete-a review. Construction Building Materials. 2010; 24: 11: 2060-2071. <https://doi.org/10.1016/j.conbuildmat.2010.03.014>
- [5] Peng H, Ge Y, Cai CS, Zhang Y, Liu Z. Mechanical properties and microstructure of graphene oxide cement-based composites. Construction Building Materials. 2019; 194: 102-109. <https://doi.org/10.1016/j.conbuildmat.2018.10.234>
- [6] Senff L, Hotza D, Lucas S, Ferreira VM, Labrincha JA. Effect of nano-SiO₂ and nano-TiO₂ addition on the rheological behavior and the hardened properties of cement mortars. Materials Science Engineering A. 2012; 532: 354-361. <https://doi.org/10.1016/j.msea.2011.10.102>
- [7] Zhao L, Guo X, Liu Y, Zhao Y, Chen Z, Zhang Y, Guo L, Shu X, Liu J. Hydration kinetics, pore structure, 3D network calcium silicate hydrate, and mechanical behavior of graphene oxide reinforced cement composites. Construction Building Materials. 2018; 190: 150-163. <https://doi.org/10.1016/j.conbuildmat.2018.09.105>
- [8] Mokhtar MM, Abo-El-Enein SA, Hassaan MY, Morsy MS, Khalil MH. Mechanical performance, pore structure and micro-structural characteristics of graphene oxide nano platelets reinforced cement. Construction Building Materials. 2017; 138: 333-339. <https://doi.org/10.1016/j.conbuildmat.2017.02.021>
- [9] Birenboim M, Nadiv R, Alatawna A, Buzaglo M, Schahar G, Lee J, Kim G, Peled A, Regev O. Reinforcement and workability aspects of graphene-oxide reinforced cement nanocomposites. Composites B Engineering. 2019; 161: 68-76. <https://doi.org/10.1016/j.compositesb.2018.10.030>
- [10] Devi SC, Khan RA. Effect of graphene oxide on mechanical and durability performance of concrete. Journal of Building Engineering. 2020; 27: 1-12. <https://doi.org/10.1016/j.jobbe.2019.101007>
- [11] Lv S, Ma Y, Qiu C, Sun T, Liu J, Zhou Q. Effect of graphene oxide nanosheets of microstructure and mechanical properties of cement composites. Construction Building Materials. 2013; 49: 121-127. <https://doi.org/10.1016/j.conbuildmat.2013.08.022>
- [12] Sharma S, Kothiyal NC. Influence of graphene oxide as dispersed phase in cement mortar matrix in defining the crystal patterns of cement hydrates and its effect on mechanical, microstructural and crystallization properties. RSC Advances. 2015; 5: 65: 52642-52657. <https://doi.org/10.1039/C5RA08078A>
- [13] Naresh Kumar T, Vishnu Vardhan K, Hari Krishna M, Nagaraja PV. Effect of graphene oxide on strength properties of cementitious materials: A review. Materials Today: Proceedings. 2021; 46: 6: 2157-2160. <https://doi.org/10.1016/j.matpr.2021.02.637>
- [14] Li W, Li X, Chen SJ, Long G, Liu YM, Duan WH. Effects of nanoalumina and graphene oxide on early-age hydration and mechanical properties of cement paste. Journal of Materials in Civil Engineering. 2017; 29: 9: 1-7. [https://doi.org/10.1061/\(ASCE\)MT.1943-5533.0001926](https://doi.org/10.1061/(ASCE)MT.1943-5533.0001926)

- [15] Li W, Li X, Chen SJ, Liu YM, Duan WH, Shah SP. Effects of graphene oxide on early-age hydration and electrical resistivity of Portland cement paste. *Construction Building Materials*. 2017; 136: 506-514. <https://doi.org/10.1016/j.conbuildmat.2017.01.066>
- [16] Li X, Korayem AH, Li C, Liu Y, He H, Sanjayan JG, Duan WH. Incorporation of graphene oxide and silica fume into cement paste: A study of dispersion and compressive strength. *Construction Building Materials*. 2016; 123: 327-335. <https://doi.org/10.1016/j.conbuildmat.2016.07.022>
- [17] Akshana V, Naveen Arasu A, Karthigaiselvi P. Experimental study on concrete by partial replacement of cement by silica fume. *Journal of Critical Reviews*. 2020; 7: 17: 3801-3805.
- [18] Bajpai P, Choudhary K, Srivastava A, Sangwan KS, Singh M. Environmental impact assessment of flyash and silica fume based geopolymer concrete. *Construction Building Materials*. 2020; 254: 120-147. <https://doi.org/10.1016/j.jclepro.2020.120147>
- [19] Süleyman Gökçe H, Hatungimana D, Ramyar K. Effect of fly ash and silica fume on hardened properties of foam concrete. *Construction Building Materials*. 2019; 194: 1-11. <https://doi.org/10.1016/j.conbuildmat.2018.11.036>
- [20] Golewski GL, Gil DM. Studies of Fracture Toughness in Concretes Containing Fly Ash and Silica Fume in the First 28 Days of Curing. *Materials*. 2021; 14: 319: 1-21. <https://doi.org/10.3390/ma14020319>
- [21] Wang Y, Cao Y, Ma Y, Xiao S, Hu J, Wang H. Fresh and hardened properties of alkali-activated fly ash/slag binders: effect of fly ash source, surface area, and additives. *Journal Sustainable Cement*. 2022; 239-262. <https://doi.org/10.1080/21650373.2021.1932637>
- [22] Das SK, Mustakim SM, Adesina A, Mishra J, Alomayri TS, Assaedi HS, Kaze CR. Fresh strength and microstructure properties of geopolymer concrete incorporating lime and silica fume as replacement of fly ash. *Journal of Building Engineering*, 2020; 32: 101780. <https://doi.org/10.1016/j.jobe.2020.101780>

Blank Page



Research Article

Integral waterproofing concrete mechanical properties with the addition of fly ash

Dwi Nurtanto^{*,a}, Mochammad Roziqin^b, Krisnamurti^c, Wiwik Yunarni Widiarti^d, Roy Firmawan^{1,e}

Dept. of Civil Eng., Faculty of Eng. University Jember, Tegalboto Campus, Jember Regency, East Java 68121, Indonesian

Article Info

Abstract

Article history:

Received 29 Dec 2022

Accepted 2 May 2023

Keywords:

Integral

Waterproofing

Concrete;

Modulus Elasticity;

Fly Ash;

Compressive

Strength;

Split Tensile Strength

The addition of waterproofing to concrete aims to reduce porosity and is expected to be more watertight. However, the addition of a waterproof layer to the concrete can reduce its performance of the concrete. Therefore, researchers are trying to innovate an integral mixture of waterproofing concrete with fly ash (FA) as a filler. FA added to the integral waterproofing concrete mix is expected to improve its mechanical properties, including the modulus of elasticity. The Madrid Parabola Formula and Desay & Khrisnan Formula are usually used in calculating the stress-strain distribution of concrete. This case aims to determine the physical and mechanical properties as well as the stress-strain distribution equation by adding FA to integral concrete waterproofing. In this study, the specimens used were cylindrical in shape with a size of 15 cm x 30 cm. The ingredients are PPC cement, sand, gravel, 1.5% integral waterproofing added (Damdex brand), and the addition of FA from cement weight 0% to 15% in 5% increment intervals. Tests for compressive strength, split tensile strength, and modulus of elasticity tests were carried out in reference to ASTM C39/C39M-18, 2018, ASTM C 496/C 496M - 04, 2004, and ASTM C 469 - 02, 2002. The results showed that the more FA was added, the more strength increased. The Desay-Khrisnan stress-strain formula is more suitable for this concrete

© 2023 MIM Research Group. All rights reserved.

1. Introduction

Concrete is the result of the bond between the paste (cement and water) with the aggregate. In some conditions, concrete is also required to be waterproof. In project construction, many workers neglect work procedures, which can cause underground structures such as basement walls or floors to leak. This requires high repair costs. Along with the times, the development of concrete technology cannot be avoided. Various kinds of proofs of this innovation have been created, one of which is integral concrete waterproofing and plasticizing admixture[1]-[3]. Waterproofing Essential is made of concrete with average conditions that cannot be waterproofed so that the need for concrete from the concrete mixture can produce waterproof concrete. The addition of waterproofing can make the concrete last longer [4]-[6]. The life of concrete can be durable because the addition of waterproofing materials reduces water absorption and permeability through the concrete capillaries.[3,7, 8]. Standard concrete has a compressive strength that is more significant than the required waterproofing concrete. The integral waterproofing method can drastically reduce concrete's compressive strength. The concrete's compressive value is below the average compressive strength [9]-[12].

*Corresponding author: dwinurtanto.teknik@unej.ac.id

^a orcid.org/0000-0001-7436-004X; ^b orcid.org/0009-0008-2547-230X; ^c orcid.org/0000-0002-7858-8073;

^d orcid.org/0000-0001-8513-2085; ^e orcid.org/0009-0000-5927-037X

DOI: <https://dx.doi.org/10.17515/resm2023.627me1229>

Res. Eng. Struct. Mat. Vol. 9 Iss. 3 (2023) 861-873

There have been many uses of industrial waste, fly ash (FA), and agricultural residues such as rice husk ash (RHA), and sugarcane bagasse ash (SBA) as a substitute for cement in concrete research [13]-[20]. This material aims to replace the depletion of natural resources and reduce CO₂ emissions in the air from cement manufacture, which will help save the environment. Previous research by replacing cement or adding additives from FA, RHA, and SBA can improve the mechanical strength of concrete. In previous studies, this waste as a substitute for paste materials or as aggregates, the mechanical properties of which can be improved with age. At the beginning of the 28th generation, the strength is still low, but after 56 days the strength will be higher or equal to normal concrete. Meanwhile, as a filler, it can improve the mechanical properties of concrete [21]- [24]. In some conditions, FA has a chemical content that can increase the binding element in cement called silica dioxide (SiO₂), thus increasing the compressive strength [25]- [28]. The use of FA material is based on the properties of this material which is similar to cement and can close the pores of the concrete thereby increasing the integral waterproofing strength of the concrete. The similarity of these properties can be seen physically and chemically [29,30]. FA material has very good physical properties, able to pass through a filter of fewer than 50 millimicrons by 5% - 27%, has a specific gravity value of 2.15-2.6 and is gray in color. The most abundant chemical content of FA is usually silica dioxide (SiO₂) with a percentage of up to 80%. Therefore, FA can be an integral filler in concrete waterproofing similar to cement.

The modulus of elasticity is the ratio of stress to strain under elastic conditions, the ability to undergo elastic deformation under applied loads. The greater the value, the greater the stiffness, but the deformation value decreases. From the results of laboratory tests, uniaxial compression tests, researchers can determine the behavior of concrete, its modulus of elasticity, using a parabolic equation of order 2. Draw a straight line measured relative to the horizontal axis with a tangent line twice the tangent. This line can be used as an assumption in calculating the modulus of elasticity of concrete before further numerical analysis is carried out [31]. In calculating the modulus of elasticity, the Madrid parabola equation and the Desay & Krishnan formula are used.

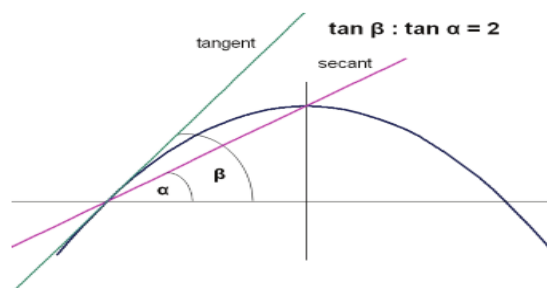


Fig. 1. Property of 2nd order parabola (P.Kmieciak, M.Kaminski)

The formula for the stress-strain relationship for the non-linear behavior of concrete structures is as follows:

- Madrid Parabola
- $$\sigma c = Ec . \varepsilon c . \left[1 - \frac{1}{2} \left(\frac{\varepsilon c}{\varepsilon c1} \right) \right], \quad \sigma c = f(Ec, \varepsilon c1) \tag{1}$$
- Desay & Krishnan

$$\sigma_c = \frac{E_c \cdot \epsilon_c}{1 + \left(\frac{\epsilon_c}{\epsilon_{c1}}\right)^2}, \quad \sigma_c = f(E_c, \epsilon_{c1}) \tag{2}$$

According to ASTM C496 from the test result at the laboratory determined that the modulus elasticity as the ratio of stress when reaching 40% of the stress collapse to the strain following the stress under these conditions :

$$E_c = \frac{(\sigma_2 - \sigma_1)}{(\epsilon_2 - \epsilon_1)} \tag{3}$$

- Where : E_c = Modulus Elasticity (Mpa)
- σ_c = Concrete Stress
- σ_{cm} = average compressive strength
- σ_2 = Stress equivalent to 40% ultimate stress (Mpa)
- σ_1 = Stress value at the time of reaching longitudinal strain, ϵ_1 (Mpa)
- ϵ_2 = Strain value at stress σ_2
- ϵ_1 = 0,00005
- ϵ_{c1} = strain ϵ at stress σ_{cm}

This study determines the mechanical properties of watertight concrete with a mixture of integral waterproofing and variations of FA filler from 0% to 15% of the total cement.

2. Experimental Work

2.1. Material

2.1.1. Fly Ash (FA)

PLTU Paiton Probolinggo is a steam power plant in East Java that uses coal as fuel. Combustion waste in the form of fly ash is used in this case. Table 1 contains the chemical content.

Table 1. Properties FA

Physical	
Soecific Gravity	3.07
Checimal Composition (%)	
Silikon dioksida	52,35
Alumnia Oksida	12,11
Ferri Oksida	12,35
Kalsium Oksida	6,79
Magnesium Oksida	10,63
Natrium Oksida	2,15
Sulfur Trioksia	2,27
Water	0,12
LOI	0,40

2.1.2. Aggregates

Lumajang river natural sand from Mount Semeru, East Java, Indonesia, is used as fine aggregate in the concrete mix. The specific gravity is 2.53, the volume weight is 1710 kg/m³, the water absorption rate is 2.78%, and the fineness level is 2.15. Coarse aggregate

obtained from crushed stone in Jember. The specific gravity of crushed stone is 2.6, the unit weight is 1390 kg/m³, the water absorption rate is 0.54%, the fineness level is 1.45, and the maximum size is 20 mm. The properties of the aggregates used in this concrete mix are given in Table 2 and Fig. 2

Table 2, Physical and mechanical properties of aggregates.

Unit	Sand	Broken Stone
Specific gravity	2.53	2.6
Volume weight (kg/m ³)	1710	1390
Water absorption (%)	2.78	0.54
Fine Modulus	2.15	1.45
Clay and fine materials (%)	1.54	0.39

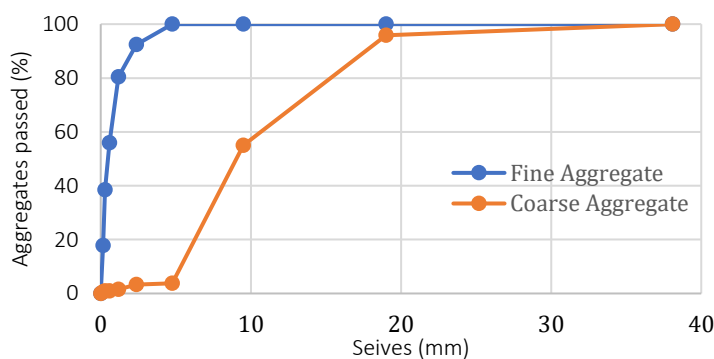


Fig 2. The grading curve of aggregates

2.1.3. Waterproofing

Waterproofing is widely available in building stores (Damdex), which functions as an added ingredient for fresh concrete so that the concrete is water seepage resistant or the concrete is watertight. It is recommended to use 0.5 -2% by weight of cement, in research using 1.5% by weight of cement.

2.2. Mix Desain

To achieve the research objective, a mixture was prepared with three variations of FA, 5%, 10%, and 15% by weight of cement. FA as a filler material in the concrete mixture. The parameters of the mix that remained constant were cement and 1.5% water proofing by weight of cement.

Table 3. Material Requirements per Concrete Cylinder for Each Variation of FA

Sample	% filler FA	Material					
		Cement (Kg)	Water (Ltr)	Sand (Kg)	Gravel (Kg)	FA (Kg)	Waterproofing (kg)
BW	0	3.26	1.30	4.35	6.00	0	0.049
BWF1	5	3.26	1.30	4.35	6.00	0.1629	0.049
BWF2	10	3.26	1.30	4.35	6.00	0.3257	0.049
BWF3	15	3.26	1.30	4.35	6.00	0.4889	0.049

2.3. Testing Procedure

Testing fresh concrete with slump test according to ASTM C143. Concrete testing by compression test according to ASTM C39 split tensile strength according to ASTM C496, Modulus of Elasticity according to ASTM C469, and absorption according to ASTM C642. The test object is cylindrical (15 x 30 cm). Tests were carried out at 28 days of concrete, and an average of five samples were recorded for each test.

3. Results and Discussion

3.1. Workability

Fresh concrete testing was carried out to determine the flowability level using the slump abrams test. In the implementation of mixing, the control variable in this study is the slump abrams test. Therefore, the use of water in the normal concrete mixing process must always be controlled. The addition of FA to the concrete mixture can increase the concrete's workability so that the fresh concrete is thinner. The slump abrams test results on integral waterproofing concrete are presented in Table 4, Fig. 3, and Fig. 4.

In previous studies, FA in a fresh concrete mixture will increase workability and reduce water addition. Such a function allows concrete planning by reducing the lower cement water factor ratio for equal workability, useful in increased strength, tighter pore structure, and increased durability. In the previous test, the relationship between the slump and FA test at the same water content shows that it is directly proportional, where the more FA additions will also show a high slump test value



Fig. 3. Slump Abrams Test Measurement on BW, BWF1, BWF2, and BWF3

Table 4. Abrams slump test results on fresh concrete

Sample	Slump test (cm)
BW	10
BWF1	10
BWF2	11
BWF3	12

Figure 4 shows the integral waterproofing (BWF) slump value of FA. As the FA value increases, the slump value also increases. Increasing slump value will give affect the performance of fresh concrete, high workability, and low viscosity.

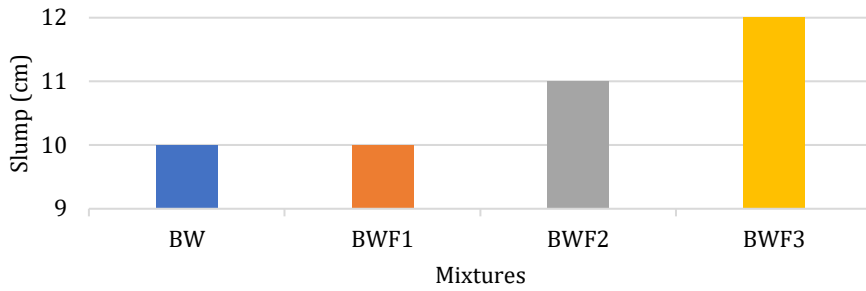


Fig. 4. Slump test value

3.2. Compressive strength

The addition of 0% to 15% FA by weight of cement into 1.5% integral watertight concrete will be tested for strength. The compressive strength of the prepared BW samples increased directly proportional to the addition of FA. Fig. 5 shows the strength of the sample at 28 days of age. Compared with the reference sample, namely BW, the BWF sample has a higher strength. With the addition of FA to BW it will close or reduce the pore size. With the FA bond polymerization process, a pozzolanic reaction is formed which contributes to increase strength of BW.

Table 5. Compressive strength

Sample	MPa
BW	33.32
BWF1	35.48
BWF2	38.69
BWF3	43.22

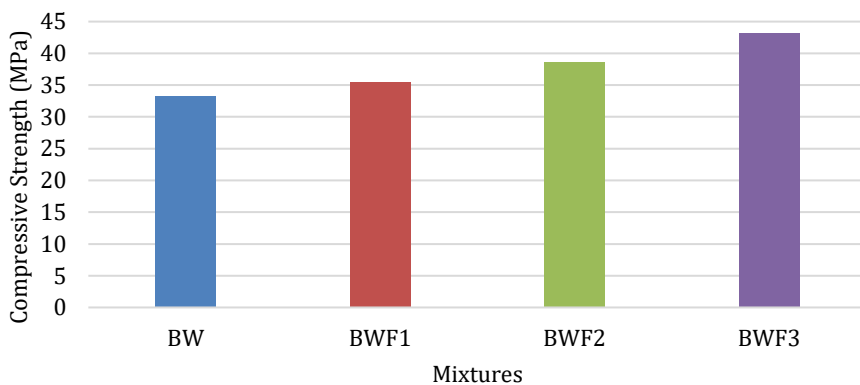


Fig. 5. Effect of addition FA on Compressive Strength BWF

The relationship between the increase in compressive strength and the increase in the number of FA is very strong. The correlation coefficient for the linear relationship is $R^2=0.9747$ according to Eq. (4)

$$y = 3.291x + 29.45 \tag{4}$$

From this relationship, the increase in compressive strength is directly related to the addition of FA, this causes the compressive strength to increase as a result of the reduced pore size of the concrete

3.3. Splitting Tensile Strength

In this case, the split tensile strength of BW with the addition of FA will be plotted in Figure 6. The highest split tensile strength value was obtained in the BWF3 composition with an FA content of 15%, with a split tensile strength value of 3.11 MPa. While the lowest split tensile strength value is in the BWF0 composition with 0% FA content with a split tensile strength of 3.04 MPa. This means that the addition of fly ash as a filler can increase the value of the split tensile strength of integral waterproofing concrete because adding fly ash as a filler or added material can improve the mechanical properties of concrete.

Table 6. Splitting tensile strength

Sample	MPa
BW	3.04
BWF1	3.07
BWF2	3.09
BWF3	3.11

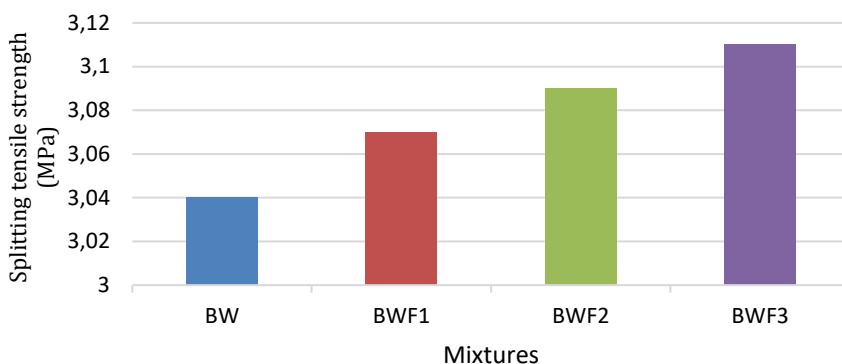


Fig. 6. Effect of addition FA on Splitting tensile Strength BWF

3.4. Modulus of Elasticity

Testing the modulus of elasticity of concrete was carried out on all samples of specimens used for compressive strength at the age of 28 days. The modulus of elasticity test is carried out until the concrete is completely destroyed. The results of the Stress–Strain test will be presented in Fig. 8, and the maximum average stress and strain can be seen in table 7. to get the value of the elastic modulus using Eq. (3)

Table 7. Strain (ϵ_{c1}) values Strain value of waterproofing integral concrete

Sample	σ_{cm} (MPa)	ϵ_{c1} (mm/mm)
BW	33.32	0.0017
BWF1	35.48	0.0021
BWF2	38.69	0.0027
BWF3	43.22	0.0029



Fig. 7. The setting for testing modulus of elasticity

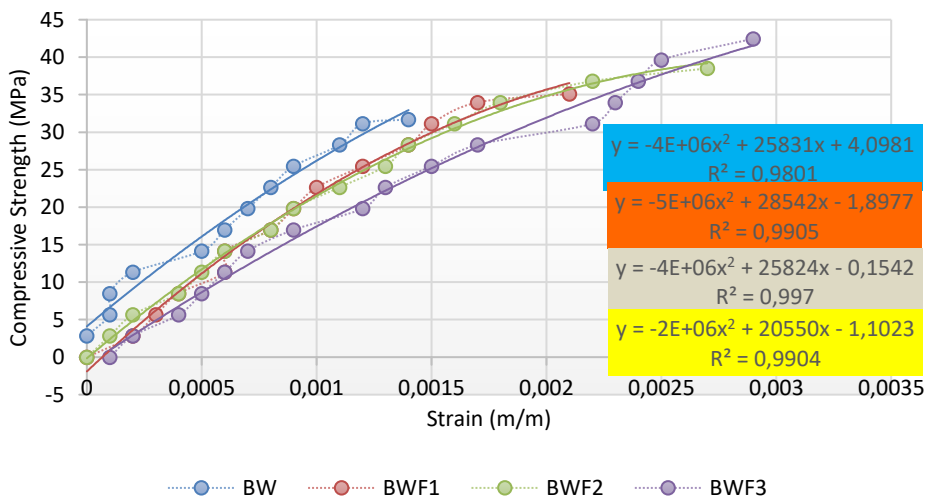


Fig. 8. Stress-strain diagram of 2nd order parabolic integral waterproofing concrete with additional FA variation

Fig. 8. shows the stress-strain relationship diagram of 2nd-order parabolic integral waterproofing concrete with an additional FA variation. To approach the σ_c - ϵ_c relationship using the Madrid parabola equation and Desay & Krishnan. In analyzing the modulus of elasticity follow the following steps (example BW):

- It is assumed from the second-order parabolic equation that the value of $E_c = 39.743,647$ MPa at $\sigma_{cm} = 33,32$ MPa. The value of E_c is obtained from the tangent twice the tangent to the angle formed by the line through the point $(\sigma_{cm}, \epsilon_{c1})$
- From the E_c above, it is graphed from the Madrid Parabola equation and the Desay & Krishnan equation
- Determine the stress value σ_1 at 0.00005 strain and determine the strain σ_2 at 0.4 σ_{cm}
- The new modulus of elasticity is obtained tangent from the straight line passing through $(\epsilon_{c2}, 0.4 \sigma_{cm})$ and $(0.00005, \sigma_1)$, $E_c = 34.680,189$ MPa (Parabola Madrid), $E_c = 37.818,252$ MPa (Desay & Krishnan)

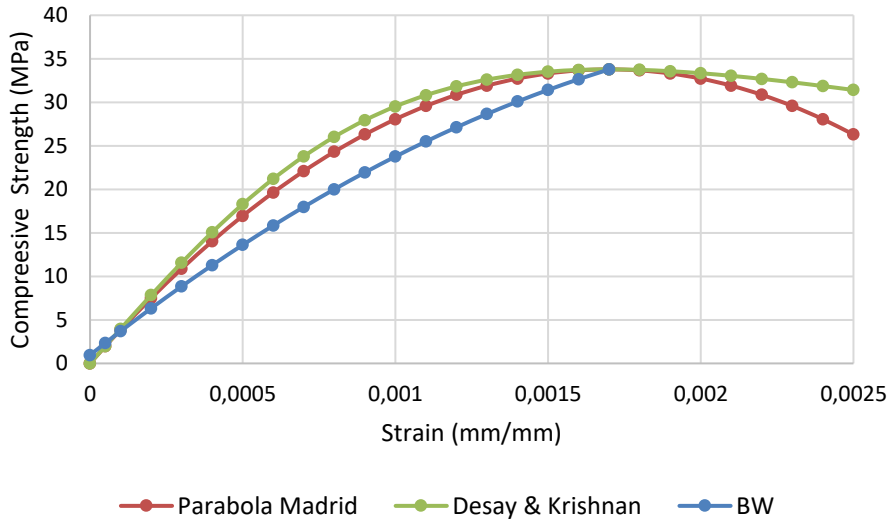


Fig. 9. Comparison of stress-strain diagram between BW concrete with Madrid Parabola and Desay & Krishnan

From the above calculation, the elastic modulus of waterproofing concrete with the addition of FA is obtained which is close to the Desay & Krishnan equation. Table 5. shows the value of the elastic modulus of several equations. With a proportion of 1.5%. Integral waterproofing concrete mix with fly ash filler variation of 0% to 15% differs from 28779.60 MPa to 37818.252 MPa (Desay & Krishnan). The results of the highest modulus of elasticity obtained the proportion of mixed waterproofing 1.5% with 0% fly ash filler. With the addition of fly ash, the behavior of the concrete will be more ductile. While the smallest elastic modulus was obtained compared to 1.5% waterproofing with 10% fly ash variation, on 1.5% fly ash variation the elastic modulus increased again. That the improvement of fly ash as an integral filler of waterproofing concrete can improve the behavior of concrete, increase its ductility and strength.[32,33]

The effect of fly ash composition on the modulus of elasticity of integral waterproofing concrete is shown in Figure 6. The equation obtained from this relationship is $y = 52.893X^2 - 1411.6X + 37573$ with $R^2 = 0.9908$. The addition of fly ash to the integral waterproofing concrete increases the performance of the waterproof concrete.[34,35]

Table 8. Modulus of Elasticity of Integral Waterproofing Concrete (MPa)

Sample	$E_c = \tan \beta = 2 \times \tan \alpha$	Parabola Madrid	Desay & Krishnan
BW	39743.647	34680.189	37818.252
BWF1	34276.667	30005.633	32664.106
BWF2	29933.778	26282.965	28589.563
BWF3	30127.034	26471.950	28779.605

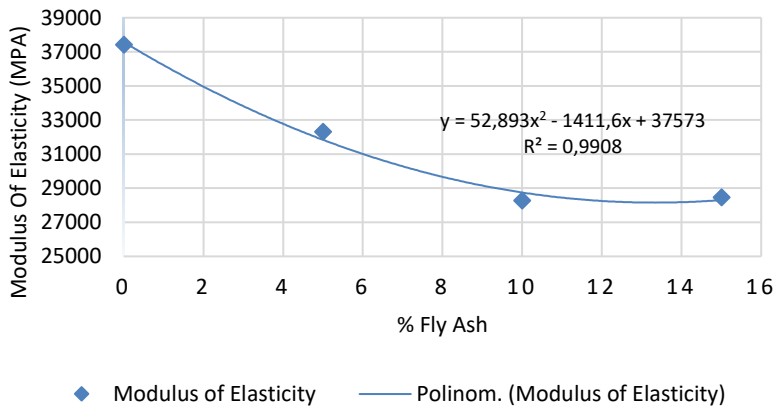


Fig. 10. Modulus of elasticity relationship with integral waterproofing concrete with the addition of fly ash

4. Conclusions

Several discussions about the integral waterproofing concrete result in decreased strength compared to normal concrete. This paper discusses the possibility of increasing the mechanical properties of integral waterproofing concrete with the addition of fly ash regarding the workability, strength, and modulus of elasticity of concrete. From this paper it can be concluded:

- The addition of FA is directly proportional to the slump value, with the highest slump value at 12 cm at 15% FA content (BWF3). The addition of fly ash to concrete waterproofing improves workability because the particle size is mostly spherical, resulting in better traceability.
- The use of 15% FA produces a compressive strength of 43.32 MPa, and an increase of 29.71% from integral concrete waterproofing without FA (BW) of 33.32 MPa. The polymerization process of silica on FA to form geopolymer chains is very important so that strong bonds in the polymer chains can reduce the pore diameter can increase their strength.
- BWF3 produces the highest split tensile strength of the others at 3.11 MPa and an increase of 2.3% compared to BW, which had a tensile strength of 3.04 MPa.
- The shape of the stress-strain relationship in the test with the FA variation tends to be close to the equation proposed by Desay & Khrisnan
- The greatest ultimate strain value occurs in BWF3 of 0.0029 mm/mm, and the lowest is in BW of 0.0017 mm/mm
- The elastic modulus values of BW, BWF1, BWF2, and BWF3 were 37818.252 MPa, 32664.106 MPa, 28589.563 MPa, and 28779.605 MPa respectively.

This conclusion reveals that it is possible to incorporate FA into construction and building materials using waterproofing, without significant changes to its mechanical properties, especially compressive strength. FA additives are cheaper than the addition of original portland cement or silica fume additives in maintaining the compressive strength of concrete by using waterproofing such as normal concrete compressive strength.[36]

Acknowledgement

The author would like to thank the Dean of the Faculty of Engineering, University of Jember, who has supported this work by borrowing tools from the structure laboratory.

References

- [1] Farfán M, Leonardo E. Caucho reciclado en la resistencia a la compresión y flexión de concreto modificado con aditivo plastificante.. *Rev ing constr.* 2018 Dec;33(3):241-50. <https://dx.doi.org/10.4067/S0718-50732018000300241>
- [2] Al-Rashed R, Jabari M. Dual-crystallization waterproofing technology for topical treatment of concrete. *Case Studies in Construction Materials.* 2020 Dec;13:e00408. <https://doi.org/10.1016/j.cscm.2020.e00408>
- [3] Li G, Huang X, Lin J, Jiang X, Zhang X. Activated chemicals of cementitious capillary crystalline waterproofing materials and their self-healing behaviour. *Construction and Building Materials.* 2019 Mar;200:36-45. <https://doi.org/10.1016/j.conbuildmat.2018.12.093>
- [4] Zhao L, Yao S, Huang X, Liu T, Qin F. Effect of Silicone Waterproofing Agent on the Properties of Ceramic Recycled Aggregate Cement Mortar. *IOP Conf Ser: Earth Environ Sci.* 2020 Aug 1;558(3):032007. <https://doi.org/10.1088/1755-1315/558/3/032007>
- [5] Waldvogel M, Zurbriggen R, Berger A, Herwegh M. Influences of temperature and opening rate of substrate cracks on the mechanical behaviour, crack-bridging ability and deformation mechanisms of one-component, cementitious, flexible waterproofing membranes. *Cement and Concrete Research.* 2020 Oct;136:106140. <https://doi.org/10.1016/j.cemconres.2020.106140>
- [6] Parah Salsabeel Jalal PSJ, Indra Kumar Pandey IKP, Ashok k Tiwari AkT, Vikas Srivastava VS. Effect of Waterproofing Systems and Materials on Environment. *J Environ Nanotechnol.* 2018;7(4):40-5.. <https://doi.org/10.13074/jent.2018.12.184326>
- [7] Meng T, Wei H, Ying K, Wang M. Analysis of the Effect of Nano-SiO₂ and Waterproofing Agent on the Water Transportation Process in Mortar Using NMR. *Applied Sciences.* 2020 Nov 6;10(21):7867. <https://doi.org/10.3390/app10217867>
- [8] Akinkulore O. Water Absorption, Sorptivity and Permeability Properties of Concrete Containing Chemical and Mineral Admixtures. *LAUJOCES.* 2021 May 1;6(2):118-127. <https://doi.org/10.36108/laujoces/1202.60.0201>
- [9] Gupta R, Biparva A. Do crystalline water proofing admixtures affect restrained plastic shrinkage behavior of concrete?. *Revista de la Asociación Latinoamericana de Control de Calidad, Patología y Recuperación de la Construcción.* 2017 Jan 31;7(1):15-24. <https://doi.org/10.21041/ra.v7i1.172>
- [10] Vijayalakshmi R, Babu DD, Mathivanan M, Sandeepkumar J, Boopathiraja V. Characteristic Study on Behaviour of Integral Crystalline Water Proofing Concrete. *International Research Journal Engineering and Technology.* 2018 June;5(6):542-546
- [11] Tuns I, Tamas FL, Mantulescu M. Waterproofing Solution of an Existing Basement

- Against Water Under Hydrostatic Pressure. Case Study. Bulletin of the Transilvania University of Braşov. 2017;10(59):211–218
- [12] Petrucci RDS, Hastenpflug D. Evaluation Of Crystalline Waterproofing Admixture On Portland Cement Concrete. Proceedings of International Structural Engineering and Construction. 2017 Jul;4(1). <https://doi.org/10.14455/ISEC.res.2017.95>
- [13] Sathe S, Zain Kangda M, Dandin S. An experimental study on rice husk ash concrete. Materials Today: Proceedings. 2023;77:724-8. <https://doi.org/10.1016/j.matpr.2022.11.366>
- [14] Subramaniam DN, Sathiparan N. Comparative study of fly ash and rice husk ash as cement replacement in pervious concrete: mechanical characteristics and sustainability analysis. International Journal of Pavement Engineering. 2022 May 20;1-18 <https://doi.org/10.1080/10298436.2022.2075867>
- [15] Nurtanto D, Junaidi I, Wahyuningtyas W, Yunarni W. Comparación de la adición de cenizas de cascarilla de arroz y cenizas de tejas a cemento de geopolímero en base a cenizas volantes con cemento Portland. Rev ing constr. 2020 Dec;35(3):287-94. <https://dx.doi.org/10.4067/S0718-50732020000300287>
- [16] Ojha PN, Singh B, Prakash S, Singh P, Mandre MK, Kumar S. Effect of high ratio fly ash on roller compacted concrete for dam construction. Res Eng Struct Mater. 2022;8(2):233–251. <https://doi.org/10.17515/resm2022.374ma1216>
- [17] YCheng Y, Cong P, Zhao Q, Hao H, Mei L, Zhang A, Han Z, Hu M. Study on the effectiveness of silica fume-derived activator as a substitute for water glass in fly ash-based geopolymer. Journal of Building Engineering. 2022 July;51:104228. <https://doi.org/10.1016/j.jobbe.2022.104228>
- [18] Liu C, Zhang W, Liu H, Zhu C, Wu Y, He C, et al. Recycled aggregate concrete with the incorporation of rice husk ash: Mechanical properties and microstructure. Construction and Building Materials. 2022 Oct;351:128934. <https://doi.org/10.1016/j.conbuildmat.2022.128934>
- [19] Amin M, Attia MM, Agwa IS, Elsakhawy Y, el-hassan KA, Abdelsalam BA. Effects of sugarcane bagasse ash and nano eggshell powder on high-strength concrete properties. Case Studies in Construction Materials. 2022 Dec;17:e01528. <https://doi.org/10.1016/j.cscm.2022.e01528>
- [20] Abdalla TA, Koteng DO, Shitote SM, Matallah M. Mechanical and durability properties of concrete incorporating silica fume and a high volume of sugarcane bagasse ash. Results in Engineering. 2022 Dec;16:100666. <https://doi.org/10.1016/j.rineng.2022.100666>
- [21] Amran M, Onaizi AM, Qader DN, Murali G. Innovative use of fly ash-finely powdered glass cullet as a nano additives for a sustainable concrete: Strength and microstructure and cost analysis. Case Studies in Construction Materials. 2022 December;17:e01688. <https://doi.org/10.1016/j.cscm.2022.e01688>
- [22] Yadav VK, Amari A, Wanale SG, Osman H, Fulekar MH. Synthesis of Floral-Shaped Nanosilica from Coal Fly Ash and Its Application for the Remediation of Heavy Metals from Fly Ash Aqueous Solutions. Sustainability. 2023;15(3):2612, <http://doi.org/10.3390/su15032612>
- [23] Nasir Amin M, Ur Rehman K, Shahzada K, Khan K, Wahab N, Abdulalim Alabdullah A. Mechanical and microstructure performance and global warming potential of blended concrete containing rice husk ash and silica fume. Construction and Building Materials. 2022 September;346:128470. <https://doi.org/10.1016/j.conbuildmat.2022.128470>
- [24] Aminu Alhaji M, Kumar Sharma P. Combined effects of rice husk ash and hybrid

- fibres on the fresh and mechanical properties of recycled aggregate concrete. *Material Today: Proceedings*. 2022;62(12):6695-6700. <https://doi.org/10.1016/j.matpr.2022.04.746>
- [25] Cho YK, Jung SH, Choi YC. Effects of chemical composition of fly ash on compressive strength of fly ash cement mortar. *Construction and Building Materials*. 2019 April;204:255-264. <https://doi.org/10.1016/j.conbuildmat.2019.01.208>
- [26] Shi S, Li H, Zhou Q, Zhang H, Basheer P, Bai Y. Alkali-activated fly ash cured with pulsed microwave and thermal oven: A comparison of reaction products, microstructure and compressive strength. *Cement and Concrete Research*. 2023 April;166:107104. <https://doi.org/10.1016/j.cemconres.2023.107104>
- [27] Bicer A. Effect of fly ash particle size on thermal and mechanical properties of fly ash-cement composites. *Thermal Science and Engineering Progress*. 2018 December;8:78-82. <https://doi.org/10.1016/j.tsep.2018.07.014>
- [28] Ojha P, Singh B, Trivedi A, Singh P, Singh A, Pede C. Short-term mechanical performance and flexural behavior of reinforced slag-fly ash-based geopolymer concrete beams in comparison to OPC-based concrete beams. *Research on Engineering Structures Materials*. 2023;9(1):31-51. <https://doi.org/10.17515/resm2022.515me0902>
- [29] Matar P, Barhoun J. Effects of waterproofing admixture on the compressive strength and permeability of recycled aggregate concrete. *Journal of Building Engineering*. 2020 November;32:101521. <https://doi.org/10.1016/j.jobe.2020.101521>
- [30] Wang D, Zhou X, Meng Y, Chen Z. Durability of concrete containing fly ash and silica fume against combined freezing-thawing and sulfate attack. *Construction and Building Materials*. 2017 August;147:398-406. <https://doi.org/10.1016/j.conbuildmat.2017.04.172>
- [31] Kmiecik P, Kamiński M. Modelling of reinforced concrete structures and composite structures with concrete strength degradation taken into consideration. *Archives of Civil and Mechanical Engineering*. 2011;11(3):623-636. [https://doi.org/10.1016/s1644-9665\(12\)60105-8](https://doi.org/10.1016/s1644-9665(12)60105-8)
- [32] Sarkar M, Maiti M, Malik MA, Xu S. Evaluation of the crack-healing performance and durability of bacteria integrated alkali-activated fly ash composites. *Journal of Building Engineering*. 2022 August;54:104642. <https://doi.org/10.1016/j.jobe.2022.104642>
- [33] Zhou Z, Li S, Cao J, Chen X, Wu Z, Zhou P. The waterproofing effect and mechanism of graphene oxide/silane composite emulsion on cement-based materials under compressive stress. *Construction and Building Materials*. 2021 November;308:124945. <https://doi.org/10.1016/j.conbuildmat.2021.124945>
- [34] Jalali UH, Afgan S. Analysis of Integral Crystalline Waterproofing Technology for Concrete. *International Research Journal of Engineering and Technology*. 2018;5(10):1076-1085.
- [35] Zhao L, Zhang M, Chen H, Xue Q, Huang Q, Zhao M. Effect of Silicone Waterproofing Agent on Properties and Microstructure of Fly Ash-cement Based Wall Insulation Materials in High-humidity Environment. *Silicon*. 2022; 14(12):6873-6879. <https://doi.org/10.1007/s12633-021-01468-8>
- [36] Omale RP. Comparative Analysis of Concrete Water-Proofing Materials. *Journal of Civil Engineering Research & Technology*. 2022;4(1):1-9. [https://doi.org/10.47363/ICERT/2022\(4\)122](https://doi.org/10.47363/ICERT/2022(4)122)

Blank Page



Technical Note

Investigation of normal concrete properties with the addition of micro reinforcement

Andi Yusra^{*1,a}, Hesti Meliana^{2b}, Lissa Opirina^{1,c}, Andrisman Satria^{1,d}

¹Department of Civil Engineering, Teuku Umar University, Meulaboh, Indonesia

²Department of Chemical Engineering, Syiah Kuala University, Banda Aceh, Indonesia

Article Info

Abstract

Article history:

Received 18 Feb 2023

Accepted 16 May 2023

Keywords:

Micro Reinforced;
Variety of additions;
Concrete Strength;
FTIR Analysis;

The research on concrete is currently developing very rapidly. One of them is research on concrete with micro reinforcement. This study aims to find out how much influence the variations in micro reinforcement used have on the strength of concrete. This study was conducted with variations in the percentage of addition of micro reinforcement with various types of micro reinforcement. In this study, FTIR analysis was also carried out to determine the absorption area and group of micro reinforcement compounds. The micro reinforcement used is Jute, Bamboo, Rattan and Plastic with an additional percentage of 0.5%; 1%; 1.5% and 2% against the weight of cement. The test was performed at the age of 28 days, with a compressive strength test. The results showed that there was a significant influence on the compressive strength of non-micro reinforcing concrete compared to micro reinforcing concrete. The optimal compressive strength of concrete with the addition of micro reinforcement (Bamboo/Rattan) was obtained in concrete with a percentage of 1.5% with an optimum compressive strength of 23.31 MPa, plastic reinforcement 22.93 MPa (addition of 1.5%), rattan micro reinforcement 22.93 MPa (addition of 2%), and hemp micro reinforcement (addition of 2%) 20,665 MPa. The results of the FTIR analysis form of the compound group and the most optimal absorption area in micro reinforcement micro-compound groups of bamboo and rattan reinforcement has 3 peaks with the form O - H, C - H and CH₂. When compared to compound groups in concrete without micro reinforcement, it only has 2 compound groups, namely, O - H and CH₂ only.

© 2023 MIM Research Group. All rights reserved.

1. Introduction

The Research about material micro reinforced which has good tensile strength, so it is expected to add ductility to normal concrete, increase compressive and tensile strength to make it more resistant to cracking. The use of rattan as a micro-reinforced material is intended to minimize the impact of poor concrete properties, including having a high enough specific gravity so that it will cause a loading effect due to its own weight. Plastic waste is used as a fine aggregate in varying amounts in burlap fiber reinforced concrete to test its suitability. The use of plastic waste as a substitute for fine aggregates. Since plastic bottles are harmful to the environment and human health, using them in concrete will help protect the environment and human health. The main component of concrete is the partial replacement of fine aggregates and coarse aggregates. Plastic fibers are artificial fibers used in concrete to increase the split tensile strength and bending strength of concrete (1), (2), (3).

*Corresponding author: andiyusra@utu.ac.id

^a orcid.org/0000-0003-4779-0815; ^b orcid.org/0000-0002-7620-5550; ^c orcid.org/0009-0003-4495-9723;

^d orcid.org/0000-0002-8870-9852

DOI: <http://dx.doi.org/10.17515/resm2023.693ma0218>

Res. Eng. Struct. Mat. Vol. 9 Iss. 3 (2023) 875-884

Micro Reinforced Concrete as a composite material consisting of ordinary concrete and other materials in the form of Micro Reinforced (rods with a diameter between 0.10 and 0.20 mm with a length of about 20 mm to 50 mm). The addition of micro reinforced material to concrete is intended to correct the weakness of the properties possessed by concrete, that is, it has low tensile strength (4), (5), (6), (7), (8). One of the important properties of concrete is ductility. Ductility i.e. the ability of a structure or its components to perform repeated alternating inelastic deformations beyond the limits of the first melting point, while maintaining a large amount of its load carrying capacity (9). The addition of micro reinforced material to concrete is to increase the energy absorption capacity of the mixed matrix, which means to increase the ductility of concrete. The addition of ductility also means the addition of concrete behavior to fatigue and shock. Micro Reinforced Concrete has advantages over micro reinforced concrete in several structural properties including ductility, resistance to shock loads (impact resistance), tensile and bending strength (tensile and bending strength), fatigue (fatigue life), resistance to shrinkage and resistance to wear (abrasion) (8), (10). Observations of various stress curves of various concrete strengths, show that generally the maximum compressive strength is *achieved* when the unit value of the ϵ' compressive strain reaches 0.002, then the value of the f'_c stress will decrease with increasing the value of the crushed test object strain at the value of ϵ' reaching 0.003-0.005. High strong concrete is more fragile and will disintegrate at a lower maximum strain value compared to low strong concrete. In concrete testing it was established that the maximum working strain taken into account on the outermost compressed concrete edge of Micro Reinforced was 0.003 as the crushed limit (9). The maximum working strain of 0.003 may not be conservative for high strong concrete with an f'_c value between (11). The addition of Micro Reinforced to normal concrete can increase the pressure at peak loads. Fibrous concrete can absorb more energy than normal concrete before crushing (12), (13), (5), (14), (15), (16), (17). Micro-Reinforced Contribution to stress – concrete strain is distinguished by two types (18), (19), (31), namely: 1). Micro reinforced materials are very fragile with matrices, shown in Figure 1 where it appears that the shrinkage of matrix collapse is much greater than the collapse strain of micro-reinforced materials. 2). A very strong micro-reinforced material with a brittle matrix shown in Figure 1 shows that the matrix limit strain capacity is lower than the micro-reinforced strain capacity. The matrix will collapse before the full potential of the micro-reinforced work, the matrix that has been cracked is held back by Micro Reinforced that contributes energy through the bonding process and the reinforced micro is pulled out. The figure is a curve of the relationship between the pressure on Micro Reinforced concrete and the brittle matrix.

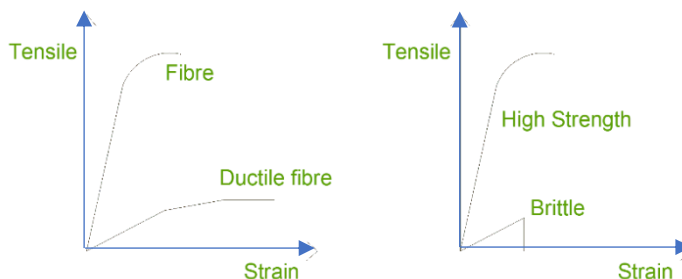


Fig. 1 Micro reinforced concrete stress-strain curve with visage matrix (31)

When the micro-reinforced material begins to be uprooted or damaged, the slope of the curve may reach zero, and the capacity of the ability to carry the load begins to decrease. This type of collapse allows maximum utilization of Micro Reinforced properties and

matrices. As a result of comparison, Figure 2 below is the data obtained from the results of a study entitled The Use of Micro Reinforced Rattan to Improve Concrete Quality, (29).

Concrete Fibre Strength

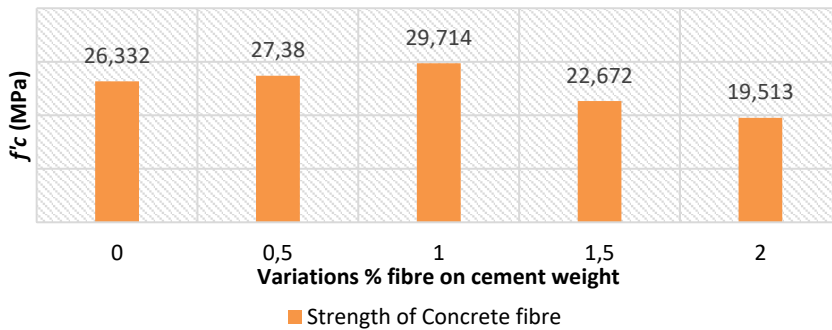


Fig. 2 The relationship of compressive strength and the percentage of micro reinforcement, [29]

The optimum load was found in the 1% Micro Reinforced rattan variation of 29,714 MPa and experienced a decrease in load if added greater than 1%. Micro Reinforced Concrete with the addition of additive ash boiler scale is made using Micro Reinforced empty oil palm bunches and boiler scale obtained from one of the palm oil processing plants in the Purwodadi Kuala Pesisir area of Nagan Regency (20). Test the average compressive strength of cylindrical concrete with the addition of empty bunches of palm micro-reinforced on concrete with a life ratio of 0% for 28 days each of 31.85 MPa. At 4% Micro Reinforced is 25.89MPa. Then 5% Micro Reinforced concrete is 26.23 MPa. In 6% micro reinforced concrete is 28.78MPa. In 7% concrete, Micro Reinforced is 30,384 MPa. At 8% of micro reinforced concrete is 30.57 MPa. The crack patterns that occurred in this study were shear and columnar crack patterns. All in all, it can be seen that the compressive strength of concrete has increased, although it is still below the normal concrete compressive strength, it is getting bigger and bigger than f'_c 25Mpa, and can be used as structural concrete (21). This shows that the more Micro Reinforced rattan is added, the less work ability of the concrete mixture. From the testing of concrete compressive strength, concrete tensile strength, and bending strength of concrete blocks, the highest concrete strength addition result on the addition of Micro Reinforced rattan is 1% of the weight of cement. The compressive strength of concrete has increased by 12.84% from normal concrete. The tensile strength of split concrete has increased by 22.17% from normal concrete. For the bending strength of concrete blocks experienced an increase of 9.69% from normal concrete (21). Rattan was chosen to be developed because in general rattan has good natural strength, is flexible and lightweight in dry conditions. Based on the results of research that has been carried out, the results obtained that rattan material with epoxy resin lamination has a compressive strength of 46.8MPa increased by 47.2% when compared to the compressive strength of rattan without lamination of 31.8MPa. The average impact strength of rattan test results before lamination with epoxy resin was 39 kJ/m² and after going through the lamination process increased by 64% to 64 kJ/m² (22).

Preservatives used to preserve micro reinforcement are boron and CCB (copper-chrome-boron) with cold bath modifications and the Boucherie method. Endurance testing refers to (23). The test results showed that boron is effective on petung bamboo to increase resistance to soil termites, dry wood termites, as well as weathering fungi, while for resistance against dry sawdust beetles, the effectiveness of boron and CCB is almost

equivalent (24). Natural fibers outperform synthetic fibers in mechanical properties, are cheaper, come from renewable resources, and are recyclable. As a result, partially replacing Meta kaolin for Portland cement reduces CO₂ emissions while extending the life of the structure. In this study, concrete was tested by Meta kaolin cement replacement and the addition of burlap fiber. The percentage of burlap fiber added is 0%, 1%, 2%, 3%, 4%, 5%, and 6%. The percentage of meta kaolin replacement is 0%, 3%, 6%, 9%, 12%, 15%, and 18%. Prepare a new mixture with 5% meta kaolin and a different percentage of Jute Fiber after analysis. The concrete value used in the analysis is M35 (25). Micro reinforcement is commonly used in the resistance and reinforcement of concrete cracks. Various fibers are usually used in concrete mixes to achieve the desired strength and resistance. Recently, in response to the problem of global warming and the need for a more sustainable society, manufacturing with natural ingredients has become more active in developing countries. Bamboo, with its low cost, rapid growth, and wide growth distribution, is expected to make a significant contribution to earthquake-resistant construction and seismic retrofit technology in developing countries. The authors investigated the mechanical behavior of bamboo fiber reinforced concrete members. The possibility of using 'Bamboo' effectively is discussed based on the results of this experiment. Similarly, results for the aspect ratios of different fibers were obtained, revealing that there is an aspect ratio of 40. An increase in the weight fraction of the fiber results in a consistent increase in ductility to the optimal content (1.0%), with a fiber aspect ratio of 40. Overall, the study found that adding bamboo micro reinforcement to concrete increases concrete strength, toughness, torque, and tensile stress. More research is needed to determine the long-term durability of concrete enhanced with bamboo micro reinforcement (26). The addition of micro reinforced materials changes a lot in the behavior of concrete after cracking, for example, there is an increase in tensile strain after concrete collapses, resulting in harder and more impact-resistant concrete. The increase in concrete hardness is strongly influenced by the concentration of Micro Reinforced and the resistance of Micro Reinforced to tensile which is mainly determined by the comparison of Micro Reinforced aspects (length/diameter ratio) and other factors such as surface shape and texture. Micro Reinforced concrete mix planning is determined based on (15). The use of Micro Reinforced in concrete mixtures is carried out after the soaking process using a solution of Sodium Hydroxide (NaOH) against micro reinforced rattan which functions to separate the dirt on the Micro Reinforced and avoid easy printing. Compressive strength is the ability of concrete to accept extensive unification compressive force. The compressive strength of concrete identifies the quality of a structure. The higher the desired strength of the structure, the higher the quality of the concrete produced (4). The compressive strength value of concrete is obtained from standard tests with a commonly used test object in the form of a cylinder. The dimensions of the standard test piece are 300 mm high, 150 mm in diameter. The compressive strength of each test piece is determined by the highest compressive (f'_c) that the test piece reaches a lifespan of 28 days due to the compressive load during the experiment. Concrete will have high compressive strength if it consists of good quality local materials. The constituent material of concrete that needs attention is that the aggregate reaches 70 - 75% of the volume of concrete (11). Tensile testing is a method of determining the strength of a material by applying a force load. Tensile test results are critical for product engineering and design as they produce material strength data. Tensile testing is used to determine the resistance of a material to slow-applied static forces. Tensile tests are usually used to supplement basic design information on material strength and as supporting data for material specifications. The tensile test curve reveals the strength and elasticity values of the test material (4). Based on the results of research conducted by the tensile strength of rattan parallel to Micro Reinforced shows a fairly high value of 481.99 kg / cm². This rattan strength has the potential to be used for building purposes, namely concrete with high tensile strength (1).

2. Material and Methods

In the treatment carried out on specimens, it is to add a varying percentage of micro reinforcement, with various types of micro reinforcement, namely: Bamboo / Rattan, Gowon, Rattan and Plastic. In this second treatment, the variation in the percentage of micro reinforcement addition was 0; 0.5; 1; 1.5; and 2%. Micro bamboo and rattan reinforcement is made by shaving so that the results of bamboo rattan shavings are long but small in diameter or square size of about 1 mm x 2 mm. The shavings are then cut into pieces with a machete so that they have a length of 20 mm. The treatment of microplastic and hemp reinforcement was also cut by 1 mm x 2 mm x 20 mm. The press weight of the plan is 25MPa for a cylinder test piece measuring 15/30 cm using a cement water factor (w/c) of 0.52. The coarse aggregation used is natural stone with a maximum aggregation diameter of 19 mm. The design of the normal concrete mixture uses the method (7), which requires a concrete design mixture taking into account its economic side and paying attention to the availability of materials in the field, ease of work, as well as the durability and strength of concrete work. Figure 3 shows the variety of different types of micro reinforcement.



Fig. 3 Micro Reinforcement Bamboo (a) and Hemp (b)



Fig. 4 Micro Plastic Reinforcement (a) and Rattan (b)

FTIR tests are performed to determine the chemical bonding information of bamboo. Such chemical bonds are indicated by distinct peaks. This test was performed for the first time to measure the bond between Betung bamboo fibers (*Dendrocalamus asper*) and rattan fibers. Here's how FTIR works:

The beginning of the substance to be measured is identified in atomic or molecular form. Infrared light, which acts as a light source, is split into two beams, one passing through the

sample and one passing through the reference beam. Then pass through the chopper. After passing through a prism or diffraction grating, the beam hits a detector and is converted into electrical signals and recorded by a recorder. An amplifier is also needed if the generated signal is very weak, (27).

The standard used is ASTM E1252 (30). Samples that can be easily tested with FTIR include polymer pellets, parts, opaque samples, fibers, powders, wire coatings and liquids. A typical infrared scan is produced in the mid-infrared portion of the light spectrum. The mid-infrared region has wave numbers between 400 and 4000 cm⁻¹, corresponding to wavelengths between 2.5 and 25 microns (10-3 mm). The Figures 3 and 4 show the shape and type of micro reinforcement used in fresh concrete mixtures. Successively 3(a) is bamboo micro-reinforcement; 3(b) Hemp micro reinforcement, 4(a) plastic micro reinforcement, and 4(b) rattan micro reinforcement. The dimensions of micro reinforcement are 2 mm x 2 mm x 30 mm.

4. Results and Discussion

Figure 5 tends to show almost the same graphic pattern in concrete with the addition of micro reinforcement, i.e. the strength of concrete decreases with the addition of micro reinforcement of 0.5 – 1 % and the strength of concrete increases again in increments of 1.5 and 2%. There is a difference with the results of the study (14), (15), (16), (29), where the most optimal concrete strength is in the addition of 1.5% fiber. This is thought to be related to the dimensions of the fibers or reinforcement used which are different from the micro reinforcement used in this study. When compared with the test object in the first treatment, the compressive strength obtained was greater than the study (14), (15), (16), (29), with an optimal compressive strength obtained of 29.714 MPa (1% fiber addition). Figure 5 shows the optimum compressive strength in the addition of micro reinforcement of 1.5% with a compressive strength obtained of 23.21 MPa, when compared to non-micro reinforcing concrete having a compressive strength of 22.65 MPa.

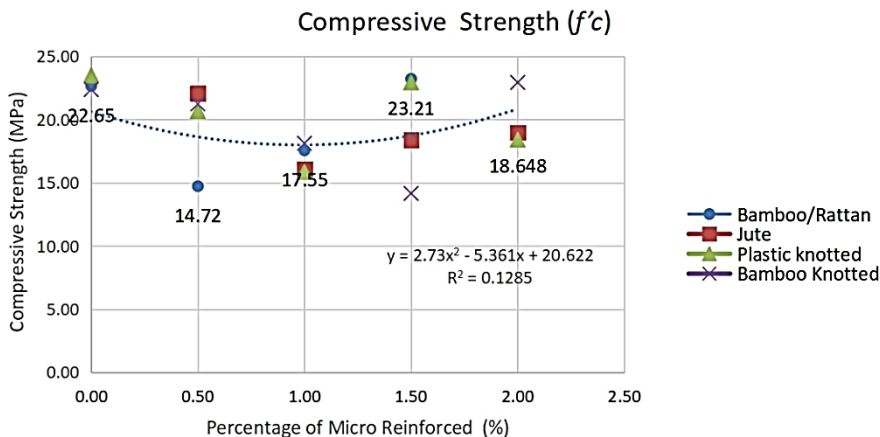
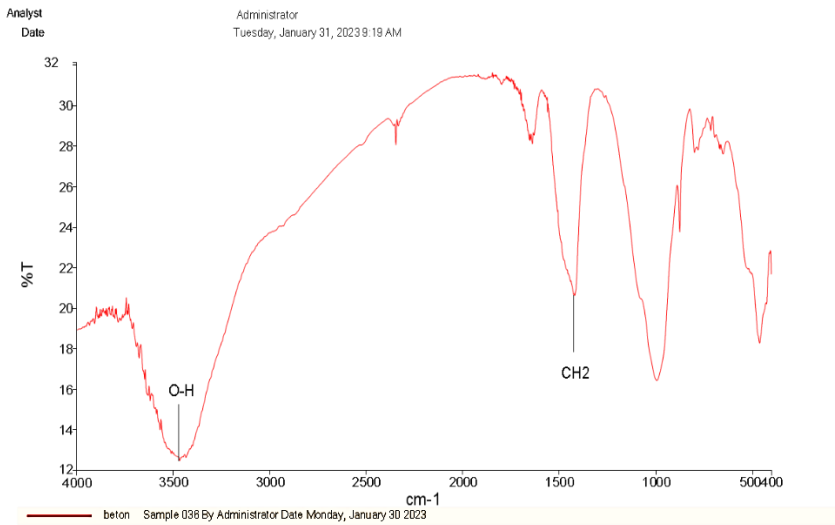


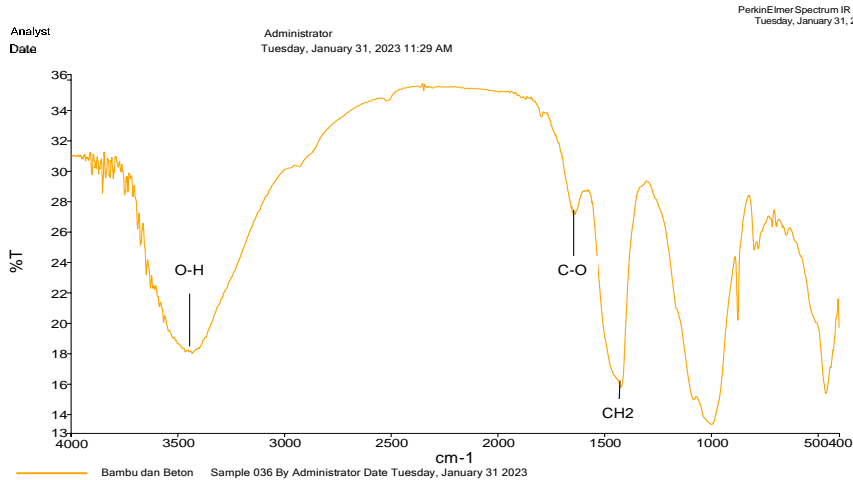
Fig. 5 Graph of the relationship of Percentage of Micro Reinforcement with concrete compressive strength



Tabel 1.
Daerah Serapan Infra Merah Beton

Daerah Serapan (cm ⁻¹)	Ikatan dan Jenis Gugus Fungsi
3467.97	O-H Stretching
1419.71	CH2 Banding

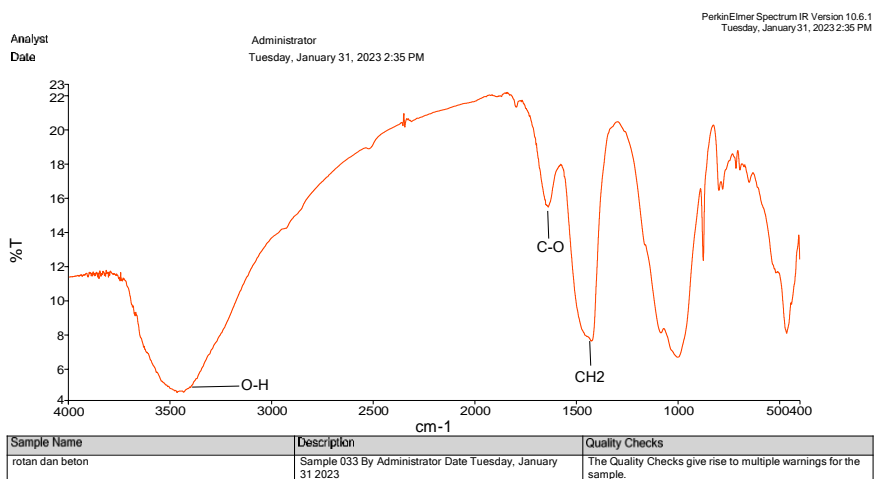
Fig. 6 Graph of Groups of micro non-reinforcing concrete compounds



Tabel 1.
Daerah Serapan Infra Merah Bambu +Beton Interpretation

Daerah Serapan (cm ⁻¹)	Ikatan dan Jenis Gugus Fungsi
3435.09	O-H Stretching
1638.43	C-O Stretching
1424.13	CH2 Banding

Fig. 7 Graph of Bamboo micro reinforcing concrete Compound Group



Tabel 1. Daerah Serapan Infra Merah Rotan +Beton Interpretation

Daerah Serapan (cm-1)	Ikatan dan Jenis Gugus Fungsi
3467.24	O-H Stretching
1638.33	C-O Stretching
1424.75	CH2 Banding

Fig. 8 Rattan micro reinforcing concrete Compound Group Graph

From the results of FTIR analysis we can see in Figure 6,7, and 8 Compound groups and peaks of the Chart. It shows the shape of the graph is almost the same but the transmittance value is different where non-micro reinforcing concrete has a higher transmittance value than micro reinforcement, bamboo and rattan. Then it can be seen that the absorption area is almost the same in the area of 3400 cm-1. For micro-compound groups of bamboo and rattan reinforcement has 3 peaks with the form O - H, C - H and CH2. When compared to compound groups in concrete without micro reinforcement, it only has 2 compound groups, namely, O - H and CH2 only.

5. Conclusions

Based on the results of data processing and discussion, the conclusions that can be drawn from the results of additional micro-research are strengthened on the strength of concrete. The optimal compressive strength of concrete with the addition of reinforced micro (Bamboo/Rattan) was obtained on concrete with a percentage of 1.5% with an optimum compressive strength of 23.31MPa, plastic 22.93MPa (addition of 1.5%), rattan 22.93MPa (addition of 2%), and Burlap (addition of 2%) 20,665MPa. It can be concluded from several variations of the addition of micro reinforcement obtained optimum compressive strength in concrete with micro reinforcement (Bamboo and Rattan), with a percentage of micro reinforcement addition of 1.5% to the weight of cement. Infrared spectra can provide information about functional clusters in compounds. Figure 6, i.e. the fiber-free concrete sample, has absorption peaks at wave number 3467.97, i.e. alcohol-phenol (H-bond) and carboxylic acid, and several peaks in the fingerprint region below 1300 cm⁻¹. Based on the nature of molecular vibrations, there are types of stretching vibrations and bending vibrations, the absorption range of stretching vibrations is in the range of wavenumbers (cm⁻¹) > 2500, and bending vibrations (bending) are in the range of wavenumbers < 2500 (cm⁻¹) range. 1500 cm⁻¹. The absorption region peaks at 2467.97 can be interpreted as an OH stretching group with an alcohol-phenol bond (H-bond) or as a carboxylic acid due to the broadening of the spectral shape. A CH2 bend appears in the peak at 1419.71 cm⁻¹ and alkanes have spectra in this region. In Figure 8 (concrete + rattan) a peak C = O appears,

extending to a wavelength of 1638.33 cm^{-1} . Presence of double bonds and/or aromatic rings. In Figure 7, the C=O bond occurs in the range 1750 to 1625 cm^{-1} where the C=O bond is a carbon group in which a functional group consisting of carbon atoms is double-bonded to an oxygen atom. The presence of peak C=O gives a specific indication of the presence of carboxylic acid in the peak at 3467.97 cm^{-1} . Since the reactivity of oxygen is more electronegative than carbon, the electron density is attracted to carbon, increasing the polarity of the bond. Of the three septa, adding rattan and bamboo to concrete results in a C=O bond.

Acknowledgement

The author expressed his gratitude to colleagues at Teuku Umar University. We also express our deepest gratitude to the research members who have helped a lot in the implementation of this research. From the initial process of making test objects, testing so that the data analysis process. So that the results of the data analysis the author can create articles that can be published in international journals with international reputation or indexed by Scopus. This research was financed by LPPM – Teuku Umar University with contract no: 013/UN59.7/SPK-PPK/06 June 2022.

References

- [1] Abdurachman A, Jasni J, Pari R, Satiti ER. The Classification Of 23 Types Of Indonesian Rattan Is Based On The Density And Tensile Strength Parallel To The Fibers. *J Forest Has Research*. 2017 Apr 14;35(1):43-52. <https://doi.org/10.20886/jphh.2017.35.1.43-52>
- [2] Salusu HD, Waldini VA, Patulak IM, Sari NM, Nurmarini E, Yusuf A, et al. Study of Physical Properties, Mechanics and Keaw Etan Rattan Manau (Calamus manan Miq.) that has gone through the cooking oil frying process. *Bul Poltanesa*. 2022; 23(2):725-730 <https://doi.org/10.51967/tanesa.v23i2.1975>
- [3] Senthil KK, Venkatachalam K, Bhakya K, Sharmidha B, Kalaivani M, Devi SG. Growth and characterization of picolinium maleate (PM) crystals. In: *AIP Conference Proceedings*. AIP Publishing LLC; 2020. p. 100014.
- [4] Mulyono T. *Concrete technology*. Yogyakarta Andi Offset. 2003;
- [5] Van CN. Steel fiber reinforced concrete. In: *Faculty of Civil Engineering Ho chi minh City university of Technology Seminar Material*. 2004. p. 108-16.
- [6] SF J. *JCI Standards for test methods of fiber reinforced concrete* S. Japan Concrete Institute, Tokyo; 1983.
- [7] Committee ACI. *State of the Art Report in Fiber Reinforced Concrete*. ACI Am Concr Inst Farmington Hills MI USA. 1982;
- [8] Tellu AT. Cladistics of some rattans (*Calamus* spp.) from Central Sulawesi based on physical and mechanical characteristic of stems. *Biodiversitas J Biol Divers*. 2006 Apr 30;7(3). <https://doi.org/10.13057/biodiv/d070306>
- [9] Yasir K, Adriana R, Pramitha K. Comparison of Earthquake Resistant Building Design Based on SNI 1726-2012 and SNI 2847-2013 with SNI 1726-2019 and SNI 2847-2019. Case Study of Indonesian International Islamic University (UIII) Student Apartment Building. In: *Proceedings of the 1st International Conference on Contemporary Risk Studies, ICONIC-RS 2022, 31 March-1 April 2022, South Jakarta, DKI Jakarta, Indonesia*. 2022. <https://doi.org/10.4108/eai.31-3-2022.2320967>
- [10] Odeyemi SO, Adisa MO, Atoyebi OD, Wilson UN, Odeyemi OT, Odeyemi SO, et al. Optimal water-cement ratio and volume of superplasticizers for blended cement-bamboo leaf ash high-performance concrete. 2022; <https://doi.org/10.17515/resm2022.382ma0108>
- [11] Dipohusodo I. *Reinforced Concrete Structures*. PT Gramedia Pustaka Utama Jkt. 1994;

- [12] Astawa MD. Struktur Beton Fiber (Bagian Materi Struktur Beton I). Surabaya; 2016.
- [13] Bentur A, Mindess S. Fibre reinforced cementitious composites. 2nd ed. London ; New York: Taylor & Francis; 2007. 601 p. (Modern concrete technology series). <https://doi.org/10.1201/9781482267747>
- [14] Paradava DD, Pitroda J. Utilization of Artificial Fibres In Construction Industry: A Critical Literature Review. Int J Eng Trends Technol. 2013; 4:4311-4319.
- [15] Turk K, Kina C, Oztekin E. Effect of macro and micro fiber volume on the flexural performance of hybrid fiber reinforced SCC. Adv Concr Constr. 2020;10(3):257-69.
- [16] Jain D, Kothari A. Hair fibre reinforced concrete. Res J Recent Sci ISSN. 2012; 2277:2502.
- [17] Skazlić M, Bjegović D. Toughness testing of ultra high performance fibre reinforced concrete. Mater Struct. 2009; 42:1025-38. <https://doi.org/10.1617/s11527-008-9441-3>
- [18] Ramadoss P, Nagamani K. Investigations on the tensile strength of high-performance fiber reinforced concrete using statistical methods. Comput Concr. 2006;3(6):389-400. <https://doi.org/10.12989/cac.2006.3.6.389>
- [19] Kishore IS, Chowdary CM. Influence of Steel Fibers as Admix in Normal Concrete Mix. Int J Civ Eng Technol. 2016;7(1): 93-103.
- [20] A. Nindiani, O. Suparno, and E. Anggraeni, "The challenge of bamboo craft industry in the VUCA era," in IOP Conference Series: Earth and Environmental Science, IOP Publishing, 2022, p. 012046 <https://doi.org/10.1088/1755-1315/1063/1/012046>
- [21] Opirina L, Azwanda A, Febrianto R. Analysis of The Mechanical Properties of Concrete Based on Fly Ash and Palm Oil Clinkers. Int J Eng Sci Inf Technol. 2021 Nov 3;1(4):31-5. <https://doi.org/10.52088/ijesty.v1i4.148>
- [22] Yusra A, Salena IY, Sari DP, Asrianur A. The Influence of Rattan Fibre Addition to The Compressive Strength of Normal Concrete. In: IOP Conference Series: Earth and Environmental Science. IOP Publishing; 2021. p. 012019. <https://doi.org/10.1088/1755-1315/832/1/012019>
- [23] Irawan AP, Daywin FJ. Peningkatan Kekuatan Tekan dan Impak Material Rotan Dengan Proses Laminasi Resin Epoksi, 2023.
- [24] Jasni J. Natural Durability Of 57 Species of Indonesian Wood with Testing Under Shade. J Forest Has Research. 2016 Sep 30;34(3):179-88.
- [25] Wardiha MW, Agustiningtyas RS, Sumawa I. The effectivity of preservative treatment in petung bamboo dan gewang using boron and CCB by cold soaking and modified Boucherie methods. Jurnal Penelit Hasil Hutan. 2018;36(2):159-70. <https://doi.org/10.20886/jphh.2018.36.2.159-170>
- [26] Anand I, Verma A, Dubey MK, Raj DV, Sethy SK. Analysis of Physical Properties of Concrete With Jute Fibre Reinforced Concrete With Partial Replacement Of Cement With Metakaolin. Int J Mech Eng. 2022; 7(4):1819-1833.
- [27] Kavitha S, Kala TF. Effectiveness of bamboo fiber as a strength enhancer in concrete. Int J Earth Sci Eng. 2016;9(03):192-6. <https://doi.org/10.17485/ijst/2016/v9i31/95347>
- [28] Pambudi A, Farid M, Hakim JAR. Morphological Analysis and Infrared Spectroscopy of Betung Bamboo Fiber (Dendrocalamus Asper) Results of the Alkalization Process as a Composite Booster for Sound Absorption.
- [29] M. D. Fauzan, (The Usage Of Rattan Fiber To Improve The Concrete Quality), Yogyakarta: Universitas Islam Indonesia, 2018.
- [30] ASTM E2809, Standard Guide for Using Scanning Electron Microscopy/X Ray Spectrometry in Forensic Paint Examinations, Annual book of ASTM Standards, Vol.08.01, American Society for Testing and Materials (ASTM), Philadelphia, USA.
- [31] Balaguru, Fiber Reinforced Cement Composite, New York: McGraw-Hill International Editions, 1992.



Research Article

Mechanical behavior and fractography analysis of Zn-Sn alloy matrix composites reinforced with nano B₄C particles

Santosh V Janamatti^{1,a}, Veerabhadrappa Algur^{2,b}, Madeva Nagaral^{3,c}, V Auradi^{4,d}

¹Dept. of Mechanical Eng., Ballari Institute of Technology and Management, Ballari, Karnataka, India

²Dept. of Mechanical Eng., Rao Bahadur Y Mahabaleswarappa Engineering College, Ballari, Karnataka, India

³Aircraft Research and Design Centre, HAL, Bengaluru, Karnataka, India

⁴Department of Mechanical Engineering, Siddaganga Institute of Technology, Tumakuru, Karnataka, India

Article Info

Article history:

Received 13 Dec 2022

Accepted 13 Mar 2023

Keywords:

Zn-Sn Alloy;

B₄C;

Stir Casting;

Hardness;

Tensile Strength;

Impact Strength

Abstract

The effect of nano-sized B₄C particulates on the Zn85-Sn15 alloy has been investigated. Composites reinforced with B₄C of (0%, 2%, 4% and 6%, by weight) are manufactured by two step stir casting. Microstructural studies carried out by SEM, EDS, and XRD and mechanical testing like tensile, hardness, and impact were performed on cast samples. The criteria for determining strength and fractography are met. EDS analysis confirms the homogeneous distribution of B₄C particles in the Zn-Sn matrix seen in SEM micrographs. XRD examination revealed the B₄C phases in the Zn-Sn alloy matrix as well. When B₄C reinforcement is added to the basic matrix alloy, it improves its hardness and tensile strength with slight decrease in the ductility and impact strength. Further, tensile and impact fractured surfaces were studied to know the different fracture mechanisms.

© 2023 MIM Research Group. All rights reserved.

1. Introduction

Materials are the starting point for determining human age and the ability to meet daily demands. For a long time, people have had access to and used materials. We can understand that human advancements are about human usage and utilization of materials for social beneficial capacities, research, and innovation if we focus on the historical environmental variables of human growth [1].

As a novel material system, metal matrix composites (MMCs) have staked a claim in a wide variety of engineering fields. Domain-specific applications for these materials can be found in a variety of fields, such as transportation, aerospace, and medicine. Increased strength, increased stiffness, resistance to corrosion and wear, superior damping characteristics, a low coefficient of thermal expansion, etc. are just some of the properties that can be combined in metal matrix composites.

It exemplifies humanity's ability to comprehend and alter nature. When a new process for creating material is developed, the benefit will also increase dramatically, and human culture will advance [2, 3]. As a result, materials have evolved into a picture of human progress and have progressed toward being achievements for separating periods of human history. B₄C nanoparticles were supported to Zinc-compound composite using a liquid metallurgical course, in which the blending strategy was accomplished while pouring the particles to avoid agglomeration of particulates and to achieve a normal homogeneous dispersion of nano particulates in the molten [4, 5].

*Corresponding author: madeva.nagaral@gmail.com

^a orcid.org/0000-0003-2653-7239; ^b orcid.org/0000-0001-6094-6197; ^c orcid.org/0000-0002-8248-7603;

^d orcid.org/0000-0001-6549-6340

DOI: <http://dx.doi.org/10.17515/resm2022.628ma1213>

Res. Eng. Struct. Mat. Vol. 9 Iss. 3 (2023) 885-899

Copper, zinc, and aluminium alloys are some of the most frequently used materials for bearing applications. These days, copper-zinc alloys and copper-tin alloys are used in a wide variety of commercial industries in place of pure copper. A lot rides on the properties constituents for MMCs to be successfully produced, used, and have their desired properties. Much of the fundamental research in MMCs has focused on the structure and behavior of the interface region. Researchers have created composites of Al, Cu, Zn, and Mg by incorporating SiC, Al₂O₃, B₄C, and graphite particles into the alloys in liquid, semisolid, and powder metallurgical forms (PM).

There are benefits to using a stir casting method, but it is still difficult to create high-quality particulate reinforced MMCs. The true challenges lie in achieving a strong bond between the Cu matrix combination and the reinforcement, limiting or avoiding the interfacial response between the framework compound and the fortification, and increasing the wettability of the fortification in the lattice material. It is common practice to add trace amounts of reactive metals like magnesium, titanium, and the like to copper melt in order to increase its wettability. In addition, wettability can be improved by employing metallic covered fortifications such as graphite, TiO₂, Al₂O₃, and SiC.

In addition, studies using B₄C as reinforcement to synthesize zinc-tin alloy with B₄C composites by liquid melt technique are extremely limited. The microstructure and mechanical properties of the prepared composites of Zn-Sn alloy with boron carbide are then analyzed.

By adding particles in preheated cast iron die by two step method. Prepared samples are machined according to ASTM principles to complete essential tests such as tensile, hardness, wear, and microstructure tests [6]. Because of its remarkable hardness, outstanding strength, high wear and impact strength, B₄C is a more prominent support material [7, 8]. The aim of this work is focusing on a wide scope of utilizations in airplane, vehicle, auto and other designing applications further writing survey uncovers that many works have been done on the utilization of micro-particles as reinforcement to blend copper-micro composites by liquid metallurgy procedure [9, 10]. The expected micro-particles molecule has thickness viable with that of aluminum and copper for all intents and purposes high hardness. Upgraded two phase mix stir cast successions is created for the composite. Delivered Zn-15Sn alloy with 500 nano size B₄C reinforcement composites are then suspended to different analyses to concentrate on mechanical and wear conduct [11, 12].

2. Experimental Details

Composites using a two-stage melt stir strategy with Zinc 85 percent-Tin15 percent wt. (Fig. 1a) were synthesized. Boron carbide particles with 2, 4 and 6 wt. % were used as the reinforcement in the Zn-Sn matrix alloy. For casting, an electric furnace with a power rating of 60 kW and a maximum temperature of 800°C is used (Fig. 2a). A graphite crucible with the required weight percent of Zn-Sn composite network material in billet shapes was placed inside the heater and kept at a temperature of roughly 450°C. At this temperature, the entire Zn-Sn compound melted, allowing the base combination to dissolve and works out the needed wt. % of B₄C powder [13, 14].

The nano B₄C composites with Zn-Sn alloy matrix with 2% B₄C are made using a liquid metallurgy method and a stir technique. Metal ingots of a specific amount of Zn-Sn alloy are loaded into an electric furnace and heated until they melt. As, zinc-tin alloys melt at around 419°C, but here, the molten metal has already been superheated to 450°C. Melting and superheating temperatures are recorded using thermocouples calibrated for the appropriate temperature range. Crucibles are filled with solid hexachloroethane (C₂Cl₆) for about three minutes to degas the superheated molten metal. Zirconium ceramic is

applied to a steel rotor mounted on a shaft stirrer to agitate the liquid metal. By rotating the stirrer at a speed of about 300 rpm, the molten metal is agitated to the point where a vortex is created. The stirrer is immersed in the molten metal, taking up about 60% of the depth in the crucible. In addition to stirring the molten metal, a small amount of nano B₄C particulates, equal to about 2% by weight of charged zinc-tin alloy, must be heated to about 300°C in a separate heater before being slowly poured into the molten metal vortex. Wettability between the Zn-Sn alloy matrix and the B₄C reinforcement particulates is brought to a point where interfacial shear strength can be established by continuing to stir the mixture for an extended period of time. The nano composites with a Zn-Sn and 2 wt.% B₄C composition are made by pouring a molten metal mixture containing a Zn-Sn alloy matrix and B₄C composites into cast iron moulds of 125 mm length and 15 mm diameter dimensions. Further, Zn-Sn alloy with 4 and 6 wt. % of nano B₄C reinforced composites were synthesized by similar process. Figure 2 (a-b) are showing the stir cast set up and die used to prepare composites.



(a)



(b)

Fig. 1 (a) Zn-Sn matrix (b) Nano B₄C particles



(a)



(b)

Fig. 2 (a) Stir cast set up (b) Cast iron die

For the purpose of determining whether or not reinforcing particles are distributed uniformly throughout the Zn-Sn alloy, the cast specimen is then subjected to a scanning electron microscopy (SEM) (TESCAN VEGA 3 LMU, Czech Republic) microstructural investigation. Both Zn-Sn alloy and Zn-Sn reinforced composites containing 2 to 6, wt.%

of B_4C are imaged microscopically. The microstructure sample is 15mm in diameter and 5mm in height.

The specimen is machined in accordance with ASTM standard E10 [15] for hardness testing. A Brinell hardness tester (Krystal Industries, Ichalkaranji) is used to get an idea of the material's tensile strength, or how tough it is. The surface of the polished specimen is flawless. The depression is made using a ball indenter with a 5 mm diameter and 250 kg of pressure. Three indentations are made into the surface of the specimen and the results are recorded and counted.

The specimens are machined in accordance with ASTM standard E8 to investigate the tensile behavior of Zn-Sn alloy and Zn-Sn alloy with various percentages of B_4C composites. Testing tensile strength, studying the behavior of Zn-Sn alloy reinforced composites under unidirectional tension, and evaluating the uniform distribution effect are all possible with the help of a computer-measured tensile machine by Instron. This specimen measures 104 mm in total length, 45 mm in gauge length, and 9 mm in gauge diameter. This tensile test is useful for assessing the mechanical properties of composites and as cast alloys. The schematic diagram of tensile test specimen is shown in Fig. 3.

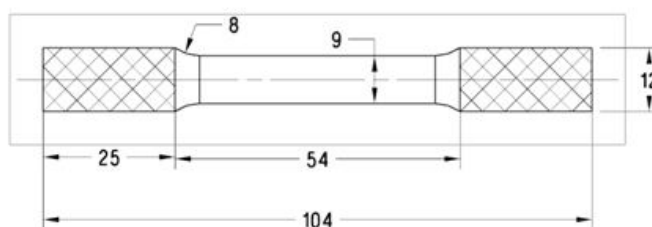


Fig. 3 Schematic diagram of tensile test specimen

Impact test is conducted by using Charpy impact testing machine. The specimen used for the impact test is shown in the Fig. 4. The test is conducted on the Zn-Sn alloy and Zn-Sn alloy with 2, 4 and 6 wt. % of nano B_4C reinforced composites as per ASTM E23 standard.

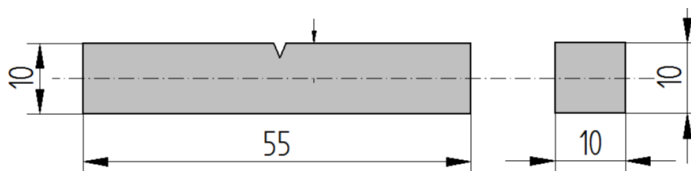


Fig. 4 Schematic diagram of impact test specimen

3. Results and Discussion

3.1. Microstructural Analysis

The microstructure of synthesized composites using as-cast Zn-Sn matrix alloy (Fig.5a), Zn-Sn-2 wt. percent B_4C (Fig.5b), Zn-Sn alloy with 4 wt. percent B_4C (Fig.5c), and Zn-Sn alloy with 6 wt. percent B_4C composites are characterized using SEM (Fig. 5d).

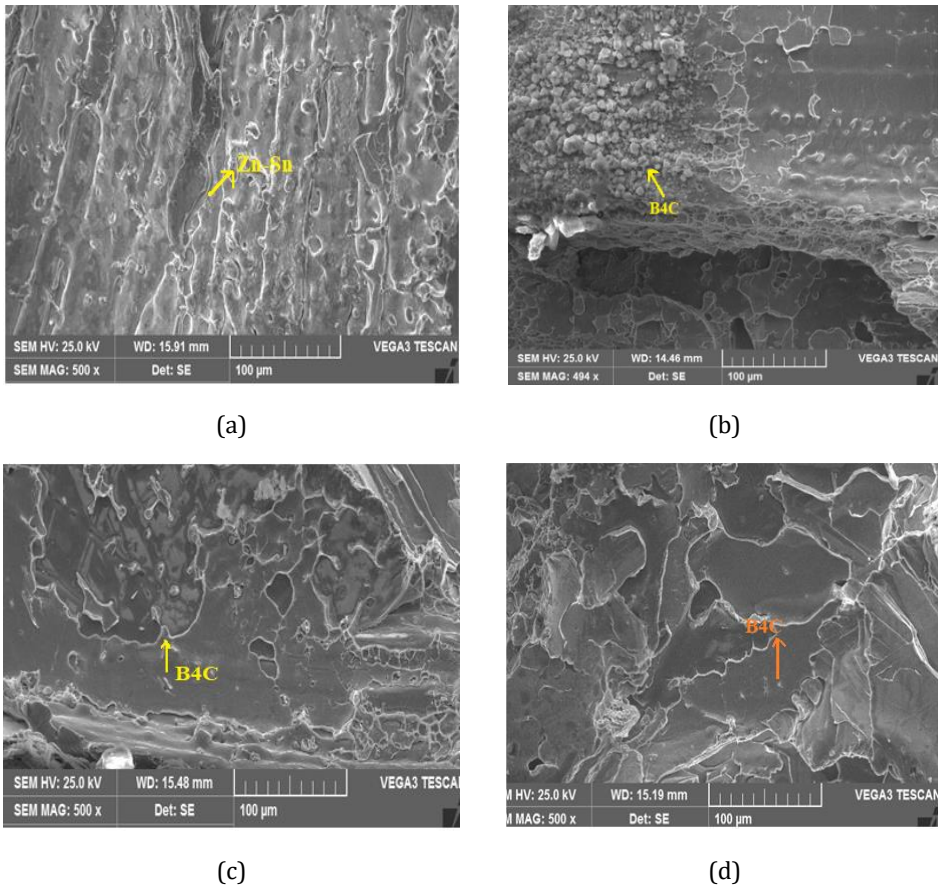
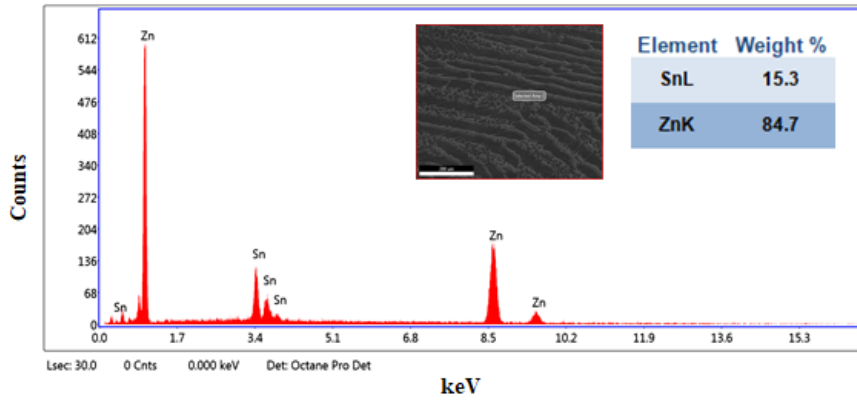


Fig. 5 SEM micrographs of (a) as-cast Zn-Sn matrix (b) Zn-Sn alloy matrix with 2 wt.% of B₄C (c) Zn-Sn alloy matrix with 4 wt. % of B₄C (d) Zn-Sn alloy matrix with 6 wt. % of B₄C composites

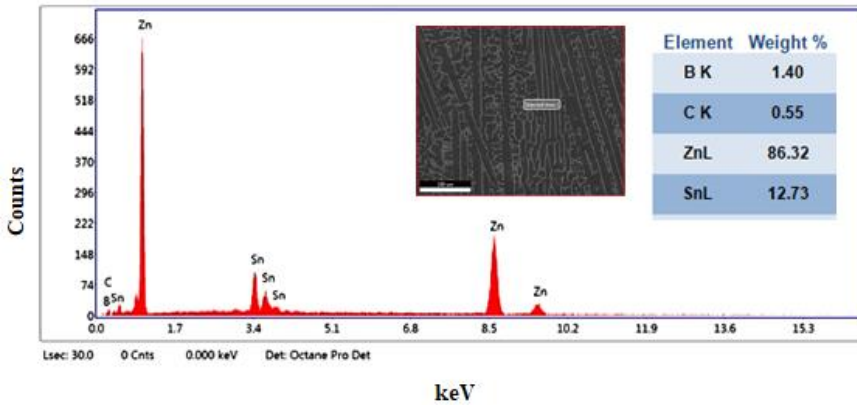
Fig. 5 (b-d) demonstrates the appropriation of B₄C support particulates in various wt. % of B₄C, and it can be seen that the particles were dissolved finely and uniformly with no formation clustering. Furthermore, due to its sophisticated two-stage support blending method, the predicted metal grid composites show remarkably low isolation [16].

Fig. 6(a) represents the EDS of the Zn-Sn matrix whereas Fig. (b-d) can demonstrate the presence of boron particles in the Zn-Sn compound lattice. By displaying B and C materials in EDS testing, this diagram further revealed that boron and carbide components may be found in the Zn-Sn alloy matrix.

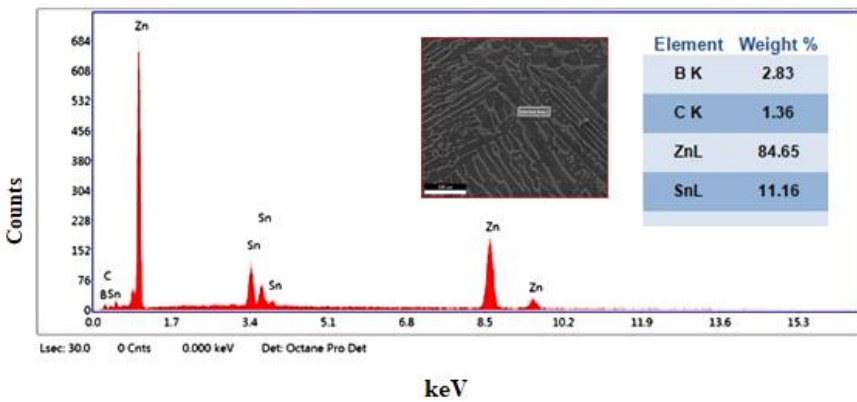
Fig. 7 shows an XRD examination of Zn-Sn alloy and Zn-Sn alloy with 6 wt. % B₄C particles (Fig. 7b). XRD investigation confirms the presence of the Sn stage over the Zn network and boron carbide stage in the Zn-Sn matrix.



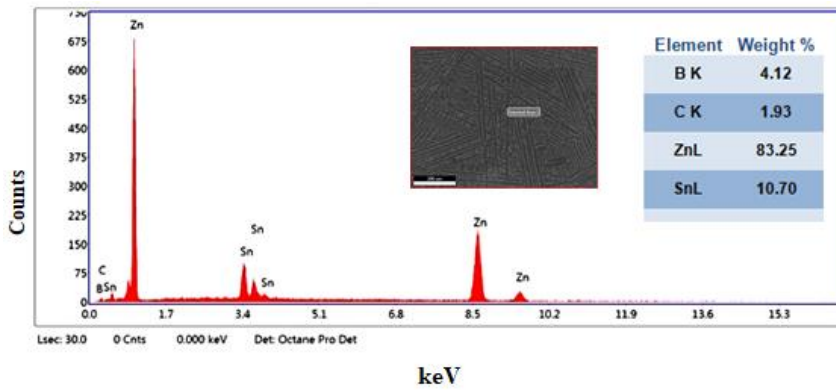
(a)



(b)

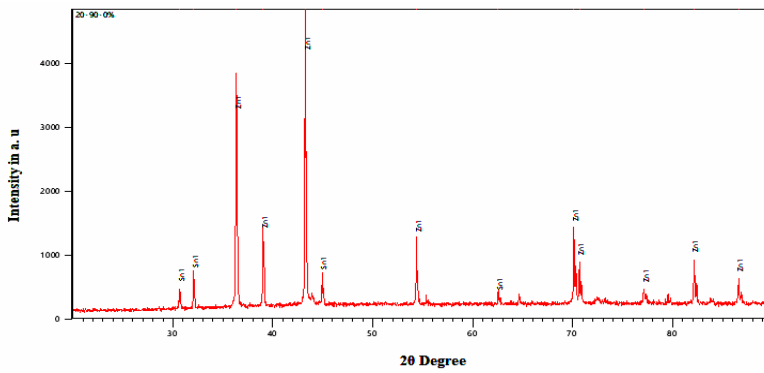


(c)

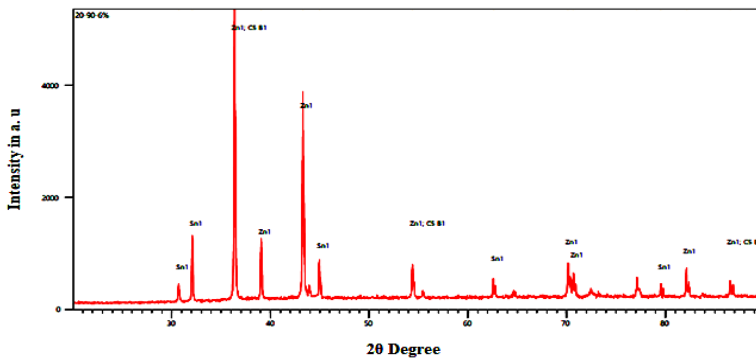


(d)

Fig. 6 EDS spectrums of (a) as-cast Zn-Sn matrix (b) Zn-Sn alloy matrix with 2 wt.% of B₄C (c) Zn-Sn alloy matrix with 4 wt. % of B₄C (d) Zn-Sn alloy matrix with 6 wt. % of B₄C composites



(a)



(b)

Fig. 7 XRD patterns of (a) as-cast Zn-Sn matrix (b) Zn-Sn alloy matrix with 6 wt. % of B₄C composites

3.2. Hardness Measurements

Hardness benefits from a combination of Zn-2, and 6wt. % in the current research. Brinell hardness analyzer has found percent B₄C composites. Fig. 8 shows the hardness of Zn-2, 4& 6, wt% of B₄C composite is higher than Zn basis matrix in terms of percentage [17]. With increasing of B₄C particles, a significant increase in the composite matrix hardness can be detected. The presence of B₄C particles in the framework Zn alloy is the main reason for this. The hardness of the composite material is improved whenever firm reinforcement is consolidated into a delicate base alloy. As can be seen in Figure.8, the Brinell hardness increases as the B₄C particles are increased. The tougher particles are responsible for the increase in hardness [18].

Table 1. Hardness of Zn-Sn alloy and its nano B₄C composites with standard deviation

Material Composition	Hardness (BHN)
Zn-Sn Alloy	82.03 ± 1.50
Zn-Sn – 2 wt. % B ₄ C	88.53 ± 1.43
Zn-Sn – 4 wt. % B ₄ C	100.20 ± 1.15
Zn-Sn – 6 wt. % B ₄ C	115.02 ± 1.16

± - SD (Standard Deviation)

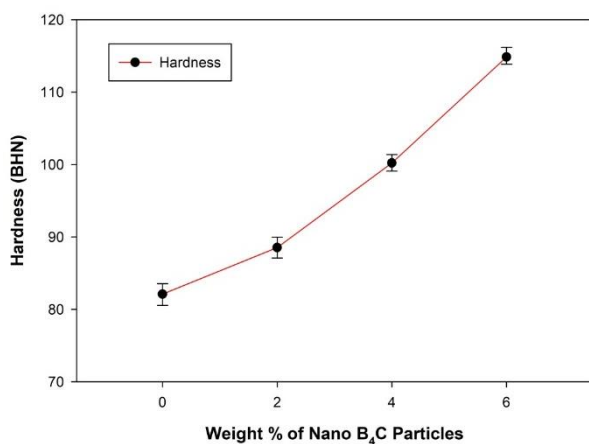


Fig. 8 Hardness of Zn-Sn alloy and its nano B₄C composites

3.3. Tensile Properties

Fig.9 shows the ultimate strength (UTS) and yield strength (YS) for Zn alloy, and 2, 4 and 6 wt. percent B₄C composites. The proximity of hard B₄C particles is credited with the improvement in ultimate and yield strength.

Ultimate and yield strength of as-cast Zn alloy with 2, 4 & 6 wt. % B₄C reinforcement, as illustrated in the Fig. 9. Boron carbide particles enhanced the yield Strength of the base matrix. Zn-Sn combination. In a fine Zn composite base network, ceramic particles are uniformly combined [19]. Many ceramics, such as boron ceramics, will resist external weight in contrast to delicate materials, and as a result, they will not twist plastically successfully, increasing their yield resistance rate.

The tensile properties of these materials might be affected by the consistency of the particle dispersion. It has been demonstrated that these are currently quite homogeneous, so it is anticipated that they will not significantly affect the trends of the

current work. Clusters can cause localized damage that compromises a material's strength and ductility. In this sense, such aggregations may be viewed as pre-loading danger zones. It is important to note that clustering is often more prevalent in composites reinforced with small particulates, despite the fact that these composites appear to have greater strength and ductility than materials containing coarse particles. Any areas of clustering must be kept to a minimum if top performance is desired, and this is especially true for nanoparticle-reinforced composites.

Table 2. Tensile properties of Zn-Sn alloy and its B₄C composites with standard deviation

Material Composition	Ultimate Tensile Strength (MPa)	Yield Strength (MPa)
Zn-Sn Alloy	315.15 ± 1.54	248.37 ± 1.21
Zn-Sn – 2 wt. % B ₄ C	330.32 ± 1.12	266.86 ± 1.33
Zn-Sn – 4 wt. % B ₄ C	357.44 ± 1.39	295.09 ± 0.97
Zn-Sn – 6 wt. % B ₄ C	394.46 ± 0.56	326.03 ± 0.94

± - SD (Standard Deviation)

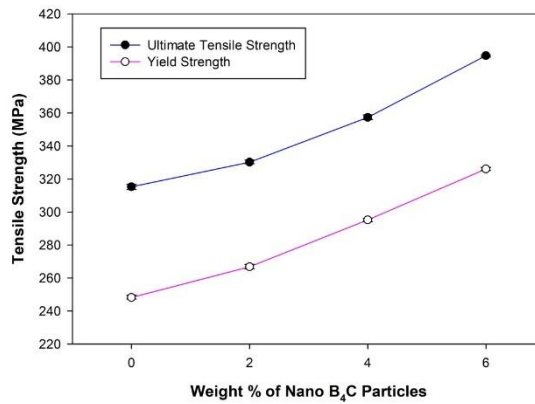


Fig. 9 Ultimate and yield strength of Zn-Sn alloy and its nano B₄C composites

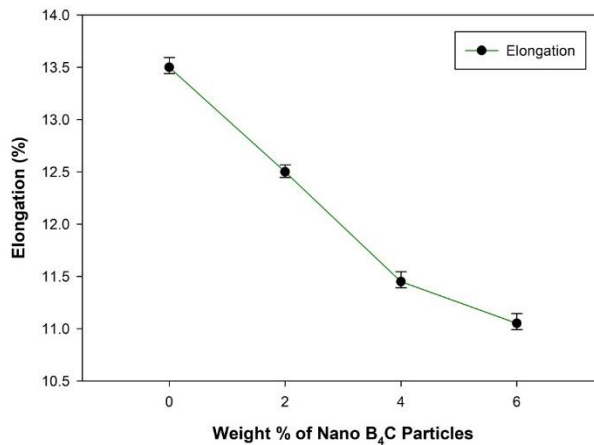
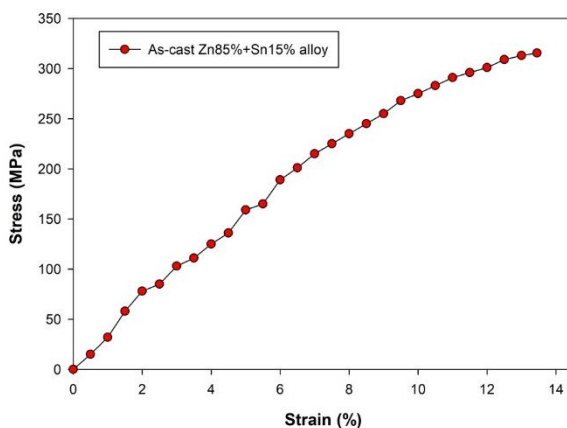


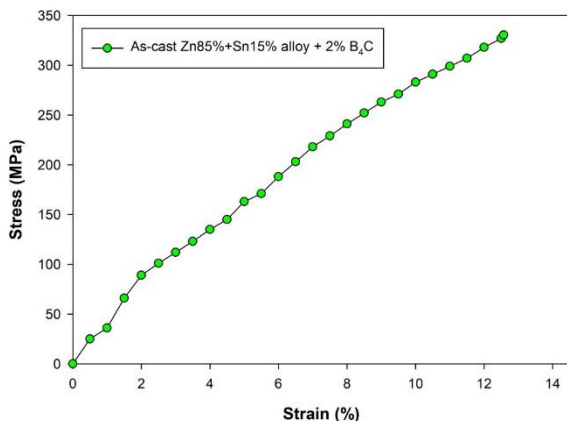
Fig. 10 Elongation of Zn-Sn alloy and its nano B₄C composites

Elongation of as-cast Zn composite with 2, 4 6 wt. % of B₄C reinforcement is shown Fig. 10. It was shown that as boron carbide particles increased in base matrix the % of elongation is reduced, as shown in Figure.11. Harder particles are consistently integrated into the Zn-Sn base alloy [20]. Due to two step stir action hard boron carbide particles are distributing uniformly throughout the base solution, hence substitution solid solution was achieved. As results, boron is influencing on delicate base alloy, then base alloy successfully opposes plastically, increasing yield strength rate and diminishes the machinability and % of elongation.

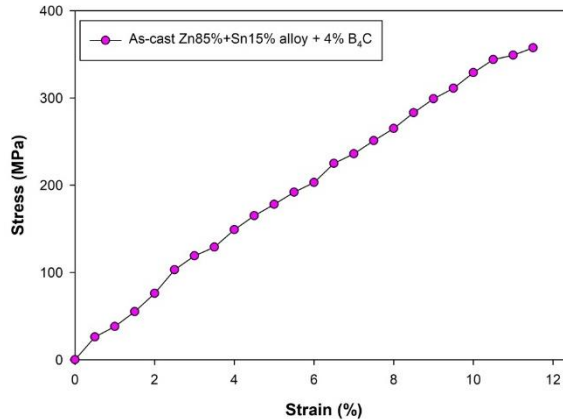
Fig. 11 (a-d) are representing stress-strain graphs of as cast Zn-Sn alloy, Zn-Sn alloy with 2, 4 and 6 wt. % of nano B₄C reinforced composites. Boron carbide reinforced Zn-Sn alloy composites exhibited superior load carrying capacity as compared to the as cast Zn-Sn alloy. The ultimate tensile stress of as cast Zn-Sn alloy is 311115 MPa, as weight percentage of B₄C particles content increased in the Zn-Sn alloy, the tensile strength increased. Zn-Sn alloy with 2, 4 and 6 weight % of boron carbide reinforced composites exhibits 330.32 MPa, 357.44 MPa and 394.46 MPa respectively with reduced strain. The increase in load carrying capacity with addition of B₄C is mainly due to the load bearing capacity of hard carbide particles during tensile loading conditions.



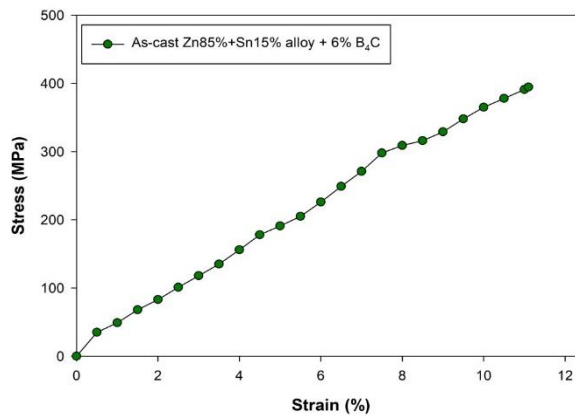
(a)



(b)



(c)



(d)

Fig. 11 Stress-strain graphs of (a) as-cast Zn-Sn matrix (b) Zn-Sn alloy matrix with 2 wt.% of B₄C (c) Zn-Sn alloy matrix with 4 wt. % of B₄C (d) Zn-Sn alloy matrix with 6 wt. % of B₄C composites

3.4. Tensile Fractography

Fig. 12 shows the tensile fractured surfaces of as-cast Zn alloy and Zn-Sn alloy with 6 percent of B₄C composites (a-b). The goal of the tensile fracture surfaces research is to see how boron carbide particles alter Zn alloy fracture behavior [21]. The particles were equally distributed throughout the matrix alloy in the current investigation, boosting microhardness, ultimate, and yield strength while lowering ductility. Interfaced cohesion between the Zn -Sn alloy matrix and B₄C particles, reinforcement fracture, and matrix failure are all causes of failure in particle-reinforced metal composites [22].

The as-cast Zn alloy's tensile cracked surface in Fig. 12 (a) shows larger and more uniform dimples, indicating malleable fracture. On the cracked surfaces of Zn alloy reinforced with 6 wt. % of B₄C particles (Fig.12b), the size dimples are less than on the as-cast Zn matrix. On the fracture surfaces of composites, electron microscopy revealed particle decohesion with the matrix and reinforcement [23]. The particle fracture is less

ductile in the majority of cases, and the surface is smooth and crisp, showing that the particle is broken rather than decreased, implying that high interface strength dominates these composites.

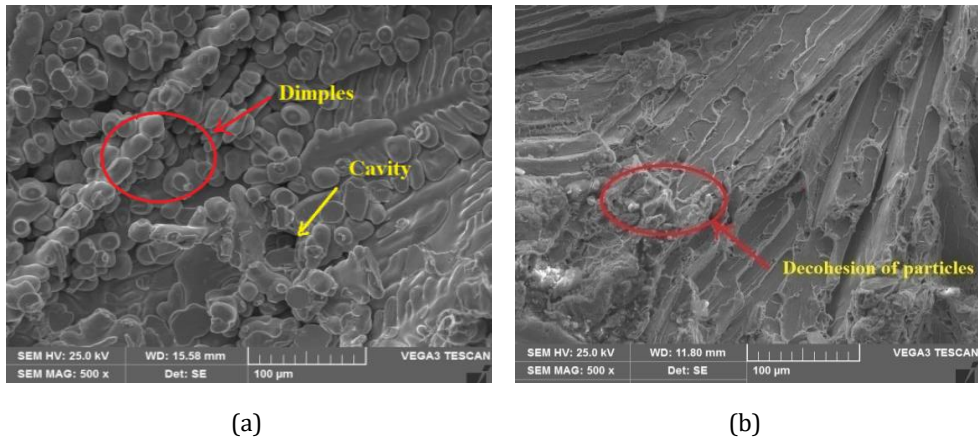


Fig. 12 Tensile fractured surfaces SEM images of (a) as-cast Zn-Sn matrix (b) Zn-Sn alloy matrix with 6 wt. % of B₄C composites

3.5. Impact Strength and Fractography

The impact strength of Zn alloy reinforced metal composites containing 2 to 6 wt.% B₄C particles is shown in Fig 13. The impact strength of Zn alloy as-cast is 3.5 J, but the impact strength of Zn-Sn alloy with 2, 4 and 6 wt.% of B₄C composites are 3.0, 2.49 and 2.0 J respectively with the addition of ceramic particles. Because of the hard particle and matrix contact, composites absorb less energy than as-cast Zn matrix. The creation of a hard interface between the matrix and reinforcement is influenced by load transfer, which is critical for improving composite brittleness [24].

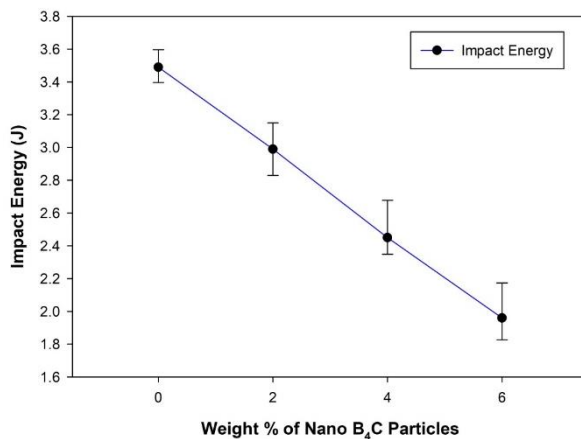


Fig. 13 Impact strength of Zn-Sn alloy and its nano B₄C composites

Impact cracked surfaces of as-cast Zn alloy, Zn-2 wt. per cent, and Zn-6 wt. percent, SEM micrographs Figure 10 depicts B₄C reinforced composites. The Zn-Sn alloy matrix has larger dimples with voids, as shown in Fig. 14 (a), while the matrix alloy tends to have smaller dimples and voids after introducing B₄C particles, as shown in Fig. 14 (b). The

soft matrix was turned into a brittle substance by the inclusion of ceramic particles. The impact strength of the newly developed composites is reduced due to strong interfacial bonding between the Zn matrix and B₄C- particles. The impact strength of the newly generated composites is lowered due to strong interfacial bonding between the Zn matrix and B₄C- particles. Brittle materials absorb fewer loads than soft or ductile materials; however, the impact strength of the newly developed composites is reduced. The fracture surfaces of particles reinforced composites containing 2 and 6 weight per cent particles indicate a sharp brittle fracture mode [25].

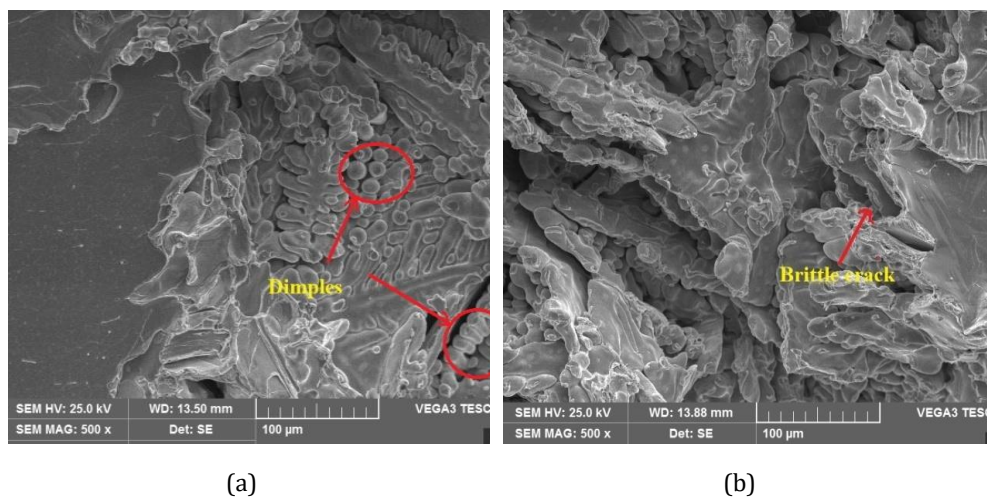


Fig. 14 Impact fractured surfaces SEM images of (a) as-cast Zn-Sn matrix (b) Zn-Sn alloy matrix with 6 wt. % of B₄C composites

4. Conclusions

A stir casting process was used to make Zn-Sn alloy with 2, 4 and 6 wt. % of B₄C composites. The prepared composites were studied for microstructural characterization by using SEM, EDS and XRD. Scanning electron micrographs were shown the dispersion of boron carbide particles in the Zn-Sn alloy matrix. Further, boron carbide particles in the Zn-Sn alloy matrix were confirmed by the EDS spectrums containing the Boron and Carbon elements, XRD patterns recognized by the Zn, Sn and B₄C phases in the prepared matrix. With the incorporation of nano sized boron carbide particles various mechanical properties like, hardness, ultimate and yield strengths were improved. The percentage improvement in the hardness of Zn-Sn alloy with 6 wt. % of boron carbide particles is 40%. As weight percentage of boron carbide particles were increased to 2 to 6 wt. % in the Zn-Sn alloy, ultimate and yield strengths were improved. Ultimate tensile strength of as-cast Zn-Sn alloy was 315.15 MPa, with 6 wt. % of nano boron carbide particles it was found 394.46 MPa. Addition of hard ceramic particles decreased ductility of Zn-Sn alloy, the lowest ductility was observed in the case of Zn-Sn alloy with 6 wt. % of B₄C particles. Stress-strain patterns of Zn-Sn alloy with boron carbide particles reinforced composites exhibited superior load carrying capacity as compared to the as-cast Zn-Sn alloy. Tensile fractured surfaces of as-cast Zn-Sn alloy indicated the ductile mode of fracture, whereas composites shown brittle fracture. Hard particles addition affected on the impact energy of Zn-Sn alloy, impact strength of Zn-Sn alloy decreased as weight percentage of boron carbide particles increased from 2 to 6 weight percentage in the Zn-Sn alloy. Further, different fracture mechanisms were observed in the case of as-cast Zn-Sn alloy and its

boron carbide reinforced composites. Hence, these Zn-Sn alloys with nano born carbide particles composites can be used for future load bearing applications.

References

- [1] Nagesh SN, Siddaraju C, Prakash SV, Ramesh MR. Characterization of brake pads by variation in composition of friction materials. *Procedia Materials Science*, 2014; 5: 295-302. <https://doi.org/10.1016/j.mspro.2014.07.270>
- [2] Manjunatha SS, Manjaiah M, Basavarajappa S. Analysis of factors influencing dry sliding wear behaviour of laser remelted plasma sprayed mo coating using response surface methodology. *Achieves of Metallurgy and Materials*, 2018; 63 (1): 217-225. <https://doi.org/10.1080/17515831.2017.1407473>
- [3] Dineshkumar S, Sriram S, Surendran R, Dhinakaran V. Experimental investigation of tensile properties of Ti-6Al-4V alloy at elevated temperature. *International Journal of Recent Technology and Engineering*, 2019; 8(1):103-107.
- [4] Prasad GP, Chittappa HC, Nagaral M, Auradi V. Influence of B4C reinforcement particles with varying sizes on the tensile failure and fractography of LM29 alloy composites. *Journal of Failure Analysis and Prevention*, 2020; 20(6): 2078-2088. <https://doi.org/10.1007/s11668-020-01021-6>
- [5] Ali Z, Muthuraman V, Rathnakumar P, Gurusamy P, Nagaral M. Studies on mechanical properties of 3 wt.% of 40 and 90 μm size B4C particulates reinforced A356 alloy composites. *Materials Today: Proceedings*, 2022; 52: 494-499. <https://doi.org/10.1016/j.matpr.2021.09.260>
- [6] Anne G, M. Ramesh MR, Shivananda Nayaka, Arya SB, Sahu S. Microstructure evolution and mechanical and corrosion behavior of accumulative roll bonded Mg-2%Zn/Al-7075 multilayered composite. *Journal of Materials Engineering and Performance*, 2017;26 (4):1726-1734. <https://doi.org/10.1007/s11665-017-2576-z>
- [7] Kumar HSV, Kempaiah UN, Nagaral M. Impact, tensile and fatigue failure analysis of boron carbide particles reinforced Al-Mg-Si (Al6061) alloy composites. *Journal of Failure Analysis and Prevention*, 2021; 21: 2177-2189. <https://doi.org/10.1007/s11668-021-01265-w>
- [8] Pathalinga PG, Chittappa HC, Nagaral M, Auradi V. Effect of the reinforcement particle size on the compressive strength and impact toughness of LM29 alloy B4C composites. *Structural Integrity and Life*, 2019;5 (7):231-236.
- [9] Nagaral M, Auradi V, Kori SA, Vijaykumar H. Investigations on mechanical and wear behavior of nano Al2O3 particulates reinforced AA7475 alloy composites. *Journal of Mechanical Engineering and Sciences*, 2019; 13(1):4623-4635. <https://doi.org/10.15282/jmes.13.1.2019.19.0389>
- [10] Harti J, Prasad TB, Nagaral M, Rao KN. Hardness and tensile behavior of Al2219-TiC metal matrix composites. *Journal of Mechanical Engineering and Automation*, 2016; 6(5A): 8-12.
- [11] Ali Z, Muthuraman V, Rathnakumar P, Gurusamy P, Nagaral M. Investigation on the tribological properties of copper alloy reinforced with Gr/ZrO2 particulates by stir casting route. *Materials Today: Proceedings*, 2020; 33: 3449-3453. <https://doi.org/10.1016/j.matpr.2020.05.351>
- [12] Balaraj V, Nagaraj K, Nagaral M, Auradi V. Microstructural evolution and mechanical characterization of micro Al2O3 particles reinforced Al6061 alloy metal composites. *Materials Today: Proceedings*, 2021; 47: 5959-5965. <https://doi.org/10.1016/j.matpr.2021.04.500>
- [13] Krishna Prasad S, Samuel Dayanand, Rajesh , Madeva Nagaral, Auradi V, Rabin Selvaraj. Preparation and Mechanical Characterization of TiC Particles Reinforced Al7075 Alloy Composites, *Advances in Materials Science and Engineering*, 2022,

- Article ID 7105189, <https://doi.org/10.1155/2022/7105189>
<https://doi.org/10.1155/2022/7105189>
- [14] Nagaral M, Auradi V, Kori SA, Reddappa HN, Jayachandran, Shivaprasad V. Studies on 3 and 9 wt. % of B4C particulates reinforced Al7025 alloy composites. In AIP Conference Proceedings, 2017; 1859, 1: 020019. <https://doi.org/10.1063/1.4990172>
- [15] Nagaral M, Deshapande RG, Auradi V, Satish BP, Samuel D, Anilkumar MR. Mechanical and wear characterization of ceramic boron carbide-reinforced Al2024 alloy metal composites. Journal of Bio-and Tribo-Corrosion, 2021; 7(1):1-12. <https://doi.org/10.1007/s40735-020-00454-8>
- [16] Nagara M, Auradi V, Bharath V. Mechanical characterization and fractography of 100 micron sized silicon carbide particles reinforced Al6061 alloy composites. Metallurgical and Materials Engineering, 2022; 28 (1): 17-32. <https://doi.org/10.30544/639>
- [17] Fazil N, Venkataramana V, Nagaral M, Auradi V. Synthesis and mechanical characterization of micro B4C particulates reinforced AA2124 alloy composites. International Journal of Engineering and Technology UAE, 2018; 7 (2.23): 225-229. <https://doi.org/10.14419/ijet.v7i2.23.11954>
- [18] Marco Z, Carlos ES, Alicia EA. Investigation on Al2O3 reinforced zinc aluminium matrix composites. Procedia Materials Science, 2015;8:424-433. <https://doi.org/10.1016/j.mspro.2015.04.093>
- [19] Jeng J, Xu J, Hua W, Xia L, Deng X, Wang S, Tao P, Ma X, Yao J, Jiang C, Lin L. Wear Performance of the lead free tin bronze matrix composite reinforced by short carbon fibers. Applied Surface Science, 2009;255:6647-6651. <https://doi.org/10.1016/j.apsusc.2009.02.063>
- [20] Ferguson JB, Schultz BF, Rohatgi PK. Zinc alloy ZA-8 shape memory alloy self healing metal matrix composite. Materials Science and Engineering A, 2015;620(3):85-88. <https://doi.org/10.1016/j.msea.2014.10.002>
- [21] Halil BK, Hasan U, Ahmet CT, Okan D, Ahmet A. Influence of sea water on mechanical properties of SiO2-epoxy polymer nanocomposites. Research on Engineering Structures and Materials, 2019;5(2):147-154.
- [22] Ahmet CT, Halil BK, Hasan U, Okan D, Ahmet A. Evaluation of low-velocity impact behavior of epoxy nanocomposite laminates modified with SiO2 nanoparticles at cryogenic temperatures. Research on Engineering Structures and Materials, 2019;5(2):115-125.
- [23] Mei Z, Zhu YH, Lee WB, Yue TM, Pang GKH. Microstructure investigation of a SiC whisker reinforced eutectoid zinc alloy matrix composite. Composite Part A: Applied Science and Manufacturing, 2006;37(9):1345-1350. <https://doi.org/10.1016/j.compositesa.2005.08.011>
- [24] Wenlong Z, Xiang M, Dongyan D. Aging behavior and tensile response of a SiCw reinforced eutectoid zinc-aluminium-copper alloy matrix composite. Journal of Alloys and Compounds, 2017;727:375-381. <https://doi.org/10.1016/j.jallcom.2017.08.130>
- [25] Uppada RK, Putti SR, Mallarapu GK. Mechanical behavior of fly ash-SiC particles reinforced Al-Zn alloy based metal matrix composites fabricated by stir casting method. Journal of Materials Research and Technology, 2019;8(1):737-744. <https://doi.org/10.1016/j.jmrt.2018.06.003>

Blank Page



Research Article

Seismic behaviour of re-entrant dominant RC frame buildings

Jahanvi Suthar^a, Sharadkumar Purohit^{*, b}

Department of Civil Engineering, School of Engineering, Institute of Technology, Nirma University, Ahmedabad-382481, Gujarat, India.

Article Info

Abstract

Article history:

Received 30 Dec 2022

Accepted 27 Mar 2023

Keywords:

Re-entrant corner;

Plan irregularity

descriptor;

Torsional response;

Semi-rigid diaphragm

Reinforced Concrete (RC) building stocks with plan and/or vertical irregularities are built routinely world-wide, despite being vulnerable to seismic forces. Irregular RC buildings with asymmetry, mass and stiffness irregularities have been well researched, however, seismic behaviour of RC building with re-entrant corner type plan irregularity is given relatively less attention. In the present study, a total of 104 re-entrant corner dominant plan irregular RC building models (C-, L-, T- and PLUS-shaped) are developed along with one regular rectangular building. Plan Irregularity Descriptors (PIDs) are summarized with their limit of regularity and are evaluated for building models. Building models have uni-directional and bi-directional re-entrant corner of A/L ratio ranging between 0.1 to 0.8 in the X-direction and between 0.2 to 0.8 in the Y-direction. Seismic response quantities; peak displacement, peak storey drift, normalized base shear and normalized overturning moments are evaluated using the equivalent static method and response spectrum method specified by the Indian seismic code. It has been found that building models yield amplified peak displacement responses in the direction perpendicular to that of applied seismic forces. Other seismic response parameters for all re-entrant RC building models fall well within code based permissible limits. A/L ratio limit specified by the Indian seismic code is found to be conservative. Out of various building models considered, C-shaped building models perform well under seismic forces, while PLUS-, L- and T-shaped RC building models with A/L ratio ≥ 0.4 , in both directions, overshoot torsional irregularity descriptor, $\frac{\Delta_{max}}{\Delta_{avg}}$.

© 2023 MIM Research Group. All rights reserved.

1. Introduction

Buildings with simple and regular configurations offer good seismic behaviour due to uniform lateral stiffness and strength distribution. However, building with irregular configurations becomes inevitable for various reasons like natural ventilation & illumination, limited availability of land, rapid urbanization and aesthetics [1,2]. Irregular buildings are broadly classified as plan and vertical irregulars, suffering substantial damage under seismic excitation has been a cause of concern for the research fraternity and is an active area of research for the past few decades [3]. Real buildings are mostly irregular due to either unsymmetric distribution of mass, stiffness, strength or a combination thereof or the presence of plan and/or vertical irregular configuration. Irregular buildings are prone to structural damage due to torsion, diaphragm deformation and stress concentration under seismic forces. Since the early 1970s, experimental and analytical research studies, have been conducted to understand the impact of irregularities on the seismic response of the building. Studies have revealed that strength and stiffness

*Corresponding author: sharad.purohit@nirmauni.ac.in

^a orcid.org/0000-0002-7959-0415; ^b orcid.org/0000-0002-2678-4320

DOI: <http://dx.doi.org/10.17515/resm2022.629me1230>

Res. Eng. Struct. Mat. Vol. 9 Iss. 3 (2023) 901-920

eccentricities modify building behaviour, leading to unsatisfactory seismic performance. Owing to complexities in modelling and the involvement of a large number of parameters, research efforts to understand the seismic behaviour of irregular buildings have been limited. Therefore, seismic design codes, worldwide, have limited guidelines with detailed discussion missing on irregularities. Prescribed limits of various types of irregularities in seismic design codes are by and large conservative and exceedance of limit is not permitted, else they recommend altering the structural configuration and/ or architectural planning. The design of irregular buildings becomes more complicated than regular buildings due to the presence of torsional response under earthquake excitation. And has been given attention in the past several decades. It is still an open area of research due to, varied provisions across seismic design codes. Seismic design codes have introduced provisions of accidental eccentricity as an additional loading condition primarily for irregular buildings.

Initial investigations on torsional response were through simplified single-storey rigid deck structures with two or three Degrees of Freedom (DoFs) supported on vertical shear-type elements. A comprehensive review paper by Anagnostopoulos et al. [4] has a detailed discussion on the torsional response of buildings from early 1938 to the time of its publication that provides a well-laid foundation. Goel and Chopra [5] studied the elastic and inelastic seismic response of plan asymmetric one-storey systems to show that the seismic response of an inelastic system is affected less by plan asymmetry compared to an elastic system. Single storey model designed by different seismic code criteria was investigated considering the nonlinear behaviour, random stiffness & strength of the structural elements and uncertain location of the Centre of Mass (CM) on the performance of a symmetric building using, deterministic and probabilistic approaches [6]. Elastic analysis of a single-storey building under a set of seismic excitations showed that the lateral-torsional response of the building is sensitive to both structural and ground motion characteristics [7]. Stathopoulos and Anagnostopoulos [8] examined shear beam type and plastic hinge type single-storey models for a set of seismic excitations to find that ductility demands of the stiff side increase while no effect on the flexible side of the shear beam type models. Peter and Iztok [9] have performed a parametric study of a single-storey asymmetric building to determine inelastic seismic response under bi-directional earthquake ground motions. Preliminary results based on a limited number of test models revealed that maximum response quantities can be obtained by performing uni-directional analyses and results can be combined by the Square Root of the Sum of Square rule though more investigations are needed. Influence of bi-directional seismic excitations on inelastic behaviour of in-plane irregular one-storey models with one symmetry axis showed that orthogonal elements always remain elastic while parallel elements undergo inelastic deformation under uniaxial analysis leading to a minor change in inelastic response of the models [10].

3D idealized buildings representing more realistic characteristics of the building as compared to the single-storey models were investigated for torsional effects under seismic excitations. Pinho et al. [11] have applied four Nonlinear Static procedures (NSPs); Capacity Spectrum Method (CSM), N2, Modal Pushover Analysis (MPA), Adaptive Capacity Spectrum Method (ACSM) on 3D SPEAR building tested in full scale under pseudo-dynamic conditions under bi-directional seismic loadings. It has been found that all NSPs yield satisfactory results while ACSM showed better capacity in capturing response under involved intensity. Bhasker and Menon [12] studied various torsional irregularity indices for capturing torsional effects under various intensity levels of seismic excitations using Multiple Strip Analysis (MSA). It has been shown that no scalar index of irregularity correlates well with seismic demand at all intensities, however, $\Delta_{max}/\Delta_{min}$ index is the most effective for low-intensity levels. Very limited research is conducted to understand

the difference between rigid and flexible floor analysis of 3D building models. Ju and Lin [13] studied L- and U-shaped FE-based 3D building models using Response Spectrum Method (RSM) with rigid and flexible floors and found that building models with shear walls are more sensitive to flexible floor analysis. Fang and Leon [14] studied the torsional behaviour of braced frames of a 3D steel structure with rigid and semi-rigid floor and showed that the ultimate strength of the structure is higher with a rigid diaphragm than a semi-rigid diaphragm. Research on plan irregular buildings with re-entrant corners is in its initial phase. Khanal and Chaulagain [1] have studied plan irregular L-shaped buildings with re-entrant corners under varying angles of the input response spectrum. It has been found that a 135-degree angle yields a significant increase in seismic response demand.

Several reconnaissance studies performed during various earthquakes; Japan (1978), Athens (1999), Bhuj (2001), Bam (2003), Nepal (2015) and Imphal (2016) have reported damages to buildings due to symmetry and predominantly irregularity [1,3,7]. One of the worth studies conducted at the National Autonomous University of Mexico (UNAM) in Mexico City for the 1985 Mexico earthquake, reveals that out of 331 surveyed severely damaged and collapsed buildings, about 8 % were soft-story structures, 42 % were corner buildings, 15 % had story stiffness eccentricities and 40 % had experienced middle and top storey collapse [2]. It has been realized from the literature review that most of the research efforts have been made to understand the seismic behaviour of asymmetric structures and relatively fewer efforts towards other types of irregular buildings, especially, buildings with plan irregularity [3]. Fig. 1 shows the research contributions, up to the paper published, in different domains of irregular structures. It is realized that seismic behaviour of plan irregular buildings with re-entrant corners of geometrical shape C-, L-, T-, PLUS-, etc. are less researched and thus, identified as a research gap.

The present paper aims to study the seismic behaviour of re-entrant dominant plan irregular ten-storey RC frame buildings of geometrical shapes, i.e., C-, L-, T- and PLUS-. PIDs defined by seismic design codes of various countries are studied, summarized and computed to establish that RC buildings possess dominant uncoupled re-entrant corner type plan irregularity. Total 32 nos. of 3D building models are developed with A/L ratio ranges between 0.1 to 0.8 in X- direction and 0.2 in Y-direction for each geometrical shape.

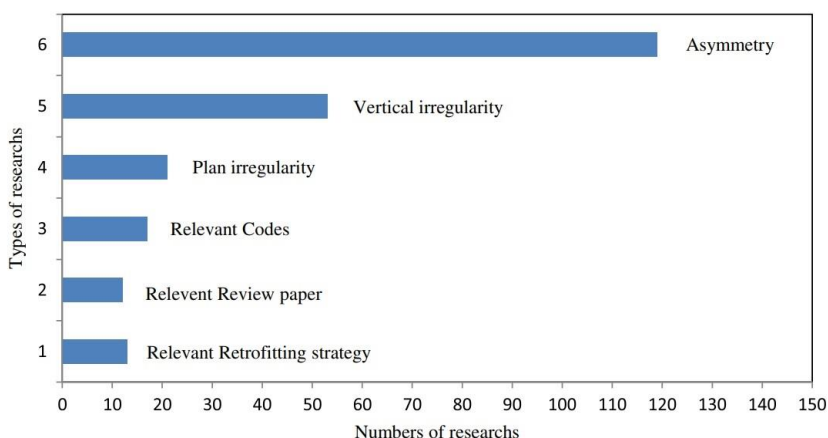


Fig. 1 Research on asymmetric/ irregular structures [3]

Seismic response parameters; peak displacement, peak storey drift, normalized base shear and normalized overturning moment are evaluated. Total of 72 nos. of 3D re-entrant dominant RC building models with an A/L ratio, which varies between 0.4 to 0.8 in the

Y-direction are developed to study the seismic behaviour of these models with bi-directional re-entrant corners. The study is extended to include the effect of rigid and flexible (semi-rigid) diaphragms on the seismic behaviour of plan irregular re-entrant dominant RC building models.

2. Plan Irregularity Descriptors (PIDs)

Seismic design codes worldwide define irregularity, both plan and vertical, for buildings with limits on regularity. Physical parameters like; projection ratio, static eccentricity, torsional radius, mass-radius of gyration, floor displacement, fundamental period of torsional mode, area of cut-outs, out-of-plane offsets, etc. with specific limits have been used by the seismic design code to quantify types, and degree of irregularity exists in the building. Stringent recommendations on irregularities are imposed to ensure the good seismic performance of a building. Table 1 summarizes various PIDs along with their definition and limits of regularity prescribed by the seismic design code of representative countries of seismically active regions. RC buildings are routinely encountered with torsional irregularity type of plan irregularity mostly due to plan asymmetry and/or stiffness asymmetry of the lateral load-resisting structural system. Thus, most PID definitions are associated with torsional irregularity while the other four types of irregularity have a single PID definition as shown in Table 1. Thus, it is evident that plan irregularities other than torsional irregularity are relatively less researched.

Table 1. Plan Irregularity Descriptors; their definition and limits of regularity for buildings

Types of Irregularity	Plan Irregularity Descriptor (PID) with description and limit of Regularity (Seismic Design Code of the Country)
Re-entrant Corner	$\frac{A}{L}$ ratio where, A = projection length and L = Plan dimension > 0.15 (India [15], Bangladesh [16], Pakistan [17], Philippines [18], Nepal [19], Korea [20], EL Salvador [21]); > 0.2 (Peru [22], Turkey [23]); > 0.25 (Algeria [24], Iran [25]); >0.3 (China [26])
	Normalized static eccentricity ratio, $\frac{e_{kx}}{L}$ or $\frac{e_{ky}}{B}$ $e_{kx} = x_r - x_m$; $e_{ky} = y_r - y_m$ where, e_k = Static eccentricity; x_m & y_m = Distance of centre of mass in X- and Y-direction, respectively; x_r & y_r = Distance of centre of rigidity in X- and Y-direction, respectively; L & B = Plan dimension in X- and Y-direction, respectively ≥ 0.1 (EL Salvador, Mexico [27]); ≥ 0.15 (Portugal [12], Algeria); ≥ 0.2 (Egypt [12], Iran [12])
Torsional Irregularity	(i) Static eccentricity (e_k) to torsional radius (r_k) ratio, $\frac{e_{kx}}{r_{kx}}$ or $\frac{e_{ky}}{r_{ky}}$ where, $r_{kx} = \sqrt{\frac{\sum(k_{xi}(y_i - y_r)^2) + \sum(k_{yi}(x_i - x_r)^2)}{\sum k_{yi}}}$; $r_{ky} = \sqrt{\frac{\sum(k_{xi}(y_i - y_r)^2) + \sum(k_{yi}(x_i - x_r)^2)}{\sum k_{xi}}}$ where, r_m = Mass radius of gyration; k_{xi} & k_{yi} = stiffness of an element in X- and Y-direction, respectively and x_i & y_i = distance of an element with respect to reference axis in X- and Y -direction, respectively ≥ 0.15 (Japan [12]); > 0.3 (Europe [28])
	(ii) Torsional radius (r_k) to Mass radius of gyration (r_m) ratio, $\frac{r_{kx}}{r_m}$ or $\frac{r_{ky}}{r_m}$, where, $r_m = \sqrt{\frac{\sum m_i d_i^2}{\sum(m_i)}}$ where, m_i = lumped mass and d_i = radial distance from CM ≤ 0.8 (Italy [12]); < 1 (Europe); $\frac{r_{kx,CM}}{r_m}$ or $\frac{r_{ky,CM}}{r_m} \leq 1$ (Greece [12])

	<p>(iii) Maximum to the minimum or average floor displacement, $\frac{\Delta_{max}}{\Delta_{min}}$ or $\frac{\Delta_{max}}{\Delta_{avg}}$ where, Δ_{max}, Δ_{min} and Δ_{avg} = Maximum, minimum and average floor displacement, respectively</p> <p>$\frac{\Delta_{max}}{\Delta_{min}} : > 1.5$ (India, Nepal); $\frac{\Delta_{max}}{\Delta_{avg}} : \geq 1.2$ (Bangladesh, China, India, Iran [12], Pakistan, Philippines, Taiwan [12], Turkey, USA [12]); ≥ 1.3 (Peru); $\frac{\Delta_{max}}{\Delta_{avg}} \geq 1.4$ (New Zealand [29], Bangladesh-extreme); ≥ 1.7 (Canada [30]); $\Delta_2 - \Delta_1 \geq 0.002H$ (Chile [31], $\Delta_2 - \Delta_1 = \text{max relative displacement between two consecutive floors and } H = \text{storey height}$); $\left(\frac{\Delta_{max}}{\Delta_{avg}}\right)_{drift} > 1.2$ (EL Salvador, Korea)</p> <p>(iv) The ratio of fundamental torsional to translational modes time period, $\frac{T_{\theta}}{T_x}$ and $\frac{T_{\theta}}{T_y}$, where, T_x and T_y = Fundamental time period of translational mode in X- and Y-direction, respectively and T_{θ} = Fundamental time period of torsional mode > 1 (India)</p>
Floor Slabs having excessive Cut-outs or Openings	<p>Opening located anywhere in the slab > 0.1 opening edge (India); > 0.15 (Algeria); > 0.3 (China) ; $> 1/3$ (Turkey); > 0.5 (Bangladesh, EL Salvador, India, Iran, Korea, Nepal, Pakistan, Peru, Philippines)</p>
Out-of-plane offsets in Vertical Elements	<p>Structural walls or frames are moved out of a plane in any storey along the height of the building India, Bangladesh, Canada, EL Salvador, Korea, Pakistan, Philippines, Nepal</p> <p>(i) In addition to (i), (a) For any single column j, the tangent of the offset angle, $\frac{a_j}{b_j} > 0.4$ (b) Average of the absolute values of the tangent of the offset angle, $\frac{\sum N_c \left \frac{a_j}{b_j} \right }{N_c} > 0.1$ where, a_j = the horizontal offset at column j b_j = the vertical distance between the base of the upper column and the top of the lower column j N_c = number of columns at the level under consideration New Zealand</p>
Non-parallel Lateral Force System	<p>Vertical structural systems resisting lateral forces are not oriented along the two principal orthogonal axes in the plan India, Bangladesh, Canada, EL Salvador, Korea, Pakistan, Philippines</p>

3. Re-entrant Dominant Irregular Building Models

A regular ten-storey RC building of plan dimension 50 m × 50 m with a square module of 5 m × 5 m each, placed symmetrically in both directions is considered as a basic plan configuration. Irregular RC buildings of various C-, L-, T- and PLUS-shaped geometrical shapes are derived by removing nos. of square modules appropriately from the basic plan configuration of a square regular building. Fig. 2 shows regular RC buildings along with C-, L-, T- and PLUS-shaped irregular RC buildings derived from regular RC building to have re-entrant corners.

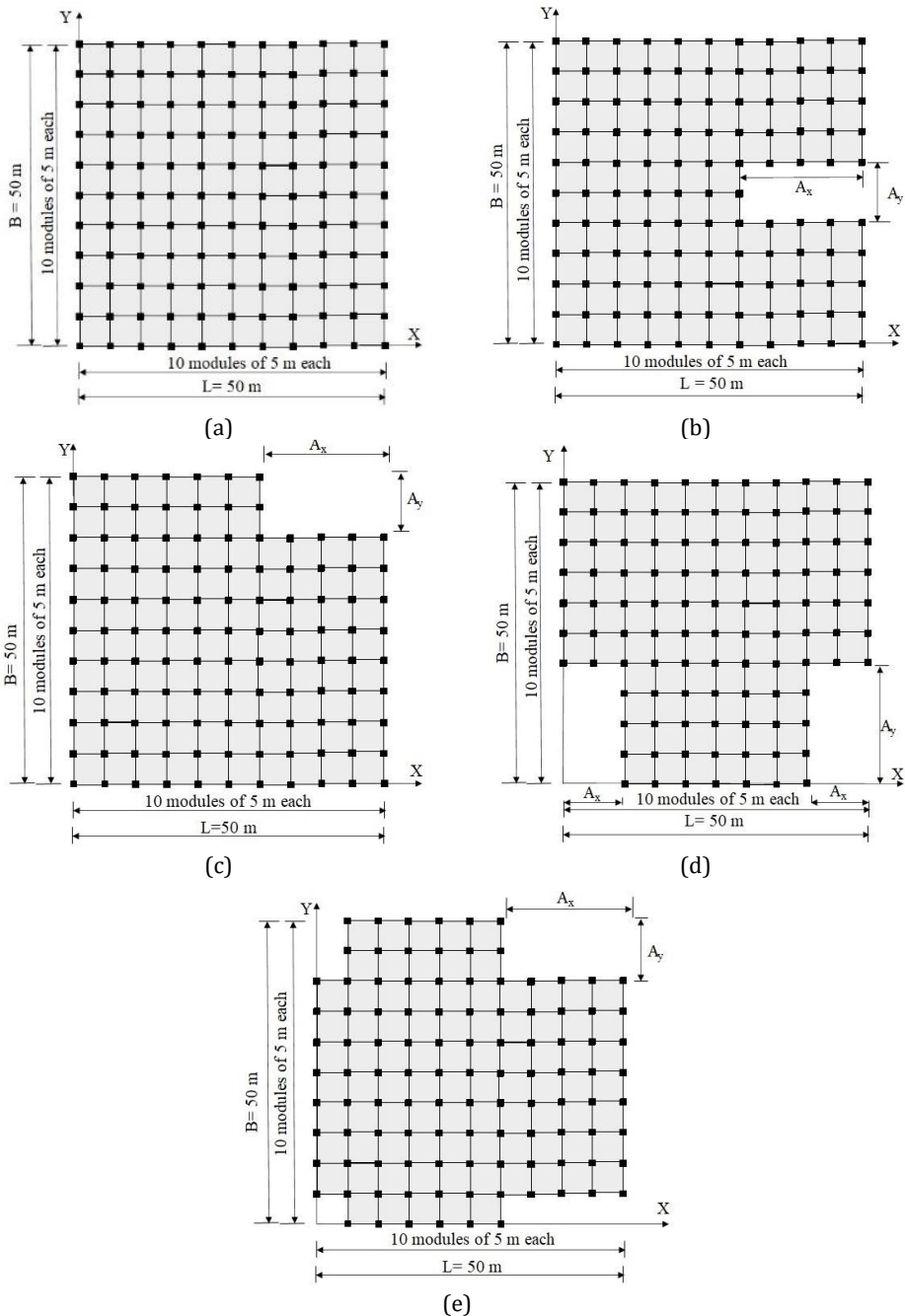


Fig. 2 Regular and plan irregular RC building models with A/L ratio 0.4 in the X-direction and 0.2 in the Y-direction, (a) Regular; (b) C-shaped; (c) L-shaped & (e) PLUS-shaped with A/L ratio 0.4 in the X direction and 0.2 in the Y-direction and (d) T-shaped with A/L ratio 0.2 in the X-direction and 0.4 in the Y-direction

Two categories of re-entrant dominant plan irregular RC building models developed are, (i) uni-directional re-entrant models having A/L ratio ranges between 0.1 to 0.8 in

X-direction with A/L ratio of 0.2 in Y-direction for C-, L- and PLUS-shaped RC building models. In T-shaped RC building models- A/L ratio of X-direction is 0.2 and in Y-direction it ranges between 0.1 to 0.8; (ii) bi-directional re-entrant models having A/L ratio ranges between 0.1 to 0.8 in X-direction with A/L ratio ranges between 0.2 to 0.8 in Y-direction for C-, L- and PLUS-shaped RC building models. In T-shaped RC building models A/L ratio varies from 0.1 to 0.8 in Y- direction with A/L ratio ranges between 0.2 to 0.4 in X-direction. RC building stocks with relatively high A/L ratio, both, uni-directional and bi-directional are practiced due to one or other reasons as discussed earlier.

Building models are analyzed and designed by, the Limit State Method (LSM) following Indian design code IS 456:2000 [32] for, gravity and lateral loading. IS 875 (Part-1, 2) [33,34], and IS 1893 (Part-1) codes are used for defining gravity and seismic loading definition, respectively.

Table 2. Geometric and design inputs for regular and irregular RC buildings

Geometric Details of RC Building	
Structural system	Moment Resisting Frame (MRF)
Shape of the building	C, L, T and PLUS
Centre-to-centre distance between frames in each direction	5 m
Typical floor height	3 m
Slab thickness	150 mm
Beam size	300 mm × 450 mm
Column sizes	600 mm × 600 mm (Typical floor nos. 1 to 3)
	500 mm × 500 mm (Typical floor nos. 4 to 6)
	400 mm × 400 mm (Typical floor nos. 7 to 10)
Diaphragm type	Semi-rigid, Rigid
Design Inputs of RC Building	
Gravity Loading Definition	
Impose load (Live load)	3 kN/m ² for a Typical floor 1.5 kN/m ² for Roof floor
Floor finish	1 kN/m ²
Seismic Loading Definition	
Seismic zone factor	0.36 (∵ seismic zone-v)
Importance factor	1.2
Response reduction factor	5 (∵ SMRF)
Soil type	Medium stiff
Damping	5 % of critical damping
Time period estimation	Code-based formula; Programme calculated
Seismic Analysis Method	
Equivalent Static Method (ESM)	---
Response Spectrum Method (RSM)	
Nos. of participating modes	Up to mass participation ≥ 90%
Participating modes	$\{ \phi_{ik} \}_x \{ \phi_{ik} \}_y \{ \phi_{ik} \}_\theta$ at the floor i in mode k Where, $x, y =$ Translational degrees of freedom $\theta =$ Rotational degree of freedom
Material Definition	
Concrete	$f_{ck} = 25$ MPa for M25 grade
Steel	$f_y = 415$ MPa for HYSD

The highest seismic zone is considered to have maximum seismic demand on plan irregular building models. The floor of the regular RC building models is modelled as rigid diaphragm while plan irregular building model have flexible floor diaphragms following recommendations by the seismic design codes for seismic analysis of irregular buildings. Table 2 summarizes geometrical and design inputs for the analysis and design of various structural elements of the RC building models.

Computational 3D models of regular and irregular RC buildings are created using commercial ETABS software (v18) by CSI corporation, USA [35]. Masonry walls are not modelled in the 3D model as; (i) non-uniform distribution of walls may lead to accidental eccentricities which increase seismic demand and (ii) Stiffness contribution of masonry wall is generally not considered in practice as walls are treated as nonstructural element. The study aims to investigate the seismic behaviour of re-entrant dominant RC buildings. RC building models are analyzed by ESM and RSM as per Indian seismic design code. Both seismic analysis methods are required to be performed for each RC building models as per Indian seismic design code as base shear and seismic response parameters are required to be scaled up by a scaling factor, $\left(\frac{V_B}{\bar{V}_B}\right)$ where \bar{V}_B is the base shear by ESM and V_B is the base shear by RSM when base shear and seismic response parameters obtained by RSM are lesser than those from ESM.

PIDs for re-entrant dominant RC building models are determined and are compared with those of regular RC building model. Table 3 summarizes PIDs for all RC building models conducted for the study and are limited to re-entrant corner and torsional irregularity types of plan irregularity only since other types of plan irregularity are absent in the RC building models. It is evident from Table 3 that all irregular RC building models are re-entrant dominant only since PIDs associated with torsional irregularity are well within prescribed limits of regularity defined by various seismic codes.

Table 3. Plan Irregularity Descriptors for regular and re-entrant dominant plan irregular RC buildings

Plan Irregularity Descriptors (PIDs)												
Building Models	$\left(\frac{A}{L}\right)$		$\left(\frac{e_k}{B}\right)$		$\left(\frac{e}{rkcs}\right)$		$\left(\frac{rkcs}{rm}\right)$	$\left(\frac{rkcm}{rm}\right)$	$\frac{T_\theta}{T_x}$	$\frac{T_\theta}{T_y}$	$\left(\frac{\Delta_{max}}{\Delta_{avg}}\right)$	
	X	Y	X	Y	X	Y	-	-	-	-	X	Y
Regular	0	0	0	0	0	0	1.062	1.062	0.930	0.930	1.064	1.064
C1* (0.1,0.2) #	0.1	0.2	0.004	0.004	0.009	0	1.033	1.033	0.935	0.931	1.064	1.065
C2 (0.2,0.2)	0.2	0.2	0.007	0.007	0.015	0	1.040	1.040	0.938	0.931	1.065	1.066
C3 (0.3,0.2)	0.3	0.2	0.009	0.009	0.020	0	1.034	1.034	0.942	0.931	1.064	1.067
C4 (0.4,0.2)	0.4	0.2	0.011	0.011	0.024	0	1.035	1.035	0.948	0.932	1.064	1.068
C5 (0.5,0.2)	0.5	0.2	0.011	0.011	0.025	0	1.038	1.038	0.953	0.933	1.063	1.069
C6 (0.6,0.2)	0.6	0.2	0.011	0.011	0.024	0	1.021	1.021	0.957	0.933	1.063	1.071
C7 (0.7,0.2)	0.7	0.2	0.009	0.009	0.020	0	1.010	1.010	0.962	0.932	1.062	1.062
C8 (0.8,0.2)	0.8	0.2	0.007	0.007	0.014	0	1.017	1.017	0.964	0.930	1.061	1.076
L1 (0.1,0.2)	0.1	0.2	0.001	0.000	0.001	0.001	1.063	1.063	0.930	0.929	1.065	1.065
L2 (0.2,0.2)	0.2	0.2	0.001	0.001	0.002	0.002	1.023	1.023	0.931	0.930	1.066	1.066
L3 (0.3,0.2)	0.3	0.2	0.001	0.002	0.003	0.004	1.064	1.064	0.931	0.930	1.068	1.068

L4 (0.4,0.2)	0.4	0.2	0.001	0.002	0.002	0.005	1.064	1.064	0.931	0.931	1.069	1.071
L5 (0.5,0.2)	0.5	0.2	0.001	0.003	0.001	0.007	1.064	1.064	0.932	0.932	1.069	1.073
L6 (0.6,0.2)	0.6	0.2	0.000	0.004	0.000	0.009	1.064	1.065	0.932	0.932	1.072	1.077
L7 (0.7,0.2)	0.7	0.2	-0.001	0.005	-0.003	0.011	1.066	1.066	0.931	0.930	1.076	1.082
L8 (0.8,0.2)	0.8	0.2	-0.003	0.006	-0.007	0.013	1.069	1.069	0.929	0.928	1.08	1.088
T1 (0.2,0.1)	0.2	0.1	0	-0.001	0	-0.003	1.065	1.065	0.929	0.929	1.066	1.066
T2 (0.2,0.2)	0.2	0.2	0	-0.002	0	-0.005	1.066	1.066	0.930	0.930	1.069	1.069
T3 (0.2,0.3)	0.2	0.3	0	-0.003	0	-0.007	1.067	1.067	0.930	0.930	1.074	1.071
T4 (0.2,0.4)	0.2	0.4	0	-0.003	0	-0.007	1.066	1.067	0.932	0.932	1.083	1.073
T5 (0.2,0.5)	0.2	0.5	0	-0.002	0	-0.006	1.066	1.066	0.934	0.934	1.092	1.074
T6 (0.2,0.6)	0.2	0.6	0	-0.001	0	-0.002	1.032	1.032	0.934	0.935	1.103	1.074
T7 (0.2,0.7)	0.2	0.7	0	0.001	0	0.003	1.026	1.026	0.933	0.934	1.116	1.075
T8 (0.2,0.8)	0.2	0.8	0	0.005	0	0.012	1.021	1.021	0.927	0.930	1.133	1.077
PLUS1(0.1,0.2)	0.1	0.2	0.000	0.000	0.000	0.001	1.066	1.066	0.929	0.929	1.069	1.068
PLUS2(0.2,0.2)	0.2	0.2	0.001	0.001	0.001	0.001	1.064	1.064	0.928	0.928	1.071	1.071
PLUS3(0.3,0.2)	0.3	0.2	0.001	0.001	0.002	0.002	1.068	1.068	0.929	0.929	1.073	1.075
PLUS4(0.4,0.2)	0.4	0.2	0.001	0.001	0.002	0.003	1.068	1.068	0.930	0.930	1.074	1.079
PLUS5(0.5,0.2)	0.5	0.2	0.000	0.002	0.000	0.004	1.068	1.068	0.930	0.930	1.075	1.084
PLUS6(0.6,0.2)	0.6	0.2	-0.001	0.002	-0.003	0.005	1.069	1.069	0.930	0.931	1.076	1.091
PLUS7(0.7,0.2)	0.7	0.2	-0.003	0.003	-0.007	0.007	1.071	1.071	0.929	0.929	1.077	1.100
PLUS8(0.8,0.2)	0.8	0.2	-0.006	0.004	-0.014	0.009	1.076	1.076	0.924	0.926	1.079	1.113

*Re-entrant RC building Model No., # (A/L ratio in X-direction, A/L ratio in Y-direction)

4. Results and Discussion

The seismic behaviour of RC building models with C-, L-, T- and PLUS- type geometrical shapes are presented in four parts; (i) unidirectional re-entrant RC building models; (ii) bi-directional re-entrant RC building models; (iii) Stress concentration in re-entrant RC building models and (iv) Diaphragm modelling of re-entrant RC building models. A three-dimensional seismic analysis of each RC building models is performed by considering both, rigid and flexible diaphragm using ETABS. Seismic response parameters; peak displacement, peak storey drift, normalized base shear ($\frac{V_B}{\Sigma W}$)-ratio of base shear to seismic weight of the building and Normalized Overturning Moment ($\frac{M_o}{\Sigma w_i h_i}$) - ratio of overturning moment with product of weight and height of the building are evaluated. PIDs evaluated for each RC building models are re-evaluated to ascertain coupling of torsional irregularity with re-entrant corner type irregularity, especially for higher unidirectional and bi-directional A/L ratio. Shear stress distribution in the diaphragm of RC building models is studied with greater emphasis on RC building models with re-entrant corners. The effect of diaphragm modelling on the seismic behaviour of re-entrant dominant RC building models are investigated.

4.1. Uni-directional Re-entrant RC Building Models

Effect of increasing A/L ratio in a uni-directional direction is studied first with a constant A/L ratio of 0.2 in orthogonal direction. 28 out of 32 plan irregular RC building models are re-entrant dominant only since they exceed limit of regularity; A/L ratio of 0.15 as per the Indian Seismic code in X-direction. A/L ratio of 0.2 in Y-direction is considered to understand the immediate impact of re-entrant corner PID exceedance in Y-direction on seismic behaviour. Peak displacement of RC building models in X- and Y-directions due to seismic force are plotted in Fig. 3(a) and Fig. 3(b). It is evident that peak displacement response of plan irregular RC building models increases w.r.t. to regular RC building model

except C-shaped re-entrant corner RC models. This is because C-shaped RC building models are symmetric about the horizontal axis with MR frames resisting lateral loads.

Most of the other types of re-entrant dominant RC building models show marginal increase of ~6 % in peak displacement response. T-shape building models; T5(0.2, 0.5); T6(0.2, 0.6); T7(0.2, 0.7) and T8(0.2,0.8) show an increase in peak displacement of 6.11 %; 8.02 %; 10.5 % and 13.98 %, respectively. It has been observed that peak displacement in Y-direction due to applied seismic force increases marginally ~5.44 % for all re-entrant corner RC building models, except PLUS type RC building models. PLUS-shaped RC building models; PLUS6(0.6,0.2), PLUS7(0.7,0.2) and PLUS8(0.8,0.2) response increase by 6.01 %, 7.9 % and 10.55 %, respectively vis-a-vis regular RC building models. C-, L- and PLUS-shaped building models with A/L ratio > 0.15 yield maximum increase of 4.75 %, 25 % and 35.04 %, respectively in Y-direction peak displacement due to X-direction seismic force.

However, this response shows maximum increase of 173 % for T-shape building models. X-direction peak displacement response due to seismic force in Y-direction of C-, L- and PLUS-shaped building models vary between 8.37 % – 48.91 %, 9.79 % – 98.15 % and 18.06 % – 161.21 %, respectively. However, this response varies between 16.75 % – 34.69 % for T-shaped building models. Fig. 3(c) and Fig. 3(d) show peak displacement response of re-entrant dominant RC building models in orthogonal directions to the applied seismic force, i.e., peak displacement in X-direction due to seismic force applied in Y-direction and vice-versa. Peak displacement of re-entrant dominant RC building models is found to be amplified for models with A/L ratio > 0.15 . This is due to coupling between re-entrant type plan irregularity with a torsional response. Re-entrant dominant RC building models of C-, L- and T-shaped show almost identical peak displacement response for A/L ratio of 0.1. However, PLUS- shape re-entrant dominant RC building models yield ~10 % increase in peak displacement response in orthogonal directions to applied seismic loads in both X- and Y-direction. Therefore, seismic code limit of A/L ratio < 0.15 seems to be underrated and such type of plan irregular RC building should be avoided. It has been observed that re-entrant corner results in to torsional displacement and thus beyond certain value of A/L ratio re-entrant plan irregularity converted to torsional irregularity.

Peak storey drift ratio of all building models is evaluated as shown in Table. 4. It has been observed that almost all building models have peak storey drift value well within permissible limit of 0.004 times height of the storey i.e., 0.012(1.2 % drift ratio). Maximum peak storey drift value obtained for T8(0.2,0.8) building model is 0.0063 (0.63 % drift ratio) only.

Fig. 4(a) and Fig. 4(b) shows normalized base shear and normalized overturning moment for all building models in the direction of applied seismic forces, i.e., X- and Y-direction. These response quantities in orthogonal directions of the applied seismic force direction are plotted in Fig. 4(c) and Fig. 4(d). It is evident from these figures that normalized base shear in the direction and orthogonal direction of applied seismic forces have similar trend and so as for normalized overturning moment. This is due to the fact that seismic response quantities are governed by ESM over RSM and these quantities are scaled up by the ratio of quantities by ESM to RSM as per Indian seismic design code. Therefore, a general term “seismic forces” is used to indicate seismic forces obtained by seismic analysis using ESM and RSM leading to identical values owing to scaling up of the value obtained by later. Detailed analysis of building models reveals that re-entrant corner with increasing A/L ratio leads to torsional response as these models had non-exceeding PIDs related to torsional irregularities as tabulated in Table 1.

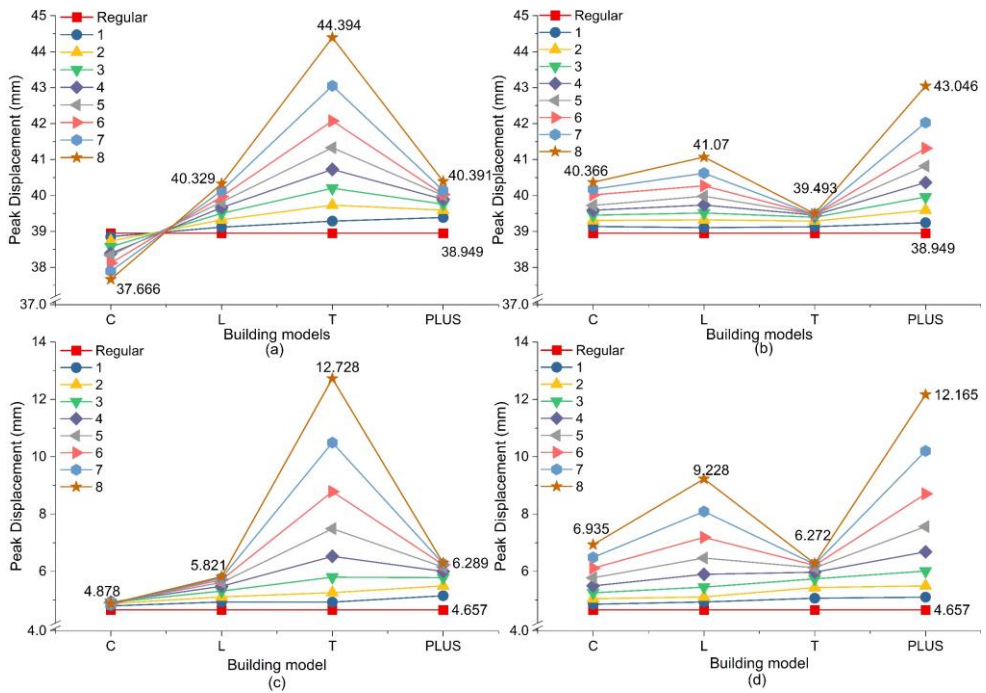


Fig. 3 Peak displacement response of regular and re-entrant dominant plan irregular RC building models, (a) Response in X-direction for seismic force RSM-X; (b) Response in Y-direction for seismic force RSM-Y; (c) Response in Y-direction for seismic force RSM-X and (d) Response in X-direction for seismic force RSM-Y

Table 4. Peak storey drift ratio of regular and re-entrant dominant plan irregular RC building models

		Peak Storey Drift									
		Regular	C1	C2	C3	C4	C5	C6	C7	C8	
X-dir.		0.0018	0.0018	0.0018	0.0018	0.0018	0.0018	0.0018	0.0018	0.0017	
Y-dir.		0.0018	0.0018	0.0018	0.0018	0.0018	0.0018	0.0019	0.0019	0.0019	
Y ← X dir.*		0.0002	0.0002	0.0002	0.0002	0.0002	0.0002	0.0002	0.0002	0.0002	
X ← Y dir.*		0.0002	0.0002	0.0002	0.0002	0.0002	0.0003	0.0003	0.0003	0.0003	
			L1	L2	L3	L4	L5	L6	L7	L8	
X-dir.		0.0018	0.0018	0.0018	0.0018	0.0018	0.0018	0.0018	0.0019	0.0019	
Y-dir.		0.0018	0.0018	0.0018	0.0018	0.0018	0.0019	0.0019	0.0019	0.0019	
Y ← X dir.		0.0002	0.0002	0.0002	0.0002	0.0002	0.0002	0.0002	0.0003	0.0003	
X ← Y dir.		0.0002	0.0002	0.0002	0.0002	0.0003	0.0003	0.0003	0.0004	0.0004	
			T1	T2	T3	T4	T5	T6	T7	T8	
X-dir.		0.0018	0.0018	0.0018	0.0019	0.0019	0.0019	0.0019	0.0020	0.0021	
Y-dir.		0.0018	0.0018	0.0018	0.0018	0.0018	0.0018	0.0018	0.0018	0.0018	
Y ← X dir.		0.0002	0.0002	0.0002	0.0003	0.0003	0.0003	0.0004	0.0005	0.0006	
X ← Y dir.		0.0002	0.0002	0.0002	0.0002	0.0003	0.0003	0.0003	0.0003	0.0003	
			PLUS1	PLUS 2	PLUS 3	PLUS 4	PLUS 5	PLUS 6	PLUS 7	PLUS 8	
X-dir.		0.0018	0.0018	0.0018	0.0018	0.0018	0.0019	0.0019	0.0019	0.0019	
Y-dir.		0.0018	0.0018	0.0018	0.0019	0.0019	0.0019	0.0019	0.0019	0.0020	
Y ← X dir.		0.0002	0.0002	0.0002	0.0003	0.0003	0.0003	0.0003	0.0003	0.0003	
X ← Y dir.		0.0002	0.0002	0.0002	0.0003	0.0003	0.0003	0.0004	0.0005	0.0005	

*-Displacement response in Y-direction due to earthquake force applied in X-direction or vice-versa.

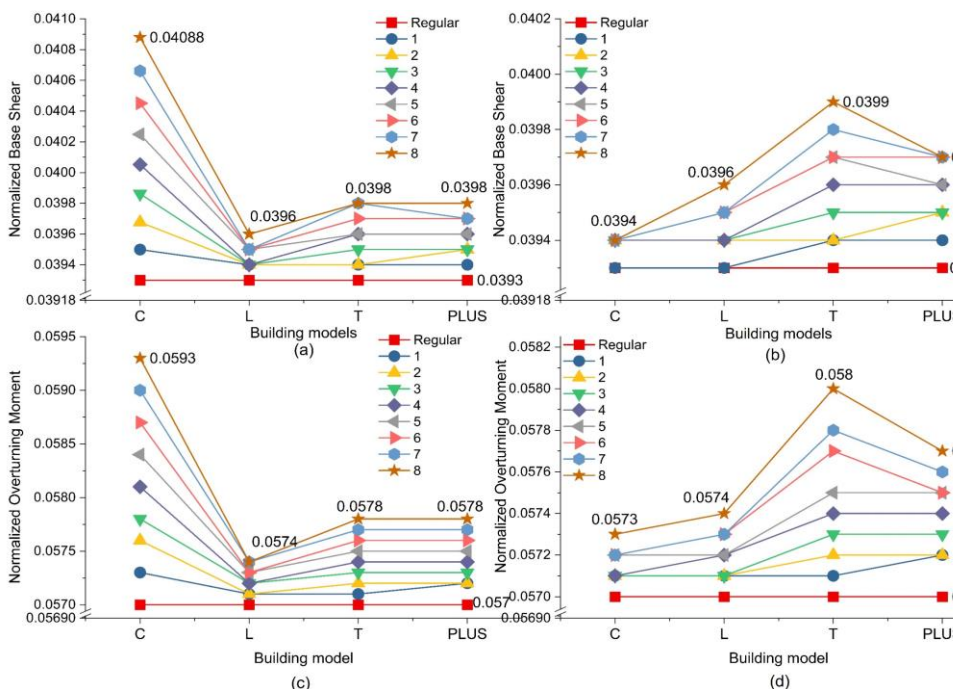


Fig. 4 (a) Normalized base shear response in X-direction for seismic force RSM-X; (b) Normalized base shear response in Y-direction for seismic force RSM-Y; (c) Normalized overturning moment response in X-direction for seismic force RSM-X and (d) Normalized overturning moment response in Y-direction for seismic force RSM-Y of regular and re-entrant dominant plan irregular RC building models

L-shaped building models; L6(0.6,0.2) to L8(0.8,0.2) as well as PLUS-shaped building models; PLUS5(0.5,0.2) to PLUS8(0.8,0.2) exceed torsional irregularity limit of 1.2 for PID; $\frac{\Delta_{max}}{\Delta_{avg}}$, at all floor levels for X-direction displacement response to Y-direction seismic force. Indian seismic code and most seismic codes world-wide have specified $\frac{\Delta_{max}}{\Delta_{avg}}$ limits under the direction of seismic force, but limit of $\frac{\Delta_{max}}{\Delta_{avg}}$ for orthogonal directions to the applied seismic direction is not specified. However, such as bi-directional torsional seismic response is typical of a re-entrant irregularity, and thus $\frac{\Delta_{max}}{\Delta_{avg}}$ limit should be specified for maximum torsional response irrespective of seismic force direction.

4.2. Bi-directional Re-entrant RC Building Models

In this section, results of seismic response studies conducted for RC building models having bi-directional re-entrant corners are reported. New building models are developed with A/L ratio in Y-direction ranges between 0.4 to 0.8 with an increment of 0.2 while A/L ratio in X-direction is between 0.1 to 0.8 as earlier building models. Building models with A/L ratio of 0.8 in Y-direction for C-shaped and ratio beyond 0.6 for T-shaped building models in the X-direction are non-realizable due to geometrical dimensions. As evident from discussion in Section 4.1 that peak displacement of orthogonal directions to applied seismic force direction shows amplification, therefore, results related to this response are reported in Table 5.

Table 5. Peak displacement response of re-entrant RC building models in orthogonal directions to the direction of seismic force

Direction of Response ← Seismic Force	$(\frac{A}{L})_y$	$(\frac{A}{L})_x$								
		Regular	0.1	0.2	0.3	0.4	0.5	0.6	0.7	0.8
C-shaped RC Building Model										
Y←X dir.	0.2	4.65	4.79	4.88	4.92	4.93	4.91	4.87	4.85	4.87
X←Y dir.	0.2	4.65	4.85	5.04	5.25	5.49	5.78	6.11	6.49	6.93
Y←X dir.	0.4	4.65	4.92	5.09	5.18	5.18	5.12	5.02	4.92	4.92
X←Y dir.	0.4	4.65	4.97	5.26	5.61	6.04	6.57	7.25	8.06	9.05
Y←X dir.	0.6	4.65	5.08	5.38	5.57	5.63	5.56	5.42	5.29	5.35
X←Y dir.	0.6	4.65	5.09	5.49	5.96	6.55	7.29	8.27	9.51	11.05
L-shaped RC Building Model										
Y←X dir.	0.2	4.65	4.93	5.11	5.31	5.48	5.61	5.71	5.77	5.82
X←Y dir.	0.2	4.65	4.93	5.11	5.45	5.90	6.46	7.18	8.09	9.22
Y←X dir.	0.4	4.65	5.23	5.90	6.51	7.03	7.43	7.70	7.82	7.79
X←Y dir.	0.4	4.65	5.03	5.45	6.39	7.03	8.23	9.97	12.3	15.67
Y←X dir.	0.6	4.65	5.81	7.18	8.60	9.97	11.17	12.09	12.53	12.34
X←Y dir.	0.6	4.65	5.12	5.71	6.53	7.70	9.44	12.09	16.13	22.54
Y←X dir.	0.8	4.65	6.64	9.22	12.27	15.67	19.23	22.60	24.98	26.23
X←Y dir.	0.8	4.65	5.19	5.82	6.64	7.78	9.51	12.35	17.23	26.23
PLUS-shaped RC Building Model										
Y←X dir.	0.2	4.65	5.15	5.49	5.78	6.00	6.15	6.23	6.26	6.28
X←Y dir.	0.2	4.65	5.10	5.49	6.01	6.68	7.56	8.70	10.20	12.16
Y←X dir.	0.4	4.65	5.83	6.73	7.48	8.17	8.68	8.96	8.95	8.69
X←Y dir.	0.4	4.65	5.35	6.04	6.89	8.17	10.02	12.72	16.67	22.49
Y←X dir.	0.6	4.65	6.90	8.71	10.69	12.72	14.56	15.70	16.34	14.96
X←Y dir.	0.6	4.65	5.47	6.23	7.32	8.96	11.59	15.70	23.18	35.84
Y←X dir.	0.8	4.65	8.56	12.16	16.7	22.4	29.09	35.84	40.23	41.07
X←Y dir.	0.8	4.65	5.54	6.28	7.28	8.69	10.95	14.96	23.01	41.07
T-shaped RC Building Model										
	$(\frac{A}{L})_x$					$(\frac{A}{L})_y$				
Y←X dir.	0.2	4.65	4.93	5.26	5.80	6.52	7.49	8.78	10.49	12.73
X←Y dir.	0.2	4.65	5.06	5.43	5.74	5.97	6.12	6.21	6.25	6.27
Y←X dir.	0.4	4.65	5.12	5.77	6.66	7.94	10.0	13.09	17.66	24.46
X←Y dir.	0.4	4.65	5.43	6.24	7.04	7.76	8.21	8.55	8.75	8.55

It has been observed that peak displacement response substantially increases ($\geq 137\%$) for $A/L \geq 0.6$ for C-, L- and PLUS-shaped building models and thus, re-entrant corner of such A/L ratio should not be permitted. T-shaped building model shows amplification of the order ($> 173\%$) in peak displacement response for both A/L 0.2 and 0.4 and therefore A/L limit of 0.15 by seismic design codes are not in agreement for such building models. Seismic analysis suggests that only C- and L-shaped building models yield reasonable peak displacement response for A/L ratio ≤ 0.4 . PLUS-shaped building model with A/L 0.4 also yields reasonable peak displacement response. Detailed investigation reveals that building models with $A/L \geq 0.6$ result into flexible projected frames also called cantilever tails and thus peak displacement response increases substantially due to deformation of such cantilever tails.

Buildings with such flexible cantilever tail(s) result in exceeding the, $\frac{\Delta_{max}}{\Delta_{avg}}$ PID limit of 1.2 while other torsional irregularity PIDs were verified to fall within the limit. Fig. 5 shows building models with A/L ratio in X- and Y-direction with, $\frac{\Delta_{max}}{\Delta_{avg}}$ PID values. Dark line indicates that building models within have the PID value < 1.2, permissible value by seismic design codes. PID, $\frac{\Delta_{max}}{\Delta_{avg}}$ is obtained for peak displacement of building model in orthogonal directions to the applied seismic force as tabulated in Table 5. Re-entrant corner type plan irregularity defined by A/L ratio with permissible limit of regularity as 0.15 by Indian seismic design code is marked in Fig. 5 with dash-dot line. It is evident from Fig. 5 that, permissible limit of regularity is quite conservative since many building models don't exceed $\frac{\Delta_{max}}{\Delta_{avg}}$ PID for A/L ratio up to 0.4 in Y-direction for C-, L- & PLUS-shaped and X-direction for T-shaped and for A/L ratio in X-direction up to 0.6, 0.3 & 0.2 for C-, L- & PLUS-shaped, respectively and in Y-direction up to 0.4 in T-shaped building models. Few building models with A/L ratio of 0.2 in Y-direction for C-, L- & PLUS-shaped and X-direction for T-shaped show $\frac{\Delta_{max}}{\Delta_{avg}}$ PID within limit for A/L ratio in X-direction up to 0.8, 0.5 & 0.4 for C-, L- & PLUS-shaped and in Y-direction up to 0.6 for T-shaped building models.

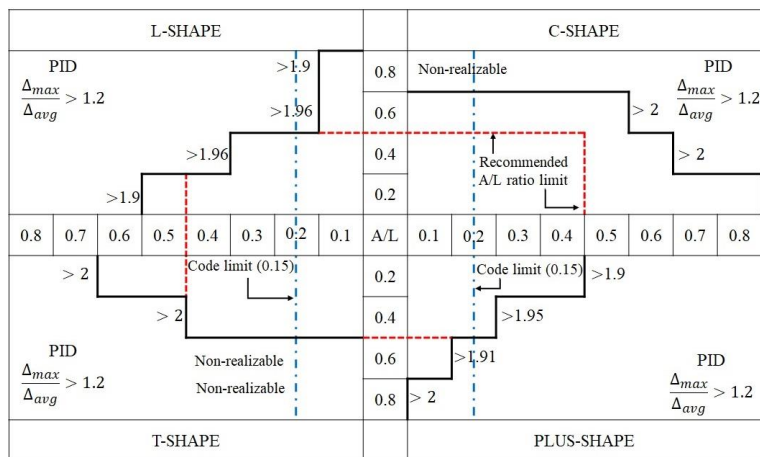


Fig. 5 Torsional response type PID, $\left(\frac{\Delta_{max}}{\Delta_{avg}}\right)$ for bi-directional re-entrant irregular RC building models

Based on this analysis, it can be recommended that the limit of regularity of A/L ratio for re-entrant corner type plan irregularity may be increased to 0.4 from present value of 0.15, as indicated by dash line in Fig. 5. Note that, school, business centre, hotel, hospital and hostel buildings typically have C-, L- and T-shaped geometry and are widely practiced world-wide. It can be realized from Fig. 5 that PLUS-shaped building models with $A/L \geq 0.6$ shows $\frac{\Delta_{max}}{\Delta_{avg}}$ PID exceeded even for A/L ratio ≤ 0.1 in X-direction. Therefore, it is not recommended to practice PLUS-shaped buildings owing to their torsional behavior with low level of re-entrant corners. Amongst various geometrical shapes of building models considered in the present study, C-shaped building models show better seismic response followed by T-shaped and L-shaped building models.

Plan irregular buildings with re-entrant corners are expected to undergo complicated deformed shapes during modal analysis [3,13]. The present study has observed such

behaviour of building models when A/L ratio become ≥ 0.4 in, both, X- and Y- directions due to cantilever tail('s) (i.e., flexible projected frames). However, complicated deformed shape of these building models is associated with higher modes which have very low time period (very high frequencies). Therefore, mass participation of such complicated deformed shape is very low ($\sim \leq 1\%$). The mass participation for re-entrant dominant building models is driven by vibration associated with high time period (low frequency) associated to fundamental translational and rotational modes.

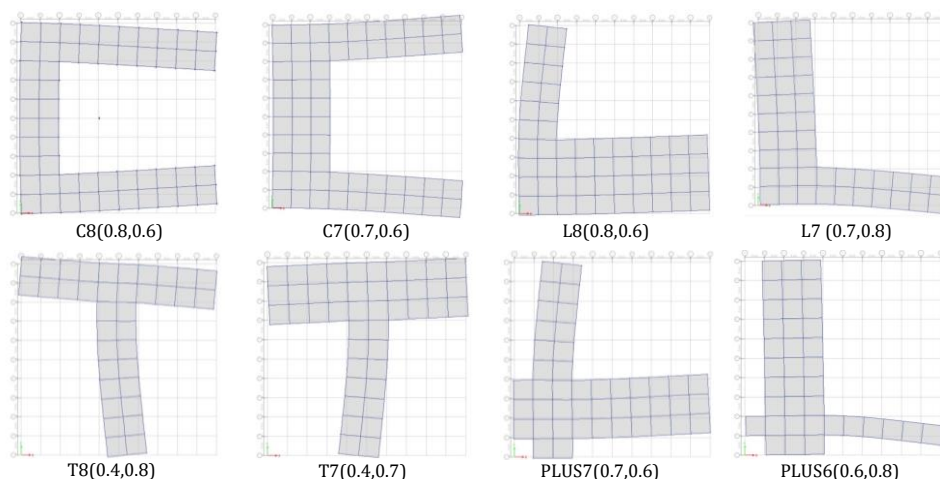


Fig. 6 Representative complicated deformed mode shapes of re-entrant RC building models

Modal analysis of building models reveal that re-entrant corner dominant building models have time period of translational mode in principal directions higher than time period of rotational mode. Though, with an increase in A/L ratio $\geq (0.7, 0.8)$ for L-shaped, $(0.4, 0.8)$ for T-shaped and $(0.8, 0.6)$ & $(0.6, 0.8)$ for PLUS-shaped in X- and Y-directions, mass participation by transitional mode decreases while it increases from rotational modes leading to translational-rotational combined modes of vibration.

Table 6 shows summary of the complicated deformed shapes of building models with their time period and mass participation ratio. It can be seen that with increasing A/L ratio, corresponding time period associated with the complicated deformed shape increases due to the flexibility of the cantilever tail('s) and reduced seismic weight of the building model. Few representatives, complicated deformed mode shapes are shown in Fig. 6 for C-, L, T- and PLUS-shaped building models

Table 6. Summary of time period and mass participation factor of complicated deformed shape of re-entrant RC building models

RC Building Model	Mode Shapes with A/L Ratio-Time period and Mass Participation Factor
C-shaped	Mode-4: (0.8, 0.2)- 0.61 sec, $\sim 0\%$, (0.8, 0.4)-0.65 sec, $\sim 0\%$, (0.8, 0.6)-0.668 sec, $\sim 0\%$
	Mode-6: (0.7, 0.6)- 0.465 sec, $\sim 0\%$
	Mode-7: (0.6, 0.2)- 0.284 sec, $\sim 0\%$, (0.7, 0.2)- 0.398 sec, $\sim 0\%$, (0.6, 0.4)-0.308 sec, $\sim 0\%$, (0.7, 0.4)- 0.428 sec, $\sim 0\%$, (0.6, 0.6)- 0.234 sec, $\sim 0\%$
	Mode-10: (0.4, 0.6)- 0.189 sec, $\sim 0\%$, (0.5, 0.6)- 0.258 sec, $\sim 0\%$
	Mode-12: (0.4, 0.6)- 0.189 sec, $\sim 0\%$
L-shaped	Mode-7: (0.7, 0.8)- 0.296 sec, $< 1\%$, (0.8, 0.8)- 0.365 sec, $< 1\%$
	Mode-10: (0.7, 0.6)- 0.192 sec, $\sim 0\%$, (0.8, 0.6)- 0.246 sec, $\sim 0\%$, (0.5, 0.8)-0.2 sec, $\sim 0\%$, (0.6, 0.8)- 0.247 sec, $\sim 0\%$

T-shaped	Mode-10: (0.6, 0.4)- 0.204 sec, < 1 %, (0.7, 0.4)-0.232 sec, < 1 %, (0.8, 0.4)-0.25 sec, ~0 %
	Mode-4: (0.8, 0.8)- 0.561 sec, ~0 %
PLUS-shaped	Mode-7: (0.8, 0.6)- 0.36 sec, < 1 %, (0.5, 0.8)- 0.281 sec, < 1 %, (0.6, 0.8)- 0.36 sec, < 1 %, (0.7, 0.8)- 0.44 sec, < 1 %
	Mode-10: (0.8, 0.4)- 0.205 sec, ~0 %, (0.7, 0.6)- 0.231 sec, ~0 %
	Mode-12: (0.6, 0.6)- 0.28 sec, ~0 %

4.3. Stress Concentration in Re-entrant RC Building Models

Re-entrant corner dominant building models are likely to have stress concentration at corner(s) due to torsional response resulting from combined translational-torsional modes of vibration. All building models are modelled with semi-rigid diaphragm following seismic design code stipulations related to irregular building. Such modelling approach enables seismic analysis to capture in-plane forces developed in the diaphragm due to inertia force of the building. Fig. 7 shows the in-plane stress distribution produce in the diaphragm of C-, L-, T- and PLUS-shaped building models for A/L ratio of 0.8 in X-direction and 0.4 in Y-direction. Von-mises shear stresses are evaluated for each building model which reveal that corners are subjected to higher shear stress. Additionally, it can be seen that, peripheral portion of diaphragms also suffered from shear stress concentration due to the flexibility of cantilevered tail(s). Most building models yield low values of shear stress at re-entrant corner (s) due to relatively lower value of $(\frac{e_x}{B})$ ratio resulting to low additional shear force by the twisting moment. As discussed earlier, complicated deformed mode shapes of the building models do not contribute significantly due to low mass participation and thus, produces negligible shear stresses in the diaphragm. Shear stress concentration at re-entrant corners may become significant, if complicated deformed mode shape contribution increases significantly due to the asymmetric mass and stiffness distribution for the building model.

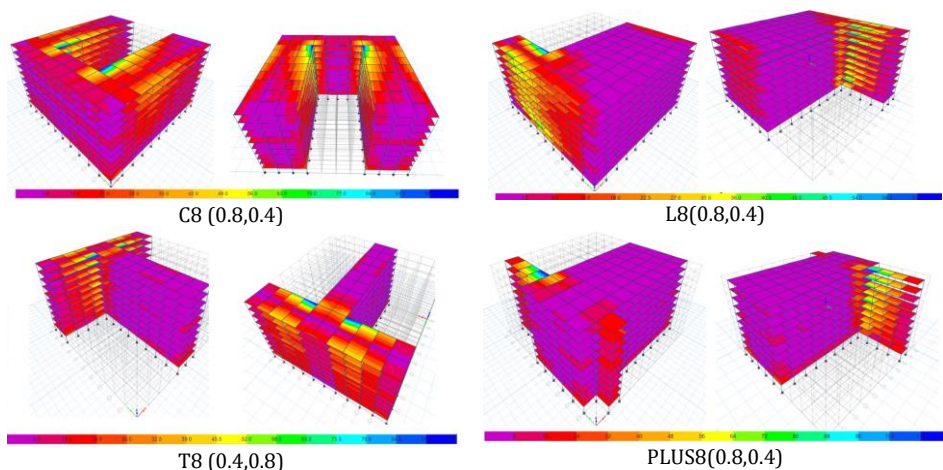


Fig. 7 In-plane stress distribution C-, L-, T- and PLUS-shaped building models

4.4. Diaphragm Modelling of Re-entrant RC Building Models

Diaphragms is an important element of the RC buildings since it transfer lateral load to vertical load resisting system. In-plane stiffness of the diaphragm relative to the stiffness of the lateral load resisting system defines rigidity or flexibility. Indian seismic design code recommends use of flexible diaphragm to perform seismic analysis of RC building with re-entrant corner as per latest version. All building models in the present study are

developed using both, semi-rigid (flexible) and rigid diaphragm modelling approach to understand effectiveness of their lateral load distribution capabilities to vertical load resisting system using ETABS. It has been found that re-entrant dominant building models with semi-rigid (flexible) diaphragm yield exactly identical seismic behaviour with that of the rigid diaphragm since semi-rigid diaphragm also have relatively higher in-plane stiffness. Though, deformation of semi-rigid diaphragm is different than rigid diaphragm where later has rigid translation only. The said observations are of good agreement with result reported by other literature [14] related to semi-rigid diaphragm.

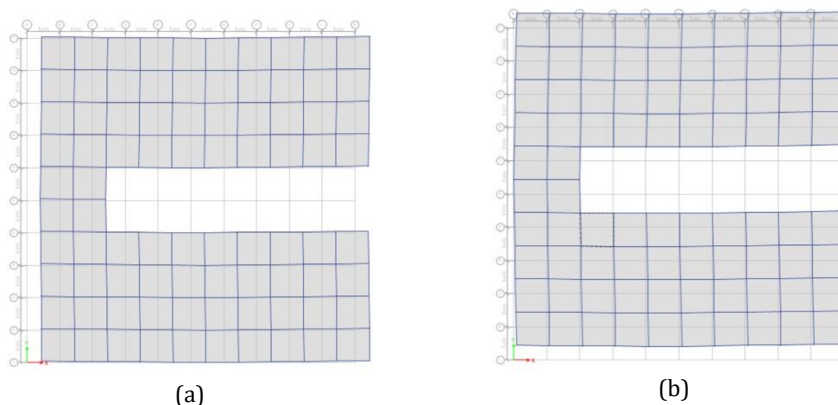


Fig. 8 Displacement profile in semi-rigid diaphragm
(a) seismic force in X-direction and (b) seismic force in Y-direction

Difference between shear force results obtained for all building models with rigid and semi-rigid diaphragm are found to be $\leq 5\%$ only. A representative, C-shaped building model with A/L ratio 0.8 in X-direction and 0.2 in Y-direction is shown in Fig. 8 for seismic force in X- and Y-directions. Peak displacement of building models with semi-rigid diaphragm are found to be higher vis-à-vis building model with a rigid diaphragm. In semi-rigid diaphragm, floors are capable of transferring internal forces which is not possible in case of rigid diaphragm.

5. Conclusions

Irregular RC buildings have suffered damages during past earthquakes and are vulnerable. Irregularities are classified as plan and vertical irregularity by seismic design codes world-wide. Present paper aims to investigate the seismic behaviour of plan dominant with re-entrant corners irregular RC buildings of C-, L-, T- and PLUS-shaped. Total 104 building models comprising of C- (24 nos.), L- (32 nos.), T-(16 nos.) and PLUS- (32 nos.) shaped with A/L ratio ranges between 0.1 to 0.8 in X-direction and of 0.2, 0.4, 0.6 and 0.8 in Y-direction for C-, L- and PLUS- shapes and A/L ratio of 0.2 and 0.4 in X-direction and of 0.1 to 0.8 in Y-direction for T-shaped models are developed along with a regular RC building model. Plan Irregularity Descriptors (PIDs) are defined and computed to ensure developed building models are re-entrant dominant. Seismic response parameters; peak displacement, peak storey drift, normalized based shear and normalize overturning moment are determined using Equivalent Static Method and Response Spectrum Method recommended by Indian Seismic design code for all building models. Combined translational-torsional modes of vibration resulting to stress concentration at re-entrant corner and other places of the building models are studied. Recommendation by seismic

design code for 3D analysis of irregular building with flexible diaphragm is investigated by modelling building models with both, rigid and flexible diaphragm approach.

The major observations of the present study are summarized as follows.

Building models show a marginal increase of ~6% in peak displacement due to seismic forces, except for T- and PLUS-shaped building models with A/L ratio ≥ 0.6 in the X-direction and 0.2 in Y-direction.

- Building models with an A/L ratio of 0.2 to 0.8 in the X-direction and 0.2 in the Y-direction yield moderate to substantial increase (34.68 % to 173.31 %) in peak displacement of orthogonal directions to the direction of seismic force applied.
- Peak storey drift response of all building models falls well within permissible limit of 0.4% of storey height by Indian seismic code.
- Normalized base shear and normalized overturning moment of building models are found to be at par with the regular building model.
- L- and PLUS-shaped building models with A/L ratio ≥ 0.5 in the X-direction exhibit torsion type PID, $\frac{\Delta_{max}}{\Delta_{avg}}$ exceeding the permissible limit of 1.2. Thus, such building models shall be modified in terms of geometric dimensions.
- Complicated deformed mode shapes are observed for increasing A/L ratio, however, these modes have insignificant mass participation due to low time period.
- Limit of re-entrant corner PID, A/L ratio of 0.15 defined by Indian seismic design code is found to be conservative. A/L ratio limit of 0.4 is recommended from the present study since beyond this limit PID, $\frac{\Delta_{max}}{\Delta_{avg}}$ exceeding permissible limit of 1.2.
- C-shaped building models perform well under seismic force for large range of A/L in X- and Y- direction.
- Shear stress values at the re-entrant corner of building models are found to be relatively low. Stress concentration is observed at the periphery of semi-rigid diaphragm for few building models.
- Building models with semi-rigid (flexible) diaphragm yield similar (difference $\leq 5\%$) lateral load force distribution in the lateral-load resisting system as that of building models with rigid diaphragm. However, peak displacement response of building models with semi-rigid (flexible) diaphragm is different and higher vis-à-vis rigid diaphragm building models.

References

- [1] Khanal B, Chaulagain H. Seismic elastic performance of L-shaped building frames through plan irregularities. *Structures*, 2020; 27: 22-36. <https://doi.org/10.1016/j.istruc.2020.05.017>
- [2] Ten-Colunga A. Conditions of structural irregularity. Relationships with observed earthquake damage in Mexico City in 2017. *Soil Dynamics and Earthquake Engineering*, 2021; 143: 106630. <https://doi.org/10.1016/j.soildyn.2021.106630>
- [3] Das PK, Dutta SC, Datta TK. Seismic behavior of Plan and Vertically Irregular Structures: State of Art and Future Challenges. *Natural Hazards Review*, 2021; 22(2): 04020062. [https://doi.org/10.1061/\(ASCE\)NH.1527-6996.0000440](https://doi.org/10.1061/(ASCE)NH.1527-6996.0000440)
- [4] Anagnostopoulos SA, Kyrkos MT, Stathopoulos KG. Earthquake induced torsion in buildings: critical review and state of the art. *Earthquakes and Structures*, 2015; 8 (2): 305-77. <https://doi.org/10.12989/eas.2015.8.2.305>
- [5] Goel RK, Chopra AK. Effects of Plan Asymmetry in Inelastic Seismic Response of the One-Story Systems. *Journal of Structural Engineering*, 1991; 117(5): 1492-513. [https://doi.org/10.1061/\(ASCE\)0733-9445\(1991\)117:5\(1492\)](https://doi.org/10.1061/(ASCE)0733-9445(1991)117:5(1492))
- [6] Escobar JA, Ayala-Milian AG. Yielding seismic response of code-designed single-storey asymmetric structures. *Earthquake Engineering and Structural Dynamics*, 1998; 27:

- 525-41. [https://doi.org/10.1002/\(SICI\)1096-9845\(199806\)27:6<525::AID-EQE731>3.0.CO;2-B](https://doi.org/10.1002/(SICI)1096-9845(199806)27:6<525::AID-EQE731>3.0.CO;2-B)
- [7] Tamizharasi G, Prasad M, Murty CVR. Criticality of controlling seismic torsional response in plan unsymmetric buildings. 16th World Conference on Earthquake Engineering, Santiago Chile, Paper No.916; 1-11, 2017.
- [8] Stathopoulos KG, Anagnostopoulos SA. Inelastic earthquake response of single-story asymmetric buildings: an assessment of simplified shear beam models. *Earthquake Engineering and Structural Dynamics*, 2003; 32:1813-831. <https://doi.org/10.1002/eqe.302>
- [9] Peter F, Iztok P. On the inelastic seismic response of asymmetric single-story structures. 8th Canadian Conference on Earthquake Engineering, Vancouver, 763-68, 1999.
- [10] Ghersi A, Rossi PP. Influence of bi-directional ground motions on the inelastic response of one-storey in plan irregular systems. *Engineering Structures*, 2001; 23: 579-91. [https://doi.org/10.1016/S0141-0296\(00\)00088-2](https://doi.org/10.1016/S0141-0296(00)00088-2)
- [11] Pinho R, Bento R, Bhatt C. Assessing the 3D irregular SPEAR building with nonlinear static procedures. The 14th World Conference on Earthquake Engineering, Beijing, 1-9, 2008.
- [12] Bhasker R, Menon A. Torsional irregularity indices for the seismic demand assessment of RC moment resisting frame buildings. *Structures*, 2000; 888-900. <https://doi.org/10.1016/j.istruc.2020.05.018>
- [13] Ju SH, Lin MC. Comparison of Building Analyses Assuming Rigid and Flexible Floors. *Journal of Structural Engineering*, 1999; 125(1): 25-31. [https://doi.org/10.1061/\(ASCE\)0733-9445\(1999\)125:1\(25\)](https://doi.org/10.1061/(ASCE)0733-9445(1999)125:1(25))
- [14] Fang CH, Leon RT. Seismic Behavior of Symmetric and Asymmetric Steel Structures with Rigid and Semirigid Diaphragms. *Journal of Structural Engineering*, 2018; 144 (10): 04018186. [https://doi.org/10.1061/\(ASCE\)ST.1943-541X.0002123](https://doi.org/10.1061/(ASCE)ST.1943-541X.0002123)
- [15] IS 1893(Part 1): 2016. Criteria for Earthquake Resistant Design of Structures, Part 1 General Provisions and Buildings, Bureau of Indian Standards, New Delhi.
- [16] BNBC 2017. Bangladesh National Building Code, Housing and Building Research Institute.
- [17] BCP SP-2007. Building Code of Pakistan, Seismic Provisions. Ministry of Housing and Works, Pakistan.
- [18] NSCP C101-10, 2010. National Structural Code of the Philippines, Vol.1, Building, Towers and other Vertical Structures, Association of Structural Engineers of the Philippines.
- [19] NBC: 105: 2020. Nepal National Building Code, Seismic Design of Buildings in Nepal.
- [20] Korean building code, AIK (Architectural Institute of Korea), 2009, Seoul: AIK.
- [21] Technical Standard for Seismic Design, Ministry of Public Works, EL Salvador, 1994.
- [22] National Building Code, 2003. Technical Standard of Building, E.030, Earthquake Resistant Design, Peru.
- [23] Turkish Seismic Code. Ministry of Public Works, Turkey, 2007.
- [24] RPA 99, 2003. Algerian Earthquake Resistant regulations, Ministry of Housing and Urban Planning, Algeria.
- [25] Iranian Code of Practice for Seismic Resistant Design of buildings, Building and Housing Research Center, Standard No. 2800, 2007.
- [26] GB 50011,2010. Code for Seismic Design of Buildings, National Standard of the People's Republic of China.
- [27] Complementary Technical Norms for Earthquake Resistant Design, Mexico City Building Code, 1995.
- [28] Eurocode 8: 2004. Design of structures for earthquake resistance Part-1, General rules, seismic actions and rules for buildings, European Committee for Standardization.
- [29] NZS 1170.5:2004. Structural Design Actions, Part 5: Earthquake actions- New Zealand.

- [30] National Building Code of Canada, 2020. Vol.1. Canadian Commission on Building and Fire Codes-National Research Council of Canada.
- [31] Nch433.Of96,1996. Chilean Standard, Seismic design of buildings, Chile.
- [32] IS 456:2000. Indian Standard- Plain and reinforced Concrete Code of Practice, Bureau of Indian Standards, New Delhi.
- [33] IS:875 (Part 1)-1987. Indian Standard- Code of Practice for Design Loads (Other than Earthquake) for buildings and Structures, Part 1 Dead Loads-Unit Weights of Building Materials and Stored Materials, Bureau of Indian Standards, New Delhi.
- [34] IS:875 (Part 2)- 1987. Indian Standard- Code of Practice for Design Loads (Other than Earthquake) for Buildings and Structures, Part 2 Imposed Loads, Bureau of Indian Standards, New Delhi.
- [35] ETABS- Building Analysis and Design, Computers & Structures, Inc.



Research Article

Prediction of performance of UHPFRC flexural member under blast loading

Rizwanullah*, a, H.K. Sharma^b

Department of Civil Engineering, National Institute of Technology, Kurukshetra, (Haryana) India

Article Info

Abstract

Article history:

Received 03 Jan 2023

Accepted 13 Mar 2023

Keywords:

*UHPFRC;
Spalling and Scabbing;
Damage behaviour;
Flexural member;
Total deformation*

An explosion within or near a building can cause terrible damage to the building. Ultra-high performance fibre reinforced concrete (UHPFRC) increases the strength and ductility of designing the structural elements with reduced sections. UHPFRC has a better load-carrying capacity, tensile strength (TS), and enhanced energy absorption capacity than the normal strength concrete (NSC) and high-performance concrete (HPC). This study focuses on understanding the behaviour of UHPFRC and HPC structural elements when subjected to the blast loading. Stress-strain behaviour, total deformation versus time response, and other ductility associated characteristics of UHPFRC based structural elements under blast loading of different charge weights were investigated. The design was carried out according to unified facilities criteria (UFC: 3-340-02). The total deformation of the beam was verified and compared with computed ANSYS R18.1 generated result. A significant reduction in total deformation was observed in UHPFRC compared to HPC and NSC structural elements. Flexural member designed to withstand a blast of 1.315 kN was found to resist a blast load of 5 kN within elastic range and up to 15 kN in the plastic field due to the inclusion of UHPFRC. The use of UHPFRC made the structural elements to reduced section dimensions thereby, decreasing the dead load, which is always advantageous in earthquake-resistant structures. UHPFRC can benefit blast-resistant facilities under high strain rates because of its extremely higher force capacity for the same size and reinforcement.

© 2023 MIM Research Group. All rights reserved.

1. Introduction

Structures under blast loading demonstrate improved strength than those subjected to static loading. The rapid strain rates in explosive-laden elements recognize the enhancement in force for composites and rebars [1]. The ultimate dynamic capacity is higher than its maximum static capacity. NSC and rebars are higher when subjected to high strain rates. HPC and UHPFRC illustrate higher compressive strength (CS), increased tensile resistance, toughness, and significant energy absorption capacity compared to NSC. UHPFRC and HPC are thus very economical to reduce the size of structural elements and develop resistance against blast loading [2].

Considerable significance has been given to blast loading effects on structures because of accidental or intentional activities due to terrorism. Therefore, it is imperative to protect civil infra-structures against blast shocks, accidental/deliberate actions worldwide target essential infrastructure facilities. There is a need to design the structures, especially of strategic importance, to withstand the effect of blast loads. Because of the nonlinear behaviour of material, dynamic response of the structure under blast loading is quite intricate and challenging to analyze. The progressive collapse of the structure is minimized by designing and constructing structural elements as blast-resistant. HPC has been found

*Corresponding author: rizwan_6170002@nitkkr.ac.in

^a orcid.org/0009-0000-4145-5798; ^b orcid.org/0000-0001-7713-1998

DOI: <http://dx.doi.org/10.17515/resm2023.633me0103>

Res. Eng. Struct. Mat. Vol. 9 Iss. 3 (2023) 921-946

to impart more strength, durability, and serviceability on this front to obtain reduced section dimensions of the features. An extensive literature review study reveals that HPC has a better ability to load carrying capacity, TS, and significant energy absorption capacity than NSC. This study concentrates on enhancing the understanding of behaviour of UHPFRC and HPC structural elements under blast loading.

2. HPC and UHPFRC

The term high performance infers an improved arrangement of structural properties like durability, stiffness, strength, energy absorption capacity, multiple cracking, etc., considering the overall cost of the material and the products manufactured. HPC is defined as concrete with superior performance and uniformity that can be accomplished using special mixing, placing, and curing techniques. The structure involves high early strength, long-term mechanical properties, durability and toughness, longer life under poor environmental conditions, flowability, and self-leveling capacity. It also has a high modulus of elasticity, low permeability, placement, and compaction without segregation and resistance to chemical attack [3]. HPC is manufactured with high-quality material ingredients and a proper mix design. It has a low water-binder ratio and excellent performance characteristics that satisfy the requirements to withstand high tensile and flexural stresses subjected to high-intensity blast loads. UHPFRC is another novel material class with exceptionally high strength and durability. It is high in strength and flexibility and is prepared by mixing cement, fine silica sand, silica fume, quartz floor, plasticizer, high-strength steel fibres (SF), and water [4].

UHPFRC, a new class of material, which was developed to overcome the comparatively brittle behaviour of HPC. Larrard FD et al. [5] presented the term UHPFRC, which required hot curing at 90° C or higher and vacuum pressure before and during the setting. Although these special procedures are advantageous to mechanical properties, they result in high-energy consumption and low production efficiency [6]. Therefore, researchers have conducted a good selection of materials to influence the mechanical and microstructural properties and durability of UHPFRC to facilitate its production and application. The typical static stress-strain behaviour of UHPFRC in compression is illustrated in Fig. 1.

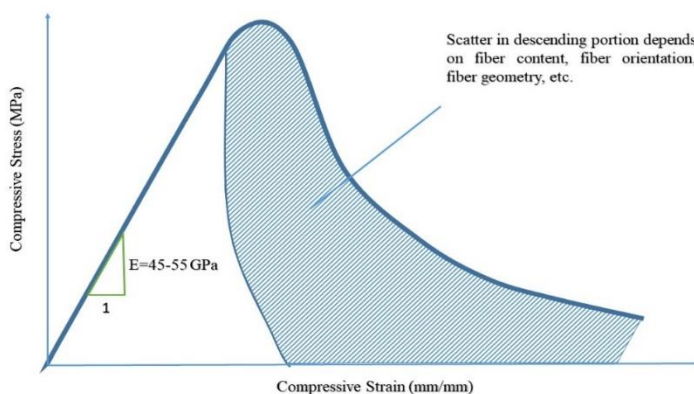


Fig. 1 Compressive stress-strain curve of UHPFRC [7]

The behaviour of UHPFRC is characterized by very high CS, more than 150 MPa, elastic modulus, TS of 4-5 % of CS, and a significantly higher post-peak ductility. Generally, the influence of SF on enhancing CS and elastic modulus is very low [8]. UHPFRC is expensive compared to NSC and requires hot curing, and the mix must be designed appropriately to

suit unique structures. The TS of UHPFRC varies from 8 to 15 MPa [9], as illustrated in Fig. 2. The tensile behaviour of UHPFRC is characterized by linear-elastic stress level corresponding to TS, strain hardening behaviour corresponding to non-continuous micro-cracks in the cementitious paste ended by single crack localization. After that, the resistance drops, and strain-softening behaviour is exhibited until complete failure. SFs strongly affect the stress-strain curve's behaviour and post-cracking non-linear descending portion.

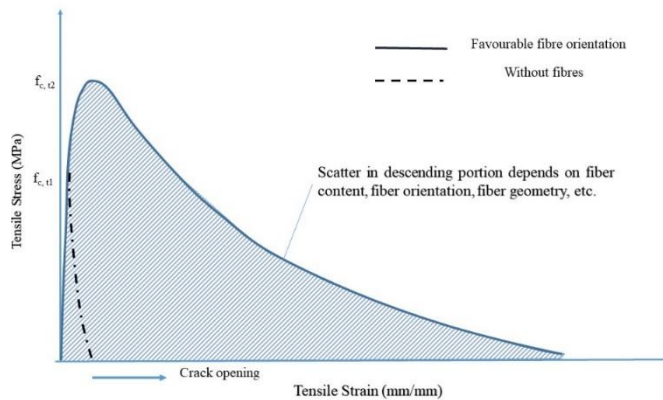


Fig. 2 Tensile behaviour of UHPFRC [7]

Structural performance assessment against blast loading is an urgent issue that needs to be addressed due to increased terrorist activities and unintentional explosions. Computer modeling involving numerical analysis is considered valuable for modeling such structures when subjected to blast loading. Therefore, the current study is intended to investigate the response of NSC, HPC, and UHPFRC structural elements using UFC 3-340-02 to explore HPC and UHPFRC structural elements using standard software ANSYS R18.1 for other blast loading conditions.

3. Explosion and Blast

The blast effect of an explosion is in the form of shock waves comprising of a high intensity shock wave front that develops outward from the surface of explosive into the adjacent air. As the wave propagates, it decays in strength, lengthens in duration, and decreases in velocity. This phenomenon is created by spherical deviation and chemical reactions, but for some after-burning related with the hot explosion products mixing with the nearby surrounding. As the wave develops in the air, the front impinges on constructions within its path, and shock pressures engulf the whole system. The magnitude and dispersal of the blast loads arising from these pressures are a function of the factors like explosive characteristics (lower or higher order detonation) and explosive weight, the location of the explosion, and magnitude of the reinforcement. The blast loading on the structures can be classed into two categories on the basis of confinement of the systems, confined explosion, and unconfined explosion [10].

3.1 Pressure and Time Profile of Blast Load

The blast pressure vs. time profile is illustrated in Fig. 3. At an arrival time t_A due to explosion, the pressure increases suddenly to a peak overpressure, P_{so} , on ambient pressure (P_o). Then, pressure decreases to the ambient level at a time t_o decrease again to an under-pressure P_{so^-} until ambient conditions are attained. The term P_{so} is denoted as

peak overpressure, incident peak overpressure, or peak overpressure. The incident peak overpressure P_{so} is augmented by a reflection factor as the shock wave comes across the structure in its path. The reflection factors, which are affected by shock wave intensity and normal incidence in the case of explosives, can raise incident pressures by an order of magnitude. Two main phases are observed during the pressure-time profile. The portion above ambient is called +ve phase of duration, denoted by t_o , and the leg below ambient is -ve phase of time, t_o^- . The -ve phase is always has a longer but lower intensity than the +ve duration. When standoff distance (SD) increases, positive-phase blast wave duration also increases, leading to a longer-duration shock pulse of lower amplitude. Blast charges close to a target inflict an impulsive and high-intensity pressure load, whereas blast charges at some distance yield a low intensity- longer-duration uniform pressure of lower intensity over the structure. Finally, in this process, the whole target is bounded by the shock wave, with diffraction and reflection effects forming shadow and focused zones around the structure. The deteriorated structure can be subjected to fragments, which may cause further destruction during the -ve phase. The ambient pressure increases and subsequently decreases forming a triangular overpressure. Brode [11] obtained peak overpressure expressions in close-in-contact conditions.

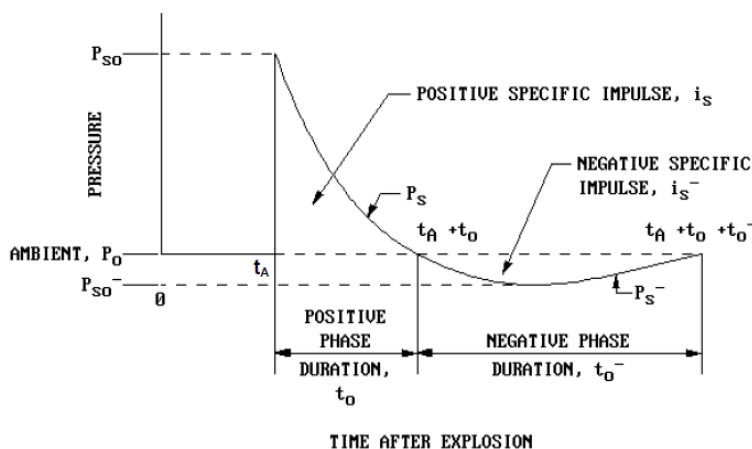


Fig. 3 Pressure vs. time profile [10]

It is crucial that the negative pressure phase marks in a vacuum in which air gets filled accordingly at a faster rate, on account of which pressure acts in a direction reverse top to the incident pressure. Therefore, just like seismic loads, blast loads are also cyclic. However, the number of cycles and frequency is inconsequential compared to the positive one. The negative amplitude, almost negligible compared to the P_o negative phase, is often neglected to simplify the analysis. Baker recommended Friedlander's equation (12) as,

$$P_s(t) = P_{so} \left(1 - \frac{t}{t_o}\right) e^{-b \frac{t}{t_o}} \tag{1}$$

Here 'P (t)' represents the incident pressure at (t), '(P_o)' is the region atmospheric pressure, '(P_{so+})' is peak positive incident over-pressure, and '(t_{pos})' is positive phase duration. The decay parameter is (b). The integrated area under the pressure history curve is called impulse. The impulse is called a positive specific impulse for the positive pressure phase, and for the negative pressure phase, it is called a negative specific impulse. Fig. 4 illustrates various strain rate values for different extreme load scenarios. The strain rate ranges in 10^{-8} s^{-1} are considered for creep and 10^3 s^{-1} for explosive loading (blast and impact loads).

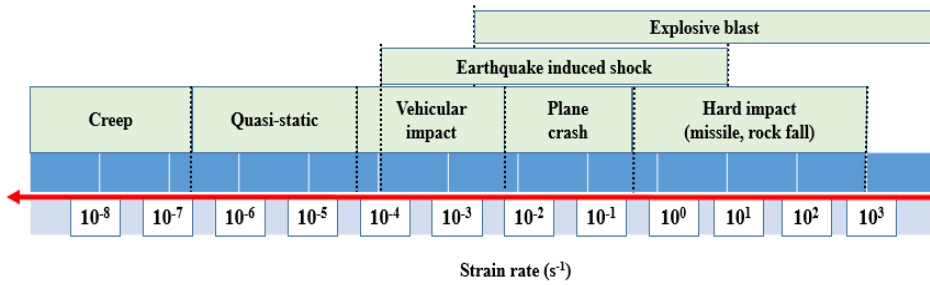


Fig. 4. Ranges of Strain rate for Concrete Structures [9]

3.2 Prediction of the Blast Wave

Many researchers also provided empirical equations for overpressures ' P_{so} ' in units of MPa, weight of charge ' w ' in kg, ' R ' is the SD in meters, and scaled distance, $[Z = \frac{R}{W^{\frac{1}{3}}}]$ in $m / (kg^{1/3})$ as tabulated in Table 1.

Table 1. Empirical equations anticipated by different authors for peak positive overpressure ' P_{so} '

S.No	Author (s)/ year	Equations
1.	Sadovskyi (1952) [13]	$P_{so} = \frac{0.085}{Z} + \frac{0.3}{Z^2} + \frac{0.82}{Z^3}$
2.	Brode (1955) [11]	$P_{so} = \frac{0.0975}{Z} + \frac{0.1445}{Z^2} + \frac{0.585}{Z^3} - 0.0019$ for $(0.01 \leq P_{so} \leq 1)$ $P_{so} = \frac{0.67}{Z^3} + 0.1$ for $(P_{so} > 1)$
3.	Adushkin and Korotkov (1961) [14]	$P_{so} = \frac{0.08}{Z} + \frac{0.28}{Z^2} - \frac{0.322}{Z^3}$
4.	Newmark and Hansen (1961) [15]	$P_{so} = 93 \left(\frac{W}{R^3} \right)^{\frac{1}{2}} + 6784 \frac{W}{R^3}$
5.	Henrych and Major (1979) [16]	$P_{so} = \begin{cases} \frac{14.072}{Z} + \frac{5.54}{Z^2} - \frac{0.375}{Z^3} + \frac{0.00625}{Z^4} & \text{for } (0.05 < Z < 0.3) \\ \frac{-6.194}{Z} - \frac{0.326}{Z^2} + \frac{2.132}{Z^3} & \text{for } (0.3 \leq Z \leq 1) \\ \frac{0.662}{Z} + \frac{4.05}{Z^2} + \frac{3.288}{Z^3} & \text{for } (1 \leq Z \leq 0.3) \end{cases}$
6.	Held (1983) [17]	$P_{so} = 2 \frac{W^{\frac{2}{3}}}{R^2}$

7.	Kinney and Graham (1985) [18]	$P_{so} = P_0 \cdot \frac{808 \left[1 + \left(\frac{Z}{4.5} \right)^2 \right]}{\left\{ \left[1 + \left(\frac{Z}{0.048} \right)^2 \right] \times \left[1 + \left(\frac{Z}{0.32} \right)^2 \right] \times \left[1 + \left(\frac{Z}{1.35} \right)^2 \right] \right\}^{\frac{1}{2}}}$
8.	Mills (1987) [19]	$P_{so} = \frac{0.108}{Z} - \frac{0.114}{Z^2} + \frac{1.772}{Z^3}$
9.	Hopkins-Brown and Bailey (1998) [20]	$P_{so} = \begin{cases} -1.245 + \frac{1.935}{Z} + \frac{0.2353}{Z^2} - \frac{0.01065}{Z^3} & \text{for } (0.05 \leq Z \leq 1.15) \\ \frac{0.0707}{Z} + \frac{0.3602}{Z^2} + \frac{0.4891}{Z^3} & \text{for } (1.15 < Z \leq 40) \end{cases}$
10.	Low and Hao (2001) [21]	$P_{so} = \begin{cases} \frac{1.050}{Z^3} - 0.0981 & \text{for } (Z \leq 1) \\ \frac{0.0745}{Z} + \frac{0.250}{Z^2} + \frac{0.637}{Z^3} & \text{for } (1 < Z \leq 15) \end{cases}$
11.	Gelfand and Silnikov (2004) [22]	$P_{so} = \begin{cases} 1.7 \times 10^3 \exp(-7.5 \times Z^{0.28}) + 0.0156 & \text{for } (0.1 \leq Z < 8) \\ 8 \times 10^3 \exp(-10.7 \times Z^{0.1}) & \text{for } (Z \geq 8) \end{cases}$
12.	Wu and Hao (2005) [23]	$P_{so} = 1.059 \times Z^{-2.56} - 0.051 \quad \text{for } (0.1 \leq Z \leq 1)$ $P_{so} = 1.008 \times Z^{-2.01} \quad \text{for } (1 < Z \leq 10)$

3.3 Structural Response with Blast Loading

The structure's behaviour under blast is usually denoted in design ranges in the form of pressure intensity as high, low, and very low, Fig. 5. At the high-pressure design zone, curve A, the duration of the load applied is short, mainly when venting of the explosion product of the detonation happens. The durations are lacking compared to the response- time of the individual elements of the structures. In the case of the low-pressure design of curve B, structures under blast pressures withstand smaller peak pressures than those related with an earlier range corresponding to curve A. Structural elements are therefore designed for the low-pressure range depending on impulse and pressure. Likewise, in the case of a very low-pressure design range, curve C, blast pressure duration is substantial compared to the response time. The structure responses designed to withstand the impact of detonations are considered in the "very low-pressure range."

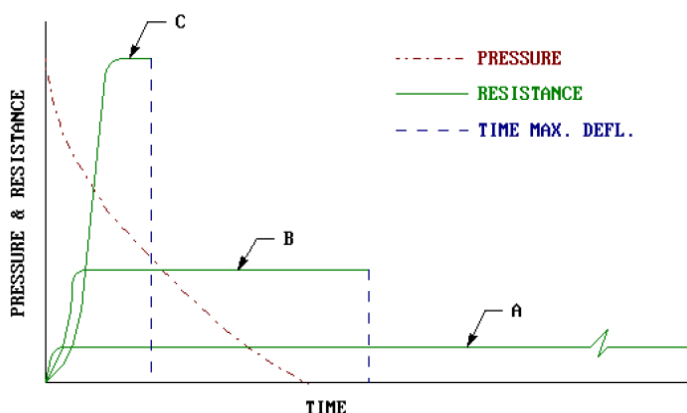


Fig. 5. Variation of structural response and blast load vs. time [24]

4. Published Literature

Luccioni, BM et al. 2004 [25] studied the failure of RC buildings caused by blast loading and validated the damage produced after the explosion. They concluded that the numerical results showed collapse under the blast load. The failure was due to the destruction of lower columns. Byfield, MP et al. 2006 [26] studied the behaviour of blast loading on structures. In recent attack happened due to the detonation of vehicle-borne devices in the Middle East, Europe, and North America. Modern commercial buildings may be vulnerable to progressive collapse, as seen during the attack on the Murrah building in 1995. Conventional beams showed a noteworthy higher flexural strength during design. Vehicle-used devices were capable of destroying the frame system at close range. Ngo, T et al. 2007 [1] extensively studied the influence of blasts on the structure. Terrorist organizations have used vehicle bombs to assault worldwide in their activities. A bomb explosion inside or nearby can inflict major damage to the structures' internal and external frames, collapse walls, window panels, and cause the loss of humans. The structural analysis and design under blast loading necessitate a deep knowledge of diverse structures' dynamic responses and blast phenomena. Yanchao, S et al. 2007 [27] conducted numerical simulations to investigate the blast wave interaction in a structural column. It was observed that when the blast wave column behaviour is considered, the influence marginally decreases the positive reflected pressure and the positive impulse increases. They concluded that the blast column interaction is significantly influenced by column size. UFC 3-340-02, 2008 [10] illustrated the step-to-step analysis and design methods. The parameters included the dynamic analysis, blast fragment, reinforced concrete (RC), and steel construction shocks. Zeynep, K et al. 2008 [28] observed a rise in the terrorist attack, and the effects of blast loading on the structure is a great concern that should be considered in the construction and design. The attacks were artificial and dynamic blast loads that were calculated similarly to wind and earthquake loads. The buildings protect to resist blast load using several techniques in structural design. Every member of the structure should be designed to stand blast load. Nystrom, U et al. 2009 [24] conducted an analytical investigation to study the influence of fragments caused by explosions. The combined blast and fragment loading effects on RC walls were investigated using a numerical simulation. Numerical simulations were conducted on the response subjected to fragments and blast loading. Wu, C et al. 2009 [29] investigated a series of test conducted on slabs under blast loading. Different types of slabs were cast and tested using UHPFRC, reinforced ultra-high performance fibre concrete (RUHPFC), and fibre reinforced polymer (FRP). The authors concluded that the UHPFRC slabs suffered less damage as compared with RC slabs when subjected to blast loading. Hassan, MZ et al. 2012 [30] investigated blast resistance of sandwich panels made up of aluminium alloy. Experimental studies were carried out using a ballistic pendulum, and it was found that the sandwich panels were damaged as the density of foam increased. The authors also concluded that the blast response of sandwich structures showed significant energy absorption. Shallan, O et al. 2014 [31] investigated the influence of blast loading on buildings for different ratios numerically. Finite element simulation on the buildings was developed using AUTODYN. Blast loads with varied SDs were applied at two distinct locations and distanced from the structure. Nicolaides, D et al. 2015 [32] studied the mechanical and fracture behaviour of UHPFRC under blast loading. The mix's water-to-binder ratio and SFs were 0.16 as 6%, respectively. The authors concluded that the CS and fracture energy obtained were obtained as 175 MPa and 26000 N/m, respectively. Conrad K et al. 2017 [33] presented the influence of axial loading and transverse reinforcement spacing on RC columns at a small-scaled distance under blast loading. An analytical study was conducted to understand the transverse reinforcement effects under blast loading on RC columns. Li et al. 2017 [34] investigated the blast resistance of segmental RC columns. The results indicated that the performance of RC columns under blast loading differs from seismic excitation on the ground. The author

performed a numerical analysis of RC columns segmentally. The central deflection of the segmental column under blast load is reduced by the addition of prestress by post-tensioning tendons. The results showed that the behaviour of segmental columns subjected to blast loading differs from that of seismic ground excitations. Yang, HW et al. 2018 [35] studied the failure behaviour of four different hemispherical shells subjected to blast loading. Simulation studies of the collapse behaviour of hemispherical shells were conducted using ANSYS and LS-DYNA. The analysis considered material and geometric non-linearities for extreme loading conditions. Experiments and computations demonstrated relatively small variation for both empty and liquid-filled shells. Kaan, T et al. 2019 [36] studied the flexural behaviour of UHPFRC beams numerically and experimentally. The fibre used in the beam is 13 mm straight fibre and 60 mm hooked fibre. The deflection of non-fibre beams varies from 8.14 to 2.11 while increasing the reinforcement ratio. Rizwanullah et al. 2020 [2] presented an extensive review to study the effect of various parameters on UHPFRC elements under blast loading. They also discussed the effects of w , blast loading with changing CS, and SD. It was observed that detailing structural elements under earthquake conditions also presents improved blast performance.

An extensive literature review conducted to study the influence of blast loading illustrated that several investigators had studied the effect of blast intensity, SD, and location of the blast in their studies. However, researchers did not consider the influence of elevated temperature on structural elements. Lee, J-Y et al. 2020 [37] investigated six RC columns of $160 \times 160 \times 2468$ mm and tested them using a shock tube. In addition to retrofitted jackets, UHPFRC was studied to calculate the influence of seismic detailing and transverse reinforcement. UHPFRC columns were improved by including seismic in the case of blast and impact resistance. Castedo, R et al. 2021 [38] investigated RC slabs under close-in explosion. The slab was subjected to 1.74 kg of trinitrotoluene (TNT) at 1 m and the other slab of 13.05 kilograms of TNT at 0.5 m.

Scaled distance determines the type of failure and damaged concrete slab area. Khadim, MMA et al. 2021 [39] studied the performance of UHPC in comparison to NSC. UHPC has exceptional CS and carries less post-cracking tensile behaviour. The beams with and without fibres were modeled in finite element analysis (FEA) and validated results with a reinforcement ratio of 0.009. Mahmud, GH et al. 2021 [40] investigated the structural behaviour of UHPFRC under bending. They have performed using different thickness and boundary conditions, i.e., simply supported and fixed ends. The failure pattern in both conditions has similar cracks. Further, very few analytical works have been done on the behaviour of HPC and UHPFRC structural elements under close-range blast conditions. No one has recommended analysis and design procedures for structural components to resist different blast loading. Mandal, J et al. 2021 [41] studied the post-blast release of kinetic energy, and some were converted into ground shock waves, which affect the shock propagation and crater depth. The present study has therefore been conducted to investigate these parameters. Anas, SM et al. 2022 [42] investigated RC structures used to store ammunition, explosives, and chemical weapons. Such structures are considered very important, like war zones under critical conditions. The structures were subjected to extreme loading conditions from blasts and explosions. Safe on-ground, free air SDs, and safe blast pressure, were forecast for both the hemispherical surface detonation (HSD) and spherical air detonation (SAD). It was concluded that the proposed shelter can withstand blast loads of 4.98 and 0.93 MPa against SAD and HSD, respectively. Yan, J et al. 2022 [43] investigated the combination of UHPC with Glass fibre reinforced concrete (GFRP) structure subjected to blast loading. The authors studied damage caused by UHPC beams for different scaled distances. Adding GFRP in the beams improves the blast resistance of UHPC compared with NSC. LL, M et al. 2023 [44] investigated critical infrastructures prone

to accidental and manmade explosions. The authors analytically evaluate the performance of RC beams/columns subjected to blast loading. The researchers concluded that the scaled distance for global and local responses of RC members can be determined as $0.78 \text{ m/kg}^{1/3}$.

Calculation of peak overpressure using UFC 3-340-02 [10]

Calculation of blast parameters for 5 kN of TNT.

Steps:

1. Given data,
Height (H_c) = 10m= 32.8 ft., Length (L) =10m= 32.8 ft.
Weight= 5 kN = 1102.31 lbs.
2. Apply a 20% safety factor to the charge weight
 $W= 1.2 (1102.31) = 1322.772 \text{ lbs.}$

3. At the point of interest, evaluate the SD, 'R', and 'Z'

$$R = \sqrt{(32.8)^2 + (32.8)^2} = 46.4 \text{ ft.}$$

$$Z = \frac{R}{W^{1/3}} = \frac{46.4}{(1322.772)^{1/3}} = 4.2 \text{ ft/lb}^{1/3}$$

4. Determine incident blast wave parameters, see Fig. (6-7)

$$P_{so} = 50 \text{ psi}$$

Positive incident impulse, ' i_s '

$$\frac{i_s}{W^{1/3}} = 35 \text{ psi-ms/lb}^{1/3}$$

$$i_s = 35 (1322.772)^{1/3} = 384.2 \text{ psi-ms}$$

Positive phase duration, t_o

$$\frac{t_o}{W^{1/3}} = 1.5 \text{ ms/lb}^{1/3}$$

$$t_o = 1.5 (1322.772)^{1/3} = 16.46 \text{ ms}$$

Arrival time, t_A

$$\frac{t_A}{W^{1/3}} = 0.9 \text{ ms/lb}^{1/3}$$

$$t_A = 0.9 (1322.772)^{1/3} = 9.88 \text{ ms}$$

For negative blast wave pressure,

Negative incident pressure, $P_{so}^- = 3 \text{ psi}$

Negative phase duration, t_o^-

$$\frac{t_o^-}{W^{1/3}} = 8 \text{ ms/lb}^{1/3}$$

$$t_o^- = 8 (1322.772)^{1/3} = 87.82 \text{ ms}$$

Positive and negative blast wave parameters and Peak overpressure for positive phase time for different TNT charge weights are tabulated in Table 2. Fig. (6-7) represent as negative and positive phase duration of free air explosion.

Table 2. Peak overpressure and time for different charge weight

Load (kN)	Peak Overpressure (MPa)	Positive Phase				Negative Phase	
		P_{so} (psi)	i_s (psi-ms)	t_o (ms)	t_A (ms)	P_{so}^- (psi)	t_o^- (ms)
5	0.344	50	384.2	16.46	9.88	3	87.82
10	0.55	80	221.3	19.63	9.68	4	99.57
15	0.655	95	269.14	23.74	7.6	7	118.7
25	1.103	160	375.41	28.16	7.5	9	140.8

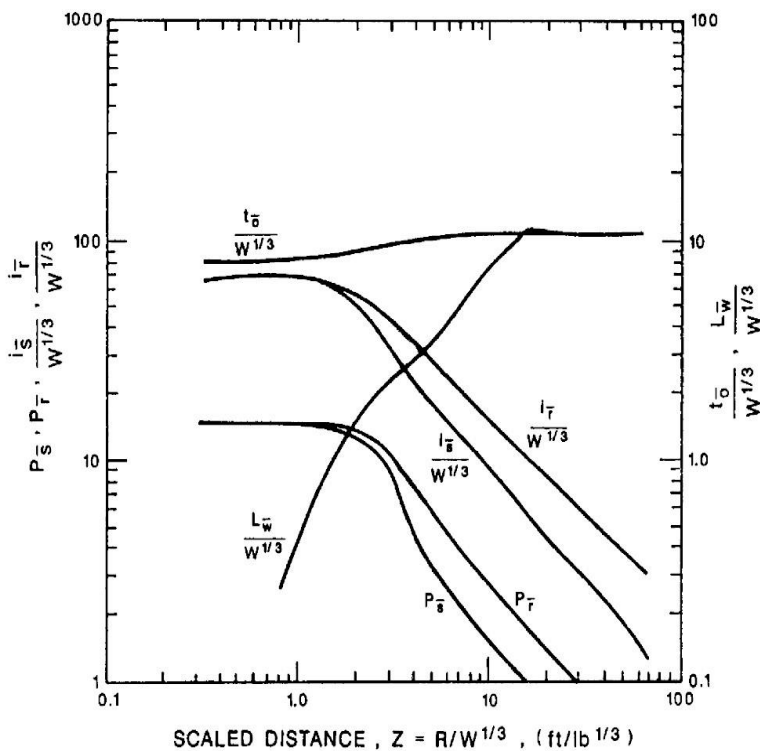


Fig. 6 Negative Phase Parameter of Free Air Explosion [10]

An interior roof slab-beam assembly has studied the behaviour of flexural members for free air blast loading shown in Fig. 8. The assembly section was analyzed and designed by UFC 3-340-02 for NSC, HPC, and UHPFRC. Free airbursts of charge weights 1.315, 5, 10, 15, and 25 kN TNT were considered for evaluating the blast wave parameters. The detonation was assumed at 10 m above the ground and 10 m away from the point of interest. An intermediate T- beam was considered for HPC and UHPFRC under blast loading from UFC 3-340-02. A free airburst was assumed to occur, and negative phase pressure was neglected due to the very low intensity of the blast. The equivalent elastic deflection, X_E

was obtained as 1.27 mm. For the natural period of the beam corresponding to 16.77 ms, blast wave parameters were calculated for different TNT charges.

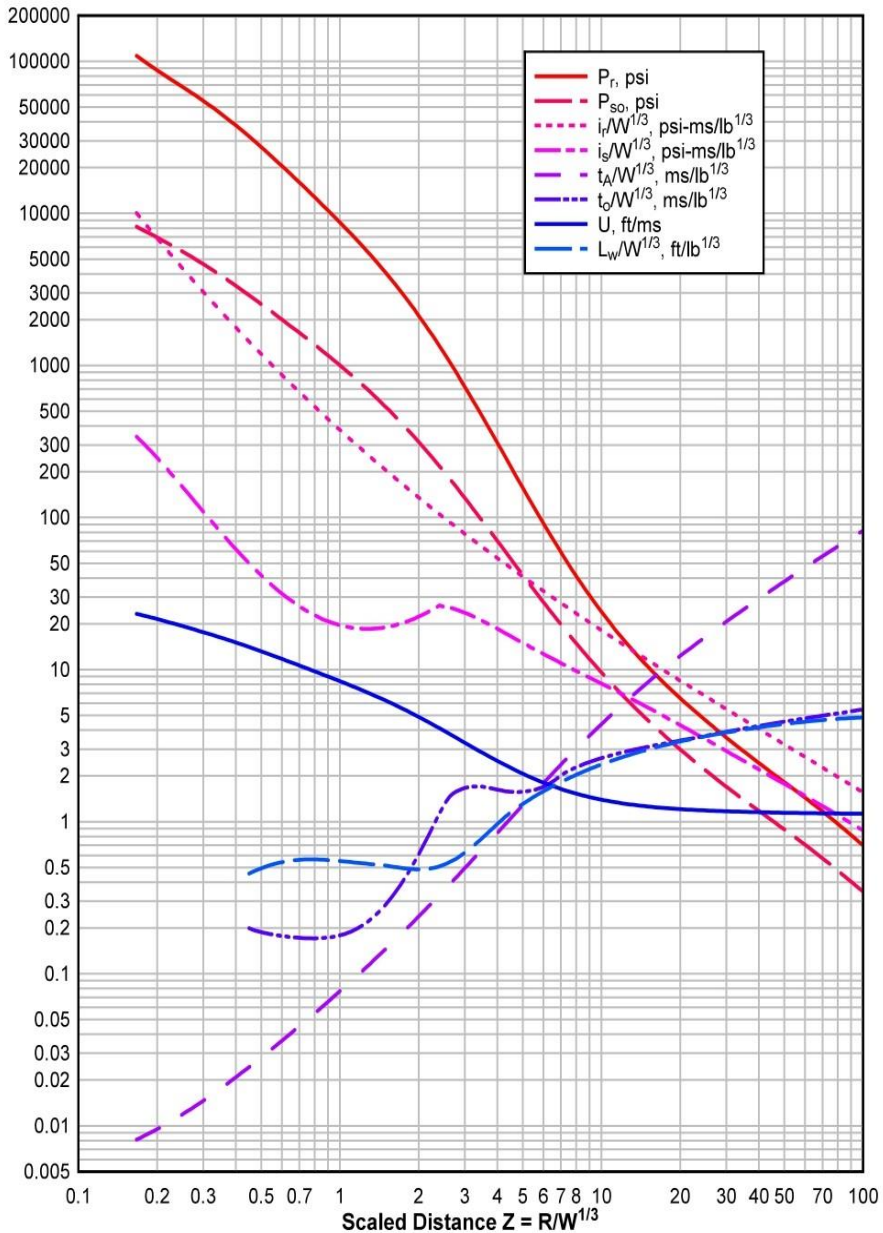


Fig. 7 Positive Phase Parameter of Free Air Explosion [10]

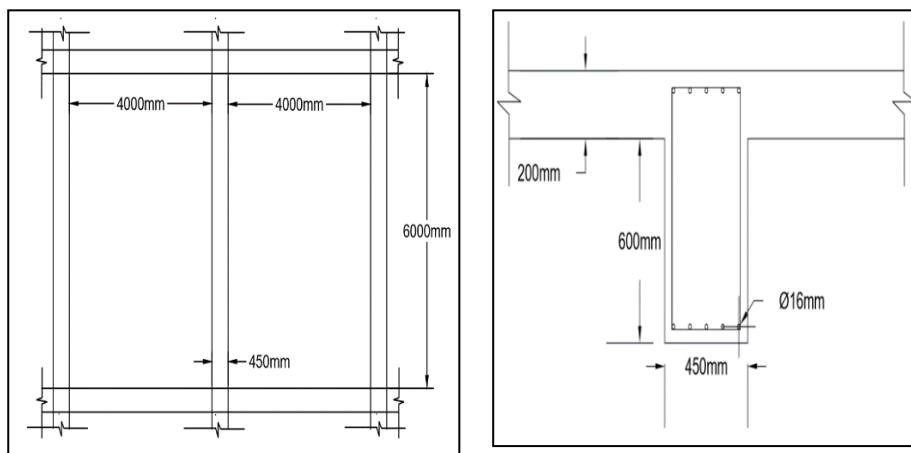


Fig. 8 Plan of an interior roof beam and section of Interior roof T- beam

5. Analytical Investigations

A finite element analysis using standard software ANSYS R18.1 was conducted to validate the typical results obtained. 3D solid elements SOLID 65 and LINK8 were used for nonlinear modeling of concrete and reinforcement for numerical simulation, as shown in Fig. 9. When cracking and concrete crushing are used, the load is gradually applied to check the possible crushing of concrete before proper load transfer takes place through a closed crack.

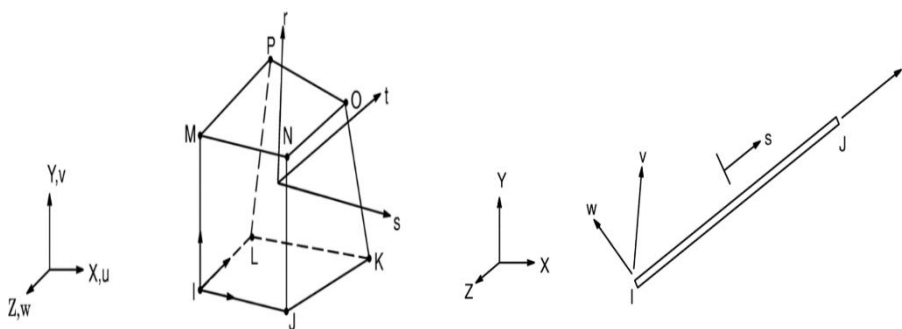


Fig. 9 Solid 65 and Link 8 Element [45]

5.1 Modelling of Interior Roof Slab Beam Assembly

Modeling the flexural member assembly was done in ANSYS R18.1 explicit dynamic software, Fig. 10. The geometry of the beam has been made in the Design Modular of explicit dynamics. The body interaction in explicit dynamics automatically made the bonded connection between steel reinforcement and concrete. UFC 3-340-02 calculates the end time of the analysis in the positive phase duration of the pressure of different blast loading conditions. Table 3 illustrates the properties of steel reinforcement and concrete for NSC, HPC, and UHPFRC, respectively.

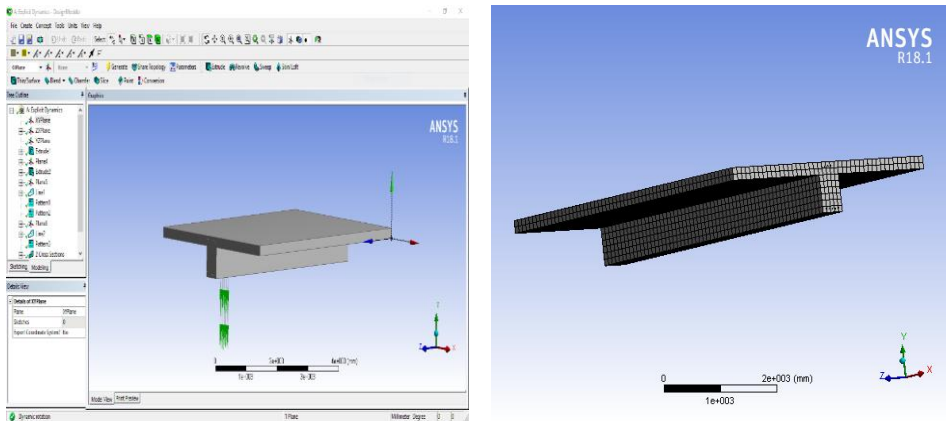


Fig. 10. Design Modular user interface of the software and meshed of interior roof

Table 3. Properties of the material

Steel Reinforcement Properties		RHT Concrete Model of NSC, HPC, and UHPFRC			
Properties/Unit	Values	Properties/Unit	Values		
Density (kN/m ³)	78.50	NSC	HPC	UHPFRC	
Young's Modulus (MPa)	200000	Density (kN/m ³)	23.14	24.00	25.00
Poisson's ratio	0.3	Specific heat (J/Kg °C)	654	654	654
Bulk Modulus (MPa)	166670	CS, f_c (MPa)	35	80	140
Shear Modulus (MPa)	76923	TS, f_t/f_c	0.1	0.15	0.2
Tensile Yield Strength (MPa)	415	Shear strength, f_s/f_c	0.18	0.2	0.28
Specific Heat (J kg ⁻¹ C ⁻¹)	434	Compressive strain rate exponent, α	0.032	0.0091	0.0091
Plastic Failure Strain	0.02	Tensile strain rate expo, δ	0.036	0.00125	0.0013
Strain-Life Parameters		Minimum strain to failure	0.01	0.01	0.01
Strength Coefficient	920	Damage constant, D_1	0.04	0.04	0.04
Strength Exponent	-0.106	Damage constant, D_2	1	1	1
Ductility Coefficient	0.213	Shear modulus (MPa)	16670	22060	22060

Cyclic Hardening Coefficient	Strain 0.2	Solid density (kN/m ³)	27.50	27.50	27.50
Porous sound speed (m/sec)			2920	3242	3242
Initial compaction pressure, P _e (MPa)			23.3	93.3	93.3
Solid compaction pressure, P _s (MPa)			6×10 ³	6×10 ³	6×10 ³
Compaction exponent, n			3	3	3

ANSYS R18.1 software was used for explicit dynamics for finite element modeling to solve time-dependent load problems. Explicit dynamics divide the problem into four categories: engineering data, geometry, model, and results. The geometry is part of the solver in which the problem has been to be taken. Explicit dynamics used the Design Modeler program to draw the geometry. In the model part of explicit dynamics, various steps are connections, meshing, analysis settings, pressure application, support fixing, and the results. Explicit dynamics automatically make connections between two different materials depending on their properties.

6. Analysis and Discussion of Results

The analytical investigation on NSC, HPC, and UHPFRC structural elements was conducted under blast loading using ANSYS R18.1 software. The characteristic CS of NSC, HPC, and UHPFRC for 35, 80, and 140 MPa, respectively, for TNT charge 5, 10, 15, and 25 kN. This paper has studied the flexural members of different magnitudes at 10 m above and away from the structures. The assembly was designed to resist an airburst of charges of 1.315 kN. The deflection corresponding to equivalent elastic deflection and maximum deflection for such a control beam (CB) has been calculated as 1.27 mm and 19.75 mm, respectively.

6.1 Stress-Strain Behaviour

The typical results of stress-strain behaviour for NSC, HPC, and UHPFRC beams for TNT charge corresponding to 5, 10, 15, and 25 kN are illustrated in Fig. 11-12, respectively. It has been observed that for a TNT charge of 5 kN, values of maximum stress have been obtained as 49.22, 48.53, and 51.57 MPa in NSC, HPC, and UHPFRC beams, respectively, whereas values of maximum strain are obtained as 0.001137, 0.001618, and 0.00026 mm/mm, in the corresponding beams. It was also found that there is no substantial change in maximum stress values corresponding to NSC and HPC beams. However, HPC beams illustrated a significant increase in elastic deformation by 142%. HPC is, therefore, found to behave more elastically than NSC. There was an increase in maximum stress value in UHPFRC in the beam, but the max strain was significantly decreased, illustrating no damage in the UHPFRC beam for a blast of 5 kN TNT. UHPFRC beam remained intact without any damage. It is also stated that stress-strain behaviour has only been plotted for ascending values for the first cycle. This trend was observed in several processes until stresses and strains were finally stabilized. An identical behaviour was observed in the case of 10 and 15 kN of TNT charges. However, in the case of the 25 kN TNT charge, the maximum strain value is significantly on the lower side, illustrating that UHPFRC, being of high strength and stiffness, behaved linearly during 25 kN of TNT.

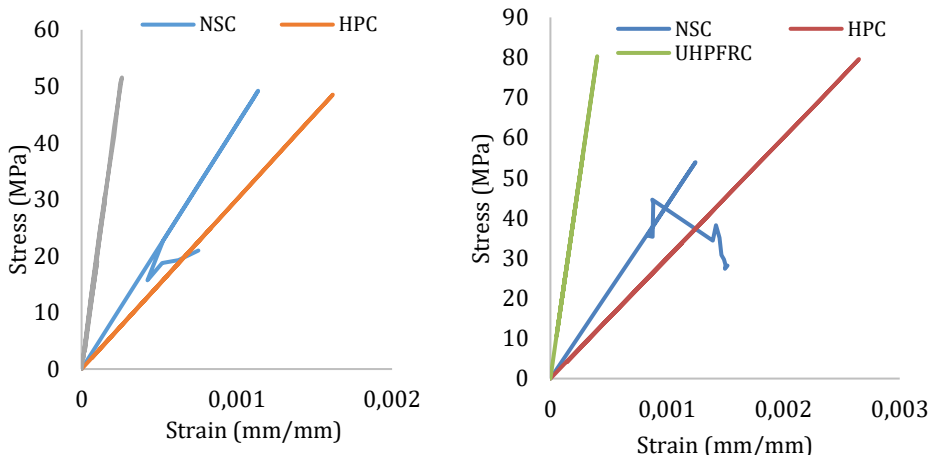


Fig. 11 Stress-Strain behaviour of NSC, HPC, and UHPFRC beams for 5 and 10 kN of TNT

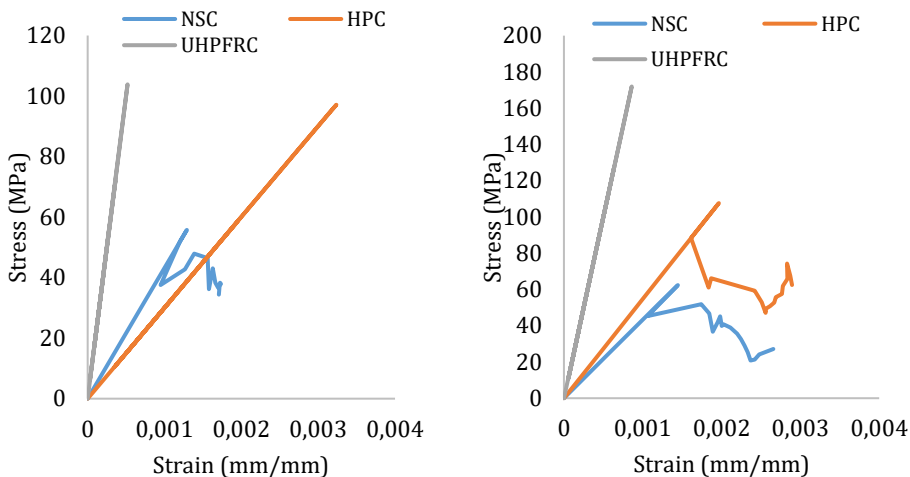


Fig.12 Stress-Strain behaviour of NSC, HPC, and UHPFRC beams for 15 and 25kN of TNT

6.2 Total Deformation-Time Behaviour

The variation of total deformation with time regarding NSC, HPC, and UHPFRC beams for TNT charge corresponding to 5, 10, 15, and 25 kN are shown in Fig. 13-14, respectively. It was found that there is a significant decrease in maximum values corresponding to NSC and HPC beams. UHPFRC beams illustrated a substantial reduction in total deformation to 0.89 mm compared to 6.89 and 5.53 mm in the case of the control beam of NSC and HPC beam for a TNT of 5 kN. UHPFRC is therefore found to illustrate significant ductility than NSC and HPC. There was a decrease in deformation value in the UHPFRC beam while demonstrating no damage in the UHPFRC beam for a blast of 5 kN TNT. UHPFRC beam remained intact without any damage. Maximum stress-strain behaviour and total deflection values of NSC, HPC, and UHPFRC are obtained at different times in these composites, as shown in Table 4. A significant reduction in total deformation was observed

in the case of HPC and UHPFRC beams compared to the control beam of NSC, clearly illustrating that HPC and UHPFRC showed tremendous resistance to blast loading compared to the NSC beam.

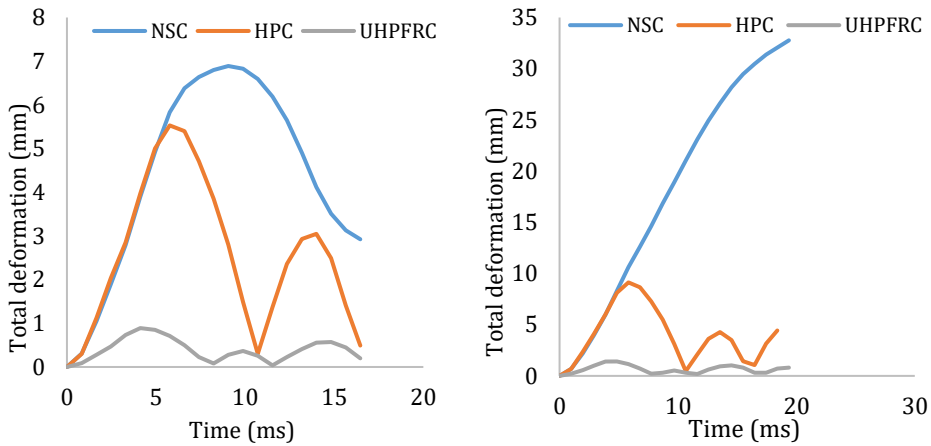


Fig.13 Total deformation and time graph of NSC, HPC, and UHPFRC for 5 and 10 kN of TNT

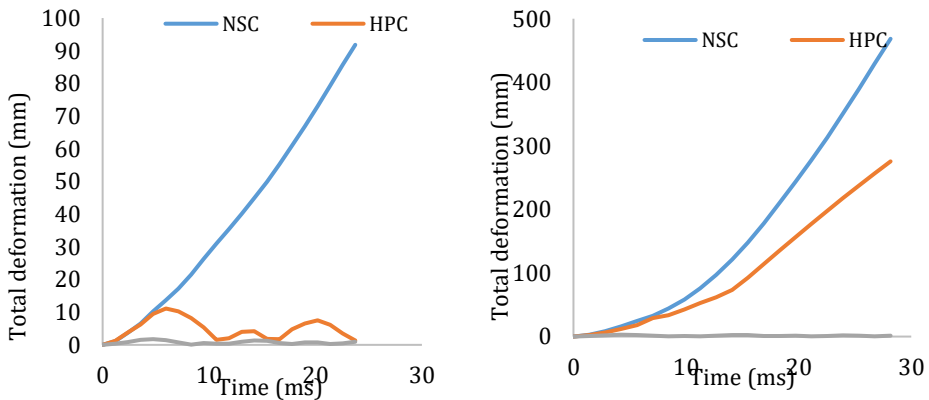


Fig.14 Total deformation and Time Graph of NSC, HPC, and UHPFRC for 15 and 25 kN of TNT

Table 4. Maximum Stress-Strain and deformation values with time for NSC, HPC, and UHPFRC

Blast Load, TNT (kN)	Time (ms)	Maximum Stress-Strain						Time (ms)	Total deformation (mm)		
		NSC		HPC		UHPFRC			NSC	HPC	UHPFRC
		Stress (MPa)	Strain (mm/mm)	Stress (MPa)	Strain (mm/mm)	Stress (MPa)	Strain (mm/mm)				
5	8.23	49.22	0.001137	-	-	-	-	9.06	6.89	-	-
	6.59	-	-	48.53	0.001603	-	-	5.77	-	5.53	-
	4.95	-	-	-	-	51.57	0.00021	4.12	-	-	0.89
10	5.81	53.92	0.001246	-	-	-	-	19.37	32.77	-	-
	5.81	-	-	79.61	0.00265	-	-	5.81	-	9.13	-

	3.88	-	-	-	-	80.31	0.0040 2	4.84	-	-	1.41
15	4.75	55.76	0.001289	-	-	-	-	23.7 4	91.8	-	-
	5.94	-	-	97.11	0.03237	-	-	5.94	-	11.11	-
	4.75	-	-	-	-	103.8 5	0.0005 2	4.75	-	-	1.74
25	4.22	62.38	0.00144	-	-	-	-	23.9 4	350.9	-	-
	4.22	-	-	107.61	0.00197	-	-	28.1 6	-	275.5 7	-
	4.22	-	-	-	-	171.9 5	0.0008 6	4.23	-	-	2.99

6.3 Equivalent Stress and Equivalent Strain Pattern

Free air explosion on flexural members was analyzed to study the equivalent stress behaviour for NSC, HPC, and UHPFRC beams under TNT charge corresponding to 5, 10, 15, and 25 kN. The worst situation is in the NSC, HPC, and UHPFRC beam under 25 kN TNT. Fig. 15-20 illustrate the response of NSC, HPC, and UHPFRC beams with plastic strain contour. NSC flexural member deformed, and spalling damage in the portion was found, which can be seen when strains are stabilized, and contours show significant cracking in NSC and HPC slabs. However, no scabbing, spalling, or peeling of concrete was observed in HPC assembly. Therefore, UHPFRC illustrated considerable strength and energy absorption capacity compared with NSC, and HPC may be conveniently used in blast-resistant structures.

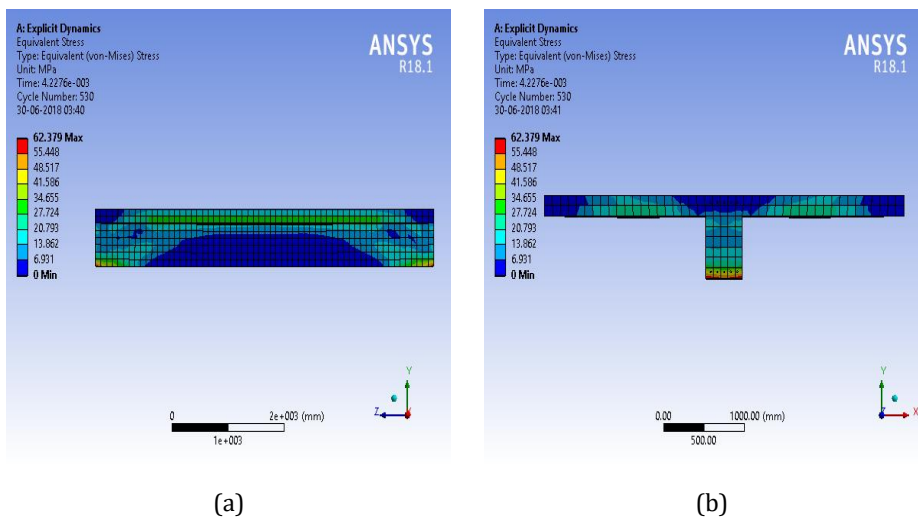
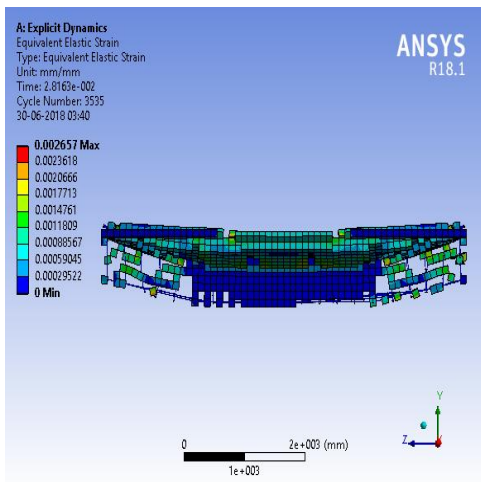
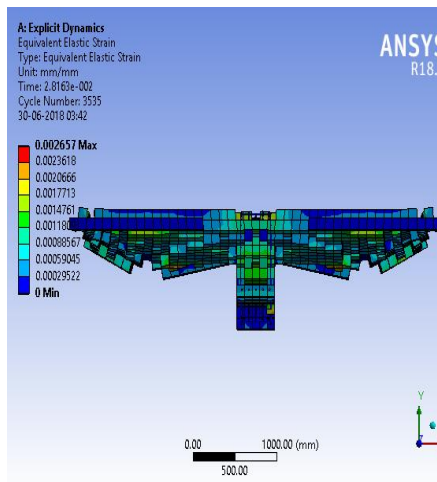


Fig. 15 (a, b) Equivalent stress pattern for NSC

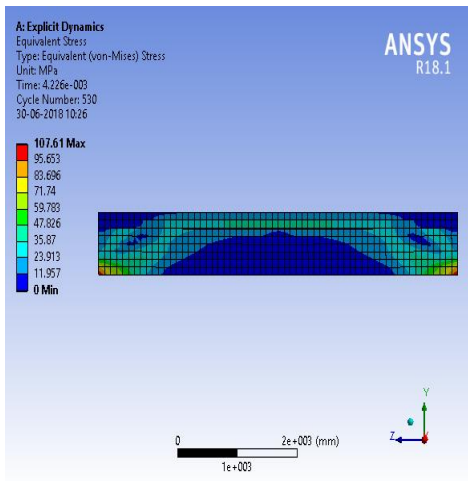


(a)

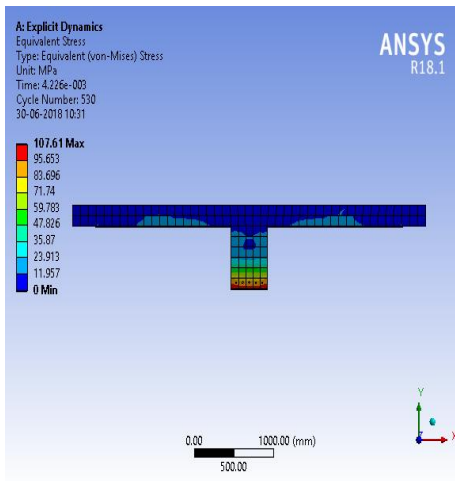


(b)

Fig. 16 (a, b) Equivalent strain pattern for NSC

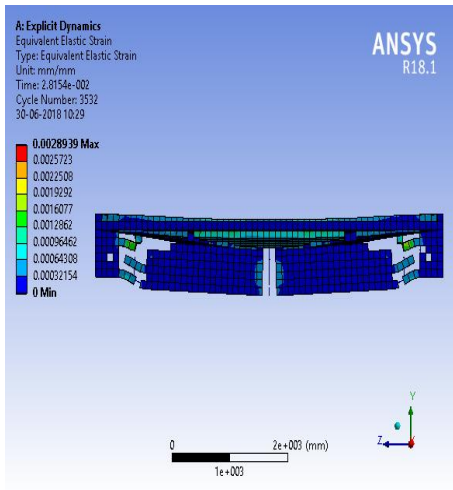


(a)

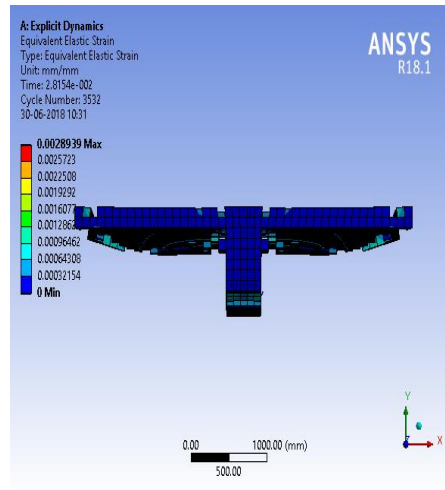


(b)

Fig. 17 (a, b) Equivalent Stress Pattern for HPC

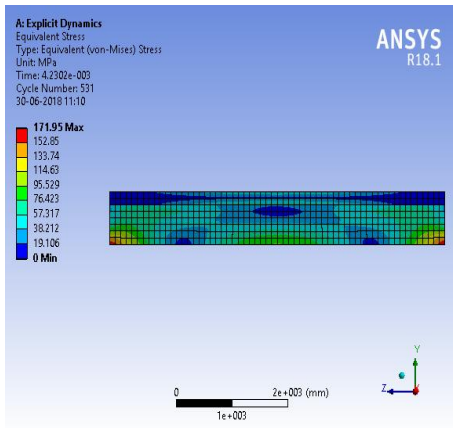


(a)

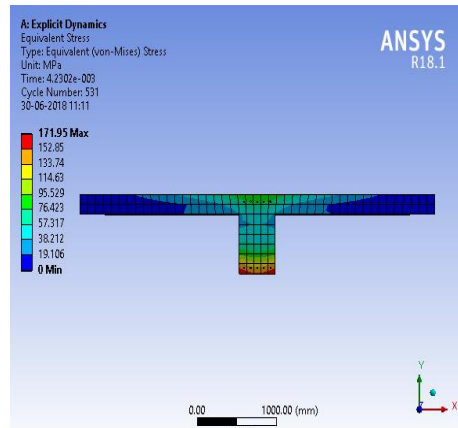


(b)

Fig. 18 (a, b) Equivalent Strain Pattern for HPC



(a)



(b)

Fig. 19 (a, b) Equivalent Stress Pattern for UHPFRC

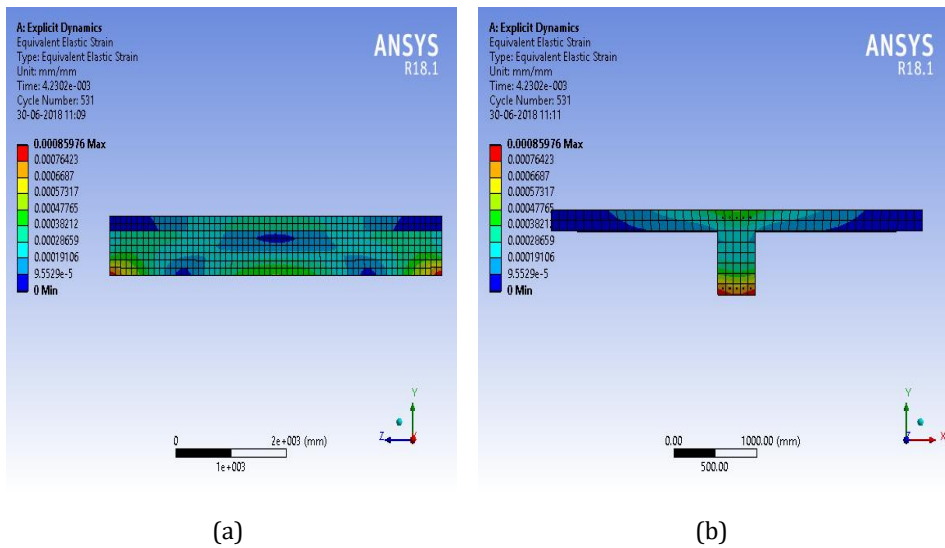


Fig. 20 (a, b) Equivalent Strain Pattern for UHPFRC

6.4 Damage Behaviour

Fig. 21-22 illustrate the damage pattern in NSC and HPC beams under 25 kN of TNT. There is no damage occurs in the UHPFRC slab beam assembly at a load intensity of 25 kN. As explained earlier, concrete crushing, spalling, and peeling is an exceedingly localized phenomenon, and the structure re-establishes its strength in the short period in UHPFRC. High CS associated with significant flexural and shear strength significantly confined damage compared to NSC.

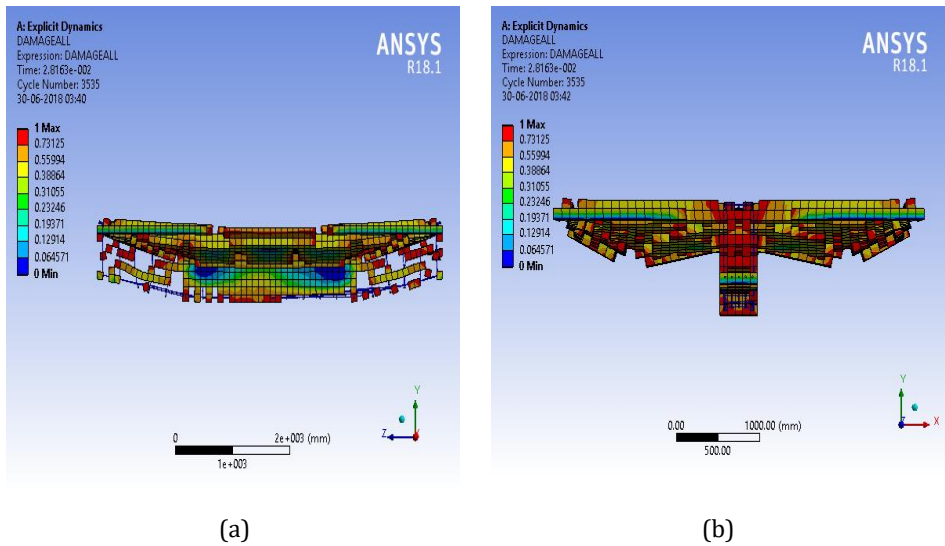


Fig. 21 (a, b) Damage Pattern of NSC

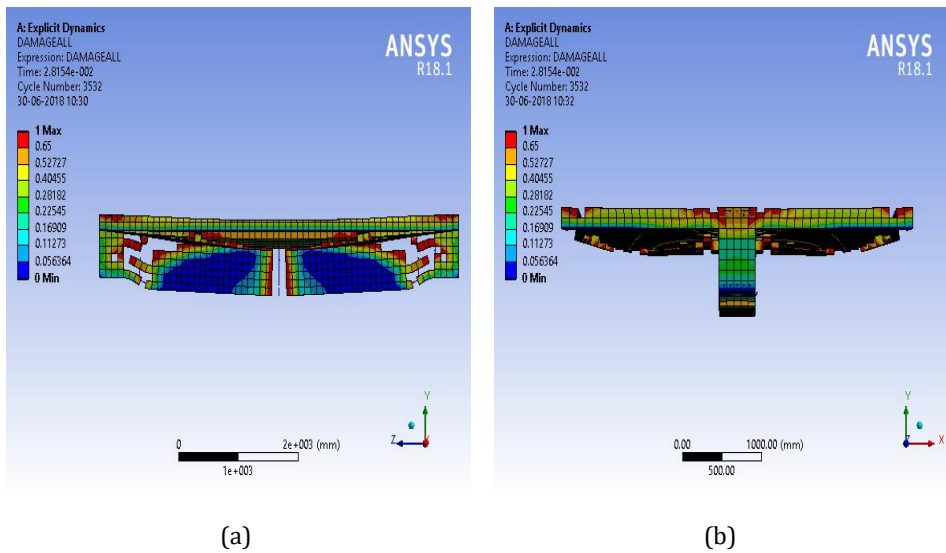


Fig. 22 (a, b) Damage Pattern of HPC

6.5 Comparison of Results

The time history curves of the flexural structural system are plotted for HPC, shown in Fig. 23. It has been observed that the dynamic analysis of the assembly gives a maximum deformation of 1.27 mm and a peak value of 1.81 mm obtained numerically. It has also been seen that higher values demonstrated a plastic deformation in HPC flexural members. Due to the wide-open cracks, the total deformation gradually decreased by 0.19 mm at 10 ms to transfer the stresses in the reinforcing bars. The use of SF reinforcement in the UHPFRC assembly has been found to significantly reduce spall damage in concrete. Therefore, it conclusively stated that the numerical model presented in this research work could reproduce the damage response of NSC, HPC, and UHPFRC assembly under blast loads. UHPFRC produced superior blast resistance capacity compared with NSC and HPC.

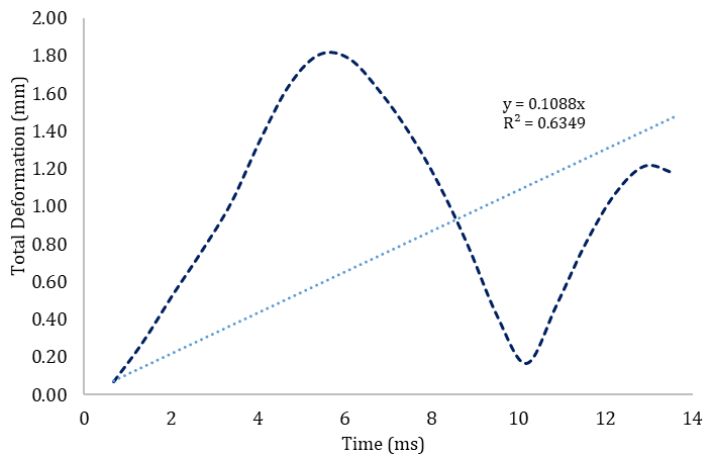


Fig. 23 Total Deformation and Time-History Curve for HPC

The pattern of peak deformation with blast intensity demonstrates that the values in NSC, HPC, and UHPFRC are minimal blast loads of 5 and 10 kN, as shown in Fig. 24. At 15 kN TNT, NSC members showed a significant deformation. At 25 kN intensity, peak deformations in NSC and HPC were increased significantly, and the structure may not survive under the blast load. However, a small deformation was shown by the UHPFRC assembly, which illustrates that the member withstands a higher blast intensity of 25 kN. The load-deformation curve calculated the values of energy absorption capacity, improved strength, stiffness, and ductility. Therefore, the UHPFRC assembly can withstand blast loads of higher intensities without appreciable damage. UHPFRC was also an efficient material that could withstand a blast of large magnitude at a small distance.

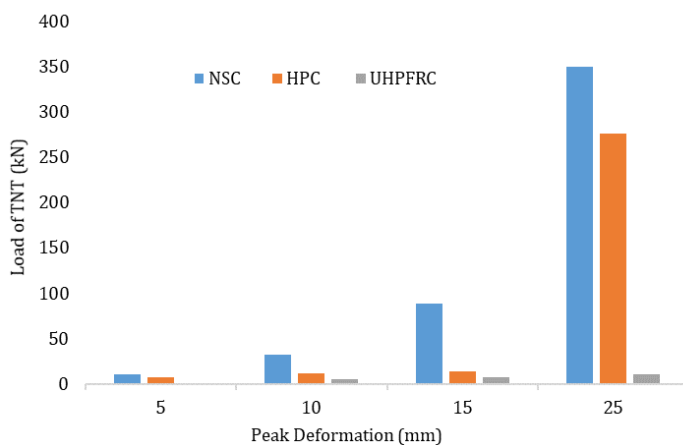


Fig. 24 Load-Deformation behaviour of different strengths of concrete

The comparison of maximum stress with blast intensity for NSC, HPC, and UHPFRC is shown in Fig. 25-26. It illustrates the exciting results at low blast loads and maximum stress developed when the blast intensity increases in the case of NSC and HPC. However, there is no variation in HPC and UHPFRC due to their improved toughness and energy absorption capacity.

At the peak blast intensity of 25 kN, a significant variation was observed for maximum stresses. The values of NSC, HPC, and UHPFRC vary in strength, compactness, and energy absorption capacity. In comparison, maximum strain values on the lower side in UHPFRC compared with NSC and HPC. After validating with UHPFRC, flexural member possesses improved resistance against blast loads of higher magnitude and can be used advantageously for structures of strategic significance near border areas and structures of national importance. Since the numerical model provides an excellent prediction of the damage to the structure, it is always possible to enhance structural performance against blast. Improving the toughness of key elements and increasing SD can further provide occupants with a reasonable chance to escape injury and death.

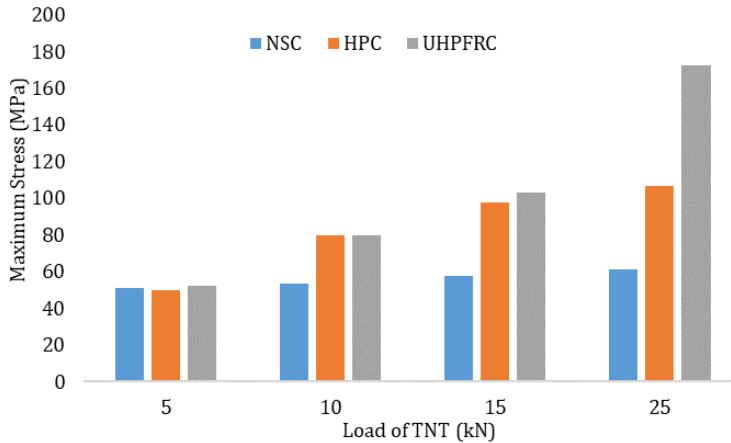


Fig. 25 Maximum Stress Vs. Blast Load Intensity Behaviour for Different Grades of Concrete

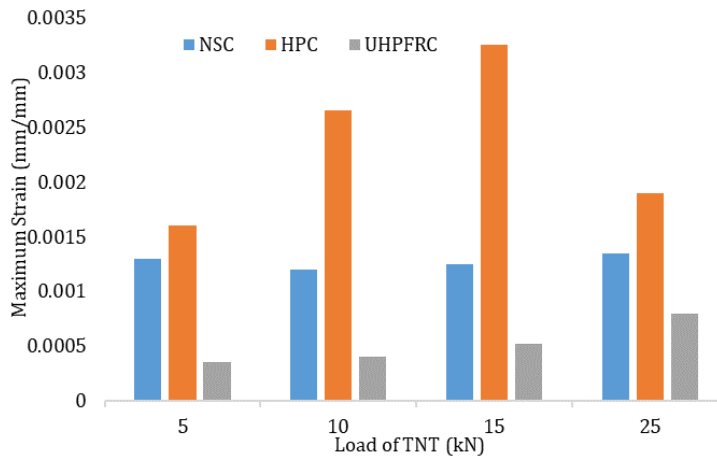


Fig. 26 Maximum Strain Vs. Blast Load Intensity for Different Grades of Concrete

7. Conclusions

The present study demonstrates the performance of NSC, HPC, and UHPFRC flexural assemblies under high strain rate conditions of blast loading. Based on the analysis and detailed investigation, the following conclusions are drawn.

- UHPFRC offers the improved capability to distribute an enormous amount of energy under blast loading compared to NSC and HPC. Hence, UHPFRC can be used to construct blast-resistant structures because of the fact that it has about four times higher force capacity for the same size and reinforcement.
- UHPFRC flexural members demonstrate greater compressive and tensile resistance against extreme conditions like blast, impact loadings.
- Compared with controlled concrete, a significant reduction in total deformation of 22 and 99% have been observed in HPC and UHPFRC.

- NSC members were severely damaged because of the weak bond with steel reinforcement under blast loads, and bond failure was observed between the composite and reinforcement when subjected to a blast load of 25 kN. HPC, however, did not fail due to de-bonding with reinforcement and offered bond resistance more effectively than NSC for more duration. UHPFRC was also capable of surviving the blast load during the entire period of blast and showed no damage.
- The flexural members are designed to resist blast load of 1.315 kN at a charge weight of 5 kN within the elastic-range, and 15 kN in the plastic- range due to HPC and UHPFRC.
- UHPFRC enhances flexural stiffness of structural members significantly thereby decreasing section dimensions, resulting in reduced dead load.
- UHPFRC was also an efficient material that could withstand a blast of large magnitude at a small distance.
- The numerical model presented in this research work could reproduce the damage response of NSC, HPC, and UHPFRC assembly under blast loads. UHPFRC produced superior blast resistance capacity compared with NSC and HPC.

References

- [1] Ngo T, Mendis P, Ramsay J. Blast Loading and Blast Effects on Structures – An Overview, EJSE Special Issue: Loading on Structures. 2007; 76–91.
- [2] Rizwanullah, Sharma HK. Influence of critical parameters on UHPFRC structural elements subjected to blast loading. SN Applied Science. 2020; 2:486. <https://doi.org/10.1007/s42452-020-2259-5>.
- [3] Büyüköztürk O, Denvid L. High performance concrete: fundamentals and application. Massachusetts Institute of Technology, Cambridge, Massachusetts, US, 2002; 1-20.
- [4] Rizwanullah, Sharma HK, Blast loading effects on UHPFRC structural elements: a review, Innovative Structure Solutions, 2022; 7:341, <https://doi.org/10.1007/s41062-022-00937-2>.
- [5] Larrad FD, Sedran T. Optimization of Ultra high performance concrete by the use of a packing model, Cement and Concrete Research, 1994; 24 (6), 997–1009.
- [6] Feylessoufi A, Crespin M, Dion P, Bergaya F, Van DH, Richard P. Controlled Rate Thermal Treatment of Reactive Powder Concretes, Advanced Cement BASED Materials, 1997; (6): 21–27.
- [7] Fehling E, Schmidt M, Walraven J, Leutbecher T, Fröhlich S. Ultra-High Performance Concrete UHPC. Fundamentals, Design, Examples. First Edition, 2015; 1-188.
- [8] Yi N-H, Kim J-HJ, Han T-S, Cho Y-G, Lee JW. Blast-resistant characteristics of ultra-high strength concrete and reactive powder concrete, Construction and Building Material, 2012;28; 694–707, <https://doi.org/10.1016/j.conbuildmat.2011.09.014>.
- [9] Thomas RJ, Sorensen AD. Review of strain rate effects for UHPC in tension, Construction and Building Materials, 2017;153; 846–856, <https://doi.org/10.1016/j.conbuildmat.2017.07.168>.
- [10] Unified Facilities Criteria (UFC) 3-340-02: Structures to resist the effects of accidental explosions, 2008; Department of the Army, the NAVY and the Air Force, Washington DC, USA, 1-1867.
- [11] Brode HL. Numerical Solutions of Spherical Blast Waves, Journal of Applied Physics, American Institute of Applied Physics, New York, 1955; 26(6), 766–775. <https://doi.org/10.1063/1.1722085>.
- [12] Karlos V, Solomos G. Calculation of blast loads for application to structural components, JRC Technical report, EUR 26456 EN.2013; <https://doi.org/10.2788/61866>.

- [13] Sadovskiy MA. Mechanical effects of air shock waves from explosions according to experiments, 2004; Selected works: Geophysics and physics of explosion, Nauka Press, Moscow.
- [14] Adushkin VV, Korotkov AI. Parameters of a shock wave near to HE charge at explosion in air. PMTF, 1961; 119-123.
- [15] Newmark NM, Hansen RJ. Design of blast resistant structures, shock and vibration handbook, Harris, Crede eds, McGraw-Hill, 1961, New York, USA.
- [16] J. Henrych, and R. Major. The Dynamics of Explosion and Its Use, NUCLEAR TECHNOLOGY, 1979, Elsevier, Amsterdam.
- [17] Held M. Blast Waves in Free Air, Propellants, Explosives Pyrotechnics, 1983; 8 (1), 1-7, <https://doi.org/10.1002/prop.19830080102>.
- [18] Kinney GF, Graham KJ. Explosive Shocks in Air, The Journal of the Acoustical Society of America, Springer-Verlag, Berlin and New York, 1985; 80(2), <https://doi.org/10.1121/1.394030>.
- [19] Mills CA. The design of concrete structure to resist explosions and weapon effects, Proceedings of the 1st International Conference on Concrete and Hazard Protections, 1987; 61-73.
- [20] Hopkins-Brown MA, Bailey A. Chapter 2 (Explosion Effects) Part 1, AASTP-4 Royal Military College of Science, 1998; Cranfield University.
- [21] Low HY, Hao H. Reliability analysis of reinforced concrete slabs under explosive loading, Structural Safety, 2001; 23 (2): 157-178, [https://doi.org/10.1016/S0167-4730\(01\)00011-X](https://doi.org/10.1016/S0167-4730(01)00011-X).
- [22] Gelfand B, Silnikov M, Translation from Russian to English Book, Blast effect caused by Explosions, 2004; DTIC, Document, London, England.
- [23] Wu C, Hao H. Modelling of simultaneous ground shock and air burst pressure on nearby structures from surface explosions, International Journal of Impact Engineering, 2005; 31(6): 699-717, <https://doi.org/10.1016/j.ijimpeng.2004.03.002>.
- [24] Nyström U, Gylltoft K. Numerical studies of the combined effects of blast and fragment loading, International Journal of Impact Engineering, 2009; 36: 995-1005, <https://doi.org/10.1016/j.ijimpeng.2009.02.008>.
- [25] Luccioni BM, Ambrosini RD, Danesi RF. Analysis of building collapse under blast loads, Engineering Structures, 2004; 26: 63-71, <https://doi.org/doi.1016/j.engstruct.2003.08.011>.
- [26] Byfield MP. Behavior and Design of Commercial Multistory Buildings Subjected to Blast, Journal of Performance of Constructed Facilities, 2006; 20(4), 324-329. [https://doi.org/10.1061/\(ASCE\)0887-3828\(2006\)20:4\(324\)](https://doi.org/10.1061/(ASCE)0887-3828(2006)20:4(324)).
- [27] Shi Y, Hao H, Li Z-X. Numerical simulation of blast wave interaction with structure columns, Shock Waves, 2007; 17: 113-133, <https://doi.org/10.1007/s00193-007-0099-5>.
- [28] Kocczaz Z, Sutcu F, Torunbalci N. Architectural and structural design for blast resistant buildings, In: The 14th World Conference on Earthquake Engineering, The 14 World Conference on Earthquake Engineering, October 12-17, 2008, Beijing, China.
- [29] Wu, C, Oehlers DJ, Rebentrost M, Leach J, Whittaker AS. Blast testing of ultra-high performance fibre and FRP-retrofitted concrete slabs, Engineering structures, 2009; 31(9): 2060-2069, <https://doi.org/10.1016/j.engstruct.2009.03.020>.
- [30] Hassan MZ, Guan Z. W, Cantwell, WJ, Langdon, GS, Nurick GN. The influence of core density on the blast resistance of foam-based sandwich structures. International Journal of Impact Engineering, 2012; 50:9-16, <https://dx.doi.org.10.1016/j.ijimpeng.2012.06.009>.
- [31] Shallan O, Eraky A, Sakr T, Emad S. Response of Building Structures to Blast Effects, International Journal of Engineering and Innovative Technology, 2014; 4:167-175.
- [32] Nicolaidis D, Kanellopoulos A., Petrou M, Savva P, Mina A. Development of a new Ultra High Performance Fibre Reinforced Cementitious Composite (UHPFRCC) for impact

- and blast protection of structures, *Construction and Building Materials*, 2015; 95:667-674, <https://dx.doi.org/10.1016/j.conbuildmat.2015.07.136>.
- [33] Kyei C, Braimah A. Effects of transverse reinforcement spacing on the response of reinforced concrete columns subjected to blast loading, *Engineering Structures*, 2017; 142:148–164, <https://doi.org/10.1016/j.engstruct.2017.03.044>.
- [34] Li J, Hao H, Wu C. Numerical study of precast segmental column under blast loads, *Engineering Structures*, 2017; 134:125–137, <https://doi.org/10.1016/j.engstruct.2016.12.028>.
- [35] Yang HW, Guan WB, Lu GY. Experimental and numerical investigations into collapse behavior of hemispherical shells under drop hammer impact. *Thin-Walled Structures*, 2018; 124:48-57, <https://doi.org/10.1016/j.tws.2017.11.034>.
- [36] Turker K, Hasgul U, Birol T, Yavas A, Yazici H. Hybrid fiber use on flexural behavior of ultra high performance fiber reinforced concrete beams, *Composite Structures*, 2019; 229:111400, <https://doi.org/10.1016/j.compstruct.2019.111400>.
- [37] Lee J-Y, Aoude H, Yoon Y-S, Mitchell D. Impact and blast behavior of seismically-detailed RC and UHPFRC-Strengthened columns, *International Journal of Impact Engineering*, 2020; 143:103628, <https://doi.org/10.1016/j.ijimpeng.2020.103628>.
- [38] Castedo R, Santos AP, Alañón A, Reifarh C, Chiquito M, López LM, Martínez-Almajano S, Pérez-Caldentey A. Numerical study and experimental tests on full-scale RC slabs under close-in explosions, *Engineering Structures*, 2021; 231:111774, <https://doi.org/10.1016/j.engstruct.2020.111774>.
- [39] Kadhim MMA, Jawdhari A, Peiris A. Development of hybrid UHPC-NC beams: A numerical study, *Engineering Structures*, 2021; 233:111893, <https://doi.org/10.1016/j.engstruct.2021.111893>.
- [40] Mahmud GH, Hassan AMT, Jones SW, Schleyer GK. Experimental and numerical studies of ultra high performance fibre reinforced concrete (UHPFRC) two-way slabs, *Structures*, 2012; 29:1763–1778, <https://doi.org/10.1016/j.istruc.2020.12.053>.
- [41] Mandal J, Goel MD, Agarwal AK. Surface and Buried Explosions: An Explorative Review with Recent Advances, *Archives of Computational Methods in Engineering*, 2021; <https://doi.org/10.1007/s11831-021-09553-2>.
- [42] Anas SM, Mehtab Alam, Mohammad Umair. Reinforced cement concrete (RCC) shelter and prediction of its blast loads capacity. *Materials Today: Proceedings*, 2022; <https://doi.org/10.1016/j.matpr.2022.09.125>.
- [43] Yan J, Liu Y, Bai F, Ni X, Xu Y, Yan Z, Huang F. Dynamic response of GFRP-reinforced UHPC beams under close-in blast loading. *Materials & Design*, 2022; 223, 111140, <https://doi.org/10.1016/j.matdes.2022.111140>.
- [44] Ma LL, Wu H, Fang Q. A unified performance-based blast-resistant design approach for RC beams/columns. *International Journal of Impact Engineering*, 2023; 173:104459, <https://doi.org/10.1016/j.ijimpeng.2022.104459>.
- [45] K. Peter. ANSYS Theory Reference Release 5.6, 1994.



Research Article

An assessment of rebound hammer test in estimating the concrete compressive strength in seawater

Philip Jun Celerinos^{*a}, Patrick Miguel Dedel^b, Nesty Vince Fernandez^c, Kathleen Ira Muñoz^d, Fatima Alaiizza Suelan^e

Civil Engineering Department, School of Engineering and Architecture, Ateneo de Davao University, Davao City, Davao del Sur, 8000, Philippines

Article Info

Abstract

Article history:

Received 21 Mar 2023

Accepted 5 May 2023

Keywords:

Compressive strength;

Direct compression;

Rebound hammer;

Reliability;

Seawater

Currently, there is a need to assess the structural integrity of concrete structures situated near or within seawater in a faster manner using a rebound hammer test. However, this test is limited to its reliability, particularly if the rebound hammer device has not been calibrated according to its specific tested environment. Hence, this study assessed the reliability of the rebound hammer test in the compressive strength estimation of concrete cured in a specific environmental condition. As such—the seawater environment, the seawater in a controlled area, and the potable water stored in a normal room condition were the environmental conditions that were considered in the study. Results showed that the rebound hammer test consistently underestimated the direct compression test in three (3) environmental conditions. It was found that the underestimated compressive strength errors ranged from 15.22% to 59% in seawater environment, 33.33% to 58.33% in seawater in a controlled area, and 37.70% to 57.57% in potable water stored in a normal room condition, respectively. Furthermore, this study also established a rebound correlation model, both graphical curve and empirical equation, which can be the basis for concrete compressive strength estimation cured in three (3) different environments.

© 2023 MIM Research Group. All rights reserved.

1. Introduction

Seawater is an aggressive and complex marine environment. If concrete structures are constructed and situated in seawater, these will cause deterioration through biological, chemical, mechanical, and physical processes [1]. Due to the perception of seawater in concrete, its durability has been a problem for many years. Hence, poor-quality cement in the concrete design mixture is not long-lasting for such aggressive and complex environments [2]. In the Philippines, particularly in Davao Region, some ongoing and upcoming major infrastructure (e.g., bridges, coastal roads, and ports) are situated near or within seawater. Most of these infrastructures are reinforced-concrete designs [3].

Generally, in the reinforced-concrete structure, the durability of concrete is determined through compressive strength. It can be measured by taking concrete samples in cylinder forms [4]. The samples are brought to laboratories and loaded in the direct compression machine until cracking failure occurs. While this method is commonly practiced in the construction industry up to this day because of its accuracy, this also requires considerable time and expenses [5]. Recently, researchers have developed a non-destructive testing technique in a faster manner to determine the in-situ concrete compressive strength. These techniques have estimated the compressive strength of the concrete structures by

*Corresponding author: pjscelerinos@addu.edu.ph

^a orcid.org/0009-0009-3919-2357; ^b orcid.org/0009-0007-6835-0321; ^c orcid.org/0009-0007-6960-5226;

^d orcid.org/0009-0001-6539-873X; ^e orcid.org/0009-0006-9891-6720

DOI: <http://dx.doi.org/10.17515/resm2023.712me0321>

Res. Eng. Struct. Mat. Vol. 9 Iss. 3 (2023) 947-967

evaluating some concrete properties and then relating the measured properties to the mechanical properties of concrete [6].

One of the most widely known non-destructive testing techniques is to use a device called the Rebound Hammer. This device measures the concrete surface hardness through the rebound principle of spring, also referred to as the rebound number, to correlate with its compressive strength. Moreover, this development provided a portable, low-cost, and easy-to-use non-destructive device [6], [7]. Studies revealed that the near-surface properties of concrete could affect the rebound readings. Consequently, it came with certain drawbacks and was limited in its reliability. Factors that contributed to its accuracy are aggregates, air voids of concrete, calibration of the rebound hammer, carbonation, concrete age, surface hardness, moisture content, and environmental temperature. These factors have demonstrated that the obtained measurements are not unique for the rebound hammer device and that the test outcome is based on the tested properties of concrete [6], [8].

Many research works have verified if the non-destructive test using the rebound hammer was a reliable technique to estimate the concrete compressive strength. Some of these findings revealed that this technique provided adequate information and was an acceptable method for conducting a fast approximation in determining the concrete compressive strength [6]–[9]. Sanchez & Tarranza (2014) [6] examined the rebound hammer test of concrete samples exposed to a brackish water environment. They found out that rebound number readings were affected by the concrete surface hardness. Also, the type of environment significantly influenced the compressive strength result from the rebound hammer test compared to the actual compressive strength result in the direct compression test. In the study of Co (2019) [8], the rebound hammer test was investigated for concrete samples cured in potable water and compared to the actual test result in the direct compression test. Hence, the rebound hammer consistently underestimated the actual compressive strength result. From the consistent underestimation, the study developed an empirical model to estimate the compressive strength of concrete when using the rebound hammer device in assessing a concrete structure.

Moreover, Brencich et al., 2020 [7], investigated the reliability of the rebound hammer test in concrete structures with different water-cement ratios cured in standard clean potable water. They concluded that the irregularities of the concrete mixture within the concrete surface significantly affected the rebound hammer readings. The interaction of the plunger in the rebound hammer and concrete sample during their test provided large dispersion in the compressive strength results. However, they also inferred that the rebound hammer test was still acceptable as a non-destructive test to estimate the compressive strength of concrete if the universal calibration curve has been developed from the actual compressive strength result of the concrete sample. Jain et al., (2022) [10] used the rebound hammer device to measure the compressive strength of the concrete samples with additive materials in the standard curing procedure. The rebound hammer readings still underestimated the compressive strength result around 34.3% to 38.1% for 28th days and 84th days after the curing period. The linear correlation graph from the rebound number versus the compressive strength obtained a 0.98 coefficient. In addition, Pushpakumara & Fernando (2023) [11] assessed the existing concrete structures exposed to splash zone partially submerged in seawater using the rebound hammer test. The study found that water quality exposure achieved the highest priority for the deterioration of concrete structures in the splash zone area. Hence, the rebound hammer still provided an adequate prediction of estimating the concrete compressive strength.

The abovementioned studies also concluded that the rebound reading estimation can only be accepted if the device has undergone calibration for a particular type of concrete. Thus,

the rebound hammer device relied on its physical condition and must be maintained regularly [12]. In addition, a rebound correlation curve must be developed from the laboratory experimentation, made with the concrete specimen, similar to the materials in the existing concrete structure [6], [7], [13]–[15]. With this, the rebound hammer test must also be evaluated in actual marine conditions, particularly in seawater, to investigate the concrete structure when subjected to extreme changes in weather conditions [6]. Therefore, to the author's knowledge, the evaluation of compressive strength in concrete samples cured in seawater using the rebound hammer test has never been reported in the existing literature, specifically in the Philippine setting. Furthermore, the development of the rebound correlation curve has yet to be provided in actual marine conditions for the particular type of concrete samples.

This present study aimed to assess the reliability of the rebound hammer test in estimating the concrete compressive strength cured in seawater. Thus, produced in this context were concrete cube samples that were cured in three environmental conditions: 1) seawater environment, 2) seawater in a controlled area, and 3) potable water stored in a normal room condition. Consequently, this study provided a distinction of the obtained concrete compressive strength using the tests of rebound hammer versus direct compression. The study also determined the carbonation development in the concrete cube samples cured in three (3) environmental conditions since carbonation development was one factor that influenced the rebound reading. It also determined the true relationships between the compressive strengths from the rebound hammer and direct compression tests, respectively. Furthermore, this work established a rebound correlation curve and equation models from the calculated rebound hammer estimation.

2. Methodology

2.1. Materials and Design Mixture

Twenty-seven (27) samples were produced for experimentation in this study. The concrete samples in a cubic shape form with a 150-mm size [6] for all sides were used, shown in Figure 1. The concrete design mixture was class A with a standard proportion of 1:2:3 ratio, and the minimum attainable compressive strength was 21 MPa (3000 psi). This ratio was equally divided by weights for cement in one-part, fine aggregates in two parts, and coarse aggregates in three parts. To produce all concrete cube samples, the following were the used materials: 1) Type 1 Ordinary Portland cement, 2) crushed-washed sand fine aggregates, and 3) 3/4-inch diameter crushed gravel. The properties of cement, fine aggregates and coarse aggregates were provided by the supplier, shown in Table 1.

The gradation of curves for fine aggregates and coarse aggregates used for experimentation is presented in Figure 2. The test for geometrical properties using the sieving method to determine the size distribution was based on BS EN 933-1 standards [16]. After preparing all materials and determining their properties, they were blended using a 0.45 water-cement ratio [17] with clean potable water for casting all concrete samples. Thereafter, the mixed concrete was poured into a cubic molder using a 3/4-inch-thick phenolic board to attain the fair-faced finish concrete surface. The abovementioned materials were supplied by Green Rise Marketing and Co., located in Davao City, Davao del Sur, Philippines.



Fig. 1 Concrete cube samples

Table 1. Properties of Materials

Materials	Parameter	Properties
Cement	Specific gravity	3.15
	Specific gravity	2.50
Fine aggregate	Fineness modulus	3.16
	Moisture content (%)	7.75
	Absorption values (%)	4.20
	Specific gravity	2.45
Coarse aggregate	Moisture content (%)	3.15
	Absorption values (%)	3.08

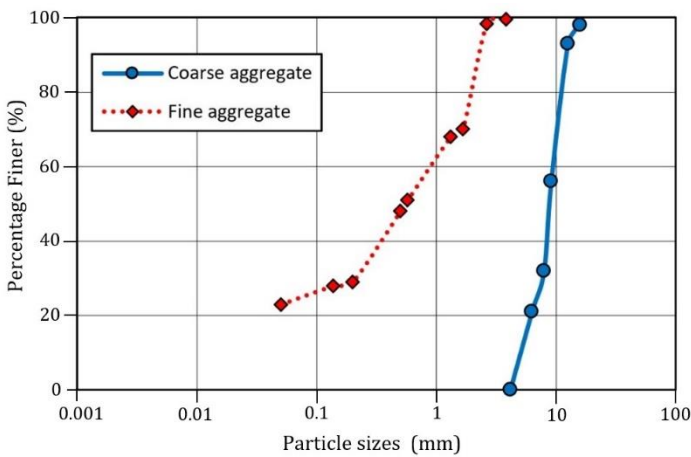


Fig. 2 Grain size distribution of fine aggregates and coarse aggregates

2.2. Curing Environments

2.2.1. Seawater Environment

The concrete cube samples were divided into three (3) groups and were cured in the following environmental conditions: 1) seawater environment, 2) seawater in a controlled area, and 3) potable water stored in a normal room condition. In the first environmental condition, nine (9) concrete cube samples were cured using the continuous immersion of

seawater in a private fish cage (Figure 3b) located at Brgy. Biao, Digos City, Davao del Sur, Philippines, shown in Figure 3a. Moreover, these samples were wrapped in a fishnet and tied with a 1/4-inch nylon rope one to two meters below the surface of seawater to ensure stable conditions during the strong presence of waves. This specific procedure measured the effect of extreme changes on weather conditions in the concrete cube samples [6]. Moreover, the authors in this present work conducted this specific curing condition in June 2022 since this month had recorded a normal range and above-normal range temperature from 23°C to 31°C [18].



Fig. 3 Seawater environment in: (a) topographic view [19] and (b) actual curing condition of concrete cube samples

2.2.2. Seawater in a Controlled Area

The second environmental condition in this study was seawater in a controlled area, shown in Figure 4. Another nine (9) concrete cube samples were cured in a controlled area at 20°C to 26°C temperature and 75% relative humidity. The concrete cube samples were placed in an emptied container that was alternately cured and filled with seawater instead of brackish water [6]. The seawater was replaced weekly in an alternate cycle of drying and wetting, in which the concrete cubes were air-dried for six (6) hours. After air-drying, the emptied container was slowly filled with seawater to immerse all concrete cube

samples fully. This condition was maintained until all nine (9) concrete cube samples were removed from the container for a rebound hammer test and a direct compression test, respectively. This procedure was consequently performed in a vacant room in Brgy. Calinan, Davao City, Davao del Sur, Philippines.



Fig. 4 Concrete cube samples cured in seawater in a controlled area

2.2.3. Potable Water in a Normal Room Condition

In the third environmental condition, the last nine (9) concrete cube samples were cured in potable water at a normal room condition, shown in Figure 5. The container with potable water was stored at a temperature from 20°C to 26°C at 75% relative humidity in a vacant room in Brgy. Calinan, Davao City, Davao del Sur, Philippines. Following the curing procedure of concrete samples in the laboratory test, this study observed the standard practice provided by ASTM C192 [20] for all nine (9) concrete cube samples. Hence, this group served as the controlled samples [6] set by the researcher as a baseline reference for the abovementioned environmental conditions.



Fig. 5 Concrete cube samples cured in potable water in a normal room condition

2.3. Equipment, Measurement and Variation of Tests

After the twenty-seven (27) concrete cube samples had been extracted from the molders and were cured in three (3) different environmental conditions, the non-destructive and the destructive tests were employed. All concrete cube samples were air-dried for twenty-four (24) hours before they were tested on the 7th, 14th, and 28th day for compressive strength. Moreover, the conventional N-type rebound hammer device, shown in Figure 6a, was used for the non-destructive test. On the other hand, the digital direct compression machine, shown in Figure 6b, was used for the destructive test with a 5000-kN maximum load capacity. The direct compression machine and the rebound hammer device used to

conduct the tests were from Terms Concrete and Materials testing Laboratory Inc. in Davao City, Davao del Sur, Philippines.

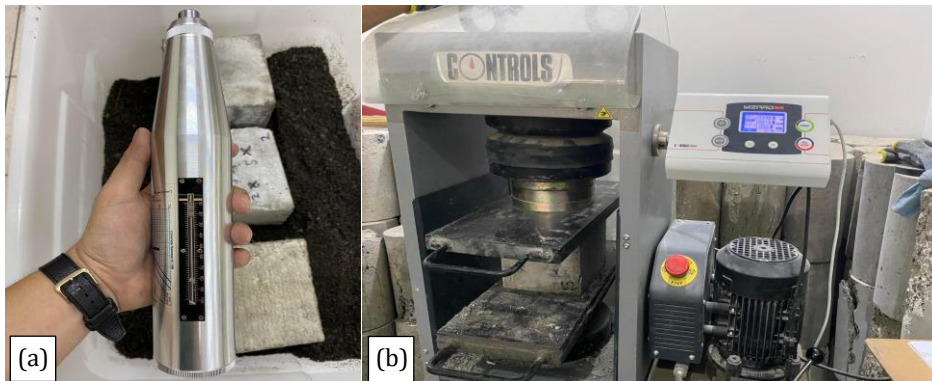


Fig. 6 Destructive and non-destructive tests using: (a) N-type rebound hammer device and (b) one unit test automatic compression machine

When the concrete cube samples were ready for testing, all samples in each group were tested first by the rebound hammer device, following the procedure set forth by ASTM (2008) [21] and ACI Committee 228 (2003) [22]. Consequently, when the rebound hammer was employed, its plunger part penetrated and struck the ten (10) marking zone [23]–[25] in each concrete cube sample. The plunger in the rebound hammer should be perpendicular to each zone and spaced 30 mm from each marked zone to achieve the desired readings. This penetration estimated the hardness of concrete for the compressive strength. All samples had visual inspection to identify the smooth surface before testing. The schematic diagram of the rebound hammer test is illustrated in Figure 7a, where the device was pressed towards the surface of each sample at the horizontal position, shown in Figure 7b. Every tested sample must lean in the solid wall so that when the rebound hammer impacted in the concrete sample, the stability condition was still achieved.

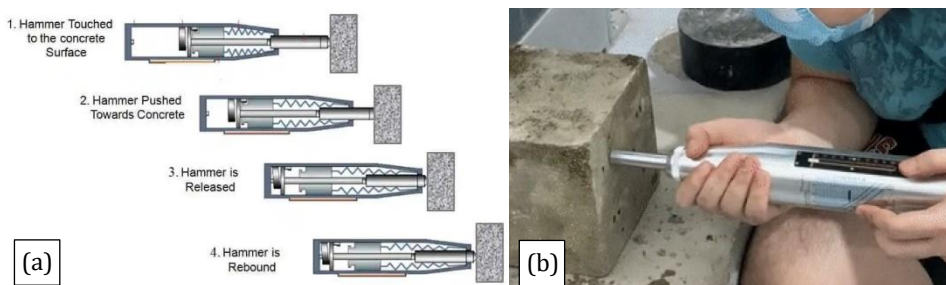


Fig. 7 Rebound hammer device in: (a) schematic diagram [26] and (b) actual position

Moreover, all concrete cube samples with the highest and lowest rebound reading numbers were discarded, and the remaining eight (8) rebound reading numbers were averaged [23], [24], [27]. The average rebound readings were taken for calculations and were compared to the rebound hammer graph provided by the manufacturer. Equation 1, shown below, was used to calculate the estimated rebound hammer compressive strength reading [7].

$$R_c(t) = R_c, 28e^{s\left(1 - \sqrt{\frac{28}{t}}\right)} \quad (1)$$

where R_c is the estimated rebound hammer compressive strength reading, s is the exponential equation provided [28] at the given time t in the designated tests at 7th, 14th, and 28th days.

Henceforth, the concrete cube samples were immediately placed in the direct compression machine and loaded for failure after the rebound hammer test was performed. The destructive test was set at a gradual load rate of 140 kg/cm² per minute until it reached the maximum compressive failure capacity. After recording the obtained compressive strength from the direct compression machine, the percentage error (*%Error*) of compressive strength reading from the rebound hammer test was determined. The percentage error used by Co (2019) [8] was employed as presented in Equation 2.

$$\%Error = \frac{R_D - R_C(t)}{R_D} \tag{2}$$

where R_D is the compressive strength from the direct compression machine, and R_c is the estimated rebound hammer compressive strength reading at the given time t in the designated tests at 7th, 14th, and 28th days.

After the concrete samples had undergone the destructive test approach in the direct compression machine, the crushed crack part of the concrete cube sample was tested using a chemical indicator that assessed the concrete carbonation. The purpose of the carbonation test in this study was to identify if concrete cube samples have been suspected of corrosion during the curing process in three (3) environmental conditions. This procedure adopted the carbonation test using a phenolphthalein [29], [30]. The phenolphthalein liquid solution has the following properties (Table 2) and was purchased in Davao Mineral Laboratories, Inc. Brgy. Lanang, Davao City, Davao del Sur, Philippines.

Table 2. Properties of phenolphthalein indicator solution

Molecular mass (g/mol)	Purity (%)	Solution in ethanol (%)	Denatured (%)	ph balance	Density at 20°C (g/mL)	color
318.328	98	1	90	8-10	0.82	clear

When phenolphthalein is applied and sprayed around 0.1 mL to 0.3 mL in the crushed crack portion of each concrete sample at contacts in alkaline, the color of the undisturbed cracked part of the concrete cube sample turns pink if it has a high pH level. In contrast, if the concrete cube sample has the presence of carbon, it will remain uncolored.

2.4. Statistical Analysis

The relationship between the readings from the rebound hammer device versus the calculated rebound hammer compressive strength and the direct compressive strength results were determined in probabilistic and statistical analysis [6], [8], [25], [31]–[33]. The correlation and regression of the Pearson r coefficient equation, presented in Equation 3, has been used in this study to identify the true relationship between the test results of the rebound hammer and the direct compression in concrete compressive strength for the twenty-seven (27) concrete cubes in three (3) environmental conditions.

$$r = \frac{n \sum xy - (\sum x)(\sum y)}{\sqrt{[n \sum x^2 - (\sum x)^2][n \sum y^2 - (\sum y)^2]}} \tag{3}$$

where the rebound reading is the independent variable x , the calculated compressive strength estimation from the test of rebound hammer and the compressive strength from

the test of direct compression are dependent variables y , and the twenty-seven (27) concrete cube samples are considered as n .

In determining the covariance of the variables considered, the computed r coefficient must be between -1 and +1. Hence, r must be a non-zero value so that the relationship between variables is evident [34]. In addition to this analysis, two (2) hypotheses were considered: 1) null hypothesis, which stated that the variables considered have no linear correlation, and 2) alternative hypothesis, which stated that the variables considered have a linear correlation. A 95% confidence level was used, with an α value equal to 0.05, in selecting the hypothesis. The α value was compared to the calculated p -value; hence, if the computed p -value was greater than α , the alternative hypothesis was accepted. In contrast, if the computed p -value was lesser than α , the accepted hypothesis was null.

3. Results and Discussion

3.1. Compressive Strength in Rebound Hammer and Direct Compression Tests

The compressive strength of all concrete cube samples placed in three (3) different curing environments was determined using a rebound hammer and direct compression tests. Table 3 shows the compressive strength results for the concrete samples cured in a seawater environment.

Table 3. Compressive strength results for rebound hammer versus direct compression at 7th, 14th and 28th days of curing in seawater

Curing days	Sample	Strength	*Number of readings										Rebound hammer (MPa)	Direct compression (MPa)	% Error
			1	2	3	4	5	6	7	8	9	10			
7	1	Rebound Reading	20	18	22	13	20	14	18	18	14	14	10.00	15.00	33.33
		Equivalent computed compressive strength (MPa)	10	10	13	10	10	10	10	10	10	10			
	2	Rebound Reading	16	16	22	18	19	17	17	20	20	19	10.00	17.00	41.18
		Equivalent computed compressive strength (MPa)	10	10	13	10	10	10	10	10	10	10			
	3	Rebound Reading	14	17	20	16	16	20	18	20	23	18	10.00	17.00	41.18
		Equivalent computed compressive strength (MPa)	10	10	10	10	10	10	10	10	14	10			
14	1	Rebound Reading	22	17	27	27	21	28	24	27	25	18	15.80	22.00	28.18
		Equivalent computed compressive strength (MPa)	12	10	20	20	12	22	16	19	17	10			
	2	Rebound Reading	26	32	30	32	21	24	23	28	20	21	16.64	24.00	30.67
		Equivalent computed compressive strength (MPa)	18	28	24	28	12	16	14	21	10	12			
	3	Rebound Reading	24	31	30	25	23	23	23	27	23	28	19.50	23.00	15.22
		Equivalent computed compressive strength (MPa)	16	26	24	17	14	14	14	20	14	21			
28	1	Rebound Reading	25	21	27	23	19	16	21	21	22	12	12.50	25.00	50.00
		Equivalent computed compressive strength (MPa)	17	12	20	14	10	10	12	12	13	10			
	2	Rebound Reading	19	20	21	19	18	15	17	18	16	22	10.25	25.00	59.00
		Equivalent computed compressive strength (MPa)	10	10	12	10	10	10	10	10	10	13			
	3	Rebound Reading	24	21	20	25	21	21	20	21	20	18	12.00	26.00	53.85
		Equivalent computed compressive strength (MPa)	16	12	10	17	12	12	10	12	10	10			

*Note that the minimum and maximum rebound readings were eliminated and the remaining eight (8) rebound readings were considered.

For the observations herein, the direct compression test results for the concrete compressive strength samples cured in a seawater environment ranged from 15 MPa to 17 MPa for the 7th day curing period, 22 MPa to 24 MPa for the 14th day curing period, and 25 MPa to 26 MPa for the 28th day curing period, respectively. The results demonstrated that the mixture of concrete achieved a compressive strength of 21 MPa (3000 psi) from the set standard mix [20]. Moreover, in Figure 8a, the results in compressive strength for the rebound hammer test underestimated all the direct compression test results. Using Equation 2 to calculate the percent error in the rebound hammer reading, it was found that the consistent underestimation for concrete cube samples cured in a seawater environment has a minimum error of 15.22% on the 14th day and a maximum error of 59% on the 28th day curing period as illustrated in Figure 8b. In comparison, the study of Co (2019) [8] has recorded minimum and maximum errors of 5.95% to 44.18%, respectively. The recorded errors in this study provided higher results because the rebound hammer device used by Co (2019) [8] was calibrated before it was used.

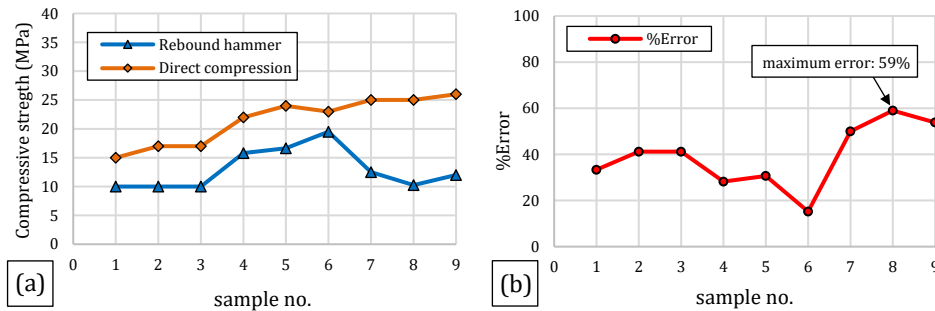


Fig. 8 Variations of concrete samples per curing periods in seawater environment versus: (a) compressive strengths from the rebound hammer and direct compression, and (b) obtained %Error

Furthermore, as the age of curing in concrete increased, the obtained compressive strength also increased. Thus, the hydration process continued [35]. The compressive strength for the rebound hammer test in this study revealed similar results to the study of Co (2019) [8], which indicated that the compressive strength results varied accordingly. However, the compressive strength of the rebound hammer test yielded only after the 14th day (Figure 8b) because the longer the concrete cube samples were cured, the higher the moisture content retained. Additionally, concrete cube samples were air-dried only after each curing period for twenty-four (24) hours instead of a much more extended period before they went through a rebound hammer test. Although the age of exposure to a particular environmental condition and the moisture content in concrete cube samples were not explored in this study, nonetheless, both factors were observed during experimentation that can influence the obtained high rebound readings percent errors [6].

Table 4 exhibits the compressive strengths of the rebound hammer and the direct compression test results of the concrete samples cured in seawater in a controlled area. Similar to Table 3, the test results of the rebound hammer underestimated all the test results in the direct compression for the compressive strength. Hence, on the 7th day curing period, when the rebound hammer test was employed, the concrete cube samples had recorded 10 MPa, while the direct compression test ranged from 15 MPa to 16 MPa compressive strengths. Subsequently, on the 14th day curing period, the rebound hammer test recorded from 10.63 MPa to 12 MPa compressive strengths, while the direct

compression test ranged from 20 MPa to 21 MPa. Also, for the curing period on the 28th day, the results in the rebound hammer test obtained 10.67 MPa to 11.63 MPa. On the other hand, the direct compression test ranged from 24 MPa to 26 MPa.

Table 4. Compressive strength results for rebound hammer versus direct compression at 7th, 14th and 28th days of curing in seawater in a controlled area

Curing days	Sample	Strength	*Number of readings								Rebound hammer (MPa)	Direct compression (MPa)	% Error		
			1	2	3	4	5	6	7	8				9	10
7	1	Rebound Reading	17	12	18	13	15	16	16	17	17	12	10.00	16.00	37.50
		Equivalent computed compressive strength (MPa)	10	10	10	10	10	10	10	10	10	10			
	2	Rebound Reading	13	18	18	17	14	14	15	18	14	17	10.00	15.00	33.33
		Equivalent computed compressive strength (MPa)	10	10	10	10	10	10	10	10	10	10			
	3	Rebound Reading	12	15	18	14	17	14	14	18	18	18	10.00	15.00	33.33
		Equivalent computed compressive strength (MPa)	10	10	10	10	10	10	10	10	10	10			
14	1	Rebound Reading	20	22	25	26	22	21	18	21	18	18	12.83	20.00	35.85
		Equivalent computed compressive strength (MPa)	10	13	17	18	13	12	10	12	10	10			
	2	Rebound Reading	10	18	23	22	18	20	21	19	19	19	10.63	20.00	46.85
		Equivalent computed compressive strength (MPa)	10	10	14	13	10	10	12	10	10	10			
	3	Rebound Reading	18	20	20	18	18	22	21	22	24	24	12.00	21.00	42.86
		Equivalent computed compressive strength (MPa)	10	10	10	10	10	13	12	13	16	16			
28	1	Rebound Reading	23	21	20	21	14	12	14	18	16	10	10.67	24.00	55.54
		Equivalent computed compressive strength (MPa)	14	12	10	12	10	10	10	10	10	10			
	2	Rebound Reading	17	22	25	23	19	18	17	16	22	22	11.63	26.00	55.27
		Equivalent computed compressive strength (MPa)	10	13	17	14	10	10	10	10	13	13			
	3	Rebound Reading	14	17	17	15	16	10	18	20	13	19	10.00	24.00	58.33
		Equivalent computed compressive strength (MPa)	10	10	10	10	10	10	10	10	10	10			

*Note that the minimum and maximum rebound readings were eliminated and the remaining eight (8) rebound readings were considered.

The underestimated compressive strength result in the second environmental condition is illustrated in Figure 9a. The results also revealed that the maximum error plotted in Figure 9b occurred on the 28th day curing period at 58.33%, the same curing period in a seawater environment where the maximum error also occurred.

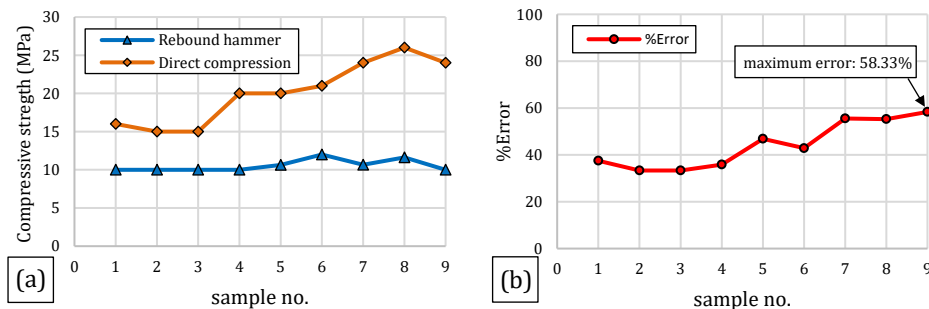


Fig. 9 Variations of concrete samples per curing periods in seawater in a controlled area versus: (a) compressive strengths from the rebound hammer and direct compression, and (b) obtained %Error

Aside from the calibration error factor and the less drying period after curing, it was also observed in the rebound hammer test that all rebound readings at the middle zones in concrete cubes had the highest results. In contrast, zones at the corner of the concrete cube samples revealed low readings. The results can be attributed to the rebound hammer device that the impact of the plunger on the nearby concrete surface edges provided a high slenderness effect [23]. Hence, the applied plunger force becomes more distributed when the rebound hammer strikes a larger zone area. Thus, the rebound readings recorded lower strength in the nearby edges and higher strength in the middle zone.

In the last environmental condition, the compressive strength results of concrete cube samples cured in potable water stored in a normal condition revealed that the compressive strengths had obtained barely higher strength, shown in Table 5. Hence, the rebound hammer test recorded 10 MPa on the 7th day of curing, while the direct compression test recorded from 17 MPa to 18 MPa compressive strengths. For the 14th day of curing, the tested concrete cube samples for the rebound hammer recorded from 13 MPa to 14.33 MPa compressive strengths.

Table 5. Compressive strength results for rebound hammer versus direct compression at 7th, 14th and 28th days of curing in potable water stored in a normal condition

Curing days	Sample	Strength	*Number of readings										Rebound hammer (MPa)	Direct compression (MPa)	% Error
			1	2	3	4	5	6	7	8	9	10			
7	1	Rebound Reading	15	13	18	13	10	18	16	15	15	18	10	18	44.44
		Equivalent computed compressive strength (MPa)	10	10	10	10	10	10	10	10	10	10			
	2	Rebound Reading	20	19	22	19	18	15	14	20	17	19	10	17	41.18
		Equivalent computed compressive strength (MPa)	10	10	13	10	10	10	10	10	10	10			
	3	Rebound Reading	16	18	22	16	17	12	16	22	17	20	10	17	41.18
		Equivalent computed compressive strength (MPa)	10	10	13	10	10	10	10	13	10	10			
14	1	Rebound Reading	20	21	22	22	20	26	20	23	22	20	13	21	38.20
		Equivalent computed compressive strength (MPa)	10	12	13	13	10	18	10	14	13	10			
	2	Rebound Reading	22	21	21	20	25	20	21	24	20	22	13	21	38.20
		Equivalent computed compressive strength (MPa)	13	12	12	10	17	10	12	16	10	13			
	3	Rebound Reading	22	24	22	20	21	20	22	24	22	22	14.33	23	37.70
		Equivalent computed compressive strength (MPa)	13	16	22	10	12	10	13	16	13	13			
28	1	Rebound Reading	21	17	19	17	18	22	14	25	18.5	21	10.88	24	54.67
		Equivalent computed compressive strength (MPa)	12	10	10	10	10	13	10	17	10	12			
	2	Rebound Reading	21	13	24	18	16	19	19	26	25	19	11.88	28	57.57
		Equivalent computed compressive strength (MPa)	12	10	16	10	10	10	10	18	17	10			
	3	Rebound Reading	21	19	27	19	18	22	16	21	21	17	11.13	25	55.48
		Equivalent computed compressive strength (MPa)	12	10	20	10	10	13	10	12	12	10			

*Note that the minimum and maximum rebound readings were eliminated and the remaining eight (8) rebound readings were considered.

In comparison, the direct compression test recorded from 21 MPa to 23 MPa. Lastly, the test results for the rebound hammer in compressive strength ranged from 10.88 MPa to 11.88 MPa for the 28th day of curing. In contrast, the direct compression test recorded from 24 MPa to 28 MPa, respectively. The test results for direct compression in three (3) environmental conditions shown in Tables 3, 4, and 5 for compressive strength have comparable results. However, in the last environmental condition, the rebound hammer test results still underestimated the compressive strength results in the direct compression, shown in Figure 10a. Likewise, the concrete compressive strength results in the rebound hammer and the direct compression tests in the last environmental condition, the maximum error reached 57.57% for the samples in potable water stored in a normal condition environment, shown in Figure 10b.

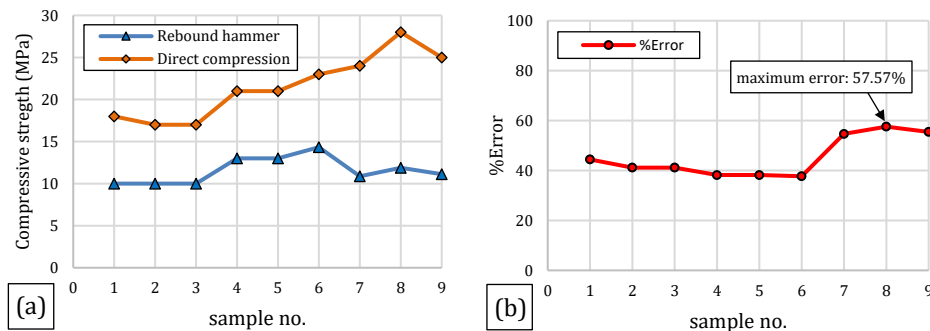


Fig. 10 Variations of concrete samples per curing periods in potable water stored in a normal condition versus: (a) compressive strengths from the rebound hammer and direct compression, and (b) obtained %Error

This maximum error is slightly lower than 1.43% compared to the maximum error of concrete cube samples in the seawater environment and 0.76% lower than the maximum error of the samples in seawater in a controlled area. The results are similar to the study of Sanchez & Tarranza (2014) [6], where the concrete cube samples cured in potable water in a normal room condition provided higher compressive strength from the direct compression test. However, compared to brackish water [6] from the seawater environment in this study, samples from the seawater environment had slightly comparable results of compressive strength versus the rebound hammer test of the samples cured in the potable water environment. Additionally, it was also observed in the rebound hammer test for all environmental conditions that the compressive strength results on the 7th day had a similar reading of 10 MPa (Tables 3, 4, and 5). This was associated with the fact that at early curing age, the rebound reading only registered and obtained a barely minimum reading from the rebound hammer device provided by the manufacturer.

Furthermore, concrete cube samples were susceptible to crack failure in nearby edge surfaces, as observed during the direct compression test. This kind of failure provided a lesser estimation of the compressive strength of concrete. Additionally, one element that influenced the inconsistent estimation of the concrete compressive strength was that when concrete cube samples were transported from one place to another, they were subjected to frequent disturbances, thereby reducing the rebound reading and compressive strength. It was advised that when using the rebound hammer device to assess the concrete

structures situated in seawater, the adjustments of rebound readings and compressive strength results in a particular setting must be developed.

3.2. Results for Carbonation Test in Three (3) Environmental Conditions

After the direct compression test was performed and cracked portions of the concrete cube samples were visible, the samples went through a carbonation test. The phenolphthalein liquid solution was immediately applied and sprayed to all the cracked portions of the samples to determine the occurrence of carbon that had been developed during the consequent curing periods. As observed in Figures 11a, 11b, and 11c, all the cracked portions in concrete cube samples turned pink.

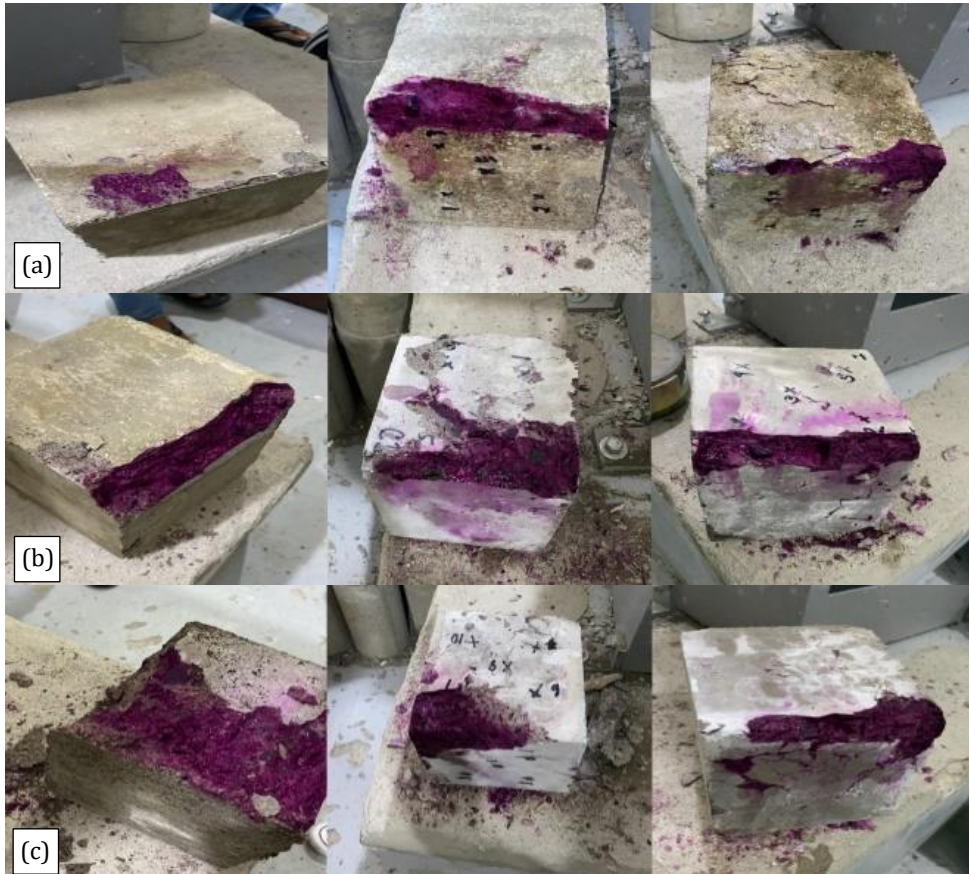


Fig. 11 Phenolphthalein solution in crack portion of concrete cube samples cured in: (a) seawater environment, (b) seawater in a controlled area, and (c) potable water stored in a normal room condition

In the carbonation test performed in this study, it can be inferred that all twenty-seven (27) concrete cube samples cured in three (3) environmental conditions had no carbon development during their designated curing periods. This test was done to verify the carbonation existence in concrete cube samples. Hence, carbon could significantly affect the rebound readings and may indicate higher than 50% inconsistency than those without carbonation [30].

Thus, the finding in this work revealed that more than 50% of the rebound reading errors were not directly influenced by carbonation development. Therefore, this contradicted the

previous result in the existing literature in the aforementioned. In addition, this finding also indicated that when the concrete cube samples were in continuous immersion in the seawater environment, any acidic agents had not intruded inside the concrete during their curing periods. Thus, in this present work, only the calibration of the rebound hammer device, less drying period after curing, the high water retained in the concrete samples, and the uneven distribution of force in the plunger of the rebound hammer device to the concrete surface were the factors that can affect the high rebound readings errors.

Furthermore, as the concrete cube samples aged in the seawater environment, seashells and other marine organisms, particularly algal species, slowly grew on the concrete surface. These organisms produced extraordinarily toxic compounds [36] that could affect the rebound hammer and direct compression tests in concrete cube samples. However, weekly cleaning maintenance on the surfaces of all nine (9) concrete cube samples cured in a seawater environment was conducted as part of the methodology in this present work to maintain the smoothness of the concrete surface. Thus, the continued growth of seashells and the development of marine organisms on concrete surfaces were prevented.

3.3. Regression and Correlation Results and Development of Correlation Models

In regression analysis for the variables considered in the seawater environment, the computed p -value of 0.000000247 between the rebound reading versus the rebound hammer compressive strength test was less than the set significant level (α). On the other hand, the computed p -value of 0.141883304 for the variation between the rebound reading versus the direct compression compressive strength test was greater than the set significant level (α). These showed that both variations had contrasting results. Hence, the null hypothesis was accepted in the former variation, while the alternative hypothesis was accepted for the latter variation.

In the calculated correlation coefficient R^2 using Equation 3 for the rebound reading versus the rebound hammer compressive strength test, the result was 98.16%, which indicates a significantly high correlation. In contrast, the rebound reading versus the direct compression compressive strength test was 28.12%, which can be considered a negligible correlation. The result of the regression and correlation analysis in the latter variation can also be observed in Figure 12a. The plotted values were dispersedly unaligned in the linear trendline. This study found that rebound readings from approximately 12 to 16 had no direct effect on the direct compression compressive strength test results in a seawater environment. These findings showed that extreme weather changes in the seawater environment with a normal range and above-normal range recorded temperatures from 23°C to 31°C [18] can also significantly affect the rebound readings.

Moreover, for the variables considered in seawater in a controlled area, the computed p -values of 0.000348684 and 0.065826142 in the variations between the rebound reading versus the rebound hammer compressive strength and the direct compression compressive strength tests in concrete cube samples were less than the set significant level (α). These showed that the considered variables had linear relationships with each other. Hence, the null hypothesis in the second environmental condition was accepted. The correlation coefficient R^2 between the rebound reading versus the rebound hammer compressive strength test was computed to have 85.62%, which was considered a high correlation result. Contrary to the former variation, the correlation coefficient R^2 of 40.40% in the rebound reading and the direct compression compressive strength test indicated a low correlation. Subsequently, the regression and correlation analysis results in both variables in seawater in a controlled area can also be observed in Figure 12b. Hence, in the former variation, the plotted values were in a consolidated arrangement in the linear trendline. On the other hand, the plotted values in the latter variation were scattered in the linear trendline.

Lastly, for concrete cubes cured in potable water stored in a normal room condition, shown in Figure 12c, the regression analysis for the variables considered had a 0.001870707 computed p -value, less than the set significant level (α). On the other hand, the computed p -value for the variation between the rebound reading versus the direct compression compressive strength test was 0.162301988, which was greater than the set significant level (α). Since both variations had contrasting results, the null hypothesis was accepted. In contrast, the alternative hypothesis was accepted for the latter variation. Hence, the correlation coefficient R^2 between the rebound reading versus the rebound hammer compressive strength test was 77.02%, which was considered a high correlation result. However, the rebound reading and the direct compression compressive strength test was 25.84%, a considerably negligible correlation.

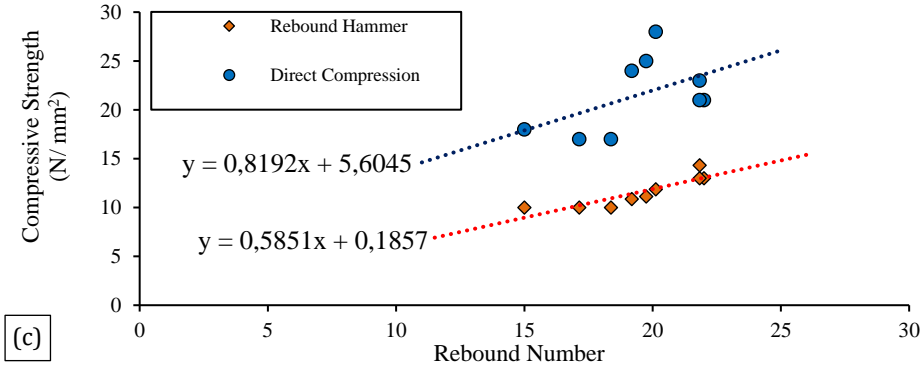
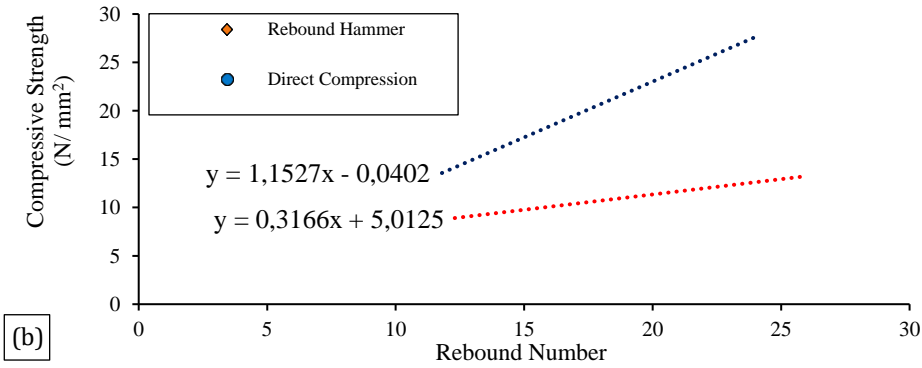
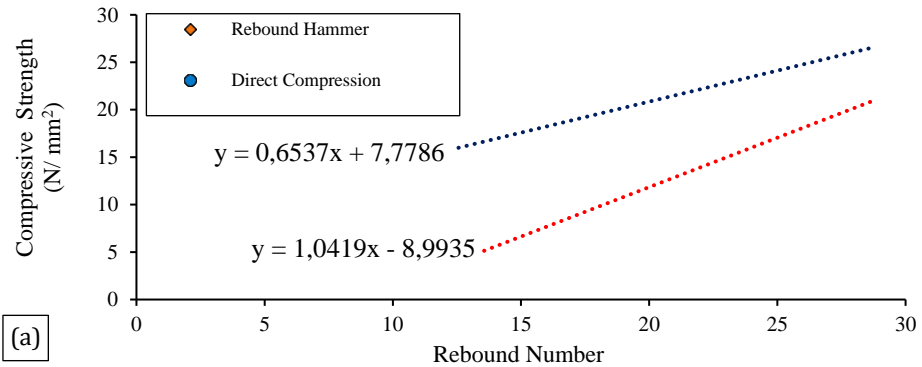


Fig. 12 Rebound correlation curve of concrete cube samples cured in: (a) seawater environment, (b) seawater in a controlled area, and (c) potable water stored in a normal room condition

The plotted values were unaligned in the linear trendline (Figure 12c) for the variation between the rebound reading versus the direct compression compressive strength test. Meanwhile, the variation between the rebound reading versus the rebound hammer compressive strength test shown in the same figure revealed that the plotted values were within the linear trendline. These indicated that the outcome of the non-destructive test using the rebound hammer in assessing all the samples was significantly far from the actual compressive strength using the correlation curve graph provided by the manufacturer. Consequently, there was a need to develop a rebound correlation model to assess the compressive strength of concrete for its reliability, either a graphical curve or an empirical equation derived from the actual compressive strength data.

Finally, this study established three (3) correlation curves for the graphical model in the rebound hammer test in concrete samples, as presented in Figure 13. The graphical model considered the rebound reading as x and the estimated compressive strength as y . The developed graphical model adopted the exponential power model of Co (2019) [8] as the rebound correlation curve graph in this work. The model increased the estimation by 7.86% in a seawater environment, 5.93% in seawater in a controlled area, and 9.15% in potable water stored in a normal room condition, respectively.

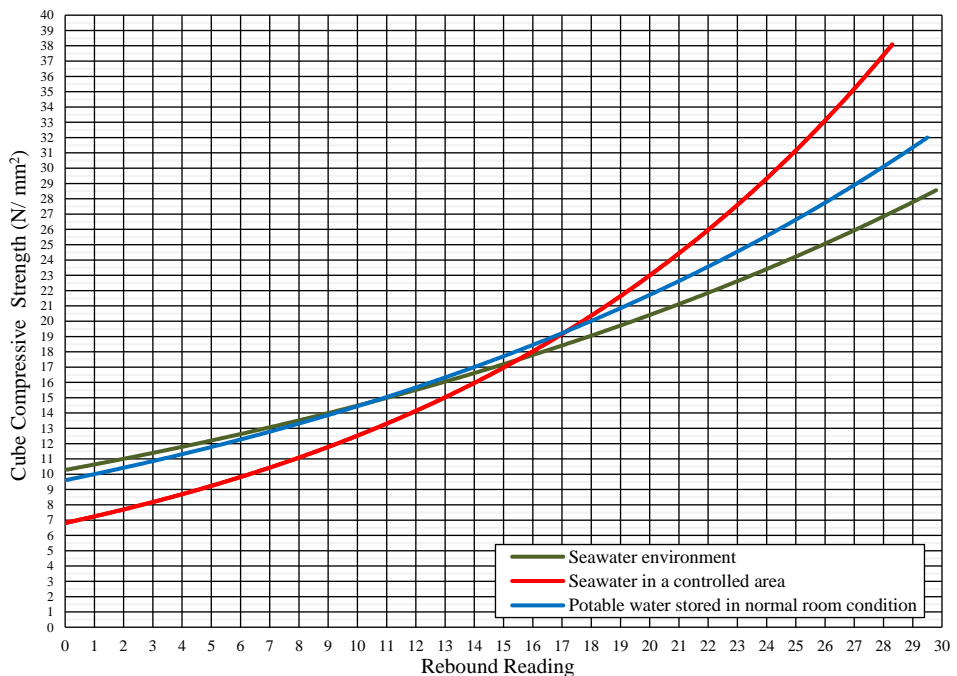


Fig. 13 Developed rebound correlation curve in three (3) environmental conditions

Aside from the graphical model, this study also established an empirical equation model for the predictor variable (rebound reading) to emerge with an outcome variable (compressive strength) when the rebound hammer test was used. The established equations can also be the basis for estimating the concrete compressive strength cured in a seawater environment (Equation 4), seawater in a controlled area (Equation 5), and

potable water stored in a normal room condition (Equation 6) for rebound hammer test, respectively.

$$Y_{(compressive\ strength)} = 10.2780e^{0.0343x_{(rebound\ reading)}} \quad (4)$$

$$Y_{(compressive\ strength)} = 6.8166e^{0.0608x_{(rebound\ reading)}} \quad (5)$$

$$Y_{(compressive\ strength)} = 9.6049e^{0.0408x_{(rebound\ reading)}} \quad (6)$$

4. Conclusions and Recommendation

The rebound correlation curve provided by the manufacturer in this study shows high dispersion in actual compressive strength results. The conventional rebound hammer device recorded low accuracy of 28.12%, 40.40%, and 25.84% in the actual concrete compressive strength estimation in three (3) environmental conditions. Therefore, the non-destructive test using the rebound hammer is inadequate to determine the actual compressive strength of concrete during the earlier days of its curing period.

The study also shows that the changes in temperature in the seawater environment, the calibration and maintenance of the rebound hammer device, less drying period of concrete samples after curing, the high water retained in the samples, and the uneven distribution of force in the plunger of the rebound hammer device to the concrete surface have greatly influenced the rebound reading which provided a high percentage error. Hence, the obtained compressive strength results were affected. It was also found that there was no carbonation development in all concrete samples in three (3) environmental conditions during their curing periods. Moreso, it was confirmed that the rebound reading was not linearly correlated with actual compressive strength results for concrete samples cured in the seawater environment and potable water stored in a normal room condition. Additionally, the rebound reading of concrete cured in seawater in a controlled area has a low correlation with the compressive strength in the direct compression test. In general, contrary to the specifications provided by the manufacturer, the rebound readings were not directly correlated with the actual compressive strength results.

Although the rebound hammer test had an inferior prediction in the actual compressive strength of concrete, still the rebound hammer device is good enough to estimate the concrete compressive strength if it is calibrated and regularly maintained to have a good condition. The study also developed rebound correlation models (graphical curve and empirical equation) as baseline references to estimate the concrete compressive strength when assessing the reinforced-concrete structure situated in seawater. The models increased the reliability estimation by 7.86%, 5.93%, and 9.15% in three (3) environmental conditions, respectively.

Acknowledgement

The corresponding author would like to thank the Faculty of the Civil Engineering Department at Ateneo de Davao University for their support. Above all, the corresponding author is grateful to Ivanne Layka, Chrisvalle Alish, and Christivanne Alish, who inspired him to do this research.

References

- [1] Bjegović D, Serdar M, Baričević A, Jelčić Rukavina M. Assessing condition of concrete pier after three decades of exposure to sea water. *Gradevinar*. 2015;67(12.):1155-64. <https://doi.org/10.14256/ICE.1188.2014>.

- [2] Melchers RE. Long-term durability of marine reinforced concrete structures. *Journal of Marine Science and Engineering*. 2020 Apr 18;8(4):290. <https://doi.org/10.3390/jmse8040290>.
- [3] Department of Public Works and Highways. Infrastructure preparation and innovation facility-output 1-roads and bridges. 2020. [Online]. Available: <https://eia.emb.gov.ph/wp-content/uploads/2020/09/IPIF1-SIDC-EIS.pdf>.
- [4] McCormac JC, Brown RH. *Design of Reinforced Concrete* (9th Edition). John Wiley & Sons, 2015.
- [5] Shang HS, Yi TH, Yang LS. Experimental study on the compressive strength of big mobility concrete with nondestructive testing method. *Advances in Materials Science and Engineering*. 2012 Oct;2012. <https://doi.org/10.1155/2012/345214>.
- [6] Sanchez K, Tarranza N. Reliability of rebound hammer test in concrete compressive strength estimation. *Int. J. Adv. Agric. Environ. Eng.* 2014;1(2):198-202. <http://dx.doi.org/10.15242/IJAAEE.C1114040>.
- [7] Brencich A, Bovolenta R, Ghiggi V, Pera D, Redaelli P. Rebound hammer test: an investigation into its reliability in applications on concrete structures. *Advances in Materials Science and Engineering*. 2020 Dec 14;2020:1-1. <https://doi.org/10.1155/2020/6450183>.
- [8] Co JRM. Assessment of the Reliability of Rebound Hammer Testing on the Estimation of Concrete Compressive Strength. BSCE thesis, Department of Civil Engineering, De La Salle University, Philippines. 2019. [Online]. Available: https://www.researchgate.net/publication/338680234_Assessment_of_the_Reliability_of_Rebound_Hammer_Testing_on_the_Estimation_of_Concrete_Compressive_Strength.
- [9] Brencich A, Cassini G, Pera D, Riotto G. Calibration and reliability of the rebound (Schmidt) hammer test. *Civil Engineering and Architecture*. 2013;1(3):66-78. <https://doi.org/10.13189/cea.2013.010303>.
- [10] Jain V, Sancheti G, Jain B. Non-destructive test analysis on concrete with rice husk ash and crushed stone additives. *Materials Today: Proceedings*. 2022 Jan 1;60:622-6. <https://doi.org/10.1016/j.matpr.2022.02.128>.
- [11] Pushpakumara BH, Fernando MS. Deterioration assessment model for splash zone of marine concrete structures. *Case Studies in Construction Materials*. 2023 Jul 1;18:e01731. <https://doi.org/10.1016/j.cscm.2022.e01731>.
- [12] Jolly MR, Prabhakar A, Sturzu B, Hollstein K, Singh R, Thomas S, Foote P, Shaw A. Review of non-destructive testing (NDT) techniques and their applicability to thick walled composites. *Procedia CIRP*. 2015 Jan 1;38:129-36. <https://doi.org/10.1016/j.procir.2015.07.043>.
- [13] Atoyebi OD, Ayanrinde OP, Oluwafemi J. Reliability comparison of schmidt rebound hammer as a non-destructive test with compressive strength tests for different concrete mix. In *Journal of Physics: Conference Series* 2019 Dec 1 (Vol. 1378, No. 3, p. 032096). IOP Publishing. <https://doi.org/10.1088/1742-6596/1378/3/032096>.
- [14] Kocáb D, Misák P, Cikrle P. Characteristic curve and its use in determining the compressive strength of concrete by the rebound hammer test. *Materials*. 2019 Aug 23;12(17):2705. <https://doi.org/10.3390/ma12172705>.
- [15] Kumavat HR, Chandak NR, Patil IT. Factors influencing the performance of rebound hammer used for non-destructive testing of concrete members: A review. *Case Studies in Construction Materials*. 2021 Jun 1;14:e00491. <https://doi.org/10.1016/j.cscm.2021.e00491>.
- [16] BS EN, 12350-2. Testing of fresh concrete, slump test. British Standards Institution, London, UK. 2019. [Online]. Available: https://kupdf.net/download/bs-en-12350-2-2009-testing-fresh-concrete-slump-test_589d516f6454a7c43cb1e8d4_pdf.
- [17] ACI Committee. Code Requirements for Environmental Engineering Concrete Structures (ACI 350-01) and Commentary (ACI 350R-01): An ACI Standard. American

- Concrete Institute. 2001. [Online]. Available: http://dl.mycivil.ir/dozanani/ACI/ACI%20350,%20Code%20Req.%20for%20Environmental%20Engineering%20Concrete%20Structures%20and%20Commentary%20-%20Hanskat%20.%20Tabat_MyCivil.ir.pdf.
- [18] World Weather. Weather in Davao in June 2022. 2022. [Online]. Available: <https://world-weather.info/forecast/philippines/davao/june-2022/>.
- [19] Google. Barangay Biao, Digos City, Davao del Sur satellite image. 2022, [Online]. Available: <https://earth.google.com>.
- [20] Lamond JF, Pielert JH. Significance of tests and properties of concrete and concrete-making materials. ASTM international, vol. 169. 2006. [Online]. Available: <http://ndl.ethernet.edu.et/bitstream/123456789/66539/1/1499.pdf>.
- [21] ASTM C. Standard test method for rebound number of hardened concrete. ASTM International West Conshohocken, Pa, USA. 2008. [Online]. Available: <https://inspectapedia.com/structure/ASTM-C805-1997.pdf>.
- [22] ACI Committee 228-Nondestructive Testing of Concrete. In-place methods to estimate concrete strength. American Concrete Institute. 2003. [Online]. Available: http://dl.mycivil.ir/dozanani/ACI/ACI%20228.1R-03%20In-Place%20Methods%20to%20Estimate%20Concrete%20Strength_MyCivil.ir.pdf.
- [23] Kolek J. Using the Schmidt rebound hammer Publication #C690227. The Aberdeen Group. 1969. [Online]. Available: <https://www.concreteconstruction.net/view-object?id=00000153-8b73-dbf3-a177-9f7b961c0000>.
- [24] Mulik N, Deo S, Dhumal K, Ghaywat V. Concrete Quality Assessment by Using Non-Destructive Test. International Research Journal of Engineering and Technology, 6: 5202-5204. 2019.
- [25] Onyeka FC. A Comparative Analysis of the Rebound Hammer and Pullout as Non-Destructive Method in Testing Concrete. European Journal of Engineering and Technology Research. 2020 May 12;5(5):554-8. DOI: <http://dx.doi.org/10.24018/ejers.2020.5.5.1903>.
- [26] Mahajan B. Rebound Hammer Test | Rebound Hammer Test Procedure | Schmidt Hammer Test Result. 2022. [Online]. Available: <https://civiconcepts.com/blog/rebound-hammer-test>.
- [27] Islam MS, Mondal BC, Islam MM. Effect of sea salts on structural concrete in a tidal environment. Australian Journal of Structural Engineering. 2010 Jan 1;10(3):237-52. <https://doi.org/10.1080/13287982.2010.11465048>.
- [28] Szilágyi K, Borosnyói A, Zsigovics I. Extensive statistical analysis of the variability of concrete rebound hardness based on a large database of 60 years experience. Construction and Building Materials. 2014 Feb 28;53:333-47. <https://doi.org/10.1016/j.conbuildmat.2013.11.113>.
- [29] Rimshin V, Truntov P. Determination of carbonation degree of existing reinforced concrete structures and their restoration. In E3S Web of Conferences 2019 (Vol. 135, p. 03015). EDP Sciences. <https://doi.org/10.1051/e3sconf/201913503015>.
- [30] Jedidi M. Evaluation of the Quality of Concrete Structures by the Rebound Hammer Method. Current Trends in Civil & Structural Engineering. 2020;5(5):1-7. <https://doi.org/10.33552/CTCSE.2020.05.000621>.
- [31] Roknuzzaman M, Hossain MB, Mostazid MI, Haque RM. Application of rebound hammer method for estimating compressive strength of bricks. Journal of Civil Engineering Research. 2017;7(3):99-104. <https://doi.org/10.5923/j.jce.20170703.02>.
- [32] Olonade KA. Influence of water-cement ratio and water reducing admixtures on the rebound number of hardened concrete. Malays. J. Civ. Eng. 2020 Nov 30;32. <https://doi.org/10.11113/mjce.v32.16219>.
- [33] Murthi P, Poongodi K, Gobinath R. Correlation between rebound hammer number and mechanical properties of steel fibre reinforced pavement quality concrete. Materials

- Today: Proceedings. 2021 Jan 1;39:142-7.
<https://doi.org/10.1016/j.matpr.2020.06.402>.
- [34] Walpole RE, Myers RH, Myers SL, Ye K. Probability & Statistics for Engineers & Scientists (9th Edition). Pearson Education, Inc. 2012.
- [35] Abd Elaty MA. Compressive strength prediction of Portland cement concrete with age using a new model. HBRC journal. 2014 Aug 1;10(2):145-55.
<https://doi.org/10.1016/j.hbrj.2013.09.005>.
- [36] Cox PA. Pharmacology, Biodiversity and. Encyclopedia of Biodiversity. 4: 523-536, 2021. <https://doi.org/10.1016/b0-12-226865-2/00221-2>.

Blank Page



Research Article

Nonlinear coupled thermal-structural analysis of precast concrete beam-to-column connections at high temperatures

Noor Azim Mohd. Radzi^a, Muhaimim Kamal^b, Shareen Azuha^c, Nur Izzatie Aqilah Mansor^d, Roszilah Hamid^e

Department of Civil Engineering, Universiti Kebangsaan Malaysia, Selangor D. E., Malaysia

Article Info

Abstract

Article history:

Received 20 Dec 2022

Accepted 18 Apr 2023

Keywords:

Finite element analysis;
Fire resistance; Beam-to-column connections;
Thermal response

This paper presents a nonlinear coupled thermal-structural analysis using ANSYS Workbench to determine precast beam-to-column connections' thermal and structural behaviour. Three precast connection models, a concrete corbel, a concrete nib, and an inverted E steel nib, are exposed to ambient and cellulose fire curves. Firstly, the precast connection models are verified based on the previous experimental result at ambient temperature. Then, the verified precast connection models are exposed to the cellulose fire curve for two hours before being loaded to failure. The results are compared with the recent experimental fire test conducted by the authors. Based on the result, finite element models at ambient temperature were validated with a percentage difference of less than 10%. However, finite element models at high temperatures were not verified due to the percentage difference exceeding 10%. The significant difference was due to the non-uniformity of sample dimensions and different test setups in the previous experiment. Finite element models for concrete corbel and inverted E steel nib have a higher stiffness than the experimental sample. However, the finite element model for concrete nib has a lower stiffness than the experimental sample. Concrete nib recorded the most significant thermal percentage deterioration (32.1 % and 57.4 %) compared to concrete corbel (22.4 % and 11.52 %) and inverted E steel nib (26.9 % and 27.9 %). The validation result of nonlinear coupled thermal-structural analysis executed using ANSYS Workbench gives good efficiency for predicting the fire performance of precast concrete corbel beam-to-column connections at high temperatures.

© 2023 MIM Research Group. All rights reserved.

1. Introduction and Objectives

Precast concrete technology is widely used around the world. The various advantages of precast concrete make it the leading choice in construction materials today. Prefabrication of concrete on structural components outside the construction site during construction will reduce the period and use of materials, thus saving costs compared to conventional construction methods (1). Precast structures contain complex precast concrete connections that contribute to the overall structure (2). Precast beam-to-column connections are one of the structural elements that are important in improving structures' behaviour. Concrete corbel and concrete nib are the most used type in precast construction. They transfer vertical loads from the beam to the columns. In addition, a new method of hybrid connection was introduced, such as an inverted E steel nib (3).

According to Eurocodes (4), fire is classified as an accidental load that must be considered in the structural design process. The connection's behaviour of precast concrete exposed to fire or high temperatures is determined by complex interactions during the heating

*Corresponding author: p100973@siswa.ukm.edu.my

^a orcid.org/0000-0003-4017-7735; ^b orcid.org/0000-0002-7389-4338, ^c orcid.org/0000-0003-1665-0393,

^d orcid.org/0000-0001-9306-4481, ^e orcid.org/0000-0002-4617-970X

DOI: <http://dx.doi.org/10.17515/resm2023.610ma1220>

Res. Eng. Struct. Mat. Vol. 9 Iss. 3 (2023) 969-987

process and depends on the composition of the mixture (5–7). When exposed to fire, the failure mode of precast concrete connection is distinguished by fire type or temperature, load system and structure. Teja (8) stated that post-fire effects on connection elements in precast structures, such as bearing, pavement, and welding, also influence moment-rotation characteristics. Fire-damaged to beam-to-column connections also reduces the rigidity of the beam structure and the integrity between the beam end and the column face, reducing the toughness of the connection. The ASTM E119 (9) and ISO 834 (10) methods provided the standard test to identify the response of structures and materials to fire. The behaviour of structural members is analysed and measured according to the period of resistance to the fire load. However, the methods focus on the individual structural members, not the structural subassembly, including beam-to-column connections. The response can only be observed and analysed in vertical structural members such as columns, walls, and dividers and transverse structural members such as beams and slabs.

Literature shows that the fire test study on the precast beam-to-column connection at high temperatures is limited compared to the study on monolithic and steel connection (11,12). An experimental study by Teja (8) on three types of precast beam-to-column connections at high temperatures only made against a temperature of 400 °C, which is too low compared to the maximum cellulose fire curve temperature (1057 °C). Radzi (13) has performed a fire test of a precast beam-to-column connection at a cellulose fire curve to overcome this gap. The test involves two types of connections commonly used in precast building construction: concrete corbel and concrete nib, and a new connection type inverted E steel nib (3). A comparison was made with the result at ambient temperature on the load-deflection and moment-rotation curves.

The use of computer software aims to simplify the calculation of complex structural analysis and can save time. Finite element simulation using computer software can perform analysis for various engineering problems. Computer software such as ABAQUS, VULCAN, ADAPTIC, DIANA, and ANSYS can be used in transient structural analysis and coupled thermal structural analysis of beam-to-column connections (14–16). Finite element simulations can confirm experimental findings, predict thermal and structural behaviour using different parameters, and improve engineering recommendations. Considerations are made based on thermal and structural constraints, thermal and structural loads, and material properties.

In this paper, a nonlinear coupled thermal-structural analysis is executed using ANSYS Workbench to determine the thermal and structural behaviour of precast beam-to-column connections (concrete corbel, concrete nib, and an inverted E steel nib) exposed to ambient and cellulose fire curve. Firstly, the finite element models are verified based on the previous experimental test result at ambient temperature (3,17,18). Since the previous experiment (3,17,18) were not made for high temperature, the comparison of the finite element simulation at high temperature was made with the experiment by Radzi (13). The study's findings are presented as load-deflection and moment-rotation curves. Finally, the thermal percentage deterioration of the connection summarised the best connection with fire resistance capability at high temperatures.

2. Description of Specimens at Ambient Temperature

This study adopted the experimental test results at ambient temperature by Abd. Rahman et al. (17) for the concrete corbel model, Mokhtar et al. (18) for the concrete nib, and Bahrami et al. (3) for the inverted E steel nib. The test setup, detail of the test specimen, material properties, and test procedure are summarised in this section. More details of this experiment can be found in the paper (3,17,18).

2.1 Concrete Corbel

The sizes of the concrete corbel components, beams and columns are shown in Fig. 1. The size of the precast beam is 160 mm x 280 mm, while the size of the precast column is 200 mm x 200 mm. Table 1 lists the concrete corbel connection's reinforcement and concrete cover details. Half-depth precast beams were installed on both sides of the corbels, followed by the installation of 2Y16 top reinforcement bars, while 2Y16 of the bottom reinforcement bars were already cast in the half beam. A second stage of concreting using wet cast-in-place concrete was carried out using simple side formwork along the beam to complete the connection between the precast beam and precast column.

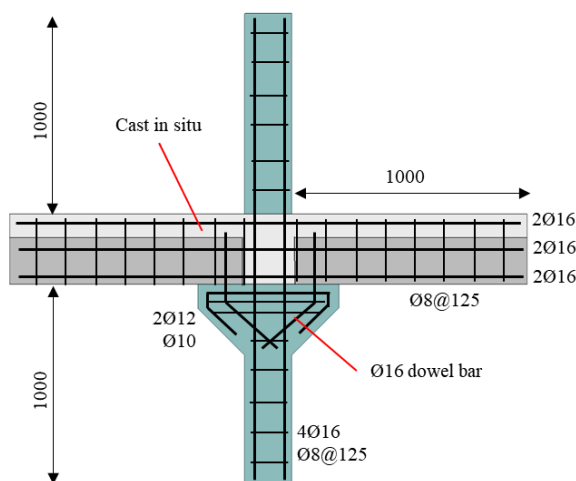


Fig. 1 Concrete corbel connection detailing (17)

Table 1. Reinforcement and concrete cover detailing (17)

Items	Descriptions
Top and bottom steel bar beam	2Y16
Stirrup beam	R8-125
Main bar column	4Y16
Stirrup column	R8-125
Dowel bar	Y16
Concrete cover of column and corbel	25mm
Concrete cover of beam	25mm

2.2 Concrete Nib

The sizes of the concrete nib components, beams and columns are shown in Fig. 2. The beam size is 300 mm x 450 mm and 1500 mm long. The column is 300 mm x 300 mm, with a total height of 3000 mm and a cross-section containing four T25 mm rebars. The tension reinforcements are fully anchored and lapped to ensure that full tensile force can be developed at this connection without slippage or failure. Flexural reinforcements were anchored inside the columns with a 90° bend. The connection used two 20 mm high-yield deformed bars as top reinforcement. The precast components' compressive strength, f_{cu} , at 28 days was 40 N/mm². The compressive strength of the infill concrete mix, f_{cui} , was designed to be 40 N/mm² in 7 days.

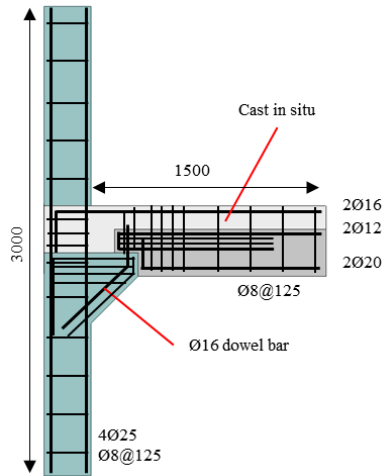


Fig. 2 Concrete nib connection detailing (18)

2.3 Inverted E Steel Nib

The sizes of the inverted E steel nib components, beams and columns are shown in Fig. 3. The beam size is 250 mm × 320 mm and 1376 mm long. The column is 250 mm × 250 mm, with a total height of 1500 mm. The precast concrete beam is placed on the embedded steel corbel in the continuous column, and the bottom threaded bars of the beam are tightened between the grooves of the corbel by two nuts and steel gaskets with a thickness of 10 mm. The space of the connection area is filled with expandable grout. After grouting, two top bars were passed through two holes in the column. Those holes are also grouted, and the connection is completed by slab concreting.

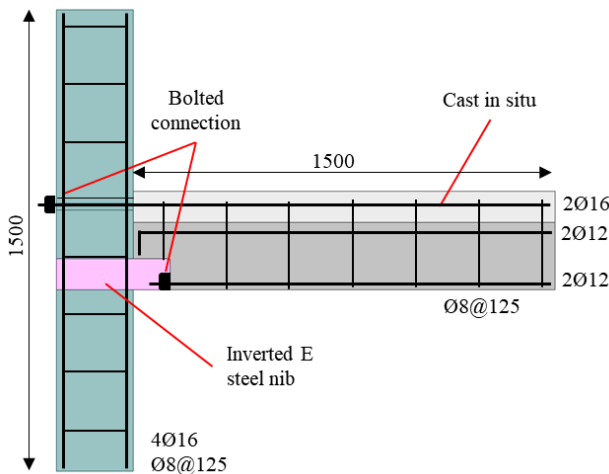


Fig. 3 Inverted E steel nib connection detailing (3)

3. Previous Study at High Temperature

Radzi (13) studied the behaviour of precast concrete beam-to-column connections subjected to standard cellulose fire exposure, as shown in Fig. 4. The behaviour of precast concrete beams to column connection specimens, namely concrete corbel, concrete nib, and inverted E steel nib, were compared with monolithic type specimens. The specimens were produced based on the IBS catalogue produced by the Public Works Department of Malaysia (JKR) and the Construction Industry Development Board of Malaysia (CIDB). The dimensions and test setup used were not uniform in this study. However, the test results by Radzi (13) can still be used as a reference for comparison purposes.

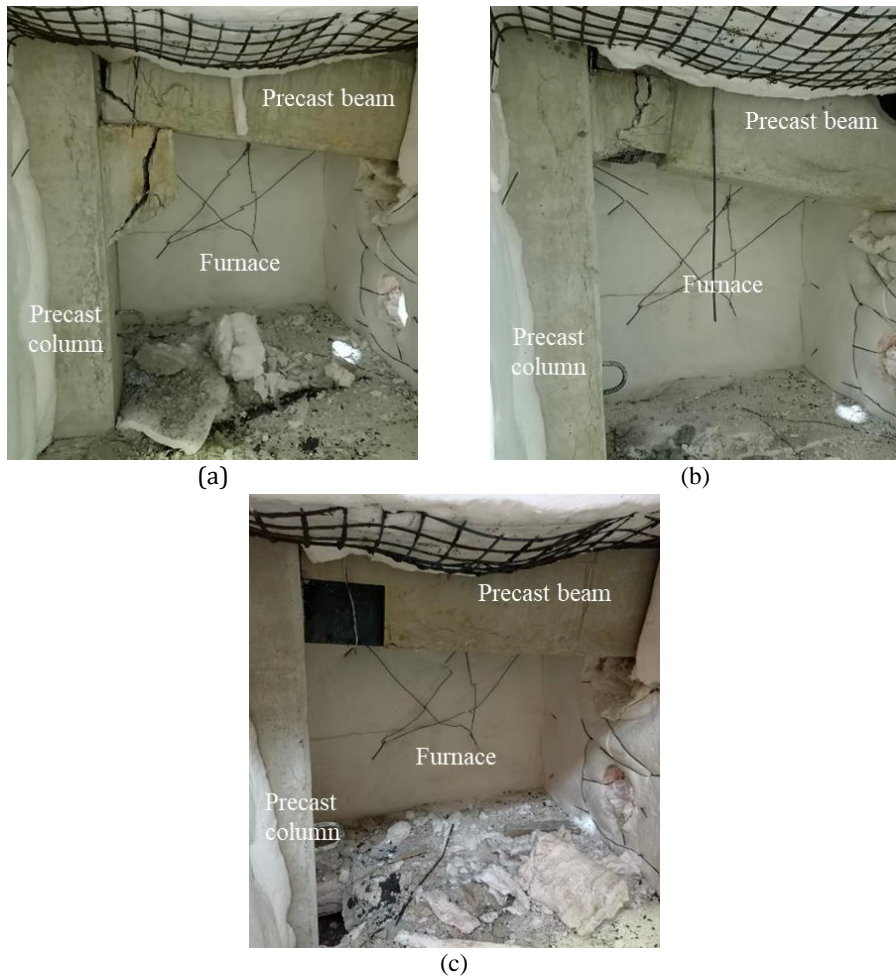


Fig. 4 Fire damaged of precast concrete beam to column connections: (a) concrete corbel, (b) concrete nib, and (c) inverted E steel nib (13).

4. Numerical Models

4.1 Finite Element Models

The details of the finite element models are given in Table 2. A total of six finite element models are provided, three for ambient temperature and three more for high temperature.

For the finite element model references, the first letter CC, CN, and EN stands for concrete corbel, concrete nib, and Inverted E steel nib, respectively, while the following letter A and HT represents the ambient and high temperature conditions. The geometric modelling was executed using additional software, SpaceClaim 2021 R2. Fig. 5 shows the geometric models produced: concrete corbel, concrete nib, and inverted E steel nib. The geometry of concrete, grout, rubber pads, and steel plates as volumes were produced by solid modelling methods. In contrast, the geometry of the steel reinforcement was produced as a line using the direct generation method. Convergence analysis subjected to an increasing static load at the end of the beam until the connection fails was done on five different mesh sizes of the beam to monolithic column connection model. The sizes were 125 mm, 100 mm, 75 mm, 50 mm, and 25 mm. The deflection values for the 50 mm and 25 mm mesh sizes show a lower gradient with a consistent deflection difference of only 0.5 mm. Because the small mesh size (25 mm) will affect the duration of the simulation solution, this thesis chooses a more appropriate and reasonable mesh size of 50 mm based on the size of the large-scale model and requires a suitable period to complete. The chosen type of mesh was linear and hexahedral in shape with six surfaces.

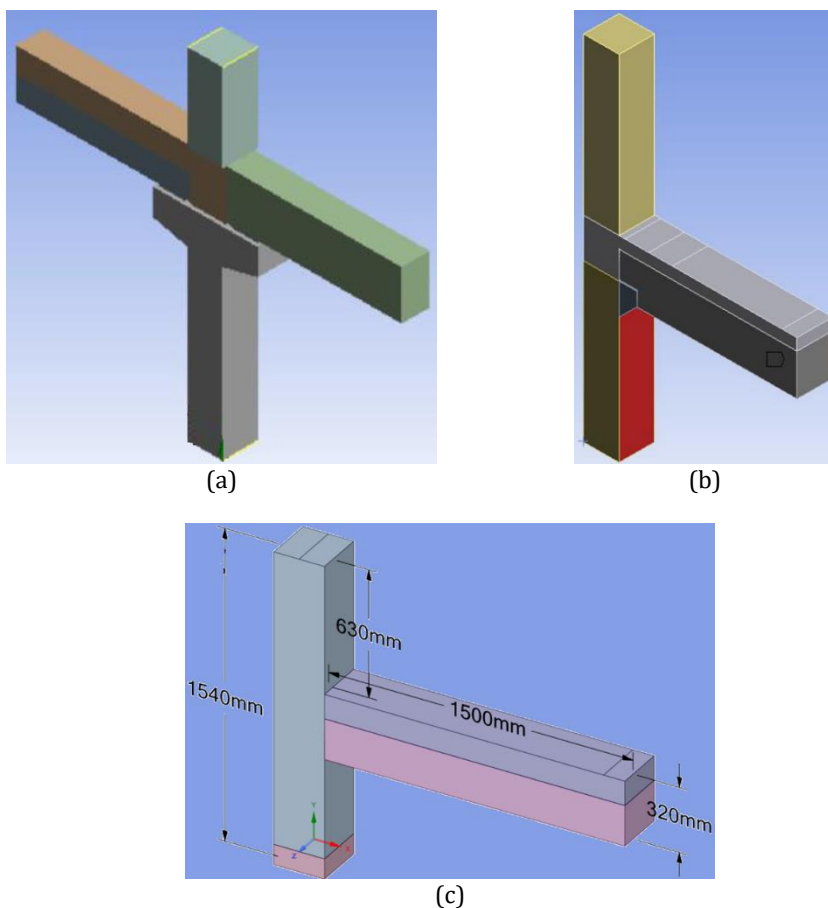


Fig. 5 Geometric modelling: (a) concrete corbel, (b) concrete nib, and (c) inverted E steel nib

Table 2. Details of finite element models at ambient temperature

Conditions	Connections	Finite Element Model References
Ambient	Concrete corbel (17)	CC-A
	Concrete nib (18)	CN-A
	Inverted E steel nib (3)	EN-A
High Temperature	Concrete corbel (17)	CC-HT
	Concrete nib (18)	CN-HT
	Inverted E steel nib (3)	EN-HT

4.2 Simulation Procedures

The nonlinear coupled thermal-structural analysis using ANSYS Workbench was performed to validate the experimental result and predict the behaviour under different parameters (19). This sequential coupling technique was chosen to connect thermal and structural analysis. The simulation procedures inside the ANSYS program are illustrated in Fig. 6. In Step 1, the transient structural analysis was executed. The material properties at ambient temperature and structural boundary conditions were assigned to the model.

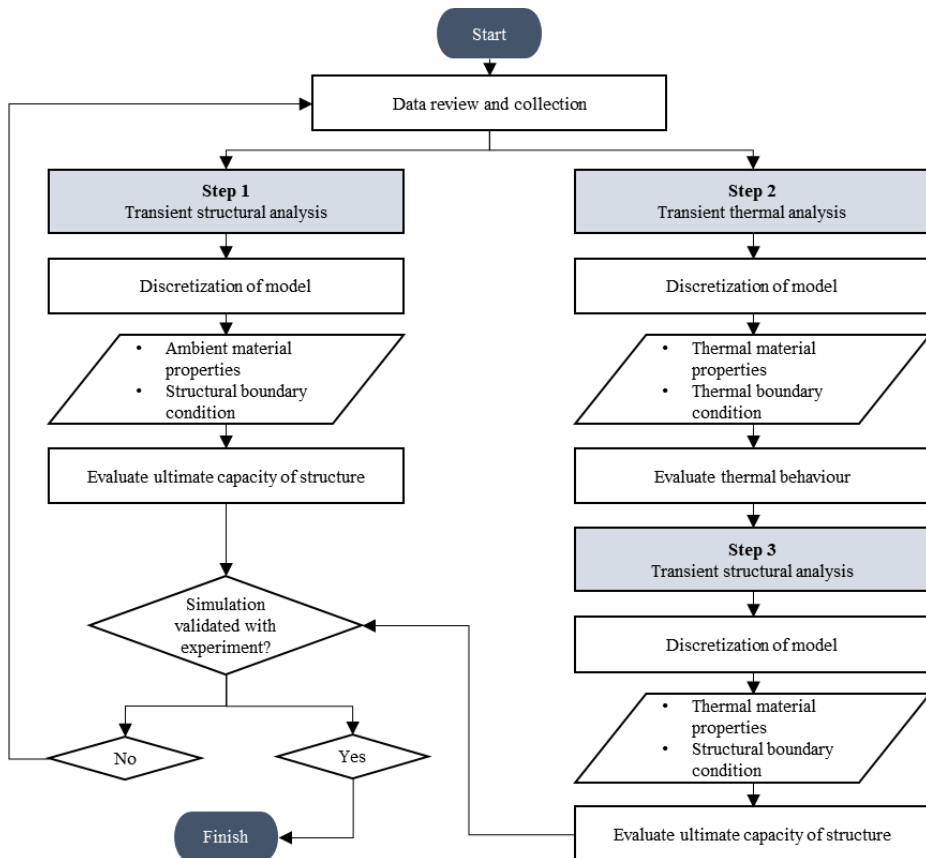


Fig. 6 Fire Finite element simulation procedures

The gradual load was applied to the end of the beam to allow for beam failure. Then, the ultimate capacity of the structure at ambient temperature was evaluated. In Steps 2 and 3, The transient thermal and structural analyses were executed. Transient thermal analysis

was performed first and followed by transient structural analysis. The temperature-dependent thermal properties and thermal boundary conditions were assigned to the model. The cellulose fire curve temperature profile was applied to the model. The temperature solution at a high temperature was evaluated. Then, the computed temperature solution was used as input data to determine the deformation and thermal stress of the structure at high temperatures.

Mesh studies are performed to determine the optimal finite element mesh, which provides a relatively accurate solution method with low calculation time. This section divides the large structure into small parts to facilitate analysis. The optimal size and short analysis period were used in this study. Trial-and-error methods for different sizes determine the optimal mesh size. In this analysis, the selected mesh size is 25 mm (for concrete nib) and 50 mm (for concrete corbel and inverted E steel nib) because it shows reasonable force convergence (Force Convergence). This value is adapted for all model components, such as concrete, reinforcement bar and stirrups. The fixed support was assigned at the top and bottom of the precast concrete column. The interface between rebar elements and concrete was assumed to be fully bonded using the discrete reinforcing method. The explosive spalling phenomena on the concrete surface during heating were neglected.

4.3 Thermal and Structural Elements

The element characteristics were described by ANSYS (20). For transient thermal analysis, SOLID278 was assigned to simulate the concrete element. SOLID278 has a 3-D thermal conduction capability. The element has eight nodes with a single degree of freedom and temperature at each node. For transient structural analysis, SOLID278 was replaced by SOLID185 to simulate the concrete element. SOLID185 was selected for or the 3-D modelling of solid structures. Eight nodes define it with three degrees of freedom at each node: translations in the directions of the nodal x, y, and z. The element has plasticity, hyper elasticity, stress stiffening, creep, large deflection, and large strain capabilities. REINF264 was assigned for the transient thermal and transient structural analysis to reinforce the elements. REINF264 has plasticity, stress stiffening, creep, large deflection, and large strain capabilities.

4.4 Materials Properties

Table 3 lists the properties of the material used in ANSYS. The thermal and mechanical material properties assigned in the simulation were according to Eurocode (4) and previous studies (21,22).

Table 3. Materials properties

Properties	Concrete	Steel
Density (Kg mm^{-3})	2.3×10^{-6}	7.8×10^{-7}
Young's modulus (MPa)	35000	2×10^5
Poisson ratio	0.2	0.3
Bulk modulus	19444	1.63×10^5
Shear modulus (MPa)	14583	77160
Coefficient of thermal expansion (C^{-1})	1.48×10^{-5}	1.6×10^{-5}
Thermal conductivity ($\text{W mm}^{-1} \text{C}^{-1}$)	0.002	0.054
Specific heat ($\text{mJ Kg}^{-1} \text{C}^{-1}$)	9×10^5	4.8×10^5

The isotropic thermal conductivity and specific heat constant pressure vary with temperature. The density, isotropic elasticity (Young's modulus and Poisson's ratio),

multilinear isotropic hardening of concrete (plastic stress-strain), and bilinear isotropic hardening of reinforcement (yield strength-tangent modulus) are varied with respect to temperature.

4.5 Process of Data Analysis

The results obtained from the experimental and simulation were load-deflection and moment-rotation curves. For the simulation result using ANSYS, the load-deflection curves were directly obtained from a combined force and total deformation appeared in the graph and tabular data, as shown in Fig. 7 (a). For the experiment, the load-deflection curves were generated based on the applied load and the vertical directional deformation data at the end of the beam, as shown in Fig. 7 (b).

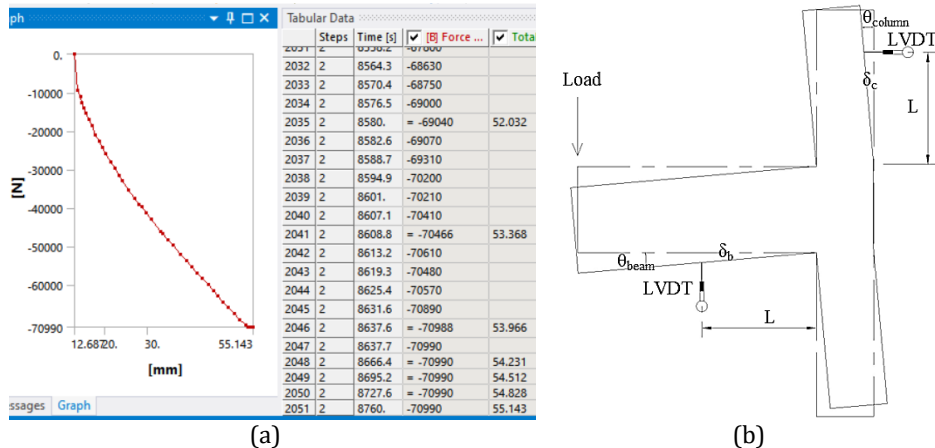


Fig. 7 Load-deflection of connections: (a) results from ANSYS and (b) experimental relationship between deflection, δ and rotation, θ

From the load result, the moment (M) was calculated according to equation (1).

$$M = (F \times d) + \left(SW_b \times \frac{d}{2} \right) \tag{1}$$

where F is the applied force (in kN), d is the distance from the fixed axis (in mm), and SW_b is the selfweight of the beam (in kN). The rotation (θ) was calculated based on the difference between the rotation in the beam (θ_{beam}) and the rotation in the column (θ_{column}) according to equation (2).

$$\theta = \left\{ \left[\tan^{-1} \frac{b}{d} \right] - \left[\tan^{-1} \frac{a}{c} \right] \right\} 100\pi/18 \tag{2}$$

where a is the deflection in the column (in mm), b is the deflection in the beam (in mm), c is the distance of the LVDT to the center of rotation of the column (in mm), and d is the distance of the LVDT to the center of rotation of the beam (in mm).

5. Results and Discussions

5.1 Concrete Corbel

5.1.1 Ambient Temperature

For model validation, Fig. 8 compares the load-deflection curves of model CC-A and the experiment by Abd. Rahman et al. (17) at ambient temperature. It is observed that the curves showed a good agreement between them. The deflection for the experiment was

45.7 mm with a maximum load of 62.4 kN. The deflection for model CC-A was 47.6 mm with a maximum load of 67 kN. The percentage difference for deflection and load was 4 % and 6.8 %, which validated the finite element model. Fig. 9 shows the moment–rotation curves of model CC-A and the experiment by Abd. Rahman (17) at ambient temperature. At the beginning of loading, there was a difference in the load value between the two curves. Model CC-A had a higher stiffness compared to the experiment. At load 67 kN, the curves showed a good agreement between them. The percentage difference for moment and rotation was 9.2 % and 7.7 %, respectively.

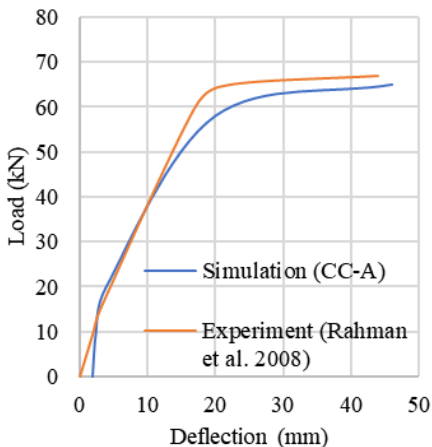


Fig. 8 Load – deflection curves of model CC-A and experiment (17) at ambient temperature

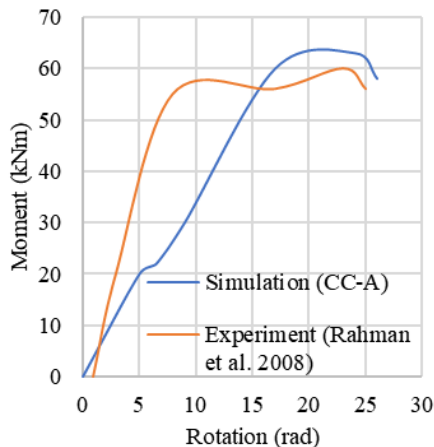


Fig. 9 Moment – rotation curves of model CC-A and experiment (17) at ambient temperature

5.1.2 High Temperature

For model validation, Fig. 10 shows the load-deflection curves of model CC-HT and the experiment by Radzi (13) at high temperatures. It is observed that there was a difference in the load value of 10 kN between the two curves. This is due to the non-uniformity of sample dimensions and different test setups in the study by Radzi (2023) (13), which was not considered in the simulation. A constant load of 10 kN was applied to the sample during the experiment. Table 4 compares the load–deflection ratio between the model CC-HT and the experiment by Radzi (13). The load–deflection ratio showed a good agreement between them, with a slight difference of 6.1%.

Table 4. Load – deflection ratio between CC-HT and experiment [9] at high temperature

Items	CC-HT [A]	Experiment (13) [B]	Differences [B] – [A]	Percentage Difference (%)
Load (kN)	52.39	60	7.61	12.68
Deflection (mm)	52.43	64.66	12.23	18.91

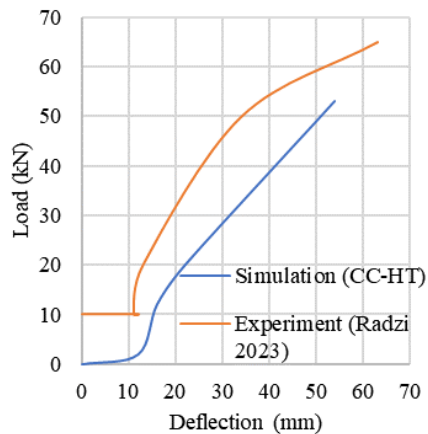
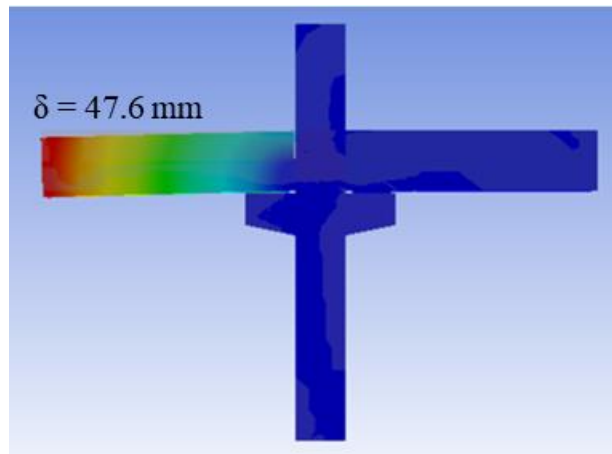


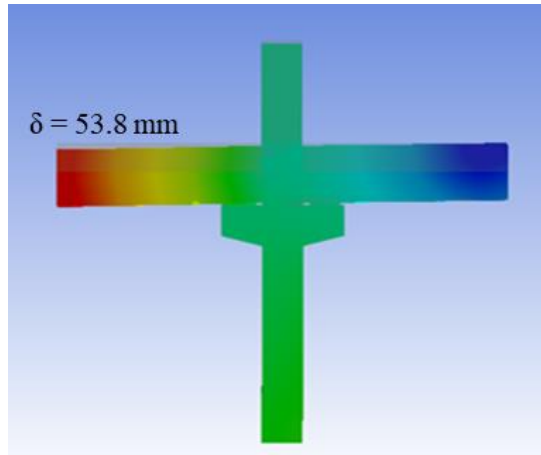
Fig. 10 Load – deflection curves of model CC-HT and experiment [9] at high temperature

5.1.3 Comparison of Ambient and High Temperature

Fig. 11 illustrates the deflection of model CC-A at ambient temperature and model CC-HT at high temperature. The comparison between these two results is important to determine the effect of the term on the model after being loaded at high temperature. The maximum deflection for model CC-A was 47.6 mm, with a maximum load of 67 kN. The maximum deflection for model CC-HT was 53.8 mm, with a maximum load of 52 kN. Observation showed that CC-A was performing better than CC-HT. Even though the deflection at ambient temperature is high, the maximum load is lower compared to the high temperature. Model CC-A had a higher stiffness compared to the CC-HT. The thermal percentage deterioration of load and displacement is 22.4 % and 11.52 %, respectively.



(a)



(b)

Fig. 11 Deflection of connection: (a) Model CC-A and (b) Model CC-HT

5.2 Concrete Nib

5.2.1 Ambient Temperature

For model validation, Fig. 12 and Fig. 13 show the deflection of model CN-A and load-deflection curves of model CN-A and the experimental test by Mokhtar et al. (18) at ambient temperature, respectively. It is observed that the curves showed a good agreement between them. In the experimental test, the deflection recorded was 8.33 mm with a maximum load of 60 kN. The deflection recorded in the simulation was 9 mm with a maximum load of 60 kN. The percentage difference for deflection was 7.8%, which validated the finite element model. Fig. 14 shows the moment-rotation curves of model CN-A and the experiment by Mokhtar et al. (18) at ambient temperature. It is observed that the curves showed a good agreement between them. The experiment specimen had a higher stiffness compared to the model CN-A. The percentage difference for rotation was 8.9%.

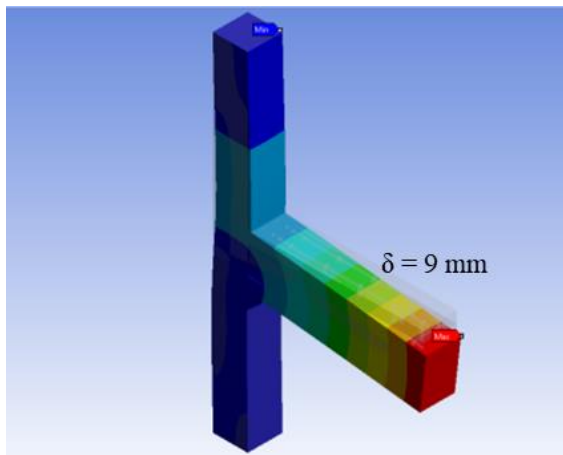


Fig. 12 Deflection of connection for model CN-A

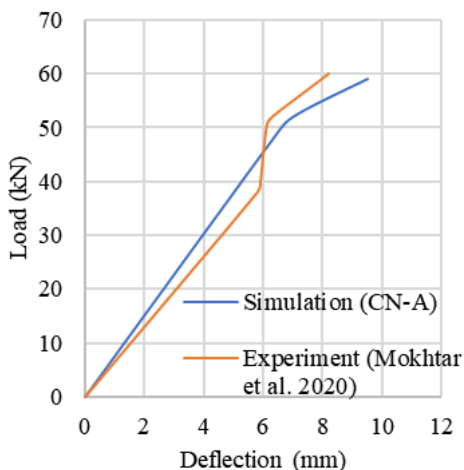


Fig. 13 Load - deflection curves of model CN-A and experiment [12] at ambient temperature

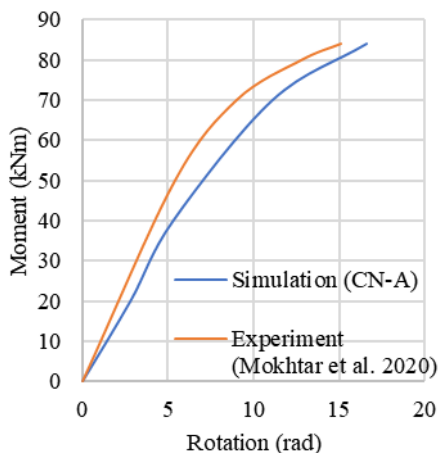


Fig. 14 Moment - rotation curves of model CN-A and experiment [12] at ambient temperature

5.2.2 High temperature

For model validation, Fig. 15 shows the load-deflection curves of model CN-HT and the experiment by Radzi (13) at high temperatures. Table 5 compares the load-deflection ratio between the model CN-HT and the experiment by Radzi (13). The load-deflection ratio showed a difference of 29.3%. This significant difference was due to the non-uniformity of sample dimensions and different test setups in the study by Radzi (2023) (13). The load in the simulation was a lateral applied at the column. The load in the experiment was vertical and applied to the beam.

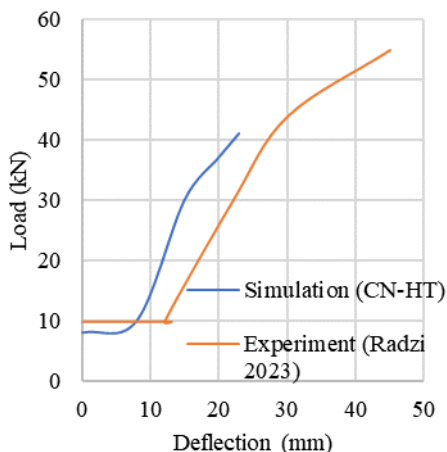


Fig. 15 Load - deflection curves of model CN-HT and experiment [9] at high temperature

Table 5. Load – deflection curves of model CN-HT and experiment (13) at high temperature

Items	CN-HT [A]	Experiment (13) [B]	Differences [B] – [A]	Percentage Difference (%)
Load (kN)	40.70	56.47	15.77	27.9
Deflection (mm)	22.93	45.26	22.33	49.34

5.2.3 Comparison of Ambient and High Temperature

Fig. 16 shows the load-deflection curves of models CN-A and CN-HT. The maximum deflection for model CN-A was 9.76 mm with a maximum load of 60 kN. The maximum deflection for model CN-HT was 22.93 mm with a maximum load of 40.7 kN. Observation showed that CN-A was performing better than CN-HT. The thermal percentage deterioration of load and displacement is 32.1 % and 57.4 %, respectively.

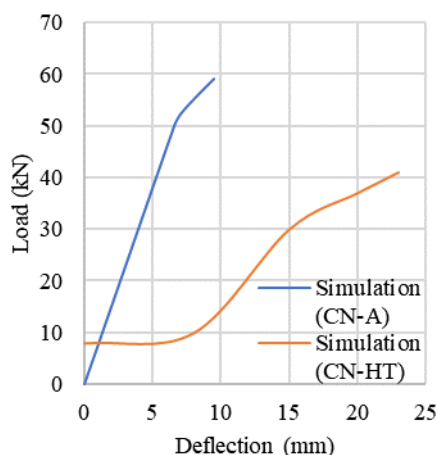


Fig. 16 Load – deflection curves of model CN-A and CN-HT

5.3 Inverted E Steel Nib

5.3.1 Ambient Temperature

For model validation, Fig. 17 and Fig. 18 show the deflection of model EN-A and load-deflection curves of model EN-A and the experimental test by Bahrami et al. (3) at ambient temperature, respectively. It is observed that the curves showed a good agreement between them. In the experimental test, the deflection recorded was 43 mm with a maximum load of 130 kN. The deflection recorded in the simulation was 39 mm with a maximum load of 130 kN. The percentage difference for deflection was 9.3 %, which validated the finite element model. Fig. 19 shows model EN-A's moment–rotation curves and the experiment by Bahrami et al. (3) at ambient temperature. It is observed that the curves showed a good agreement between them. Model EN-A had a higher stiffness compared to the experiment. The percentage difference for rotation was 8.5%.

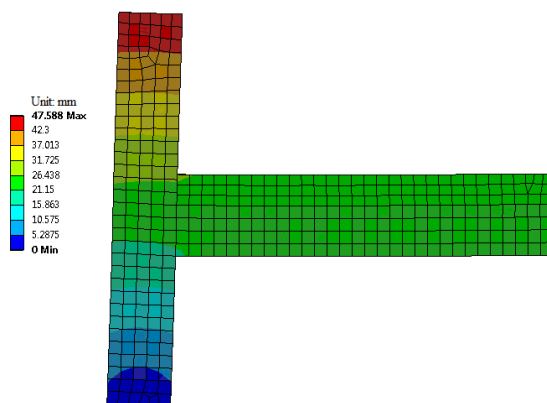


Fig. 17 Deflection of model EN-A

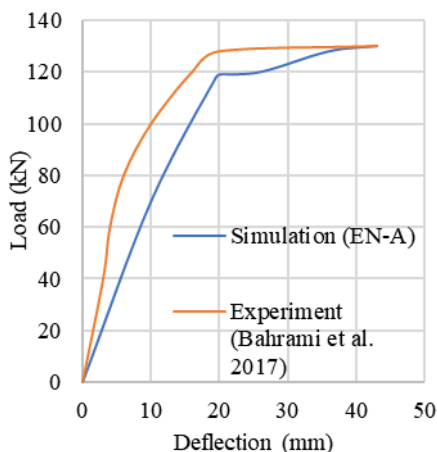


Fig. 18 Load – deflection curves of model EN-A and experiment [3] at ambient temperature

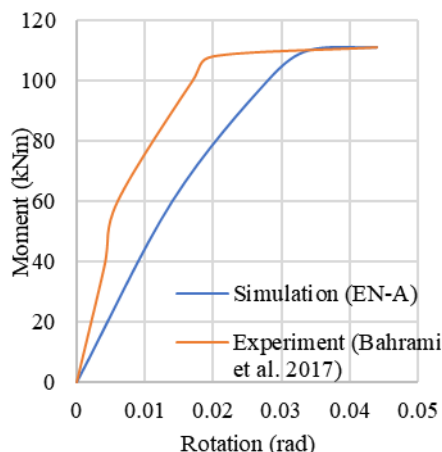


Fig. 19 Moment - rotation curves of model EN-A and experiment [3] at ambient temperature

5.3.2 High temperature

For model validation, Fig. 20 shows the load-deflection curves of model EN-HT and the experiment by Radzi (13) at high temperatures. Table 6 compares the load–deflection ratio between the model CN-HT and the experiment by Radzi (13). The load–deflection ratio showed a difference of 24.2%. This significance was due to the non-uniformity of sample dimensions and different test setups in the study by Radzi (2023) (13). The load in the simulation was a lateral applied at the column. The load in the experiment was a vertically applied beam.

Table 6. Load – deflection curves of model CN-HT and experiment (13) at high temperature

Items	EN-HT [A]	Experiment (13) [B]	Differences [B] – [A]	Percentage Difference (%)
Load (kN)	92	63	29	31.52
Deflection (mm)	60.1	54.3	5.8	9.7

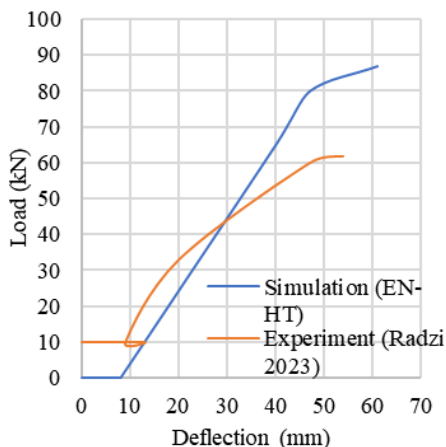


Fig. 20 Load – deflection curves of model EN-HT and experiment [9] at high temperature

5.3.3 Comparison of Ambient and High Temperature

Fig. 21 shows the load-deflection curves of models EN-A and EN-HT. The maximum deflection for model EN-A was 43.04 mm with a maximum load of 130 kN. The maximum deflection for model CN-HT was 59.51 mm with a maximum load of 94.68 kN. Observation showed that CN-A was performing better than CN-HT. The thermal percentage deterioration of load and displacement is 26.9 % and 27.9 %, respectively.

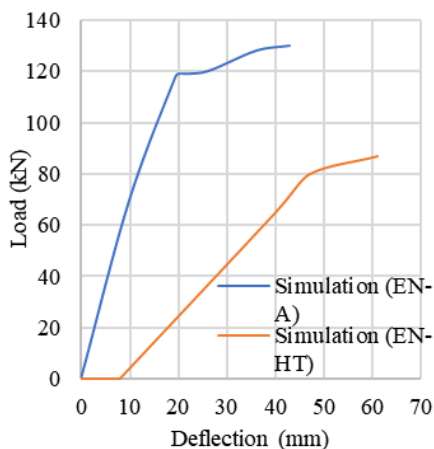


Fig. 21 Load – deflection curves of model EN-A and EN-HT

6. Results Comparison

Table 7 lists the validation of finite element models based on the previous experiment at ambient temperature (3,17,18) and high temperature (13). The percentage difference for finite element models at ambient temperature was less than 10 %, which validated the finite element model. However, the percentage difference for finite element models at high temperatures exceeded 10 %, which were not validated the finite element model. This significant difference was due to the non-uniformity of sample dimensions and different

test setups in the study by Radzi (2023) (13). The load in the simulation was a lateral applied at the column. The load in the experiment was vertically applied to the beam.

Table 7. Validation of finite element models

Connections	Validation with Previous Experiment	
	Ambient [3], [11], [12]	High Temperature [9]
Concrete corbel	√	×
Concrete nib	√	×
Inverted E steel nib	√	×

√ = Validated, percentage difference less than 10%

× = Not validated, percentage difference more than 10%

Table 8 lists the comparison of thermal percentage deterioration based on load and deflection values at high temperatures compared to ambient temperatures. Concrete nib recorded the most significant thermal percentage deterioration (32.1 % and 57.4 %) compared to concrete corbel (22.4 % and 11.52 %) and inverted E steel nib (26.9 % and 27.9 %). The concrete corbel and inverted E steel nib models had an additional strength factor by the vertical dowel reinforcement and the stiffness of the E steel component compared to the concrete nib.

Table 8. Thermal percentage deterioration of finite element models

Connections	Thermal Percentage Deterioration (%)	
	Load	Deflection
Concrete corbel	22.4	11.52
Concrete nib	32.1	57.4
Inverted E steel nib	26.9	27.9

7. Conclusions

Based on the results of nonlinear coupled thermal-structural analysis using ANSYS Workbench on three precast connection models presented in this paper, the following conclusions can be drawn on the nonlinear coupled thermal-structural analysis of precast concrete beam-to-column connections:

- Finite element models CC-A, CN-A, and EN-A at ambient temperature were validated with a less than 10% percentage difference. However, finite element models CC-HT, CN-HT, and EN-HT at high temperatures were not verified due to the percentage difference exceeding 10 % due to the non-uniformity of sample dimensions and different test setups between the simulation and the experimental study by Radzi (2023) (13).
- At ambient temperatures, the finite element models CC-A dan EN-A have a higher stiffness than the experimental sample. However, the CN-A finite element model has a lower stiffness than the experimental sample.
- At high temperatures, the concrete nib recorded the most significant thermal percentage deterioration (32.1 % and 57.4 %) compared to concrete corbel (22.4 % and 11.52 %) and inverted E steel nib (26.9 % and 27.9 %). The concrete corbel and inverted E steel nib models had an additional strength factor by the vertical dowel reinforcement and the stiffness of the E steel component compared to the concrete nib.
- The post-fire effects on connection elements in precast structures such as bearing pads, grouting, and welding influenced the thermal percentage deterioration.

Fire-damaged to beam-to-column connections reduce the rigidity of the beam structure and the integrity between the beam end and the column connection.

- The validation result of nonlinear coupled thermal-structural analysis executed using ANSYS Workbench gives good efficiency for predicting the fire performance of precast concrete corbel beam-to-column connections at high temperatures.

Conflicts of Interest

The authors declare that they have no known conflict of financial interests or personal relationships that could have appeared to influence the work reported in this paper. This work was supported by the Universiti Kebangsaan Malaysia Research University Grant (grant no. GUP-2018-027).

References

- [1] Hollý I, Harvan I. Connections in precast concrete elements. *Key Eng Mater.* 2016;691:376-87. <https://doi.org/10.4028/www.scientific.net/KEM.691.376>
- [2] Fatema T. Study on Connection Between Precast Concrete Beam and Cast-in-Situ Column in Prefabricated Building Frames. *J Eng Appl Sci.* 2006;1(1):33-8.
- [3] Bahrami S, Madhkhani M, Shirmohammadi F, Nazemi N. Behavior of two new moment resisting precast beam to column connections subjected to lateral loading. *Eng Struct [Internet].* 2017;132:808-21. <https://doi.org/10.1016/j.engstruct.2016.11.060>
- [4] European Committee For Standardization. Eurocode 2: Design of concrete structures - Part 1-2: General rules - Structural fire design. Vol. 1. 2011.
- [5] Eid F, Heiza K, Elmahroky M. Behavior and Analysis of Reinforced Self-Compacted Concrete Beam Column Connection Subjected to Fire. *Am J Sci Eng Technol.* 2017;
- [6] Kien DD, Trinh D Van, Toan KT, Danh LB. Fire Resistance Evaluation of Reinforced Concrete Structures. *Proc 2020 5th Int Conf Green Technol Sustain Dev GTSD 2020.* 2020;588-92. <https://doi.org/10.1109/GTSD50082.2020.9303102>
- [7] Yakudima AG et al. Impact of Fire on Steel Reinforcement In Reinforced Concrete Structures. 2015;5(10):46.
- [8] Teja CS, Moturu TS, Yaswanth Kumar G, Khan HA, Kumar GY, Khan HA. Effect of Fire on Prefabricated Concrete Beam Column Connections. *Int J Recent Technol Eng.* 2019;8(2):1433-6. <https://doi.org/10.35940/ijrte.B2092.078219>
- [9] ASTM. ASTM E119-07: Standard methods of fire test of building construction and materials. ASTM - Am Soc Test Mater. 2007;1-21.
- [10] ISO. Fire-resistance tests - Elements of building construction - Part 2: Requirements and recommendations for measuring furnace exposure on test samples. ISO 834-2. Geneva; 1999.
- [11] Mao CJ, Chiou YJ, Hsiao PA, Ho MC. Fire response of steel semi-rigid beam-column moment connections. *J Constr Steel Res.* 2009; <https://doi.org/10.1016/j.jcsr.2008.12.009>
- [12] Mahale HD, Kandekar SB. Behaviour of steel structure under the effect of fire loading. *Int J Eng Res Appl* www.ijera.com [Internet]. 2016;6(5):42-6. Available from: www.ijera.com
- [13] Radzi NAM. Kelakuan Terma dan Struktur Sambungan Rasuk ke Tiang Konkrit Pratuang Luaran Pada Suhu Tinggi. Ph.D Thesis. Ph.D Thesis, Universiti Kebangsaan Malaysia; 2023.
- [14] Radzi NAM, Hamid R, Mutalib AA, Kaish ABMA. A Review of Precast Concrete Beam-to-Column Connections Subjected to Severe Fire Conditions. *Adv Civ Eng [Internet].* 2020;2020:1-23. <https://doi.org/10.1155/2020/8831120>

- [15] Radzi NAM, Hamid R, Mutalib AA, Kaish ABMA. A Review of the Structural Fire Performance Testing Methods for Beam-to-Column Connections. *Adv Civ Eng.* 2021;2021:1-36. <https://doi.org/10.1155/2021/5432746>
- [16] Dzolev I, Cvetkovska M, Ladjinovic D, Radonjanin V, Raseta A. Fire Analysis of a Simply Supported Reinforced Concrete Beam Using Ansys Workbench. 2016;(September).
- [17] Rahman ABA, Ghazali AR, Abd. Hamid Z. Comparative study of monolithic and precast concrete beam-to-column connections. *Malaysian Constr Res J.* 2008;2(1):42-55.
- [18] Mokhtar R, Ibrahim Z, Jumaat MZ, Hamid ZA, Hazim A, Rahim A. Behaviour of Semi-rigid Precast Beam-to-column Connection Determined Using Static and Reversible Load Tests. *Measurement* [Internet]. 2020;108007. <https://doi.org/10.1016/j.measurement.2020.108007>
- [19] Radzi NAM, Muniandy S, Ismasafie FS, Hamid R. Nonlinear Coupled Thermal-Structural Analysis of Monolithic and Precast Concrete Corbel Beam-to-Column Connection. In: *Proceedings of The 17th East Asian-Pacific Conference on Structural Engineering and Construction*, 2022. Springer; 2023. p. 581-196. https://doi.org/10.1007/978-981-19-7331-4_47
- [20] ANSYS Inc. *Mechanical APDL Element Reference*. Vol. 15317. 2010. 1-1416 p.
- [21] Tjitradi D, Eliatun E, Taufik S. 3D ANSYS Numerical Modeling of Reinforced Concrete Beam Behavior under Different Collapsed Mechanisms. *Int J Mech Appl* [Internet]. 2017;7(1):14-23. Available from: <http://journal.sapub.org/mechanics>
- [22] Elshorbagy M, Abdel-Mooty M. The coupled thermal-structural response of RC beams during fire events based on nonlinear numerical simulation. *Eng Fail Anal.* 2020. <https://doi.org/10.1016/j.engfailanal.2019.104297>

Blank Page



Review Article

Approaches considering non-linearity in soil-foundation-interaction: A State of the Art Review

Vishal Kumar Mourya^{*1a}, Gaurav Pandey^{1b}, Dharendra Patel^{1c}, Rajesh Kumar^d

¹Department of Civil Engineering, IIT (BHU) Varanasi, India

Article Info

Abstract

Article history:

Received 17 Jan 2023

Accepted 09 May 2023

Keywords:

*Continuum Modelling;
Beam-on-nonlinear
Winkler Foundation
model;
Macro Modelling;
Centrifuge Experiment;
1-g Test*

Seismic excitation causes the soil to begin acting nonlinearly at higher strain. Hence, the nonlinearity of the soil, foundation, and structure should be appropriately considered. This can be achieved by proper modelling of soil-structure-foundation interaction (SSI). The continuum, Winkler-based, and Macroelement models are the major modelling techniques for considering SSI. The continuum method involves determining absorbing boundaries, the size of the soil domain, soil element size, constitutive soil model, and soil structure interface. In contrast, the Winkler-based model uses nonlinear spring and dashpot to represent inelastic behaviour and energy dissipation properties of soil, respectively. Macroelement replaces the entire soil foundation arrangement with one element at the bottom of the superstructure. The trade-off between the advantageous effects of the SSI model, particularly in terms of energy dissipation, and its unfavourable effects, such as settling or tilting, should also be optimised during the analysis and design phases. The present paper aims to provide a concise review and comparative analysis of the several methodologies proposed by the researchers that consider the nonlinearity in soil-foundation-structure interaction (SSI). The importance of the study lies in the adoption of an approach that reduces computational effort and time. Moreover, the experimental works are also reviewed with regard to the soil structure interaction. It can be inferred from the current study that various approaches have some benefits and drawbacks; thus, these approaches can opt accordingly.

© 2023 MIM Research Group. All rights reserved.

1. Introduction

Soil structure interaction (SSI) is considered a multidisciplinary field that combines soil and structural dynamics, earthquake engineering, geomechanics and geophysics, material science, and various other technical fields. Following the successful result of SSI, many theories, methodologies and experimental settings are employed to continue the study of SSI. Several analytical methods, numerical methods, analytical-numerical techniques, experiments, and prototype observation paved the roadways for SSI analysis after technology advancement.

Nonlinearity in the superstructure, foundation, and soil can be geometric nonlinearity, material nonlinearity, or both. Consideration of the nonlinearity of soil-structure-foundation is crucial for better accuracy of results simulating the actual behaviour of the entire system. Nonlinearity comes into the scenario due to various reasons, including (a) deformation in the seismic force-resisting element of the superstructure, (b) foundation structural element yielding, (c) gapping between foundation base and soil (e.g., base

*Corresponding author: vishalkmourya.rs.civ18@itbhu.ac.in

^a orcid.org/0009-0009-4348-9911; ^b orcid.org/0009-0008-3750-3097; ^c orcid.org/0009-0004-1633-2437;

^d orcid.org/0000-0001-5145-588X

DOI: <http://dx.doi.org/10.17515/resm2023.646me0117>

uplift), (d) soil yielding, which can get amplified by pore-pressure-induced strength loss. Modelling nonlinearity has become easy with the advancement in computation techniques suggested by researchers.

Typically, structural components are modelled as skeletal, but soil can be either modelled as a skeletal spring or a continuum. Early research into SSI analysis, often known as the "Winkler Model," began in the 1860s. Following this, different soil idealisation types were examined using two-parameter and three-parameter models that solely consider the elasticity of the soil [1]. The majority of Winkler's nonlinear model is also covered in the subsequent sections. With the introduction of FEM in the 1960s, the concept of modelling soil as a continuum emerged. This led to the development of numerous constitutive relations for modelling soil as linear or nonlinear elastic and elastoplastic. Popular constitutive relations include, for instance, Linear Elastic Model, Mohr-Coulomb Model, Hyperbolic Model, Strain Hardening Model, etc. [2]. The concept of incorporating an interface element between two distinct materials was first proposed in the 1970s. The interface makes it possible to simulate how the structure and soil move in relation to one another [3]. Macroelement concept was introduced in foundation engineering, which allows taking into account the coupling phenomena involved in SSI while avoiding the complexity and the numerical cost of nonlinear finite element dynamic analysis. It is equipped with a nonlinear "constitutive law" (defined by the mean of the relationship between forces and displacements) formulated in accord with the theory of plasticity or hypo-plasticity and making it possible to model the dynamic couplings (linear and nonlinear) in several directions between the superstructure, the soil and the foundation [5]. The primary contribution of this novel technique is to consider all such nonlinearities and the coupling between different degrees of freedom.

Summarising concepts discussed in the above paragraph, classification of SSI analysis with nonlinear soil and foundation behaviour can be done majorly in three ways: (1) continuum models, (2) beam-on-nonlinear Winkler foundation models, and (3) Microelement modelling. This study reviewed previous methods adopted to model nonlinearity in SSI analysis. The study also discusses various advantages, disadvantages and applicability of the abovementioned techniques.

Many experiments were performed to verify the result obtained from the analysis methods discussed in the previous section. Shake table and centrifuge tests are the major experiments performed, but a few full-scale models have been conducted in recent days. A concise review of some experimental setups relevant to numerical technique is also presented herein.

2. Modelling Approaches

2.1. Continuum Approach

Continuum modelling of the soil gives its precise and meticulous behavioural response for an SSI problem. The idea of the elastic continuum comes from using Boussinesq's theory for estimating static stresses. This well-known theory assumes the soil domain to be semi-infinite (soil boundary extended infinity in one direction), homogeneous, isotropic, linear elastic solid. Development in the continuum approach enabled the complete and thorough modelling of the semi-infinite soil domain using finite elements. Other assumptions of such theories are realised in the continuum approach, as shown in Fig. 1. Different continuum methods proposed by many researchers are presented hereafter.

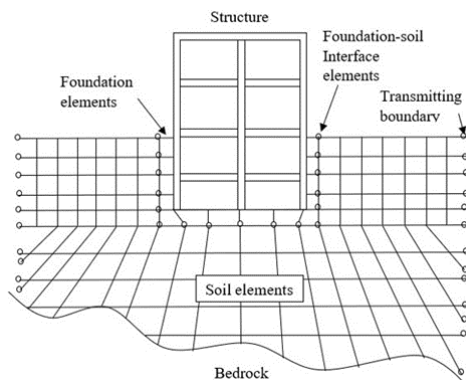


Fig. 1 Schematic illustration of SSI using continuum modelling by FEM (NIST, 2012)

2.1.1 Finite Element Method

FEM is known to be an efficient and multifaceted technique for performing numerical analyses because its applicability is extensive and can be applied to many classes of problems. Also, it can deal with real and complex tasks. To address the SSI problem, FEM considers specific parameters that are discussed below.

a. Absorbing Boundaries

The soil domain should be large enough to deal with the problem of radiation damping generated due to wave propagation within semi-infinite space, which increases a substantial amount of time and internal memory for complete FE analysis. To find an optimal solution (i.e., to reduce computation time and scale of soil domain), wave-absorbing boundaries can be adopted. All boundaries are generally classified into elementary, local and consistent (global) boundaries, which are briefly discussed below.

Elementary boundaries are typically employed in static analyses. Since this boundary is unable to simulate the wave energy radiation toward the infinite soil domain, it is more practical in situations where the wave energy radiation has little impact, such as the interface between soft and hardened soils. A few examples of elementary boundary conditions are Free field, fixed boundaries, and tie boundary conditions. In the soil-pile interaction analysis of a pile embedded in a deep multi-layered soil under seismic excitation, Peiris et al. [6] made successful implementation of elementary boundary conditions.

The viscous boundary produces the absorbing effect by employing a viscous damper or dashpot attached to the boundary element. It gives better results when the boundary is positioned at a suitable distance from the region of interest [7]. Absorbing boundary conditions for the dashpot system can be computed using Eq (1) and represented schematically, as shown in Fig. 2.

$$\begin{aligned} \sigma &= a\rho v_p w \\ \tau &= b\rho v_s u \end{aligned} \tag{1}$$

where σ and τ are the normal and shear stress, ρ is unit mass, v_p and v_s are the primary wave and secondary wave velocities at the boundary, w and u are the normal and tangential velocities, a and b are the dimensionless parameters.

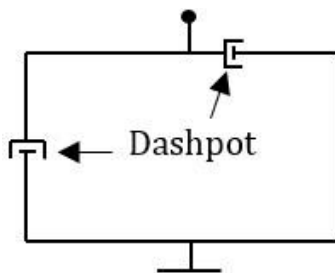


Fig. 2 Viscous boundary element

Another such boundary is the unified boundary proposed [8], which is quite similar to the viscous boundary [7]; the difference arises in the value of the dimensionless parameter, which varies with the value of Poisson's ratio of soil. The viscous boundaries were found most appropriate to apply in time domain analysis among the numerous absorbing boundaries [9].

Another idea to overcome finite boundary difficulties was the infinite element [10]. The formulation of the infinite element is the same as that of finite elements; addition is the domain mapping. This element doesn't require any other boundary condition (BC) to simulate zero displacements at infinity which is an added advantage over other BC. In the case of SSI analysis, frequency-based dynamic infinite elements were used to describe the far-field response of a 2D layered half-space. Nonlinear analysis was not possible because the formulation was frequency-based [11].

Kelvin elements [12] work more effectively than viscous dampers, provided their constants are properly calculated. While using the Kelvin element, the required mesh size of the soil element also gets reduced. The predominant frequency of loading governs the stiffness and damping constant values in the Kelvin model, and the stiffness value can be calculated using Eq (2). Kelvin element can be represented as shown in Fig. 3.

$$k_r = \frac{G}{r_0} [S_{u1}(a_0, \nu, D) + iS_{u2}(a_0, \nu, D)] \tag{2}$$

where k_r refers to the complex stiffness, r_0 refers to the distance in a plan between the foundation's centre and the node to which a Kelvin element is coupled, G refers to the modulus of rigidity of the soil, S_{u1} and S_{u2} are the dimensionless quantities obtained from closed-form solutions, a_0 ($= \frac{r_0 \omega}{v_s}$, where ω is the excitation frequency and v_s is the shear wave velocity of the soil medium) is the dimensionless frequency, i is the imaginary unit, ν is the Poisson's ratio, and D is the damping ratio of the material.

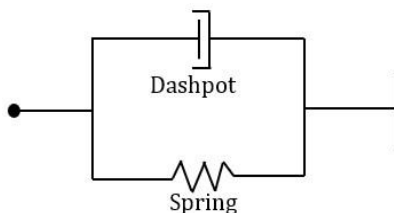


Fig. 3 Diagram representing Kelvin element

An advanced plasticity-based constitutive soil model and hierarchical single surface (HiSS), employed with the Kelvin element to perform the dynamic analysis of soil-pile interaction of single pile and pile groups. It was found that the suggested model performs satisfactorily with the Kelvin element [13].

A viscous spring artificial boundary (VSAB) condition was developed by modifying the spring constant and damping coefficient in the spring-dashpot system and using it to solve the dynamic excitation problem [14]. The values of the constants are calculated from Eq (3).

$$\begin{aligned} k_1 &= k_2 = \lambda_t \frac{G}{R} A \\ c_1 &= c_2 = \rho v_s A \\ k_3 &= \lambda_n \frac{G}{R} A \\ c_3 &= \rho v_p A \end{aligned} \quad (3)$$

where c_1 , c_2 and c_3 are the damper and k_1 , k_2 and k_3 are spring constants in x, y and z directions, respectively, v_p and v_s are primary wave and secondary wave velocities, G is the modulus of rigidity of soil, ρ denotes mass density, R represents the distance between the load point and the soil boundary, A is the total area contributing from surrounding nodes, λ_n and λ_t represents the constant in normal and tangential directions of the boundary in modified form.

The wave radiation issue in an infinite soil domain can be addressed by coupling the finite and infinite elements at their junction [15]. The dynamic SSI problem of the semi-infinite soil domain was examined using the finite elements in conjunction with 2D and 3D infinite elements in ABAQUS [16]. Domain Reduction Method (DRM) combined with Perfectly-Matched-Layers (PMLs) using ABAQUS to absorb outgoing waves perfectly [17].

b. Domain of Soil Model

To determine the sufficiency of the range in the horizontal direction of the soil domain, two criteria were taken into consideration: (a) a shear soil column formed of the identical material under linear elastic undamped conditions should have an outcome as close as viable to that of a soil column away from the boundary, and (b) the nonlinear vertical soil reaction should be modest in contrast to the horizontal response at any point in the realm of computation [18]. The horizontal distance of soil lateral boundaries must be at least five times more than the width of the structure, usually up to 60 m. Since the greatest amplification of wave generally occurs up to the depth of 30 m of the soil profile, recommended depth of bedrock can be up to 30 m while performing numerical analysis [19].

c. Size of Soil Element

The accuracy and reliability of SSI analysis results may get altered due to the size (Δx) of the element and the time-step (Δt) size used to model soil. Proper wave propagation is not guaranteed when the elements assumed to discretise the soil are of inappropriate size. The size of the elements should not be more than $\left(\frac{1}{8}\right)^{th}$ of the minimum wavelength (λ_{min}) or maximum frequency (f_{max}) of the seismic wave radiation travelling through the soil domain [20] and can be evaluated as per Eq. (4). This condition assures that even the shortest wavelength can easily propagate through the soil medium. To ensure

stability and accuracy while performing the numerical analysis for time-step (Δt) size, Eq. (5) can be used [21].

$$\Delta x = \frac{\lambda_{min}}{8} = \frac{v_s}{8f_{max}} \tag{4}$$

$$\Delta t = \frac{\Delta x}{v_p} \tag{5}$$

where v_p and v_s are longitudinal and shear wave velocities, respectively.

d. Soil Constitutive Model

The constitutive soil model consists of mathematical equations representing the nonlinearity of soil using a single element which can be further used in numerical computations to represent the relationship between stress and strain of a particular type of soil. Some of the constitutive models are discussed in Table 1.

Table 1. Different constitutive soil model

Type of Model	Model	References	Attributes
Elastic	Hooke's Law	[22]	It represents the linear elastic behaviour of soil but doesn't hold well for the elastoplastic behaviour of soil.
	Hyperbolic	[23]	Calculating the tangential modulus at any point of stress during loading can represent nonlinear elasticity, but because hardening behaviour is ignored during unloading, it cannot be applied.
Simple Elastic Plastic	Mohr-Coulomb	[24]	It is used where strength is dominating criterion, hexagonal failure cone is used to represent the real failure pattern. After achieving the maximum strength, it fails to incorporate the softening effect.
	Drucker-Prager	[25]	It is the same as Mohr-Coulomb but uses a simple cone to represent the failure pattern. The strength parameter shows valid representation but stiffness nonlinearity is not considered.

Critical State	Modified Cam Clay	[26]	It describes the strength, dilatancy and critical state of the soil and also represents loading and unloading effectively since the nonlinearity is modelled by hardening plasticity. It may allow for unrealistically high shear stresses.
	Elastic-viscoplastic	[27]	It is developed to describe the rate-sensitive behaviour of normally consolidated clay, and viscoplastic strain is used as a hardening parameter.
Single Yield Surface	Single Hardening	[28]	It is developed for frictional materials based on elasticity and plasticity. Elastic behaviour is represented by Hooke's law, while plastic behaviour is by failure criterion, yield criterion and non-associated flow rule.
Double Hardening	PLAXIS Hardening	[29]	Friction hardening and cap hardening are used in this model to simulate plastic shear under deviatoric loading and volumetric plastic strain under primary compression, respectively. Excludes both creep and anisotropic stiffness strength.

e. Soil Structure Interface

Another critical parameter that needs to be taken into account is interface modelling. Modelling of interfaces helps to understand the phenomenon of slip, bonding & rebonding between soil and structure. The most common interface elements are two-node elements, continuum elements comprising finer meshing, zero thickness, and thin-layer elements (Fig.4). Dashpot elements and node-to-node spring elements are examples of two-node elements. Interface behaviour may be represented for certain scenarios by refining a conventional finite element mesh adjacent to the interface and imparting appropriate characteristics [30]. Viladkar et al. [31] pointed out that one of the primary drawbacks of the methodology proposed by [30] is its inability to properly mimic the failure or slip plane when two types of materials are sandwiched. A widely employed interface element obtained from Goodman's hypothesis relates to the stresses and relative displacement of nodes. It is known as a zero-thickness element since it is a four-node element with no thickness. On the other hand, zero-thickness elements have drawbacks, such as being prone to inaccuracies in normal stress and deformation calculations [32]. In finite element analyses, zero-thickness interfaces are better for modelling solid-on-solid contact [33]. Another option is to think of the soil-structure contact as a thin layer or continuum. It was proposed to overcome the mentioned difficulties of zero-thickness elements. Thin-layer elements are preferable to zero-

thickness elements because both field and simple shear tests reveal the presence of a transition zone alongside the interface of two stiff bodies [34]. A simple shear test can be used to measure the thickness of the thin-layer interface [35]. Formulation of an isoparametric interface is applied between soil and footing base to assess the behaviour of shallow foundations when subjected to eccentrically inclined load [36].

FEM necessitates the usage of distinct transmitting boundaries or infinite elements, which might result in inaccuracies. Despite the addition of transmitting boundaries, the whole structure-soil model is still huge. Analysis using FEM needs a significant amount of time and internal memory compared to other continuum approaches, which limits its application in certain problems. Moreover, a detailed review of modelling SSI systems using FEM is available [37].

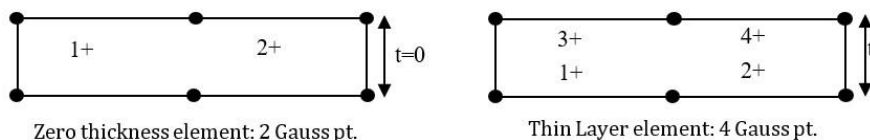


Fig. 4. Interface element

2.1.2 Boundary Element Method

The boundary element method (BEM), another numerical approach in progress to FEM, is more favourable than FEM since it simply needs a surface (or boundary) discretisation, which helps to meet the radiation condition without the requirement of complex non-reflecting boundaries.

The indirect BEM produced fairly accurate findings among the several BEM formulations (the weighted residual formulation, the direct and indirect BEM) [38]. Boundary integral problem approach applicability broadened from isolated foundations to numerous rigid foundations of various shapes and sizes laid on an elastic or viscoelastic half-space, applied with the seismic waves along with other possible external stresses. It is observed that the discretisation of the foundation had a considerable impact on the computed impedance functions in the case of relatively minor separations [39-40]. It also found that numerical outcomes documented by some authors [41-42] in the scenario of diminishing a small gap between the foundations contain an error. The time-domain BEM, combined with the Stokes fundamental solutions, was used to solve a 3D structural system composed of a large rigid square footing lying on isotropic, homogeneous and linear elastic half-space [43].

Furthermore, some investigations have been done on the interaction of nearby rigid foundations on a multi-layer viscoelastic soil media. A 3D frequency-domain-based BEM framework is used in aggregation with infinite space fundamental solutions and the successive stiffness technique to simulate a soil medium of several layers [44-46]. A boundary element technique of the substructure deletion approach is available for seismic evaluation of the dynamic soil-structure interaction among numerous embedded foundations [47-49]. In the frequency domain BEM, an impedance function is developed on and below the foundation surface [50]. The difficulty of applying BEM in the event of heterogeneous media is one of its drawbacks. Similarly, the benefit will be lost if BEM is used to solve a nonlinear issue.

2.1.3 Finite Element - Boundary Element Method

BEM, in conjunction with FEM employed to solve the differential equations of several SSI cases; one such example is the transient analysis of dynamic soil-structure interaction (DSSI) administered to SH motion [51]. Coupled boundary element with finite element method used for three-dimensional soil foundation interaction where boundary elements represent the soil medium. The condition of equilibrium and continuity along the soil and structure interface was used to ensure the continuity of both elements [52]. Finite element-boundary elements coupling models are used to study the dynamic interaction between three-dimensional mass lumped and distributed structures applied to harmonic excitation constructed on square foundations embedded in soil media [53]. The attributes of seismic response of a nuclear power plant composed of a reactor, control and a turbine building examined that was shaken by an artificially induced motion using 3D BEM and 2D FEM [54]. BEM was also used in conjunction with FEM to analyse the DSSI of coupled shear walls [55] and adjacent piled buildings [56]. Finite Element - Boundary Element - Infinite Element - Infinite Boundary Element technique devised to account for various SSI effects. The approach was shown to be capable of earthquake-resistant design and evaluation of structures, mainly of nuclear power plants based on multi-layered soil deposits. The whole structure was dealt with in the frequency domain. Also, the combined model reduces the computational effort by representing the nonlinearity of the near-field soil in an equivalent linear fashion [57].

BEM, on the other hand, isn't well adapted to inhomogeneous or anisotropic media. As a result, researchers intended to develop a technique that included the benefits of both the Finite element and Boundary element methods. In the outcome, the Scaled Boundary Finite Element Method (SB-FEM) is a semi-analytical technique that came into existence [58]. DSSIA-3D software improved by adding a novel approach in which the concept of SBFEM was used to model unbounded soil and the FEM employed in the modelling structure [59]. An alternate method [60] for the computational homogenisation of heterogeneous structures is presented using the idea of the Scaled Boundary Finite Element Method (SBFEM).

Besides the aforementioned methods, the Domain Reduction Method (DRM) came into existence, wherein the whole domain was separated into two sub-domains, (a) one for simulating earthquake origin and propagation path effect, removing localised features and (b) the other for modelling local site effects. The size of the domain considered for analysis was also significantly reduced [61]. Evaluation using DRM resulted in a 50% reduction in computing time compared to traditional absorption boundaries with viscous dashpot systems [62].

2.2 Winkler-based approaches

To describe the general behaviour of the soil-structure interface, Winkler-based techniques may only make use of one-dimensional spring elements or one-dimensional spring elements in addition to two-dimensional or three-dimensional soil components. The Winkler spring technique is desirable in design due to its simplicity and little computational effort. Since it is a spring-based model, its mechanical aspect can be easily calibrated. These characteristics of the Winkler-based approach signify its advantage over the continuum approach.

Initiating with the revolutionary effort of McClelland and Focht [63], Beam-on-Nonlinear Winkler foundation (BNWF) models have been carry forwarded for several decades for analysing the behaviour of foundations mostly for piles subjected to static loads case [64] and then taken forwarded to the application of subjected dynamic loads [65-66]. Multiple

executions of the dynamic p-y technique were attempted, and it found that the characteristics of the nonlinear springs and dashpots can affect computations [67]. Dynamic nonlinear response output of offshore pile assessed in a both qualitative and quantitative manner [68]. Issue of complete interaction among the whole soil-pile raft-superstructure arrangement addressed in the study bearing in mind the change in design forces of various components in the structure, which were left out in previous studies [69]. The Nonlinear Winkler model for the composite caisson-piles foundation is by joining the caisson and the pile group. The nonlinear four-spring Winkler model is used for the caisson, and the axial-lateral coupled vibration equations are deduced for the pile group [70].

The methodology adopted for the pile foundation proposed above is taken further to the shallow foundation. Some of the early efforts to use a model based on the Winkler approach for capturing the rocking response of shallow footing are discussed hereafter. With the use of elastic-perfectly-plastic springs and coulomb slider elements, an analytical framework was created to predict the moment-rotation behaviour of rigid foundations. Coulomb slider elements manage to capture the uplift of the foundation, whereas elastic-plastic springs are believed to respond to compression only [71-72]. A model was developed based on two methods: (i) a two-spring model and (ii) a distributed Winkler spring model. The author developed three mechanisms to consider nonlinearity at the foundation interface: (i) viscous dampers, (ii) elastic-perfectly plastic springs, and (iii) an impact mechanism permitting energy dissipation at impact [73]. An analytical framework is presented to evaluate the rocking response of a single-degree-of-freedom system while considering the foundation uplift, along with an expression to estimate the base shear of a flexible structure allowed to uplift. The framework considers individual springs as linear elastic [74]. At the base of a shearwall structure, Nakaki and Hart [75] utilised separately and individually positioned vertical elastic springs along with viscous dampers. The property of the Winkler spring used in this study has zero tension capacity and elastic compression resistance. A nonlinear stiffness degrading hysteretic model was used to model the inelastic shearwall structure. The Winkler-type finite element model reflects the nonlinear behaviour of shallow strip footing subjected to lateral cyclic loading. This model uses the nonlinear spring backbone curve calibrated against the pile. The main limitation of the model was the calibration done mostly with moment-dominated strip footings [76]. The study [77] includes a foundation uplift in performance-based design as in continuation of the prior study. To capture the cyclic response of shallow foundations, Allotey and Naggar used a Winkler-based modelling approach in which linear backbone curves were adopted from the earlier work performed by the author. According to their findings, the model can anticipate the moment-rotation and settlement reaction fairly well. On the other hand, the model cannot accurately reflect the sliding response, which could be due to the absence of coupling amongst the various forms of deformation [78-79].

The BNWF model incorporated in OpenSees comprises elastic beam-column elements simulating structure-foundation behaviour and independent zero-length soil elements simulating soil-foundation behaviour, as shown in Fig. 5. The developed model is only suitable for two-dimensional analysis, and it has also been discovered that the model underpredicts sliding response [80]. An investigation [81] assessed the influence of SSI effects on the seismic performances of 2D moment-resisting reinforced concrete frames by means of FEM and BNWF. The finding suggests adopting the FEM model in the case of a four-story 2D structure can reduce seismic demand by up to 50% for maximum inter-story drift ratio and up to 20% for maximum base shear when compared to a fixed-base model.

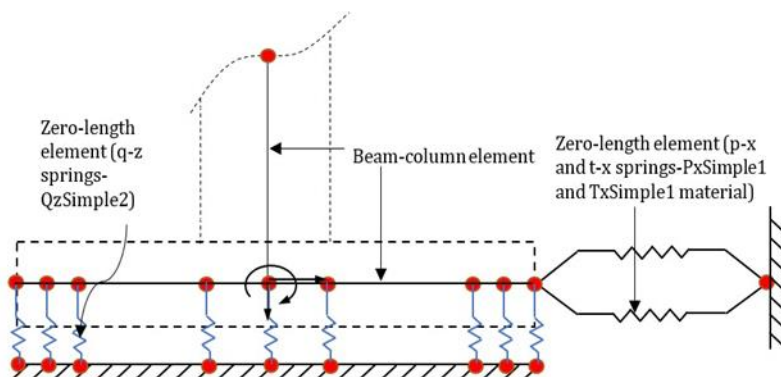


Fig. 5 Schematic diagram of a Beam-on-Nonlinear Winkler Foundation [80]

In contrast, modelling by adopting the BNWF model can change the seismic demand only if the structure has a longer time period (eight-story 2D frame) constructed on very soft soils. Although, the reductions compared to a fixed-base model (up to 20% for maximum base shear and maximum inter-story drift ratio) are less than what a full FEM model would have given as an outcome, as shown in Fig. 6. The fixed-base assumption overestimates the design of the shear wall element while underestimating the design of the coupled moment frame [82]. The influence of nonlinear SSI on the seismic response of acceleration-sensitive non-structural components of a four-story steel moment-resisting frame is investigated. The results suggest that nonlinear SSI positively impacts the performance of the non-structural components of the structure [83].

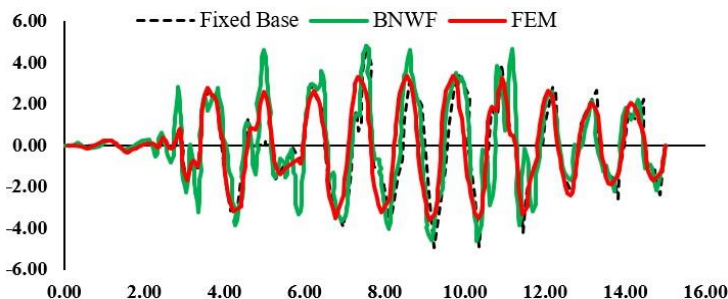


Fig. 6 Acceleration of top storey of 4-storey building

Study [84] aimed to examine the impact of SSI on the seismic outcome and susceptibility of RC structures. Authors [85] reviewed several soil-foundation-interaction models focusing on raft foundations.

2.3 Macro Modelling

Since the finite element approach contains computational complexity and requires a thorough understanding of the concept, specifically to deal with the numerical intricacy pertaining to the soil-foundation-structure behaviour during severe earthquakes, it is barely an alternative for this purpose. Another discussed a simpler technique, the beam-on-nonlinear-Winkler-foundation (BNWF) family is easy to perform. However, it is

pointed out that the BNWF model cannot suitably take care of the coupling between its different degrees of freedom [86-87].

The nonlinear macro element (NLME) concept, which involves replacing the complete soil foundation arrangement with one element at the base of the superstructure, has garnered increasing attention in recent years. In this approach, the foundation and the soil arrangement are treated as a macro element, and a 3 DOF (in case of 2D) or 6 DOF (in case of 3D) model is developed to describe the vertical and horizontal force-displacement, moment-rotation behaviour of a point at the centre of footing. The coupling between the different DOFs of macroelement represents the key improvement over the BNWF technique.

The concept of nonlinear macro-element (NLME) was first put forward to estimate settlement and rotation for strip footings placed on the sand under the joint action of eccentric and inclined loading. Here, isotropic-hardening elastoplastic law allows the coupling of displacement and rotations [4]. Furthermore, several NLMEs-based models have been proposed for various types of loading, foundation geometry, and soil type. For example, a bounding surface plasticity concept was added to the previous model and expanded to cyclic loading [88]. Macro-element frameworks [89] were used to investigate nonlinear dynamic soil-structure interaction (DSSI) subjected to seismic excitation, utilising an elastic-perfectly plastic concept of the model described in the earlier study [4]. A coupled plasticity-uplift model was adopted to incorporate footing uplift into the macro-element formulation. The proposed model was limited to strip footings placed on cohesive soils subjected to seismic loads [90-91]. A stiffness degradation model was introduced to consider lowering the soil-footing contact area to capture minor detail of the observed rocking response [92]. A coupling factor in the soil-foundation stiffness matrix helps to include the uplift in the nonlinear microelement plasticity model of the initial phase [93]. Grange S et al. [94] extended the work of Cremer et al. [5] to 3D circular footing and incorporated uplift with the plasticity model framework.

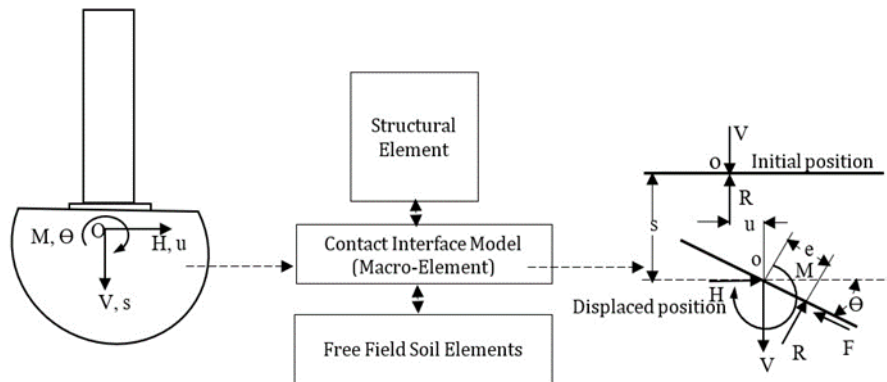


Fig. 7 Macro-element contact interface model [97]

A macro-element model has been developed using the theory of hypoplasticity for modelling shallow foundations on sands. The projected approach uses a simpler mathematical framework, allowing easy application in existing structural analysis FE codes [95]. The numerical implementation of the 6-dof hypoplastic microelement is proposed in the form of the Finite Element code incorporated in Abaqus [96]. The contact interface model (as shown in Fig. 7) proposed [97] to track the progress of the soil-

footing contact area. The critical contact area ratio (A/A_c) is defined as the ratio of the footing area (A) to the required footing contact area for vertical and shear loads (A_c). Six model input variables, mainly user-defined and the contact interface model, are required to capture the fundamental properties of shallow foundations under coupled cyclic loading, such as load capacities, energy dissipation, stiffness deterioration, and deformations.

Chatzigogos CT et al. [98] presented bounding surface plasticity in combination with the uplift formulation suggested by [89]. Further, Figini R et al. carry forwarded the previous research on dense sand [99]. A macro-element was proposed [100] for a single pile in cohesive soil exposed to the lateral earthquake force imposed at the head of the pile. The method relies on a nonlinear elastic constitutive model integrated with a boundary plasticity model. It represents the elastic behaviour under small displacement using the elastic linear impedances suggested by Gazetas [101] and incorporated in EC8 [102].

A macro-element presented [103] for a single vertical pile in sand devised within hypo-plasticity theory inspired by macro-element formulation for the shallow foundation of Salciarini et al. [95]. Generalised load and displacement vectors are used to characterise the behaviour of the pile are shown below:

$$t = \{V, H, M\}^T \tag{6}$$

$$u = \{w, u, \theta\}^T \tag{7}$$

Also, the below-recommended matrix can be used to calculate the elastic stiffness matrix regulating the elastic response of the microelement:

$$\kappa^e = \begin{bmatrix} k_v & 0 & 0 \\ 0 & \alpha k_{hh} & \alpha^{2/3} k_{hm} \\ 0 & \alpha^{2/3} k_{hm} & \alpha^{1/3} k_{mm} \end{bmatrix} \tag{8}$$

Where α is the dynamic interaction factor and k_v , k_{hh} , k_{mm} and k_{hm} represents the vertical, horizontal, rotational and combined horizontal-rotational elastic stiffness at the head part of the pile, respectively.

The macro-element formulation suggested above can be adapted for single batter piles in the sand [104] and cassion foundations in the sand [105]. The inability to account for changes in geometry and loading boundary conditions in previous studies was accounted for in the model proposed by F. Pisano et al. [106].

The macroelements for deep foundations developed to date have several limitations that do not allow reproducing (at least in a direct way) the response of a pile group under seismic loading. A newly established frequency-dependent macroelement technique is capable of reproducing the dynamic attributes of the system at multiple levels of increasing ground shaking [107].

Failure surface (point A):

$$\left(\frac{H'}{\xi N \mu H_o}\right)^2 + \left(\frac{M'}{\xi N \mu M_o}\right)^2 - 1.5 \frac{H'}{(\xi N \mu H_o)} \frac{M'}{(\xi N \mu M_o)} - \left[1 - \left(\frac{V'}{\xi N \mu V_o}\right)^2\right] = 0 \quad \mathbf{A} (H', M', V')$$

Failure surface (point B):

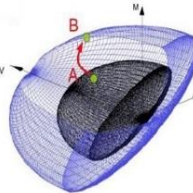
$$\left(\frac{H^*}{N \mu H_o}\right)^2 + \left(\frac{M^*}{N \mu M_o}\right)^2 - 1.5 \frac{H^*}{(N \mu H_o)} \frac{M^*}{(N \mu M_o)} - \left[1 - \left(\frac{V^*}{N \mu V_o}\right)^2\right] = 0 \quad \mathbf{B} (H^*, M^*, V^*)$$


Fig. 8. Loading and failure surfaces of the hypoplastic macroelement model for a single vertical pile [103]

3. Experimental Works

The result and conclusions at which many researchers arrived by adopting different approaches mentioned in the review above for soil foundation modelling need to be validated or complemented by performing experimental work. Experiments performed by researchers are reviewed hereafter, some validating the soil foundation models.

3.1 N-g Centrifuge Experiments

Centrifuge experiments are based on the concept of scaling down a prototype design in terms of geometry by introducing a higher gravitational force (e.g., $N = 20$ -100 times that of gravity). The methodology turns out in the preservation of prototype soil stresses at the model size due to similitude and scaling rules [108]. The centrifuge is a significant instrument for examining the performance and getting better outcomes of the soil-foundation system relating to the rocking shallow foundation because the nonlinearity in the system is primarily due to the soil's unpredictable behaviour. Several centrifuge tests were performed on the strip and square footings accompanying the shearwall and several other structures for different types of loading (monotonic, lateral cyclic and dynamic) [109-111]. Moreover, Ugalde executed tests on a model bridge pier supported by shallow footings [112]. Another study discussed shallow footings supporting a shearwall and a moment frame as part of a combined load-resisting system. The influence of the combined nonlinearity of structure and foundation on the response of the complete structural system is demonstrated in the centrifuge test [113]. Centrifuge experiments were conducted to find out how the degree of liquefaction influences the seismic and post-seismic settlement of shallow foundations lying on saturated sand [114]. The introduction of a new centrifuge tube-actuator was used to discharge spherical projectiles at single-degree-of-freedom (s dof) models resting on sand-filled shallow foundations. This enables the generation of dynamic impulse excitation, which is utilised to assess dynamic rocking stiffness in modest strains [115].

A comparison of dynamic p-y analysis results with the result of dynamic centrifuge model testing shows satisfactory agreement across a wide range of ground motions [116]. Geotechnical centrifuge tests were used to look at the dynamic reactions of soil foundation models with different pile arrangements, and they estimated both kinematic and inertial interaction [117]. The theoretical concept of the BNWF model is complemented by performing a centrifuge test [80].

A set of dynamic centrifuge tests was conducted to evaluate the impacts of soil conditions and structural variables on SSI effects, resulting in a dataset that might be critical for engineering practice [118]. Test performed on single-degree-of-freedom (s dof) system to obtain a period-lengthening ratio (PLR) for the different seismic intensities, which

represents the nonlinear properties of soil; the result shows the PLR of sdof system increases with peak ground acceleration at the surface [119].

3.2 1-g Experiments

To study the SSI impacts of shallow foundations, one-g experiments can be conducted employing either input at the base (e.g., using a shake table) or inertial loading (e.g., by structure-mounted hydraulic jacks). These tests have an advantage over centrifuge tests in preserving genuine soil-to-structure size scaling. Tests are, however, restricted by large scale, which significantly raises experimentation expenses. Also, the soil box's size constraint may result in boundary effects on the free-field soil conditions. Barlett tested small plate footing (simulating the real scenario) of size 0.5m×0.25m placed on clay. In contrast, Wiessing performed the cyclic test on identical footing supported on sand [120-121]. These experiments found that a spread footing can yield soil at a moment less than the moment carrying capacity of the column and can prevent the formation of a hinge at the base of the column. By performing the shake table test, Gazetas and Stokes demonstrated the trustworthiness of the impedance functions enlisted in Gazetas [122-123]. To study the true failure mechanism of the foundation, shake table experiments were performed on a strip footing positioned on dry four-layered sand embedded at various depths into the deposit. It is observed when eccentricity is introduced; the seismic bearing capacity is reduced [124]. Particle Image Velocimetry (PIV) paired with the aid of photogrammetry and rapid filming to monitor the seismic effect on soil and investigate the failure mechanism of a shallow foundation on a one-g shaking table. Moment effects are severe for structures with a centre of mass at a considerable height from the foundation level, leading to a significant decline in bearing capacity due to uplift. The failure mechanism was shown to be influenced by the depth of embedment and surcharge [125]. Overturning moments at the soil-foundation interface were studied by Paolucci et al. [92] through the use of a shake table test.

Performing the shake table test, assessment of the effects of pile arrangements, pile caps, and superstructures on time period elongation and damping ratio of a system under sinedwells, white noise and natural EQ motion done [126]. A five-storey scaled-down model structure was put on a shake table to observe the response of two structures, one with the fixed base condition and the other assisted by model piles embedded in soft clay. The result indicated that as the structure height increases, the response amplifies in SSI conditions, which can alter the functioning of the structure [127].

The majority of experiments to assess the effect of SSI on structure uses shake table testing or dynamic centrifuge model studies. But a full-scale dynamic test on a portal frame railway bridge was recently performed [128]. Amendola et al. [129] conducted full-scale field tests on soil-structure interaction to calculate the foundation impedance function.

Gajan et al. [130] correlated rocking foundation performance characteristics with capacity parameters and parameters relating to earthquake demand by taking data from 142 centrifuge and shaking table tests that included a different type of soil, varying foundation geometry, different structural models and ground motion.

4. Conclusions

Since nonlinearity in soil and structure is considered the most critical aspect, it leads to the failure of the entire system. Different methodologies proposed by the researchers are reviewed in this study to find out the best way to model nonlinearity in soil-structure

interaction (SSI). The following conclusions are made from this extensive review presented:

FEM helps model the nonlinearity of soil, structure, and foundation to give results similar to the actual scenario but is time-consuming and computationally expansive due to the huge soil domain. The boundary condition, size and soil element type are critical aspects of energy dissipation to reduce the soil domain. The review shows the possibility of evolving a particular technique [17].

Selecting a constitutive model for different soil conditions requires special attention. The Mohr-Coulomb, Modified Cam Clay, and Hyperbolic models are most commonly used. The hyperbolic model is frequently applied in SSI problems pertaining to drained and undrained soil conditions [131].

Adopting FEM in the direct approach can result in reductions in the calculation of the seismic demand of up to 50% in the case of maximum inter-storey drift ratio, whereas up to 20% in the case of maximum base shear when compared to a fixed-base model.

BEM came as an alternative to FEM, reducing the effort to discretise the soil-structure element. But it has its shortcoming in dealing with heterogeneous media and solving the nonlinear issue.

The idea of combining FEM and BEM suggested by researchers reduces computation effort and time. The theoretical development of combined FEM-BEM technique in the application of DSSI has been taken way forward, yet hardly any commercial software uses this concept.

Beam-on-nonlinear Winkler Foundation (BNWF) model evolves as a technique that uses spring to tackle the problem of a huge soil domain and its nonlinearity. Still, the main drawback is the model under-predicts sliding response. In addition, other Winkler's hypothesis also fails to depict the continuum nature of the soil, which is practically unacceptable in seepage, stress analysis, etc.

Only longer-period structures on extremely soft soil modelled using the BNWF technique can affect the assessment of the seismic demand.

In the context of both maximum base shear and maximum inter-storey drift ratio, the reductions in seismic demand estimations compared to a fixed-base model are lower (up to 20%) than what a FEM model predicts.

The primary distinction between the FEM and BNWF approaches might be linked to how the overall damping is characterised. Comparing simplified and rigorous techniques of validating the damping percentage typically provided by different codes using synthetic graphs could be an intriguing future development.

The inclusion of radiation damping into the macroelement formulations is a significant issue that has not yet been fully covered in the existing macroelement models. Considering its significance in the overall response of the system, the issue must be addressed in future.

Several experimental setups have been established to validate numerical results, but few experiments have been performed in the field. Therefore, more experimental studies are necessary to improve understanding of SSI nonlinearity.

References

- [1] Selvadurai APS. Idealized Soil Response Models for the Analysis of Soil-Foundation Interaction. Elastic Analysis of Soil-Foundation Interaction, 1st edition, Amsterdam Elsevier Scientific Publishing Company, 1979:13-42, ISBN 9780444596284. <https://doi.org/10.1016/B978-0-444-41663-6.50007-5>
- [2] Brinkgreve RB. Selection of soil models and parameters for geotechnical engineering application. In Soil constitutive models: Evaluation, selection, and calibration, Austin, Texas, United States, 69-98, 2005. [https://doi.org/10.1061/40771\(169\)4](https://doi.org/10.1061/40771(169)4)
- [3] Barros RC, de Vasconcelos LAC, Nogueira CL, Silveira RAM. Interface elements in geotechnical engineering-some numerical aspects and applications. In: XXXVIII Iberian Latin- American congress on computational methods in engineering, Florianópolis, SC, Brazil, 1-20, 2017. <https://doi.org/10.20906/CPS/CILAMCE2017-0174>
- [4] Nova R, Montrasio L. Settlement of shallow foundations on sand. Geotechnique. 1991; 41(2):243-256. <https://doi.org/10.1680/geot.1991.41.2.243>
- [5] Cremer C, Pecker A, Davenne L. Cyclic macro-element for soil-structure interaction: material and geometrical nonlinearities. International Journal for Numerical and Analytical Methods in Geomechanics. 2001;25(13):1257-1284. <https://doi.org/10.1002/nag.175>
- [6] Peiris T, Thambiratnam D, Perera N, Gallage C. Soil-pile interaction of pile embedded in deep layered marine sediment under seismic excitation. Structural Engineering International. 2014;24(4):521-531. <https://doi.org/10.2749/101686614X13854694314720>
- [7] Lysmer J, Kuhlemeyer RL. Finite dynamic model for infinite media. Journal of the engineering mechanics division. 1969;95(4):859-77. <https://doi.org/10.1061/JMCEA3.0001144>
- [8] White W, Lee IK, Valliappan S. Unified boundary for finite dynamic models. Journal of the Engineering Mechanics Division. 1977;103(5):949-64. <https://doi.org/10.1061/JMCEA3.0002285>
- [9] Jingbo L, Yandong L. A direct method for analysis of dynamic soil-structure interaction based on interface idea. Developments in geotechnical engineering, Elsevier. 1998;83:261-276. [https://doi.org/10.1016/S0165-1250\(98\)80018-7](https://doi.org/10.1016/S0165-1250(98)80018-7)
- [10] Zienkiewicz OC, Emson C, Bettess P. A novel boundary infinite element. International Journal for Numerical Methods in Engineering. 1983;19(3):393-404. <https://doi.org/10.1002/nme.1620190307>
- [11] Yun CB, Kim DK, Ki, JM. Analytical frequency-dependent infinite elements for soil-structure interaction analysis in two-dimensional medium. Engineering Structures. 2000;22(3):258-271. [https://doi.org/10.1016/S0141-0296\(98\)00070-4](https://doi.org/10.1016/S0141-0296(98)00070-4)
- [12] Novak M, Mitwally H. Transmitting boundary for axisymmetrical dilation problems. Journal of engineering mechanics. 1988;114(1):181-7. [https://doi.org/10.1061/\(ASCE\)0733-9399\(1988\)114:1\(181\)](https://doi.org/10.1061/(ASCE)0733-9399(1988)114:1(181))
- [13] Maheshwari B, Truman K, El Naggar M, Gould P. Three-dimensional nonlinear analysis for seismic soil-pile-structure interaction. Soil Dynamics and Earthquake Engineering. 2004;24(4):343-356. <https://doi.org/10.1016/j.soildyn.2004.01.001>
- [14] Liu J, Du Y, Du X, Wang Z, Wu J. 3D viscous-spring artificial boundary in time domain. Earthquake Engineering and Engineering Vibration. 2006;5(1):93-102. <https://doi.org/10.1007/s11803-006-0585-2>
- [15] Godbole PN, Viladkar MN, Noorzai J. Nonlinear soil-structure interaction analysis using coupled finite-infinite elements. Computers & Structures. 1990;36:1089-1096. [https://doi.org/10.1016/0045-7949\(90\)90216-0](https://doi.org/10.1016/0045-7949(90)90216-0)

- [16] Ismail S, Kaddah F, Raphael W. Seismic Soil Structure Interaction Response of Midrise Concrete Structures on Silty Sandy Soil. *Jordan Journal of Civil Engineering*. 2020;14: 117-135. <https://doi.org/10.2174/1874149502014010262>
- [17] Zhang W, Seylabi EE, Taciroglu E. An ABAQUS toolbox for soil-structure interaction analysis. *Computers and Geotechnics*. 2019;114:103143. <https://doi.org/10.1016/j.compgeo.2019.103143>
- [18] Zhang Y, Conte JP, Yang Z, Elgamal A, Bielak J, Acero G. Two-dimensional nonlinear earthquake response analysis of a bridge-foundation-ground system. *Earthquake Spectra*. 2008;24:343-386. <https://doi.org/10.1193/1.2923925>
- [19] Rayhani MH, El Nagggar MH. Numerical Modeling of Seismic Response of Rigid Foundation on Soft Soil. *International Journal of Geomechanics*. 2008;8(6):336-346. [https://doi.org/10.1061/\(ASCE\)1532-3641\(2008\)8:6\(336\)](https://doi.org/10.1061/(ASCE)1532-3641(2008)8:6(336))
- [20] Kuhlemeyer RL, Lysmer J. Finite element method accuracy for wave propagation problems. *Journal of the Soil Mechanics and Foundations Division*. 1973;99(5):421-7. <https://doi.org/10.1061/JSFEAQ.0001885>
- [21] Nilsson CM, Jones CJ. Theory manual for WANDS 2.1 wave number domain FE-BE software for structures and fluids, 2007.
- [22] Ranjan G, Rao ASR. *Basic And Applied Soil Mechanics*, 2nd edition, India New Age International Pvt Ltd., 2005, ISBN 81-224-1223-8.
- [23] Duncan JM, Chang CY. Nonlinear analysis of stress and strain in soils. *Journal of the soil mechanics and foundations division*. 1970;96(5):1629-53. <https://doi.org/10.1061/JSFEAQ.0001458>
- [24] Smith IM, Griffiths DV, Margetts L. *Programming the finite element method*, 5th edition, United Kingdom, John Wiley & Sons, 2014. ISBN 978-1-119-97334-8.
- [25] Drucker DC, Prager W. Soil mechanics and plastic analysis or limit design. *Quarterly of applied mathematics*. 1952;10(2):157-65. <https://doi.org/10.1090/qam/48291>
- [26] Roscoe KH, Burland JB. On the generalised behaviour of 'wet' clay. *Engineering Plasticity*. 1968;48:535-609.
- [27] Adachi T, Oka F. Constitutive equation for normally consolidated clays based on elasto-viscoplasticity. *Soil and Foundations*. 1982;22:57-70. https://doi.org/10.3208/sandf1972.22.4_57
- [28] Kim MK, Lade PV. Single hardening constitutive model for frictional materials: I. Plastic potential function. *Computers and geotechnics*. 1988;5(4):307-24. [https://doi.org/10.1016/0266-352X\(88\)90009-2](https://doi.org/10.1016/0266-352X(88)90009-2)
- [29] Brinkgreve RBJ, and Vermeer PA. *PLAXIS finite element code for soil and rock analysis- Version 7*, Balkema Rotterdam, 1997.
- [30] Griffiths D. Numerical Studies of Soil-Structure Interaction Using a Simple Interface Model. *Canadian Geotechnical Journal*. 1988;25:158-162. <https://doi.org/10.1139/t88-016>
- [31] Viladkar M, Godbole P, Noorzaeei J. Modelling of Interface for Soil-Structure Interaction Studies. *Computers and Structures*. 1994;52(4):765-779. [https://doi.org/10.1016/0045-7949\(94\)90358-1](https://doi.org/10.1016/0045-7949(94)90358-1)
- [32] Hu L, Pu J. Testing and Modeling of Soil-Structure Interface. *Journal of Geotechnical and Geoenvironmental Engineering*. 2004;130(8):851-860. [https://doi.org/10.1061/\(ASCE\)1090-0241\(2004\)130:8\(851\)](https://doi.org/10.1061/(ASCE)1090-0241(2004)130:8(851))
- [33] Mayer M, Gaul L. Modeling of Contact Interfaces Using Segment-to-segment-elements for FE Vibration Element. *IMAC-XXIII: Conference and Exposition on Structural Dynamics*. Society for Experimental Mechanics, 2005.

- [34] Desai CS, Zaman MM, Lightner JG, Siriwardane HJ. Thin-layer element for interfaces and joints. *International Journal for Numerical and Analytical Methods in Geomechanics*. 1984;8(1):19-43. <https://doi.org/10.1002/nag.1610080103>
- [35] Wei W, Tinghao L. Study on Shear Behaviour of Soil-Structure Interface. *International Conference on Engineering Computation*, IEEE Computer Society, 127-130, 2009.
- [36] Viladkar MN, Zedan AJ, Saran S. Nonlinear elastic analysis of shallow footings subjected to eccentric inclined loads. *Geomechanics and Geoengineering*. 2015;10(1):45-56. <https://doi.org/10.1080/17486025.2014.902117>
- [37] Dhadse GD, Ramtekkar GD, Bhatt G. Finite element modeling of soil structure interaction system with interface: a review. *Archives of Computational Methods in Engineering*. 2021;3415-32. <https://doi.org/10.1007/s11831-020-09505-2>
- [38] Wolf JP, Darbre GR. Dynamic-stiffness matrix of soil by the boundary-element method: conceptual aspects. *Earthquake engineering & structural dynamics*. 1984;12(3):385-400. <https://doi.org/10.1002/eqe.4290120307>
- [39] Wong HL. The coupled translations and rotations caused by the weight distribution of nearby buildings. In *Proceedings of the symposium on applications of computer methods in engineering*. University of Southern California, Los Angeles, 1977.
- [40] Wong HL, Luco JE. Dynamic interaction between rigid foundations in a layered half-space. *Soil Dynamics and Earthquake Engineering*. 1986;5:149-58. [https://doi.org/10.1016/0267-7261\(86\)90018-7](https://doi.org/10.1016/0267-7261(86)90018-7)
- [41] Sato T, Kawase H, Yoshida K. Dynamic response analysis of rigid foundations subjected to seismic waves by boundary element method. In *Proceedings of the fifth international conference on boundary elements*. Hiroshima, Japan: Springer-Verlag, 765-74, 1983.
- [42] Yoshida K, Sato T, Kawase H. Dynamic response of rigid foundations subjected to various types of seismic waves. In *Proceeding of the eighth World conference on earthquake engineering*, San Francisco, California, USA, 745-52, 1984.
- [43] Karabalis DL, Huang CFD. 3-D foundation-soil-foundation interaction. In *Proceedings of the ninth international conference on boundary element technology*, Paris, France, 197-209, 1994.
- [44] Karabalis DL, Mohammadi M. Foundation-soil-foundation dynamics using a 3-D frequency domain BEM. In *Proceedings of the thirteenth conference on boundary element*, Istanbul, Turkey, 447-56, 1991. https://doi.org/10.1007/978-94-011-3696-9_36
- [45] Karabalis DL, Mohammadi M. 3-D dynamic foundation-soil-foundation interaction on a layered soil medium. *Advances in Boundary Element Methods*, Civil-Comp Press, Edinburgh. 1996:73-80.
- [46] Karabalis DL, Mohammadi M. 3-D dynamic foundation-soil-foundation interaction on layered soil. *Soil Dynamics and Earthquake Engineering*. 1998;17:139-52. [https://doi.org/10.1016/S0267-7261\(97\)00047-X](https://doi.org/10.1016/S0267-7261(97)00047-X)
- [47] Romanini E. Dynamic structure-soil-structure interaction by the substructure deletion method. In *Proceedings of the eighteenth world conference on the boundary element method*, Braga, Portugal, 465-70, 1996.
- [48] Betti R, de Mesquita Neto E, Romanini E. Dynamic interaction between embedded foundations by the substructure deletion method. In *Proceedings of the eleventh conference on engineering mechanics*, Fort Lauderdale, Florida, USA, 314-7, 1996.
- [49] Betti R. Effect of the dynamic cross-interaction in the seismic analysis of multiple embedded foundations. *Earthquake Engineering and Structural Dynamics*.

- 1997; 26(10): 1005-19. [https://doi.org/10.1002/\(SICI\)1096-9845\(199710\)26:10<1005::AID-EQE690>3.0.CO;2-E](https://doi.org/10.1002/(SICI)1096-9845(199710)26:10<1005::AID-EQE690>3.0.CO;2-E)
- [50] Çelebi E, Firat S, Çankaya I. The evaluation of impedance functions in the analysis of foundations vibrations using boundary element method. *Applied Mathematics and Computation*. 2006;173(1):636-667. <https://doi.org/10.1016/j.amc.2005.04.006>
- [51] Eilouch MA, Sandhu RS. A mixed method for transient analysis of soil-structure interaction under SH-motion. *Earthquake engineering & structural dynamics*. 1986;14(4):499-516. <https://doi.org/10.1002/eqe.4290140402>
- [52] Wang S. Coupled boundary and finite elements for dynamic structure (3D)-foundation-soil interaction. *Computers and structures*. 1992; 44(4):807-812. [https://doi.org/10.1016/0045-7949\(92\)90465-C](https://doi.org/10.1016/0045-7949(92)90465-C)
- [53] Wang S, Schmid G. Dynamic structure-soil-structure interaction by FEM and BEM. *Computational Mechanics*. 1992;9: 347-57. <https://doi.org/10.1007/BF00370014>
- [54] Imamura A et al. Seismic response characteristics of embedded structures considering cross interaction. In: *Proceeding of the tenth world conference on earthquake engineering*. Rotterdam: Balkema, 1719-24, 1992.
- [55] Capuani D, Klein R, Antes H, Tralli A. Dynamic soil-structure interaction of coupled shear walls by boundary element method. *Earthquake engineering and structural dynamics*. 1995;24(6):861-879. <https://doi.org/10.1002/eqe.4290240606>
- [56] Padron LA, Aznarez JJ, Maeso O. Dynamic structure-soil-structure interaction between nearby piled buildings under seismic excitation by BEM-FEM model. *Soil dynamics and earthquake engineering*. 2009;29(6):1084-96. <https://doi.org/10.1016/j.soildyn.2009.01.001>
- [57] Chuhan Z, Xinfeng C, Guanglun W. A coupling model of FE-BE-IE-IBE for nonlinear layered soil-structure interactions. *Earthquake Engineering and Structural Dynamics*. 1999;28(4):421-441. [https://doi.org/10.1002/\(SICI\)1096-9845\(199904\)28:4<421::AID-EQE824>3.0.CO;2-I](https://doi.org/10.1002/(SICI)1096-9845(199904)28:4<421::AID-EQE824>3.0.CO;2-I)
- [58] Wolf JP. *The scaled boundary finite element method*. John Wiley & Sons, 2003, ISBN 0-471-48682-5.
- [59] Wegner J, Yao M, Zhang X. Dynamic wave-soil-structure interaction analysis in the time domain. *Computers and structures*. 2005;83(27):2206-2214. <https://doi.org/10.1016/j.compstruc.2005.04.004>
- [60] Talebi H, Silani M, Klusemann B. The scaled boundary finite element method for computational homogenization of heterogeneous media. *International Journal for Numerical Methods in Engineering*. 2019;118(1):1-7. <https://doi.org/10.1002/nme.6002>
- [61] Bielak J, Loukakis K, Hisada Y, and Yoshimura C. Domain Reduction Method for Three-Dimensional Earthquake Modeling in Localised Regions, Part I: Theory. *Bulletin of the Seismological Society of America*, 2003; 93(2): 817-824. <https://doi.org/10.1785/0120010251>
- [62] Zdravkovic L, Kontoe S. Some issues in modelling boundary conditions in dynamic geotechnical analysis. In *12th international conference of international association for computer methods and advances in geomechanics*, India, 1-6, 2008.
- [63] McClelland B, Focht Jr JA. Soil modulus for laterally loaded piles. *Transactions of the american society of civil engineers*. 1958;123(1):1049-63. <https://doi.org/10.1061/TACEAT.0007599>

- [64] Matlock H. Correlations for design of laterally loaded piles in soft clay. Proceedings, 2nd Offshore Technology Conference, Houston, Texas, 577-594,1970. <https://doi.org/10.4043/1204-MS>
- [65] Penzien J. Soil-pile-foundation interaction. Earthquake Engineering, Prentice Hall, New York, 1970.
- [66] Nogami T, Otani J, Konagai K, Chen HL. Nonlinear soil-pile interaction model for dynamic lateral motion. Journal of Geotechnical Engineering. 1992;118(1),89-106. [https://doi.org/10.1061/\(ASCE\)0733-9410\(1992\)118:1\(89\)](https://doi.org/10.1061/(ASCE)0733-9410(1992)118:1(89))
- [67] Wang S, Kutter BL, Chacko JM, Wilson DW, Boulanger RW, Abghari A. Nonlinear seismic soil-pile-structure interaction. Earthquake Spectra. 1998; 4(2),377-396. <https://doi.org/10.1193/1.1586006>
- [68] El Naggar MH, Shayanfar M, Kimiaei M, Aghakouchak A. Simplified BNWF model for nonlinear seismic response analysis of offshore piles with nonlinear input ground motion analysis. Canadian Geotechnical Journal. 2005;42:365-380. <https://doi.org/10.1139/t04-103>
- [69] Saha R, Dutta S, Haldar S. Effect of raft and pile stiffness on seismic response of soil-piled raft-structure system. Structural Engineering and Mechanics. 2015;55:161-189. <https://doi.org/10.12989/sem.2015.55.1.161>
- [70] Huang Maosong, Tu Wenbo, Gu Xiaoqiang. Time domain nonlinear lateral response of dynamically loaded composite caisson-piles foundations in layered cohesive soils. Soil Dynamics and Earthquake Engineering. 2018;106:113-130. <https://doi.org/10.1016/j.soildyn.2017.12.015>
- [71] Barlett PE. Foundation rocking on a clay soil. Master's thesis, University of Auckland, New Zealand, 1976.
- [72] Taylor PW, Bartlett PE, Weissing PR. Foundation rocking under earthquake loading. 10th International Conference on Soil Mechanics and Foundation Engineering, Stockholm, 313-322, 1981.
- [73] Psycharis IN. Dynamic behavior of rocking structures allowed to uplift. PhD thesis, California Institute of Technology, 1981.
- [74] Chopra A, Yim SC. Simplified earthquake analysis of structures with foundation uplift. Journal of Structural Engineering. 1985;111(4):906-930. [https://doi.org/10.1061/\(ASCE\)0733-9445\(1985\)111:4\(906\)](https://doi.org/10.1061/(ASCE)0733-9445(1985)111:4(906))
- [75] Nakaki DK, Hart GC. Uplifting response of structures subjected to earthquake motions. US-Japan Coordinated Program for Masonry Building Research. Report; 1987.
- [76] Harden CW, Hutchinson T, Martin GR, Kutter BL. Numerical modeling of the nonlinear cyclic response of shallow foundations. Report No. 2005/04, Pacific Earthquake Engineering Research Center, PEER, 2005.
- [77] Harden CW, Hutchinson T, Moore M. Investigation into the effects of foundation uplift on simplified seismic design. Earthquake Spectra. 2006;22(3):663-692. <https://doi.org/10.1193/1.2217757>
- [78] Allotey N, El Naggar MH. An investigation into the Winkler modeling of the cyclic response of rigid footings. Soil Dynamics and Earthquake Engineering. 2008;28(1):44-57. <https://doi.org/10.1016/j.soildyn.2007.04.003>
- [79] Allotey N, El Naggar MH. Analytical moment-rotation curves for rigid foundations based on a Winkler model. Soil Dynamics and Earthquake Engineering. 2003;23:367-381. [https://doi.org/10.1016/S0267-7261\(03\)00034-4](https://doi.org/10.1016/S0267-7261(03)00034-4)
- [80] Raychowdhury P, Hutchinson TC. Performance evaluation of a nonlinear Winkler-based shallow foundation model using centrifuge test results. Earthquake Engineering and Structural Dynamics. 2009;38(5):679-698. <https://doi.org/10.1002/eqe.902>

- [81] Tomeo R, Bilotta A, Ptilakis D, Nigro E. Soil-structure interaction effects on the seismic performances of reinforced concrete moment resisting frames. *Procedia Engineering*. 2017;199:230-5. <https://doi.org/10.1016/j.proeng.2017.09.006>
- [82] Marzban S, Banazadeh M, Azarbakht A. Seismic performance of reinforced concrete shear wall frames considering soil-foundation-structure interaction. *The Structural Design of Tall and Special Buildings*. 2014;23(4):302-18. <https://doi.org/10.1002/tal.1048>
- [83] Raychowdhury P, Ray-Chaudhuri S. Seismic response of non-structural components supported by a 4-story SMRF: Effect of nonlinear soil-structure interaction. *Structures*. 2015;3:200-210. <https://doi.org/10.1016/j.istruc.2015.04.006>
- [84] Tahghighi H, Mohammadi A. Numerical evaluation of soil-structure interaction effects on the seismic performance and vulnerability of reinforced concrete buildings. *International Journal of Geomechanics*. 2020;20(6):04020072. [https://doi.org/10.1061/\(ASCE\)GM.1943-5622.0001651](https://doi.org/10.1061/(ASCE)GM.1943-5622.0001651)
- [85] Pandey, G., Patel, D., Mourya, V., Kumar, R., Kumar, S. A Review on Soil-Foundation-Interaction Models. *Journal of Rehabilitation in Civil Engineering*. 2023;11(3):158-179.
- [86] Harden CW, Hutchinson TC. Beam-on-nonlinear-Winkler-foundation modeling of shallow, rocking-dominated footings. *Earthquake Spectra*. 2009;25:277-300. <https://doi.org/10.1193/1.3110482>
- [87] Pender M. Seismic design and performance of surface foundations. 4th International Conference on Earthquake Geotechnical Engineering, Thessaloniki, Greece, 25-28, 2007.
- [88] di Prisco C, Nova R, Sibilìa A. Shallow Footings Under Cyclic Loading: Experimental Behaviour and Constitutive Modeling. *Geotechnical Analysis of Seismic Vulnerability of Historical Monuments*. Patron: Bologna, 2003.
- [89] Paolucci R. Simplified evaluation of earthquake induced permanent displacements of shallow foundations. *Journal of Earthquake Engineering*. 1997;1:563-579. <https://doi.org/10.1080/13632469708962378>
- [90] Crémer C, Pecker A, Davenne L. Cyclic macro-element for soil-structure interaction: material and geometrical nonlinearities. *International Journal for Numerical and Analytical Methods in Geomechanics*. 2001;25:1257-1284. <https://doi.org/10.1002/nag.175>
- [91] Crémer C, Pecker A, Davenne L. Modelling of nonlinear dynamic behaviour of a strip foundation with microelement. *Journal of Earthquake Engineering*. 2002;6:175-212. <https://doi.org/10.1080/13632460209350414>
- [92] Paolucci R, Shirato M, Yilmaz MT. Seismic behaviour of shallow foundations: shaking table experiments vs. Numerical modelling. *Earthquake Engineering and Structural Dynamics*. 2008;37:577-595. <https://doi.org/10.1002/eqe.773>
- [93] Shirato M, Paolucci R, Kuono R, Nakatani S, Fukui J, Nova R, di Prisco C. Numerical simulation of model tests of pier-shallow foundation systems subjected to earthquake loads using an elasto-uplift-plastic macro element. *Soils and Foundations*. 2008;48(5): 693-711. <https://doi.org/10.3208/sandf.48.693>
- [94] Grange S, Kotronis P, Mazars J. A macro-element to simulate 3D soil-structure interaction considering plasticity and uplift. *International Journal of Solids and Structures*. 2009;46(20):3651-3663. <https://doi.org/10.1016/j.ijsolstr.2009.06.015>
- [95] Salciarini D, Tamagnini C. A hypoplastic macroelement model for shallow foundations under monotonic and cyclic loads. *Acta Geotechnica*. 2009;4(3):163-176. <https://doi.org/10.1007/s11440-009-0087-2>

- [96] Salciarini D, Bienen B, Tamagnini C. A hypoplastic macroelement for shallow foundations subject to six-dimensional loading paths. In *Geotechnical Engineering: New Horizons*, Cavtat-Dubrovnik, Croatia, 2011.
- [97] Gajan S, Kutter B. A contact interface model for shallow foundation subjected to combined cyclic loading. *Journal of Geotechnical and Geoenvironmental Engineering*. 2009;135:407-419. [https://doi.org/10.1061/\(ASCE\)1090-0241\(2009\)135:3\(407\)](https://doi.org/10.1061/(ASCE)1090-0241(2009)135:3(407))
- [98] Chatzigogos CT, Figini R, Pecker A, Salençon J. A macroelement formulation for shallow foundations on cohesive and frictional soils. *International Journal for Numerical and Analytical Methods in Geomechanics*. 2011;35:902-935. <https://doi.org/10.1002/nag.934>
- [99] Figini R, Paolucci R, Chatzigogos CT. A macro-element model for non-linear soil-shallow foundation-structure interaction under seismic loads: theoretical development and experimental validation on large scale tests. *Earthquake Engineering & Structural Dynamics*. 2012;41(3):475-93. <https://doi.org/10.1002/eqe.1140>
- [100] Correia A. A pile-head macro-element approach to seismic design of monoshaft-supported bridges. Ph.D. thesis, ROSE School, IUSS Pavia, Italy, 2011.
- [101] G. Gazetas. Foundation vibrations. *Foundation Engineering Handbook*, 2nd edition, Boston, Springer, 1991:553-593, ISBN 978-1-4757-5271-7. https://doi.org/10.1007/978-1-4615-3928-5_15
- [102] EN 1998-5. Eurocode 8: Design of structures for earthquake resistance Part 5: Foundations, retaining structures and geotechnical aspects.
- [103] Zheng Li, Panagiotis K, Sandra E, Claudio T. A hypoplastic macroelement for single vertical piles in sand subject to three-dimensional loading conditions. *Acta Geotechnica*. 2015;11(2):373-390. <https://doi.org/10.1007/s11440-015-0415-7>
- [104] Zheng Li, Panagiotis K, Sandra E, Claudio T. A hypoplastic macroelement formulation for single batter piles in sand. *International Journal for Numerical and Analytical Methods in Geomechanics*. 2018;42(12):1346-1365. <https://doi.org/10.1002/nag.2794>
- [105] Zhuang J, Zhen-Yu Y, Panagiotis K, Zheng L, Claudio T. A hypoplastic macroelement model for a caisson foundation in sand under monotonic and cyclic loadings. *Marine Structures*. 2019;66:16-26. <https://doi.org/10.1016/j.marstruc.2019.02.002>
- [106] Pisanò F, Flessati L, Di Prisco C. A macroelement framework for shallow foundations including changes in configuration. *Géotechnique*. 2016;66(11):910-926. <https://doi.org/10.1680/jgeot.16.P.014>
- [107] Lesgidis N, Sextos A, Kwon OS. A frequency-dependent and intensity-dependent macro-element for reduced order seismic analysis of soil-structure interacting systems. *Earthquake Engineering & Structural Dynamics*. 2018;47(11):2172-2194. <https://doi.org/10.1002/eqe.3063>
- [108] Kutter B. Dynamic centrifuge modeling of geotechnical structures. *Transportation Research Record 1336*, University of California, Davis, 1997.
- [109] Rosebrock KR, Kutter BL. Soil-foundation structure interaction: Shallow foundations. *Centrifuge Data Report for the KRR01 Test Series*: Center for Geotechnical Modeling Data Report UCD/CGMDR-01, University of California, Davis, 2001a.
- [110] Gajan S, Phalen J, Kutter B. Soil-foundation structure interaction: Shallow foundations: Centrifuge data report for the ssg02 test series. *Center for Geotechnical Modeling Data Report UCD/CGMDR-02*, University of California, Davis, 2003a.
- [111] Thomas J, Gajan S, Kutter B. Centrifuge tests on square footings. Master's thesis, University of California, Davis, 2004.

- [112] Ugalde J. Centrifuge tests on bridge columns on shallow square footings. Master's thesis, University of California, Davis, 2007.
- [113] Chang B, Thomas JM, Raychowdhury P, Gajan L, K B, Hutchinson TC. Soil-foundation-structure interaction: Shallow foundations. Centrifuge Data Report for the JMT02 Test Series: SSRP 07/24, University of California, Davis, 2007.
- [114] Mehrzad B, Jafarian Y, Lee CJ, Haddad AH. Centrifuge study into the effect of liquefaction extent on permanent settlement and seismic response of shallow foundations. *Soils and Foundations*. 2018;58(1):228-240. <https://doi.org/10.1016/j.sandf.2017.12.006>
- [115] Taeseri D, Laue J, Martakis P, Chatzi E, Anastasopoulos I. Static and dynamic rocking stiffness of shallow footings on sand: centrifuge modelling. *International Journal of Physical Modelling in Geotechnics*. 2018;18(6):315-39. <https://doi.org/10.1680/jphmg.17.00024>
- [116] Boulanger RW, Curras CJ, Kutter BL, Wilson DW, Abghari A. Seismic soil-pile-structure interaction experiments and analyses. *Journal of geotechnical and geoenvironmental engineering*. 1999;125(9):750-9. [https://doi.org/10.1061/\(ASCE\)1090-0241\(1999\)125:9\(750\)](https://doi.org/10.1061/(ASCE)1090-0241(1999)125:9(750))
- [117] Hussien MN, Tobita T, Iai S, Karray M. Soil-pile-structure kinematic and inertial interaction observed in geotechnical centrifuge experiments. *Soil Dynamics and Earthquake Engineering*. 2016;89:75-84. <https://doi.org/10.1016/j.soildyn.2016.08.002>
- [118] Martakis P, Taeseri D, Chatzi E, Laue J. A centrifuge-based experimental verification of soil-structure interaction effects. *Soil Dynamics and Earthquake Engineering*. 2017;103:1-14. <https://doi.org/10.1016/j.soildyn.2017.09.005>
- [119] Kil-Wan Ko, Jeong-Gon Ha, Heon-Joon Park, Dong-Soo Kim. Investigation of Period-Lengthening Ratio for Single-Degree-of-Freedom Structures Using Dynamic Centrifuge Test. *Journal of Earthquake Engineering*. 2021;25(7),1358-1380. <https://doi.org/10.1080/13632469.2019.1576557>
- [120] Barlett PE. Foundation rocking on a clay soil. Master's thesis, University of Auckland, New Zealand, 1976.
- [121] Wiessing PR. Foundation rocking on sand. School of Engineering Report No. 203, University of Auckland, New Zealand, 1979.
- [122] Gazetas G, Stokoe KH. Free vibration of embedded foundations: theory versus experiment. *Journal of geotechnical engineering*. 1991;117(9):1382-401. [https://doi.org/10.1061/\(ASCE\)0733-9410\(1991\)117:9\(1382\)](https://doi.org/10.1061/(ASCE)0733-9410(1991)117:9(1382))
- [123] Gazetas G. Formulas and charts for impedances of surface and embedded foundations. *Journal of geotechnical engineering*. 1991;117(9):1363-81. [https://doi.org/10.1061/\(ASCE\)0733-9410\(1991\)117:9\(1363\)](https://doi.org/10.1061/(ASCE)0733-9410(1991)117:9(1363))
- [124] Maugeri M, Musumeci G, Novita D, Taylor CA. Shaking table test of failure of a shallow foundation subjected to an eccentric load. *Soil Dynamics and Earthquake Engineering*. 2000;20:435-444. [https://doi.org/10.1016/S0267-7261\(00\)00091-9](https://doi.org/10.1016/S0267-7261(00)00091-9)
- [125] Knappett JA, Haigh SK, Madabhushi SPG. Mechanisms of failure for shallow foundations under earthquake loading. *Proceedings, 11th International Conference on Soil Dynamics and Earthquake Engineering*, University of California, Berkeley, 713-725, 2004.
- [126] Durante MG, Di Sarno L, Mylonakis G, Taylor CA, Simonelli AL. Soil-pile-structure interaction: experimental outcomes from shaking table tests. *Earthquake Engineering & Structural Dynamics*. 2016;45(7):1041-61. <https://doi.org/10.1002/eqe.2694>
- [127] Subramanya KG, Govindaraju L, Ramesh Babu R. Shake table studies on the dynamic response of pile supported framed structure in soft soil. *Civil Engineering*

- and Architecture. 2020;8(6):1313-1324.
<https://doi.org/10.13189/cea.2020.080615>
- [128] Zangeneh A, Svedholm C, Andersson A, Pacoste C, Karoumi R. Identification of soil-structure interaction effect in a portal frame railway bridge through full-scale dynamic testing. Engineering Structure. 2018;159:299-309.
<https://doi.org/10.1016/j.engstruct.2018.01.014>
- [129] Amendola C, de Silva F, Vratsikidis A, Pitilakis D, Anastasiadis A, Silvestri F. Foundation impedance functions from full-scale soil-structure interaction tests. Soil Dynamics and Earthquake Engineering. 2021;141:106523.
<https://doi.org/10.1016/j.soildyn.2020.106523>
- [130] Gajan S, Soundararajan S, Yang M, Akchurin D. Effects of rocking coefficient and critical contact area ratio on the performance of rocking foundations from centrifuge and shake table experimental results. Soil Dynamics and Earthquake Engineering. 2020;141:106502. <https://doi.org/10.1016/j.soildyn.2020.106502>
- [131] Stark TD, Vettel JJ, Fitzwilliam SM, Ebeling RM. Soil-Structure Interaction Parameters for Silts. Washington DC: US Army Corps of Engineers, 1991.

Blank Page



Research Article

Sensitivity indices of RC beams considering construction sequence analysis for RC high-rise building

Nehal Mahadevbhai Desai^a, Sandip Vasanwala^b

Department of Civil Engineering, SVNIT, India

Article Info

Abstract

Article history:

Received 31 Oct 2022

Accepted 02 Mar 2023

Keywords:

Construction sequence method of analysis;
Sensitivity index;
Bending moment;
Time-dependent properties of concrete

Construction Sequence Analysis (CSA) is a technique that simulates real-time onsite construction procedures like timing, sequential loading, and construction sequence. This study compares the bending moment at various sections of beams using the CSA- Construction Sequence Analysis and LSA-Linear Static Analysis methods. Four 40-storeyed RC buildings of different spans are studied to consider the long-term effect of concrete properties like creep and shrinkage. The effects for 30 years from the application of live load in the CSA methods were analysed. It is essential to know the sensitivity of a beam for bending moments concerning the CSA method compared to the LSA method. Knowing how the sensitivity of beams varies concerning span in RC buildings is essential. The study divides beams into five different sensitivity categories. According to the study, the LSA approach provides 3.6% higher to 70.24% lower, 42.29% higher to 111.49% lower, and 17% higher to 44% lower left-end support, right-end support, and mid-span moments, respectively, than the CSA method in beams of normal categories. The study also concluded that RC shear walls increase the sensitivity of surrounding beams. These beams are categorized into the most vulnerable categories among all, and these categories seem absent in a plan without RC walls. The study concludes that it is advisable to adopt the CSA method with time-dependent effects of concrete when designing RC moment frame high-rise buildings. The analysis is done using MIDAS Gen-17 software.

© 2023 MIM Research Group. All rights reserved.

1. Introduction

Structural engineers analyse and design an RC building by simultaneously applying all loads to the building models using the Linear Static analysis method. However, an RC structure is gradually loaded due to stage-wise construction of the walls, floors, and structural components. Upon construction completion, the live load is applied in the form of occupancy. Using the Construction Sequence Analysis (CSA) method, all loads are applied according to the construction order, and application timing corresponds to actual construction.

According to Chakrabarti et al. (1978)[3] and Chang-Koon Choi et al. (1992)[4], the CSA approach reports responses that are different from the typical Linear Static Analysis (LSA) method, which is a one-step analysis method. Due to the time-dependent characteristics of concrete, Kwak & Kim (2006)[14] proposed a construction sequence method for analysis for designing RC buildings. Dinar et al. (2014) [10] and Correia & Lobo (2017)[5] investigated the effect of sequential self-weight on construction. Ha et al. (2017)[12] recommended considering the time-dependent effect of the concrete during the design stage of tall buildings and created an algorithm for the construction stage to evaluate the

^{*}Corresponding author: nehal.desai@scet.ac.in

^a orcid.org/0000-0001-8767-5649; ^b orcid.org/0000-0003-0083-6257

DOI: <http://dx.doi.org/10.17515/resm2022.572st1031>

Res. Eng. Struct. Mat. Vol. 9 Iss. 3 (2023) 1015-1037

results with a laser survey. Afshari et al. (2017)[1] suggested an improved correction factor approach. When employing the CSA approach, Secer & Arslan (2018) [16] and Zucca et al. (2018) [17] both discovered a sizable change in vertical column displacements. Elansary et al. (2021) [11] found that one-step analysis results in an unsafe solution in some element zones and an uneconomic solution in others. Since creep and shrinkage are ongoing processes, the CSA method will yield different results at various points in the analysis. Most of these investigators omitted the role of time and primarily assessed responses during live load application. Nehal et al. [6] have concluded that “98% to 99% of the total 50th-year axial shortening, and beam moments respectively are observed on completion of 30 years from the time of live load application. Therefore, it is advised to analyse using the CSA method up to a minimum time of 30 years after the application of the live load, taking the effects of creep and shrinkage into account, rather than up to 50 years, as the procedure is time-consuming and laborious.” In this study, all models were analysed up to 30 years after the application of live load, considering the effects of creep and shrinkage.

Vishal et al. (2000) [19] analysed G+19 floors, while Dubey & Bhadauria (2017) [11] analysed 50-floor RC buildings but studied only axial shortening for comparison with the conventional one-step method. Most investigators concentrated the study on axial shortening and differential shortening of vertical members. They overlooked the study of the effect of this axial shortening on the bending moment of beams. Thus, to fill this gap, additional research is required to study and compare the changes that occur in beam moments by CSA and LSA methods. Hence, the stakeholders of the construction industry would realise the significance of the CSA method and understand the importance of adopting it. The study calculates the sensitivity of beams by comparing the bending moment at different sections of beams induced in the CSA the LSA method at every floor level of building models. Beams were divided into different categories based on their sensitivity Index (SI). Four RC moment framed building models with and without RC shear walls of the same plan area, but different spans were selected to evaluate the effect of various beam spans. The building models were analysed using Midas Gen 17[15]. The code of practice of the Indian Roads Congress -IRC: 112-2011[13] was used to consider the long-term effects of concrete-like creep and shrinkage in CSA. This study's analysis and design are undertaken as per the Indian standard code of practice.

2. Materials and Methods

2.1. Building Models

Four 40-storied RC framed building models of symmetrical plans with varying plan grids, as shown in Table 1 and Fig. 1(a)-1(d), were selected for this study. The floor height of the models was 3.2m. Models were analysed and designed using the Indian Standard Code of Practice, with a live load of 2 kN/m², floor finishing load of 1 kN/m², and brick wall load of 6.5 kN/m by the LSA method.

Table 1. Details of building models

Models	Plan size, mxm	Beam grid, m x m	Total storey numbers	Specific details
Plan A	40 X 40	8 X 8	40	With Central Shear Wall
Plan B	40 X 40	5.72 X 5.72	40	With Central Shear Wall
Plan C	40 X 40	4.44 X 4.44	40	With Central Shear Wall
Plan A0	25 X 25	5 x 5	40	Without Shear wall

The designed cross-sections of structural members for all building models are shown in Table 3. Properties of the grade of concrete and steel used for modelling buildings are specified in Table 2.

Table 2. Properties of materials

Material properties	Reinforcement grade -Fe 415	Concrete grade -M 25
Yield Stress	415 N/mm ²	-
Compressive strength after 28 days of curing	-	25 N/mm ²
Modulus of Elasticity	2X10 ⁵ N/mm ²	2.5X10 ⁴ N/mm ²
Weight per unit volume	76.973 kN/m ³	23.6 kN/m ³
Poisson's Ratio	-	0.2

Table 3. Cross-sections of members

Floor No.	Column size, m x m				Shear wall size, mm		
	Plan A	Plan B	Plan C	Plan A0	Plan A	Plan B	Plan C
1st to 5th	1.6 x1.6	1.3x1.3	1.1x1.1	1.6 x1.6	550	500	500
6th to 10th	1.4x1.4	1.2x1.2		1.4x1.4	550	500	500
11th to 15th	1.3x1.3	1.1x1.1	0.9x0.9	1.3x1.3	450	400	400
16th to 20th	1.2x1.2	1.0x1.0	0.8x0.8	1.2x1.2	450	400	400
26th to 30th	1.0x1.0	0.8x0.8	0.6x0.6	1.1x1.1	350	300	300
31st to 35th	0.9x0.9	0.7x0.7	0.5x0.5	1.0x1.0	250	200	200
36th to 40th	0.7x0.7	0.6x0.6	0.4x0.4	0.9x0.9	250	200	200
Beam Size	0.35x0.75	0.3x0.6	0.3x0.5	0.7x0.7	-	-	-

All models with the same design cross-section were analysed by the CSA method. Stage-wise construction loads were applied to all RC building models considering a construction cycle of seven days. The formwork was undertaken to cast the first slab, and the first slab concreting was done on the third day of construction. As shown in Table 4, different loads were applied at different stages following the actual on-site construction sequence and its timing.

As per the time period study of Nehal et al. [6], all models were analysed up to a minimum time of 30 years after the application of the live load, considering the effects of creep and shrinkage.

2.2. Material Properties Related to Creep & Shrinkage

To calculate the long-term shortening due to creep and shrinkage in the CSA method, basic equations for creep co-efficient and the drying shrinkage strain given in IRC: 112-2011^[12] (ANNEXURE A-2, page no.237 to 240) code were used.

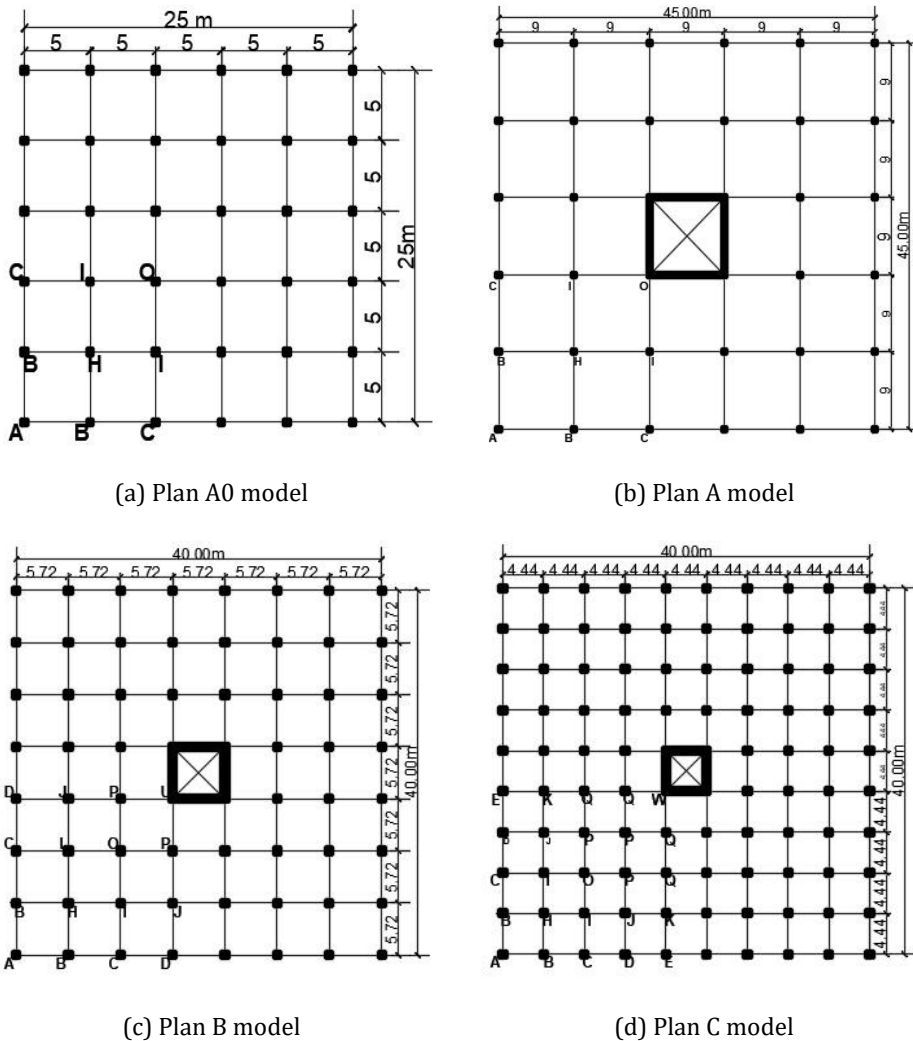


Fig. 1 Plan of different building models

Factors considered while calculating the co-efficient of creep include relative humidity, concrete age at loading, cross-sectional area, concrete strength, notional size of the member in mm, the perimeter of the member in contact with the atmosphere, age of concrete in days at the time considered, cement type, and the temperature adjusted age of concrete at loading in days. Similarly, the parameters considered for calculating the shrinkage strain are mean compressive strength, type of cement, and relative humidity.

As per the equations given in IRC: 112-2011[12], MIDAS Gen-17 calculates the long-term shortening due to creep and shrinkage in the CSA method based on above mentioned parameters.

2.3. Sequential Loads on Building Models

Stage-wise construction loads were applied on all RC building models and analysed by the CSA method for a construction cycle of seven days. The formwork was undertaken for the first slab casting and concreting of the first slab was done on the third day of construction.

As shown in Table 4, different loads were applied at different stages following the actual onsite construction sequence and its timing. These stage-wise loading sequences and timing for all stages were activated considering long-term properties of concrete like creep and shrinkage. The analysis was undertaken for 30 years for the RC building models.

Table 4. Stage-wise sequential loading for the CSA method

Sr. No	Type of load	Starting floor	The load cycle begins at/with	Cycle time
1	Self-weight of RC members	the first floor	On the first day of first stage one, i.e., on 22nd day, when the age of first-floor slab is 19 days	7 days
2	Load of the brick wall	the first floor	On the first day of fifth stage, i.e., on the 29th day	7 days
3	Load of floor finishing	the first floor	On the first day of sixth stage, i.e., on the 36th day	7 days
4	Live load	on all floors	At the last stage i.e., after allowing 90 days for occupancy after completion of construction work including finishing work.	Single time

3. Results and Discussion

In this study, the self-weight of structural members, a load of a brick wall, a load of floor finishing, and a live load were applied stage-wise as per construction sequence and scheduled timing, in line with the actual construction, as explained in Table 4. This changes the structural responses in the CSA method. Since the analysis was undertaken for 30 years from the application of live load, the time-dependent properties of concrete, like creep and shrinkage, also change the bending moment of beams in the CSA analysis method.

3.1. Sensitivity Analysis

The bending moments induced in LSA and CSA methods at left-end support, mid-span, and right-end support for all beams of all four building models were compared. To measure the level of sensitivity of moments, the dimensionless coefficient Sensitivity Index- 'SI' was introduced.

$$\text{Sensitivity Index (SI)} = \frac{\text{Bending Moment induced in CSA method}}{\text{Bending Moment induced in LSA method}}$$

SI coefficient for all beams on every floor for all plans were calculated, tabulated, and plotted in a graph.

3.2. Sensitivity Categories for Left End Moments

Graph of Sensitivity Index v/s Storey numbers, for left-end Moment, for a beam 'AB' of Plan C was plotted in Fig. 2.

It was observed that SI at the left end of beam 'AB' increases from 0.772 to 1.006 as moving from the top (40th) storey to the 8th storey. After that, SI again reduces to 0.972 from the 7th to the 1st storey. As storey numbers increase, the left-end moment sensitivity increases from the 8th floor. The LSA method provides a 0.6% lesser to 22.76 % higher bending moment than the CSA method when moving from the bottom to the top storey (at the left end). The higher storeys were more vulnerable in comparison to the lower storeys.

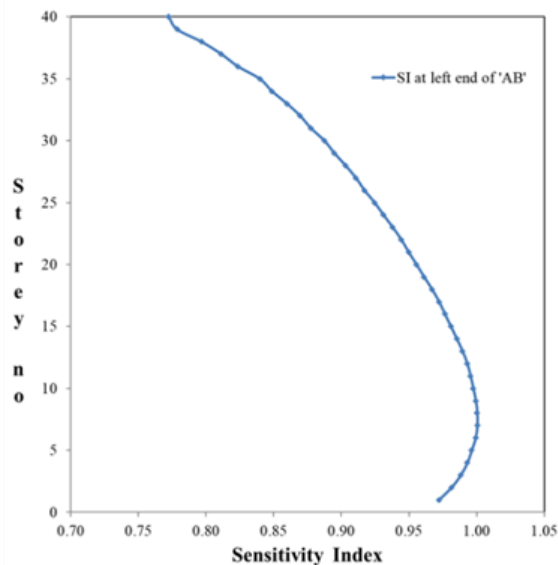


Fig. 2 Sensitivity Graph of beam 'AB' of Plan C

The SI at the left end of beam 'O1P1' increases from 0.964 to 1.345 while moving from 1st floor to 40th floor as shown in Fig. 3. From 1st to 10th storey, LSA provides 3.57% higher moments than CSA. From the 10th to the 34th storey LSA provides 31.3% lesser moments than CSA. On the 34th and 39th floor, 'SI' suddenly increases to 1.313 & 1.346, respectively, i.e. LSA provides 31.3% to 34.6% lower bending moments than CSA.

Similarly, as per Fig. 3, in Beam 'BC', 'SI' reduces from 0.964 to 0.848 while moving from the 1st floor to the 40th floor, i.e. LSA provides 3.57% to 15.2% higher values than CSA. However, sensitivity in Beam 'DE' & 'EF' 'SI' varies in a range of 0.959 to 0.961 for all storeys, i.e. LSA provides 4.1% to 3.9% higher moments than LSA. The deviation of a moment in CSA from LSA is comparatively lesser here as storey numbers increase.

From the 'Sensitivity index of left end moment V/S floor number' for beams of all building models as shown in Fig. 3, Fig. 4(a)-4(c) and Fig. 5, the following observations were made:

- Sensitivity index V/S floor number graph of left end moment of beams 'AB', 'GH', and 'MN' of Plan A model show a similar pattern and range of sensitivity Index.
- Similarly, the sensitivity index graph of the left end moment of beams 'AB', 'GH', 'MN' and 'RS' of the Plan B model, beams 'AB', 'GH', 'MN', M1N1' and 'TS' of Plan C model and beams 'AB', 'GH' and 'MN' of Plan A0 model also show a similar pattern and range of Sensitivity index.

All these beams were grouped into one category, which is CAT-III.

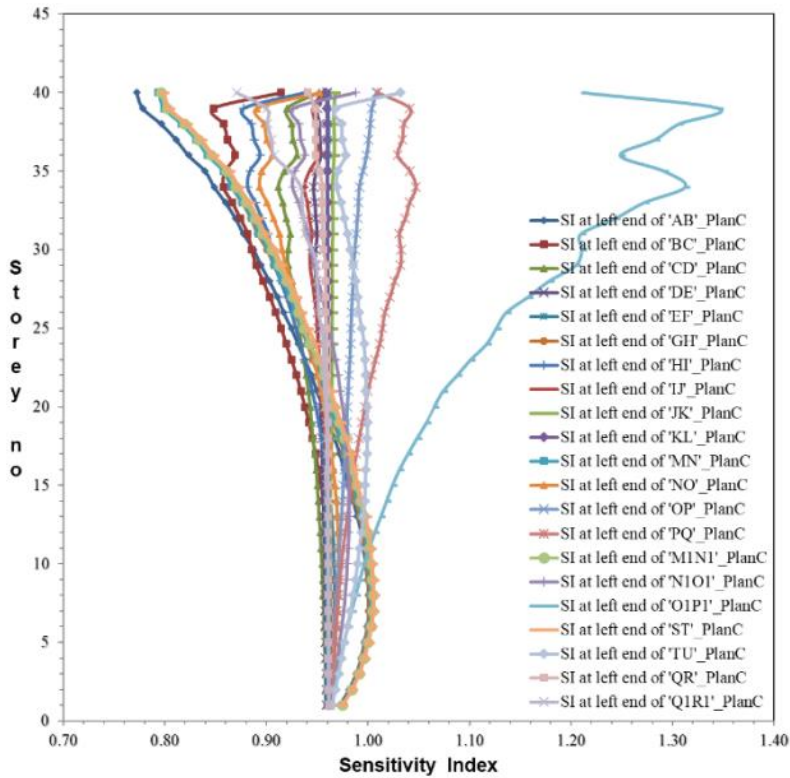
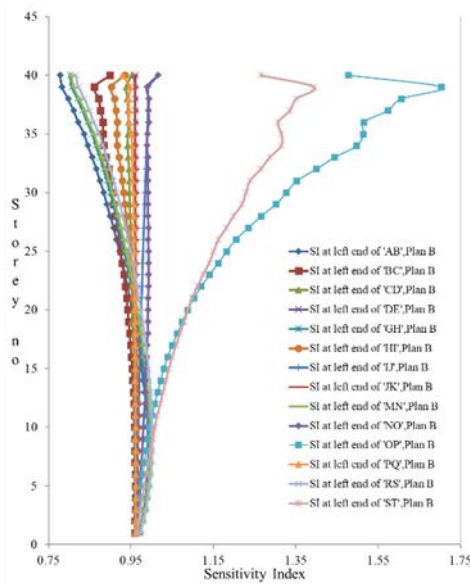
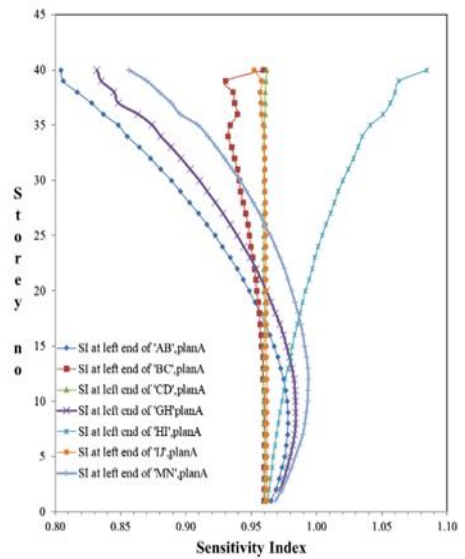


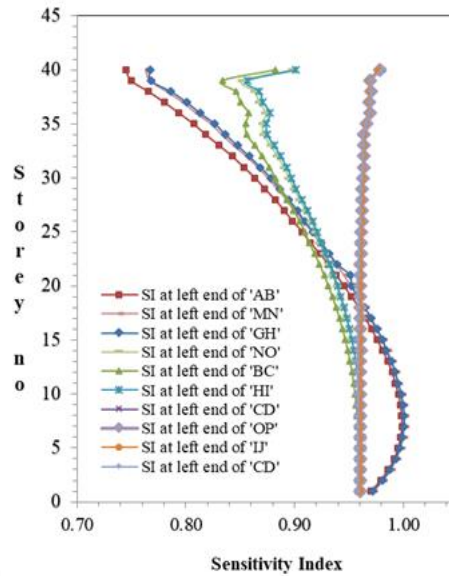
Fig. 3 Sensitivity Graph at Left end for all beams, Plan C



(a) Plan B model



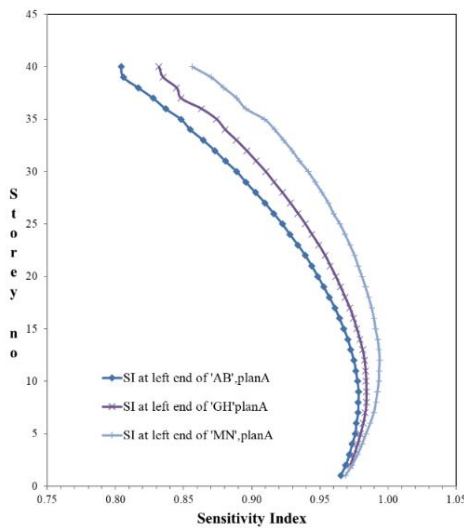
(b) Plan A model



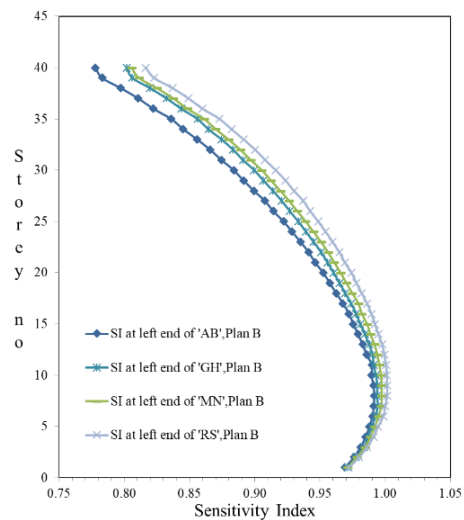
(c) Plan A0 model

Fig. 4 Sensitivity Graph at Left end for building models

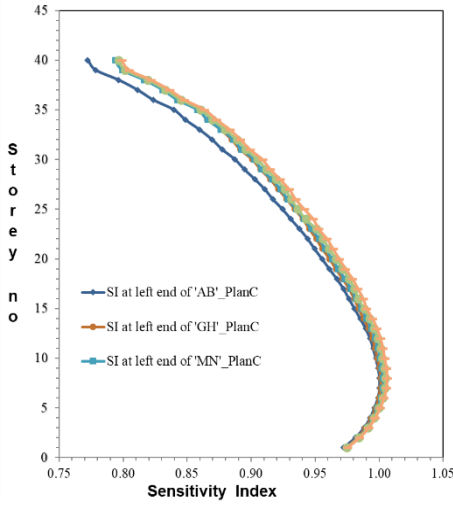
A different set of graphs with a similar pattern and range of SI were identified from the left-end support moments in beams of all models, as shown in Fig.3 and Fig.4. Finally, all beams were divided into five different categories. Beams of CAT I, CAT II, CAT III, CAT IV and CAT-V with their Sensitivity range are shown in Fig. 5-9 and tabulated in Table 5. the following observations were made:



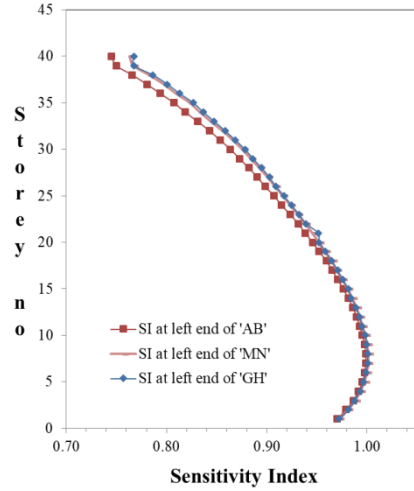
(a) Plan A model



(b) Plan B model



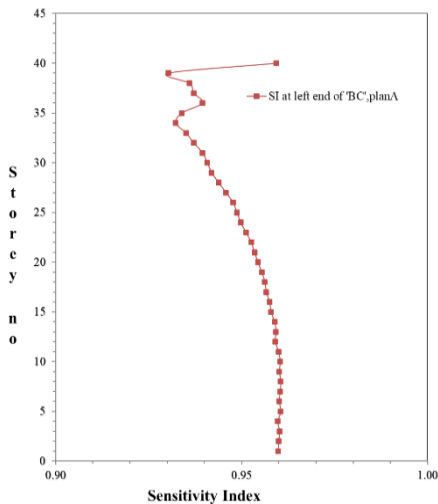
(c) Plan C model



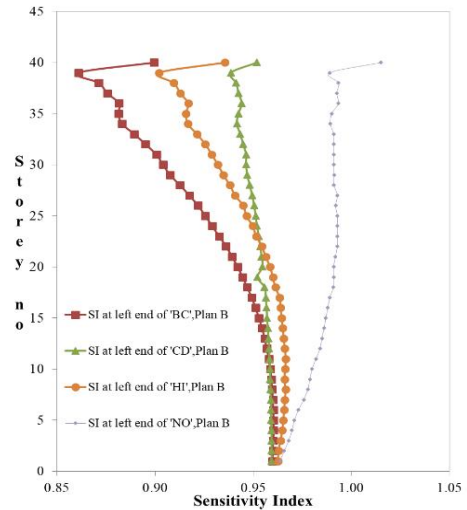
(d) Plan A0 model

Fig. 5 Sensitivity graph at left-end support for beams of CAT III

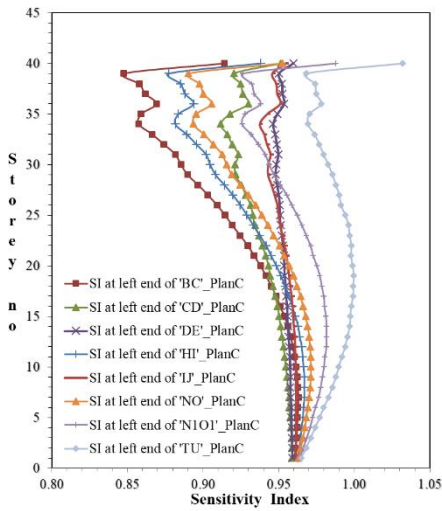
- As shown in Fig. 5, in Cat-III, the value of SI increases up to the 7th and 8th floors. Later it reduces up to the top floor in all building models. As shown in Fig. 6 to 8, in CAT-II, CAT-IV and CAT-V, the sensitivity of the bending moment increases as the building floors increase for all categories of building models. While in CAT-I beams, as shown in Fig. 9, the SI shows highly vulnerable values.
- In Category-III beams, as shown in Fig. 5, the SI varies from 0.8042 to 0.994 in Plan A, 0.78 to 1.0014 in Plan B, 0.7724 to 1.006 in Plan C and 0.745 to 1.00 in Plan A0. Thus, LSA provides 19.58% to 0.61% higher, 22% higher to 0.14 % lower, 22.76% higher to 0.6% lower and 25.5% higher left end bending moment in Plan A, Plan B, Plan C and Plan A0, respectively.



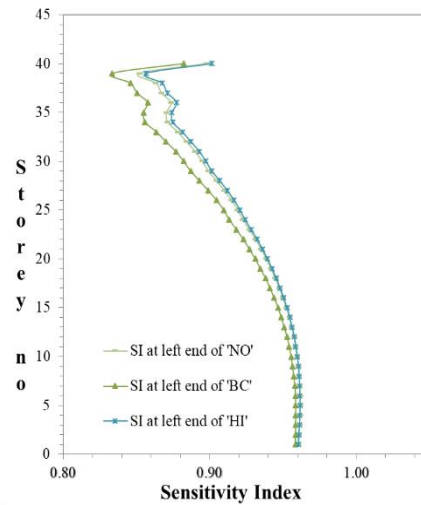
(a) Plan A model



(b) Plan B model



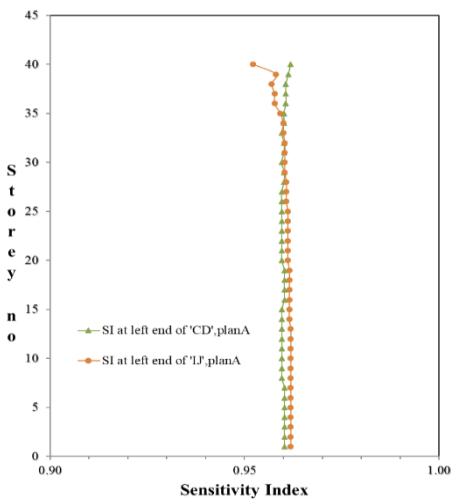
(c) Plan C model



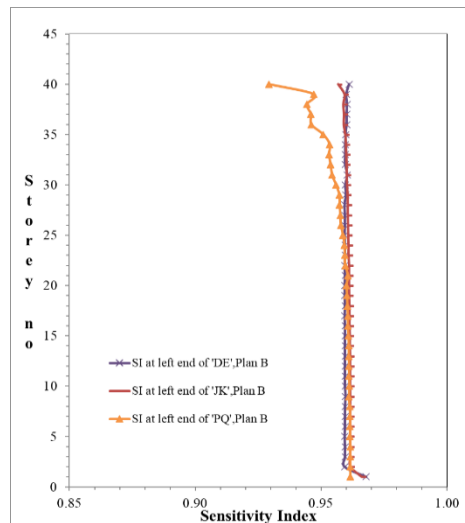
(d) Plan A0 model

Fig. 6 Sensitivity graph at left-end support for beams of CAT IV

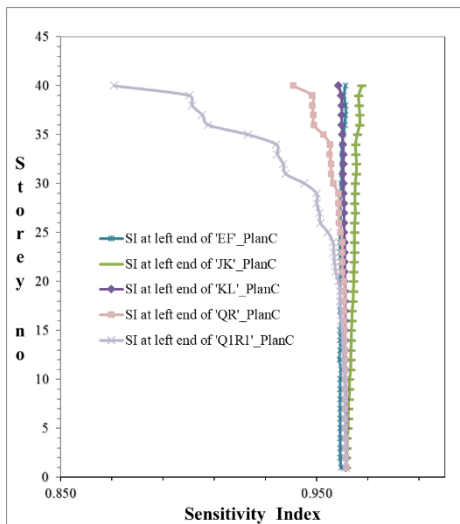
- In Category-IV beams, as shown in Fig. 6, the SI varies from 0.930 to 0.9605 in Plan A, 0.8609 to 1.0165 in Plan B, 0.8478 to 1.0320 in Plan C, and 0.830 to 0.977 in Plan A0. Thus, LSA provides 7% to 3.95% higher, 13.91% higher to 1.65% lower, 15.22% higher to 3.2% lower and 17% to 2.3% higher left-end bending moment in Plan A, Plan B, Plan C, and Plan A0, respectively.



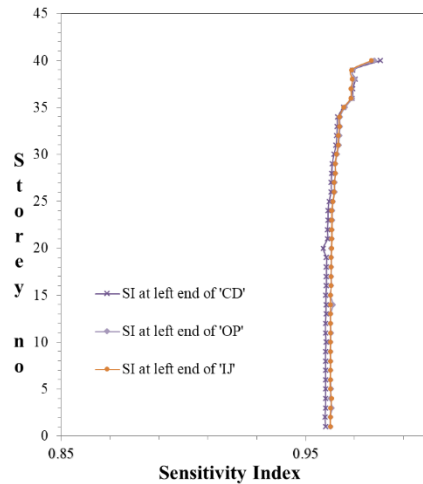
(a) Plan A model



(b) Plan B model



(c) Plan C model

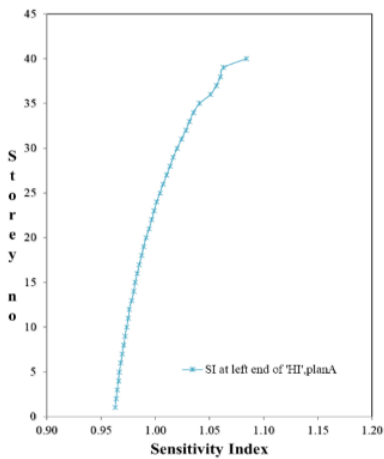


(d) Plan A0 model

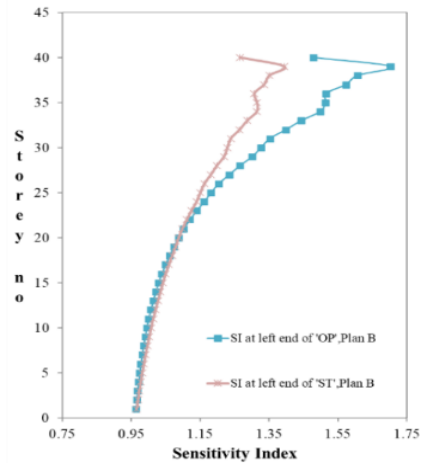
Fig. 7 Sensitivity graph at left-end support for beams of CAT V

- In Category-V beams, as shown in Fig. 7, the SI varies from 0.9522 to 0.9619 in Plan A, 0.9222 to 0.9679 in Plan B, 0.8709 to 0.9676 in Plan C and 0.957 to 0.981 in Plan A0. Thus, LSA provides 4.78% to 3.81% higher, 7.78% to 3.21% higher, 12.91% to 3.24% higher and 4.3% to 1.9% higher left-end bending moment in Plan A, Plan B, Plan C, and Plan A0 respectively.
- In Category-II beams, as shown in Fig. 8, the SI varies from 0.963 to 1.084 in Plan A, 0.9640 to 1.7024 in Plan B and 0.9643 to 1.3452 in Plan C. Thus, LSA provides 3.7% higher to 8.4% lower, 2.6% higher to 70.24% lower, and 3.6% higher to 34.52% lower left end bending moment in Plan A, Plan B, and Plan C, respectively.
- In Category-I beams, as shown in Fig. 9, the SI varies from 3.48 to -11.087 in Plan A, -1.0937 to 4.8316 in Plan B and -10.209 to 36.9457 in Plan C. Thus, LSA provides 248% to 108% lower, 209.34% to 383.16% lower, and 110.209% to 3594.57% lower left end bending moment in Plan A, Plan B, and Plan C, respectively. CAT-I beams surrounding the RC shear walls were the most vulnerable and sensitive category among all categories.
- As the span increases, the sensitivity index decreases, i.e. the difference between the left end moment by the CSA method and LSA method in all categories of beams.
- In Plan A0, only three categories, CAT-III, CAT-IV and CAT-V, were observed. CAT-I and CAT-II, which were highly vulnerable, seem absent here. Hence RC shear walls increase sensitivity.
- The study of all the beams suggests that LSA provides 3.6% higher to 70.24% lower, 25% higher to 0.14% lower, 17% to 3.2% lower, and 12.91% to 1.9% higher left-end support bending moments in CAT-II, CAT-III, CAT-IV and CA-V, respectively.
- While left-end support moments of CAT-I behave very irregularly, the LSA provides 110% to 3594.57% lower right-end support bending moments.
- Hence, sensitivity varies from CAT-I to Cat-V in descending order while progressing from CAT-I to CAT-V in the case of left-end support moments. The most sensitive category is CAT-I.

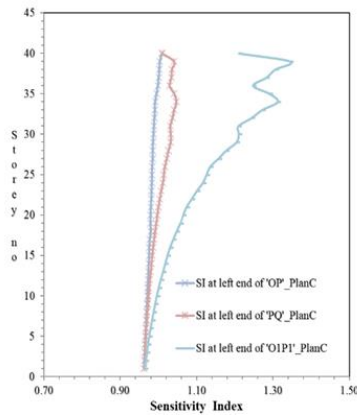
- Sensitivity of the left-end moment increases as storeys increase in all categories except CAT-I. In CAT-I beams of Plan A and Plan B models, the maximum variation in SI is at intermediate floors. Maximum variation in SI is at higher floors in CAT-I beams of the Plan C model.



(a) Plan A model

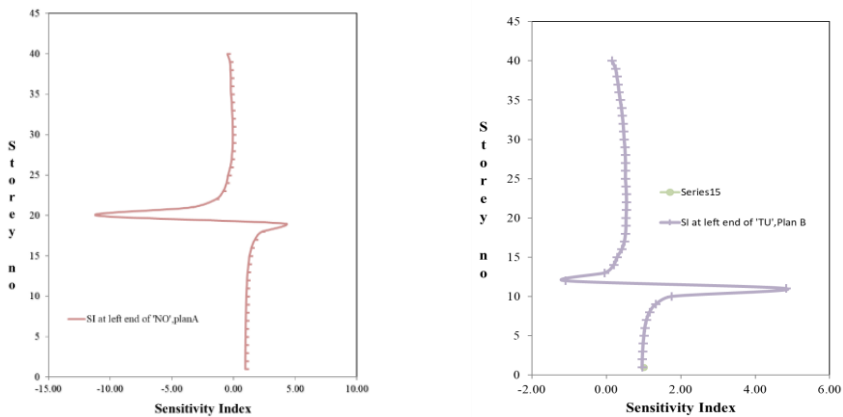


(b) Plan B model



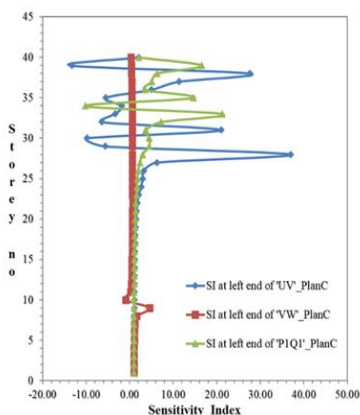
(c) Plan C model

Fig .8 Sensitivity graph at left-end support for beams of CAT II



(a) Plan A model

(b) Plan B model



(c) Plan C model

Fig. 9 Sensitivity graph at left-end support for beams of CAT I

Beams are presented with colour codes, as per their categories as shown in Fig. 10

3.3. Sensitivity Categories for Right-End Support Moments

A similar pattern of SI graphs was observed in the ‘sensitivity index of the right end moment V/S storey number for beams in all plans. All beams were divided into the same five categories, CAT I, CAT II, CAT III, CAT IV and CAT V. Beams of all plans as per their categories and sensitivity range are tabulated in Table 6. Fig. 11 shows a graph of ‘SI V/s storey number’ for CAT III, which was found critical for right-end support moments. Observations are listed below:

- The maximum to minimum SI range of right-end beam moments varies from 0.588 to 1.155, 0.8299 to 1.105, 00.89 to 62.97to -105.82, 0.8858 to 2.1149 and 0.8755 to 0.97966 in CAT-I, CAT-II, CAT-III, CAT-IV and CAT-V, respectively.
- LSA provides 42.29 % higher to 15.5% lower, 17.01% higher to 10.5% lower, 11.75% higher to 111.49% lower and 2.034% to 12.45% higher right-end support bending moments in CAT-I, CAT-II, CAT-IV and CAT-V, respectively.

Table 5. Range of Sensitivity Index of left end moments for all Categories

Categories of beams	Range of left end moment SI for various categories of beams of various plans					SI-Range amongst all models
	Plan A	Plan B	Plan C	Plan A0		
CAT-I	Beams	NO	TU	UV, P1Q1,VW	NA	LSA gives 110.21 % to 3594.57% lower
	SI-range	3.48 to -11.087 LSA gives 248%lower To 1087% lower BM	-1.0937 to 4.8316 LSA gives 209.34% lower to 383.16% lower BM	-10.209 to 36.9457 LSA gives 110.209% Lower to 3594.57% lower BM		
CAT-II	Beams	HI	OP, ST	O1P1, PQ, OP	NA	LSA gives 3.6%higher To 70.24% lower BM
	SI-range	0.963 to 1.084 LSA gives 3.7% higher to 8.4% lower BM	0.9640 to 1.7024 LSA gives 3.6% higher to 70.24% lower BM	0.9643 to 1.3452 LSA gives 3.6%higher to 34.52% lower BM		
CAT -III	Beams	AB, GH, MN	AB, GH, MN, RS	AB, GH, MN, M1N1, ST	AB,GH,MN	LSA gives 25% higher to 0.14% lower BM
	SI-range	0.8042 to 0.994 LSA gives 19.58% to 0.61% higher BM	0.78 to 1.0014 LSA gives 22% Higher to 0.14% lower BM	0.7724 to 1.006 LSA gives 22.76% higher to 0.6% lower BM	0.745 to 1.00 LSA gives 0 to 25.5% higher BM	
CAT -IV	Beams	BC	BC, HI, CD, NO, IJ	BC, HI, NO, CD,N1O1,IJ, DE, UT	BC,HI, NO	LSA gives 17% to 3.2% lower BM
	SI-range	0.930 to 0.9605 LSA gives 7% to 3.95% higher BM	0.8609 to 1.0165 LSA gives 13.91% higher to 1.65% lower BM	0.8478 to 1.0320 LSA gives 15.22% to 3.2% lower BM	0.830 to 0.977 LSA gives 17% to 2.3% higher BM	
CAT -V	Beams	CD,IJ	PQ, JK,DE	JK,EF,KL, QR,Q1R1	CD,OP,IJ	LSA gives 12.91% to 1.9% higher BM
	SI-range	0.9522 to 0.9619 LSA gives 4.78% to 3.81% higher BM	0.9222 to 0.9679 LSA gives 7.78% to 3.21% higher BM	0.8709 to 0.9676 LSA gives 12.91% to 3.24% higher BM	0.957 to 0.981 LSA gives 4.3% to 1.9% higher BM	

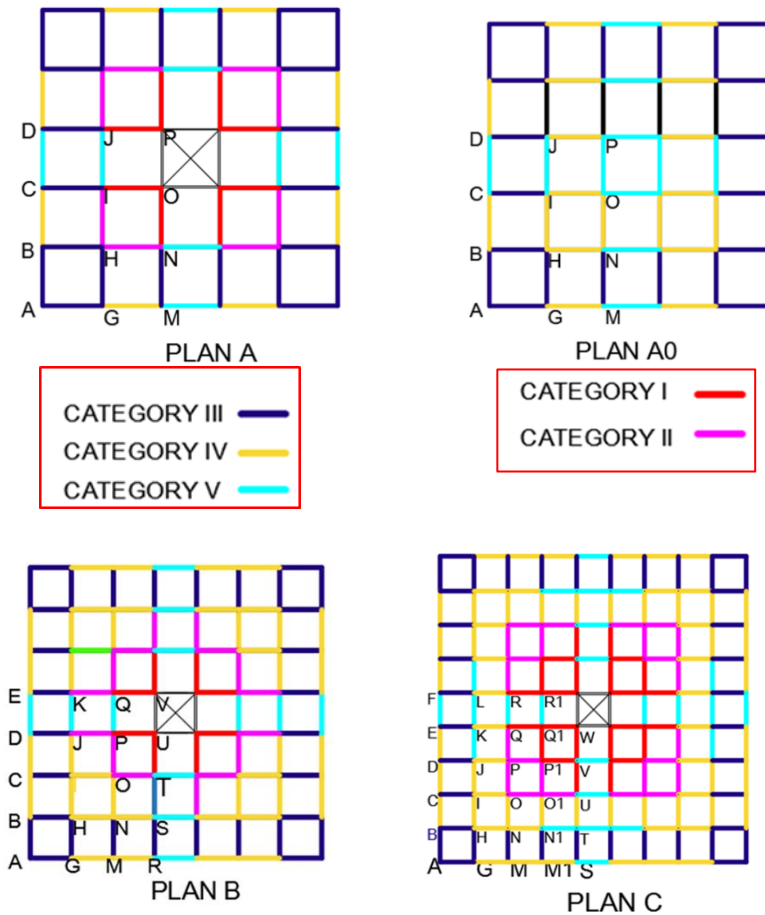
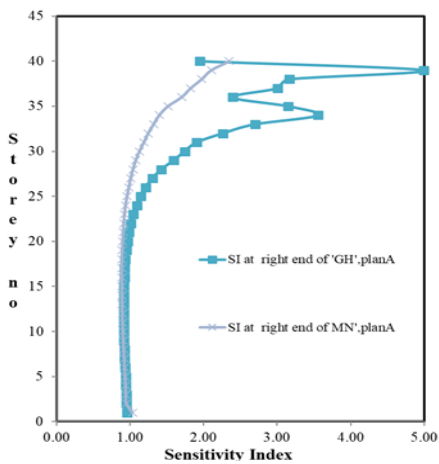


Fig. 10 Different categories of beams of Plan A, Plan B, Plan C and Plan A0 models

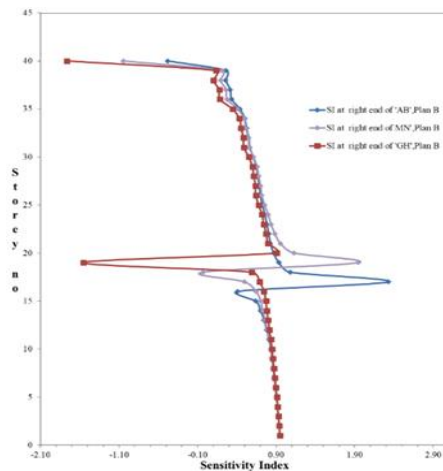
- While right-end support moments of CAT-III behave very irregularly. LSA provides 19.5775% higher to 6197 % lower right-end support moments. Hence sensitivity varies in descending order from CAT-V, CAT-II, CAT-I, and CAT-IV for right-end support moments. The most sensitive category is CAT-III.
- Sensitivity of the right-end moment increases as storeys increase in all categories except CAT-III. In CAT-III beams of Plan B, Plan C and Plan A0 models, the maximum variation in SI is at intermediate floors, while in the Plan A model, it is at higher floors.

A similar pattern of graphs with a similar range of SI was observed in the ‘sensitivity index of mid-span moment V/S floor number’ for beams in all plans. All beams were divided into the same four categories, CAT I, CAT II, CAT III and CAT IV. Beams of all plans as per their categories and range of sensitivity are tabulated in Table 7. While Fig. 12 shows a graph of ‘SI v/s storey number’ for CAT III, which was found very critical for mid-span moments. Observations are listed below:

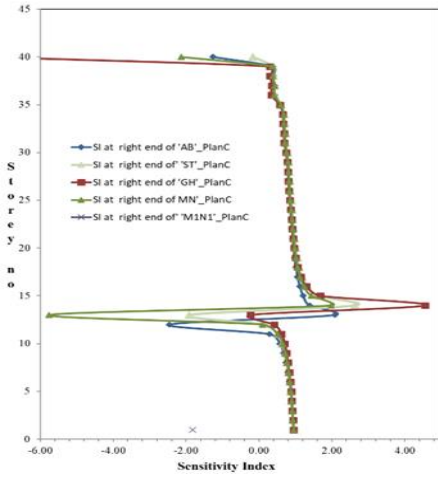
- The range of maximum to minimum SI of right-end beam moments varies from 0.3723 to 1.1435, 0.9047 to 1.0761, 0.2820 to 1.1016, 0.830 to 1.0745 and 0.957 to 1.4442 in CAT-I, CAT-II, CAT-III, CAT-IV and CAT-V, respectively.
- The LSA provides 9.53% higher to 7.58% lower, 17% higher to 7.45% lower and 4.3% higher to 44% lower mid-span bending moments in CAT-II, CAT-IV and CAT-V, respectively.
- While the range of mid-span moments of CAT-I and CAT-III was large, the LSA provides 62.77% higher to 14.35% lower and 71.8% higher to 10.16% lower mid-span moments in CAT-I and CAT-III beams, respectively. Hence the sensitivity of CAT-III was larger than CAT-I, CAT-IV, CAT-IV and CAT-II in descending order in the case of mid-span moments. The most sensitive categories were CAT-III and CAT-I, with CAT-I being the most sensitive.
- The sensitivity of the mid-span moment increases as storeys increase in all categories. However, significant variation was observed in the top 10 to 15% of the floors. In CAT-III beams, the SI remains constant up to 60% to 62.5%, 37.5% to 40%, 30% to 32.5% and 27.5% of floors in Plan A, Plan B, Plan C and Plan A0 models. The SI suddenly increases at a significantly higher range up to the top floor. The number of storeys up to which the SI graph remains constant also increases the span increases.
- In CAT-I beams, the SI remains constant up to 47.5%, 27.5% and 22.5% of floors in Plan A, Plan B and Plan C models. Later SI suddenly increases at a significantly high range up to the top floor. The number of storeys up to which the SI graph remains constant increases as the span increases.
- In this category of mid-span moments, as the span decreases, the sensitivity of beam moments increases in all categories of beams.



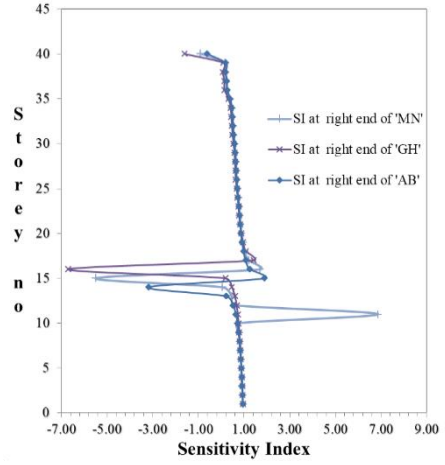
(a) Plan A model



(b) Plan B model

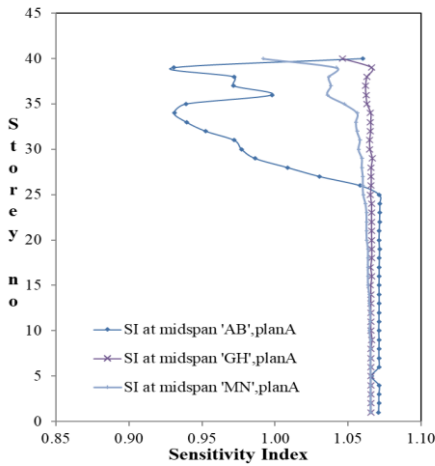


(c) Plan C model

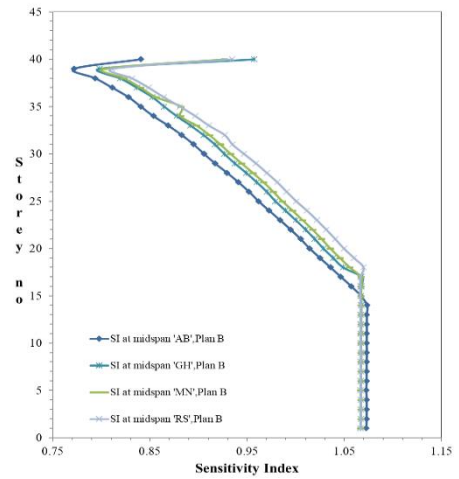


(d) Plan A0 model

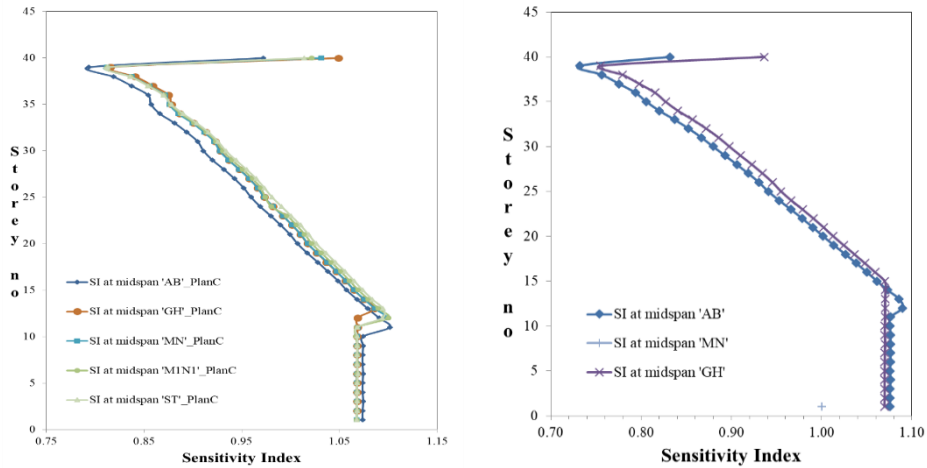
Fig. 11 Sensitivity graph at right-end support for beams of CAT III



(a) Plan A model



(b) Plan B model



(c) Plan C model

(d) Plan A0 model

Fig. 12 Sensitivity graph at mid-span for beams of CAT III

Table 6. Range of Sensitivity Index of Right End Moments for all Categories

Categories of beams		Range of right-end moment SI for various categories of beams of various plans				SI-Range amongst all models
		Plan A	Plan B	Plan C	Plan A0	
CAT-I	Beams	NO	TU	UV,P1Q1,VW		
	SI-range	0.67 to 0.96 LSA gives 33% to 4% higher BM	0.961 to 0.577 LSA gives 3.925% to 42.29% higher BM	0.588 to 1.155 LSA gives 41.2% higher to 15.5% lower BM	NA	LSA gives 42.29% higher to 15.5% lower BM
CAT-II	Beams	HI	OP,ST	O1P1,PQ,OP		
	SI-range	0.89 to 0.96 LSA gives 11% higher to 4% higher BM	0.955 to 1.105 LSA gives 4.473% higher to 10.5% lower BM	0.8299 to 0.974 LSA gives 17.01% higher to 2.58% higher BM	NA	LSA gives 17.01% higher to 10.5% lower
CAT -III Irregular	Beams	AB,GH, MN	AB,GH,MN,RS	AB,GH,MN, M1N1,ST	AB,GH, MN	
	SI-range	0.89 to 62.97 to -105.82	-0.47912 to 3.559 to -15.5379	4.5484 to -7.397	1.887 to 6.868 to -3.188	LSA gives 19.5775% higher to 6197% lower

		LSA gives 19.577% Higher to 6197% lower to BM	LSA gives 147.92%/1653.79% lower to 255.88% lower BM	LSA gives 354.84% lower to 839.72% lower BM	LSA gives 88.7 % lower to 586.8 % to 218.8% lower BM	
CAT -IV	Beams	BC	BC,HI,CD, NO,IJ	BC,HI,NO, CD,N1O1, IJ,DE, TU	BC,HI, NO	
		1.01 to 0.96	0.9585 to 1.28397	0.8858 to 2.1149	0.939 to 1.44	LSA gives 11.75% higher to 111.49 lower % BM
	SI-range	LSA gives 4% higher to 1% lower BM	LSA gives 7.15% higher to 28.397 % lower BM	LSA gives 11.75% higher to 111.49% lower BM	LSA gives 6.1 % higher to 44% lower BM	
CAT -V	Beams	CD,IJ	PQ, JK,DE	QR, Q1R1	CD, OP, IJ	
		0.95 to 0.96	0.92924 to 0.97966	0.8755 to 0.9676	0.958 to 0.981	LSA gives 2.034% higher to 12.45% higher BM
	SI-range	LSA gives 5% to 4% higher BM	LSA gives 7.076% to 2.034% higher BM	LSA gives 12.45% higher to 3.24% higher BM	LSA gives 4.2 % higher to 1.9% higher BM	

Table 7. Range of Sensitivity Index of Mid-Span Moments for all Categories

Categories of beams	Range of mid-span moment SI for various categories of beams of various plans					SI-Range amongst all models
	Plan A	Plan B	Plan C	Plan A0		
CAT -I	Beams	NO	TU	UV,P1Q1, VW		
		0.672265 to 1.064252	0.4189 to 1.0688	0.3723 to 1.1435	NA	LSA gives 62.77% higher to 14.35% lower BM
	SI-range	LSA gives 32.77% higher to 6.4252% lower BM	LSA gives 58.11% higher to 6.88% lower BM	LSA gives 62.77% higher to 14.35 % lower BM		
CAT-II	Beams	HI	OP,ST	O1P1,PQ,OP	NA	

CAT -III	SI-range	1.042581 to 1.066484	0.9047 to 1.0758	0.9446 to 1.0761		LSA gives 9.53 % higher to 7.58% lower BM
		LSA gives 6.6484 % lower to 4.2581% lower BM	LSA gives 9.53% higher to 7.58% lower BM	LSA gives 5.54 % higher to - 7.61 % lower BM		
	Beams	AB,GH, MN	AB,GH, MN,RS	AB,GH,MN, M1N1,ST	AB,GH MN,	
		0.930755 to 1.0718	0.7718 to 1.0734	0.2820 to 1.1016	0.745 to 1.00	LSA gives 71.8% higher to 10.16% lower BM
	SI-range	LSA gives 6.9245% higher to 7.18637% higher BM	LSA gives 22.82% higher to 7.34% lower BM	LSA gives 71.8% higher to 10.16% lower BM	LSA gives 0 to 25.5% higher to BM	
		Beams	BC	BC,HI,CD, NO,IJ	BC,HI,NO, CD,N101, IJ, DE, TU	BC,HI, NO
SI-range	1.040438 to 1.0718736		0.9949 to 1.0736	0.9737 to 1.0745	0.830 to 0.977	LSA gives 17% higher to 7.45% lower BM
	Beams	4.044% less to 7.18736% higher BM	LSA gives 0.51% higher to 7.36% lower BM	LSA gives 2.63 % higher to 7.45% lower BM	LSA gives 17% to 2.3% higher BM	
CAT -IV		SI-range	CD,IJ	PQ, JK, DE	JK,EF,KL, QR,Q1R1	CD,OP,IJ
	1.066 to 1.086		1.068 to 1.146		0.957 to 0.981	LSA gives 4.3% higher to 44% lower BM
CAT -V	SI-range	LSA gives 6.58% lower to 8.61% lower BM	LSA gives -6.75% lower to - 14.59% lower BM	LSA gives 5.76% lower to 44.42% lower BM	LSA gives 4.3% To 1.9% higher BM	

4. Conclusion

The study concludes:

- Building models of various spans are divided into five different sensitivity categories as per the behavioural patterns of the beams.
- In the case of left end beam moments, CAT-I beams surrounding the RC shear walls are the most vulnerable among all categories. The sensitivity varies from CAT-I to Cat-V in descending order while progressing from CAT-I to CAT-V in case of left-end support moments. The sensitivity of the left-end moment increases as storeys increase in all categories except CAT-I. In CAT-I, the beams of Plan A and Plan B models, the maximum variation in SI is observed at intermediate floors. While in CAT-I beams of the Plan C model, maximum variation in SI is observed at higher floors.
- The sensitivity varies in descending order from CAT-V, CAT-II, CAT-I, and CAT-IV in the case of right-end support moments. The most sensitive category is CAT-III. The sensitivity of the right-end moment increases as storeys increase in all

categories except CAT-III. In CAT-III beams of Plan B, Plan C and Plan A0 models, the maximum variation in SI occurs at intermediate floors. While in CAT-III beams of the Plan A model, the maximum variation in SI is observed at higher floors.

- The sensitivity of CAT-III is larger than CAT-I, CAT-IV, CAT-IV and CAT-II in descending order in the case of mid-span moments. The most sensitive categories are CAT-III and CAT-I, with CAT-I being the most sensitive. The sensitivity of the mid-span moment increases as storeys increase in all categories. However, significant variation is observed in the top 10% to 15% of floors in CAT-I. In CAT-III beams, the SI remains constant up to 60% to 27.5% of the total storey in various plan models, and in CAT-I beams, the SI remains constant up to 47.5% to 22.5% of the total storey in various plan models. Later the SI suddenly increases at a significantly high range up to the top floor. As the span increases, the number of storeys up to which the SI graph remains constant also increases.
- After studying all the beams, it is observed that LSA provides 3.6% higher to 70.24% lower left-end support bending moments in CAT-II, CAT-III, CAT-IV and CAT-V, respectively. While left-end support moments of CAT-I behave very irregularly, the most sensitive category is CAT-I in the case of left-end support moments.
- LSA provides 42.29% higher to 111.49% lower right-end support bending moments in CAT-I, CAT-II, CAT-IV and CAT-V. In contrast, right-end support moments of CAT-III behave very irregularly. Hence the most sensitive category is CAT-III.
- LSA provides 17% higher to 44% lower mid-span bending moments in CAT-II, CAT-IV and CAT-V. At the same time, the range of mid-span moments of CAT-III and CAT-I behave very irregularly.
- In Plan A0 type building models, only three categories, CAT-III, CAT-IV and CAT-V, are observed. CAT-I and CAT-II, which are highly vulnerable, seem absent here. Hence, the RC shear walls increase sensitivity.
- As span decreases, the sensitivity of beam moments increases in all categories of beams.

The study concludes that it is advisable to use the CSA method considering the effects of concrete's time-dependent properties when designing RC moment-frame high-rise buildings.

5. Limitations of the Study

The study is undertaken for symmetrical RC frame high-rise buildings considering a construction cycle of seven days with an occupancy period of 90 days in the CSA method. Analysis and design are undertaken as per the Indian standard code of practice.

Acronym

CSA: Construction Sequence Analysis considering creep and shrinkage.

LSA: Linear Static Analysis Method.

SI: Sensitivity Index.

Plan A, Plan B: RC building model of plan A, plan B, etc.

RC: Reinforced Concrete.

CAT: Category.

BM: Bending Moment

References

- [1] Afshari MJ, Kheyroddin A, Gholhaki M. Simplified sequential construction analysis of buildings with the new proposed method. *Structural Engineering and Mechanics*, 2017; 63(1), 77-88.
- [2] Casalegno C, Sassone M, Chiorino MA. Time-Dependent Effects In Cable-stayed Bridges Built by Segmental Construction, Proc. of Third International fib Congress incorporating the PCI Annual Convention and Bridge Conference. Washington DC, 2010.
- [3] Chakrabarti SC, Nayak GC, Agarwala SK. Effect of sequence of construction in the analysis of multistoreyed building frame. *Building and Environment*, 1978; 13(1), 1-6. [https://doi.org/10.1016/0360-1323\(78\)90002-1](https://doi.org/10.1016/0360-1323(78)90002-1)
- [4] Choi CK, Chung HK, Lee DG, Wilson EL. Simplified building analysis with sequential dead loads-CFM. *Journal of Structural Engineering*, 1992;118(4),944-954. [https://doi.org/10.1061/\(ASCE\)0733-9445\(1992\)118:4\(944\)](https://doi.org/10.1061/(ASCE)0733-9445(1992)118:4(944))
- [5] [https://ascelibrary.org/doi/abs/10.1061/\(ASCE\)0733-9445\(1993\)119%3A7\(2274\)](https://ascelibrary.org/doi/abs/10.1061/(ASCE)0733-9445(1993)119%3A7(2274))
- [6] Correia R, Lobo PS. Simplified assessment of the effects of columns shortening on the response of tall concrete buildings. *Procedia Structural Integrity*, 2017; 5, 179-186. <https://doi.org/10.1016/j.prostr.2017.07.095>
- [7] Desai NM, Vaswanala S. Influence of time period and derivation of critical storey limit for RC frame buildings using construction sequence method of analysis. *Res. Eng. Struct. Mater.*, 2023; 9(1): 195-208. <https://doi.org/10.17515/resm2022.414st0309>
- [8] Desai N, Vaswanala S. Comparative study of modified construction stage analysis and construction stage analysis for RC buildings., *Proceedings of International Structural Engineering and Construction*, 2022; 9:1 ISEC Press. [https://doi.org/10.14455/10.14455/ISEC.2022.9\(1\).STR-61](https://doi.org/10.14455/10.14455/ISEC.2022.9(1).STR-61)
- [9] Desai N, Vaswanala S. Influence of timespans on construction sequence analysis of RC buildings., *Proceedings of International Structural Engineering and Construction*, 2022; 9:1 ISEC Press. [https://doi.org/10.14455/10.14455/ISEC.2022.9\(1\).STR-71](https://doi.org/10.14455/10.14455/ISEC.2022.9(1).STR-71)
- [10] Dinar Y, Rasel MM, Chowdhury MJA, Ashraf MA. Chronological construction sequence effects on reinforced concrete and steel buildings. *the International Journal of Engineering and Science (IJES)*, 2014; 3(1), 52-63.
- [11] Dubey A, Bhadauria SS. Comparative analysis of a 50 Storey RCC Frame with shear wall for conventional loading and construction sequence loading. *International Research Journal of Engineering and Technology (IRJET)*. 2017;4(5):1419-24.
- [12] Elansary AA, Metwally MI, El-Attar A. Staged Construction Analysis of Reinforced Concrete Buildings with Different Lateral Load Resisting Systems, *Engineering Structures*, 2021; 242, p.112535. <https://doi.org/10.1016/j.engstruct.2021.112535>
- [13] Ha T, Kim S, Lee S. Prediction of time-dependent lateral movement induced by differential shortening in tall buildings using construction stage analysis. *International Journal of High-Rise Buildings*, 2017; 6(1), 11-19. <https://doi.org/10.21022/IJHRB.2017.6.1.11>
- [14] IRC:112, Code of Practice for Concrete Road Bridges, Indian Roads Congress. New Delhi, 2011.
- [15] Kwak HG, Kim JK. Time-dependent analysis of RC frame structures considering construction sequences. *Building and Environment*, 2006;41(10), 1423-1434. <https://doi.org/10.1016/j.buildenv.2005.05.013>
- [16] MIDAS Gen software Engineering Manual: Integrated Solution System for Building and General Structures; available from the URL: http://en.midasuser.com/product/gen_overview.asp
- [17] Secer M, Arslan T. Effects of Construction Sequence on Reinforced Concrete Building Analysis. In *International Conference on Numerical Modelling in Engineering* pp. 123-134). Springer, Singapore 2018. https://doi.org/10.1007/978-981-13-2405-5_10

- [18] Zucca M, Longarini N, de Socio F, Migliori I. Construction stage analysis for a new mixed structure building in Milan. *International Journal of Structural Glass and Advanced Materials Research*, 218; 2(1), 66-72.
<https://doi.org/10.3844/sgamrsp.2018.66.72>
- [19] Vishal N, Kannan MR, Keerthika L. Seismic Analysis of Multi-Storey Irregular Building with Different Structural Systems. *Int. J. of Recent Tech. and Eng.* 2020; 8(6):3146-55.
<https://doi.org/10.35940/ijrte.F8813.038620>

Blank Page



Research Article

Predicting strength of concrete by ensemble technique

Monali Kirange^{a,1}, Lomesh Mahajan^{*,b,2}

¹Department of Computer Engineering, RCPET's IMRD, Shirpur, 425405, India

²Department of Civil Engineering, R. C. Patel Institute of Technology, Shirpur, Affiliated to Dr. Babasaheb Ambedkar Technological University, Lonere, India

Article Info

Abstract

Article history:

Received 03 Jan 2023

Accepted 03 Feb 2023

Keywords:

Compressive strength;

Cement;

Concrete;

Ensemble technique;

Decision Tree.

The developing countries share similar attributes at all the regions. Still 43% of urban population did not escape from slums live hoods. As many developing countries focuses on the infrastructural development and try to improve people living standards. This infrastructural built-up activity consumes lots of concrete and other construction materials. These construction materials possess different properties from place to place. Cementitious composites undergo transformations in their fundamental properties due to regional variations in environmental conditions. Therefore, their mechanical strength computing tools plays crucial role. When topic touches with concrete, one of the most important characteristics is the compressive strength. Predicting the strength of concrete has traditionally been done with using mechanical means, but in recent years few soft computing methods have become important tools. In this research, we apply two methods to compute the Compressive strength of fly ash concrete based on the results of our own experimental findings. To anticipate concrete strength, this study investigated the properties of all the materials involved. The ensemble methodology and the decision tree were two of the success-forecasting methodologies that were investigated, and comparative assessments were made on them. The R^2 value for the ensemble methodology was determined to be 0.96, which was much higher than the DT method's 0.76. In addition to k-fold Cross Validation, the findings of the trials are further supported by assessments of root mean square error (RMSE) and root mean error (RME). Ensemble approaches are good for minimizing model variance, improving prediction accuracy. Combining many models to make a single forecast from all their potential predictions eliminates variation.

© 2023 MIM Research Group. All rights reserved.

1. Introduction

Concrete's strength, durability, resilience, and adaptability make it a go-to material for a broad range of building projects. This remarkable substance is put to use in the production of a broad variety of buildings, roads, and walkways. During building, concrete is employed for its strength, longevity, and adaptability. These superior qualities have made concrete the material of choice for both commercial and residential building projects because to its dependability and widespread application in the building trade. Standard concrete consists primarily of cement, water, and rocks and gravel of varying sizes [1-3]. Greenhouse gases (GHG) are mostly caused by the cement manufacturing process and huge incorporation in concrete infrastructure [4]. When it comes to CO₂ emissions, the cement industry is among the worst offenders [5]. If four billion tonnes of cement are produced per year, the same quantity of CO₂ pollutant is also discharged into the environment [6]. Making use of waste or repurposed materials is suggested to lessen this effect [7]. Reduced concrete use has further environmental benefits [8]. Many types of industrial waste

*Corresponding author: loms786@gmail.com

^a orcid.org/0000-0003-3310-6832; ^b orcid.org/0000-0002-8275-170X

DOI: <http://dx.doi.org/10.17515/resm2023.632me0103>

Res. Eng. Struct. Mat. Vol. 9 Iss. 3 (2023) 1039-1060

products (e.g. G G B S, Granite Powder, Fly Ash (F) [9]) can be used as a cement substitute. Hardened concrete will benefit from these additional raw materials and, simultaneously, lower its carbon footprint by as much as 80 percent without sacrificing quality.

In the process of mix design, the compressive strength (C.S) is regarded as one of the most important qualities and study of concrete structures. Additives, such as chemical or mineral admixtures, can be added to concrete either before or after it sets to improve its basic components. The quality of concrete can be affected by the cementitious mixes used [10]. Lab tests of concrete's strength are necessary for every project [11]. Concrete factories have a hard time with strength prediction because of this. In ancient times [12], the strength became an important criterion for heterogeneous building. Due to worldwide standards and sustainable development, the mineral additives used for making concrete found key role in the environment [13]. Fly ash, a sustainable substance, can be used as a dependable substitute for cement in renovations, alterations, and major building projects. Concrete's mechanical and rheological properties are enhanced [14].

It is not easy to strike a balance between cost and quality when considering the quantity of each suitable concrete material to use, as determining the C.S of concrete takes a lot of time and work. Scientists have spent the better part of a decade creating artificial methods for picking the most effective strength prediction techniques [15] to help them save time and money in the lab. Complex concrete mixtures are difficult to locate and predict. The C.S of concrete is determined in the laboratory by breaking cylinders and conventional cubes after they have been cast for a specified period of time [16]. This method's application has reached a plateau of near-universal acceptance. However, laboratory testing will certainly be expensive and time-consuming. It takes a lot of time and money to set up apparatus and conduct tests on specimens using the conventional, established laboratory methods.

Recently, researchers have been putting a lot of effort into developing prediction scenarios for a variety of mechanical features in concrete with the use of tearing technologies like artificial intelligence (AI) and machine learning (ML) [15,17]. Using methods such as supervised learning, it is possible to estimate a great many parameters (W/C, SCBA%, FA, CC, CA), although with varying degrees of accuracy in the regression, classification, clustering, and reinforcement learning [22].

2. Machine Learning [ML] Overview

The primary focus should be placed on the development of prediction algorithms for machine learning, the most sophisticated kind of AI. This is due to the fact that several patterns in large datasets can be objectively recognized in order to carry out a certain task. This artificial zone, labelled Intelligence, is what gives computers the ability to perform the intricate and laborious activities that would otherwise be impossible for them to do. Tasks that tested the robots' precision and difficulty. Through a series of computational procedures, we were able to create a programme that, rather than having to be explicitly programmed to recognize patterns, could infer them automatically from the available data. These algorithms outperform human-written code because they have independently learned logics from the data at hand. These algorithms are the product of computational learning theory, which permits the acquisition of data-point-specific properties necessary for the interpretation of knowledge and the rapid generation of solutions from any number of publicly available datasets. It is possible to employ extra image data in conjunction with an algorithm that has been trained to distinguish between benign and malignant lesions on imaging.

As can be seen in Fig. 1, the AI subfields are structured in a hierarchical fashion. A few broad classifications for ML models are provided below. The ML phylogenetic trees can be

broken down into several distinct groups. The ML are known as Supervised Learning, Unsupervised Learning, and Reinforcement Learning.

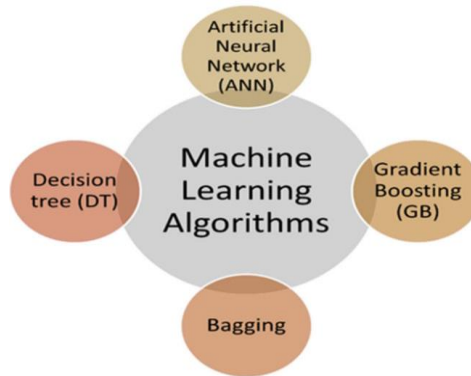


Fig. 1 AI's subfields

Popular and widely used approaches to supervised machine learning include the decision tree, boosting, S V M, AdaBoost, bagging, ANNs, and gene expression modulation. For unsupervised learning, the available datasets are often quite limited for the output labels are scant or nonexistent in several cases. The purpose of these models is rather to determine the interrelationship and/or expose the dormant parameters based on the findings.

3. Literature Review

Ensemble techniques are a kind of statistical and numerical learning approach that mimics the human interpersonal learning behavior of polling a group of experts before reaching a major decision. To improve the accuracy and reliability of their recommendations in supervised and unsupervised learning situations, ensembles integrate the judgements, learning algorithms, perspectives on the data, and other features of several learning machines. A N N, G E P, and deep learning are now popular developments technology utilized for predicting a wide range of scientific issues [23, 24]. Specifically, S V M is more robust in nonlinear regression settings than other approaches [25]. It has high generalizability and may provide better global optimal solutions. Despite having a tree-like form and using nodes and roots to distribute data, the results of the prediction [26] differ from the Decision tree (D-T) and Random Forest (R-F). While R-F relies on a randomized sampling of unique particulars among the elements that build the trees used for projection, DT makes use of an extensive database that includes the variable of interest to it. The next step is to prove that the mean prediction is right by tying it to as many votes as feasible. Using inspiration from Darwinian evolution, GEP, a cutting-edge M-L computer algorithm, was created [27]. It achieves this by using an expression tree to depict the connection's non-linearity. Machine learning (ML) techniques are often used to glean previously unknown patterns, data points, and connections from a massive repository of information. Despite this, the process employs databases, machine learning, and statistical analysis. There are two unique techniques that may be used for both modelling and prediction. For one, there is the time-honored, single-model approach; for the other, there is the ensemble-algorithm technique [28]. Evidence from the first studies of these methods shows that, relative to solo ML models, ensemble procedures improve accuracy [29]. With the use of

the training data, ensemble learning models first perfect the weaker/slower learners, and then merge them with the stronger/faster learners to create a perfect learner [30].

Several machine learning techniques have been utilized for performance prediction over a wide range of criteria for quite some time. However, throughout the course of the last several years, a clear trend toward a larger usage of them in engineering field has emerged. Because of the high accuracy with which they predict property values (mechanical). Since nonlinear behavior is more accurate than linear behavior, the underlying theory of ML is identical to that of conventional algorithms. Statistical methods such as ANN, the decision tree algorithm D-T, support vector machines SVM, R-F, GEP, and D-L, and others are extensively used in the evaluation of perceptible mechanical qualities [31]. To compute the shear strength of concrete beams, the study by [32] used 11 distinct methods. Study [33] used ANN in tandem with the multi-objective grey wolves optimizer to forecast the mechanical properties of silica fume concrete with high precision. C.S estimates for concrete were calculated using D-T, ANN, and SVM by the researcher [34].

Utilizing an ANN system, researcher [35] determined the C.S and tensile strength of discarded concrete. Concrete C.S was estimated [36] using SVM, and outcomes were contrasted to those obtained using ANN and DT models in coastal situations. To foretell the durability of lightweight foamed concrete, Researcher [37] used a number of machine learning techniques. One study [38] used a machine learning technique to identify a reinforced concrete durability feature. Suguru. [39] used machine learning to create a robotic system for detecting cracks in concrete. Images of the concrete were utilized for data collection, and deep learning was put to use to spot the cracks. Accuracy of machine learning models is evaluated by researchers [40,41].

There is a lot of variability in the testing model, and one way to deal with it is via an ANN [42]. The broad use of ANN in C.S prognosis has received support from many academics. The feed forward ANN classification (multilayer perception), consists of 03 layers: Input, hidden, and output (MLP). For the power prediction model, these more traditional neural nodes are more convenient to operate with [43, 44]. For the objective of foretelling the C.S of fly ash concrete mixes, this research makes use of a variety of categorical criteria. The goal is to make it easier to create a universal M-L model that can capture a broad range of mixture characteristics. In furthermore, the models will use a wide range of Fly Ash concrete mixtures rather than only using the results of earlier studies. Since a cement composite's primary function as a construction material is compression, its mechanical strength is prized above all others. Studies have shown that ordinary compressive strengths are within the range of 25 to 115 MPa [45-49, 72]. Generative ensemble approaches, on the other hand, produce groups of base learners that manipulate the base supervised learning or the data frame structure to enhance the base learners' variety and performance. In this situation, the fundamental problem with the ensemble method is not the mixing approach, but rather the manner in which various base learners are generated. Methods such as resampling, which divide the input space and train base learners on bootstrap samples reproduces of the data; random subspace algorithms, which produce diversified base learners by using varying random selection sub-sets of features; and combination of experts methods, which divide the input space and train an ensemble of neural networks to conduct an impactful estimation at each assigned territory separately, are all examples.

Table 1. Trends of adopting soft computing techniques for the prediction of various terms

Sr No	Reference and Year	Algorithm and Method adopted by Researchers	Dataset Used	Output (Prediction Parameter)	alternative mineral admixture used)
1	Researcher [50]	Convolutional Neural Network Regression (CNN), Ensemble Regression models	345	Compressive Strength (C-S)	sludge-cement
2	Researcher [51]	A N N, G E P, and Gradient boosting tree (GBT) models	232	C-S	demolition waste
3	Researcher [52]	support vector regression (SVR), grid search (GS) optimization algorithm,	559	C-S	Not Used
4	Researcher [53]	ensemble deep neural network models	270	C-S	Fly ash
5	Researcher [54]	(BPNN), (MARS), (RVM)	629	C-S	Not Used
6	Researcher [55]	ensemble algorithm (GEP, DT and Bagging)	270	(C-S)	Fly ash
7	Researcher [21]	Individual and ensemble modelling (A N N, bagging and boosting)	1030	C-S	Fly ash
8	Researcher [18]	Individual algorithm (A N N, GEP, D-T)	642	Chloride Concentration	Fly ash
9	Researcher [56]	Data Envelopment (DEA)	114	C-S	Fly ash
10	Researcher [57]	Multivariate (MV)	21	C-S	Crumb Rubber
11	Researcher [58]	Support vector machine (S V M)	25	C-S	Fly Ash
12	Researcher [59]	SVM	115	Slump Value, L-box	Fly Ash
13	Researcher [60]	Adaptive neuro fuzzy inference system (ANFIS-ANN)	7	C-S	POFA
14	Researcher [20]	Gene expression programming (GEP)	277	Axial Capacity	Not Used
15	Researcher [61]	G E P	357	C-S	Not Used
16	Researcher [62]	R-F and G E P	357	C-S	Not Used
17	Researcher [63]	A N N	205	C-S	Fly Ash, GGBFS, SF, RHA
18	Researcher [64]	Intelligent rule enhanced multiclass SVM and fuzzy rules (IREMSVM-FR)	114	C-S	Fly Ash
19	Researcher [65]	R-F	131	C-S	Fly ash, GGBFS
20	Researcher [66]	M A R S	114	C-S, Slump value	Fly ash
21	Researcher [67]	Random Kitchen Sink Algorithm (RKSA)	40	C-S, Slump value, V-funnel	Fly Ash
22	Researcher [68]	Adaptive neuro fuzzy inference system (ANFIS)	55	C-S	Not Used
23	Researcher [69]	A N N	114	C-S	Fly Ash
24	Researcher [70]	A N N	69	C-S	Fly Ash
25	Researcher [71]	ANN, DT, GEP	100	C-S	Fly Ash

4. Research Significance

Since the turn of the century, computer technologies have become more efficient, reducing the need for laborious manual labor. There are fewer validations at civil engineers' disposal in this burgeoning sector of transdisciplinary domain utilization. The little literature on ANN strategies and their application to C.S. prediction. Through the use of cutting-edge ML techniques, costly manual labor in the lab and expensive raw materials may be avoided. This study's significance and novelty stem from (a) its novelty and (b) its applicability to current issues, such as the ASTM's experimental works for fly ash concrete (FAC) (c) using ML methods for FAC model development.

This research focuses on ML (discrete-event neural network) and boosting techniques for making predictions of strength. The use of concrete that contains fly ash was explored during the whole experimental procedure. Actual results were predicted and compared using ML. Quality of these findings provided by various ML algorithms and their applicability. This research also gives a means of comparing and evaluating the results of experiments conducted using individual and ensemble ML approaches. Both statistical tests and k-fold performance models were evaluated for cross-validation [71]. The purpose of this analysis is to look at how different inputs affect the reliability of the expected output. Such applications were utilized to evaluate the predictive efficacy of different approaches.

5. Experimental Program

The fundamental components of concrete have been thoroughly analyzed in accordance with IS Code and ASTM standards. Experiments were conducted using Type-1; 53Grade cement (Ordinary Portland). For both the cement utilized and the studies conducted, the standard specifications indicated by ASTM C150 were taken into account. Cement bags had airtight polythene coverings placed on top of them to prevent the bags from absorbing moisture from the air. Table 2 and Table 3 provide the chemical and physical characteristics of fly ash and cement, respectively.





Fig. 2 shows a glimpse of experimental work that were subjected to compressive testing

The fine aggregate's quality was determined by testing that met the requirements of the ASTM standard. Coarse aggregates with a standard thickness of less than 20 mm were sourced locally and used into the fresh concrete that was formulated to meet ASTM standards. Coarse Aggregate (CA) and Fine Aggregate (FA) physicochemical parameters are listed in Table 4. (Fa).

Table 2. Physical Analysis of cement (C)and fly ash (F)

Sr No	Material	Property	Measured Unit	Obtained Value
1	C	Specific surface area	Cm ² /gm	8299
2	C	Specific Gravity	gm/cm ²	3.1
3	C	Insoluble residue	Percent	0.5
4	C	Particle Size	µm	1.65
5	C	Loss of Ignition	Percent	2.29
6	F	Retention on 45-micron Sieve	Percent	33
7	F	Lime Reactivity	N/mm ²	7
8	F	Soundness test using Autoclave Expansion	Percent	0.06
9	F	Drying Shrinkage	Percent	0.05
10	F	C.S compare to cement mortar cube	Percent	81

Table 5 summarizes the results of the tests performed on the different mix proportions (a, b, c). Specimens with a diameter of 100mm and a height of 200mm were cast with a w/c of 0.4 - 0.6. the specimens were cured at 27 degrees Celsius for 3, 7, 14, 28, and 90 days. The C.S. performed to ASTM C39 standards after curing properly. To achieve the desired mix workability attribute, the hit-and-trial approach was examined with the superplasticizer dosage. Fig. 2 is a view inside laboratory procedures.

Table 3. Chemical Analysis of fly ash (F) and cement (C)

Sr No	Chemical Compound	C	F
1	Calcium Oxide-(CaO)	65.82	2.35
2	Iron Oxide-(Fe ₂ O ₃)	3.63	26.87
3	Silica-(SiO ₂)	18.99	50.9
4	Alumina-(Al ₂ O ₃)	6.94	4.27
5	Magnesium Oxide -(MgO)	1.98	1.52
6	Sodium Oxide-(Na ₂ O)	0.10	0.11
7	Potassium Oxide- (K ₂ O)	0.45	1.47

Table 4. Physical Analysis of Coarse Aggregate (C-a) and Fine Aggregate (F-a)

Sr No	Aggregate Type	Property	Measured Unit	Result	Standards Followed
1	C-a	Bulk Sp. Gr.	No Unit	2.75	ASTM C128, C127
2	F-a	Bulk Sp. Gr.	No Unit	2.65	ASTM C128, C127
3	C-a	Moisture Content	Percent	0.75	ASTM C566
4	F-a	Moisture Content	Percent	1.10	ASTM C566
5	C-a	Moisture Absorption	Percent	1.40	ASTM C128/ C127
6	F-a	Moisture Absorption	Percent	1.10	ASTM C128/ C127
7	C-a	Fineness Modulus	No Unit	-	ASTM C136
8	F-a	Fineness Modulus	No Unit	2.45	ASTM C136
9	C-a	Nominal Maximum Size	Mm	20	-
10	F-a	Nominal Maximum Size	Mm	4.70	-
11	C-a	Rodded Unit Weight	kg/m ³	1580	ASTM C29
12	F-a	Rodded Unit Weight	kg/m ³	-	-

Table 5a. Mix proportions conducted of specimens (sr. no 1 to 33)

Sample no	Cement (kg/m ³ .)	Fly Ash (kg /m ³ .)	Water (kg/m ³ .)	Superplasti cizer (Kg/m ³ .)	Coarse aggregate (kg/m ³ .)	Fine aggregate (kg /m ³ .)	Curing Period (days)	CS (N/mm ²)
1	185.5	102	166.6	7.7	1009.5	908.5	90	39.4
2	170.5	127.9	161.5	8	1093.1	801.6	3	18.23
3	180.5	127.9	165.8	8	1093.1	801.7	14	24.46
4	160.5	127.9	161.8	8	1093.1	807.1	28	28.53
5	241.9	126.1	184	5.9	1060.7	782.4	14	23.03
6	211.9	126.1	183.9	5.9	1060.7	782.4	28	22.93
7	211.9	125.1	183.9	5.9	1060.7	782.4	56	34.33
8	239.8	118.8	191.6	4.8	1032.5	761.7	90	33.43
9	195.1	124.7	160.5	10.1	1091.2	805.7	3	10.61
10	190.5	124.7	161.6	10.1	1091.2	805.7	14	24.22
11	167.9	168.8	172.1	4.7	1061.7	783.2	3	12.9
12	135.9	163.8	176.2	4.7	1061.7	783.2	14	28.61
13	165	161.8	172.1	4.7	1061.7	783.2	28	26.32
14	230.4	118.7	194.9	6.3	1031.2	760.7	3	16.59

15	228.5	119.7	191	6.3	1031.2	760.7	14	22.43
16	229.5	118.7	194.9	6.3	1031.2	760.7	90	43.49
17	247.9	94.6	186.4	7.2	953	850.1	3	22.55
18	237.9	92.6	188.4	7.2	953	850.1	14	27.72
19	247.9	92.6	186.4	7.2	953	850.1	90	48.95
20	250.3	96.2	187.1	5.7	960	864.3	3	13.9
21	250.8	96.2	186.2	5.7	960	864.3	14	28.52
22	212.3	125.4	158.7	8	1088.5	802.6	3	19.54
23	212.4	125.2	181.6	6	1031.5	760.8	14	32.04
24	251.6	124.7	188.2	6.6	1031.5	813.8	56	36.02
25	251.7	123.3	181.3	6.6	1031.5	760.8	90	46.32
26	181.6	123.3	169.3	7.8	1058.7	813.8	3	15.73
27	181.6	123.3	170.3	7.8	1058.7	813.8	14	24.05
28	181.6	123.3	169.3	7.8	1058.7	780.9	28	29.91
29	182.3	124.9	170.3	7.8	1058.7	780.9	56	38.89
30	181.2	122.3	169.3	7.8	1058.7	780.9	90	47.89
31	249.9	125.3	168	9.6	964.3	868.1	90	47.11
32	229.9	125.3	160.3	12	977	878.7	3	23.23
33	220.6	125.3	145.8	12.6	1009.1	902.9	28	32.86
34	210.6	125.3	143	12.2	1089.9	804	56	63.67
35	220.6	125.2	140.8	12.2	1089.9	804	90	63.44
36	213.5	125.2	154.5	10.4	1056.6	779.5	28	44.27
37	213.5	125.3	154.7	10.4	1056.6	779.5	56	48.26
38	213.5	125.3	154.5	10.4	1056.6	779.5	90	55.21
39	213.3	125.3	155.3	11.9	1055.4	778.6	3	20.76
40	213.3	125.3	154.3	11.9	1055.4	803.1	14	38.1

Table 5b. Mix proportions conducted of specimens (sr. no 34 to 66)

Sample no	Cement (kg/m ³ .)	Fly Ash (kg /m ³ .)	Water (kg/m ³ .)	Superplasti cizer (Kg/m ³ .)	Coarse aggregate (kg/m ³ .)	Fine aggregate (kg /m ³ .)	Curing Period (days)	CS (N/mm ²)
41	213.3	125.3	155.4	11.9	1055.4	803.1	28	43.56
42	213.3	125.3	154.3	11.9	1055.4	803.6	56	50.55
43	213.3	125.3	155.2	11.9	1055.4	803.1	90	59.52
44	218.7	125.3	158.2	11.5	1081.8	798	56	41.33
45	218.7	125.3	159.8	11.5	1081.8	798	90	46.37
46	375.8	125.3	216.4	0	1006.6	765.5	3	20.1
47	190.1	125.3	165.3	10.1	1082.1	802	14	21.34
48	164.8	125.3	163.5	0	1008.7	904	28	27.23
49	190.1	125.3	165	10.1	1082.1	802	28	27.79
50	249.8	125.3	192.5	5.5	952	860.3	28	29.33
51	213.3	125.3	158.9	11.9	1046.7	775	28	45.73
52	194.5	125.3	171.2	7.7	1001.1	904.9	28	40.39
53	251.2	125.3	192.6	6	1046.7	757.4	28	38.11
54	309.8	125.3	189.6	0	939.3	715.3	28	42.06
55	279.8	125.3	189.6	0	939.3	703.1	7	37.69

56	290	125.3	183.3	0	1072.3	757.4	7	24.3
57	252.3	125.3	186.4	0	1114.7	787.4	7	14.23
58	338.8	125.3	196.7	0	971.1	803.1	3	19.36
59	256.8	125.3	192.5	0	971.1	859.6	90	28.66
60	253.8	125.3	192.4	0	971.1	802.8	90	29.78
61	306.8	125.3	193.2	0	971.1	802.6	28	30.45
62	306.8	125.3	190.9	0	971.1	802.6	90	37.04
63	289.8	125.3	191.9	0	939.1	758.1	28	47.41
64	296.8	125.3	191	0	939.1	758.1	90	52.3
65	298.8	125.3	187	0	969.1	766.1	3	18.23
66	287.8	125.3	188.3	0	969.1	761.1	7	22.33
67	288.8	125.3	188.3	0	969.1	762.1	14	30.34
68	291.8	125.3	187	0	969.1	766.1	28	34.67
69	330.8	125.3	191.9	0	981.1	804.1	90	41.22
70	348.8	125.3	191.9	0	1050.1	809.1	3	17.71
71	294.8	125.3	185	0	1072.1	772.5	28	28.31
72	237.8	125.3	184.9	0	1121.1	792.1	28	17.96
73	295.8	125.2	191	0	1088.1	768.6	7	17.95
74	322.3	125.3	203.1	0	977.1	843.1	14	25.23
75	321.8	124.9	201.2	0	977.1	803.3	28	27.27
76	321.8	125.2	202.4	0	977.1	823.1	90	31.69
77	301.8	125.3	202.4	0	977.1	820.1	28	27.23
78	312.3	125.1	182.1	0	1043.1	737.1	28	41.2
79	316.8	125.3	192.2	0	939.1	724.1	3	27.41
80	209.8	125.3	142.2	0	899.1	899.1	7	50.53

Table 5c. Mix proportions conducted of specimens (sr. no 34 to 66)

Sample no	Cement (kg/m ³ .)	Fly Ash (kg /m ³ .)	Water (kg/m ³ .)	Superplastic izer (Kg/m ³ .)	Coarse aggregate (kg/m ³ .)	Fine aggregate (kg /m ³ .)	Curing Period (days)	CS (N/mm ²)
81	220.7	125.3	142.2	0	899.1	899.1	28	73.23
82	143.8	125.3	157.9	18.2	946.1	847.1	28	18.54
83	147.8	125.3	158.1	16.2	1005.1	833.1	28	21.07
84	325.8	125.1	198.8	11.2	804.1	795.1	28	40.9
85	289.8	125.3	220.2	11.2	901.1	716.1	28	10.71
86	299.6	125.3	211.2	10.1	881.3	730.7	28	26.93
87	147.9	125.1	158.9	16.3	1004.9	833.2	28	20.1
88	326.3	125.3	193	11	804.2	795.6	28	36.73
89	276.2	125.3	217.1	11.2	900.8	716	28	10.67
90	150.5	125.3	164.3	15.8	1077.6	690.1	28	16.56
91	190.6	125.3	184.8	11.3	982.6	814.1	28	16.33
92	190.7	125.3	167.9	11.8	994.3	787.1	28	19.78
93	188.5	125.3	182.1	11.9	1026.4	735.1	28	21.13
94	297.9	125.1	189.1	6.3	882.1	818.1	28	42.76
95	318.7	125.3	212.4	5.9	863.6	728.1	28	37.21
96	355.7	125	196	11.2	804.5	772.1	28	37.39
97	199.6	125.3	185.1	12.8	852.4	859.6	28	19.13

98	278.5	125.3	170	10.3	928.4	785.1	28	42.28
99	305.5	125	217	10.6	942.2	796.3	28	42.89
100	318.5	125.3	196	11.2	856.3	736.5	28	43.6

The modelling was carried out using a total of seven inputs and one result (i.e. C.S). Table 6 lists the individual variables that make up this input dataset. Table 6 presents the frequency distribution information, while Table 7 describes the statistical distribution. Using a histogram, figure 4 depicts the intensity that was included into the C-S calculation.

Table 6. Dataset properties for Input- output variables

Parameter	Min value	Max value
C (kg/m ³)	135.9	375.8
Water content (kg/m ³)	141.4	220.9
F (kg/m ³)	92.6	168.8
Superplasticizer (% by mass)	0	18.2
Aggregate F-a (kg/m ³)	690.1	908.5
Curing period (days)	3	90
Aggregate C-a (kg/m ³)	804.1	1121.1
C.S (MPa)	10.6	73.23

There are a number of techniques that may be used to calculate C.S., some of which are listed below: i) boosting algorithm; ii) Decision tree (D-T). Fig.3 shows a simplified schematic flowchart of the algorithms for the D-T . The anaconda software was used to run the models. schematic flowchart of the algorithms for the D-T . The anaconda software was used to run the models.

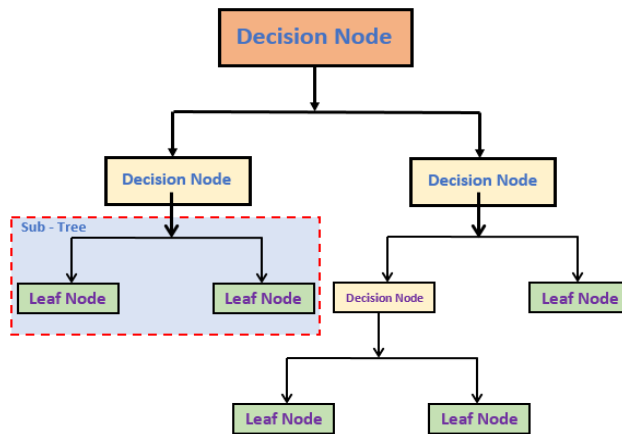
Table 7. Details of parameters study

Sr. No.	Parameters	Cement kg/m ³	Fly Ash kg/m ³	Water kg/m ³	Super Plasticizer kg/m ³
1	Mean or Avg	241.2	123.8	178.7	6.4
3	Median	230.35	124.8	184.2	7
2	Std. Deviation	55.62	10.13	18.01	4.9
2	Std. Error	5.62	1.02	1.82	0.5
4	Mode	213.5	124.8	191.3	0
6	Sample Variance	3093.8	102.65	324.33	24.4
7	Kurtosis	-0.8	9.8	-0.6	-1.1
8	Skewness	0.27	0.55	-0.08	-0.02
9	Maximum	376	168.3	220.5	18
10	Minimum	136.1	92.1	141.1	0
11	Range	239.9	76.2	79.4	18
12	Sum	24120	12385.4	17877.1	642.6
13	Count	100	100	100	100

Table 7(Con.). Details of parameters study

Sr. No.	Parameters	Coarse Aggregate kg/m ³	Fine Aggregate kg/m ³	Days	Comp. Strength MPa
1	Mean or Avg	1001.3	793.27	33.67	30.49
3	Median	1006.2	794.9	28	27.52
2	Std. Deviation	71.36	48.00	28.81	13.00
2	Std. Error	7.21	4.85	2.91	1.31
4	Mode	1055.6	800	28	17.11
6	Sample Variance	5092.88	2304.07	830.20	169.06
7	Kurtosis	0.3	0.7	-0.1	0.2
8	Skewness	-0.77	0.17	1.06	0.67
9	Maximum	1118	905.4	90	72.11
10	Minimum	801	650	3	9.49
11	Range	317	255.4	87	62.62
12	Sum	100130	79327.3	3367.0	3049.3
13	Count	100	100	100	100

The decision tree is well-known as an efficient and straightforward approach to categorization. It's a model that looks like a tree and uses a set of specified criteria to sort data into several classifications. D-T oversees the classification process using criteria determined from the nature of the incoming data. The decision tree's behavior is planned such that the classification and regression trees share no characteristics at all.



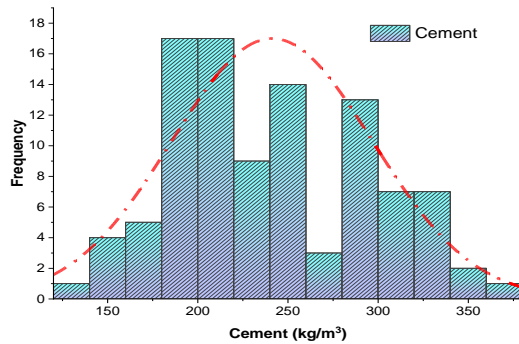
(a)

Fig. 3 Flow Chart of Decision Tree Technique (D-T)

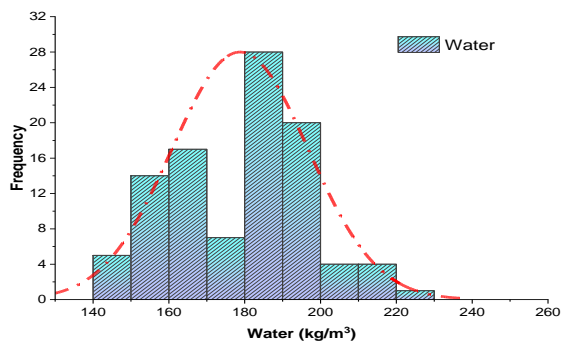
In contrast to artificial neural networks (ANNs), the usage of a structure that is based on decision trees gives explicitness. Because the process of decision tree clustering imitates the process of human thought, it is easy for even communities who are not technically oriented to grasp the behavior. However, in comparison to the simple decision tree, the majority of more sophisticated tree-based designs are relatively complicated. Despite this, every single tree-based model that was used in this investigation was a decision tree-based model. Because of this, it is very necessary to explain the process that a decision tree regressor goes through.

6. Results and Discussion

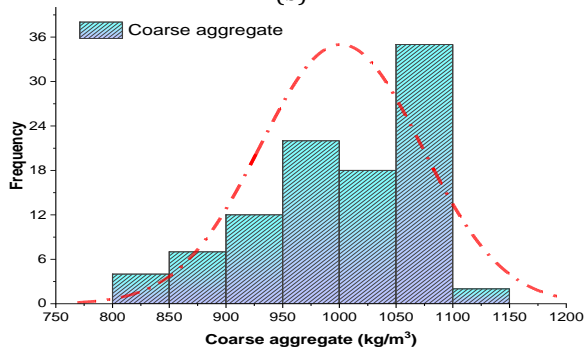
The results of the decision tree fly ash binder concrete prediction model are shown in Figure 5. Figure 5(a) shows that the DT has a higher $R^2 = 0.76$ when projecting the concrete C-S. The limit of the modelled error ranges from 0.001 MPa to 21.40 MPa, even with average error observed to be 4.22 MPa. Furthermore, the output results and model's performance correlated with each other's. Two-thirds of the findings show that the data lies within 7 MPa, with high accuracy; one-third of the results show that the data found between value 7 MPa to 10 MPa, with low precision; and one result shows that space exists at a pressure higher than 20 MPa, with low precision.



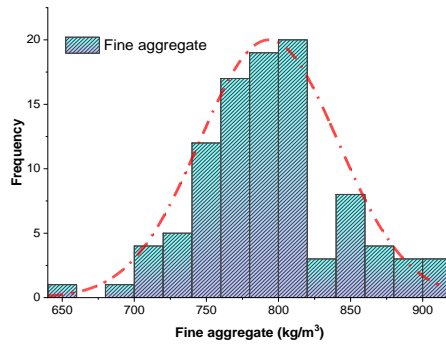
(a)



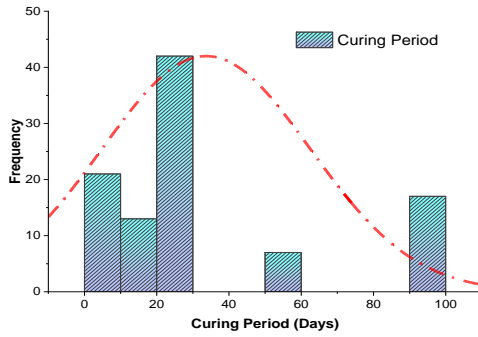
(b)



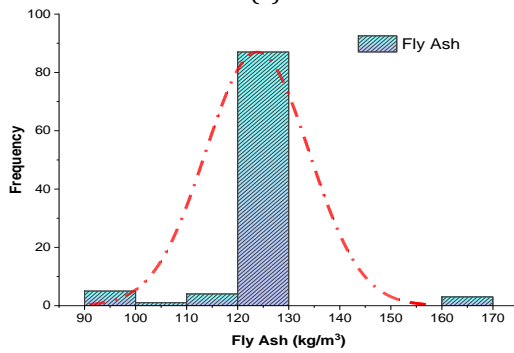
(c)



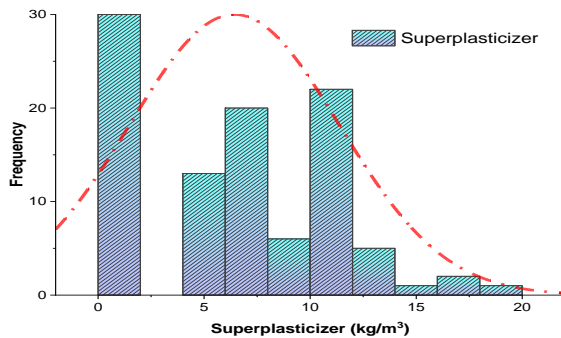
(d)



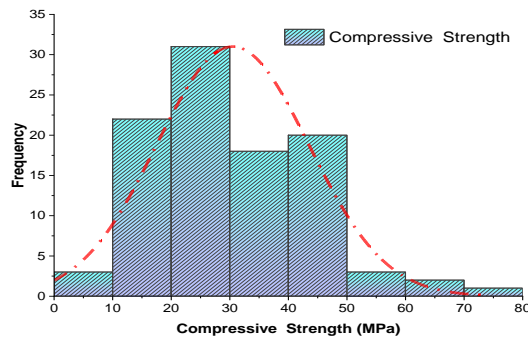
(e)



(f)



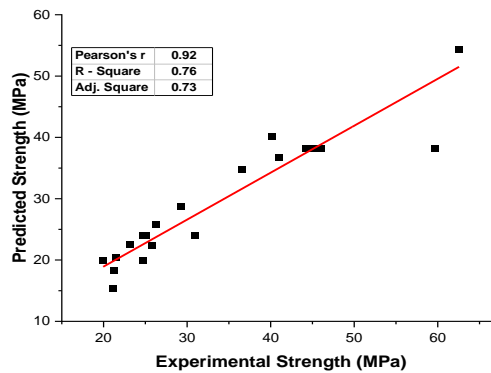
(g)



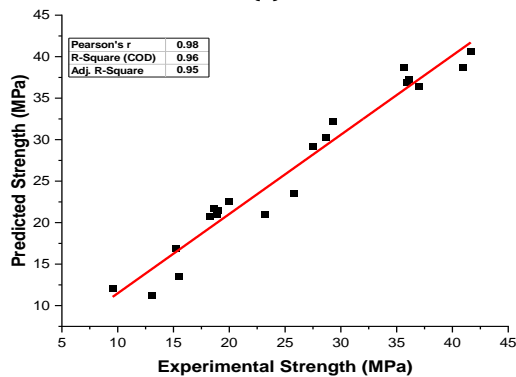
(h)

Fig. 4 Histogram of concentration used for computing the C-S

The effectiveness of the ensemble (boosting) algorithm often used estimate the C.S of concrete was substantially higher when compared here to other machine learning techniques employed for this study. You may get a sense of its efficiency by looking at Figure 5(a), which shows the relationship between the actual and ideal output. The estimated standard deviation is 2.0 MPa, with a range of 0.57 to 3.0 MPa, as shown in Fig. 5(b). Furthermore, the fact that all error data found less than 4 MPa demonstrates the reliability.



(a)



(b)

Fig. 5 (a) Performance of DT algorithm (b) Boosting Regressor algorithm

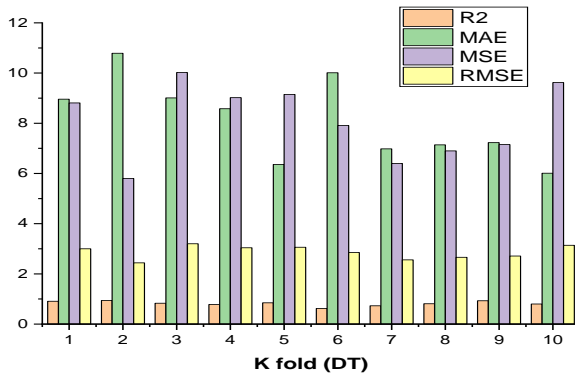
6.1 K-fold Cross validation

Multiple tasks may benefit from the use of the J. knife test and the K-fold cross validation algorithm test, including reducing the impact of bias in a random training data selection, excluding less-representative examples from the data collection, and reducing the severity of overfitting issues. The stratified 10-fold validation method has been proven reliable and is often used to maximize productivity with minimal hardware and software requirements. Similarly, this study employs a ten-fold analysis, albeit it does so by splitting the data into k distinct subsets.

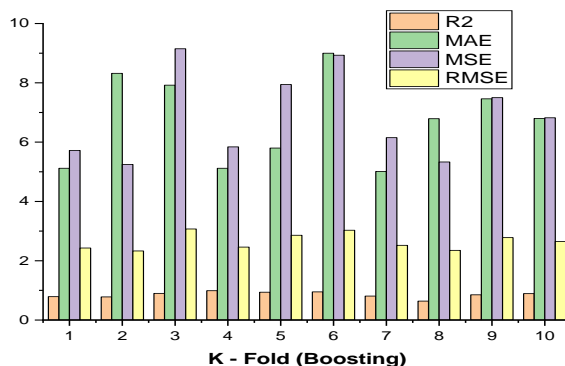
The collected information may be partitioned into distinct categories, of which several are required for the analysis. It is not feasible to validate the model by using more than one data subset in the verification process. separate attempts at the procedure are required to get a result that is representative of the norm. The statistical tests' findings were also used into an evaluation of the models' performance. Evidence for the model's efficacy was derived from the formulations that were created in accordance with the underlying study.

The attempted approach of k-fold cross validation is employed to ascertain how much the bias and variance of the testing set have been reduced. But there is noticeable variation in the results produced by each of learning methods. The BR model has a substantially better R^2 value and far fewer mistakes compared to decision tree models. Further, as can be shown in Fig. 6(a), the Decision tree (D-T) model has an average R^2 value of 0.78, with values as high as 0.90 and as low as 0.58. Validation error rates that drop indicate that the models have been improved. Values of 8.08 MPa, 8.04 MPa, and 2.82 MPa may be seen in the decision tree shown in Figure 6(a). As can be seen in Fig. 6(b), the average R^2 for the boosting regressor ranges from 0.82 to 0.62, with a maximum of 0.97. The lowest mean absolute errors (MAE), mean standard errors (MSE), and root mean squared errors (RMSE) for BR are shown in 6(b) as 6.714% MPa, 6.806% MPa, and 2.59% MPa, respectively.

More so, statistical tests conducted on the dataset showed that the ensemble ML approach had lower error rates than the other methods used (D-T). The findings for the bagging regressor (B-R) reveal an error of 3.69 MPa (mean absolute error), 24.76 MPa (mean standard error), and 4.79 MPa when statistical tests are done (root mean squared error). Coefficient of determination (R^2) is directly related to this test; higher R^2 value once again for model corresponds to lower R^2 value due to less error.



(a)



(b)

Fig.6 "K-fold" cross-validation; (a) DT model and (b) Boosting regressor

6. Conclusion

- Ensemble approaches are good for minimizing model variance, improving prediction accuracy. Combining many models to make a single forecast from all their potential predictions eliminates variation.
- The foundation of this research is a thorough analysis of M-L algorithms used on fly ash-based concrete. Decision tree (D-T), and bagging regressor (B-R) were some of the supervised machine learning methods analyzed for their ability to predict the C.S of fly ash-mixed concrete. In addition, the performances of the individual machine learning algorithms were compared to those of the ensemble machine learning method.
- There is less discordance between observed and predicted outcomes when using distinct machine learning techniques. In contrast to regression, it may accommodate several answers and outputs at once. The field of research known as "machine learning" is dedicated to understanding how to duplicate and implement certain cognitive features of the machine learning tool in order to create technological products and build relevant hypotheses.
- Nonetheless, the ensemble was found to be a fairly strong and significantly reliable way, as demonstrated by the value of its coefficient correlation (R^2), which was equal to 0.96 when compared to the total accuracy of the independent ML techniques. This was accomplished by using a bagging regressor. There is an average R^2 value 0.76 for the D-T.
- Mean absolute error (3.6 MPa), mean squared error (24.6), and root mean squared error (4.9) are all less than they are when using other methods, further demonstrating the superior accuracy of the bagging regressor.
- The model's accuracy was confirmed using the K-fold cross validation method, which corroborates the bagging regressor's usefulness.
- Statistical analysis done on the dataset showed that the ensemble ML approach yields lower error rates than the other individual methods used (D-T). The use of statistical checks additionally verifies that bagging regressor shows an improvement in model performance by reducing the amount of error that exists between the outcomes that were sought and those that were predicted.
- It has been found that ensemble machine learning methods are an effective and helpful tool for addressing a broad range of structural engineering issues, and it is

anticipated that the usage of these algorithms will rise over the duration of the subsequent years.

References

- [1] Possan, E, Thomaz WA, Aleandri GA, Felix EF, dos Santos AC. CO₂ uptake potential due to concrete carbonation: A case study. *Case Stud. Constr. Mater.* 2017, 6, 147–161.
- [2] Barkhordari, MS, Tehranizadeh M, Scott MH. Numerical modelling strategy for predicting the response of reinforced concrete walls using Timoshenko theory. *Mag. Concr. Res.* 2021, 73, 988–1010.
- [3] Venkateswarlu K, Deo S, Murmu M. Effect of Super absorbent polymer on workability, strength and durability of Self consolidating concrete. *Int. J. Eng.* 2021, 34, 1118–1123.
- [4] Yan H., Q. Shen, L.C.H. Fan, Y. Wang, L. Zhang, Greenhouse gas emissions in building construction: a case study of one peking in Hong Kong, *Build. Environ.* 45, 2010, 949–955, <https://doi.org/10.1016/j.buildenv.2009.09.014>.
- [5] Xiao H., Z. Duan, Y. Zhou, N. Zhang, Y. Shan, X. Lin, G. Liu, CO₂ emission patterns in shrinking and growing cities: a case study of Northeast China and the Yangtze River Delta, *Appl. Energy.* 251, 2019, 113384 <https://doi.org/10.1016/j.apenergy.2019.113384>.
- [6] Benhelal E., G. Zahedi, E. Shamsaei, A. Bahadori, Global strategies and potentials to curb CO₂ emissions in cement industry, *J. Clean. Prod.* 51, 2013, 142–161, <https://doi.org/10.1016/j.jclepro.2012.10.049>.
- [7] Kajaste R., M. Hurme, Cement industry greenhouse gas emissions – Management options and abatement cost, *J. Clean. Prod.* 112, 2016, 4041–4052, <https://doi.org/10.1016/j.jclepro.2015.07.055>.
- [8] Batayneh M., I. Marie, I. Asi, Use of selected waste materials in concrete mixes, *Waste Manag.* 27, 2007, 1870–1876, <https://doi.org/10.1016/j.wasman.2006.07.026>.
- [9] Shubbar AA, H. Jafer, A. Dulaimi, K. Hashim, W. Atherton, M. Sadique, The development of a low carbon binder produced from the ternary blending of cement, ground granulated blast furnace slag and high calcium fly ash: an experimental and statistical approach, *Constr. Build. Mater.* 187, 2018, 1051–1060, <https://doi.org/10.1016/j.conbuildmat.2018.08.021>.
- [10] Gursel AP, Masanet E, Horvath A, Stadel A. Life-cycle inventory analysis of concrete production: a critical review. *Cement and Concrete Composites.* 51, 2014, 38-48.
- [11] Mehta PK. Greening of the concrete industry for sustainable development. *Concrete International*, 24, 2002, 7 23- 28.
- [12] Mahajan LS, Bhagat SR. Strength Assessment of Concrete using Fly Ash and Metakaolin, In proceeding: International Conference on Advances in Concrete Technology materials and construction practices, Excel India Publishers, New Delhi, 2016, 113-114.
- [13] Li VC, Wang S, Wu C, Tensile Strain-Hardening Behavior of Polyvinyl Alcohol Engineered Cementitious Composite (PVA-ECC). *Materials Journal*, 2001; 98: 483-492
- [14] Wang S, Li VC. Engineered Cementitious Composites with High-Volume Fly Ash., *ACI Materials Journal*, 104, 2007, 233-241
- [15] Mahajan L, Bhagat S., An artificial neural network for the prediction of the strength of supplementary cementitious concrete. *Res. Eng. Struct. Mater.*, 8(2), 2022, 421-430. <http://dx.doi.org/10.17515/resm2022.341st0918tn>
- [16] Li M, H. Hao, Y. Shi, Y. Hao, Specimen shape and size effects on the concrete compressive strength under static and dynamic tests, *Constr. Build. Mater.* 161, 2018, 84–93, <https://doi.org/10.1016/j.conbuildmat.2017.11.069>.
- [17] Feng DC, Z.T. Liu, X.D. Wang, Y. Chen, J.Q. Chang, D.F. Wei, Z.M. Jiang, Machine learning-based compressive strength prediction for concrete: an adaptive boosting approach,

- Constr. Build. Mater. 230, 2020, 117000, <https://doi.org/10.1016/j.conbuildmat.2019.117000>.
- [18] Ahmad A, F. Farooq, KA. Ostrowski, K. 'Sliwa-Wieczorek, S. Czarnecki, Application of novel machine learning techniques for predicting the surface chloride concentration in concrete containing waste material, *Materials* (Basel). 14, 2021, 2297, <https://doi.org/10.3390/ma14092297>.
- [19] Khan MA, Memon SA, Farooq F., Javed MF, Aslam F., R. Alyousef, Y. Sun, Compressive strength of fly-ash-based geopolymer concrete by gene expression programming and random forest, *Adv. Civ. Eng.* 2021, 1–17, <https://doi.org/10.1155/2021/6618407>.
- [20] Javed MF, Farooq F, Memon SA, Akbar A, Khan MA, F. Aslam, R. Alyousef, H. Alabduljabbar, S.K.U. Rehman, S.K. Ur Rehman, S. Kashif, U. Rehman, New prediction model for the ultimate axial capacity of concrete-filled steel tubes: a nevolutionary approach, *Crystals*. 10, 2020, 1–33, <https://doi.org/10.3390/cryst10090741>.
- [21] Farooq F, Ahmed W, Akbar A, Aslam F, Alyousef R., Predictive modeling for sustainable high-performance concrete from industrial wastes: a comparison and optimization of models using ensemble learners, *J. Clean. Prod.* 292, 2021, 126032, <https://doi.org/10.1016/j.jclepro.2021.126032>.
- [22] Javed MF, Amin MN, Shah MI, Khan K, Iftikhar B, Farooq F, Aslam F, Alyousef R, Alabduljabbar H, Applications of gene expression programming and regression techniques for estimating compressive strength of bagasse ash-based concrete, *Crystals*. 10, 2020, 1–17, <https://doi.org/10.3390/cryst10090737>.
- [23] Fouquier A, Robert S, Suard F, St'ephan L, Jay A, State of the art in building modelling and energy performances prediction: a review, *Renew. Sustain. Energy Rev.* 23, 2013, 272–288, <https://doi.org/10.1016/j.rser.2013.03.004>.
- [24] Bhagat SR, Suryawanshi GA, Monali Mahajan, Lomesh S. Mahajan, Artificial neural network techniques for evaluation of pollution, *IOP Conf. Series: Earth and Environmental Science* 796, 2021, 012052, <https://doi.org/10.1088/1755-1315/796/1/012052>
- [25] Lv Y, Liu J, Yang T, Zeng D., A novel least squares support vector machine ensemble model for NOx emission prediction of a coal-fired boiler, *Energy*. 55, 2013, 319–329, <https://doi.org/10.1016/j.energy.2013.02.062>.
- [26] Dou J., Yunus AP, Tien Bui D, A. Merghadi, M. Sahana, Z. Zhu, C.W. Chen, K. Khosravi, Y. Yang, B.T. Pham, Assessment of advanced random forest and decision tree algorithms for modeling rainfall-induced landslide susceptibility in the Izu-Oshima Volcanic Island, Japan, *Sci. Total Environ.* 662, 2019, 332–346, <https://doi.org/10.1016/j.scitotenv.2019.01.221>.
- [27] Zhang D, Tsai JP, Machine learning and software engineering, *Softw. Qual. J.* 11, 2003, 87–119, <https://doi.org/10.1023/A:1023760326768>.
- [28] J.S. Chou, A.D. Pham, Enhanced artificial intelligence for ensemble approach to predicting high performance concrete compressive strength, *Constr. Build. Mater.* 49, 2013, 554–563, <https://doi.org/10.1016/j.conbuildmat.2013.08.078>.
- [29] Galar M, Fernandez A, Barrenechea E, Bustince H, Herrera F., A review on ensembles for the class imbalance problem: bagging-, boosting-, and hybrid-based approaches, *IEEE Trans. Syst. Man Cybern. Part C Appl. Rev.* 42, 2012, 463–484, <https://doi.org/10.1109/TSMCC.2011.2161285>.
- [30] Gomes HM, Barddal JP, Enembreck F, Bifet A., A survey on ensemble learning for data stream classification, *ACM Comput. Surv.* 50, 2017, 1–36, <https://doi.org/10.1145/3054925>
- [31] Rahman J, Ahmed KS, Khan NI, Islam K, Mangalathu S., Data-driven shear strength prediction of steel fiber reinforced concrete beams using machine learning approach, *Eng. Struct.* 233, 2021, 111743. <https://doi.org/10.1016/j.engstruct.2020.111743>.
- [32] Jesika Rahman, Khondaker Sakil Ahmed, Nafiz Imtiaz Khan, Kamrul Islam, Sujit Mangalathu, Data-driven shear strength prediction of steel fiber reinforced concrete

- beams using machine learning approach, *Engineering Structures*, Volume 233, 2021, 111743, <https://doi.org/10.1016/j.engstruct.2020.111743>.
- [33] Behnood A, Golafshani EM, Predicting the compressive strength of silica fume concrete using hybrid artificial neural network with multi-objective grey wolves, *J. Clean. Prod.* 202, 2018, 54–64, <https://doi.org/10.1016/j.jclepro.2018.08.065>.
- [34] Güçlüer K, Özbeyaz A, S. G'öymen, O. Günaydın, A comparative investigation using machine learning methods for concrete compressive strength estimation, *Mater. Today Commun.* 27, 2021, 102278, <https://doi.org/10.1016/j.mtcomm.2021.102278>.
- [35] Getahun MA, Shitote SM, Abiero Gariy ZC, Artificial neural network based modelling approach for strength prediction of concrete incorporating agricultural and construction wastes, *Constr. Build. Mater.* 190, 2018, 517–525, <https://doi.org/10.1016/j.conbuildmat.2018.09.097>.
- [36] Ling H, Qian C, Kang W, Liang C, Chen H, Combination of support vector machine and K-Fold cross validation to predict compressive strength of concrete in marine environment, *Constr. Build. Mater.* 206, 2019, 355–363, <https://doi.org/10.1016/j.conbuildmat.2019.02.071>.
- [37] Zaher M. Yaseen, RC. Deo, A. Hilal, AM. Abd, LC. Bueno, S. Salcedo-Sanz, ML. Nehdi, Predicting compressive strength of lightweight foamed concrete using extreme learning machine model, *Adv. Eng. Softw.* 115, 2018, 112–125, <https://doi.org/10.1016/j.advengsoft.2017.09.004>.
- [38] Taffese WZ, Sistonen E, Machine learning for durability and service-life assessment of reinforced concrete structures: recent advances and future directions, *Autom. Constr.* 77, 2017, 1–14, <https://doi.org/10.1016/j.autcon.2017.01.016>.
- [39] Yokoyama S, Matsumoto T., Development of an automatic detector of cracks in concrete using machine learning, in, *Procedia Eng.*, Elsevier Ltd, 2017, 1250–1255, <https://doi.org/10.1016/j.proeng.2017.01.418>.
- [40] Ben W, Chaabene, Flah M, Nehdi ML, Machine learning prediction of mechanical properties of concrete: critical review, *Constr. Build. Mater.* 260, 2020, 119889, <https://doi.org/10.1016/j.conbuildmat.2020.119889>.
- [41] Su M, Zhong Q, Peng H, Li S, Selected machine learning approaches for predicting the interfacial bond strength between FRPs and concrete, *Constr. Build. Mater.* 270, 2021, 121456, <https://doi.org/10.1016/j.conbuildmat.2020.121456>.
- [42] Gunasekara C, Setunge S, Law DW, Willis N, Burt T. Engineering Properties of Geopolymer Aggregate Concrete. *Journal of Materials in Civil Engineering*, 30, 2018, 11 04018299.
- [43] Peng CH, Yeh IC, Lien LC. Building Strength Models for High-Performance Concrete at Different Ages using Genetic Operation Trees, Nonlinear Regression, and Neural Networks. *Engineering Composites*, 26, 2010, 61-73.
- [44] Shi L, Lin STK, Lu Y, Ye L, Zhang YX. Artificial Neural Network Based Mechanical and Electrical Property Prediction of Engineered Cementitious Composites. *Construction and Building Materials*, 174, 2018, 667-74
- [45] Bilim C, Atis CD, Tanyildizi H, Karahan O. Predicting the Compressive Strength of Ground Granulated Blast Furnace Slag Concrete using Artificial Neural Network, *Adv. Eng. Soft.* 40 (5), 2009, 334-340. <https://doi.org/10.1016/j.advengsoft.2008.05.005>
- [46] Sahoo S, Das BB, Mustakim S. Acid, Alkali, and Chloride Resistance of Concrete Composed of Low-Carbonated Fly Ash. *Journal of Materials in Civil Engineering*, 29(3), 2016; 1-12, 04016242. [https://doi.org/10.1061/\(ASCE\)MT.1943-5533.0001759](https://doi.org/10.1061/(ASCE)MT.1943-5533.0001759)
- [47] Mahajan LS, Bhagat SR. Investigation of the Relationship between Splitting Tensile Strength and Compressive Strength for Prediction of Splitting Tensile Strength of Fly Ash Concrete, In: *Proceedings, 3rd International Conference on Innovative Technologies for Clean and Sustainable Development at NITTTTR, Chandigarh, India 2020.*
- [48] Ankur M, Rafat S, Pratap SB, Salima A, Grzegorz L, Danuta BH. Influence of Various Parameters on Strength and Absorption Properties of Fly Ash Based Geopolymer

- Concrete Designed by Taguchi Method, *Construction and Building Materials*, 150, 2017, 817-824. <https://doi.org/10.1016/j.conbuildmat.2017.06.066>
- [49] Hashmi AF, Shariq M, Baqi A. Haq Moinul, Optimization of Fy Ash Concrete Mix - a Solution for Sustainable Development, *Materials Today: Proceedings*, 26(2), 2020; 3250-3256. <https://doi.org/10.1016/j.matpr.2020.02.908>
- [50] Jinrui Zhang, Wenjun Niu, Youzhi Yang, Dongshuai Hou, Biqin Dong, Machine learning prediction models for compressive strength of calcined sludge-cement composites, *Construction and Building Materials*, Volume 346, 2022, 128442, <https://doi.org/10.1016/j.conbuildmat.2022.128442>
- [51] Babatunde Abiodun Salami, Mudassir Iqbal, Abdulazeez Abdulraheem, Fazal E. Jalal, Wasii Alimi, Arshad Jamal, T. Tafsirojjaman, Yue Liu, Abidhan Bardhan, Estimating compressive strength of lightweight foamed concrete using neural, genetic and ensemble machine learning approaches, *Cement and Concrete Composites*, Volume 133, 2022, 104721, <https://doi.org/10.1016/j.cemconcomp.2022.104721>.
- [52] Woubishet Zewdu Taffese, Leonardo Espinosa-Leal, Prediction of chloride resistance level of concrete using machine learning for durability and service life assessment of building structures, *Journal of Building Engineering*, Volume 60, 2022, 105146, <https://doi.org/10.1016/j.jobe.2022.105146>
- [53] Mohammad Sadegh Barkhordari, Mohsen Tehranizadeh, Response estimation of reinforced concrete shear walls using artificial neural network and simulated annealing algorithm, *Structures*, Volume 34, 2021, 1155-1168, <https://doi.org/10.1016/j.istruc.2021.08.053>.
- [54] Panagiotis G. Asteris, Athanasia D. Skentou, Abidhan Bardhan, Pijush Samui, Paulo B. Lourenço, Soft computing techniques for the prediction of concrete compressive strength using Non-Destructive tests, *Construction and Building Materials*, Volume 303, 2021, 124450, <https://doi.org/10.1016/j.conbuildmat.2021.124450>.
- [55] Ahmad A, Farooq F, Niewiadomski P, Ostrowski K, Akbar A, Aslam F, Alyousef R., Prediction of compressive strength of fly ash based concrete using individual and ensemble algorithm, *Materials (Basel)*. 14, 2021, 1-21, <https://doi.org/10.3390/ma14040794>.
- [56] Balf FR, Kordkheili HM, Kordkheili AM, A new method for predicting the ingredients of self-compacting concrete (SCC) including fly ash (FA) using data envelopment analysis (DEA), *Arab. J. Sci. Eng.*, 2020, 1-22, <https://doi.org/10.1007/s13369-020-04927-3>
- [57] Bušić R, Benšić M, Miličević I, Strukar K, Prediction models for the mechanical properties of self-compacting concrete with recycled rubber and silica fume, *Materials (Basel)*. 13, 2020, 1821, <https://doi.org/10.3390/MA13081821>.
- [58] Azimi-Pour M, Eskandari-Naddaf H, Pakzad A, Linear and non-linear SVM prediction for fresh properties and compressive strength of high volume fly ash self-compacting concrete, *Constr. Build. Mater.* 230, 2020, 117021, <https://doi.org/10.1016/j.conbuildmat.2019.117021>.
- [59] Saha P, Debnath P, Thomas P, Prediction of fresh and hardened properties of selfcompacting concrete using support vector regression approach, *Neural Comput. Appl.* 32, 2020, 7995-8010, <https://doi.org/10.1007/s00521-019-04267-w>.
- [60] Al-Mughanam T, Aldhyani THH, B. Alsubari, M. Al-Yaari, Modeling of compressive strength of sustainable self-compacting concrete incorporating treated palm oil fuel ash using artificial neural network, *Sustain.* 12, 2020, 1-13, <https://doi.org/10.3390/su12229322>.
- [61] Aslam F, Farooq F, Amin MN, Khan K, Waheed A, Akbar A, Javed MF, Alyousef R, Alabduljabbar H., Applications of gene expression programming for estimating compressive strength of high-strength concrete, *Adv. Civ. Eng.* 2020, 1-23, <https://doi.org/10.1155/2020/8850535>.
- [62] Farooq F, Amin MN, Khan K, Sadiq MR, Javed MF, Aslam F, Alyousef R, A comparative study of random forest and genetic engineering programming for the prediction of

- compressive strength of high strength concrete (HSC), Appl. Sci. 10, 2020, 1–18, <https://doi.org/10.3390/app10207330>.
- [63] Asteris PG, Kolovos KG, Self-compacting concrete strength prediction using surrogate models, Neural Comput. Appl. 31, 2019, 409–424, <https://doi.org/10.1007/s00521-017-3007-7>
- [64] Selvaraj S, Sivaraman S., Prediction model for optimized self-compacting concrete with fly ash using response surface method based on fuzzy classification, Neural Comput. Appl. 31, 2019, 1365–1373, <https://doi.org/10.1007/s00521-018-3575-1>.
- [65] Zhang J, Ma G, Huang Y, Sun J., F. Aslani, B. Nener, Modelling uniaxial compressive strength of lightweight self-compacting concrete using random forest regression, Constr. Build. Mater. 210, 2019, 713–719, <https://doi.org/10.1016/j.conbuildmat.2019.03.189>.
- [66] Kaveh A, Bakhshpoori T., Hamze-Ziabari SM, M5' and mars based prediction models for properties of selfcompacting concrete containing fly ash, Period. Polytech Civ. Eng. 62, 2018, 281–294, <https://doi.org/10.3311/PPci.10799>.
- [67] Sathyan D, Anand KB, Prakash AJ, Premjith B, Modeling the fresh and hardened stage properties of self-compacting concrete using random kitchen sink algorithm, Int. J. Concr. Struct. Mater. 12, 2018, 1–10, <https://doi.org/10.1186/s40069-018-0246-7>.
- [68] Vakhshouri B, Nejadi S, Prediction of compressive strength of self-compacting concrete by ANFIS models, Neurocomputing. 280, 2018, 13–22, <https://doi.org/10.1016/j.neucom.2017.09.099>.
- [69] Belalia Douma O, Boukhatem B, Ghrici M, Tagnit-Hamou A, Prediction of properties of self-compacting concrete containing fly ash using artificial neural network, Neural Comput. Appl. 28, 2017, 707–718, <https://doi.org/10.1007/s00521-016-2368-7>.
- [70] Abu Yaman M, Abd Elaty M, Taman M, Predicting the ingredients of self compacting concrete using artificial neural network, Alexandria Eng. J. 56, 2017, 523–532, <https://doi.org/10.1016/j.aej.2017.04.007>.
- [71] Mahajan LS, Bhagat S, Machine learning approaches for predicting compressive strength of concrete with fly ash admixture, Research on Engineering Structures & Materials. 8 (4), 2022. <https://doi.org/10.17515/resm2022.534ma0927>
- [72] Wangwen Huo, Zhiduo Zhu, He Sun, Borui Ma, Liu Yang, Development of machine learning models for the prediction of the compressive strength of calcium-based geopolymers, Journal of Cleaner Production, Volume 380, Part 2, 2022, 135159. <https://doi.org/10.1016/j.jclepro.2022.135159>



Research Article

Evaluation of cement-treated ferrochrome slag and quarry dust composites for base and sub-base layers of flexible pavement

CH Ajay^{1*}, K Durga Rani^{2,b}

¹Research Scholar, Civil Engineering Department, Andhra University, Visakhapatnam, Andhra Pradesh, India

²Professor, Civil Engineering Department, Andhra University, Visakhapatnam, Andhra Pradesh, India

Article Info

Abstract

Article history:

Received 10 Oct 2022

Accepted 15 May 2023

Keywords:

Ferrochrome slag;

Quarry dust; gradation;

Cement stabilization;

Ultrasonic pulse

velocity;

Unconfined

compressive strength;

This study explores the use of ferrochrome slag as cement-bound granular layers of flexible pavement. To meet MoRTH design criteria, ferrochrome slag (FS) gradation was improved by incorporating quarry dust (Q) in proportions of 10%, 20%, 30%, 40%, and 50% (by weight). Only FS70Q30 and FS60Q40 composites have satisfied the gradation requirements of cementitious sub-base and base courses of flexible pavement. Unconfined compressive strength (UCS) and ultrasonic pulse velocity (UPV) tests were performed under OMC and MDD conditions on ferrochrome slag and quarry dust composites stabilized with cement in proportions of 2% to 10% (by weight of the aggregate mix) and curing periods of 3, 7, 14 and 28 days. FS70Q30 and FS60Q40 mixes exhibited a significant increase in strength and wave velocities with increasing cement content and curing periods. The UCS of FS60Q40 mixes was 1.03 to 1.62 times that of FS70Q30 mixes, and no significant variation in UPV was observed. An equation with a high regression factor (R-square >0.98) was formulated to correlate UCS and UPV values with cement content. Based on the developed statistical equation, the predicted minimum cement content for FS60Q40 mixes was found to be 12-16% lower than FS70Q30 mixes.

© 2023 MIM Research Group. All rights reserved.

1. Introduction

Traditionally, aggregates for road construction were deployed through extensive mining activities. Uncontrolled mining has led to the depletion of natural aggregates and increased demand for alternative pavement construction materials. Industrial byproducts have driven a special interest in launching a new era in construction activities in place of conventional materials. Industrial byproducts such as waste foundry sand, blast furnace slag, steel slag, bottom ash, copper slag, and fly ash are used in large quantities in concrete applications for producing better strength, durability, and environmentally friendly concrete [1, 2]. Owing to its environmental concerns, there was a minimal analysis of the functionality of ferrochrome slag in transportation engineering applications. Every metallurgical processing industry has massive deposits piled over huge areas, which result in the leaching of toxic elements into the ground in events of saturation. In this case, ferrochrome slag occupies the available land and contains toxic metals that can cause leaching. Residual chromium in ferrochrome slag is liable for leaching and results in environmental contamination [3]. Magnetic separation and crushing followed by the jiggling process produce about 59% of the residual chromium from the slag [4]. Presently,

*Corresponding author: ajay.chappa91@gmail.com

^a orcid.org/0009-0001-0728-1461; ^b orcid.org/0009-0004-1847-6012

DOI: <http://dx.doi.org/10.17515/resm2023.559.ma1010>

two challenges have to be addressed 1) preventive measures to reduce chromium leaching from slag and 2) to characterize it as pavement material for its maximum utility. So adequate research on its use in view of its environmental concern may maximize the benefit of ferrochrome slag as pavement construction material and reduce several environmental issues.

To meet the design standards of MoRTH, ferrochrome slag gradation has to be improved to use in granular sub-base and base course of flexible pavement. So there was a need to explore cost-effective alternative materials. Quarry dust was a primary byproduct of the rock processing industry, accounting for 20-25% of output. Around 175 million tons of dust was generated from various sources like mining, crusher units, and quarry units [5]. These non-biodegradable wastes were deposited, blown, and entrapped as particulate matter in the air creating an environmental problem. Humans and animals can also easily inhale this dust at a quarry site [6, 7]. So its emissions should be controlled to reduce the problem. This study used quarry dust from 10% to 50% (with 10% intervals) to improve the gradation of ferrochrome slag. The use of ferrochrome slag and quarry dust materials in flexible pavement layers is an economical and sustainable solution to renew natural resources.

2. Background Studies

Sanghamitra et al. reported that ferrochrome slag aggregate had good mechanical properties, and its use in granular layers can lessen the demand for conventional aggregate [2,8]. The unconfined compressive strength, California bearing ratio (CBR), and shear strength of red soil was found to be improved by stabilizing it with ferrochrome slag and ferrochrome ash in proportions of 10%-50% (with 10% intervals) [9]. It can also be used as a subbase material through improvement in gradation of ferrochrome slag by proportioning with soil (i.e., slag: soil, 80:20) [10]. According to the marshall stability test, the slag-based mixtures were better in confrontation with the water effect than the conventional bituminous concrete mixture [11].

However, concerns have been outstretched due to residual chromium (Cr) in slag, which can leach and create ecological issues. Lind et al. constructed a ferrochrome slag road base and found minimal migration of chromium to the surrounding soil and groundwater [12]. Even at ambient temperature, ferrochrome slag remained in stable condition and was under regulatory terms of the United States Environmental Protection Agency (USEPA)[13] Though it was stable at ambient temperature, to ensure safe disposal and to prevent heavy metal leaching, solid waste has to be solidified using the right stabilization technology [14]. Complex calcium chromate was created on stabilization with Portland cement, reducing the solubility of Cr(VI) [15]. It was influential in stabilizing ferrochrome dust using cement mixtures and revealed that the leaching behavior of immobilized ferrochrome was within acceptable limits [16]. This remarkable effect of solidification was also proven to be effective in the immobilization of chromium in concrete applications reported by Panda CR et al [17]. Due to the good mechanical properties of the ferrochrome slag aggregate, it also exhibits high performance than conventional aggregates [18-24]. In this context, it is advantageous to use ferrochrome slag in cement-treated granular bases to immobilize chromium (VI) in CSH phases and to address the environmental issue.

Cement-treated or cement-bound layers include granular materials and measured quantities of cement and water, compacted to reach maximum density. Granular materials can be a combination of locally available materials and waste materials. Cement stabilization of weak subgrade helps in the economical design of pavement due to increased modulus and reduced vertical strain [25]. A granular subbase and base course with 2% cement stabilization were found to be suitable for low-traffic roads [26]. In recent studies, reclaimed asphalt pavement materials, recycled concrete aggregate, and industrial wastes were also cement treated to reduce dumping and environmental issues. Cement-treated recycled asphalt aggregates can be economically used as a replacement for virgin aggregate up to 30% in bounded layers of pavement [27-29]. So, cement-stabilized ferrochrome mixtures as road bases could be a better solution to keep heavy metal leaching within allowable limits without posing environmental issues [30, 31].

Here are some studies that focused on the use of quarry dust. The CBR of laterite soil can be considerably improved with 30% quarry dust addition, and further stabilizing it with 6% cement satisfies the criteria for a base course [32]. Fly ash and quarry dust mixed in a ratio of 1:2 up to 45% proportion in expansive soil can strengthen the subgrade soil [33]. Even its performance effectively decreases the swelling index of expansive clay soils [34]. When high plasticity silty soil was proportioned with quarry dust, the CBR value of the subgrade increased significantly [35]. The rutting resistance was also improved with the inclusion of quarry byproducts and RAP as coarse aggregate in the cement-treated granular layers of flexible pavement [36].

In this study, an attempt was made to check the suitability of ferrochrome slag and quarry dust as cement-bound pavement layers. Ferrochrome slag and quarry dust were blended in different proportions (90/10, 80/20, 70/30, 60/40, 50/50 of FS/Q) to check suitability as cement-bound subbase and base course in flexible pavements. Depending on the specifications stipulated by the MoRTH, 70/30 and 60/40 gradations were finalized to stabilize with cement content ranging from 2% to 10% (by dry weight of the mixture). The cement-treated ferrochrome slag-quarry dust samples were prepared and tested for unconfined compressive strength and ultrasonic pulse velocity test at different moist curing durations. Based on the desired UCS strength specified by the MoRTH, arrived at optimum levels of cement contents for use as cement-bound pavement layers.

3. Research Significance

Globally ferrochrome slag has been widely investigated for concrete applications due to its ability to encapsulate in calcium silicate hydrate (CSH) phases and increase Cr (VI) volatilization. Although environmental impact assessment studies have asserted that chromium leaching was within permissible limits, its use in pavement layers is minimal. Thus framework was developed to study the strength properties of cementitious ferrochrome slag and quarry dust composites through the UCS and UPV tests. This study helps practicing engineers enhance the utility of ferrochrome slag in cement-bound pavement layers.

4. Materials and Methods

4.1. Materials

Ferrochrome slag was collected from Jindal Stainless Steel Industry, Vizianagaram, Andhra Pradesh (AP). Quarry dust was collected from a nearby quarry in Vizianagaram, AP. As per IS 2386 [37], sieve analysis was performed to analyze the grain size distribution. Ferrochrome slag and quarry dust were classified as poorly graded gravel and poorly graded silty sand. The gradation curves and their corresponding IS soil classification are presented in Fig.2 and Table 3. It can be observed from the sieve analysis, ferrochrome slag has a maximum size of 10mm and a minimum size of 1.18mm, indicating that there was a deficiency of fines less than 1.18mm. Since ferrochrome has no fines, it was less sensitive to water and also there was in need to improve its gradation. Hence, mechanical stabilization of ferrochrome slag was done by mixing it with quarry dust in proportions of 90/10, 80/20, 70/30, 60/40, and 50/50 so as to improve its gradation for use as sub-base and base course material [38]. The attributes of ferrochrome slag and quarry dust are depicted in Tables 1 and 2. Ferrochrome slag and quarry dust used in this study are presented in Fig.1

The sieve analysis of the different gradations and their respective Indian soil classification systems are presented in Fig.2 and Table 3. Based on the sieve analysis from Table 3, FS90Q10 was classified as a well-graded aggregate but failed to satisfy the gradation limits specified by MoRTH as shown in Fig.2 [39]. Whereas, FS80Q20 and FS50Q50 mixtures were within the gradation limits but classified as poorly graded material as shown in Table 3. FS70Q30 and FS60Q40 composites satisfied the MoRTH gradation limits and were classified as well-graded materials. So in this study, cement stabilization was carried out by considering two gradations, i.e., FS70Q30 and FS60Q40.

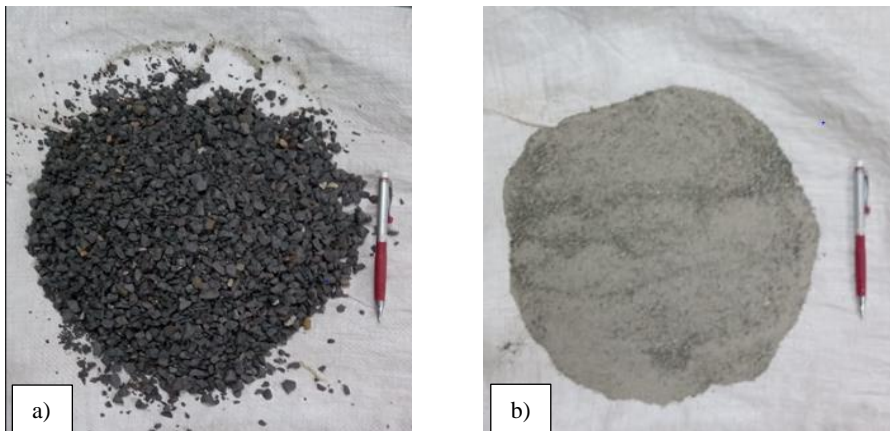


Fig.1. Materials used in this study a) Ferrochrome slag and b) Quarry dust

Table 1. Physical properties of the ferrochrome slag [40]

Physical Property	Test Value	Maximum allowable limits specified by MoRTH (2013)
Specific gravity	3.16	NA
Water absorption, %	0.37	2.0
Aggregate impact value, %	9.63	30
Angularity number	8	0-11
Flakiness and elongation Index, %	20.37	35
Los angeles abrasion Value, %	22.39	40
Soundness (based on MgSO ₄) %	2.83	18

Table 2. Physical properties of quarry dust

Property	value
Specific gravity	2.55
Liquid limit	NP
Plastic limit	NP
Optimum moisture content (OMC), %	10.36
Maximum dry density (MDD), g/cc	2.047
California bearing ratio (CBR), %	24.3

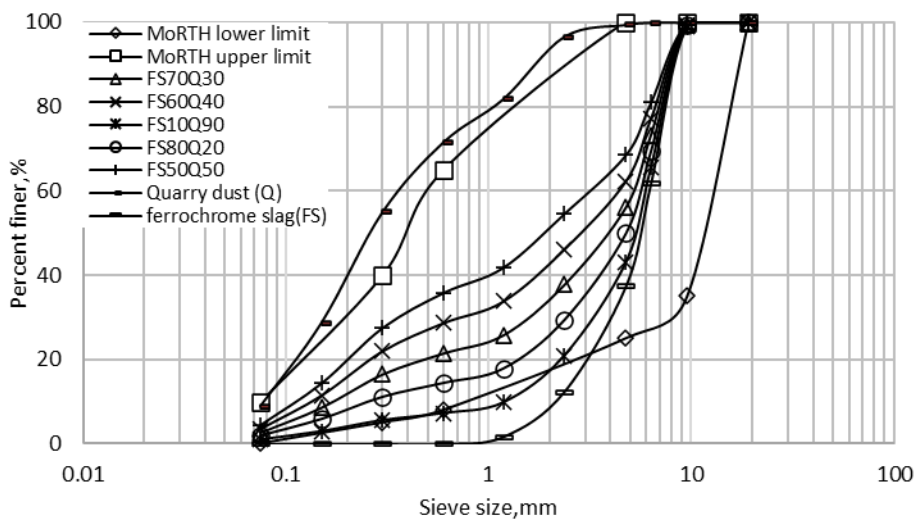


Fig. 2. Grain size distribution curves of ferrochrome slag, quarry dust and their combinations

Table 3. IS soil classifications of ferrochrome slag, quarry dust and their combinations

Mix	Coefficient of Uniformity (C_u)	Coefficient of Curvature (C_c)	IS Soil Classification
Ferrochrome slag (FS)	3	1.33	GP
Quarry dust(Q)	4.5	9	SP-SM
FS90Q10	4.83	1.38	GW
FS80Q20	20	4	GP
FS70Q30	29	2.64	SW
FS60Q40	32.3	1.05	SW
FS50Q50	30	0.44	SP

4.2 Preparation of samples

Initially, air-dried ferrochrome slag and quarry dust samples were mixed in the required proportions (FS70Q30 and FS60Q40). Cement content of 2 to 10% (by dry weight of the aggregate mix) was then added to the FS70Q30 and FS60Q40 mixtures. Ferrochrome slag, quarry dust, and cement are mixed thoroughly to ensure homogeneity before mixing with water. Care was taken to complete mixing and compaction within 30 minutes after the addition of water, as initial hydration would occur. A heavy compaction rammer weighing 4.89 kg was used to compact cement-treated mixtures in 5 layers to determine compaction properties as per IS 4332 part III [41]. Optimum moisture content (OMC) and maximum dry density (MDD) were ascertained for each cement content of FS70Q30 and FS60Q40 mixes. Cement-treated ferrochrome slag and quarry dust mixes of cylindrical size (100 mm dia. X 200 mm height) were prepared at OMC and MDD for conducting unconfined and ultrasonic pulse velocity tests. The experimental program resulted in 10 mixtures, and their details are depicted in Table 4.

Table 4. Experimental matrix

Mix proportion	Ferrochrome slag (FS), %	Quarry dust (Q), %	Cement content (C), %	Number of replicates	Type of test
FS70Q30	70	30	2	03	<ul style="list-style-type: none"> • Compaction characteristics • UCS test* • UPV test*
			4		
			6		
			8		
			10		
FS60Q40	60	40	2	03	<ul style="list-style-type: none"> • UPV test*
			4		
			6		
			8		
			10		

*Note; Tests conducted at 3, 7, 14, and 28 days of moist curing

4.3. Tests

4.3.1. Unconfined Compressive Strength (UCS)

UCS test was carried out as per IS4332 part V [42] on cement-treated ferrochrome slag mixtures. This test was conducted to evaluate the interfacial contact of ferrochrome slag with cement dust matrix in terms of strength. The samples were prepared with heavy compaction effort and compacted in 5 layers in steel cylindrical split molds (100 mm X 200 mm). All UCS samples were demolded after 24 hours of casting for sample retention.

Polyethylene plastic covers were wrapped around the specimens (Fig.3) to prevent moisture loss into the atmosphere after demolding and to allow cement hydration to occur with OMC. The compressive load was applied to the specimens up to failure, and the corresponding failure load was recorded. The average of the three samples was taken as the test value.



Fig.3 Cylindrical test specimens wrapped in polyethylene sheet

4.3.2 Ultrasonic Pulse velocity test (UPV)

The UPV was performed as per IS 516 [43] on cement-treated ferrochrome slag and quarry dust composites. A longitudinal wave was transmitted through the specimen through transducers fixed at one surface and another at the point of defined length. The second transducer, located at a distance of "L," converts the created pulse into electrical energy. The amount of time (t) required for a wave to traverse a predetermined distance, "L," was determined electronically. The velocity of the longitudinal wave through the test specimen was determined by dividing the predetermined length "L" with the corresponding transmission time "t". The quality of cement-stabilized ferrochrome slag and quarry dust composites was evaluated by measuring their wave velocity.

5. Results and Discussion

5.1. Compaction Characteristics

The OMC and MDD of cement-stabilized FS70Q30 and FS60Q40 composites at different cement contents were determined and their compaction curves are presented in Fig.4. From Table 5, the OMC and MDD of FS70Q30 are found to be 6.68% to 7.38% and 2.43g/cc to 2.46g/cc, respectively, for cement contents of 2% - 10%. The OMC and MDD of FS60Q40, for 2-10% cement contents, ranged from 6.33% to 6.81% and 2.387g/cc to 2.424g/cc, respectively. It was observed that the MDD of FS70Q30 mixes was higher than FS60Q40 mixes due to a higher proportion of ferrochrome slag in the FS70Q30 mixes. The overall change in OMC ranged from 6.33 to 7.38%, which shows an insignificant change with an increase in cement content, and these findings agree with previous studies [44,27]. MDD

of FS70Q30 and FS60Q40 mixes were found to increase up to 6% cement content due to reduced void ratio, as shown in Table 5. This may also be due to the difference in specific gravities of quarry dust(2.55) and cement(3.11) [45]. As a result, cement being finer than the quarry dust fills the available voids in the mix, thereby increasing the dry density and reducing the void ratio. Cement content above 6% leads to flocculation of mixtures, which causes a slight change in MDD and increased void ratios of cement-treated mixtures [46].

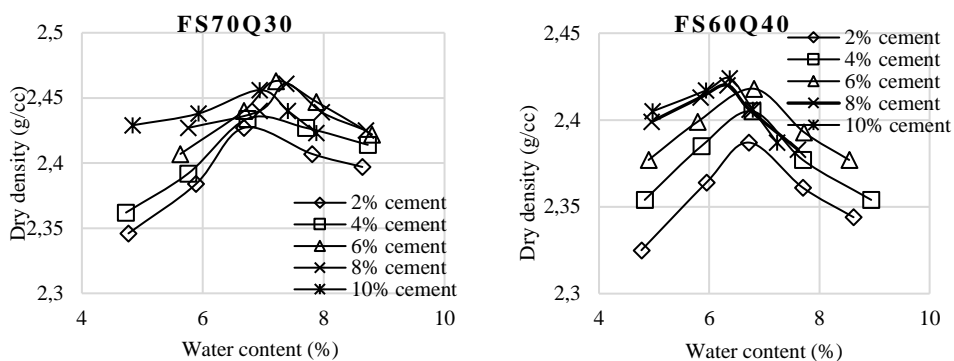


Fig.4 Compaction curves of cement stabilized FS70Q30 and FS60Q40 mixes corresponding to various cement contents

Table 5. Compaction characteristics of FS70Q30 and FS60Q40

Cement content (%)	FS70Q30			FS60Q40		
	OMC (%)	MDD (g/cc)	Void ratio (e)	OMC (%)	MDD (g/cc)	Void ratio (e)
0	6.17	2.392	0.208	6.43	2.368	0.193
2	6.68	2.427	0.192	6.72	2.387	0.186
4	6.74	2.434	0.191	6.78	2.406	0.178
6	7.21	2.463	0.178	6.81	2.418	0.174
8	7.38	2.461	0.181	6.33	2.420	0.175
10	6.94	2.456	0.184	6.37	2.424	0.175

5.2. Physical Examination

From visual inspection, it was found that FS60Q40 mixtures has a well-finished surface texture covering all the voids, as shown in Fig.5. The FS60Q40, with sufficient fines, provides good bonding and requires less cement than FS70Q30, with a deficiency of fines [47]. It was seen from Fig.6 that when FS60Q40 mix (with 2% cement content) was held together in our hands, it formed a lump indicating inter-granular bonding of quarry dust with cement, whereas FS70Q30 mix failed to form a lump in the absence of fines.

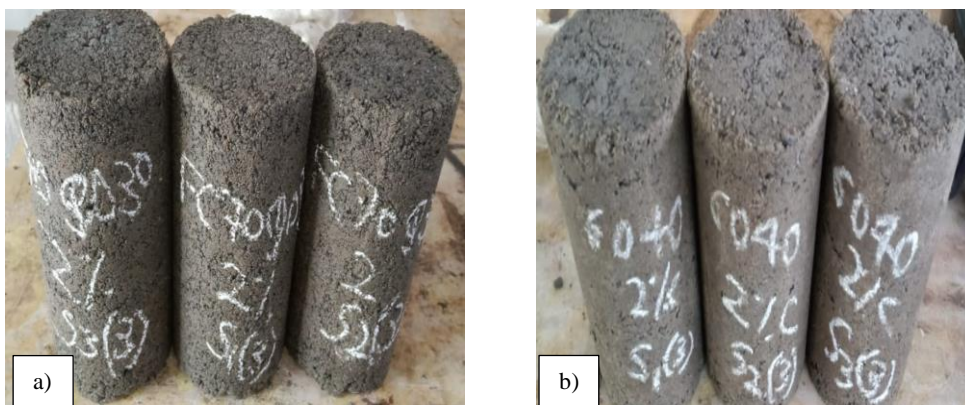


Fig.5 Variation of surface texture a) FS70Q30+2% b) FS60Q40+2%

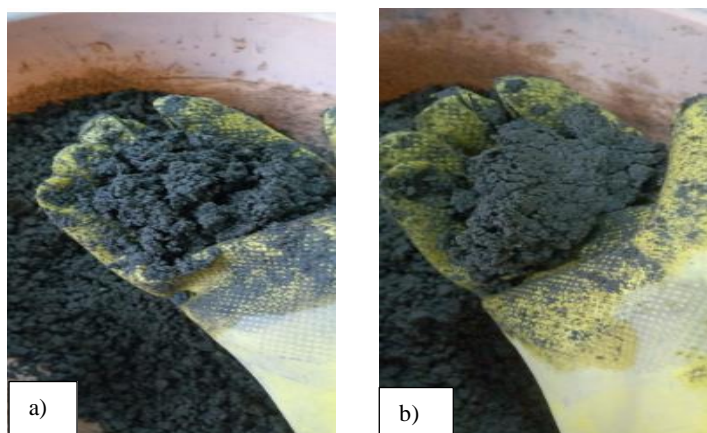


Fig.6 Variation of clump formation a) FS70Q30+2% b) FS60Q40+2%

5.3. Unconfined Compressive Strength (UCS)

The UCS of cement stabilized FS70QD30 and FS60QD40 mixtures corresponding to moist curing periods of 3, 7, 14, and 28 days for various percentages of cement (2-10%) are presented in the form of a bar graph in Fig.7. 3 samples were prepared for each cement content and curing duration (120 specimens). The standard deviations (SD) of the strengths for each cement content were calculated, and their deviation bars are depicted in Fig.7. The overall SD of the mixtures was in the range of 0.03 MPa to 1.47 MPa.

5.3.1 Effect of cement on UCS of the FS70Q30 and FS60Q40 mixes

Experimental results indicated an increase in UCS values with cement content as shown in Fig. 8. An increase in cement content resulted in the densification of the mix due to the gradual filling of pores with cement and more cementitious action[45]. The ferrochrome slag could hardly influence the hydration process as it was less sensitive to water. The high angularity of ferrochrome slag contributed to good interlocking and increased shear strength of the cement-bound mixtures. Therefore, the inclusion of quarry dust in the

mixtures provided the necessary fines for the cement hydration to occur effectively. [48,49].

The UCS values at three days of moist curing ranged from 0.859 MPa to 9.904 MPa for the FS70Q30 mix and 1.090 MPa to 10.980 MPa for the FS60Q40 mix. UCS values at seven days of moist curing ranged from 0.946 MPa to 11.178 MPa for the FS70Q30 mix and 1.128 MPa to 12.630 MPa for FS60Q40. UCS values at 14 days of moist curing ranged from 1.689 MPa to 17.480 MPa for the FS70Q30 mix and 1.916 MPa to 20.540 MPa for FS60Q40. UCS values at 28 days of moist curing ranged from 1.989 MPa to 23.850 MPa for the FS70Q30 mix and 2.814 MPa to 24.995 MPa for FS60Q40, indicating a significant increase in strength with the cement content increment. The maximum UCS of 24.995 MPa was reported at 10 % cement content of the FS60Q40 and a minimum UCS of 0.946 MPa at 2% cement content of FS70Q30. The major increase in strength was recorded at 4% cement content of all the mixtures with respect to 2%. Further, it was noticed that the UCS strength of FS60Q40 was between 1.03 to 1.62 times the UCS of FS70Q30 at all cement contents and curing durations. The percentage of voids in the FS60Q40 mix was found to be 3.1 to 4.9% lower than FS70Q30 mix. This reduced void ratio was due to more quarry fines in FS60Q40 providing more significant contact points with cement than in FS70Q30 [50]. This allows for an efficient hydration process due to increased cement contact points, a more solid matrix, and increased strength in FS60Q40. Therefore, for a given cement content, FS60Q40 provided higher compressive strength when compared to FS70Q30.

5.3.2 Effect of curing period on UCS

Fig.7 indicates that the UCS values improve notably with longer curing periods for all mixtures [51, 26] Hydration time plays a crucial role in filling the pores with calcium hydroxide. As the curing period increases, the water available in the pores (OMC) reacts with the cement to form CSH (hardened paste).

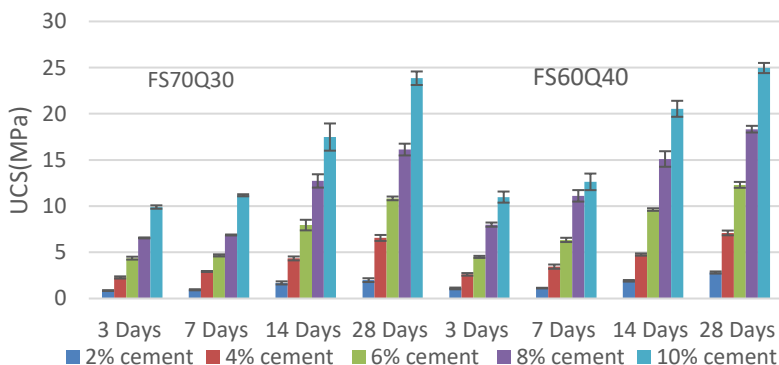


Fig.7 Variation of UCS with curing period

Initially, during compaction, the voids were filled with water (OMC) and un-hydrated cement dust particles. After obtaining the final strength, the voids were filled with hardened paste (CSH). These phenomena can be well noted through the attainment of strength with the curing period. Cement-treated mixtures gained only 34% to 44% of their

28-day UCS strength at 3 days of moist curing. About 42% to 60% of their 28-day UCS strength was achieved in 7 days. During the first 14 days of moist curing, strength was achieved between 66% and 85% of their 28-day UCS strength. IRC-37[52] recommends UCS strength of 7 days as a quick assessment for minimum cement requirement for the sub-base and base course of flexible pavement.

5.3.3. Minimum cement requirement based on UCS

According to IRC 37 [52], the recommended UCS values range from 1.5 to 3.0 MPa for cementitious sub-base and 4.5 to 7 MPa for cementitious base course at 7 days of moist curing. The percentage of cement content requirements for stabilizing ferrochrome slag and quarry dust composites is depicted in Table 3 based on the correlation developed between cement content (C) and UCS. Regression analysis was done to correlate UCS values against different cement contents. It can be observed in Fig.7 that a power function can be set up to assess the relationship between UCS and cement content for FS70Q30 and FS60Q40 mixes. In one of the studies, it was stated that a logarithmic relationship could be developed to correlate cement content and UCS (eq.1) at 28 days of curing [30]. Regression curves, their respective power function equation, and correlation factors are presented in Fig.8.

$$UCS = 6.27\ln(PC) - 1.898; R^2 = 0.965 \quad (1) [30]$$

Where PC is Portland cement and UCS is the unconfined compressive strength of cement-bound ferrochrome slag.

Table 6. Cement requirement for FS70Q30 and FS60Q40 mixes

Moist curing days	FS70Q30 mix		FS60Q40 mix	
	Cement requirement (%)		Cement requirement (%)	
	Sub-base	Base course	Sub-base	Base course
3	2.95 - 4.67	6.11 - 8.19	2.64 - 4.21	5.58 - 7.58
7	2.69 - 4.30	5.66 - 7.64	2.36 - 3.69	4.80 - 6.39
14	1.88 - 3.02	3.98 - 5.39	1.75 - 2.77	3.64 - 4.88
28	1.60 - 2.54	3.33 - 4.46	1.26 - 2.11	2.84 - 3.94

As seen from the predicted curves, their regression coefficients for cement-treated FS70Q30 and FS60Q40 composites are found to be greater than 0.99. Since the value of the regression coefficient was nearly equal to one, the relationship between UCS and cement content developed from experimental data was significant in evaluating the UCS of cement-treated composites. The mean standard errors of the predicted values for the FS70Q30 mixes at 3, 7, 14, and 28 days were found to be 0.22MPa, 0.461MPa, 0.218MPa, and 0.46MPa. For FS60Q40 mixes, the standard errors were found to be 0.387MPa, 0.821MPa, 0.287 MPa, and 0.094MPa at 3, 7, 14, and 28 days, respectively. The observed standard errors were minimal for all the composites, indicating that the predicted values were close to the experimental observations.

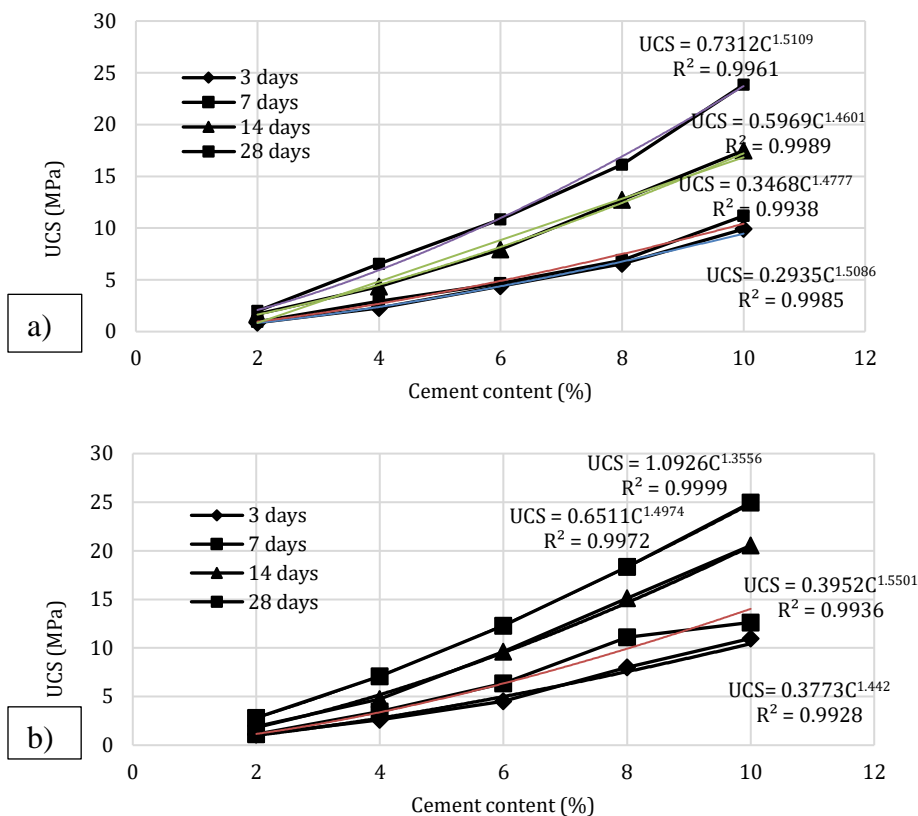


Fig.8 Variation of UCS with cement content a) FS70Q30 b) FS60Q40

Table 3 shows that due to the increased compressive strength of FS60Q40 over FS70Q30, the minimum cement requirement for FS70Q30 was higher than the FS60Q40. The minimum cement requirement for FS70Q30 is 2.7% and 5.7% for use as a sub-base and base course to attain the desired UCS values of 1.5 MPa and 4.5 MPa respectively. Similarly, 2.4% and 4.8% for FS60Q40 to use as sub-base and base courses. The minimum cement requirement for FS60Q40 was about 12-16% lower than that of FS70Q30. Based on seven days of compressive strength, MoRTH recommends a minimum of 2% cement content for the stabilization of sub-base and base courses in flexible pavements. However, from the analysis, the minimum cement content for 7-day UCS was found to be more than 2% as shown in Table 3.

5.4 Ultrasonic Pulse Velocity (UPV)mixes

UPV tests were conducted on cylindrical specimens of 100mm diameter and 200mm height moist cured for 3, 7, 14, and 28 days. The ultrasonic pulse was made to propagate through the cylindrical specimen along the 200mm length of the specimen using transducers positioned at each end of the specimen. 3 samples were prepared for each cement content and curing duration (120 specimens). The standard deviations (SD) of UPV values for each cement content were calculated, and their deviation bars are depicted in

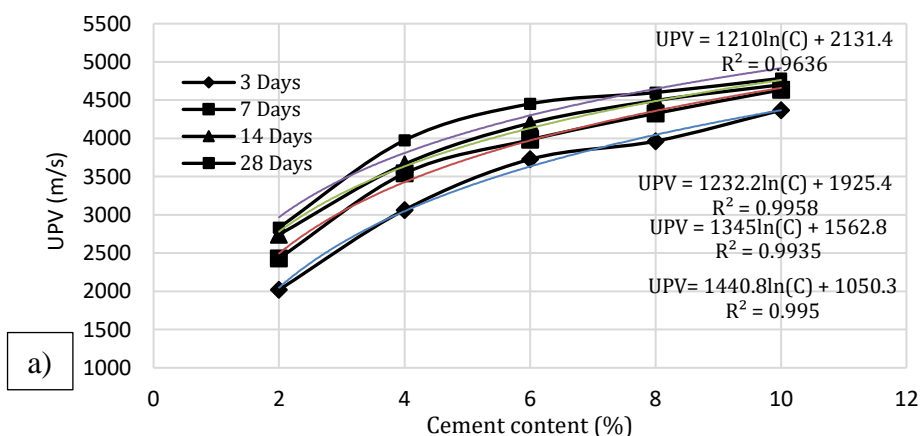
Fig.10. The overall SD of the cement-treated mixtures was found to be between 20.74m/s and 94.32m/s.

5.4.1. Effect of Cement on UPV

UPV values are plotted against the cement contents, as shown in Fig.9. In both FS70Q30 and FS60Q40 mixtures, an increase in UPV value was observed with cement content increment. It can be attributed to the fact that the filling of voids with an increase in cement content and the binding effect of cement [45]. Due to the reduced void ratio up to 6% cement content in both composites, a noticeable increase in UPV is observed. At higher cement contents (8% and 10%), a slight increase in UPV was observed as the cement to be filled exceeded the voids to be filled in the mix. A maximum increase in velocity was observed for 4% cement content with respect to 2% of all mixtures. The logarithmic variation can be set up to assess the relationship between UPV and cement content for FS70Q30 and FS60Q40 mixes, as shown in Fig.9. This relationship was in good agreement with one of the studies eq. 2 at 28 days of curing [30]. There is no noticeable difference between UPV values for the FS70Q30 and FS60Q40 mixes. The UPV values of FS70Q30 are almost identical to those of the FS60Q40 mix.

$$UPV = 1.171\ln(PC) + 1.388; R^2 = 0.993 \quad UPV \text{ in Km/s} \quad (2)[30]$$

The UPV values at three days of moist curing ranged from 2021 to 4367 m/s for the FS70Q30 mix and 2136 to 4272 m/s for FS60Q40. For seven days of moist curing, ranged from 2432 to 4634 m/s for the FS70Q30 mix and 2430 to 4412 m/s for FS60Q40. UPV values at 14 days of moist curing ranged from 2742 to 4701 m/s for the FS70Q30 mix and 2889 to 4564 m/s for FS60Q40. UPV values at 28 days of moist curing ranged from 2834 to 4784 m/s for the FS70Q30 mix and 3084 to 4691 m/s for FS60Q40.



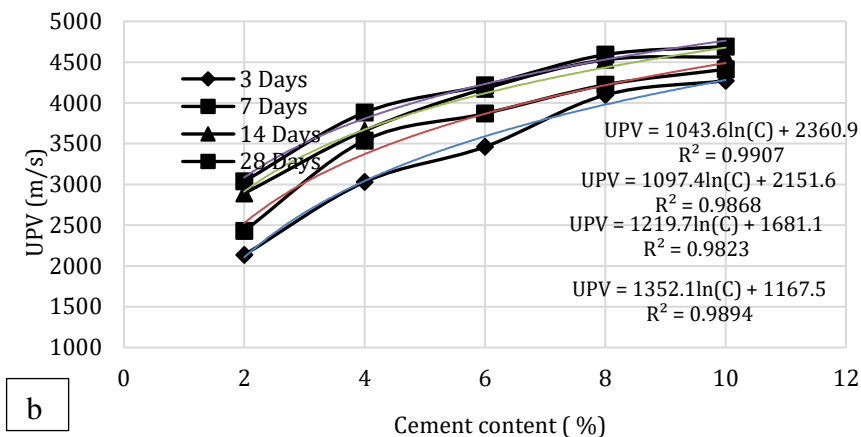


Fig. 9 Variation of UPV with the cement content a) FS70Q30 b) FS60Q4

As seen from the predicted curves, their regression coefficients for cement-treated FS70Q30 and FS60Q40 composites are found to be greater than 0.98. Since the value of the regression coefficient was near to one, the relationship between UPV and cement content developed from experimental data was significant in evaluating the UPV of cement-treated composites. The mean standard errors of predicted values for the FS70Q30 mix were found to be between 45.28m/s and 135.45m/s, and for the FS60Q40 mix, it was between 57.55m/s and 93.01m/s. The observed standard errors were minimal for all the cement composites, indicating that the predicted values were close experimental observations. The UPV values for FS70Q30 for minimum cement contents of 2.7% and 5.7% were found to be 2899 m/s and 3904 m/s, respectively. For FS60Q40, the UPV values corresponding to 2.4% and 4.8% are 2749 m/s and 3595 m/s, respectively.

5.4.2. Effect of Curing Period on UPV

It can be observed (Fig. 10) that the UPV value increased as the curing time of both FS70Q30 and FS60Q40 mixtures increased. This could be another sign that the hydration process has occurred, resulting in the densification of the composites with the increase in curing duration. In the early curing periods, relatively low values of UPV were observed due to the entrapped air and water in the voids of the mix. The influence of the entrapped air and undissolved water attenuates the pulse velocity. In the later stages of curing period, the entrapped air and water reduce, solid percolation path occurs due to the development of hydration products. As the hydration process progresses bridging between the particles takes place with a more connected path. This accelerates the UPV in the mixes with increase in curing period. At higher curing periods, the UPV slowly increases and remains stable as the maximum hydration products formed covering most of the voids in the mix. All cement-treated mixes achieved 70.29% to 91.30% of their 28-day curing velocities at 3-day moist curing. For 7-day curing, the velocities achieved ranged from 79.96% to 96.86% of their 28-day curing speeds. Similarly, for 14-day moisture curing, velocities ranging from 92.13% to 99.01% of their 28-day velocities were obtained. A significant

improvement in velocities with an increasing curing period was observed for 2% cement-treated mixes when compared to all mixtures.

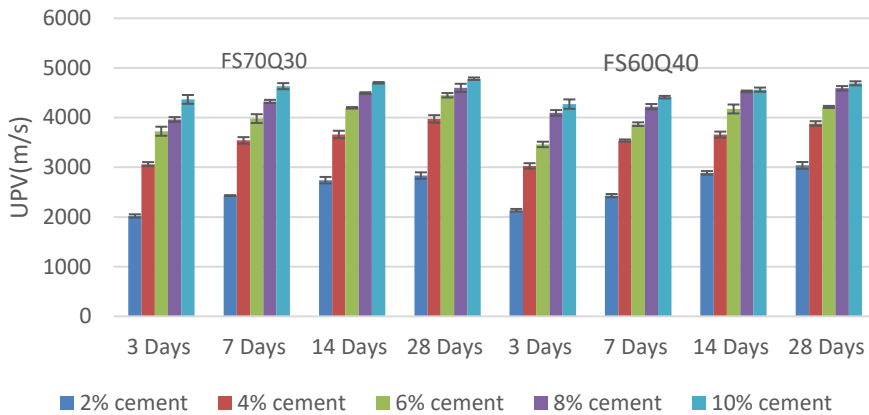


Fig.10 Variation of UPV with curing period

6. Microstructure Analysis

To analyze the behavior of the material at the microscopic level, a scanning electronic microscope (SEM) was conducted on the FS70Q30 and FS60Q40 composites. SEM images are obtained to evaluate pores and hydration products as depicted in Fig. 11. The FS70Q30 has a large number of voids and rod-like crystals (Ettringite) when compared to the FS60Q40. The cement hydration product CSH gel formed around the aggregate (Agg.) can be evident from the two images. FS70Q30 was also observed to be less compact, while the FS60Q40 structure was more closely packed. This can be attributed to the higher strength of the FS60Q40 mix than FS70Q30 for a given cement content.

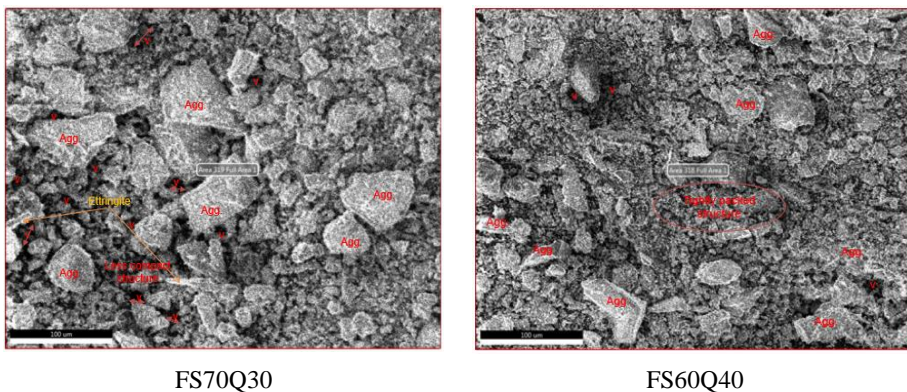


Fig. 11 SEM images at 4% cement contents for both the composites

7. Conclusions

The present study attempts to explore and comprehend the behavior of ferrochrome slag and quarry dust composites upon cement stabilization for sustainable development. The following conclusions are drawn from the study.

- From the particle size analysis, ferrochrome slag(FS) was classified as poorly graded material and has a deficiency of fines below 1.18mm. Hence, quarry dust(Q) was incorporated in different proportions to enhance the gradation of ferrochrome slag to make it suitable as cement-bound layers of flexible pavements. Only FS70Q30 and FS60Q40 mixes were classified as well-graded materials and satisfied the gradation limits specified by the MoRTH.
- The OMC and MDD of the cement-treated mixes were found to be in the range of 6.33 to 7.38% and 2.387 to 2.456g/cc respectively. No appreciable variation in OMC with increasing cement content was found. While MDD increased up to a cement content of 6% due to the filling of voids with cement resulting in a reduced void ratio. However, the addition of cement beyond 6% resulted in flocculation of the mixes thereby increasing the void ratio and subsequent decrease in MDD.
- The high angularity of the ferrochrome slag contributed to the overall strength of the composites, while quarry dust inclusion provided sufficient fines for the cement hydration to occur.
- The unconfined compressive strength (UCS) and ultrasonic pulse velocities (UPV) of the cement-treated composites increased with an increase in cement content. This can be attributed to the gradual filling of voids and the densification of the mixes with increasing cement.
- The UCS of FS60Q40 mixes was found to be 1.03 to 1.62 times higher than the UCS of FS70Q30 mixes. The higher proportion of quarry dust in FS60Q40 mixes over FS70Q30 resulted in a reduced void ratio and enhanced contact area with cement particles. A greater inter-contact surface with cement helps in the effective hydration process, thereby increasing the strength of FS60Q40 mixes.
- The statistical equations developed in the study can be useful in predicting UCS and UPV values for a given cement content. The high correlation factors of the developed equations indicate that the dependency of UCS and UPV on cement content was well established. These equations were also useful for estimating the corresponding cement content for desired UCS values specified by the MoRTH.
- The minimum cement required for use as a cementitious sub-base and base courses was found to be in the range of 2.4% to 2.7% and 4.8% to 5.7% respectively. Due to higher compressive strengths of FS60Q40 mixes, the minimum cement contents required for stabilization was found to be 12-16% lower than FS70Q30 mixes.
- The UCS increased significantly with increasing curing time. The 7-day strengths of the cement-treated mixtures were found to be between 40% and 60% of the 28-day strengths. Longer curing periods were essential for effective cement hydration to attain maximum strength. Even with lower cement contents with prolonged curing periods can help in achieving minimum strength.

- Cement-stabilized ferrochrome slag and quarry dust composites (FS70Q30 and FS60Q40) may be used as cementitious sub-base and base courses in flexible pavements. However, further investigations through durability and field testing need to be carried.

Competing interests

The authors have no relevant financial or non-financial interests to disclose. The corresponding author declares that no funding, grants or any other support was received during the progress of the work and preparation of the manuscript.

References

- [1] Dash MK, Patro SK, Rath AK. Sustainable use of industrial-waste as partial replacement of fine aggregate for preparation of concrete–A review. *International Journal of Sustainable Built Environment*. 2016 Dec 1;5(2):484-516. <https://doi.org/10.1016/j.ijsbe.2016.04.006>
- [2] Ojha PN, Singh A, Singh B, Trivedi A, Kaura P. Recent Research On Iron, Steel, Copper and Ferrochrome Slag For Utilization In Construction Industry. 2022 Dec.
- [3] Shen H, Forssberg E. An overview of recovery of metals from slags. *Waste management*. 2003 Jan 1;23(10):933-49. [https://doi.org/10.1016/S0956-053X\(02\)00164-2](https://doi.org/10.1016/S0956-053X(02)00164-2)
- [4] Ramachandra Rao S Chapter 8 – Metallurgical Slags, Dust and Fumes.” *Waste Management Series 7* 2007 Sep: 269-327.
- [5] Sairanen M, Rinne M, Selonen O. A review of dust emission dispersions in rock aggregate and natural stone quarries. *International Journal of Mining, reclamation and environment*. 2018 Apr 3;32(3):196-220. <https://doi.org/10.1080/17480930.2016.1271385>
- [6] Bluvshstein N, Mahrer Y, Sandler A, Rytwo G. Evaluating the impact of a limestone quarry on suspended and accumulated dust. *Atmospheric Environment*. 2011 Mar 1;45(9):1732-9. <https://doi.org/10.1016/j.atmosenv.2010.12.055>
- [7] Olusegun O, Adeniyi A, Adeola GT. Impact of granite quarrying on the health of workers and nearby residents in Abeokuta Ogun State, Nigeria. *Ethiopian journal of environmental studies and management*. 2009;2(1).
- [8] Sanghamitra B, Reddy CN. Potential of Ferro chrome slag as construction material. *Indian Highway*. 2017 Jun;45(6):11-7.
- [9] Das BB. Characterization of ferrochrome slag as an embankment and pavement material (Doctoral dissertation).
- [10] Sinha AK, Havanagi VG, Kanaujia VK. Chrome slag in embankment and pavement construction. *Highw. Res. J*. 2017:45-54.
- [11] Yilmaz M, Kok BV. Effects of ferrochromium slag with neat and polymer modified binders in hot bituminous mix. *Indian J Eng Mater Sci*. 2009;16(5):310-8. <http://hdl.handle.net/11508/8772>
- [12] Lind BB, Fällman AM, Larsson LB. Environmental impact of ferrochrome slag in road construction. *Waste Management*. 2001 Jun 1;21(3):255-64. [https://doi.org/10.1016/S0956-053X\(00\)00098-2](https://doi.org/10.1016/S0956-053X(00)00098-2)

- [13] Panda CR, Mishra KK, Nayak BD, Rao DS, Nayak BB. Release behaviour of chromium from ferrochrome slag. *International Journal of Environmental Technology and Management*. 2012 Jan 1;15(3-6):261-74. <https://doi.org/10.1504/IJETM.2012.049227>
- [14] Risk Reduction Engineering Laboratory (US), Center for Environmental Research Information (US). *Stabilization/solidification of CERCLA and RCRA wastes: Physical tests, chemical testing procedures, technology screening, and field activities*. Center for Environmental Research Information; 1989.
- [15] Wang S, Vipulanandan C. Solidification/stabilization of Cr (VI) with cement: Leachability and XRD analyses. *Cement and concrete research*. 2000 Mar 1;30(3):385-9. [https://doi.org/10.1016/S0008-8846\(99\)00265-9](https://doi.org/10.1016/S0008-8846(99)00265-9)
- [16] Bulut U, Ozverdi A, Erdem M. Leaching behavior of pollutants in ferrochrome arc furnace dust and its stabilization/solidification using ferrous sulphate and Portland cement. *Journal of hazardous materials*. 2009 Mar 15;162(2-3):893-8. <https://doi.org/10.1016/j.jhazmat.2008.05.114>
- [17] Panda CR, Mishra KK, Panda KC, Nayak BD, Nayak BB. Environmental and technical assessment of ferrochrome slag as concrete aggregate material. *Construction and Building Materials*. 2013 Dec 1;49:262-71. <https://doi.org/10.1016/j.conbuildmat.2013.08.002>
- [18] Hang M, Wang J, Zhou X, Sun M. Design and Study of Physical and Mechanical Properties of Concrete Based on Ferrochrome Slag and Its Mechanism Analysis. *Buildings*. 2023 Jan;13(1):54. <https://doi.org/10.3390/buildings13010054>
- [19] Gericke WA. Environmental solutions to waste products from ferrochrome production. *Proceedings of the 8th International Ferroalloys*. 1998 Jun 7:51-8.
- [20] Acharya PK, Patro SK. Utilization of ferrochrome wastes such as ferrochrome ash and ferrochrome slag in concrete manufacturing. *Waste Management & Research*. 2016 Aug;34(8):764-74. <https://doi.org/10.1177/0734242X1665>
- [21] Zelić J. Properties of concrete pavements prepared with ferrochromium slag as concrete aggregate. *Cement and Concrete Research*. 2005 Dec 1;35(12):2340-9. <https://doi.org/10.1016/j.cemconres.2004.11.019>
- [22] Rajashekar K, Reddy CS. An experimental study on use of ferrochrome slag aggregate in concrete making. *ICI Journal*. 2015 Jan;15(4):25-9.
- [23] Mallick T, Mishra SP, Nayak Sipalin SM. Part substitute of river sand by Ferrochrome slag in cement concrete: Industrial waste disposal. *Journal of Xidian University*. 2020;14(4).
- [24] Sheen YN, Huang LJ, Sun TH, Le DH. Engineering properties of self-compacting concrete containing stainless steel slags. *Procedia engineering*. 2016 Jan 1;142:79-86. <https://doi.org/10.1016/j.proeng.2016.02.016>
- [25] Sargand SM, Houry I, Gray J, Al-Jhayyish A. Incorporating chemical stabilization of the subgrade in pavement design and construction practices. *ORITE*; 2014 Oct.
- [26] Hossain AS, Hoque AM, Zaniewski JP. Stabilization of alluvial soils with cement and cement-rice husk ash blend for low-volume road construction in Bangladesh. *Transportation Research Record*. 1991(1291). <http://onlinepubs.trb.org/Onlinepubs/trr/1991/1291vol1/1291-071.pdf>

- [27] Kasu SR, Manupati K, Muppireddy AR. Investigations on design and durability characteristics of cement treated reclaimed asphalt for base and subbase layers. *Construction and building materials*. 2020 Aug 20;252:119102. <https://doi.org/10.1016/j.conbuildmat.2020.119102>
- [28] Chakravarthi S, Boyina A, Singh AK, Shankar S. Evaluation of cement treated reclaimed asphalt pavement and recycled concrete pavement bases. *International Journal of Pavement Research and Technology*. 2019 Nov;12:581-8. <https://doi.org/10.1016/j.conbuildmat.2020.119102>
- [29] Xuan DX, Molenaar AA, Houben LJ. Evaluation of cement treatment of reclaimed construction and demolition waste as road bases. *Journal of Cleaner Production*. 2015 Aug 1;100:77-83. <https://doi.org/10.1016/j.jclepro.2015.03.033>
- [30] Yilmaz A, KARAŞAHİN M. Compressive strength of cement-bound base layers containing ferrochromium slag. *Turkish Journal of Engineering and Environmental Sciences*. 2013 Oct 1;37(3):247-58.
- [31] Kambole C, Paige-Green P, Kupolati WK, Ndambuki JM. Ferrochrome slag aggregate: physical-chemical characteristics and potential use in lightly cemented road bases. *World Journal of Engineering*. 2023 Jan 11;20(1):93-102. <https://doi.org/10.1108/WJE-12-2020-0666>
- [32] Eze-Uzomaka OJ, Agbo D. Suitability of quarry dust as improvement to cement stabilized-laterite for road bases. *Electronic Journal of Geotechnical Engineering*. 2010;15:1053-66.
- [33] Sabat AK, Bose B. Improvement in geotechnical properties of an expansive soil using fly ash -quarry dust mixes. *Electron J Geotech Eng*. 2013;18 Q(January 2013):3487-500.
- [34] Sudhakar S, Duraisekaran E, Dilli Vignesh G, Kanna GD. Performance evaluation of quarry dust treated expansive clay for road foundations. *Iranian Journal of Science and Technology, Transactions of Civil Engineering*. 2021 Dec;45:2637-49. <https://doi.org/10.1007/s40996-021-00645-4>
- [35] Priyankara NH, Wijesooriya RM, Jayasinghe SN, Wickramasinghe WR, Yapa ST. Suitability of quarry dust in geotechnical applications to improve engineering properties. *Engineer: Journal of the Institution of Engineers, Sri Lanka*. 2009 Jul 27;42(3).
- [36] Qamhia II, Tutumluer E, Ozer H, Shoup H, Beshears S, Trepanier J. Evaluation of chemically stabilized quarry byproduct applications in base and subbase layers through accelerated pavement testing. *Transportation Research Record*. 2019 Mar;2673(3):259-70. <https://doi.org/10.1177/0361198118821099>
- [37] IS:2386- Part I. Method of test for aggregate for concrete. Part I - Particle size and shape. *Indian Stand*. 1963;(Reaffirmed 2002).
- [38] IRC SP 89 part-I. Guidelines for Soil and Granular Material Stabilization Using Cement, Lime & Fly Ash. *Indian Roads Congr*. 2010;
- [39] MoRTH. Specifications for Road and Bridge Work. *Indian Roads Congress*. 2013. p. 1-883.
- [40] Ajay CH, Rani KD. Ferrochrome Slag characterization and its compatibility with Quarry dust in Flexible pavement. In *IOP Conference Series: Earth and Environmental Science* 2022 Mar 1 (Vol. 982, No. 1, p. 012008). IOP Publishing.

- [41] IS: 4332 (Part-3). Test for Determination of Moisture Content–Dry Density Relation for Stabilized Soils Mixtures. Bur Indian Stand. 2010;
- [42] IS: 4332 (Part-V) 1970 (Reaffirmed 1995). Method for Determination of Unconfined Compressive Strength Of Stabilized Soils. Bur Indian Stand New Delhi, India. 2010.
- [43] IS 516 (part5/Sec 1). Method for Determination of Non-destructive testing of concrete. Bur Indian Stand New Delhi, India 2018.
- [44] Prasad AC, Reddy CS. The Potential of Cement Stabilized Gravelly Soils as Construction Material. InProc. of Indian Geotechnical Conference-2011, Kochi, India 2011 Dec 15 (pp. 493-496).
- [45] Guotang Z, Wei S, Guotao Y, Li P, Degou C, Jinyang J, Hao H. Mechanism of cement on the performance of cement stabilized aggregate for high speed railway roadbed. Construction and Building Materials. 2017 Jul 30;144:347-56. <https://doi.org/10.1016/j.conbuildmat.2017.03.194>
- [46] Mustaque Hossain AS. Cement and cement-rice husk ash stabilization of selected local alluvial soils (1986).
- [47] Portland Cement Association. Soil-cement construction handbook. Portland Cement Assn; 1979.
- [48] Ashtiani RS, Little DN. Acceptability criteria for high fines content aggregate pavement layers. 2007 Dec 31.
- [49] Puppala AJ, Saride S, Sirigripet SK, Williammee R, Dronamraju VS. Evaluation of cemented quarry fines as a pavement base material. InGeoCongress 2008: Geotechnics of waste management and remediation 2008 (pp. 312-319).
- [50] Huddleston IJ. Cement stabilization of poor quality national forest bedrock materials for road construction. dissertation Work. 1978;(June):1–191
- [51] Fedrigo W, Núñez WP, López MA, Kleinert TR, Ceratti JA. A study on the resilient modulus of cement-treated mixtures of RAP and aggregates using indirect tensile, triaxial and flexural tests. Construction and Building Materials. 2018 May 20;171:161-9. <https://doi.org/10.1016/j.conbuildmat.2018.03.119>
- [52] IRC 37. Guidelines for the Design of Flexible Pavements. Indian Roads Congr 53. Delhi, India 2018.



Research Article

Experimental investigation along with 3-D Finite Element Analysis to determine the stress bearing ability of concrete containing waste plastic aggregates

Lalit Pawar^{*1,a}, Keshav K. Sangle^{1,b}, Yuvaraj L. Bhirud^{2,c}

¹Department of Structural Engineering, Veermata Jijabai Technological Institute, Mumbai, India

²Department of Civil Engineering, SNJB's LSKBJ COE, Chandwad, Nashik, India

Article Info

Abstract

Article history:

Received 23 Jul 2022

Accepted 06 Mar 2023

Keywords:

Design management;
Geometric modeling;
Engineering analysis;
Finite Element Method

Earth is becoming more and more polluted as a result of the unrelenting growth of plastic garbage in land surface. Also, plastic wastes are regarded as the most hazardous of the wastes produced in today's society because they take a long time to biodegrade and account for 85% of all garbage produced globally. However, the use of these plastic waste products in the building sector can help to alleviate the strength of the concrete structures while lowering the current environmental issues. Hence, in this research aggregate waste plastics were added to the concrete mixture to increase the strength of the concrete. In which aggregate waste plastics are added to the concrete mix in three different types of structures like cube, cylinder and beam which are then checked for its mechanical properties using compressive test, split tensile test, and flexural test respectively. Finally, the strength of concrete at various plastic proportions with three different structures under varying loading conditions is investigated using Finite Element Method (FEM) in Abaqus software and the results are discussed and the optimal specimen of the concrete mixture are determined. The result obtained showed high compressive, splitting tensile, and flexural strength values of concrete since coarse particles are replaced with plastic in amounts of 10%, 20%, 30 % and 40% which outperforms traditional mix that have higher percentages of more than 40% plastic waste, indicating the worst-case scenario in mechanical properties.

© 2023 MIM Research Group. All rights reserved.

1. Introduction

The ever-increasing volume of solid waste items all across the world has provided a new waste management dilemma. Waste management that is insufficient and inefficient, pollutes the environment and harms water and land. Plastic-based solid waste products account for a significant portion of all waste materials created across the world [1]. Polyethylene is the most common type of plastic waste, followed by polypropylene, polyethylene Terephthalate, and polystyrene [2]. Fortunately, waste plastics may be reused or turned into other goods in a variety of ways by recycling. Recycling is the act of converting waste materials into new goods in order to avoid wasting potentially useful materials [3]. The economy and the environment would benefit by replacing plastic resources with recycled or discarded products. Different sorts of waste plastic, for example, are produced on a daily basis, with the bulk of it ending up in open areas and landfills which can be incorporated into concrete [4]. The use of waste metalized plastic fibers in the manufacturing of concrete has shown a path toward sustainable and green building, with the added benefit of a safe waste plastics disposal option [5]. Consequently, waste plastic has demonstrated that the features of plastics are suitable for the production of new concrete, subject to certain constraints. With the growing need for concrete in

*Corresponding author: lalitraj1@gmail.com

^a orcid.org/0000-0002-8338-0626; ^b orcid.org/0000-0003-0618-7526; ^c orcid.org/0000-0001-9596-2823

DOI: <http://dx.doi.org/10.17515/resm2022.483st0723>

Res. Eng. Struct. Mat. Vol. 9 Iss. 3 (2023) 1081-1099

building sites, these resources are also becoming increasingly scarce, necessitating the search for alternatives [6].

Concrete cracks are regarded as a leading sign of structural degradation and long-term durability. In most developed nations, crack examination is a standard part of routine maintenance [7]. The cracking behavior of concrete has an impact on the load capacity of concrete structures [8]. The cracking pattern is linked to failure modes ranging from flexural to flexural-shear failure, affecting in load failure. Even if concrete offers various advantages, including high compressive strength, toughness, and other long-term durability characteristics. Concrete, on the other hand, is a brittle substance with low tensile strength [9]. However, adding fibers to concrete can help overcome these flaws, resulting in more ductile concrete with narrower fissures. Reduced fracture width reduces the entry of hostile species into concrete, improving its durability. Asbestos, rubber, glass, plastic, and bamboo fibers are some of the fibers that can be added to the concrete mix. Recently, there is being much research going on the use of recycled garbage and virgin plastic components in traditional concrete. Plastic fibers may be made from both new and recycled materials [10-14]. Especially, waste plastics can be used with concrete in two ways: as plastic fibers in fiber-reinforced concrete and as plastic aggregate in place of natural aggregates (coarse or fine) [15].

Jainet et al [16] investigated the workability, density, compressive and flexural strength, water permeability, static and dynamic modulus of elasticity, and abrasion resistance properties of concrete by adding different percentages (0,0.1,1,2,3, and 5%) of waste plastic bags by weight of concrete is a non-structural concrete additive that used in non-structural projects. Such modified concrete appears to be a particularly environmentally beneficial form of WPB disposal that minimizes natural resource loss. Building park benches, stone curbs, temporary buildings, roads, pathways, and concrete barriers are all examples of scenarios where their modified concrete is used. This enhanced concrete can also withstand freeze-thaw cycles. However, their work further needs to include a durability test. Samuel et al [17] experimentally tested the PET pulverized mix with the concrete. In concrete, crushed PET was used in percentages of 5%, 10%, and 15% by weight of conventional fine aggregate. There were four distinct types of concrete specimens made, as well as a control. After 3 days, 7 days, 14 days, and 28 days of curing, the flexural and compressive strengths of the concrete specimens were measured. The concrete specimen with 5% PET by weight exhibited higher compressive strength than the other specimens, according to the findings. However, the experiment did not look into the mechanical impact of the specimens due to higher load gradients.

Wu et al [18] presented a new test method for measuring the complete load-displacement curve of concrete under mixed mode I-II fracture. For their project, three-point bending beams with a multi-segment notch in the midspan were used. The notch depth ratio of the first segment and the inclination angle of the last segment affected the ratio of stress intensity factors. Following the recommended strategy to get the whole load vs. displacement curves for the K_{II}/K_I ratio up to 1.23 was less difficult than using the current testing methods. The complete crack propagation process was replicated using the finite element approach and their result are found. However, the stress and strain did not take their work. Rohden et al [19] their research looked at the possibility of using hard-to-recycle plastic waste as a polymeric component in high-strength concrete, with a focus on the capacity to reduce heat-induced spalling and its impact on mechanical properties. The garbage correlates to soft and hard plastic, particularly domestic polymers, which are typically disposed of in landfills while being theoretically recyclable. Mechanical and physical properties, cracking, mass loss, and the incidence of spalling in high strength concrete samples constructed with either plastic waste or polypropylene fibers were tested after a 2-hour exposure to 600 C. In addition, the effect of plastic aggregate-

produced concrete on beam structures and other structural parts must be investigated. However, for [16] durability test is needed, for [17] experiment did not look into the mechanical impact of the specimens due to higher load gradients, for [18] stress and strain did not take their work, and for [19] the effect of plastic aggregate produced concrete on beam structures and other structural parts must be investigated. The main contributions of this paper are as follows: Improve the strength of concrete under a heavy load by adding plastic wastes with polycarboxylic-based super plasticizers as aggregate. Investigating the mechanical behavior of concrete with various proportions of waste plastic aggregate using various strength tests using three different shaped structures. Thus determining the optimal addition of plastic reinforcement to improve the strength of concrete structures.

2. Experimental Program

2.1. Materials and Methods

This research investigated the binder made out of Portland cement (CEM II 52.5 R) and plastic waste. The sand-to-binder ratio was set at 0.4. Silica sand with a mesh size of 106 to 120 μm (120 to 150 mesh) was included in the mix. A polycarboxylic-based superplasticizer was present in all of the combinations (30 percent solid content). To explore the influence of plastics on the load resistance of concrete with appropriate workability of the new mixture and aggregate plastic dispersion, the concrete was prepared with 0 to 40% plastic wastes to get adequate ductility. After being ground and melted, the post-consumption waste plastic is collected and chopped into little pieces. After cooling, the same particles are utilized as coarse aggregate in concrete. The diagram of plastic wastes aggregate is depicted in Figure 1.



Fig. 1. Plastic wastes aggregate

2.2. Materials and Methods

To produce the specimens, five different proportions of plastic waste were mixed into the concrete: 0%, 10%, 20%, 30%, and 40%, respectively. The 0% represents pure concrete specimens that have not been contaminated with plastic waste. The specimens were created and tested in order to evaluate the effects of incorporating plastic trash into traditional concrete. The above-mentioned proportions are used to make three sorts of specimens: a cube, a cylinder, and a beam specimen. The cube is prepared with dimensions $150 \times 150 \times 150 \text{ mm}^3$ so that the surface area of the cube is 135000 mm^2 . The cylindrical specimen is made with dimensions having a diameter of 150 mm and height of 300 mm with a surface area of 176625 mm^2 and the beam is made with dimensions $150 \times 150 \times 700 \text{ mm}^3$. The diagram of fabricated specimens is a) Cube b) Cylindrical specimen and c)

Rectangular beam are depicted in Figure 2. The chemical and physical properties of the Portland cement and silica sand are tabulated in Tables 1 and 2.



Fig. 2. Fabricated specimens (a) cube (b) cylindrical specimen and (c) rectangular beam

Table 1. Chemical properties of portland cement and silica sand

Chemical Composition	Portland Cement	Silica Sand
Calcium Oxide (CaO)	63.40	0.02
Silicon Dioxide (SiO_2)	21.60	99.79
Aluminum Oxide (Al_2O_3)	4.45	0.06
Sulphur Trioxide (SO_3)	1.92	-
Ferric Oxide (Fe_2O_3)	5.35	0.02
Magnesium Oxide (MgO)	1.65	0.01
Sodium Oxide (Na_2O)	0.11	0.02
Potassium Oxide (K_2O)	0.22	0.01
Loss of Ignition (LOI)	0.78	0.07

Table 2. Physical properties of portland cement and silica sand

Physical Properties	Portland Cement	Silica Sand
Initial setting time (minutes)	170	5.75 min for 20% SF
Final setting time (minutes)	225	16.50 min for 20% SF
Specific gravity	3.10	2.60
Blaine specific surface area(m^2/kg)	340	—
28-day compressive strength(MPa)	42.5	20.70

2.3 Testing Methods

The cube concrete samples were made according to BS EN 12390-2, 3:2009. After 24 hours, the concrete cubes were removed and submerged in water for 90 days. The cubes were then removed from the water tank and dried at room temperature, with the mass of the specimens being monitored until they achieved a stable weight. The initial mass of all concrete specimens was measured before the thermal exposure test, and the specimens were subsequently evaluated for a non-destructive UPV test using ASTM C597-0 criteria. Moreover, the proposed cube specimens, cylindrical specimens, and rectangular specimens are checked the compressive strength, flexible strength, and split tensile strength by using a compressive testing machine and a universal testing machine. The compressive strength test was performed on the compressive testing machine. The compressive strength of all samples increased with the increase of curing age. The mechanical characteristics of the newly tested concrete were determined using three types of specimens, as shown in Table 3.

Table 3. Three types of specimens.

Specimen Shape	Dimensions	Type of Test
Cubes	150x150x150 mm ³	Compressive strength test
Cylinders	150 x300 mm	Split tensile strength test
Rectangular Beams	150x150x700 mm ³	Flexural strength test

2.3.1 Compressive Strength Test

The primary mechanical characteristic required in the construction of concrete buildings is compressive strength, which is one of the most essential qualities of concrete. Concrete compressive strength is determined by adding aggregate plastic dispersion with 0% to 40 %. Each strength test was performed on five cube specimens, with the average taken. The compressive strength was measured at different temperatures such as 35°C, 600°C, and 800°C. The compression test setup of the cube specimen is depicted in Figure 3. The compressive strength of the specimen is calculated using the formula

$$CT = p / A \quad (1)$$

Where

p – Maximum load

A – Cross-sectional area of the material resisting the load



Fig. 3. Compression test setup of cube specimen

2.3.2 Flexural Strength Test

Flexural testing is performed to assess a material's flex or bending qualities. It entails inserting a sample between two points or supports and beginning a load with a third point. The proposed beam has 3 points and the dimensions are $150 \times 150 \times 150$ with load at the center. Each strength test was performed on four cube specimens, with the average taken. Flexural strength was tested using flexural strength testing equipment, and it was found that flexural strength had been reduced by adding the waste plastic aggregates. The Flexural strength test setup of the beam specimen is depicted in Figure 4. The flexural strength of the beam is calculated using the formula

$$FS = pL/wf^2 \quad (2)$$

Where

p – Maximum load

L – supported length (cm)

w – Width of the specimen (cm)

f – failure point depth (cm)

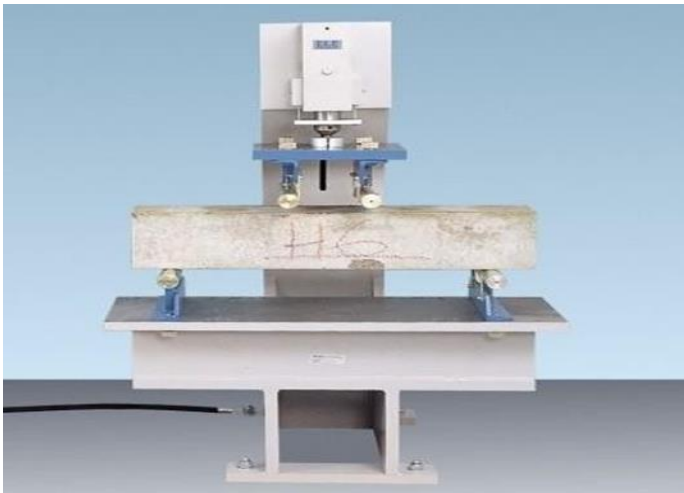


Fig. 4. Flexural strength test setup of beam specimen

2.3.3 Split Tensile Strength

A cylindrical specimen with a diameter of 150 mm and a length of 300 mm was used to test split tensile strength. The split tensile strength test setup of the cylindrical specimen is depicted in Figure 5. The specimen's split tensile strength is computed using the equation

$$T = 2p / \pi ld \quad (3)$$

Where

p – max applied load indicated by the testing machine

l – length of the specimen in mm

d – diameter of the specimen in mm



Fig. 5. Split tensile strength test setup of a cylindrical specimen

The 3D finite element analysis has been carried out for the proposed plastic waste aggregation mixture. The model is simulated on Abacus 6.14-5 with Windows 10 and a 64-bit processor considering 8 GB of RAM.

3. Results and Discussion

The compressive strength, flexural strength, and split tensile strength of the proposed plastic waste aggregation mixture have been evaluated. In addition to the experimental work in the laboratory, the 3D finite element analysis has been carried out through Abaqus software, which is presented in this section to describe model parameter of three types of specimens such as cube, cylinder, and Beam are depicted in Table 4.

Table 4. Model parameter of three types of specimen

Model parameter	Cube	Cylinder	Beam
Length (mm)	1	200	700
Width (mm)	1	-	150
Height (mm)	1	-	150
Radius (mm)	-	50	-

The mesh size depends on total number of nodes and total number of elements which are 313120 and 28320, respectively and General 3D solid, C3D4 is the element type. In order to add plastic aggregate to concrete, 0.3% of steel fibre by weight of cement is added to provide bonding between the concrete and plastic aggregate.

3.1 Experimental Test Results

The results of compressive strength, flexural strength, and split tensile strength for all types of concrete members experimentally were summarized in Tables 5, 6, and 7, the first group of specimens was tested with 0% waste plastic aggregate in order to be reference values for comparing other results. The waste plastic aggregate was mixed with proportions gradually starting from 10,20,30 reaching up to 40% then these samples were tested to find the effect of adding the waste plastic aggregates. Overall compressive strength of concrete is improved by adding 30% of plastic in mixture which reach maximum range of 36.59% compared to 0%. The compressive, tensile, and flexural strength s increased when comparing the results without adding waste plastic aggregates.

The increasing strength of a) cube, b) cylinder, and c) beam specimens are depicted in Figure 6.

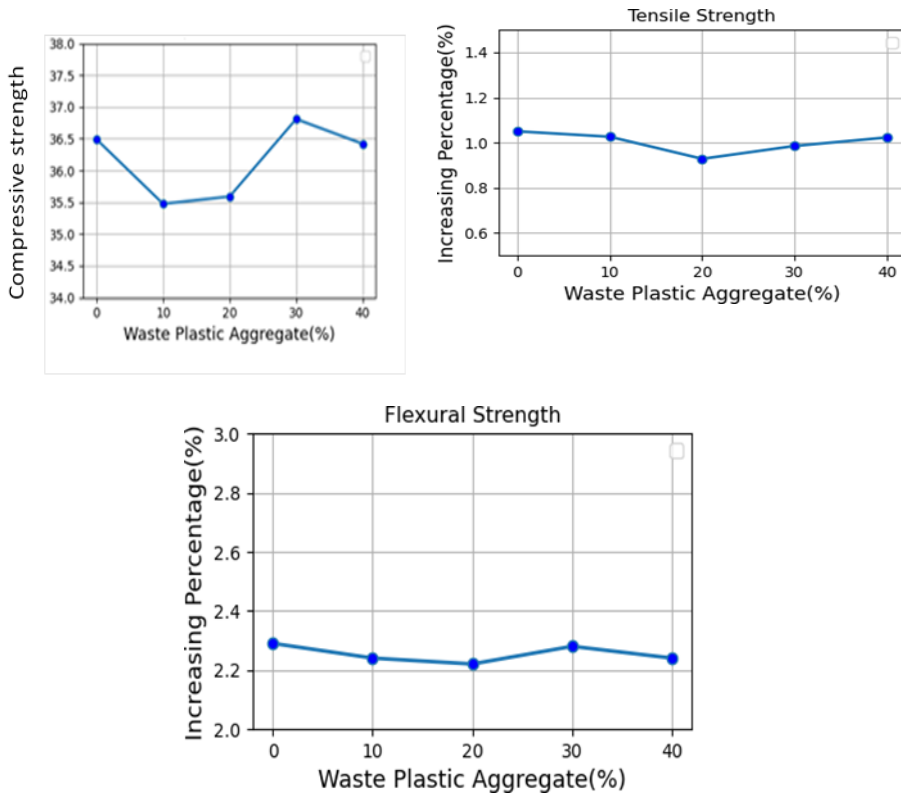


Fig. 6. Strength of cube, cylinder, and beam specimens

The graphs plotted in Figure 6 represent the strength of the cube, cylinder, and beam specimens at 35 degrees Celsius for 0%, 10%, 20%, 30%, and 40 % plastic addition. The specimens were kept at 35 degrees Celsius and weighed a maximum of 9.44 kg with no plastic added therefore the increasing strength of cube, cylinder, and beam in 0% waste plastic aggregate was 36.49%, 1.06%, and 2.29% respectively. Similarly, for 10 % addition, the maximum weight is 9.32 kg for 35°C the strength of the cube, cylinder, and beam are 35.47%, 1.02%, and 2.43% respectively. The strength of percentage for the 20% addition of waste plastic aggregate and the maximum weight is 9.20 kg in cube, cylinder, and beam specimens are 36.81%, 0.985%, and 2.289% respectively. The strength percentage for the 30% addition of waste plastic aggregate and the maximum weight is 9.08 kg in cube, cylinder, and beam specimens are 36.81%, 0.985%, and 2.289% respectively. Moreover, 40 % of additional plastic waste aggregate the maximum weight is 9.43% in cube, cylinder, and beam specimens 36.42%, 1.02%, and 2.24% respectively. The physical characteristics of the parameters are quantified in the cube material model are density, young's modulus, and Poisson ratio have values of 7.8E-008, 210000, and 0.33, respectively. Graphical representation and table of compressive strength test on the cube are shown in Figure 7 and Table 5.

Figure 7 shows the compressive strength test graph for the cube concrete with added waste plastic aggregates (10%, 20%, 30%, and 40%) specimen for 35°C, 600°C, and 800°C respectively. The compressive strength values of the proposed cube concrete values are

tabulated in Table 5. As a result, comprehensive strength is increased due to a stronger link between the plastic and the concrete matrix, which improved the stress transfer between the plastic waste aggregates and unlocked their full capacity to withstand stress and strain.

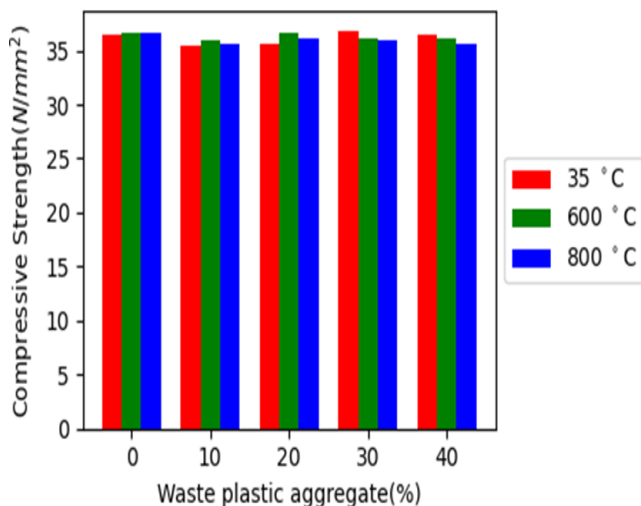


Fig. 7. Compressive strength test graph on the cube

Table 5. Compressive strength test values on the cube

Mix Specification	Value (N/mm ²)	Value (N/mm ²)	Value (N/mm ²)	Value (N/mm ²)	Value (N/mm ²)
Proportion of waste plastic	0%	10%	20%	30%	40%
35°C	36.49	35.47	35.59	36.81	36.81
600°C	36.65	36.04	36.64	36.11	36.11
800°C	36.63	35.69	36.06	35.87	35.63

Waste plastic aggregates of 36.49, 36.65, and 36.63 were used to raise the strength of a cube by 0% for varied proportions of 35°C, 600°C, and 800°C. Similar to this, adding 10% more plastic waste aggregates increases strength by 35.47%, 36.04%, and 35.69%; adding 20% more, 35.59, 36.64, 36.06; adding 30% more, 36.81%, 36.11, and 35.87%; and adding 40% more, 36.81%, 36.11%, and 35.63%.

Graphical representation and table of split tensile strength on the cylinder are shown in Figure 8 and Table 6.

The split tensile strength test on the cylinder graph is shown in Figure 11. The cylinder concrete with plastic waste aggregates specimen was tested at 35°C, 600°C, and 800°C temperatures respectively. The split tensile strength test values on the cylinder is

tabulated in Table 6. The physical characteristics of the parameters are quantified in the cylinder material model are density, young's modulus, and Poisson ratio have values of 7.8E-008, 210000, and 0.33, respectively. These parameters result in stress values of 450, 700 and plastic strain values of 0, 0.02. As a result, split tensile strength increased due to the use of plastic aggregate.

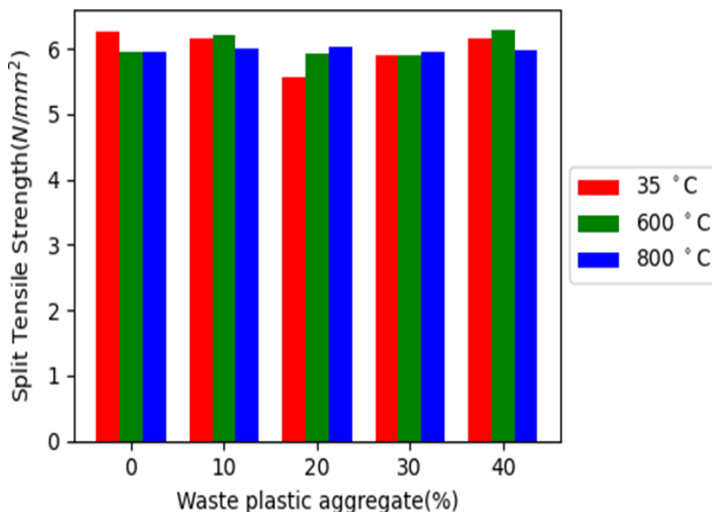


Fig. 8. Split tensile strength test graph on the cylinder

Table 6. Split tensile strength test values on the cylinder

Mix Specification	Value (N/mm ²)	Value (N/mm ²)	Value (N/mm ²)	Value (N/mm ²)	Value (N/mm ²)
Proportion of waste plastic	0%	10%	20%	30%	40%
35°C	6.35	6.16	5.57	5.91	6.17
600°C	5.96	6.2	5.98	5.89	6.29
800°C	5.96	6.01	6.03	5.94	5.98

To enhance the split tensile strength of cylinders under different proportions, such as 35°C, 600°C, and 800°C of plastic waste with 0%, 10%, 20%, 30%, and 40%. Aggregates of waste plastic in 0% are 6.35% at 35°C, 5.96% at 600°C, and 5.96% at 800°C. Comparable to 10% the strength is improved by 6.16%, 6.2%, and 6.01%, and 20% to increase strength by 5.57%, 5.98%, 6.03%, and in 30% to increase strength by 5.91%, 5.89%, and 5.94% finally in 40% to increase strength by 6.17%, 6.29%, 5.98%. Graphical representation and table of Flexural strength test on beam are shown in Figure 9 and Table 7.

Figure 12 shows the flexural strength test graph for the beam concrete with added waste plastic aggregates (10%, 20%, 30%, and 40%) specimen for 35°C, 600°C, and 800°C temperatures respectively. The flexural strength values of the proposed beam concrete

values are tabulated in table 7. The physical characteristics of the parameters are quantified in the beam material model are density, young's modulus, and Poisson ratio that have values of 7.8E-008, 210000, and 0.33, respectively. These parameters result in stress values of 690, 700, 750, 850,900, and 950,990 and plastic strain values of 0, 0.007, 0.039, 0.05, 0.065, 0.1, and 0.13. As a result, increased flexural strength due to increased load absorption by the plastics found in the concrete matrix.

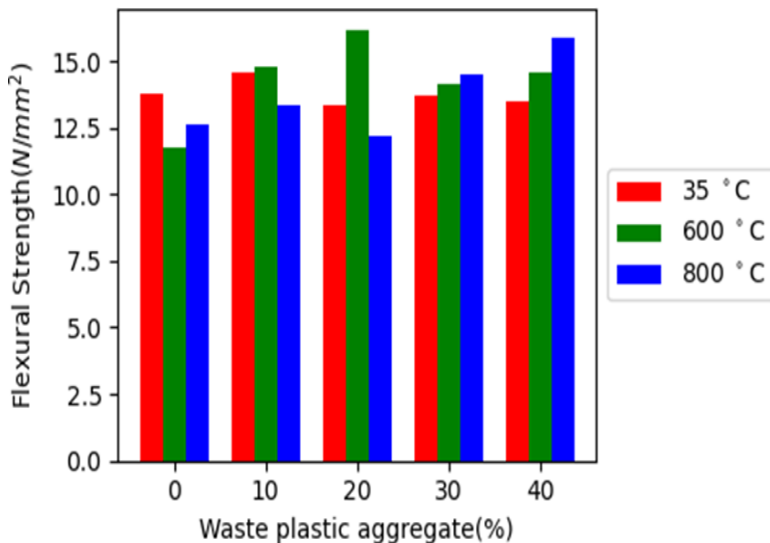


Fig. 9. Flexural strength test graph on beam

Table 7. Flexural strength test values on beam

Mix Specification	Value (N/mm²)	Value (N/mm²)	Value (N/mm²)	Value (N/mm²)	Value (N/mm²)
Proportion of waste plastic	0%	10%	20%	30%	40%
35°C	13.79	14.59	13.32	13.73	13.49
600°C	11.77	14.81	16.17	14.11	14.57
800°C	12.59	13.36	12.17	14.5	15.9

To enhance the flexural strength based on beam for under different proportions, such as 35°C, 600°C, and 800°C of plastic waste with 0%, 10%, 20%, 30%, and 40%. Aggregates of waste plastic in 0% are 13.79% at 35°C, 11.77% at 600°C, and 12.59% at 800°C. Comparable to 10% to improve strength by 14.59%, 14.81%, and 13.36%, and 20% to increase strength by 13.32%, 16.17%, 12.17%, and in 30% to increase strength by 13.73%, 14.11%, and 14.5% finally in 40% to increase strength by 13.49%, 14.57%, 15.9%

3.2 3-D Finite Element Analysis

The proposed system results and findings obtained from the data of Finite Element Method (FEM) Abaqus software are discussed in this section. The 3-model specimen taken cube concrete, cylinder concrete, and beam concrete were created and meshed in Abaqus with waste plastic aggregates of 0%, 10%, 20%, 30%, and 40%. The analysis result of concrete cube, concrete cylinder, and concrete beam containing each percentage of waste plastic aggregates was discussed.

3.3 Cube Specimen

The proposed cube model under the compressive strength test is depicted in Figure 10 (a & b).

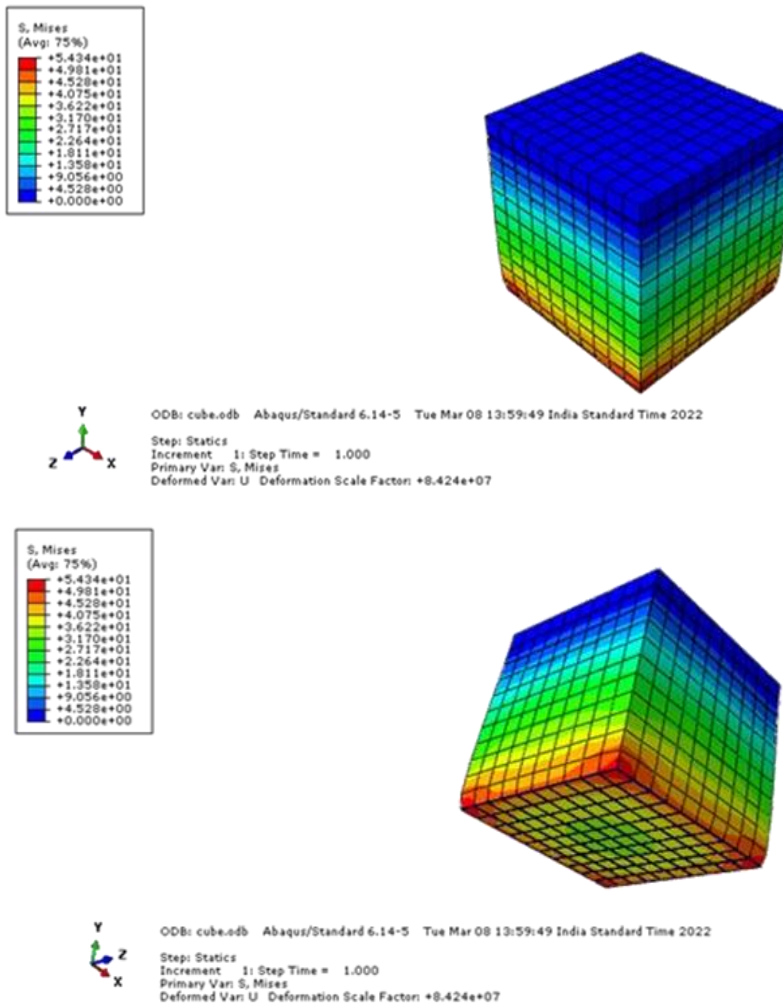
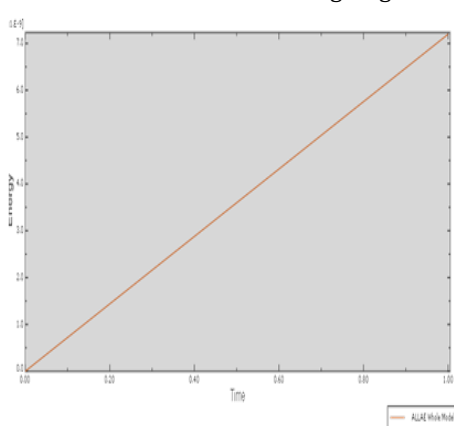


Fig. 10. (a-b) Proposed cube model under compressive strength test

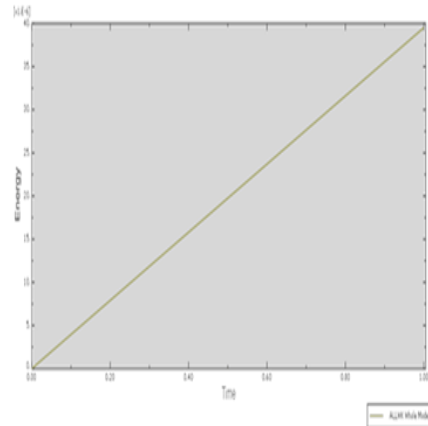
The 3-D finite element cube concrete model was employed to simulate the compressive strength test which are illustrated in Figure 10. Figure 10 showed 4-types of color which are blue, green, yellow, and red. Two different views of cube model are depicted in Figures 10 (a) and (b). The load has been applied on two ends of the cube. The maximum stress

value of the cube is $+5.434e+01$ and the minimum stress value of the cube is $+4.528e+00$. Artificial energy (ALLAE) of whole model of cube are depicted in Figure 11 (a), External work (ALLWK) of whole model of cube are depicted in Figure 11(b). Total strain energy (ALLTE) of whole model of cube are depicted in Figure 11 (c). Recoverable strain energy (ALLSE) whole model of cube are depicted in Figure 11 (d). The proposed cube model of stress and strain are depicted in Figure 11(e & f).

Figure 11(a) illustrates the artificial energy (ALLAE) of the proposed plastic waste aggregate cube model. The variable ALLAE of the presented model represents the total energy expended as artificial strain energy, whereas ALLSE represents the elastic, or recoverable, strain energy. ALLAE comprises both viscous and elastic components; however, because the viscous word is generally dominating, the majority of the energy that goes into artificial strain energy is lost. The artificial energy of the proposed cube concrete model has been increased linearly as 0.01 J in 0.01 seconds and 7.2 J in 1.00 seconds due to strength of confinement effect on concrete as well as a greater connection between the plastic and the concrete matrix. Figure 11(b) illustrates the external work applied on the whole cube concrete model for testing, which can be evaluated only for the whole model. The model can sustain while applying 5J energy in 0.10 seconds then the sustainability increases linearly to withstand for 40 J energy in 1.00 seconds. Figure 11(c) depicts the total strain energy of the proposed cube concrete model, which has been evaluated by the addition of recoverable strain energy (ALLSE), energy dissipated by rate-independent and rate-dependent plastic deformation (ALLPD), energy dissipated by viscoelasticity (ALLCD), artificial strain energy (ALLAE), energy dissipated through quiet boundaries (ALLQB), electrostatic energy (ALLEE), and energy dissipated by damage (ALLDMD). ALLTE is obtained as sustaining 7.5 J in 0.20 seconds then increases to sustain 40 J in 1.00 seconds. Figure 11(d) illustrates the recoverable strain energy of the proposed waste plastic mixture cube model. In steady-state dynamic analysis, ALLSE is the cyclic mean value. When applying 5.0 J energy in 0.10 seconds, the model can be recovered to the same after deformation. The waste plastic admixtures cube model strain and stress is depicted in figure 11 (e) and (f). From the figure (e), when time increased from 0.01 seconds to 1.00 seconds as well as the proposed cube model strain decreased. At same as the figure (f) shows, the stress of the whole model is decreased when the time is increased due to stress and strain value is calculated using original cross-sectional area.



(a)



(b)

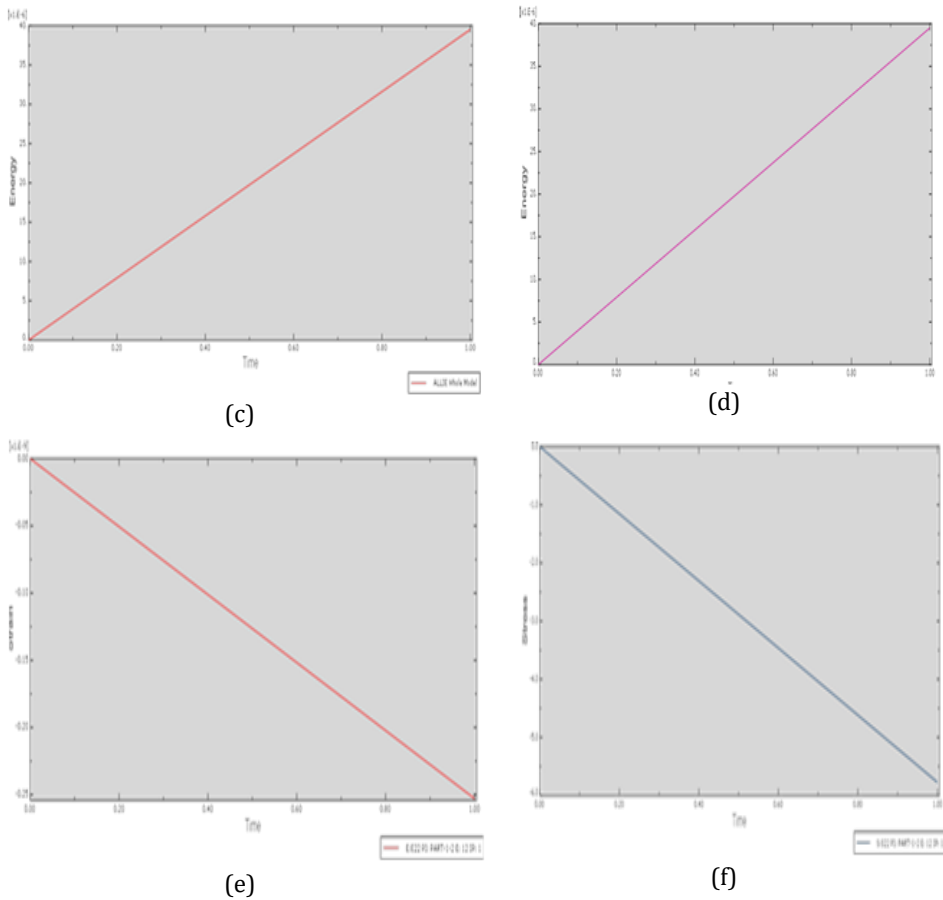


Fig. 11. (a) Artificial energy (ALLAE) of whole model of cube (b) External work (ALLWK) of whole model of cube (c) Total strain energy (ALLTE) of whole (d) Recoverable strain energy (ALLSE) of whole model of cube (e) stress and strain of proposed cube model

3.3.1 Cylinder Specimen

The proposed cylinder model under split tensile strength test are depicted in Figure 12 (a& b).

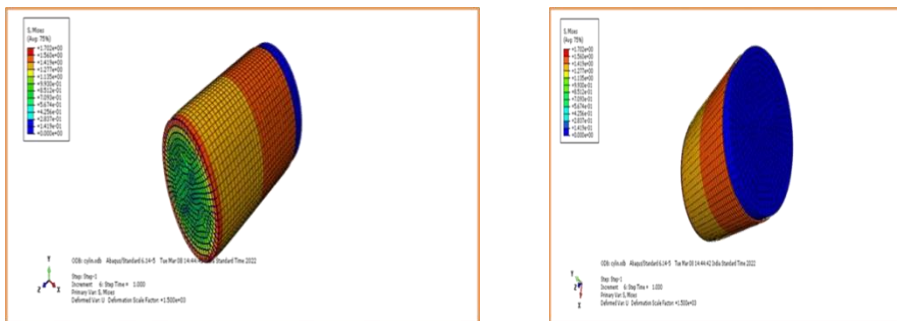


Fig. 12. (a-b) Proposed cylinder model under split tensile strength test

The 3-D finite element cylinder concrete model was employed to simulate the split tensile strength test which are illustrated in Figure 12. In Figure 12 showed 4-types of color which are blue, green, yellow, and red. The maximum stress value of the cylinder is ++10702e+00 and the minimum stress value of the cylinder is +1.419e-01. Two different views of cylinder model are depicted in figure 12 (a) and (b). The load has been applied on two ends of the cylinder. The recoverable strain energy (ALLSE) of whole model of cylinder are depicted in Figure 13 (a). Artificial energy (ALLAE) of whole model of cylinder are depicted in Figure 13 (b). The stress and strain of proposed cylinder model are depicted in Figure 13 (c) & (d).

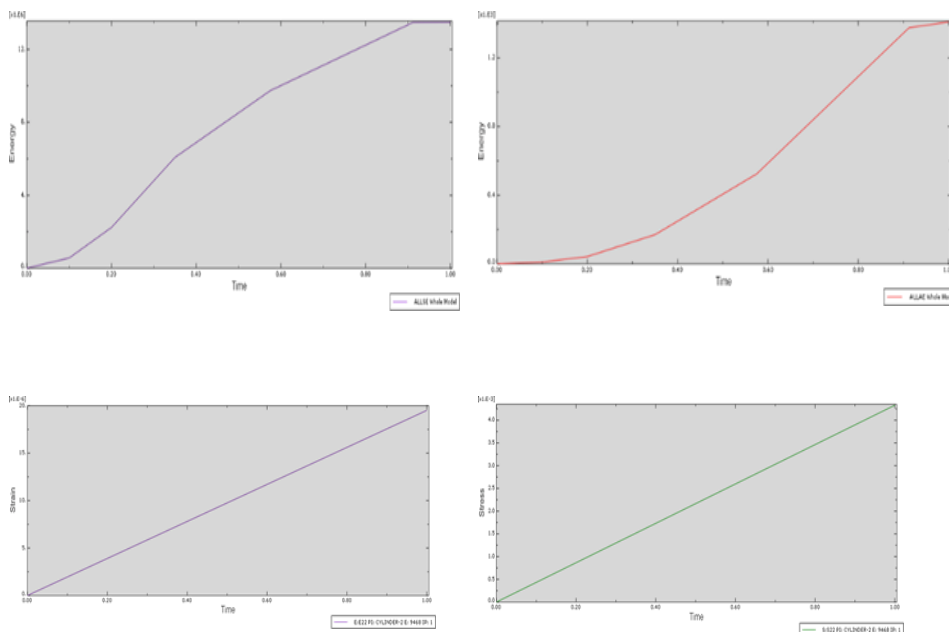


Fig. 13. (a) Recoverable strain energy (ALLSE) of whole model of cylinder (b) Artificial energy (ALLAE) of whole model of cylinder (c&d) stress and strain of proposed cylinder model

The recoverable strain energy of the suggested waste plastic mixed cylinder type is shown in Figure 13(a). ALLSE is the cyclic mean value in steady-state dynamic analysis. The model can be restored to its original shape after deformation with 3.5 J energy applied in 0.20 seconds. The proposed plastic waste aggregate cylinder model's artificial energy (ALLAE) is shown in Figure 13 (b). The artificial energy of the proposed cylinder concrete model has been increased linearly as 0.01 J in 0.20 seconds and 1.3 J in 1.00 seconds. The substitution of polycarboxylic-based superplasticizer for the fine aggregate led to an increase in split tensile strength which improve the mechanical qualities of this concrete. Figure 13 (c) and (d) exhibit the waste plastic admixtures cube model strain and stress. From the figure (c), when time increased from 0.01 seconds to 1.00 seconds as well as the proposed cube model strain decreased. At same as the figure (d) shows, the stress of the whole model is decreased when the time is increased.

3.3.2 Beam Specimen

The proposed model under flexural strength test in beam specimen are depicted in Figure 14 (a&b) .

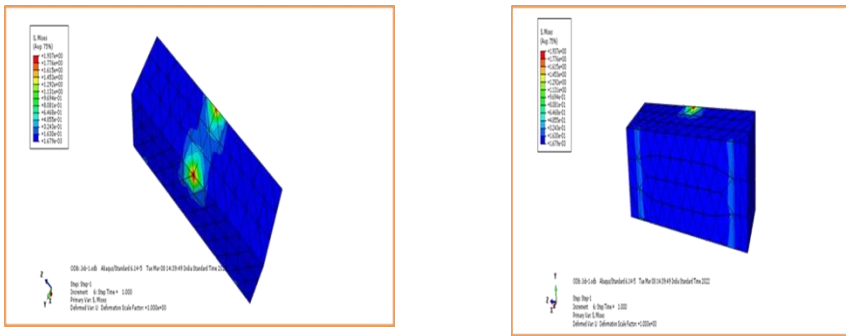


Fig. 14. (a-b) Proposed beam model under flexural strength test

The 3-D finite element beam concrete model was employed to simulate the flexural strength test which are illustrated in figure 14. To reduce mesh size, triangular meshing is utilized instead of rectangular mesh by cutting the diagonals of the quadrilateral structured mesh but the mesh values are coarse hence mesh optimization has been done to get optimum mesh values by lowering the energy function. Two different views of beam model are depicted in figure 14(a) and (b). The load has been applied on two ends of the beam. The maximum stress value of the beam is $+1.937e+00$ and the minimum stress value of the beam is $+1.679e+03$. The total strain energy (ALLTE) of whole model of beam are depicted in Figure 15 (a). The recoverable strain energy (ALLSE) whole model of beam are depicted in Figure 15 (b).

Figure 15 (a) shows the total strain energy of the proposed beam concrete model, which was calculated by adding recoverable strain energy (ALLSE), energy dissipated by rate-independent and rate-dependent plastic deformation (ALLPD), energy dissipated by viscoelasticity (ALLCD), artificial strain energy (ALLAE), energy dissipated through quiet boundaries (ALLQB), electrostatic energy (ALLSE), and energy dissipated by damage (ALLDMD). ALLTE achieved by maintaining 0.02 J for 0.20 seconds, then increasing to 2.5 J for 1.00 seconds due to limited addition of aggregate plastic waste in concrete. The recoverable strain energy of the suggested waste plastic mixed beam model is shows in Figure 15 (b). The model restored to its original shape after deformation with 0.02 J energy applied in 0.20 seconds. The comparison graph of force and displacement curve are depicted in Figure 16.

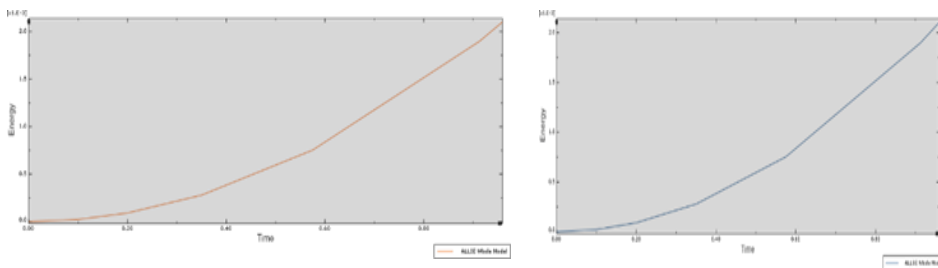


Fig. 15. (a) Total strain energy (ALLTE) of whole model of beam (b) Recoverable strain energy (ALLSE) of whole model of beam

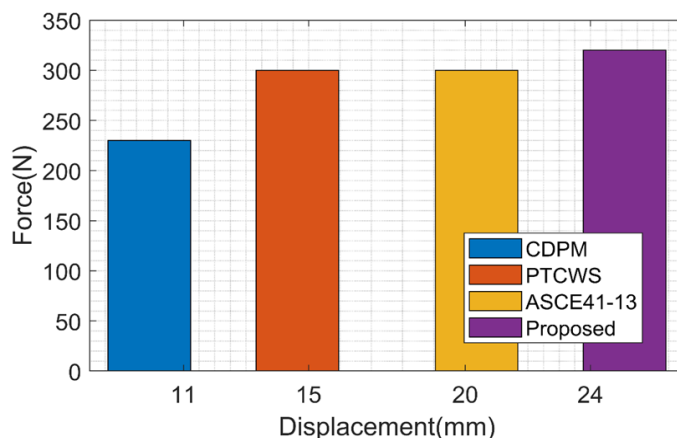


Fig. 16. Comparison graph of force and displacement

Figure 16 shows proposed model achieved high performance compared to other models in terms of force and displacement which increased the strength and workability of nonstructural concrete while using less plastic, and that can be used to improve the mechanical properties of concrete. When the concrete has hardened and the tension on the reinforcing steel has been relieved, the concrete is compressed by an internal force. Loads cause the concrete's compressive force to decrease and the reinforcing steel to experience increased stress. The relationship between force and displacement is inverse. Although the greatest range of displacement is only 24, the maximum range of force is over 300.

Overall when compared to compressive strength, the reduction in split tensile strength and flexural strength caused by the presence of plastic aggregate was considerably less due to inadequate bonding between the concrete and plastic aggregate. By volumes of 10%, 20%, 30%, and 40%, coarse particles in concrete can be also substituted with plastic. However, the use of plastic in non-structural concrete is encouraged because it exhibits higher workability and reduces environmental waste due to plastic's durability, waterproofing, and insulating properties. It is advised that up to 30% of the volume be replaced; up to this point, the M25 concrete's typical strength was attained. Another discovery is that non-structural lightweight elements can be used with 40 and 50% substitution by volume. As a result, the utilization of waste plastic aggregate can efficiently be employed from the perspectives of conservation, cost-effectiveness, and energy conservation.

4. Conclusion

Plastics waste aggregates are added to mixtures of concrete to maximize the strength in order to increase the load of the structure. Three different specimens, including cubes, cylinders, and beams, are used to assess the durability of the concrete. The cube concrete model's artificial energy has been increased linearly from 0.01 J in 0.01 seconds to 7.2 J in 1.00 seconds in order to test the compressive strength of the model. As time goes on, stress and strain will decrease. When the artificial energy of the concrete cylinder has been increased linearly as 0.01 J in 0.20 seconds and 1.3 J in 1.00 seconds in order to test the strength for split tensile strength, time-increasing stress and strain would eventually diminish. The artificial concrete beam's strength was evaluated for flexural tensile strength with an increment of 2.5 J for 1.00 seconds and these models are under various temperatures such as 35°C, 600°C, and 800°C temperatures. The strength of the concretes

is identified from the results and concluded from the results 40% addition of the plastic waste in cube increased the strength by 36%, in cylinder the strength is increased by 6%, and in beam the strength is increased by 14.65%. As a result, the strength of the proposed cube, cylinder, and beam model is maximized using waste plastic aggregate, which lowers the cost of using non-structural concrete. However, one of the biggest problems of using plastic as concrete reinforcement is that it is prone to corrosion, especially on the surface of the concrete when exposed to saltwater without the proper safeguards. Hence, it is advised to continue researching how plastic trash performs over the long term in concrete as well as its long-term effects on the ecosystem.

References

- [1] Jain, Abhishek, et al. "Evaluation of concrete containing waste plastic shredded fibers: Ductility properties." *Structural Concrete* 22.1 (2021): 566-575. <https://doi.org/10.1002/suco.201900512>
- [2] Ghuge, Jeevan, et al. "Utilization of waste plastic in manufacturing of paver blocks." *System* 6.04 (2019): 1967-1970.
- [3] Bhushaiah, Rajarapu, Shaik Mohammad, and D. Srinivasa Rao. "Study of plastic bricks Made from waste Plastic." *International Research Journal of Engineering and Technology* 6.4 (2019):
- [4] Khatib, Jamal M., et al. "Structural assessment of reinforced concrete beams incorporating waste plastic straws." *Environments* 7.11 (2020): 96. <https://doi.org/10.3390/environments7110096>
- [5] Mustafa, Maher Al-Tayeb, et al. "Effect of partial replacement of sand by plastic waste on impact resistance of concrete: experiment and simulation." *Structures*. Vol. 20. Elsevier, 2019.
- [6] Saxena, Rajat, et al. "Impact resistance and energy absorption capacity of concrete containing plastic waste." *Construction and Building Materials* 176 (2018): 415-421. <https://doi.org/10.1016/j.conbuildmat.2018.05.019>
- [7] Kim, Hyunjun, et al. "Performance assessment method for crack repair in concrete using PZT-based electromechanical impedance technique." *NDT & E International* 104 (2019): 90-97. <https://doi.org/10.1016/j.ndteint.2019.04.004>
- [8] Słowik, Marta. "The analysis of failure in concrete and reinforced concrete beams with different reinforcement ratio." *Archive of applied mechanics* 89.5 (2019): 885- 895. <https://doi.org/10.1007/s00419-018-1476-5>
- [9] Rashid, Khuram, et al. "Cracking behavior of geopolymer concrete beams reinforced with steel and fiber reinforced polymer bars under flexural load." *Composites Part B: Engineering* 186 (2020): 107777. <https://doi.org/10.1016/j.compositesb.2020.107777>
- [10] Khatib, J.; Jahami, A.; Elkordi, A.; Baalbaki, O. Structural performance of reinforced concrete beams containing plastic waste caps. *Mag. Civ. Eng.* 2019, 91, 73-79. <https://doi.org/10.2139/ssrn.3510113>
- [11] Jahami, A.; Khatib, J.; Baalbaki, O.; Sonebi, M. Prediction of Deflection in Reinforced Concrete Beams Containing Plastic Waste. *SSRN Electron. J.* 2019, 551- 555. <https://doi.org/10.2139/ssrn.3510113>
- [12] Khatib, J.; Jahami, A.; Baalbaki, O. Flexural characteristics of reinforced concrete beams containing lightweight aggregate in the tensile zone. In *Proceedings of the Fifth International Conference on Sustainable Construction Materials and Technologies*, Kingston University, London, UK, 14-17 July 2019; ISSN 2515-3048 (Print); ISSN 2515-3056 (Online). *Environments* 2020, 7, 0096 13 of 14.
- [13] Jahami, A.; Khatib, J.; Firat, S. Load deflection characteristics of reinforced concrete beams incorporating fibers made of waste plastic straw. In *Proceedings of the 2nd*

- International Turkish World Engineering and Science Congress, Antalya, Turkey, 7- 10 November 2019; pp. 326-333.
- [14] Khatib, Jamal M., et al. "Structural assessment of reinforced concrete beams incorporating waste plastic straws." *Environments* 7.11 (2020): 96. <https://doi.org/10.3390/environments7110096>
- [15] Khatib, Jamal M., et al. "Structural assessment of reinforced concrete beams incorporating waste plastic straws." *Environments* 7.11 (2020): 96. <https://doi.org/10.3390/environments7110096>
- [16] Jain, Abhishek, et al. "Fresh, strength, durability and microstructural properties of shredded waste plastic concrete." *Iranian Journal of Science and Technology, Transactions of Civil Engineering* 43.1 (2019): 455-465. <https://doi.org/10.1007/s40996-018-0178-0>
- [17] Umasabor, Richie I., and Samuel C. Daniel. "The effect of using polyethylene terephthalate as an additive on the flexural and compressive strength of concrete." *Heliyon* 6.8 (2020): e04700. <https://doi.org/10.1016/j.heliyon.2020.e04700>
- [18] Wu, Zhi-Min, et al. "A new test method for the complete load-displacement curve of concrete under mixed mode I-II fracture." *Theoretical and Applied Fracture Mechanics* 108 (2020): 102629. <https://doi.org/10.1016/j.tafmec.2020.102629>
- [19] Rohden, Abrahão Bernardo, et al. "Effects of plastic waste on the heat-induced spalling performance and mechanical properties of high strength concrete." *Materials* 13.15 (2020): 3262. <https://doi.org/10.3390/ma13153262>



Content

- 675 Vascularized mini cooling channels to achieve temperature uniformity: Battery thermal management and electronic cooling
- 687 Vibration energy harvesting using telescopic suspension system for conventional two-wheeler and EV
- 709 Tensile and compressive mechanical properties of ZA27/ molybdenum disulfide, metal matrix composite
- 719 Kinetic evaluation of the stabilization efficiency of the phosphite and urea derivative based stabilizers against epoxy based stabilizers on the thermal degradation of plasticized poly (vinyl chloride)
- 743 Effect of nano-sized clay and waste glass powder on rheological and hardened properties of self-compacting concrete
- 763 Seasonal variation in aerosol optical depth and study of PM2.5-AOD empirical relationship in Raipur, Chhattisgarh, India
- 775 Green corrosion inhibitors for steel and other metals in basic media: A mini-review
- 791 The effect of mechanical surface roughness for polyvinyl chloride (PVC) and aluminum joining
- 805 Prediction and optimization of heat treatment effects on hardness and electrical conductivity of aluminum composite reinforced with nano alumina based on response surface methodology
- 827 Influence of MWCNTS on mechanical and in vitro biocompatibility properties of PMMA bone cement for orthopedic application
- 843 Optimization of high performance concrete composites by using nano materials
- 861 Integral waterproofing concrete mechanical properties with the addition of fly ash
- 875 Investigation of normal concrete properties with the addition of micro reinforcement
- 885 Mechanical behavior and fractography analysis of Zn-Sn alloy matrix composites reinforced with nano B4C particles
- 901 Seismic behaviour of re-entrant dominant RC frame buildings
- 921 Prediction of performance of UHPFRC flexural member under blast loading
- 947 An assessment of rebound hammer test in estimating the concrete compressive strength in seawater
- 969 Nonlinear coupled thermal-structural analysis of precast concrete beam-to-column connections at high temperatures
- 989 Approaches considering non-linearity in soil-foundation-interaction: A State-of-the-Art Review
- 1015 Sensitivity indices of RC beams considering construction sequence analysis for RC high-rise building
- 1039 Predicting strength of concrete by ensemble technique
- 1061 Evaluation of cement-treated ferrochrome slag and quarry dust composites for base and sub-base layers of flexible pavement
- 1081 Experimental investigation along with 3-D Finite Element Analysis to determine the stress bearing ability of concrete containing waste plastic aggregates